Understanding Complex Systems

Springer : COMPLEXITY

Santo Banerjee
Lamberto Rondoni *Editors*

Applications of Chaos and Nonlinear Dynamics in Science and Engineering - Vol. 4

Springer

Springer Complexity

Springer Complexity is an interdisciplinary program publishing the best research and academic-level teaching on both fundamental and applied aspects of complex systems – cutting across all traditional disciplines of the natural and life sciences, engineering, economics, medicine, neuroscience, social and computer science.

Complex Systems are systems that comprise many interacting parts with the ability to generate a new quality of macroscopic collective behavior the manifestations of which are the spontaneous formation of distinctive temporal, spatial or functional structures. Models of such systems can be successfully mapped onto quite diverse "real-life" situations like the climate, the coherent emission of light from lasers, chemical reaction-diffusion systems, biological cellular networks, the dynamics of stock markets and of the internet, earthquake statistics and prediction, freeway traffic, the human brain, or the formation of opinions in social systems, to name just some of the popular applications.

Although their scope and methodologies overlap somewhat, one can distinguish the following main concepts and tools: self-organization, nonlinear dynamics, synergetics, turbulence, dynamical systems, catastrophes, instabilities, stochastic processes, chaos, graphs and networks, cellular automata, adaptive systems, genetic algorithms and computational intelligence.

The three major book publication platforms of the Springer Complexity program are the monograph series "Understanding Complex Systems" focusing on the various applications of complexity, the "Springer Series in Synergetics", which is devoted to the quantitative theoretical and methodological foundations, and the "SpringerBriefs in Complexity" which are concise and topical working reports, case-studies, surveys, essays and lecture notes of relevance to the field. In addition to the books in these two core series, the program also incorporates individual titles ranging from textbooks to major reference works.

Understanding Complex Systems

Founding Editor: S. Kelso

Future scientific and technological developments in many fields will necessarily depend upon coming to grips with complex systems. Such systems are complex in both their composition – typically many different kinds of components interacting simultaneously and nonlinearly with each other and their environments on multiple levels – and in the rich diversity of behavior of which they are capable.

The Springer Series in Understanding Complex Systems series (UCS) promotes new strategies and paradigms for understanding and realizing applications of complex systems research in a wide variety of fields and endeavors. UCS is explicitly transdisciplinary. It has three main goals: First, to elaborate the concepts, methods and tools of complex systems at all levels of description and in all scientific fields, especially newly emerging areas within the life, social, behavioral, economic, neuro- and cognitive sciences (and derivatives thereof); second, to encourage novel applications of these ideas in various fields of engineering and computation such as robotics, nano-technology and informatics; third, to provide a single forum within which commonalities and differences in the workings of complex systems may be discerned, hence leading to deeper insight and understanding.

UCS will publish monographs, lecture notes and selected edited contributions aimed at communicating new findings to a large multidisciplinary audience.

More information about this series at
http://www.springer.com/series/5394

Santo Banerjee • Lamberto Rondoni
Editors

Applications of Chaos and Nonlinear Dynamics in Science and Engineering - Vol. 4

Springer

Editors
Santo Banerjee
Institute for Mathematical Research
University Putra Malaysia
Serdang
Malaysia

Lamberto Rondoni
Dipartimento di Scienze Matematiche
Politecnico di Torino
Torino
Italy

ISSN 1860-0832 ISSN 1860-0840 (electronic)
Understanding Complex Systems
ISBN 978-3-319-17036-7 ISBN 978-3-319-17037-4 (eBook)
DOI 10.1007/978-3-319-17037-4

Library of Congress Control Number: 2013938159

Springer Cham Heidelberg New York Dordrecht London

Printed on acid-free paper

Springer International Publishing AG Switzerland is part of Springer Science+Business Media (www.springer.com)

Preface

This is the fourth volume of the collection of essays entitled *Applications of Chaos and Nonlinear Dynamics in Science and Engineering*, which has been addressed to Master and Ph.D. Students, as well as to specialists of disciplines other than the hard sciences, in order to help them familiarize with the theory and the applications of nonlinearity, and its use in describing complex phenomena.

As illustrated in the previous volumes, terms such as nonlinear dynamics, chaos and complexity have pervaded the vocabulary of almost all fields of science and technology. As a matter of fact, current mathematical descriptions of evolving phenomena consist of nonlinear ordinary or partial differential equations, of various kinds of stochastic processes and of nonlinear space and time discrete iterative schemes. In the deterministic cases, a typical situation is that in which the propagation of uncertainties is exponential in time, a phenomenon known as sensitive dependence on initial conditions, and concisely and suggestively called deterministic chaos.

To understand the reasons why certain terms have become common in many different fields, it suffices to observe that nonlinearities appear in feedback phenomena, which are ubiquitous in nature, and generically in the evolution equations of systems consisting of interacting parts or interacting with an external environment. Furthermore, any measurement one may perform, like any estimate of the initial state of any material object, is bound to be affected by uncertainties, which propagate in time leading to the conclusion that a degree of unpredictability is intrinsic, in practice as well as in principle, to all time dependent phenomena. For this reason, the study of nonlinear evolutions is commonly associated with statistical concepts, and relies on measures such as the Lyapunov exponents and various kinds of dynamical entropies.

In the previous volumes, we have presented a vast collection of examples, treated explicitly and in moderately technical terms. Indeed, these concepts have in the past decades turned useful in countless practical applications—beyond the mathematical and physical literature in which they have been mostly developed—ranging from engineering to biology, medicine, computer and telecommunication sciences, etc. We have thus followed an approach which we deem suitable to a vast

readership, proposing essays written in the form of tutorials. In this last volume, we complete our survey and introduction to nonlinear, chaotic and complex phenomena, considering some issues of higher theoretical content than in the previous volumes, but preserving the mildly technical style of the previous volumes.

Part I concerns nonlinearities in transport of energy and matter, with one contribution by L. Stricker and L. Rondoni on models of heat transport and their mechanical properties, one contribution on the general theory of diffusion, by G. Boffetta, G. Lacorata and A. Vulpiani, and one contribution by M. Colangeli on the relation between the Boltzmann equation and hydrodynamics.

In Part II, we have three contributions on chaos and synchronization in complex networks: one by J. Stroud, M. Barahona and T. Pereira on modular networks, one by P. Carl on the evolution of climate, and one by A. Tai and S. Jalan on the use of random matrices. The chapters are well illustrated with recent developments on the subject area and possible practical applications.

Part III has two contributions on phase space reconstruction and on biological patterns, respectively, by S. K. Palit, S. Mukherjee, S. Banerjee, M.R.K. Ariffin and D. K. Bhattacharya, and by M. Banerjee. The theories are well illustrated and supported with analytical and numerical results.

Part IV concerns the use of chaos in field programmable gate arrays. This chapter is very useful as an introduction to the subject area.

We hope that this collection of examples, combined with those reported in the previous three volumes have covered a sufficiently wide spectrum of subjects, in terms suitable to a wide audience, interested in importing dynamical concepts in their disciplines, without recourse to sophisticated mathematical tools. The concepts of nonlinear dynamics are indeed proving more and more useful in all fields of research.

Serdang, Malaysia — S. Banerjee
Torino, Italy — L. Rondoni
26 January 2015

Contents

Part I
Nonlinearity in Transport, Mechanical Models and Hydrodynamics

Chapter 1
Microscopic Models for Vibrations in Mechanical Systems Under Equilibrium and Non-equilibrium Conditions

Laura Stricker and Lamberto Rondoni

Abstract Equilibrium Thermodynamics studies states of macroscopic objects that do not change in time when isolated from their environment. This requires chemical, mechanical and thermal equilibrium which together amount to thermodynamic equilibrium. A non-equilibrium state can be established putting the system in contact with more than one reservoir of heat, mass, or other physical quantities. The dynamical evolution of a system of particles representing a macroscopic bar in both equilibrium and non-equilibrium conditions is illustrated by means of a simple one-dimensional molecular dynamics model, illustrating how macroscopic phenomena may be qualitatively understood with microscopic toy models. In particular, a system of hard point-particles undergoing only binary collisions is considered. A conservative force is applied on one of the end particles to reproduce the cohesion of the bar. Non-equilibrium conditions are obtained by adding two deterministic thermostats acting on the first and on the last particle of the bar. In the equilibrium case, we determine the values of macroscopic and microscopic proprieties of the system, such as length, linear density, specific kinetic energy, average energy per particle, and position of the centre of mass of control groups located in different parts of the bar. In the non-equilibrium case, we focus on length oscillations, and we demonstrate their dependence on the characteristic parameters of the thermostats. Although highly idealized, this model reproduces an important qualitative aspect of metal bars: hardening.

L. Stricker
Max Planck Institute for Dynamics and Self-Organization, Göttingen, Germany
e-mail: laura.stricker@ds.mpg.de

L. Rondoni (✉)
Dipartimento di Scienze Matematiche, Politecnico di Torino, C.so Duca degli Abruzzi 24, 10129 Torino, Italy

INFN, Sezione di Torino, Via P. Giuria 1, 10125 Torino, Italy
e-mail: lamberto.rondoni@polito.it

S. Banerjee, L. Rondoni (eds.), *Applications of Chaos and Nonlinear Dynamics in Science and Engineering - Vol. 4*, Understanding Complex Systems,
DOI 10.1007/978-3-319-17037-4_1

1.1 Introduction: Thermal Baths

Chains of oscillators constitute a very popular kind of models, used to understand the behaviour of macroscopic objects from the point of view of their microscopic constituents. The first of these models is the Fermi–Pasta–Ulam model [9], which consists of a linear chain of interacting particles providing a minimal framework for studies of ergodicity, dynamical relaxation and diffusion laws, with given interparticle interaction potentials, initial and boundary conditions [3, 10, 13]. In this tutorial, we demonstrate that the conceptually simple framework of one-dimensional N-particle systems can be consistently used to model the qualitative thermo-mechanical behaviour of solids. In particular, we consider a chain of particles, with one fixed and one free end, to study the variations of length, in response to external forces or to temperature changes. We provide both theoretical considerations and numerical results from molecular dynamics simulations, which allow direct access to any quantity of interest. These kinds of chains have been considered mostly to study heat conduction, cf. [3, 10, 13] for recent reviews on the subject, and [4–6] for some of the few works on thermo-mechanical properties.

In the theoretical study of statistical mechanics, a proper modelling of the interaction with thermal reservoirs has a crucial role. At equilibrium, this is usually done by means of well-established methods, such as the micro-canonical molecular dynamics and Monte Carlo simulations. Out of equilibrium, the lack of a general theoretical framework enforces the definition of the interaction with thermal baths. From a conceptual point of view, the procedure requires considering non-equilibrium states in the infinite system limit. For example, one could imagine to have an infinite chain of particles, with initial conditions such that all the atoms on the right and those on the left of a certain finite subset are in equilibrium at different temperatures. The subset defines the system that we want to study. However, the only case in which the above mentioned approach can be fully worked out is the case of harmonic chains [14–17]. In such a system, it is possible to derive the degrees of freedom corresponding to the reservoirs' dynamics. Therefore the existence of stationary non-equilibrium states of the system can be proved at the cost of dealing, however, with arbitrarily large energy fluctuations. In general, when non-linear effects appear, the evolution of the heat baths cannot be described anymore by means of standard techniques. However, non-linear chains can still be studied, by assuming that the non-linearity is restrained to the system of interest, while the semi-infinite particle chains (i.e. the two reservoirs) can undergo only linear interactions [1].

Following this approach, the existence of an invariant measure (not explicitly know) has been proved for non-equilibrium systems, in chains of highly non linear coupled oscillators undergoing large temperature gradients [8]. This is analogous to energy conservation in equilibrium systems.

1.1.1 Stochastic Baths

A traditional way to implement the interaction with reservoirs is the introduction of simultaneous random forces and dissipation, in agreement with the fluctuation-dissipation theorem. Hence, the reservoirs are not influenced by the dynamics of the system. For instance, in the case of a chain of particles with equal mass m, the following system of Langevin equations is derived:

$$m\ddot{q}_i = F\left(q_i - q_{i-q}\right) - F(q_{i+1} - q_i) + (\xi_+ - \lambda_+\dot{q}_i)\,\delta_{i1} + (\xi_- - \lambda_-\dot{q}_i)\,\delta_{iN} \tag{1.1}$$

where $(\xi_+ - \lambda_+\dot{q}_i)\,\delta_{i1}$, $(\xi_- - \lambda_-\dot{q}_i)\,\delta_{iN}$ are the forces acting respectively on the first and the Nth particle.

λ_- and λ_+ are the dissipation coefficients producing the slowing down forces $-\lambda_+\dot{q}_i\delta_{i1}$, $-\lambda_-\dot{q}_i\delta_{iN}$. ξ_- and ξ_+ are the independent Wiener processes (stochastic forces) with vanishing average, and variance $2\lambda_\pm k_B T_\pm$, with T the absolute temperature and k_B the Boltzmann constant. For non-linear forces, this model can be treated only numerically.

Once the non-equilibrium steady state condition is reached, the average heat flux can be derived from the temperature profile. The average energy exchanged between the first particle and the adjacent reservoir is the *heat flux j*

$$j\,(\lambda, N) = \frac{\lambda_+}{m_1}\,(T_+ - T_1)$$

Similarly at the other extreme of the system of interest. Then, at the microscopic level one commonly considers each reservoir as an ideal one-dimensional gas of particles with mass $M_\pm$, interacting with the chain through elastic collisions [18]. A simple strategy consists in selecting a random sequence of instants t_i, in which every thermostated atom collides with a particle of the corresponding reservoir. A natural choice for the distribution $W(\tau)$ of the intervals τ among consecutive collisions is the Poissonian distribution

$$W\,(\tau) = \frac{1}{\tau}e^{-\frac{\tau}{\overline{\tau}}}$$

with $\overline{\tau}$ the average collision time. If we consider the reservoir positioned on the left of the system of interest, the velocity of the first particle changes due to collisions from $\dot{q}_{1B}$ (before collision) to $\dot{q}_{1A}$ (after collision)

$$\dot{q}_{1A} = \dot{q}_{1B} + \frac{2M_+}{m + M_+}\,(v - \dot{q}_{1B})$$

where the gas particles velocity v is a random variable with a Maxwellian probability distribution $P(v)$

$$P_+(v) = \sqrt{\frac{M_+}{2\pi k_B T_+}} \cdot e^{-\frac{M_+ v^2}{2k_B T_+}}$$

When $M_\pm = m$, the procedure simplifies and it amounts to equating the particle velocity after collision to the random variable v, so that the colliding particles merely exchange their velocities. In the limit case $M_\pm << m$, the interaction with the heat baths become of Langevin kind, as in (1.1), with $\lambda_\pm = 2M_\pm/\overline{\tau}$. This method is computationally easier, because it does not imply dealing with stochastic differential equations and integration can be performed with conventional algorithms. Moreover, it is physically consistent, because damping is not imposed a priori in the model, but is intrinsically generated by the dynamics. A similar approach, consists in determining the collision times for the interaction with "thermal walls" located at the two extremes of the particle chain. This method has the advantage of allowing the inclusion of pressure effects. In this case, the velocity of the thermostated particles is randomized at every collision with the wall. The sign of the component of the velocity normal to the wall has be inverted, while its absolute value must be distributed following a Maxwellian distribution centered on the wall temperature [19].

1.1.2 Deterministic Baths

Different kinds of deterministic heat baths are commonly used [7, 11] in order to give a self-consistent description of non-equilibrium processes and to overcome the difficulties related to stochastic processes. Two possible modelling strategies are the application of the thermostating forces only to the extremes of the particles chain or to the whole chain.

1.1.2.1 Application of Forces to the Extremes of the Particle Chain

Non-equilibrium conditions are reached by applying two forces at the extremes of the particles chain. The most popular scheme in the molecular dynamics community is the *Nosè–Hoover thermostat* [7]. With this thermostat, the evolution of the particles in contact with the thermal bath α is governed by the equation:

$$m\ddot{q}_i = F(q_i - q_{i-1}) - F(q_{i+1} - q_i) - \begin{cases} \zeta_+ \dot{q}_i \;\; if \;\; i \in S_+ \\ \\ \zeta_- \dot{q}_i \;\; if \;\; i \in S_- \end{cases} \tag{1.2}$$

where $S_\pm$ are two groups of $N_\pm$ particles in contact with the reservoir, respectively at the beginning and at the end of the chain; $F(q_i - q_{i-1})$ and $F(q_{i+1} - q_i)$ are the internal forces within the particle of the chain; $\zeta_\pm \dot{q}_i$ express the interaction of the particles at the two extremes of the chain with the baths. $\zeta_\pm$ are the thermal bath variables, i.e. the two auxiliary variables modelling the microscopic action of the thermostat. The dynamics of $\zeta_\pm$ is governed by the equations

$$\dot{\zeta}_\pm = \frac{1}{\Theta_\pm^2}\left(\frac{1}{k_B T_\pm N_\pm}\sum_{i\in S_\pm} m\dot{q}_i^2 - 1\right) \tag{1.3}$$

where $k_B T_\pm N_\pm$ are the reference kinetic energies and $\Theta_\pm$ are the response times of the thermostats. If the kinetic temperature of the particles belonging to $S_\pm$ is higher than $T_\pm$, then $\zeta_\pm$ increases, thus producing a dissipation in (1.2). Vice versa, energy is fed into the system if the kinetic temperature becomes lower than $T_\pm$. Therefore, $\zeta_\pm$ introduces a stabilizing feedback around the prescribed temperature $T_\pm$. It has been demonstrated that in equilibrium this approach reproduces the canonical distribution.

In the $\Theta \to 0$ limit, the Nosè–Hoover thermostat reduces to the *isokinetic* (*or Gaussian*) *thermostat*. Here the energy is conserved in an exact-fashion and the action of the thermal bath can be described without introducing any further dynamical variable, because $\zeta_\pm$ becomes an explicit function of $\dot{q}$:

$$\zeta_\pm = \frac{\sum_{i\in S_\pm} \dot{q}_i \left[F(q_i - q_{i-1}) - F(q_{i+1} - q_i)\right]}{\sum_{i\in S_\pm} \dot{q}_i^2} \tag{1.4}$$

This model can be derived from variational methods, by imposing kinetic energy conservation by means of non-holonomous constraints [12]

The dynamic equations of the Nosé–Hoover class of deterministic thermostats have an Hamiltonian structure in a properly enlarged phase space, and a simple analysis shows that they are invariant respect to time reversal, since $\dot{q}_i \to -\dot{q}_i$ for $i = 1, \ldots, N$ and $\zeta_\pm \to -\zeta_\pm$. This property is one of the main reasons of the large success of this class of thermostats, since dissipation is not included a priori but emerges from the dynamical evolution. In particular, at equilibrium, $\langle \zeta_\pm \rangle = 0$, hence the bath does not destroy the microscopic reversibility. Conversely, out of equilibrium conditions $\langle \zeta_+ \rangle + \langle \zeta_- \rangle > 0$ and this value can be related to the entropy production [7, 11]

1.1.2.2 Application of an External Field to the Whole Particles System

In order to keep the system in a stationary nonequilibrium state, a fictitious external field can be applied, acting on all the system [7], the main advantage of this approach

being the possibility to work with homogeneous systems with, e.g. a uniform temperature along the whole sample, although one intends to represent e.g. a thermal gradient. With this approach, periodic boundaries conditions at the two extremes can be applied, in order to reduce the effects of the finite dimensionality of the system. Such procedure is usually referred to as the "Evans' algorithm of heat flux" and has been applied to the problem of heat conduction in a one-dimensional lattice [7, 20].

In order to implement this kind of thermostat, a fictitious force is applied to every particle i. In order to stabilize the dynamics at a prescribed temperature, a thermostat rule is also enforced. The equation of motion of the i-th particle then becomes:

$$m\ddot{q}_i = F(q_i - q_{i-1}) - F(q_{i+1} - q_i) + F_e D_i - \zeta \dot{q}_i \tag{1.5}$$

where $F_e D_i$ represents the fictitious heat flux and D_i can be defined as [7]:

$$D_i = \frac{1}{2}\left[F(q_{i+1} - q_i) + F(q_i - q_{i-1})\right] - \frac{1}{N}\sum_{j=!}^{N} F\left(q_{j+1} - q_j\right) \tag{1.6}$$

If we consider a *Gaussian thermostat*,

$$\zeta = \frac{1}{2K_0}\sum_{j=1}^{N} \dot{q}_j \left[F(q_i - q_{i-1}) - F(q_{i+1} - q_i) + F_e D_j\right]$$

$$K_0 \doteq \frac{m}{2}\sum_{j=1}^{N} \dot{q}_j^2$$

1.1.3 Control Parameter of a Thermostat

In all the models employed to describe a thermal bath, there is at least one parameter controlling the force acting on the particle that interacts with the bath. This parameter can be, e.g. the time between consecutive collisions or the dissipation velocity λ in the Langevin equation, or the inverse of the time constant Θ in the Nosè–Hoover model. Fixing the control parameter is a practical matter generally approached empirically, taking care that different choices do not substantially modify the simulation results. As a general approach, the control parameter should be chosen of the order of some characteristic frequencies of the system [7]. The heat flux through the system is generally depending on this choice.

For Nosè–Hoover thermostats, the heat flux vanishes when the response time Θ tends to zero. This is the limit case of a strictly isokinetic bath. Therefore, this kind of bath is not suitable to describe heat transport. In the opposite limit case, for $\Theta \to \infty$, the heat flux does not vanish although the action of the thermal baths becomes irrelevant. One explanation of this behavior is given by the fact that the

variable ζ, though slowly, reaches the same asymptotic values, for time constants Θ arbitrary big. By plotting the values of ζ, i.e. its probability distribution function (PDF) for different values of Θ, it can be seen that all the curves have a Gaussian profile centred around the same mean value, but with different standard deviations. In particular, the standard deviations differ among them by the same factor as the time constants. Hence, in the limit case of $\Theta \to 0$, the PDF of ζ becomes a Dirac delta function centred at a fixed dissipation value depending only on the chain length, the energy and the temperature gradient. This may seem to contrast with the fluctuation-dissipation theorem, suggesting that, for $\Theta \to 0$, fluctuations disappear, the dissipation remaining finite. However, in order to obtain a correct measure of the fluctuations, for finite Θ the integration must be performed on a time sufficiently long that the correlations decay and the validity of the fluctuation-dissipation theorem is recovered. We conclude that, when one uses the natural units for the description of the system, Θ should be taken of order 1, for numerical simulations. Small values of Θ imply a small heat flux, while large values of Θ require a long simulation time, in order to guarantee the decay of correlations. Clearly, the $\Theta = 0$ case is singular, and should not be considered in this context.

1.2 Model

Our model consists of N identical particles in one line, interacting with each other's nearest-neighbours via hard core collisions and obeying Newtonian dynamics (Fig. 1.1).

In other words, collisions take place instantaneously and particles do not deform, thus leading to momentum conservation. Also, we limit the nature of collisions to *binary* events, i.e. events involving only two particles at a time. The collection of these particles, which may be thought of as an ensemble of *point particles* on a straight line, localized by their x coordinate and endowed with velocity v, is considered in order to represent a solid bar.

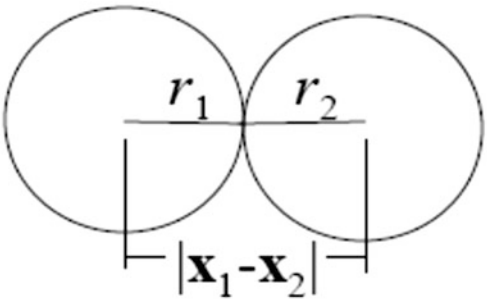

Fig. 1.1 Schematic representation of particles collisions, which are only of the head-on kind

For the simulations, we consider *event-driven* evolutions: proceeding in time by steps of different duration, targeted by the instants when collisions occur. A collision is identified by the condition:

$$|x_i(t) - x_{i\pm1}(t)| = r_i + r_{i\pm1} \tag{1.7}$$

where $x_i(t)$, $x_{i\pm1}(t)$ indicate the coordinates of particle i and its adjacent particle at time t and $r_i, r_{i\pm1}$ are the respective radii of the two particles. The point-particle hypothesis ($r_i = r_{i\pm1} = 0$) simplifies (1.7) into:

$$\begin{cases} x_i(t) = x_{i\pm1}(t) & , \ i = 2, N \\ x_1(t) = 0 \end{cases}$$

By solving these equations with respect to t, we find $\bar{t}$, the instant when collision occurs. In particular, for $\bar{t} > 0$, collision will occur in the future, for $\bar{t} = 0$ collision is taking place in the present instant and for $\bar{t} < 0$ collision has already occurred. Momentum and energy conservation, determine the dynamic conditions of the particles immediately after collision:

$$v_G = v_{G'} \tag{1.8}$$

$$\begin{aligned} v_{1,rel} &= -v'_{1,rel} \\ v_{2,rel} &= -v'_{2,rel} \end{aligned} \tag{1.9}$$

where $v_G, v_{G'}$ are the velocities of the centre of mass, before and after the collision, $v_{1,rel}, v'_{1,rel}$ are the relative velocity of particle 1 in the reference frame of the centre of mass, before and after collision and similarly $v_{2,rel}, v'_{2,rel}$ for particle 2. In order to model both the air pressure and, especially, the cohesion of the bar, we introduce a constant force F, acting on the last particle (Fig. 1.2).

In the equilibrium case, the dynamics of the system consists of uniformly accelerated motion for the last particles and uniform motion for the other particles:

$$\begin{cases} x_i(t) = x_i(t_0) + \dot{x}_i(t_0)t & , \ i = 1, (N-1) \\ x_N(t) = x_N(t_0) + \dot{x}_N(t_0)t - \dfrac{1}{2}\dfrac{F}{m_N}t^2 \end{cases}$$

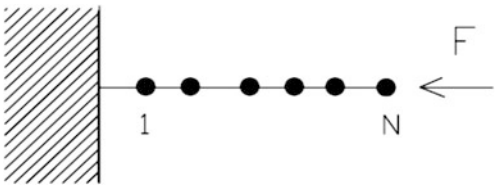

Fig. 1.2 A schematic representation of the microscopic structure of the bar

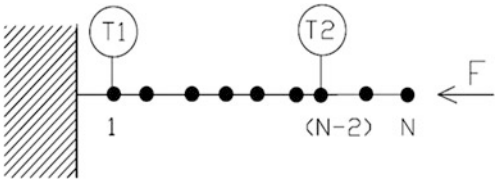

Fig. 1.3 Model of the system of particles in non-equilibrium conditions

which can be discretized as:

$$\begin{cases} x_i^{(j)} = x_i^{(j-1)} + \dot{x}_i^{(j-1)} \Delta t_{coll} & , \ i = 1, (N-1) \\ x_N^{(j)} = x_N^{(j-1)} + \dot{x}_N^{(j-1)} \Delta t_{coll} - \dfrac{1}{2} \dfrac{F}{m_N} \Delta t_{coll}^2 \end{cases}$$

where index i refers to the particle, j to the time instant and $\Delta t_{coll} = t^{(j)} - t^{(j-1)}$ is the time to collision. The conservative nature of F and the absence of dissipation in both the motion and the collision of particles ensure the total conservation of energy. Then, the system's invariant state is said to represent a "thermodynamic equilibrium" state.

In the non-equilibrium case, we study the effects of a temperature gradient by applying two simple deterministic thermostats, of the kind known as Berendsen thermostat [11], at the two ends of the bar (Fig. 1.3).

Deterministic thermostats are mathematical objects used to enforce mechanical constraints on particles systems, when these constraints are meant to enforce certain thermodynamic conditions. This can be achieved in many different ways [11]. For instance, the Gaussian isokinetic thermostat enforces the instantaneous conservation of the kinetic energy $K = p^2$, where p is the magnitude of the momentum of the particle it is applied to.

The general form of the corresponding dynamics is expressed by the equation of motion for momentum:

$$\dot{\vec{p}}_i = \vec{F}_i - \alpha \vec{p}_i \tag{1.10}$$

where $\vec{p}_i = \vec{p}_i(t) = m\vec{v}_i$ is the momentum of particle i, $\vec{F}_i$ is the external force applied to particle i, and $\left(-\alpha \vec{p}_i\right)$ is the force applied by the thermostat to particle i with α a kind of dynamical viscosity, which however gives energy to the system if this is slowing down, in order to keep K fixed. In the *one-dimensional case* the constraint that K be constant in time means:

$$2 p_i \dot{p}_i = 0 \tag{1.11}$$

which leads to:

$$\alpha = \frac{p_i F_i}{K} \tag{1.12}$$

In the one-dimensional case, the general formulation reduces to a trivial expression: the only way to ensure the conservation of the momentum magnitude of a particle, is to preserve the momentum itself. In order to do so, the resulting force applied to the particle must be null. Therefore the thermostat should apply a force $\left(-\alpha \vec{p}_i\right)$ equal and opposite to the external force F. As mentioned above, below we demonstrate that the Gaussian isokinetic thermostat is a limit case of the Nosé–Hoover thermostat.

1.2.1 Nosè–Hoover Thermostat

This kind of thermostats enforces conservation of the average of the kinetic energy, rather than its instantaneous value. Let this quantity be denoted by $\langle K \rangle = \left\langle p^2 \right\rangle$, where p is the momentum modulus of the particle the thermostat is applied to, and the symbol $\langle\rangle$ represents a time average. The general formulation of the equations of motion for the momentum is given by:

$$\dot{p}_i = F_i - \frac{\zeta}{m_i} p_i \tag{1.13}$$

where $\frac{\zeta}{m_i} p_i$ is the bath term and ζ is the thermal bath variable, following the equation:

$$\dot{\zeta} = \frac{1}{\theta^2} \left(\frac{1}{k_B T N} \sum_{i,S} \frac{p_i^2}{m_i} - 1 \right) \tag{1.14}$$

where $k_B TN$ is the reference kinetic energy K_{ref}, θ is the response time of the thermostat and N is the number of groups of S particles in contact with the thermal bath. If the thermostat is applied only to one particle, (1.14) becomes :

$$\dot{\zeta} = \frac{1}{\theta^2} \left(\frac{p_i^2}{m_i} - 1 \right) \tag{1.15}$$

1.2.2 Berendsen Thermostat

A simplified version of the Nosè–Hoover thermostat can be derived imposing the i-th particle itself as thermal bath, therefore $\zeta = p_i$. When this thermostat is applied to a particle having momentum $\vec{p}$, it enforces convergence of p^2 to the value K_{ref}

over a time scale θ, while the sign of p is left unperturbed. Its general formulation is given by:

$$\dot{p}_i = F_i - \frac{1}{\theta}\left(\frac{{p_i}^2}{K_{ref}} - 1\right) p_i \tag{1.16}$$

where K_{ref} is the reference kinetic energy p_{ref}^2 and θ is the characteristic relaxation time, i.e. the time scale to reach K_{ref} and F_i is the external force applied to the particle. The term $-\frac{1}{\theta}\left(\frac{{p_i}^2}{K_{ref}} - 1\right) p_i$ represents the force that the thermostat applies to the particle. For a better understanding of the physical meaning of (1.16), let's neglect F_i. Through dimensional analysis, we deduce that θ represents a time scale, while $-\left(\frac{{p_i}^2}{K_{ref}} - 1\right) p_i \equiv \Delta p_i$ is the momentum change enforced by the thermostat, during this time interval. Different cases can be evidenced:

– If $p_i^2 = K_{ref} \quad i.e. \quad |p_i| = \sqrt{K_{ref}}$

$$\Delta p_i = 0 \quad \Rightarrow \quad \dot{p}_i = 0 \quad \rightarrow \quad p_i = const$$

The quantity $\sqrt{K_{ref}}$ is a limit value for $|p_i|$. When this threshold is reached, the first derivative $\dot{p}_i$ goes to zero and p_i becomes a constant.

– If $p_i^2 > K_{ref} \quad i.e. \quad |p_i| > \sqrt{K_{ref}}$

- $p_i > 0 \quad \rightarrow \quad \Delta p_i < 0 \quad \Rightarrow \quad \dot{p}_i < 0 \quad \rightarrow \quad p_i \downarrow$
- $p_i < 0 \quad \rightarrow \quad \Delta p_i > 0 \quad \Rightarrow \quad \dot{p}_i > 0 \quad \rightarrow \quad p_i \uparrow$
- $p_i = 0 \quad \rightarrow \quad \Delta p_i = 0 \quad \Rightarrow \quad \dot{p}_i = 0 \quad \rightarrow \quad p_i = const$

– If $p_i^2 < K_{ref} \quad i.e. \quad |p_i| < \sqrt{K_{ref}}$

- $|p_i| < \sqrt{K_{ref}}$
- $p_i < 0 \quad \rightarrow \quad \Delta p_i < 0 \quad \Rightarrow \quad \dot{p}_i < 0 \quad \rightarrow \quad p_i \downarrow$
- $p_i = 0 \quad \rightarrow \quad \Delta p_i = 0 \quad \Rightarrow \quad \dot{p}_i = 0 \quad \rightarrow \quad p_i = const$

The monotonic trend of Δp_i ensures that the sign of p_i is not modified by the thermostat (Figs. 1.4 and 1.5).

The time scale θ represents the characteristic time needed for p^2 to converge to K_{ref}:

$$\theta \uparrow \quad \Rightarrow \quad |\dot{p}| \downarrow \quad \Rightarrow \quad p^2 \rightarrow K_{ref} \text{ slower}$$

$$\theta \downarrow \quad \Rightarrow \quad |\dot{p}| \uparrow \quad \Rightarrow \quad p^2 \rightarrow K_{ref} \text{ faster}$$

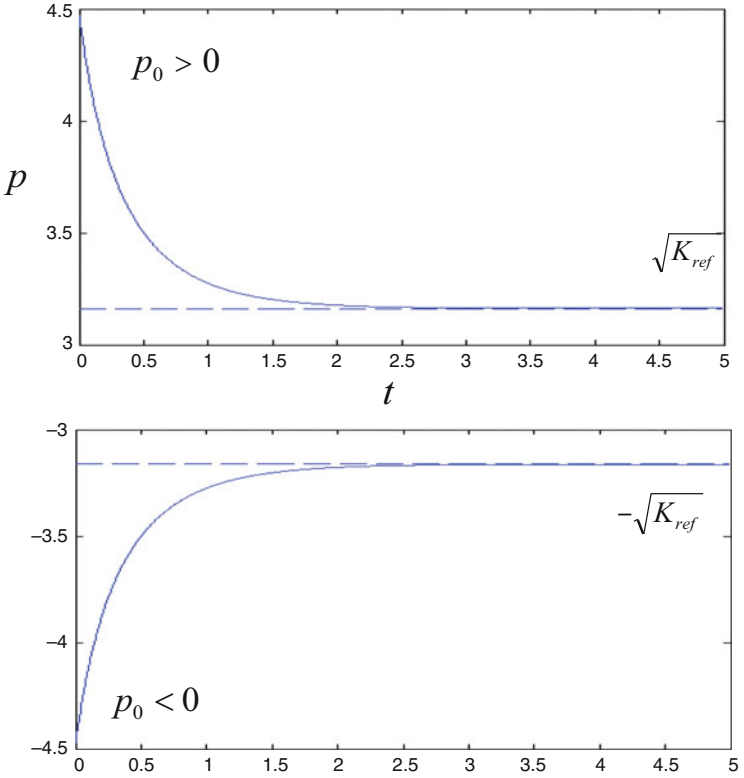

Fig. 1.4 Time evolution of p when $|p_i| > \sqrt{K_{ref}}$ (A = 0.5)

In the θ to zero limit, the Nosè–Hoover thermostat can be regarded as a Gauss thermostat

$$\theta \to 0 \quad \Rightarrow \quad |\dot{p}| \to \infty \quad \Rightarrow \quad p^2 \to K_{ref} \ \text{ instantaneous}$$

A major problem connected with the use of thermostats in our one-dimensional framework, is that they can do an infinite amount of work, balancing the force F, and eventually leading the system length to diverge. Consider indeed the Berendsen thermostat, applied on the Nth particle, (1.16) becomes

$$\dot{p}_N = F_N - \frac{1}{\theta}\left(\frac{{p_N}^2}{K_{ref}} - 1\right) p_N$$

Now, impose the condition $\dot{p}_N = 0$ i.e.

$$F_N - \frac{1}{\theta}\left(\frac{{p_N}^2}{K_{ref}} - 1\right) p_N = 0 \tag{1.17}$$

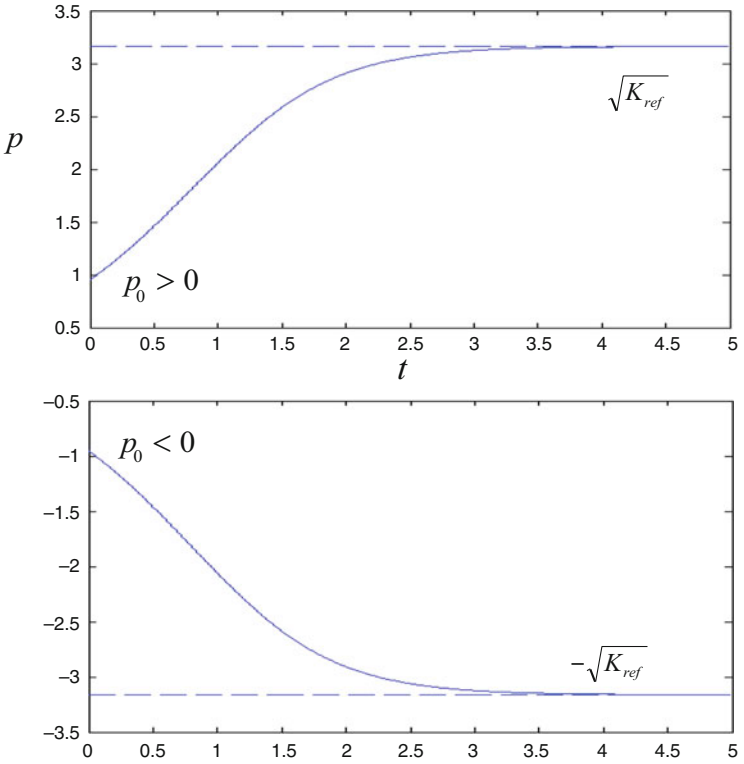

Fig. 1.5 Time evolution of p when $|p_i| < \sqrt{K_{ref}}$ (A $= -10$)

Equation (1.17) admits three possible solutions $\overline{p}_1, \overline{p}_2, \overline{p}_3$. Once one of these values is reached, p_N will not change anymore, as $\dot{p}_N = 0$. If this value of p_N is positive, the length of the bar will increase indefinitely, because the force that the thermostat applies to the particle will never be balanced by external force F.

If:

$$\begin{cases} p\left(\bar{t}\right) = \overline{p}_1 \ \vee \ p\left(\bar{t}\right) = \overline{p}_2 \ \vee \ p\left(\bar{t}\right) = \overline{p}_3 \ \Rightarrow \ \dot{p} = 0 \\ p\left(\bar{t}\right) > 0 \end{cases}$$

then: $x_N \to \infty$

Therefore, the potential energy associated with the N-th particle will grow without bounds.

$$\left(E_{pot}\right)_N = x_N \cdot F \to \infty$$

1.2.2.1 Remedies

In order to avoid the divergence of the system, two approaches at least are possible:

- Introduction of a *containing wall*, limiting the free movement of the last particle (Fig. 1.6)
- Different masses (e.g. m, $\mathrm{M} = m/3$) in such a way that, next to the last thermostatted particle, there is an other one with higher mass, simulating the effect of a containing wall (Fig. 1.7)

In our simulations, we adopted the second approach, in order to be able to compare the non-equilibrium and the equilibrium cases. As a precautionary measure, we also decided to apply the second thermostat to a particle situated $N_{particles}$ before the end of the bar $\left(N_{particles} = 10\right)$. The equations of motion of the thermostated particles now take the form:

$$\dot{p} = F - \frac{1}{\theta}\left(\frac{p^2}{K_{ref}} - 1\right) p \tag{1.18}$$

where $F = 0$. This leads to:

$$\log \frac{p^2(t)\left[p^2(t_0) - K_{ref}\right]}{p^2(t_0)\left[p^2(t) - K_{ref}\right]} = \frac{2}{\theta}\left(t - t_0\right)$$

and setting

$$\frac{p^2(t_0) - K_{ref}}{p^2(t_0)} \doteq A(t_0) \tag{1.19}$$

we find:

$$\frac{A(t_0)p^2(t)}{p^2(t) - K_{ref}} = e^{\frac{2}{\theta}(t-t_0)} \tag{1.20}$$

Fig. 1.6 Model with thermostats and containing wall

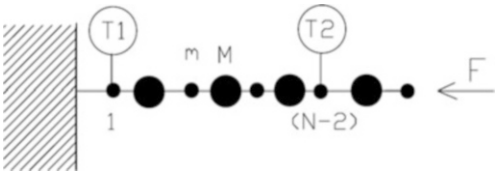

Fig. 1.7 Model with thermostats and alternated masses

The sign of $\left[p^2(t) - K_{ref}\right]$ doesn't change when the value of t increases, because $A(t_0)$ is constant, $p^2(t) > 0$, $e^{2(t-t_0)/\theta} > 0$ for $\forall t$. Thus, K_{ref} represents a limit value for $p^2(t)$ since:

$$t \to \infty \quad \Rightarrow \quad p^2(t) - K_{ref} = 0$$

An explicit expression for p can be derived from (1.20):

$$p(t) = \pm \frac{\sqrt{K_{ref}} \cdot e^{(t-t_0)/\theta}}{\sqrt{e^{2(t-t_0)/\theta} - A(t_0)}} \tag{1.21}$$

As the thermostat cannot modify the sign of $p(t)$, the sign $+$ in (1.21) holds for $p(t_0) > 0$, while the sign $-$ holds for $p(t_0) < 0$. From (1.24), using the definition of momentum $p(t) = m\dot{x}(t)$, we get:

$$\dot{x}(t) = \pm \frac{\sqrt{K_{ref}}}{m} \frac{e^{(t-t_0)/\theta}}{\sqrt{e^{2(t-t_0)/\theta} - A(t_0)}} \tag{1.22}$$

where the sign $+$ holds for $\dot{x}(t_0) > 0$, while the sign $-$ holds for $\dot{x}(t_0) < 0$. Equation (1.22) is valid for

$$e^{\frac{2}{\theta}(t-t_0)} - A(t_0) > 0 \Rightarrow A(t_0) < e^{\frac{2}{\theta}(t-t_0)}$$

As $t \geq t_0$, we have $e^{2(t-t_0)/\theta} \geq 1$. Hence:

$$A(t_0) = \frac{p^2(t_0) - K_{ref}}{p^2(t_0)} < 1 \tag{1.23}$$

If (1.23) did not hold, we would get $p^2(t_0) - K_{ref} \geq p^2(t_0)$, which is impossible since $K_{ref} > 0$. Therefore $\dot{x}(t)$ is always defined and, integrating by separation of variables, we find:

$$\begin{aligned} x(t) = \; & x(t_0) \pm \frac{\theta\sqrt{K_{ref}}}{m} \cdot \left[\log\left(e^{\frac{t-t_0}{\theta}} + \sqrt{e^{\frac{2(t-t_0)}{\theta}} - A(t_0)} \right) \right. \\ & \left. - \log\left(1 + \sqrt{1 - A(t_0)} \right) \right] \end{aligned} \tag{1.24}$$

where the $+$ sign holds for $\dot{x}(t_0) > 0$ and the $-$ sign holds for $\dot{x}(t_0) < 0$.

The equations of collision for the thermostated particles are derived, in analogy with the equations of collision of the other particles, by equating the position of the two colliding particles

$$\begin{aligned} x_{i\_thermo}(t) &= x_{i\_thermo\pm1}(t) \quad if \quad i_{thermo} = 2, N \\ x_{i\_thermo}(t) &= 0 \qquad if \; i_{thermo} = 1 \end{aligned}$$

In particular, one can take $i_{thermo1} = 1$, $i_{thermo2} = N - 10$, which yields:

$$x_{i\_thermo1}(t_0) \pm \frac{\theta_1 \sqrt{K_{ref,1}}}{m_{i\_thermo1}} \log\left(\frac{e^{(t-t_0)/\theta_1} + \sqrt{e^{2(t-t_0)/\theta_1} - A_1(t_0)}}{1 + \sqrt{1 - A_1(t_0)}}\right) = 0 \quad (1.25)$$

$$\begin{aligned} x_{i\_thermo1}(t_0) &\pm \frac{\theta_1 \sqrt{K_{ref,1}}}{m_{i\_thermo1}} \log\left(\frac{e^{(t-t_0)/\theta_1} + \sqrt{e^{2(t-t_0)/\theta_1} - A_1(t_0)}}{1 + \sqrt{1 - A_1(t_0)}}\right) \\ &= x_{i\_thermo1+1}(t_0) + \dot{x}_{i\_thermo1+1}(t_0)\,(t - t_0) \end{aligned} \quad (1.26)$$

$$\begin{aligned} x_{i\_thermo2}(t_0) &\pm \frac{\theta_2 \sqrt{K_{ref,2}}}{m_{i\_thermo2}} \log\left(\frac{e^{(t-t_0)/\theta_2} + \sqrt{e^{2(t-t_0)/\theta_2} - A_2(t_0)}}{1 + \sqrt{1 - A_2(t_0)}}\right) \\ &= x_{i\_thermo2\pm1}(t_0) + \dot{x}_{i\_thermo2\pm1}(t_0)\,(t - t_0) \end{aligned} \quad (1.27)$$

The sign + holds for $\dot{x}_j(t_0) > 0$, the sign − holds for $\dot{x}_j(t_0) < 0$ with j = i_thermo1, i_thermo2. Equation (1.25) has an analytic solution, which can be found by rewriting it as:

$$C_1 - e^z = \sqrt{e^{2z} - A_1(t_0)} \quad (1.28)$$

$$\begin{cases} C_1 \doteq \left[1 + \sqrt{1 - A_1(t_0)}\right] e^{\mp x_1(t_0) \frac{m_1}{\theta_1 \sqrt{K_{ref,1}}}} \\ z \doteq \Delta t / \theta_1 \end{cases}$$

If $\dot{x}_1(t_0) > 0$, the sign − holds in the expression of C_1 while, if $\dot{x}_1(t_0) < 0$, the sign + holds. Equation (1.27) can be rewritten as:

$$\begin{cases} \left[\sqrt{1 - A_1(t_0)} + 1\right] \underbrace{e^{-x_1(t_0) \frac{m_1}{\theta_1 \sqrt{K_{ref,1}}}}}_{<1} = \sqrt{e^{2z} - A_1(t_0)} + e^z \quad if \;\; \dot{x}_1(t_0) > 0 \\ \left[\sqrt{1 - A_1(t_0)} + 1\right] \underbrace{e^{x_1(t_0) \frac{m_1}{\theta_1 \sqrt{K_{ref,1}}}}}_{>1} = \sqrt{e^{2z} - A_1(t_0)} + e^z \quad if \;\; \dot{x}_1(t_0) < 0 \end{cases}$$

At the initial instant:

$$z = 0 \quad \rightarrow \quad \left[\sqrt{1 - A_1(t_0)} + 1\right] = \sqrt{e^{2z} - A_1(t_0)} + e^z \quad (1.29)$$

As we proceed in time, the right hand side of (1.27) increases, the left hand side remaining constant, and therefore

$$\begin{cases} \left[\sqrt{1 - A_1(t_0)} + 1\right] e^{-x_1(t_0) \frac{m_1}{\theta_1 \sqrt{K_{ref,1}}}} < \left[\sqrt{1 - A_1(t_0)} + 1\right] \quad if \;\; \dot{x}_1(t_0) > 0 \\ \left[\sqrt{1 - A_1(t_0)} + 1\right] e^{x_1(t_0) \frac{m_1}{\theta_1 \sqrt{K_{ref,1}}}} > \left[\sqrt{1 - A_1(t_0)} + 1\right] \quad if \;\; \dot{x}_1(t_0) < 0 \end{cases}$$

If we continue to increase z, we get:

$$\begin{cases} if \quad \dot{x}_1(t_0) > 0 \quad \rightarrow \quad \nexists \bar{z} \quad s.a. \quad \left[\sqrt{1-A_1(t_0)}+1\right] e^{\frac{-x_1(t_0)}{\theta_1}\frac{m_1}{\sqrt{K_{ref,1}}}} = \sqrt{e^{2\bar{z}} - A_1(t_0)} + e^{\bar{z}} \\ if \quad \dot{x}_1(t_0) > 0 \quad \rightarrow \quad \exists \bar{z} \quad s.a. \quad \left[\sqrt{1-A_1(t_0)}+1\right] e^{\frac{x_1(t_0)}{\theta_1}\frac{m_1}{\sqrt{K_{ref,1}}}} = \sqrt{e^{2\bar{z}} - A_1(t_0)} + e^{\bar{z}} \end{cases}$$

For $\dot{x}_1(t_0) > 0$ a positive solution for (1.27) cannot be found, while for $\dot{x}_1(t_0) < 0$ it always exists (in the limit case it's given by $\bar{t} \rightarrow \infty$). These theoretical results confirm the physical constraint that the thermostat cannot change the velocity direction of its application particle. As the wall is positioned on the left side of the system, a particle with initially rightward-oriented velocity will never hit it, while a particle with leftward-oriented velocity, will necessary collide with the wall at some instant. By solving Eq. (1.28) with respect to z, and substituting $z = \Delta t/\theta_1$, an expression is derived for the time that the first thermostated particle will take to impact against the wall:

$$(\Delta t_{coll})_1 = \theta_1 \log\left[\frac{{C_1}^2 + A_1(t_0)}{2C_1}\right] \tag{1.30}$$

where

$$e^z + \sqrt{e^{2z} - A_1(t_0)} = D_1 e^{E_1 z} \tag{1.31}$$

$$\begin{cases} D_1 \doteq \left[1 + \sqrt{1 - A_1(t_0)}\right] e^{\frac{\pm m_1}{\theta_1\sqrt{K_{ref,1}}}[x_2(t_0) - x_1(t_0)]} \\ E_1 \doteq \frac{m_1}{\sqrt{K_{ref,1}}}\dot{x}_2(t_0) \\ z \doteq \Delta t/\theta_1 \end{cases}$$

With these expressions, and considering the various cases that can be realized in time, one may now perform the numerical simulations.

1.3 Results

1.3.1 Equilibrium

We investigate the time evolution of several macroscopic and microscopic properties of the bar, by considering their average values and their standard deviations, both instantaneously, at each time j, and averaging over sets of 500 time steps, to mimic the temporal resolution of the measurement instrument. A macroscopic

measurement, indeed, amounts to averaging over very many microscopic times, because the instrument needs time to equilibrate with the measured object. Analogously, calculating spatial averages over longitudinal portions of the bar provides us with a method to model the space resolution of the measurement instrument: the readings given by the measurement tools are averages also over definite spatial scales, which depend on the resolution of the measurement tool. In the following, we consider the following quantities:

- Macroscopic properties
  - Total length of the bar: position of the last particle x_N
  - Linear density: $\rho_k = \frac{\sum_{i=1}^{N_k} m_i}{\Delta l_k} = \frac{m_{TOT,k}}{\Delta l_k}$
  - Specific kinetic energy: $(e_{kin})_k = \frac{1}{\Delta l_k} \sum_{i=1}^{N_k} \left(\frac{1}{2} m_i \dot{x}_i^2 \right)$

    Here, k is the index of the longitudinal element of space, which is occupied by the bar; its length is Δl_k; N_k is the number of particles that it includes. We take all length elements to be equal, so that we can write: $\Delta l_k = dx$ for all k.
- Microscopic properties
  - Average kinetic energy: $\left(\overline{E}_{kin}\right)_k = \frac{1}{N_k} \sum_{i=1}^{N_k} \left(\frac{1}{2} m_i \dot{x}_i^2 \right)$
  - Position of the centre of mass of groups of N_G particles, which are located at the ends and of the bar):

$$x_G = \frac{\sum_{i=1}^{N_G} m_i x_i}{\sum_{i=1}^{N_G} m_i}$$

    where G is the index of the group of particles under consideration.

We considered different scenarios, for $N = 200$ and $N = 300$. For the initial conditions, we adopt three different possibilities:

1. *random uniform distribution* over a reference length $(l_0)_{IC1} = 10$ natural units of the system with fixed total energy $(E_{tot})_{IC1}$. We found that this initial condition corresponds to an *elongation* of $\Delta x_N = 2$, compared to the stationary length, i.e. the average of the position x_N, which is the effective length of the bar.
2. *random uniform distribution* over a reference length $(l_0)_{IC2}$ shorter than in case 1:

$$(l_0)_{IC2} = \frac{1}{3}(l_0)_{IC1};\ (E_{tot})_{IC2} = (E_{tot})_{IC1}$$

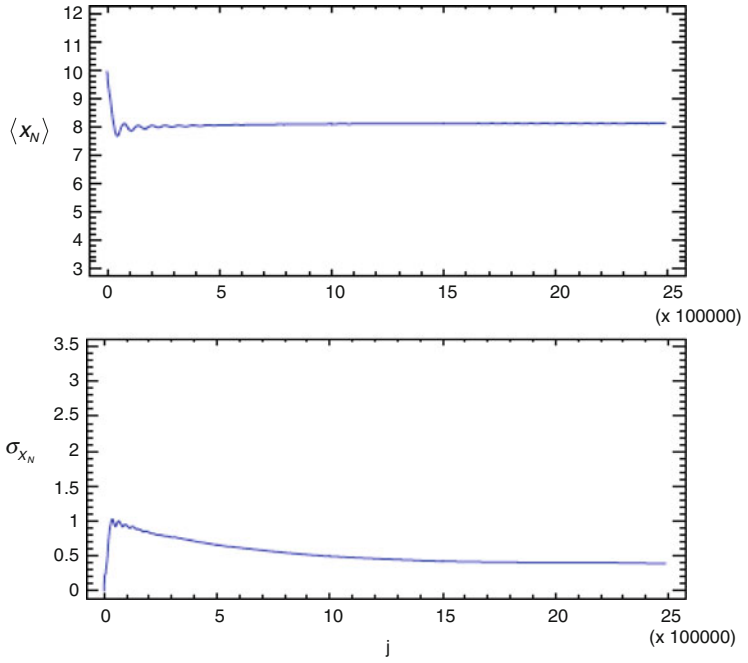

Fig. 1.8 Convergence of the average value and standard deviation of the total length of the bar x_N, with time (j = time step). Parameters: 200 particles, total time = 1,000, $F = 10$, alternating masses, initial condition 1 (elongation)

with total energy equal to case 1, and with initial condition corresponding to a *compression* of $\Delta x_N = -5$ compared to the stationary average of x_N.

3. *random uniform distribution* as in case 2, but with an initial condition corresponding to an *elongation* of, $\Delta x_N = 2$ compared to the stationary average value of x_N.

Concerning the masses of the particles, we studied the cases of all equal masses, $m_0 = 1$, and the case of alternating masses, of values m_0 and $m_0/3$. For the values of the forces applied forces on the last particle, we took: $F = 10$ as the cohesion force, and $F = 2.5, 5, 7.5, 12.5, 15, 17.5, 20, 22.5$ in order to study elasticity. Here, a force smaller than 10 amounts to pulling the bar, and a force large than 10 amounts to compressing it.

To test whether the system reaches a steady state, we considered the time evolution of the averages and of the standard deviations of various properties of the bar, realizing that the length of the bar settles rather rapidly on an apparently stationary value, as illustrated for one case by Fig. 1.8.

The system is *microscopically* (*i.e. mechanically*) *conservative*, because there is no dissipation. By construction, there is no exchange of energy with any environment, and collisions are elastic. Nevertheless, the system appears to be

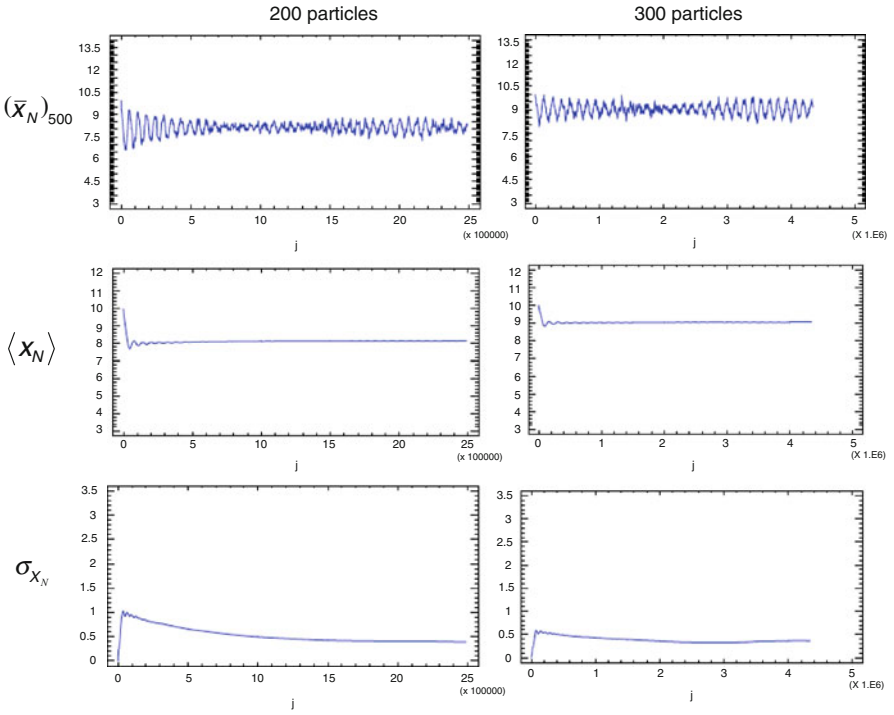

Fig. 1.9 Comparison between simulations with 200 and 300 particles: bar length. Parameters: total time = 1,000, F = constant, alternated masses, initial condition = elongation

macroscopically (*collectively*) *irreversible*, because it evolves towards a condition of statistical dynamic equilibrium. This condition depends neither on the type (1, 2 or 3) of initial condition, nor on its quantitative realization, which involves the magnitude of the initial difference between the initial and the final length of the bar. The only parameters that affect it appear to be the number of particles N and the total energy of the system E_{tot}. Of course, this kind of system is bound to recur in the long time limit, i.e. to return arbitrarily close to its initial condition, but that is possible only in principle, as in practice recurrence would take many lifetimes of the universe to be verified.

When the number of particles N increases, the model fits better the physics of a macroscopic object, in the sense the standard deviations of the fluctuations of the different properties decreases with respect to the mean values. For example, considering the total length of the bar, given the same reference value l_0, rising the number of particles from 200 to 300, we get the behaviour of Fig. 1.9, corresponding to:

$$\langle x_N \rangle_{200\_pp} < \langle x_N \rangle_{300\_pp} < l_0$$

$$(\sigma_{x_N})_{200\_pp} = (\sigma_{x_N})_{300\_pp}$$

$$\frac{(\sigma_{x_N})_{200\_pp}}{\langle x_N \rangle_{200\_pp}} > \frac{(\sigma_{x_N})_{300\_pp}}{\langle x_N \rangle_{300\_pp}}$$

It is easy to see that there is a correlation between the kinetic energy per particle and the kinetic energy per unit length, for large N. This relation can be expressed by:

$$\begin{cases} \langle (e_{kin})_k \rangle \cong C_k \cdot \left\langle \left(\overline{E}_{kin}\right)_k \right\rangle \\ \sigma_{(e_{kin})_k} \cong C_k \cdot \sigma_{\left(\overline{E}_{kin}\right)_k} \end{cases}$$

where $(e_{kin})_k$ is the specific kinetic energy averaged over the length of the kth bar segment, $(\bar{E}_{kin})_k$ is the average kinetic energy averaged over the number of particles of the kth bar segment, N_k and C_k is a constant depending on N_k. Indeed, by definition one has:

$$\left(\overline{E}_{kin}\right)_k = \frac{\langle E_k \rangle}{l_k} \quad (e_{kin})_k = \left\langle \frac{E_k}{N_k} \right\rangle$$

We now define the specific number of particle per bar interval k as $n_k \equiv \langle N_k \rangle / l_k$ and we notice that simulations show that $n_k \approx const$. Therefore, we can write:

$$\left(\overline{E}_{kin}\right)_k = \frac{\langle E_k \rangle}{\langle N_k \rangle} n_k$$

If we assume, as supported by our simulations, that the distributions of the various properties are Gaussian, we have:

$$(e_{kin})_k = \left\langle \frac{E_k}{N_k} \right\rangle = \left\langle \frac{\langle N(t) \rangle \, (\overline{e}_{kin})_k + \sqrt{N} (\overline{e}_{kin})_k (t)}{\langle N \rangle + \sqrt{N}} \right\rangle$$

Then, for large N, $\sqrt{N}$ can be neglected with respect to N, so that

$$(e_{kin})_k = \frac{\langle N(t) \, \langle (\overline{e}_{kin})_k \rangle \rangle}{\langle N \rangle} = \frac{\langle E_k \rangle}{\langle N \rangle} = \frac{\left(\overline{E}_{kin}\right)_k}{n_k}$$

And, in particular:

$$n_k = C_k = \frac{l_k}{N_k}$$

As time passes, the density gradient at the end of the bar diminishes, in agreement with the physics of the problem, as there is no wall at the end of the bar. Figure 1.10 shows the time evolution of the density distribution along the bar, averaged over time, from the beginning of the simulation to the current instant, for both elongation and compression initial conditions. Three times are examined: the beginning of the

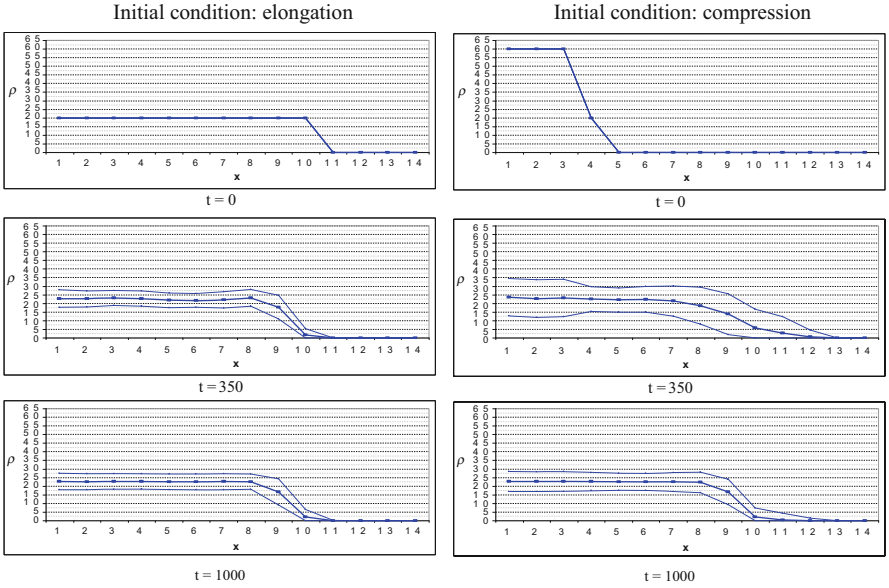

Fig. 1.10 Density distribution along the bar, in three different moments: at the beginning (*top*), during the transient (*middle*), in stationary conditions (*bottom*). The band gives the range of the possible oscillations in time and its limits are given by $\langle\rho\rangle \pm \sigma_\rho$. Parameters: 200 particles, $F =$ constant, equal masses

simulation, one time along the transient, and when steady state is reached. At the beginning, the density is constant along the bar, because we took a uniform particle distribution as initial condition. Consequently, at the end of the bar, the density gradient is initially very steep, because the borders of the physical object are sharply defined. As expected, when initial elongation is considered, the density in the centre of the bar, $\langle\rho\rangle = 2$, is lower than the stationary one. Conversely, when we start with compression, the initial density $\langle\rho\rangle = 6$ is higher than the stationary one. In the steady state, the two initial conditions have converged to the same density profile, about the average value $\langle\rho\rangle = 2.75$ with $\sigma_\rho = 0.5$. However, major differences appear during the transient. With an initial elongation $\Delta x_N = 2$, the oscillations in the transient states are much wider than those concerning the initial compression $\Delta x_N = -5$. During the transient, the average density is not uniform along the bar. In particular, the transient gradient at the end of the bar is lower than the initial and final gradients. This happens because oscillations in time cause a rarefaction at the free extreme, therefore the borders of the bar are not sharply defined during the transient.

Interestingly, our model has a stress-strain behaviour qualitatively similar to those of real bars undergoing tensile testing, as demonstrated by our results for a range of forces between 2.5 and 22.5. As our model needs the application of a compressive force, while experimental tensile results are generally referred to traction tests, in order to be able to compare the curves, we considered as the

Table 1.1 Load test cycle in equilibrium conditions of the bar

F	$\langle x_N \rangle$	s	e
2.5	12.6	0.888888889	0.726027397
5	9.6	0.777777778	0.315068493
7.5	8.6	0.666666667	0.178082192
10	8	0.555555556	0.095890411
12.5	7.8	0.444444444	0.068493151
15	7.6	0.333333333	0.04109589
17.5	7.5	0.222222222	0.02739726
20	7.4	0.111111111	0.01369863
22.5	7.3	0	0

F is the applied constant force, $\langle x_N \rangle$ is the average length of the bar at steady state, s is the stress and e is the strain. All these values are expressed in natural units

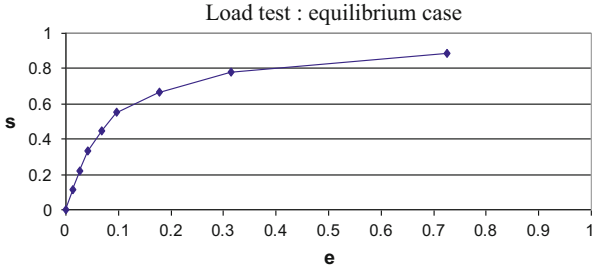

Fig. 1.11 Stress-strain curve looks like the typical experimental curves for metallic materials. The curve from simulations qualitatively reproduces the trend of the real ones, presenting a first part where the strain increases linearly with the applied stress, followed by a part where a power law holds

unloaded condition of the bar the case when we had the maximum applied force ($F_0 = 22.5$). Therefore the other forces could be considered as traction forces (Table 1.1).

Following the classical definitions, the stress of the bar s and the corresponding deformation e are calculated as

$$s = \left| \frac{F - F_0}{F_0} \right|; \quad e = \frac{l - l_0}{l_0} = \frac{\langle x_N \rangle - \langle x_N \rangle_0}{\langle x_N \rangle_0}$$

where F_0 and l_0 were respectively the restraining force and the length of the bar corresponding to the unloaded condition. The curve that we found (Fig. 1.11) is strikingly similar to the real curves of metallic materials. In particular, we observe a part with elastic behaviour, and a section where plastic deformation appears.

1.3.2 Non-equilibrium

Here, we consider the total length of the bar, in non-equilibrium conditions imposed by a temperature gradient, caused by different temperatures at the ends of the chain. We found that the following parameters affect mean and standard deviations of this quantity:

- *Average reference kinetic energy of the thermostats, i.e. average temperature of the bar*

$$\left(\overline{E}_{kin}\right)_{REF} = \frac{(E_{kin})_{REF\_1} + (E_{kin})_{REF\_2}}{2}$$

  The final average bar length $\langle x_N \rangle$ increases with the average reference kinetic energy of the thermostats $(\bar{E}_{kin})_{REF}$. As the kinetic energy is related to the temperature, this means that the bar length increases when the temperature rises, which is in agreement with the physics of the system.
- *Relaxation constants* $\theta_1 ; \theta_2$

  If we decrease the relaxation constants, the average value and the standard deviation of the bar length converge to higher values.

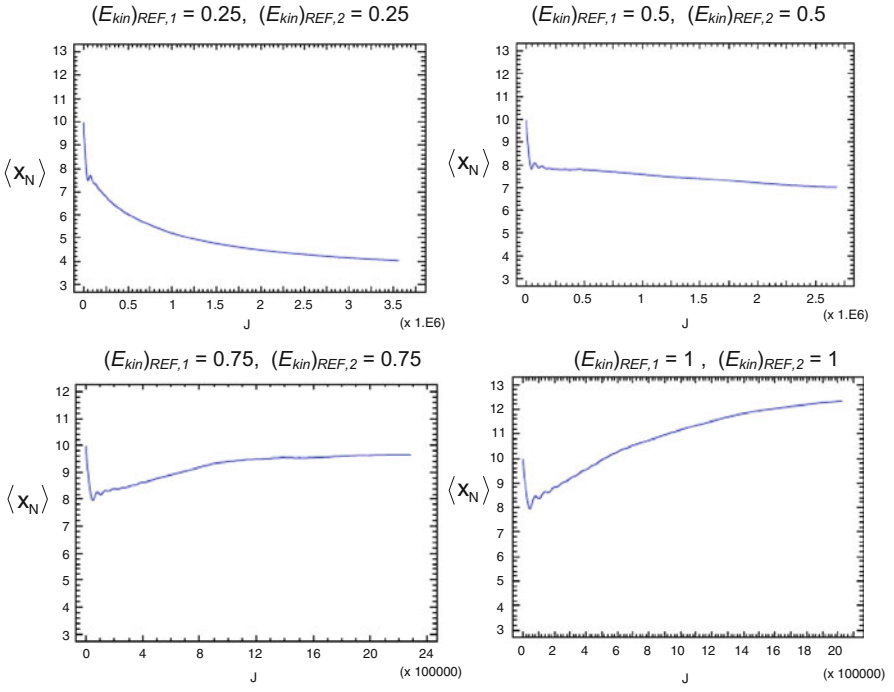

Fig. 1.12 Dependence of the average length of the bar on its imposed temperature. We imposed a temperature gradient $\Delta T = 0$ between the thermostats and an increasing average temperature $\overline{T}$. The length of the bar increases with the temperature. *j* is the index of the time instant

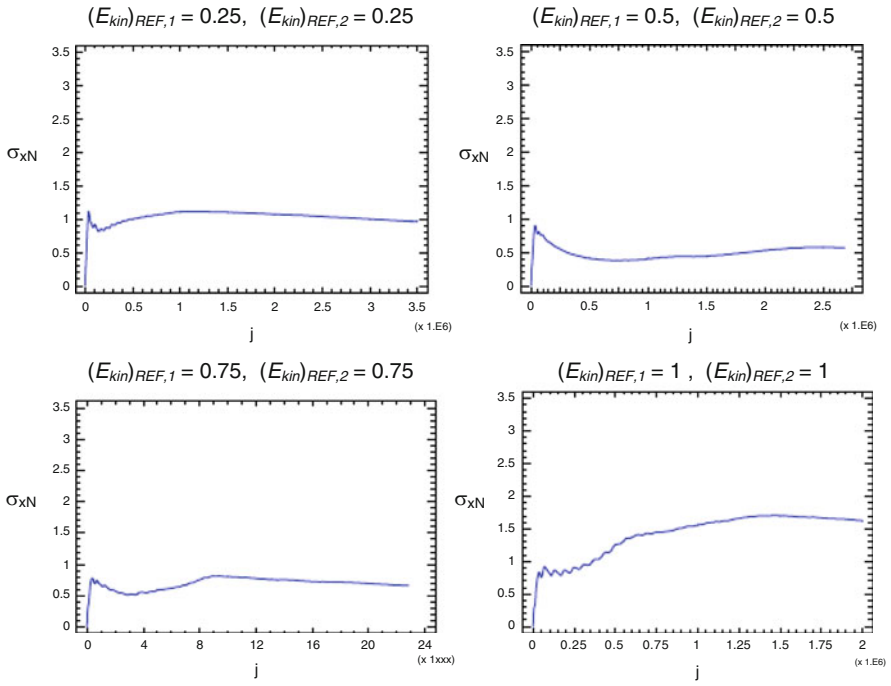

Fig. 1.13 Dependence of the standard deviation of the length of the bar on the thermostats temperatures, with vanishing temperature gradient, $\Delta T = 0$. Unlike the average length, the standard deviation always converges, but it doesn't have a monotonic trend when the temperature rises. The fastest convergence is found with the lowest temperatures, while the slowest convergence is found for the highest ones

In analogy with the equilibrium case, we run several simulations with different applied forces F at the end of the bar. When we heated up the bar by setting a temperature gradient between its two ends, we found stress-strain curves with the same qualitative characteristics as the experimental curves of most common metallic materials. When a plastic material is deformed, accumulation of dislocations produces hardening, which opposes further deformation. However, if some heat is given to the material, dislocations can move again and the material can deform. The curves that we found from our simulations, prove that these mechanisms are shared by our particles systems as well. Even in a simple one-dimensional model, localized agglomerates can originate and be redistributed by means of heat flows, thus allowing further deformation. Figures 1.12 and 1.13 illustrate cases with equal temperatures at the borders of the bar, in order to show how equilibrium is reached in the presence of thermostats. Table 1.2 and Fig. 1.14 demonstrate the hardening due to the temperature variations.

Table 1.2 Load test in non-equilibrium conditions with $v_{REF,1} = v_{REF,2} = 1.4$, corresponding to $(E_{kin})_{REF,1} = 0.98$, $(E_{kin})_{REF,2} = 0.32$

F	$\langle x_N \rangle$	s	e
2.5	27	0.888888889	5.75
5	15	0.777777778	2.75
7.5	11	0.666666667	1.75
10	8.5	0.555555556	1.125
12.5	7	0.444444444	0.75
15	6	0.333333333	0.5
17.5	5	0.222222222	0.25
20	4.5	0.111111111	0.125
22.5	4	0	0

F is the constant force, $\langle x_N \rangle$ is steady state bar length, s is the stress and e is the strain

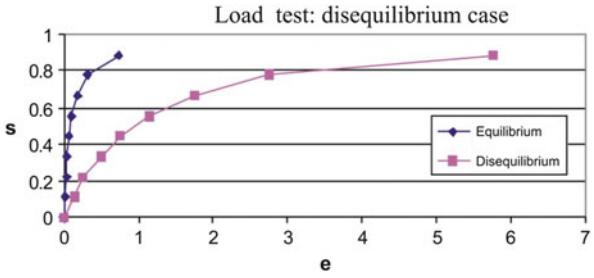

Fig. 1.14 Stress-strain curves look like those of metallic materials, for rising temperatures

1.4 Conclusions

Simulations of the equilibrium conditions of a bar made of hard point particles prove that even very simple models may qualitatively reproduce the macroscopic physical behaviour of solid bars. This is typical in statistical physics, which has provided understanding of an incredible variety of phenomena by means of explicitly treatable idealized models.

In our investigation, both the bar and the thermostats are described by over-simplified interacting particles and mechanical forces. Nevertheless, the fact that macroscopic systems are observed on a very coarse grained scale, which makes largely irrelevant the details of the myriad of microscopic degrees of freedom [2], allows us to obtain sensible results. In particular, we found that the average values and standard deviations of the main macroscopic and microscopic collective properties of our particle systems converge in relatively short times to the relevant stationary values. Although the equilibrium model is microscopically reversible, it results macroscopically irreversible: different initial conditions evolve into the same equilibrium state, which depends only on the number of particles and on their total energy. Consistently with equilibrium statistical mechanics, the probability distribution of the fluctuations of the various observables are Gaussian, with decreasing relative variance for growing number of particles.

In non-equilibrium conditions, we found that our systems reach a steady state only for a certain range of average temperatures, beyond which the bar length indefinitely diverges or collapses. Similar kinds of instabilities are known. Here the problem is that the thermostats which we have adopted manifest their unphysical peculiarities when the dissipation is too strong. This is another common feature of statistical mechanical models and, indeed, of mathematical models of real phenomena in general. A mathematical model is constructed with the intent to understand the role of various elements contributing to a phenomenon of interest. For this reason and also for the practical need to let the model be amenable to detailed study, mathematical models are necessarily incomplete, and are desired to be so. Therefore, their applicability is always restricted to a certain range of parameters and phenomena. Better models apply more extensively than others, but outside a certain range of applicability, they are all bound to fail.

Within the applicability range of our model, we found that the stationary bar length depends on the average of the thermostats reference temperatures, and the temperatures standard deviations. In particular, we obtained that a lower average temperature corresponds to lower final length and smaller oscillations of the bar, as physically expected. At equal average temperatures, the convergence velocity is influenced by the absolute value of the temperature difference of the two thermostats. Regardless of their sign, lower gradients result in a faster convergence both of average values and standard deviations of the bar length, thus stabilizing the system, in agreement with its physical behaviour.

The convergence velocity is also affected by the relaxation constants of the thermostats, which represent the efficiency of the energy exchange between bar and thermostats. When they are equal, their increase produces a slower convergence, as expected from the analysis of the thermostats equations. In fact, higher values of these constants correspond to lower efficiency of the thermostats. However, when the relaxation constants differ, the relation between their value and the convergence velocity still needs to be clarified.

Particularly interesting are the results obtained by changing the force at the free ends of the bar, both in equilibrium and in non-equilibrium conditions, as they qualitatively reproduced the typical experimental stress-strain curves of metallic materials. Such analogy is also extended to the way these curves change when the temperature increases.

We are aware of no simpler microscopic mechanical system capable of reproducing such thermo-mechanical features as the hardening phenomenon, under a temperature gradient.

Acknowledgements The research leading to these results has received funding from the European Research Council under the European Community's Seventh Framework Program (FP7/2007-2013)/ERC grant agreement no. 202680. The EC is not liable for any use that can be made of the information contained herein.

References

1. Bonetto, F., Lebowitz, J., Rey-Bellet, L.: In: Fokas, A., Grigoryan, A., Kibble, T., Zegarlinski, B. (eds.) Mathematical Physics 2000. Imperial College, London (2000)
2. Castiglione, P., Falcioni, M., Lesne, A., Vulpiani, A.: Chaos and Coarse Graining in Statistical Mechanics. Cambridge University Press, Cambridge (2008)
3. Dahr, A.: Adv. Phys. **57**, 457 (2008)
4. Conti, L., et al. J. Stat. Mech. P12003 (2013)
5. Conti, L., et al.: Phys. Rev. E **85**, 1 (2012)
6. De Gregorio, P., et al.: Phys. Rev. B **84**, 1 (2011)
7. Evans, D.J., Morriss, G.: Statistical Mechanics of Nonequilibrium Liquids. Cambridge University Press, Cambridge (2008)
8. Peierls, E.: Quantum Theory of Solids. Oxford University Press, London (1955)
9. Fermi, E., Pasta, J., Ulam, S.: Los Alamos Document LA-190 (1955)
10. Gallavotti, G.: The Fermi-Pasta-Ulam Problem: A Status Report. Springer, Berlin (2007)
11. Jepps, O.G., Rondoni, L.: J. Phys. A Math. Theor. **43**, 133001 (2010)
12. Lanczos, C.: The Variational Principles of Mechanics. Courier Dover Publications, New York (2012)
13. Lepri, S., Livi, R., Politi, A.: Phys. Rep. **377**, 1 (2003)
14. Maeda, A., Munakata, T.: Phys. Rev. E **52**, 234 (1995)
15. Nosé, S.: J. Chem. Phys. **81**, 511 (1984)
16. O'Connor, A.J., Lebowitz, J.L.: J. Math. Phys. **15**, 692 (1974)
17. Payton, D.N., Rich, M., Visscher, W.M.: Phys. Rev. **160**, 706 (1967)
18. Rubin, R.J., Greer, W.L.: J. Math. Phys. **12**, 1686 (1971)
19. Tehver, R., Toigo, F., Koplik, J., Banavar, J.R.: Phys. Rev. E **57**, R17 (1998)
20. Zhang, F., Isbister, D.J., Evans, D.J.: Phys. Rev. E **61**, 3541 (2000)

Chapter 2
Chaos, Transport and Diffusion

Guido Boffetta, Guglielmo Lacorata, and Angelo Vulpiani

Abstract This chapter presents basic elements of chaotic dynamical system theory. The concept of Lyapunov exponent, predictability time and Lagrangian chaos are introduced together with examples. The second part is devoted to the discussion of Lagrangian chaos, in particular in two dimensions, and its relation with Eulerian properties of the flow. The last part of the chapter contains an introduction to diffusion and transport processes, with particular emphasis on the treatment of non-ideal cases.

2.1 Some Basic Elements of Dynamical Systems

A dynamical system may be defined as a deterministic rule for the time evolution of state observables. Well known examples are the ordinary differential equations (ODE) in which time is continuous:

$$\frac{d\mathbf{x}(t)}{dt} = \mathbf{f}(\mathbf{x}(t)), \qquad \mathbf{x}, \mathbf{f} \in \mathbb{R}^d; \tag{2.1}$$

and maps in which time is discrete:

$$\mathbf{x}(t+1) = \mathbf{g}(\mathbf{x}(t)), \qquad \mathbf{x}, \mathbf{g} \in \mathbb{R}^d. \tag{2.2}$$

G. Boffetta (✉)
Department of Physics, University of Torino, Via Pietro Giuria 1, 10125 Torino, Italy
e-mail: boffetta@to.infn.it

G. Lacorata
CNR ISAC, Str. Prov. Lecce-Monteroni, 73100 Lecce, Italy
e-mail: G.Lacorata@isac.cnr.it

A. Vulpiani
Department of Physics and CNR ISC, University of Rome "La Sapienza", P.le Aldo Moro 5, 00185 Roma, Italy
e-mail: Angelo.Vulpiani@roma1.infn.it

S. Banerjee, L. Rondoni (eds.), *Applications of Chaos and Nonlinear Dynamics in Science and Engineering - Vol. 4*, Understanding Complex Systems,
DOI 10.1007/978-3-319-17037-4_2

In the case of maps, the evolution law is straightforward: from $\mathbf{x}(0)$ one computes $\mathbf{x}(1)$, and then $\mathbf{x}(2)$ and so on. For ODE's, under rather general assumptions on $\mathbf{f}$, from an initial condition $\mathbf{x}(0)$ one has a unique trajectory $\mathbf{x}(t)$ for $t > 0$ [50]. Typically, exception made for the linear case and other few situations (integrable systems), it is not possible to find an explicit solution $\mathbf{x}(t)$. On the other hand, via the qualitative analysis, sometimes it is possible to obtain some features of the system, for instance the stability of fixed points or the existence of periodic orbits. Examples of regular behaviors are shown in Fig. 2.1.

A rather natural question is the possible existence of less regular behaviors i.e. different from stable fixed points, periodic or quasi-periodic motion. After the seminal works by Lorenz, Hénon and Chirikov (to mention just the most eminent scientists of Chaos) it is now well established that deterministic systems can have an irregular and unpredictable behavior. As a relevant system, originated in a

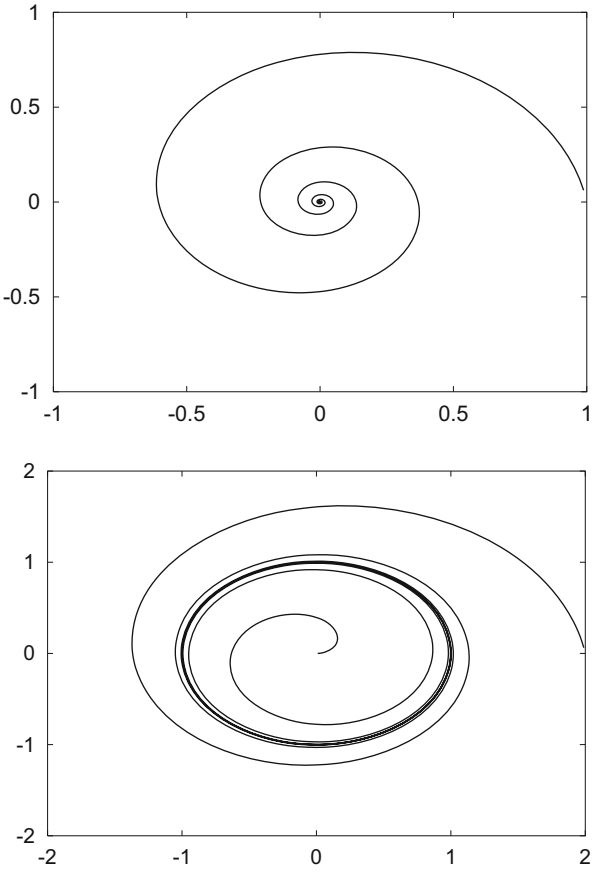

Fig. 2.1 Examples of regular attractors: fixed point (*above*) and limit cycle (*below*)

geophysical context, we mention the celebrated Lorenz model [44]:

$$\begin{aligned} \frac{dx}{dt} &= -\sigma(x-y) \\ \frac{dy}{dt} &= -xz + rx - y \\ \frac{dz}{dt} &= xy - bz \end{aligned} \tag{2.3}$$

This system is related to the Rayleigh-Benard convection under very crude approximations. The quantity x is proportional the circulatory fluid particle velocity; the quantities y and z are related to the temperature profile; σ, b and r are dimensionless parameters. Lorenz studied the case with $\sigma = 10$ and $b = 8/3$ at varying r (which is proportional to the Rayleigh number). It is easy to see by linear analysis that the fixed point $(0, 0, 0)$ is stable for $r < 1$. For $r > 1$ it becomes unstable and two new fixed points appear:

$$C_{+,-} = (\pm\sqrt{b(r-1)}, \pm\sqrt{b(r-1)}, r-1), \tag{2.4}$$

these are stable for $r < r_c = 24.74$. A nontrivial behavior, i.e. non periodic, is present for $r > r_c$, as is shown in Fig. 2.2.

In this "strange", chaotic regime one has the so called sensitive dependence on initial conditions. Consider two trajectories, $\mathbf{x}(t)$ and $\mathbf{x}'(t)$, initially very close and denote with $\Delta(t) = ||\mathbf{x}'(t) - \mathbf{x}(t)||$ their separation. Chaotic behavior means that if $\Delta(0) \to 0$, then as $t \to \infty$ one has $\Delta(t) \sim \Delta(0) \exp \lambda_1 t$, with $\lambda_1 > 0$, see Fig. 2.3.

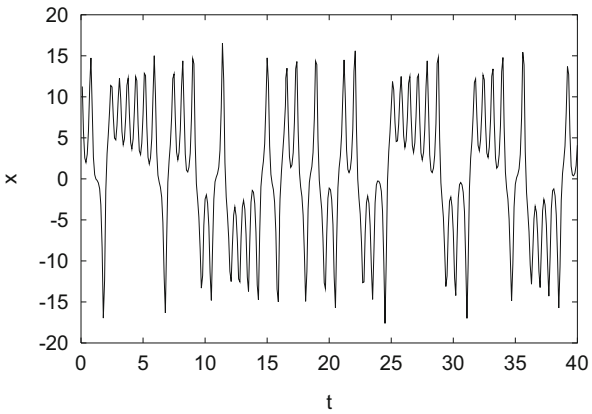

Fig. 2.2 Example of aperiodic signal: the x variable of the Lorenz system (2.3) as function of time t, for $r = 28$

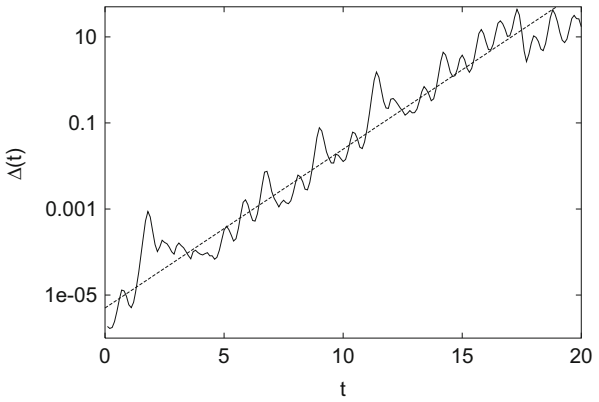

Fig. 2.3 The growth of a generic infinitesimal perturbation $\Delta(t)$ in the Lorenz model (2.3) as function of time t, for $r = 28$. The *dashed line* represent the exponential growth $\Delta(0) \exp \lambda_1 t$

Let us notice that, because of its chaotic behavior and its dissipative nature, i.e.

$$\frac{\partial \dot{x}}{\partial x} + \frac{\partial \dot{y}}{\partial y} + \frac{\partial \dot{z}}{\partial z} < 0, \tag{2.5}$$

the attractor of the Lorenz system cannot be a smooth surface. Indeed the attractor has a self-similar structure with a fractal dimension between 2 and 3. The Lorenz model (which had an important historical relevance in the development of chaos theory) is now considered a paradigmatic example of a chaotic system.

The main mark of the so-called deterministic chaos is the sensitive dependence on initial conditions: arbitrarily small initial errors are fastly amplified. The mean growth rate of the trajectory separation is measured by the first (or maximum) Lyapunov exponent, defined as

$$\lambda_1 = \lim_{t\to\infty} \lim_{\Delta(0)\to 0} \frac{1}{t} \ln \frac{\Delta(t)}{\Delta(0)}, \tag{2.6}$$

As long as $\Delta(t)$ remains sufficiently small (i.e. infinitesimal, strictly speaking), one can regard the separation as a tangent vector $\mathbf{z}(t)$ whose time evolution is

$$\frac{dz_i}{dt} = \sum_{j=1}^{d} \frac{\partial f_i}{\partial x_j}|_{\mathbf{x}(t)} \cdot z_j, \tag{2.7}$$

and, therefore,

$$\lambda_1 = \lim_{t\to\infty} \frac{1}{t} \ln \frac{||\mathbf{z}(t)||}{||\mathbf{z}(0)||}. \tag{2.8}$$

In principle, λ_1 may depend on the initial condition $\mathbf{x}(0)$, but this dependence disappears for ergodic systems. In general there exist as many Lyapunov exponents, conventionally written in decreasing order $\lambda_1 \geq \lambda_2 \geq \lambda_3 \geq \ldots$, as the independent coordinates of the phase space [7]. Without entering the details, one can define the sum of the first k Lyapunov exponents as the growth rate of an infinitesimal k-dimensional volume in the phase space. In particular, λ_1 is the growth rate of material lines, $\lambda_1 + \lambda_2$ is the growth rate of $2D$ surfaces, and so on. A numerical widely used efficient method is due to Benettin et al. [7].

It must be observed that, after a transient, the growth rate of any generic small perturbation (i.e. distance between two initially close trajectories) is measured by the first (maximum) Lyapunov exponent λ_1, and $\lambda_1 > 0$ means chaos. In such a case, the state of the system is unpredictable on long times. Indeed, if we want to predict the state with a certain tolerance Δ then our forecast cannot be pushed over a certain time interval T_P, called predictability time, given by:

$$T_P \sim \frac{1}{\lambda_1} \ln \frac{\Delta}{\Delta(0)}. \tag{2.9}$$

The above relation shows that T_P is basically determined by $1/\lambda_1$, seen its weak dependence on the ratio $\Delta/\Delta(0)$. To be precise one must state that, for a series of reasons, relation (2.9) is too simple to be of actual relevance [14].

2.2 Lagrangian Chaos

A problem of great interest concerns the study of the spatial and temporal structure of the so-called passive fields, indicating by this term passively quantities driven by the flow, such as the temperature under certain conditions [48]. The equation for the evolution of a passive scalar field $\theta(\mathbf{x}, t)$, advected by a velocity field $\mathbf{v}(\mathbf{x}, t)$, is

$$\partial_t \theta + \nabla \cdot (\mathbf{v}\,\theta) = \chi\, \nabla^2 \theta \tag{2.10}$$

where $\mathbf{v}(\mathbf{x}, t)$ is a given velocity field and χ is the molecular diffusion coefficient.

The problem (2.10) can be studied through two different approaches. Either one deals at any time with the field θ in the space domain covered by the fluid, or one deals with the trajectory of each fluid particle. The two approaches are usually designed as "Eulerian"and "Lagrangian", although both of them are due to Euler [40]. The two points of view are in principle equivalent.

The motion of a fluid particle is determined by the differential equation

$$\frac{d\mathbf{x}}{dt} = \mathbf{v}(\mathbf{x}, t) \tag{2.11}$$

which also describes the motion of test particles, for example a powder embedded in the fluid, provided that the particles are neutral and small enough not to perturb the velocity field, although large enough not to perform a Brownian motion. Particles of this type are commonly used for flow visualization in fluid mechanics experiments, see [55]. Let us note that the true equation for the motion of a material particle in a fluid can be rather complicated [47].

It is now well established that even in regular velocity field the motion of fluid particles can be very irregular [2, 29]. In this case initially nearby trajectories diverge exponentially and one speaks of *Lagrangian chaos*. In general, chaotic behaviors can arise in two-dimensional flow only for time dependent velocity fields in two dimensions, while it can be present even for stationary velocity fields in three dimensions.

If $\chi = 0$, it is easy to realize that (2.10) is equivalent to (2.11). In fact, we can write

$$\theta(\mathbf{x}, t) = \theta_o(T^{-t}\mathbf{x}) \tag{2.12}$$

where $\theta_o(\mathbf{x}) = \theta(\mathbf{x}, t = 0)$ and T is the formal evolution operator of (2.11) ,

$$\mathbf{x}(t) = T^t\mathbf{x}(0). \tag{2.13}$$

Taking into account the molecular diffusion χ, (2.10) is the Fokker-Planck equation of the Langevin equation [20]

$$\frac{d\mathbf{x}}{dt} = \mathbf{v}(\mathbf{x}, t) + \eta(t) \tag{2.14}$$

where η is a Gaussian process with zero mean and variance

$$\left\langle \eta_i(t)\, \eta_j(t') \right\rangle = 2\chi\delta_{ij}\, \delta(t - t'). \tag{2.15}$$

In the following we will consider only incompressible flow

$$\nabla \cdot \mathbf{v} = 0 \tag{2.16}$$

for which the dynamical system (2.11) is conservative. In two dimensions, the constraint (2.16) is automatically satisfied assuming

$$v_1 = \frac{\partial \psi}{\partial x_2}, \qquad v_2 = -\frac{\partial \psi}{\partial x_1} \tag{2.17}$$

where $\psi(\mathbf{x}, t)$ is the *stream function*. Inserting (2.17) into (2.11) the evolution equations become

$$\frac{dx_1}{dt} = \frac{\partial \psi}{\partial x_2}, \qquad \frac{dx_2}{dt} = -\frac{\partial \psi}{\partial x_1}. \tag{2.18}$$

Formally (2.18) is a Hamiltonian system with the Hamiltonian given by the stream function ψ.

2.2.1 Examples of Lagrangian Chaos

As a first example we consider a $3d$ stationary velocity field, the so-called ABC flow

$$\mathbf{v} = (A \sin z + C \cos y,\ B \sin x + A \cos z,\ C \sin y + B \cos x) \tag{2.19}$$

where A, B and C are non zero real parameters. Because of the incompressibility condition, the evolution $\mathbf{x}(0) \to \mathbf{x}(t)$ defines a volume preserving, dynamics.

Arnold [4] argued that (2.19) is a good candidate for chaotic motion. Let us briefly repeat his elegant argument. For a steady state solution of the $3d$ Euler equation one has:

$$\begin{aligned} \nabla \cdot \mathbf{v} &= 0 \\ \mathbf{v} \times (\nabla \times \mathbf{v}) &= \nabla \alpha \\ \alpha &= \frac{P}{\rho} + \frac{\mathbf{v}^2}{2} \end{aligned} \tag{2.20}$$

where P is the pressure and ρ the density. As a consequence of the Bernoulli theorem [41], $\alpha(\mathbf{x})$ is constant along a streamline—that is a Lagrangian trajectory $\mathbf{x}(t)$. One can easily verify that chaotic motion can appear only if $\alpha(\mathbf{x})$ is constant (i.e. $\nabla\alpha(\mathbf{x}) = 0$) in a part of the space. Otherwise the trajectory would be confined on a $2d$ surface $\alpha(\mathbf{x}) =$ constant, where the motion must be regular as a consequence of general arguments [50]. In order to satisfy such a constraint, from (2.20) one has the Beltrami condition:

$$\nabla \times \mathbf{v} = \gamma(\mathbf{x})\, \mathbf{v}. \tag{2.21}$$

The reader can easily verify that the field $\mathbf{v}$ given by (2.19) satisfy (2.21) (in this case $\gamma(\mathbf{x}) =$ constant). Indeed, numerical experiments by Hénon [29] provided evidence that Lagrangian motion under velocity (2.19) is chaotic for typical values of the parameters A, B, and C (see an example in Fig. 2.4).

In a two-dimensional incompressible stationary flows the motion of fluid particles is given by a time independent Hamiltonian system with one degree of freedom and, since trajectories follow iso-ψ lines, it is impossible to have chaos. However, for explicit time dependent stream function ψ the system (2.19) can exhibit chaotic motion [50].

In the particular case of time periodic velocity fields, $\mathbf{v}(\mathbf{x}, t + T) = \mathbf{v}(\mathbf{x}, t)$, the trajectory of (2.11) can be studied in terms of discrete dynamical systems: the

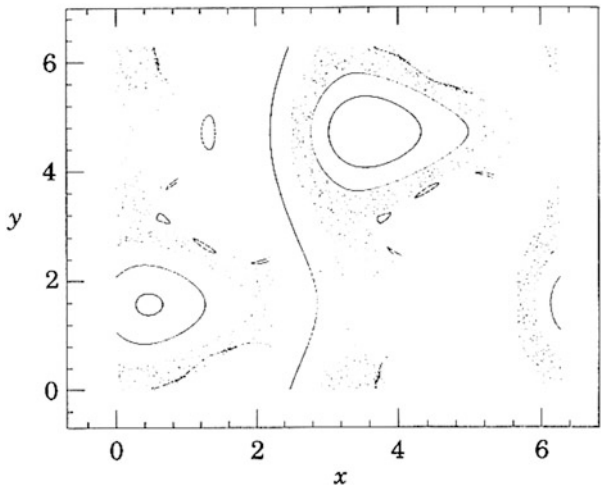

Fig. 2.4 Intersections with the Poincaré section, plane $z = 0$, of eight trajectories of the ABC flow with parameters $A = 2.0$, $B = 1.70$, $C = 1.50$

position $\mathbf{x}(t+T)$ is determined in terms of $\mathbf{x}(t)$. The map $\mathbf{x}(t) \to \mathbf{x}(t+T)$ will not depend on t thus (2.11) can be written in the form

$$\mathbf{x}(n+1) = \mathbf{F}[\mathbf{x}(n)], \tag{2.22}$$

where now the time is measured in units of the period T. Because of incompressibility, the map (2.22) is conservative:

$$\left|\det A[\mathbf{x}]\right| = 1, \qquad \text{where} \qquad A_{ij}[\mathbf{x}] = \frac{\partial F_i[\mathbf{x}]}{\partial x_j}. \tag{2.23}$$

An explicit deduction of the form of $\mathbf{F}$ for a general $2d$ or $3d$ flow is usually very difficult. However, in some simple model of can be deduced on the basis of physical features [3, 19].

2.2.2 *Eulerian Properties and Lagrangian Chaos*

In principle, the evolution of the velocity field $\mathbf{v}$ is described by partial differential equations, e.g. Navier-Stokes or Boussinesq equations. However, often in weakly turbulent situations, a good approximation of the flow can be obtained by using a Galerkin approach, and reducing the Eulerian problem to a (small) system of F ordinary differential equations [15, 42]. The motion of a fluid particle is then

described by the $(d + F)$-dimensional dynamical system

$$\frac{d\mathbf{Q}}{dt} = \mathbf{f}(\mathbf{Q}, t) \qquad \text{with } \mathbf{Q},\ \mathbf{f} \in \mathbb{R}^F \tag{2.24}$$

$$\frac{d\mathbf{x}}{dt} = \mathbf{v}(\mathbf{x}, \mathbf{Q}) \qquad \text{with } \mathbf{x},\ \mathbf{v} \in \mathbb{R}^d \tag{2.25}$$

where d is the space dimensionality and $\mathbf{Q} = (Q_1, \ldots Q_F)$ are the F variables, usually normal modes, which are a representation of the velocity field $\mathbf{v}$. Note that the Eulerian equations (2.24) do not depend on the Lagrangian part (2.25) and can be solved independently.

In order to characterize the degree of chaos, three different Lyapunov exponents can be defined [24]:

- (a) λ_E for the Eulerian part (2.24);
- (b) λ_L for the Lagrangian part (2.25), where the evolution of the velocity field is assumed to be known;
- (c) λ_T per for the total system of the $d + F$ equations.

These Lyapunov exponents are defined as:

$$\lambda_\mathrm{E,L,T} = \lim_{t\to\infty} \frac{1}{t} \ln \frac{|\mathbf{z}(t)^{(\mathrm{E,L,T})}|}{|\mathbf{z}(0)^{(\mathrm{E,L,T})}|} \tag{2.26}$$

where the evolution of the three tangent vectors $\mathbf{z}$ are given by the linearized stability equations for the Eulerian part, for the Lagrangian part and for the total system, respectively:

$$\frac{dz_i^{(\mathrm{E})}}{dt} = \sum_{j=1}^{F} \left.\frac{\partial f_i}{\partial Q_j}\right|_{\mathbf{Q}(t)} z_j{}^{(\mathrm{E})}, \qquad \mathbf{z}^{(\mathrm{E})} \in \mathbb{R}^F \tag{2.27}$$

$$\frac{dz_i^{(\mathrm{L})}}{dt} = \sum_{j=1}^{d} \left.\frac{\partial v_i}{\partial x_j}\right|_{\mathbf{x}(t)} z_j{}^{(\mathrm{L})}, \qquad \mathbf{z}^{(\mathrm{L})} \in \mathbb{R}^d \tag{2.28}$$

$$\frac{dz_i^{(\mathrm{T})}}{dt} = \sum_{j=1}^{d+F} \left.\frac{\partial G_i}{\partial y_j}\right|_{\mathbf{y}(t)} z_j{}^{(\mathrm{T})}, \qquad \mathbf{z}^{(\mathrm{T})} \in \mathbb{R}^{F+d} \tag{2.29}$$

and $\mathbf{y} = (Q_1, \ldots, Q_F, x_1, \ldots, x_d)$ and $\mathbf{G} = (f_1, \ldots, f_F, v_1, \ldots, v_d)$. The meaning of these Lyapunov exponents is evident:

- (a) λ_E is the mean exponential rate of the increasing of the uncertainty in the knowledge of the velocity field (which is, by definition, independent on the Lagrangian motion);

- (b) λ_L estimates the rate at which the distance $\delta x(t)$ between two fluid particles initially close increases with time, when the velocity field is given, i.e. a particle pair in the same Eulerian realization;
- (c) λ_T is the rate of growth of the distance between initially close particle pairs, when the velocity field is not known with infinite precision.

There is no general relation between λ_E and λ_L. One could expect that in presence of a chaotic velocity field the particle motion has to be chaotic. However, the inequality $\lambda_L \geq \lambda_E$—even though typically valid—sometimes does not hold, e.g. in some systems like the Lorenz model [24] and in generic $2d$ flows when the Lagrangian motion happens around well defined vortex structures [6] as discussed in the following. On the contrary, one has [22]

$$\lambda_T = \max(\lambda_E, \lambda_L). \tag{2.30}$$

2.2.3 Lagrangian Chaos in Two Dimensional Flows

Let us now consider the two-dimensional Navier-Stokes equations with periodic boundary conditions at low Reynolds numbers, for which we can expand the stream function ψ in Fourier series and takes into account only the first F terms [15, 42],

$$\psi = -i \sum_{j=1}^{F} k_j^{-1} Q_j e^{i\mathbf{k}_j \mathbf{x}} + \text{c.c.}, \tag{2.31}$$

where c.c. indicates the complex conjugate term and $\mathbf{Q} = (Q_1, \ldots, Q_F)$ are the Fourier coefficients. Inserting (2.31) into the Navier-Stokes equations and by an appropriate time rescaling, we obtain the system of F ordinary differential equations

$$\frac{dQ_j}{dt} = -k_j^2 Q_j + \sum_{l,m} A_{jlm} Q_l Q_m + f_j, \tag{2.32}$$

in which f_j represents an external forcing.

Franceschini and coworkers have studied this truncated model with $F = 5$ and $F = 7$ [15, 42]. The forcing were restricted to the 3^{th} mode $f_j = \text{Re}\,\delta_{j,3}$ [42]. For $F = 5$ and $\text{Re} < \text{Re}_1 = 22.85\ldots$, there are four stable stationary solutions, say $\hat{\mathbf{Q}}$, and $\lambda_E < 0$. At $\text{Re} = \text{Re}_1$, these solutions become unstable, via a Hopf bifurcation [46], and four stable periodic orbits appear, still implying $\lambda_E = 0$. For $\text{Re}_1 < \text{Re} < \text{Re}_2 = 28.41\ldots$, one thus finds the stable limit cycles:

$$\mathbf{Q}(t) = \hat{\mathbf{Q}} + (\text{Re} - \text{Re}_1)^{1/2} \delta\mathbf{Q}(t) + O(\text{Re} - \text{Re}_1) \tag{2.33}$$

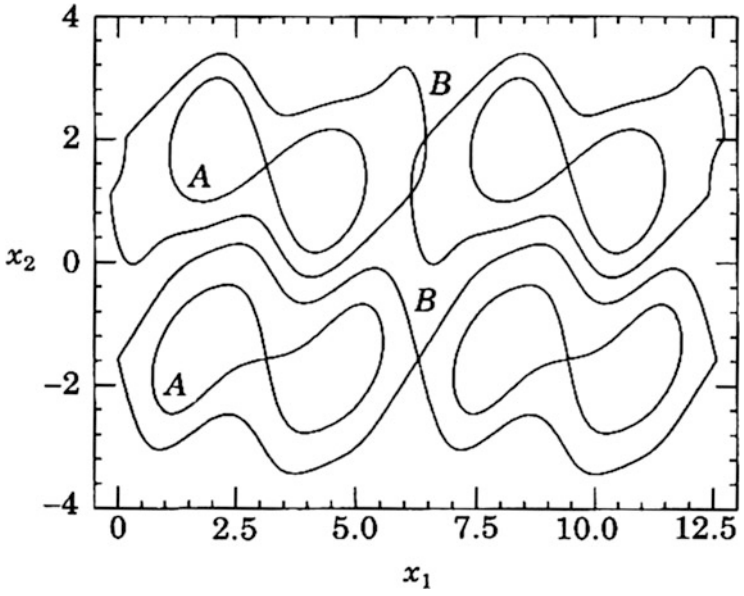

Fig. 2.5 Structure of the separatrices in the 5-mode model (2.31) with $\mathrm{Re} = \mathrm{Re}_1 - 0.05$

where $\delta\mathbf{Q}(t)$ is periodic with period

$$T(\mathrm{Re}) = T_0 + O(\mathrm{Re} - \mathrm{Re}_1) \qquad T_0 = 0.7328\ldots \tag{2.34}$$

At $\mathrm{Re} = \mathrm{Re}_2$, these limit cycles lose stability and there is a period doubling cascade toward Eulerian chaos.

Let us now discuss the Lagrangian behavior of a fluid particle. For $\mathrm{Re} < \mathrm{Re}_1$, the stream function is asymptotically stationary, $\psi(\mathbf{x}, t) \to \hat{\psi}(\mathbf{x})$, and the corresponding one-dimensional Hamiltonian is time-independent, therefore Lagrangian trajectories are regular. For $\mathrm{Re} = \mathrm{Re}_1 + \epsilon$ the stream function becomes time dependent

$$\psi(\mathbf{x}, t) = \hat{\psi}(\mathbf{x}) + \sqrt{\epsilon}\,\delta\psi(\mathbf{x}, t) + O(\epsilon), \tag{2.35}$$

where $\hat{\psi}(\mathbf{x})$ is given by $\hat{\mathbf{Q}}$ and $\delta\psi$ is periodic in $\mathbf{x}$ and in t with period T. The region of phase space, here the real two-dimensional space, adjacent to a separatrix is very sensitive to perturbations, even of very weak intensity. Figure 2.5 shows the structure of the separatrices, i.e. the orbits of infinite periods at $\mathrm{Re} = \mathrm{Re}_1 - 0.05$.

Indeed, generically in one-dimensional Hamiltonian systems, a periodic perturbation gives origin to stochastic layers around the separatrices where the motion is chaotic, as consequence of unfolding and crossing of the stable and unstable manifolds in domains centered at the hyperbolic fixed points [21, 50]. One has strong numerical evidence for the existence of the chaotic regions, see Fig. 2.6.

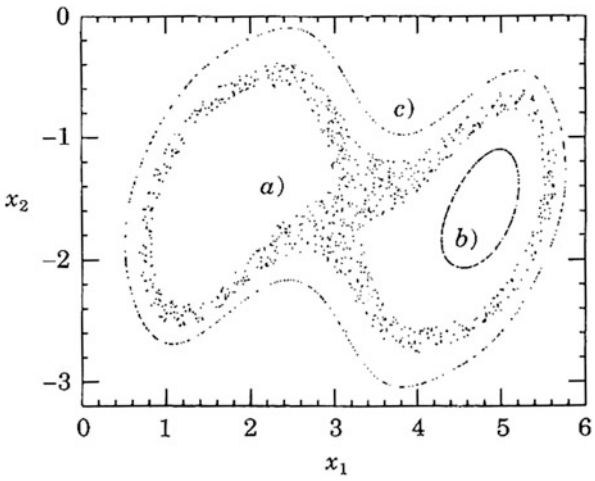

Fig. 2.6 Poincaré map for three trajectories of the 5-mode model with $\mathrm{Re} = \mathrm{Re}_1 + 0.05$. The initial conditions are selected close to a separatrix, case *a)* ($x_1(0) = 3.2$, $x_2(0) = -1.6$), or far from the separatrices, cases *b)* ($x_1(0) = 4.3$, $x_2(0) = -2.0$) and *c)* ($x_1(0) = 4.267$, $x_2(0) = -3.009$)

Chaotic and regular motion for small $\epsilon = \mathrm{Re}_1 - \mathrm{Re}$ can be studied by the Poincaré map

$$\mathbf{x}(nT) \to \mathbf{x}(nT + T). \tag{2.36}$$

The period $T(\epsilon)$ is computed numerically. The size of the stochastic layers rapidly increase with ϵ. At $\epsilon = \epsilon_c \approx 0.7$ they overlap and it is practically impossible to distinguish between regular and chaotic zones. At $\epsilon > \epsilon_c$ there is always diffusive motion.

We stress that this scenario for the onset of Lagrangian chaos in two-dimensional fluids is generic and does not depend on the particular truncated model. In fact, it is only related to the appearance of stochastic layers under the effects of small time-dependent perturbations in one-dimensional integrable Hamiltonian systems. As consequence of a general features of one-dimensional Hamiltonian systems we expect that a stationary stream function becomes time periodic through a Hopf bifurcation as occurs for all known truncated models of Navier-Stokes equations.

We have seen that there is no simple relation between Eulerian and Lagrangian behaviors. In the following, we shall discuss two important points:

- (i) what are the effects on the Lagrangian chaos of the transition to Eulerian chaos, i.e. from $\lambda_E = 0$ to $\lambda_E > 0$.
- (ii) whether a chaotic velocity field ($\lambda_E > 0$) always implies an erratic motion of fluid particles.

The first point can be studied again within the $F = 5$ modes model (2.32). Increasing Re, the limit cycles bifurcate to new double period orbits followed by a period doubling transition to chaos and a strange attractor appears at $\mathrm{Re}_c \approx 28.73$, where λ_E becomes positive. These transitions have no signature on Lagrangian

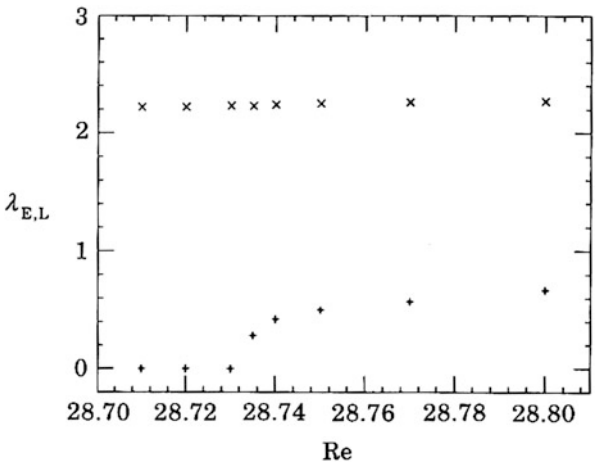

Fig. 2.7 Lyapunov exponents λ_E (+) and λ_L (×) as function of Re around Re_c, for the 5-mode model

behavior, as it is shown in Fig. 2.7, i.e. the onset of Eulerian chaos has no influence on Lagrangian properties.

This feature should be valid in most situations, since it is natural to expect that in generic cases there is a strong separation of the characteristic times for Eulerian and Lagrangian behaviors.

The second point—the conjecture that a chaotic velocity field always implies chaotic motion of particles—looks very reasonable. Indeed, it appears to hold in many systems [22]. Nevertheless, one can find a class of systems where it is false, e.g. Eqs. (2.24), (2.25) may exhibit Eulerian chaoticity $\lambda_{\mathrm{E}} > 0$, even if $\lambda_{\mathrm{L}} = 0$ [6].

Consider for example the motion of N point vortices in the plane with circulations Γ_i and positions $(x_i(t), y_i(t))$ $(i = 1, ..N)$ [1]:

$$\Gamma_i \frac{dx_i}{dt} = \frac{\partial H}{\partial y_i} \tag{2.37}$$

$$\Gamma_i \frac{dy_i}{dt} = -\frac{\partial H}{\partial x_i} \tag{2.38}$$

where

$$H = -\frac{1}{4\pi} \sum_{i \neq j} \Gamma_i \Gamma_j \ln r_{ij} \tag{2.39}$$

and $r_{ij}^2 = (x_i - x_j)^2 + (y_i - y_j)^2$.

The motion of N point vortices is described in an Eulerian phase space with $2N$ dimensions. Because of the presence of global conserved quantities, a system of three vortices is integrable and there is no exponential divergence of nearby

trajectories in phase space. For $N \geq 4$, apart from non generic initial conditions and/or values of the parameters Γ_i, the system is chaotic [1].

The motion of a passively advected particle located in $(x(t), y(t))$ in the velocity field defined by (2.37)–(2.38) is given

$$\frac{dx}{dt} = -\sum_i \frac{\Gamma_i}{2\pi} \frac{y - y_i}{R_i^2} \tag{2.40}$$

$$\frac{dy}{dt} = \sum_i \frac{\Gamma_i}{2\pi} \frac{x - x_i}{R_i^2} \tag{2.41}$$

where $R_i^2 = (x - x_i)^2 + (y - y_i)^2$.

Let us first consider the motion of advected particles in a three-vortices (integrable) system in which $\lambda_E = 0$. In this case, the stream function for the advected particle is periodic in time and the expectation is that the advected particles may display chaotic behavior. The typical trajectories of passive particles which have initially been placed respectively in close proximity of a vortex center or in the background field between the vortices display a very different behavior. The particle seeded close to the vortex center displays a regular motion around the vortex and thus $\lambda_L = 0$; by contrast, the particle in the background field undergoes an irregular and aperiodic trajectory, and λ_L is positive.

We now discuss a case where the Eulerian flow is chaotic i.e. $N = 4$ point vortices. Let us consider again the trajectory of a passive particle deployed in proximity of a vortex center. As before, the particle rotates around the moving vortex. The vortex motion is chaotic; consequently, the particle position is unpredictable on large times as is the vortex position. Nevertheless, the Lagrangian Lyapunov exponent for this trajectory is zero (i.e. two initially close particles around the vortex remain close), even if the Eulerian Lyapunov exponent is positive, see Fig. 2.8.

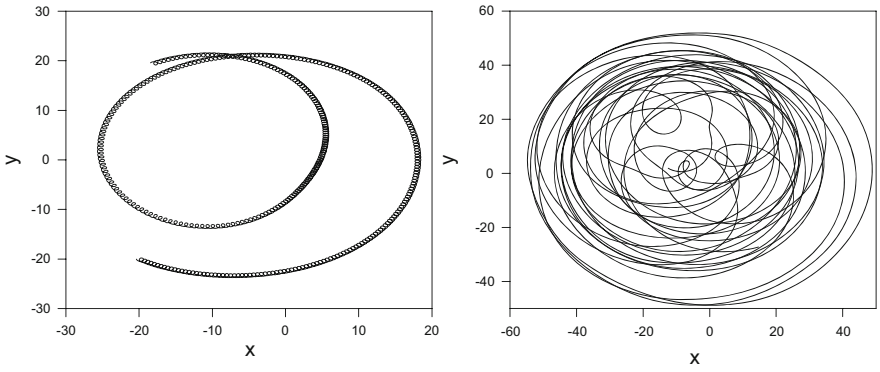

Fig. 2.8 Particle trajectories in the four-vortex system. Eulerian dynamics in this case is chaotic. The *left panel* shows a regular Lagrangian trajectory while the *right panel* shows a chaotic Lagrangian trajectory. The different behavior of the two particles is due to different initial conditions

This result indicates once more that there is no strict link between Eulerian and Lagrangian chaoticity.

One may wonder whether a much more complex Eulerian flow, such as $2d$ turbulence, may give the same scenario for particle advection: i.e. regular trajectories close to the vortices and chaotic behavior between the vortices. It has been shown that this is indeed the case [6] and that the chaotic nature of the trajectories of advected particles is not strictly determined by the complex time evolution of the turbulent flow.

We have seen that there is no general relation between Lagrangian and Eulerian chaos. In the typical situation Lagrangian chaos may appear also for regular velocity fields. However, it is also possible to have the opposite situation, with $\lambda_{\mathrm{L}} = 0$ in presence of Eulerian chaos, as in the example of Lagrangian motion inside vortex structures. As an important consequence of this discussion we remark that it is not possible to separate Lagrangian and Eulerian properties in a measured trajectory, e.g. a buoy in the oceanic currents [49]. Indeed, using the standard methods for data analysis [27], from Lagrangian trajectories one extracts the total Lyapunov exponent λ_{T} and not λ_{L} or λ_{E}.

2.3 Transport and Diffusion

2.3.1 The Random Walk Model for Brownian Motion

The simplest model of diffusion is the one-dimensional random walk. The walker moves on a line making discrete jumps $v_i = \pm 1$ at discrete times. The position of the walker, started at the origin at $t = 0$, will be

$$R(t) = \sum_{i=1}^{t} v_i \tag{2.42}$$

Assuming equiprobability for left and right jumps (no mean motion), the probability that at time t the walker is in position x will be

$$p_t(R = x) = prob\left[\begin{matrix}\frac{t-x}{2}\ steps - 1\\ \frac{t+x}{2}\ steps + 1\end{matrix}\right] = \frac{1}{2^t}\binom{t}{\frac{t+x}{2}} \tag{2.43}$$

For large t and x (i.e. after many microscopic steps) we can use Stirling approximation and get

$$p_t(x) = \sqrt{\frac{t}{2\pi(t^2 - x^2)}}\exp\left[-\frac{t+x}{2}\ln\frac{t+x}{2} - \frac{t-x}{2}\ln\frac{t-x}{2}\right] \tag{2.44}$$

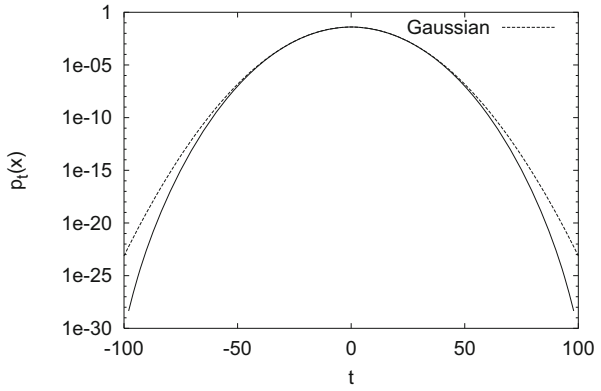

Fig. 2.9 Probability distribution function of the one-dimensional random walk after $t = 100$ steps. The *dashed line* is the Gaussian distribution

The core of the distribution recovers the well known Gaussian form, i.e. for $x \ll t$ from (2.44) we get

$$p_t(x) = \sqrt{\frac{1}{2\pi t}} \exp\left(-\frac{x^2}{2t}\right) \tag{2.45}$$

From (2.45) one obtains that the variance of the displacement follows diffusive behavior, i.e.

$$\langle x^2(t) \rangle = 2t \tag{2.46}$$

We stress that (2.45) is valid only asymptotically (i.e. for $t \to \infty$). This is a consequence of central limit theorem which assures Gaussian distributions and diffusive behavior in the limit of many independent jumps. In Fig. 2.9 we show the pdf $p_t(x)$ at step $t = 100$ compared with the Gaussian approximation. Deviations are evident in the tails.

The Gaussian distribution (2.45) can be obtained as the solution of the diffusion equation which governs the evolution of the probability in time. This is the Fokker-Planck equation for the particular stochastic process. A direct way to relate the one-dimensional random walk to the diffusion equation is obtained by introducing the master equation, i.e. the time evolution of the probability [26]:

$$p_{t+1}(x) = \frac{1}{2} p_t(x-1) + \frac{1}{2} p_t(x+1)\,. \tag{2.47}$$

In order to get a continuous limit, we introduce explicitly the steps Δx and Δt and write

$$\frac{p_{t+\Delta t}(x) - p_t(x)}{\Delta t} = \frac{(\Delta x)^2}{2\Delta t} \frac{p_t(x+\Delta x) + p_t(x-\Delta x) - 2p_t(x)}{(\Delta x)^2}\,. \tag{2.48}$$

Now, taking the limit $\Delta x, \Delta t \to 0$ in such a way that $(\Delta x)^2/\Delta t \to 2D$ (the factor 2 is purely conventional) we obtain the diffusion equation

$$\frac{\partial p(x,t)}{\partial t} = D\frac{\partial^2 p(x,t)}{\partial x^2}\,. \tag{2.49}$$

The way the limit $\Delta x, \Delta t \to 0$ is taken reflects the scaling invariance property of diffusion equation. The solution to (2.49) is readily obtained as

$$p(x,t) = \frac{1}{\sqrt{4\pi Dt}}\exp\left(-\frac{x^2}{4Dt}\right)\,. \tag{2.50}$$

Diffusion equation (2.49) is here written for the probability $p(x,t)$ of observing a marked particle (a tracer) in position x at time t. The same equation can have another interpretation, in which $p(x,t) = \theta(x,t)$ represents the concentration of a scalar quantity (marked fluid, temperature, pollutant) as function of time. The only difference is, of course, in the normalization.

2.3.2 Less Simple Transport Processes

As already stated time decorrelation is the key ingredient for diffusion. In the random walker model it is a consequence of randomness: the steps v_i are random uncorrelated variables and this assures the applicability of central limit theorem. But we can have a finite time correlation and thus diffusion also without randomness. To be more specific, let us consider the following deterministic model (standard map [21]):

$$\begin{cases} J(t+1) = & J(t) + K\sin\theta(t) \\ \theta(t+1) = \theta(t) + J(t+1) & \mod 2\pi \end{cases} \tag{2.51}$$

The map is known to display large-scale chaotic behavior for $K > K_c \simeq 0.9716$ and, as a consequence of deterministic chaos, $J(t)$ has diffusive behavior. For large times, $J(t)$ is large and thus the angle $\theta(t)$ rotates rapidly. In this limit, we can assume that at each step $\theta(t)$ decorrelates and thus write

$$\langle J(t)^2\rangle = K^2\langle\sum_{t'=1}^{t}\sin\theta(t')\rangle^2 \simeq K^2\langle\sin^2\theta\rangle t = 2Dt \tag{2.52}$$

The diffusion coefficient D, in the random phase approximation, i.e. assuming that $sin\theta(t)$ is not correlated with $sin\theta(t')$ for $t \neq t'$, is obtained by the above expression as $D_{RPA} = K^2/4$. In Fig. 2.10 we plot a numerical simulation obtained with the standard map. Diffusive behavior is clearly visible at long time.

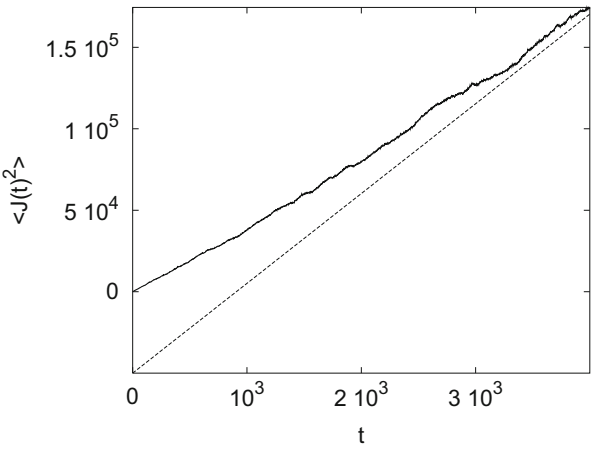

Fig. 2.10 Square dispersion $\langle J(t)^2 \rangle$ for the standard map at $K = 10.5$. The *dashed line* is the RPA prediction

The two examples discussed above are in completely different classes: stochastic for the random walk (2.42) and deterministic for the standard map (2.51). Despite this difference in the microscopic dynamics, both lead to a macroscopic diffusion equation and Gaussian distribution. This demonstrates how diffusion equation is of general applicability.

2.3.3 *Advection–Diffusion*

Let us now consider the more complex situation of dispersion in a non-steady fluid with velocity field $\mathbf{v}(\mathbf{x}, t)$. For simplicity will we consider incompressible flow (i.e. for which $\nabla \cdot \mathbf{v} = 0$) which can be laminar or turbulent, solution of Navier-Stokes equation or synthetically generated according to a given algorithm. In presence of $\mathbf{v}(\mathbf{x}, t)$, the diffusion equation (2.49) becomes the *advection-diffusion* equation for the concentration $\theta(\mathbf{x}, t)$ (2.10). This equation is linear in θ but nevertheless it can display very interesting and non trivial properties even in presence of simple velocity fields, as a consequence of Lagrangian chaos. In the following we will consider a very simple example of diffusion in presence of an array of vortices. The example will illustrate in a nice way the basic mechanisms and effects of interaction between deterministic ($\mathbf{v}$) and stochastic (D) components.

Let us remark that we will not consider here the problem of transport in turbulent velocity field. This is a very classical problem, with obvious and important applications, which has recently attracted a renewal theoretical interest as a model for understanding the basic properties of turbulence [52].

Before going into the example, let us make some general consideration. We have seen that in physical systems the molecular diffusivity is typically very small. Thus in (2.10) the advection term dominates over diffusion. This is quantified by the Peclet number, which is the ratio of the typical value of the advection term to the diffusive term

$$Pe = \frac{v_0 l_0}{D} \tag{2.53}$$

where v_0 is the typical velocity at the typical scale of the flow l_0. With $\tau_0 \simeq l_0/v_0$ we will denote the typical correlation time of the velocity.

The central point in the following discussion is the concept of *eddy diffusivity*. The idea is rather simple and dates back to the classical work of Taylor [54]. To illustrate this concept, let us consider a Lagrangian description of dispersion in which the trajectory of a tracer $\mathbf{x}(t)$ is given by (2.11). Being interested in the limit $Pe \to \infty$, in the following we will neglect, just for simplicity, the molecular diffusivity D, which is generally much lesser that the effective dynamical diffusion coefficient.

Starting from the origin, $\mathbf{x}(0) = 0$, and assuming $\langle \mathbf{v} \rangle = 0$ we have $\langle \mathbf{x}(t) \rangle = 0$ for ever. The square displacement, on the other hand, grows according to

$$\frac{d}{dt}\langle \frac{1}{2}\mathbf{x}(t)^2 \rangle = \langle \mathbf{x}(t) \cdot \mathbf{v}_L(t) \rangle = \int_0^t \langle \mathbf{v}_L(s) \cdot \mathbf{v}_L(t) \rangle ds \tag{2.54}$$

where we have introduced, for simplicity of notation, the Lagrangian velocity $\mathbf{v}_L(t) = \mathbf{v}(\mathbf{x}(t), t)$. Define the Lagrangian correlation time τ_L from

$$\int_0^\infty \langle \mathbf{v}_L(s) \cdot \mathbf{v}_L(0) \rangle ds = \langle \mathbf{v}_L(0)^2 \rangle \tau_L \tag{2.55}$$

and assume that the integral converge so that τ_L is finite. From (2.54), for $t \gg \tau_L$ we get

$$\langle \mathbf{x}(t)^2 \rangle = 2\tau_L \langle \mathbf{v}_L^2 \rangle t \tag{2.56}$$

i.e. diffusive behavior with diffusion coefficient (eddy diffusivity) $D^E = \tau_L \langle \mathbf{v}_L^2 \rangle$.

This simple derivation shows, once more, that diffusion has to be expected in general in presence of a finite correlation time τ_L. Coming back to the advection-diffusion equation (2.10), the above argument means that for $t \gg \tau_L$ we expect that the evolution of the concentration, for scales larger than l_0, can be described by an effective diffusion equation, i.e.

$$\frac{\partial \langle \theta \rangle}{\partial t} = D^E_{ij} \frac{\partial^2 \langle \theta \rangle}{\partial x_i \partial x_j} \tag{2.57}$$

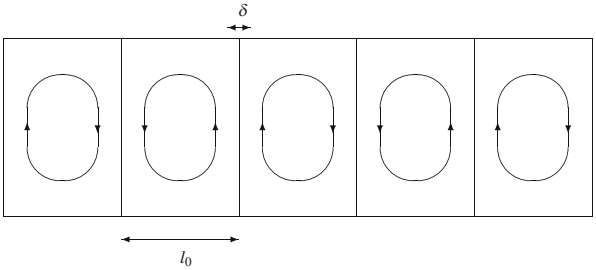

Fig. 2.11 Cellular flow model. l_0 is the size of vortices, δ is the thickness of the boundary layer

The computation of the eddy diffusivity for a given Eulerian flow is not an easy task. It can be done explicitly only in the case of simple flows, for example by means of homogenization theory [9, 45]. In the general case it is relatively simple [9] to give some bounds, the simplest one being $D^E \geq D$, i.e. the presence of a (incompressible) velocity field enhances large-scale transport. To be more specific, let us now consider the example of transport in a one-dimensional array of vortices (cellular flow) sketched in Fig. 2.11. This simple two-dimensional flow is useful for illustrating the transport across barrier. Moreover, it naturally arises in several fluid dynamics contexts, such as, for example, convective patterns [53].

Let us denote by v_0 the typical velocity inside the cell of size l_0 and let D the molecular diffusivity. Because of the cellular structure, particles inside a vortex can exit only as a consequence of molecular diffusion. In a characteristic vortex time $\tau_0 \sim l_0/v_0$, only the particles in the boundary layer of thickness δ can cross the separatrix where

$$\delta^2 \sim D\tau_0 \sim D\frac{l_0}{v_0}\,. \tag{2.58}$$

These particles are ballistically advected by the velocity field across the vortex so they see a "diffusion coefficient" l_0^2/τ_0. Taking into account that this fraction of particles is δ/l_0 we obtain an estimation for the effective diffusion coefficient as

$$D^E \sim \frac{\delta}{l_0}\frac{l_0^2}{\tau_0} \sim \sqrt{Dl_0v_0} \sim DPe^{1/2} \tag{2.59}$$

The above result, which can be made more rigorous, was confirmed by nice experiments made by Solomon and Gollub [53]. Because, as already stressed above, typically $Pe \gg 1$, one has from (2.59) that $D^E \gg D$. On the other hand, this result do not mean that molecular diffusion D plays no role in the dispersion process. Indeed, if $D = 0$ there is not mechanism for the particles to exit from vortices.

Diffusion equation (2.57) is the typical long-time behavior in generic flow. There exist also the possibility of the so-called anomalous diffusion, i.e. when the

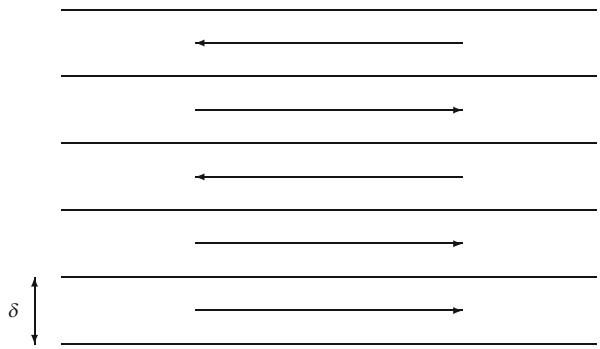

Fig. 2.12 Random shear of $\pm v_0$ velocity in strips of size δ

spreading of particle do not grow linearly in time, but with a power law

$$\langle x^2(t)\rangle \sim t^{2\nu} \tag{2.60}$$

with $\nu \neq 1/2$. The case $\nu > 1/2$ (formally $D^E = \infty$) is called super-diffusion; sub-diffusion, i.e. $\nu < 1/2$ (formally $D^E = 0$), is possible only for compressible velocity fields.

Super-diffusion arises when the Taylor argument for deriving (2.56) fails and formally $D^E \to \infty$. This can be due to one of the following mechanisms:

(a) the divergence of $\langle \mathbf{v}_L^2 \rangle$ (which is the case of *Lévy flights*), or
(b) the lack of decorrelation and thus $T_L \to \infty$ (*Lévy walks*). The second case is more physical and it is related to the existence of strong correlations in the dynamics, even at large times and scales.

One of the simplest examples of Lévy walks is the dispersion in a quenched random shear flow [16, 32]. The flow, sketched in Fig. 2.12, is a super-position of strips of size δ of constant velocity v_0 with random directions.

Let us now consider a particle which moves according to the flow of Fig. 2.12. Because the velocity field is in the x direction only, in a time t the typical displacement in the y direction is due to molecular diffusion only

$$\delta y \sim \sqrt{Dt} \tag{2.61}$$

and thus in this time the walker visits $N = \delta y/\delta$ strips. Because of the random distribution of the velocity in the strips, the mean velocity in the N strips is zero, but we may expect about $\sqrt{N}$ unbalanced strips (say in the right direction). The fraction of time t spent in the unbalanced strips is $t\sqrt{N}/N$ and thus we expect a displacement

$$\delta x \sim v_0 \frac{t}{\sqrt{N}} \,. \tag{2.62}$$

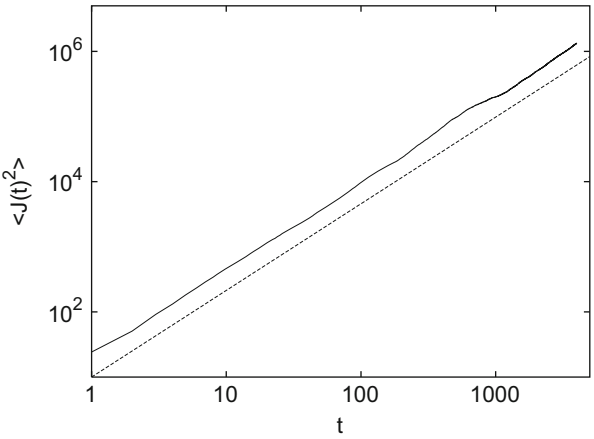

Fig. 2.13 Square dispersion $\langle J(t)^2 \rangle$ for the standard map at $K = 6.91\ldots$. The *dashed line* is $t^{1.33}$

From (2.61) we have $N \sim \sqrt{Dt}/\delta$ and finally

$$\langle \delta x^2 \rangle \sim \frac{v_0^2 \delta}{\sqrt{D}} t^{3/2} \tag{2.63}$$

i.e. a super-diffusive behavior with exponent $\nu = 3/4$.

The origin of the anomalous behavior in the above example is in the quenched nature of the shear and in the presence of large stripes with positive (or negative) velocity in the x direction. This leads to an infinite decorrelation time for Lagrangian tracers and thus to a singularity in (2.56). We conclude this example by observing that for $D \to 0$ (2.63) gives $\langle \delta x^2 \rangle \to \infty$. This is not a surprise because in this case the motion is ballistic and the correct exponent becomes $\nu = 1$.

As it was in the case of standard diffusion, also in the case of anomalous diffusion the key ingredient is not randomness. Again, the standard map model (2.51) is known to show anomalous behavior for particular values of K [56]. An example is plotted in Fig. 2.13 for $K = 6.91\ldots$ in which one find $\langle J(t)^2 \rangle \sim t^{1.33}$.

The qualitative mechanism for anomalous dispersion in the standard map can be easily understood: a trajectory of (2.51) for which $K \sin \theta^* = 2\pi m$ with m integer, corresponds to a fixed point for θ (because the angle is defined modulo 2π) and linear growth for $J(t)$ (ballistic behavior). It can be shown that the stability region of these trajectories in phase space decreases as $1/K$ [31, 56] and, for intermediate value of K, they play a important role in transport: particles close to these trajectories feel very long correlation times and perform very long jumps. The contribution of these trajectory, as a whole, gives the observed anomalous behavior.

Now, let us consider the cellular flow of Fig. 2.11 as an example of sub-diffusive transport. We have seen that asymptotically (i.e. for $t \gg l_0^2/D$) the transport is diffusive with effective diffusion coefficient which scales according to (2.59). For

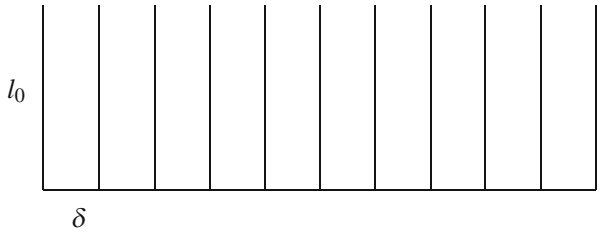

Fig. 2.14 The comb model geometry

intermediate times $l_0/v_0 \ll t \ll l_0^2/D$, when the boundary layer structure has set in, one expects anomalous sub-diffusive behavior as a consequence of fraction of particles which are trapped inside vortices [58]. A simple model for this problem is the comb model [28, 32]: a random walk on a lattice with comb-like geometry. The base of the comb represents the boundary layer of size δ around vortices and the teeth, of length l_0, represent the inner area of the convective cells. For the analogy with the flow of Fig. 2.11 the teeth are placed at the distance $\delta \sim \sqrt{Dl_0/v_0}$ (2.58) (Fig. 2.14).

A spot of random walker (dye) is placed, at time $t = 0$, at the base of the comb. In their walk on the x direction, the walkers can be trapped into the teeth (vortices) of dimension l_0. For times $l_0/v_0 \ll t \ll l_0^2/D$, the dye invades a distance of order $(Dt)^{1/2}$ along the teeth. The fraction $F(t)$ of active dye on the base (i.e. on the separatrix) decreases with time as

$$F(t) \sim \frac{\delta}{(Dt)^{1/2}} \tag{2.64}$$

and thus the effective dispersion along the base coordinate b is

$$\langle b^2(t) \rangle \sim F(t) Dt \sim \delta (Dt)^{1/2} \tag{2.65}$$

In the physical space the corresponding displacement will be

$$\langle x^2(t) \rangle \sim \langle b^2(t) \rangle \frac{l_0}{\delta} \sim l_0 (PeDt)^{1/2} \tag{2.66}$$

i.e. we obtain a sub-diffusive behavior with $\nu = 1/4$.

The above argument is correct only for the case of free-slip boundary conditions. In the physical case of no-slip boundaries, one obtains a different exponent $\nu = 1/3$ [58]. The latter behavior has been indeed observed in experiments [18].

2.3.4 Beyond the Diffusion Coefficient

From the above discussion it is now evident that diffusion, being an asymptotic behavior, needs large scale separation in order to be observed. In other words, diffusion arises only if the Lagrangian correlation time τ_L (2.55) is finite *and* the observation time is $t \gg \tau_L$ or, according to (2.57), if the dispersion is evaluated on scales much larger than l_0.

On the other hand, there are many physical and engineering applications in which such a scale separation is not achievable. A typical example is the presence of boundaries which limit the scale of motion on scales $L \sim l_0$. In these cases, it is necessary to introduce non-asymptotic quantities in order to correctly describe dispersion. Before discussing the non-asymptotic statistics let us show, with an example, how it can be dangerous to apply the standard analysis in non-asymptotic situation. We consider the motion of tracers advected by the two-dimensional flow generated by 4 point vortices in a disk. The evolution equation is given by (2.37) and (2.39) but now in (2.39), instead of $\ln r_{ij}$, one has to consider the Green function $G(r_{ij})$ on the disk [43].

A set of 10,000 tracers are initially placed in a very small cloud in the center of the disk. Because of the chaotic advection induced by the vortices, at large time we observe the tracers dispersed in all the disk. In the following we will consider *relative* dispersion, i.e. the mean size of a cluster of particles

$$R^2(t) = \langle |\mathbf{x}(t) - \langle \mathbf{x}(t) \rangle|^2 \rangle \tag{2.67}$$

Of course, for separation larger than the typical scale of the flow, l_0, the particles move independently and thus we expect again the asymptotic behavior

$$R^2(t) \simeq 2Dt \qquad \text{if} \qquad R^2(t)^{1/2} \gg l_0 \tag{2.68}$$

For very small separation we expect, assuming that the Lagrangian motion is chaotic,

$$R^2(t) \simeq R^2(0) e^{2\lambda t} \qquad \text{if} \qquad R^2(t)^{1/2} \ll l_0 \tag{2.69}$$

where λ is the Lagrangian Lyapunov exponent [22].

The computation of the standard dispersion for the tracers in the point vortex model is plotted in Fig. 2.15. At very long time $R^2(t)$ reaches the saturation value due to the boundary.

For intermediate times a power-law behavior with an anomalous exponent $\nu = 1.8$ is clearly observable. Of course the anomalous behavior is spurious: after the discussion of the previous section, we do not see any reason for observing super-diffusion in the point vortex system. The apparent anomaly is simply due to the lack of scale separation and thus to the crossover from the exponential regime (2.69) to the saturation value.

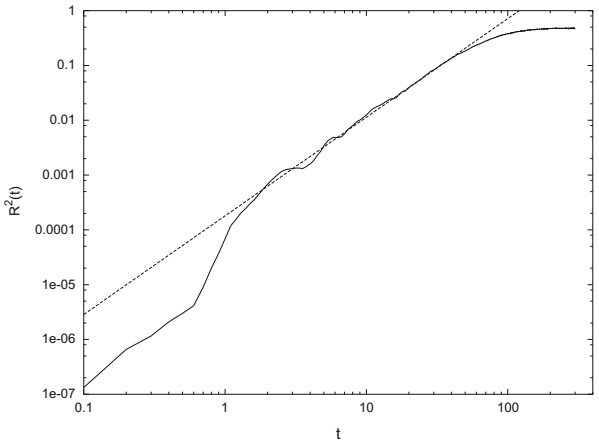

Fig. 2.15 $R^2(t)$ computed for the four point vortex system. The *dashed line* is the power law $\langle R^2(t)\rangle \sim t^{1.8}$

To partially avoid this kind of problem, it has been introduced a new indicator based on *fixed scale* analysis [5, 12]. The idea is very simple and it is based on exit time statistics. Given a set of thresholds $\delta_n = \delta_0 r^n$, one measures the exit time $T_i(\delta_n)$ it takes for the separation $R_i(t)$ to grow from δ_n to δ_{n+1}. The factor r may be any value > 1, but it should be not too large in order to have a good separation between the scales of motion.

Performing the exit time experiment over N particle pairs, from the average doubling time $\langle T(\delta)\rangle = 1/N \sum_i T_i(\delta)$, one defines the Finite Size Lyapunov Exponent (FSLE) as

$$\lambda(\delta) = \frac{\ln r}{\langle T(\delta)\rangle} \tag{2.70}$$

which recovers the standard Lagrangian Lyapunov exponent in the limit of very small separations $\lambda = \lim_{\delta\to 0} \lambda(\delta)$.

The finite size diffusion coefficient $D(\delta)$ is defined, within this framework, as

$$D(\delta) = \delta^2 \lambda(\delta) \tag{2.71}$$

For standard diffusion $D(\delta)$ approaches the diffusion coefficient D (see (2.68)) in the limit of very large separations ($\delta \gg l_0$). This result stems from the scaling of the doubling times $\langle T(\delta)\rangle \sim \delta^2$ for normal diffusion.

Thus, according to (2.68)–(2.69), the asymptotic behaviors of the FSLE are

$$\lambda(\delta) \sim \begin{cases} \lambda & \text{if} \quad \delta \ll l_0 \\ D/\delta^2 & \text{if} \quad \delta \gg l_0 \end{cases} \tag{2.72}$$

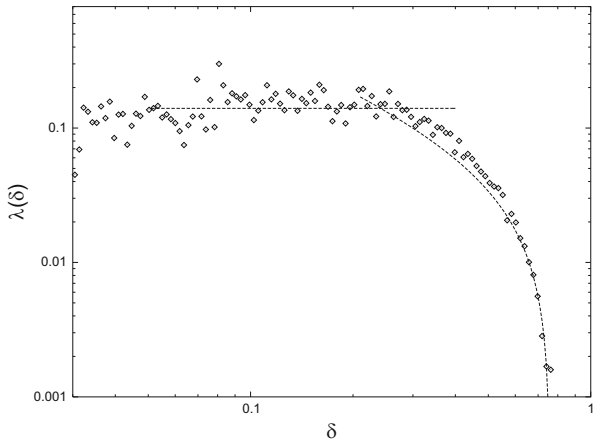

Fig. 2.16 FSLE $\lambda(\delta)$ for the tracers advected by the point vortex system. The *horizontal line* represent the Lagrangian Lyapunov exponent ($\lambda \simeq 0.14$). The *dashed curve* is the saturation regime with $\delta_{max} = 0.76$

In presence of boundary at scales $L \sim l_0$, the second regime is not observable. For separation very close to the saturation value $\delta_{max} \simeq L$ one expects the following behavior to hold for a broad class of systems [5]:

$$\lambda(\delta) \propto \frac{\delta_{max} - \delta}{\delta} \tag{2.73}$$

Let us now come back to the point vortex system. The FSLE for this problem is plotted in Fig. 2.16.

With the finite scale analysis one clearly see that only two regime survive: exponential at small scales (chaotic advection) and saturation at large scale. The apparent anomalous regime of Fig. 2.15 is a spurious effect induced by taking the average at fixed time.

The finite scale method can be easily applied to the analysis of experimental data [11]. An example is the study of Lagrangian dispersion in a experimental convective cell. The cell is a rectangular tank filled with water and heated by a linear heat source placed on the bottom. The heater generates a vertical plume which induces a general two-dimensional circulation of two counter-rotating vortices. For high values of the Rayleigh number (i.e. heater temperature) the flow is not stationary and the plume oscillates periodically. In these conditions, Lagrangian tracers can jump from one side to the other of the plume as a consequence of chaotic advection (Fig. 2.17).

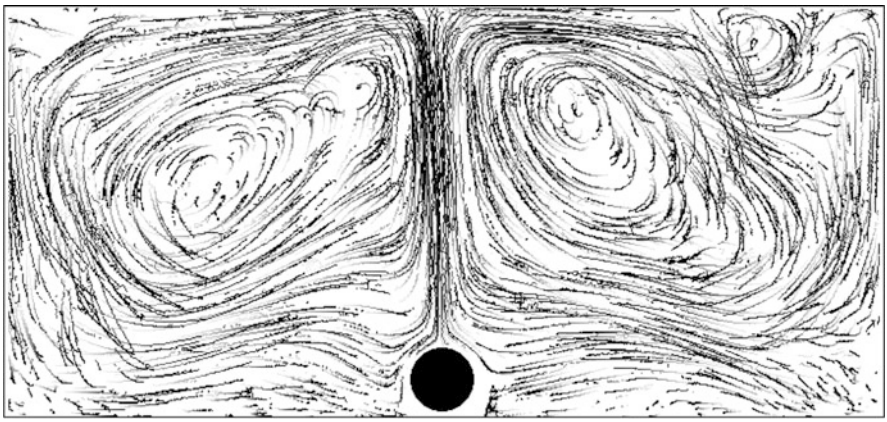

Fig. 2.17 An example of trajectories obtained by PTV technique in the convective cell at $Ra = 2.39 \times 10^8$. The vertical thermal plume is clearly observable. The *dark circle* on the bottom represents the heat source

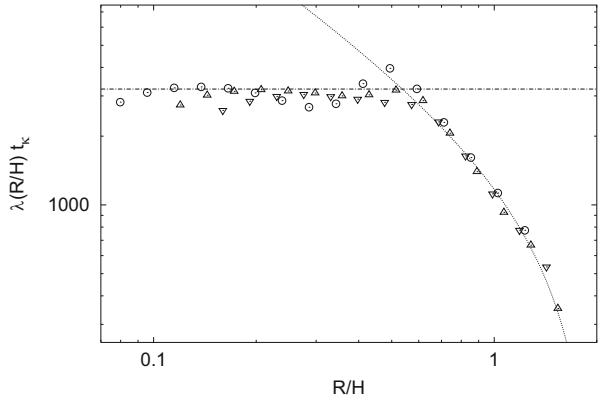

Fig. 2.18 FSLE $\lambda(\delta)$ computed for the convective cell at different initial separations (*different symbols*). The *straight line* is the Lyapunov exponent and the *dashed curve* represents the saturation regime

The study of Lagrangian dispersion has been done by means of the FSLE [11]. In Fig. 2.18 we plot the result for $Ra = 2.39 \times 10^8$. Again, because there is no scale separation between the Eulerian characteristic scale l_0 (vortex size) and the basin scale L we cannot expect diffusion behavior. Indeed, the FSLE analysis reveals the chaotic regime $\lambda(\delta) = \lambda$ at small scales and the saturation regime (2.73) at larger scale.

2.4 Barriers to Transport and Local Mixing Maps

The finite-scale Lyapunov exponent technique has been successfully applied to many other numerical and experimental situations, from the pair dispersion in fully developed turbulence [10], to the analysis of tracer motion in ocean and atmosphere [8, 35, 36, 38, 39], to laboratory experiments [37]. It has by now become a standard tool in the analysis of Lagrangian dispersion. Here we want briefly recall some applications of this methodology to cases in which a local, rather than global, description of the Lagrangian dispersion properties can have relevance to issues like the non homogeneous mixing of tracers inside a fluid, existence of persistent coherent structures in the velocity field, inhibition of mixing due to barrier effects between dynamically different regions of the flow. In this regard, the FSLE turns out to be the optimal indicator of the local mixing rate, and, more in general, a diagnostic tool of the ergodic properties of the flow.

Let us consider a $2D$ meandering jet model, Fig. 2.19, as prototype of energetic non linear currents like the Gulf Stream of the Polar Vortex. The flow is defined by a stream-function Ψ of the form [17, 51]:

$$\Psi = \frac{A}{k} \tanh \frac{k[y - B_0 \cos(k_0 x)]}{\sqrt{1 + B_0^2 k_0^2 \sin^2(k_0 x)}} - cy\,, \tag{2.74}$$

where x and y are the spatial coordinates of a fluid particle; A and k are velocity scale of the jet and cross-stream wavenumber, respectively; $k_0 = 2\pi/l_0$ and l_0 are wavenumber and spatial wavelength of the meanders, respectively; B_0 gives the amplitude of the meanders; the denominator defines the width of the jet and, last,

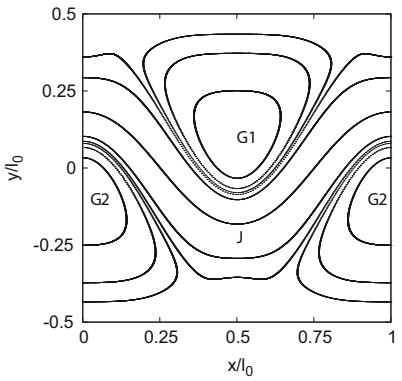

Fig. 2.19 Meandering jet model: (J) region of open streamlines (jet), in which fluid particles move from left to right; (G1) and (G2) regions of closed streamlines (gyres) with, respectively, anti-clockwise and clockwise rotation. In this plot the ratio between down-stream and cross-stream wavenumbers is $k_0/k \simeq 0.8$, and the ratio between meander amplitude and down-stream wavelength is $B_0/l_0 = 0.16$

c is a counter-stream velocity of the retrograde flow in the far field away from the central jet. Lagrangian trajectories are integrated according to (2.17) and (2.18), with Ψ given by (2.74).

In absence of an explicit time dependence in the stream-function, the flow is steady and particle trajectories coincide with the Ψ-isolines. In steady conditions, the initial positions of a set of particles completely determine the transport properties: tracers initially located inside the jet (open streamlines) travel downstream without bound, while tracers initially located inside a lateral vortex (closed streamlines) remain confined there all the time. Chaotic trajectories can be generated, for example, by replacing B_0 with $B(t)$ defined as:

$$B(t) = B_0 + \varepsilon \cdot \cos(\omega t)\,. \tag{2.75}$$

This term induces a periodic oscillation of the meanders, with period $T_p = 2\pi/\omega$ and amplitude ε, around the mean value B_0. The values of the perturbation parameters, ω and ε, control the width of the chaotic layer inside which Lagrangian trajectories display strong sensitivity to small perturbations [50]. In particular, keeping ω fixed, the amplitude ε can be varied to pass from a weakly chaotic regime, in which chaos is confined in a thin layer around the separatrices of the flow, to a strong chaotic regime, in which any subset of the spatial domain contains chaotic motions, i.e. in conditions of overlap of the resonances [21]. Let us observe that in actual geophysical systems there can be natural transitions between these two limit cases, e.g. in presence of a periodic forcing that modulates the amplitude of the time-dependent term in the stream-function. In order to evaluate the spatial distribution of the local mixing rate on finite scales, the local FSLE can be defined as:

$$\lambda_{\delta,r}(x,y) = \frac{1}{T(x,y)} \ln \frac{\Delta}{\delta} \tag{2.76}$$

where $T(x,y)$ is the time taken by a perturbation (i.e. trajectory separation) having size δ in (x,y) to grow up to size $\Delta = r \cdot \delta$, with $r > 1$. In practical applications, the growth factor r can be even several orders of magnitude larger than $O(1)$, depending on the resolution of the trajectories, in order to distinguish regions with different dynamical properties, e.g. chaotic/non chaotic, from each other. The logic behind the use of this diagnostic tool is to set the final distance Δ, i.e. setting r at fixed δ, at a value comparable with the size of the hypothetical coherent structures in the velocity field. If the coherent structures last for a sufficiently long time, then their effects to tracer transport across the domain can be detected qualitatively and quantitatively by the local FSLE mapping.

In Fig. 2.20 we show the local mixing rates for the meandering jet model in the two cases: weak perturbed conditions, with a chaotic layer confined around the separatrices (upper panel) and strong perturbed conditions, with the chaotic layer extended to all the available space (lower panel). In the first case, black spots in the FSLE field correspond to no dispersion beyond a certain separation scale, in the middle of the gyres and in the center of the jet, i.e. far from the separatrices; in the

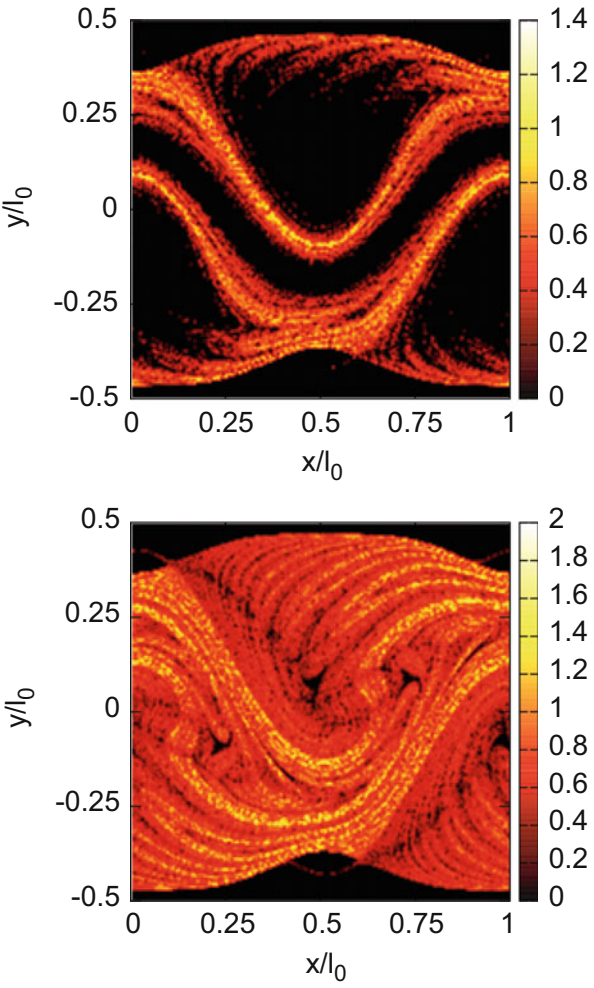

Fig. 2.20 FSLE maps for the meandering jet model: weak chaos, central barrier (*upper panel*); strong chaos, no barrier (*lower panel*). Spatial coordinates are measured in unit of the stream wavelength l_0; the local FSLE $\lambda_{\delta,r}(x, y)$ is measured in unit of the inverse characteristic time τ_a^{-1} of the jet. Parameters set up: $\delta/l_0 \simeq 10^{-3}$; $r \simeq 10^2$; $B_0/l_0 = 0.16$; $\varepsilon/B_0 \simeq 0.15$ (*upper panel*) and $\varepsilon/B_0 \simeq 0.3$ (*lower panel*)

second case, every point of the domain is "turned on", meaning that every region of the flow results to be accessible to any trajectory starting from arbitrary initial conditions (ergodic property).

This technique was applied for the first time to geophysical data in the work by Boffetta et al. [13], where the barrier effect of the Antarctic Polar Vortex against tracer mixing between high and low latitudes was analyzed and discussed. Other authors have later adopted this type of strategy in various atmospheric and oceanic systems [23, 25, 30, 33, 34, 57], where the role of coherent Lagrangian structures is assumed to characterize mixing and transport properties in non asymptotic conditions.

2.5 Conclusions

In this chapter we have reviewed some basic concepts of chaotic dynamical systems, related in particular to the predictability properties of trajectories in the phase space. We have considered the physically relevant example of Lagrangian chaos in which the phase space coincides with the physical space. By considering some specific examples, we have discussed the relation between Lagrangian chaos and the Eulerian properties of the advecting flow, showing that Lagrangian chaos can be present even in period of stationary flow. In the last part of the chapter we have shown how concepts and techniques of stochastic processes can be used to describe transport properties in chaotic systems. We discussed the generic appearance of diffusive behavior and the conditions under which anomalous diffusion can be expected. Realistic limitations, such as the presence of boundaries, and their effects on the asymptotic properties of transport have been discussed. At last, recent analysis techniques based on the measure of the Finite-Scale Lyapunov Exponent, i.e. the generalization of the maximum Lyapunov exponent to non infinitesimal perturbations, have been described and discussed as established indicators of both global and local properties of relative dispersion.

References

1. Aref, H.: Integrable, chaotic and turbulent vortex motion in two-dimensional flows. Ann. Rev. Fluid Mech. **15**, 345–389 (1983)
2. Aref, H.: Stirring by chaotic advection. J. Fluid Mech. **143**, 1–21 (1984)
3. Aref, H., Balachandar, S.: Chaotic advection in a Stokes flow. Phys. Fluids **29**, 3515–3521 (1986)
4. Arnold, V.I.: Sur une propriété topologique des applications globalement canoniques de la mécanique classique. C. R. Acad. Sci. Paris A **261**, 3719–3722 (1965)
5. Artale, V., Boffetta, G., Celani, A., Cencini, M., Vulpiani, A.: Dispersion of passive tracers in closed basins: beyond the diffusion coefficient. Phys. Fluids A **9**, 3162–3171 (1997)
6. Babiano, A., Boffetta, G., Provenzale, A., Vulpiani, A.: Chaotic advection in point vortex models and two-dimensional turbulence. Phys. Fluids A **6**, 2465–2474 (1994)
7. Benettin, G., Giorgilli, A., Galgani, L., Strelcyn, J.M.: Lyapunov characteristic exponents for smooth dynamical systems and for Hamil- tonian systems; a method for computing all of them. Meccanica **15**, 9–30 (1980)
8. Berti, S., Dos Santos, F.A., Lacorata, G., Vulpiani, A.: Lagrangian drifter dispersion in the southwestern Atlantic Ocean. J. Phys. Oceanogr. **41**, 1659–1672 (2011)
9. Biferale, L., Crisanti, A., Vergassola, M., Vulpiani, A.: Eddy diffusivities in scalar transport. Phys. Fluids **7**, 2725–2734 (1995)
10. Boffetta, G., Celani, A.: Pair dispersion in turbulence. Physica A **280**, 1–9 (2000)
11. Boffetta, G., Cencini, M., Espa, S., Querzoli, G.: Chaotic advection and relative dispersion in an experimental convective flow. Phys. Fluids **12**, 3160–3167 (2000)
12. Boffetta, G., Celani, A., Cencini, M., Lacorata, G., Vulpiani, A.: Non-asymptotic properties of transport and mixing. Chaos **10**(1), 50–60 (2000)
13. Boffetta, G., Lacorata, G., Redaelli, G., Vulpiani, A.: Barriers to transport: a review of different techniques. Physica D **159**, 58–70 (2001)

14. Boffetta, G., Cencini, M., Falcioni, M., Vulpiani, A.: Predictability: a way to characterize complexity. Phys. Rep. **356**(6), 367–474 (2002)
15. Boldrighini, C., Franceschini, V.: A five-mode truncation of the plane Navier-Stokes equations. Commun. Math. Phys. **64**, 159–170 (1979)
16. Bouchaud, J.P., Georges, A.: Anomalous diffusion in disordered media: statistical mechanisms, models and physical applications. Phys. Rep. **195**, 127–293 (1990)
17. Bower, A.S.: A simple kinematic mechanism for mixing fluid parcels across a meandering jet. J. Phys. Oceanogr. **21**, 173–180 (1991)
18. Cardoso, O., Tabeling, P.: Anomalous diffusion in a linear array of vortices. Europhys. Lett. **7**, 225–230 (1988)
19. Chaiken, J., Chu, C.K., Tabor, M., Tan, Q.M.: Lagrangian turbulence in Stokes flow. Phys. Fluids **30**, 687–694 (1987)
20. Chandrasekhar, S.: Stochastic problems in physics and astronomy. Rev. Mod. Phys. **15**, 1–89 (1943)
21. Chirikov, B.V.: A universal instability of many dimensional oscillator systems. Phys. Rep. **52**, 263–379 (1979)
22. Crisanti, A., Falcioni, M., Paladin, G., Vulpiani, A.: Lagrangian chaos: transport, mixing and diffusion in fluids. Riv. Nuovo Cim. **14**, 1–80 (1991)
23. d'Ovidio, F., Isern-Fontanet, J., Lopez, C., Hernandez-Garcia, E., Garcia-Ladona, E.: Comparison between Eulerian diagnostics and finite-size Lyapunov exponents computed from altimetry in the Algerian basin. Deep Sea Res. I **56**, 15–31 (2009)
24. Falcioni, M., Paladin, G., Vulpiani, A.: Regular and chaotic motion of fluid-particles in two-dimensional fluids. J. Phys. A: Math. Gen. **21**, 3451–3462 (1988)
25. Garcia-Olivares, A., Isern-Fontanet, J. Garcia-Ladona, E.: Dispersion of passive tracers and finite-scale Lyapunov exponents in the Western Mediterranean Sea. Deep Sea Res. I Oceanogr. Res. Pap. **54**(2), 253–268 (2007)
26. Gardiner, C.W.: Handbook of Stochastic Methods. Springer, Berlin (1985)
27. Grassberger, P., Procaccia, I.: Estimation of the Kolmogorov entropy from a chaotic signal. Phys. Rev. A **28**, 2591–2593 (1983)
28. Havlin, S., Ben-Avraham, D.: Diffusion in disordered media. Adv. Phys. **36**, 695–798 (1987)
29. Hénon, M.: Sur la topologie des lignes de courant dans un cas particulier. C. R. Acad. Sci. Paris A **262**, 312–314 (1966)
30. Hernandez-Carrasco, I., Lopez, C., Hernandez-Garcia, E., Turiel, A.: How reliable are finite-size Lyapunov exponents for the assessment of ocean dynamics? Ocean Model. **36**, 208–218 (2011)
31. Ichikawa, Y.H., Kamimura, T., Hatori, T.: Stochastic diffusion in the standard map. Physica D **29**, 247–255 (1987)
32. Isichenko, M.B.: Percolation, statistical topography, and transport in random media. Rev. Mod. Phys. **64**, 961–1044 (1992)
33. Joseph, B., Legras, B.: Relation between kinematic boundaries, stirring and barriers for the Antarctic Polar Vortex. J. Atmos. Sci. **59**, 1198–1212 (2002)
34. Koh, T.-Y., Legras, B.: Hyperbolic lines and the stratospheric Polar Vortex. Chaos **12**(2), 382–394 (2002)
35. Lacasce, J.H.: Statistics from Lagrangian observations. Prog. Oceanogr. **77**, 1–29 (2008)
36. Lacasce, J.H., Ohlmann, C.: Relative dispersion at the surface of the Gulf of Mexico. J. Mar. Res. **61**, 285–312 (2003)
37. Lacorata, G., Espa, S.: On the influence of a β-effect on Lagrangian diffusion. Geophys. Res. Lett. **39**, L11605 (2012)
38. Lacorata, G., Aurell, E., Vulpiani, A.: Drifter dispersion in the Adriatic Sea: Lagrangian data and chaotic model. Ann. Geophys. **19**, 1–9 (2001)
39. Lacorata, G., Aurell, E., Legras, B., Vulpiani, A.: Evidence for a $k^{-5/3}$ spectrum from the EOLE Lagrangian balloon in the low stratosphere. J. Atmos. Sci. **61**, 2936–2942 (2004)
40. Lamb, H.: Hydrodynamics. Dover Publications, New York (1945)
41. Landau, L.D., Lifshitz, L.: Fluid Mechanics. Pergamon Press, New York (1987)

42. Lee, J.: Triad-angle locking in low-order models of the 2D Navier-Stokes equations. Physica D **24**, 54–70 (1987)
43. Lin, C.C.: On the motion of vortices in two dimensions. Proc. Natl. Acad. Sci. USA **27**, 575–577 (1941)
44. Lorenz, E.N.: Deterministic nonperiodic flow. J. Atmos. Sci. **20**, 130–141 (1963)
45. Majda, A.J., Kramer, P.R.: Simplified models for turbulent diffusion: theory, numerical modeling and physical phenomena. Phys. Rep. **314**, 237–574 (1999)
46. Marsden, J.E., McCracken, M.: The Hopf Bifurcation and Its Applications. MIT Press, Cambridge, MA (1975)
47. Maxey, M.R., Riley, J.J.: Equation of motion for a small rigid sphere in a non uniform flow. Phys. Fluids **26**, 883–889 (1983)
48. Moffat, H.K.: Transport effects associated with turbulence, with particular attention to the influence of helicity. Rep. Prog. Phys. **46**, 621–664 (1983)
49. Osborne, A.R., Kirwan, A.D., Provenzale, A., Bergamasco, L.: A search for chaotic behaviour in large and mesoscale motions in the Pacific Ocean. Physica D **23**, 75–83 (1986)
50. Ott, E.: Chaos in Dynamical Systems. Cambridge University Press, Cambridge (1993)
51. Samelson, R.M.: Fluid exchange across a meandering jet. J. Phys. Oceanogr. **22**, 431–440 (1992)
52. Shraiman, B.I., Siggia, E.D.: Scalar Turbulence. Nature **405**, 639–646 (2000)
53. Solomon, T.H., Gollub, J.P.: Passive transport in steady Rayleigh-Bénard convection. Phys. Fluids **31**, 1372–1379 (1988)
54. Taylor, G.I.: Diffusion by continuous movements. Proc. Lond. Math. Soc. **2**, 196–211 (1921)
55. Tritton, D.J.: Physical Fluid Dynamics. Oxford Science Publications, Oxford (1988)
56. Vergassola, M.: In: Benest, D., Froeschlé, C. (eds.) Analysis and Modelling of Discrete Dynamical Systems, vol. 229. Gordon & Breach, Amsterdam (1998)
57. Wei, X., Ni, P., Zhan, H.: Monitoring cooling water discharge using Lagrangian coherent structures: a case study in Daya Bay, China. Mar. Pollut. Bull. **75**, 105–113 (2013)
58. Young, W., Pumir, A., Pomeau, Y.: Anomalous diffusion of tracer in convection rolls. Phys. Fluids **1**, 462–469 (1989)

Chapter 3
Small Scale Hydrodynamics

Matteo Colangeli

Abstract The purpose of this work is to offer a brief survey of some of the mathematical methods useful to bridge different levels of description, i.e. from the set-up of classical kinetic theory of gases to hydrodynamics. Most of the standard mathematical techniques, in this field, stem from the seminal Chapman–Enskog expansion, which constitutes an important success in kinetic theory, as it made possible to formally derive the Navier-Stokes hydrodynamics from the Boltzmann equation. Yet, almost a century of effort to extend the hydrodynamic description beyond the Navier-Stokes-Fourier approximation failed even in the case of small deviations around the equilibrium, due to the onset of instabilities which also cause the violation of the H-Theorem. A different route, in kinetic theory, is represented by the recent Invariant Manifold method. The latter technique allows one to restore stability in the hydrodynamic equations, which remain thus applicable even at short length scales, under the hypothesis of validity of the Local Equilibrium condition.

3.1 Introduction

A certain number of techniques have been designed, in kinetic theory of gases, to derive macroscopic time evolution equations from the Boltzmann equation. Most of these methods require the single-particle distribution function to be parameterized by a set of distinguished fields, such as the standard hydrodynamic ones: the number (or mass) density, momentum vector, and temperature. This stands as a plausible assumption as long as the microscopic dynamics enjoys a vast separation of time and length scales, and provided that the condition of Local Equilibrium is granted. Furthermore, the derivation of hydrodynamics from kinetic theory is often understood in terms of the so-called *hydrodynamic limit* of the Boltzmann equation. Loosely speaking, one is interested, typically, in the scaling of the Boltzmann equation with respect to some reference macroscopic length and time scales, which are expected to largely dominate the intrinsic kinetic scales. Nonetheless, it makes

M. Colangeli (✉)
Gran Sasso Science Institute, Via. F. Crispi 7, 00167 L'Aquila, Italy
e-mail: matteo.colangeli@gssi.infn.it

S. Banerjee, L. Rondoni (eds.), *Applications of Chaos and Nonlinear Dynamics in Science and Engineering - Vol. 4*, Understanding Complex Systems,
DOI 10.1007/978-3-319-17037-4_3

sense to consider the extension of the hydrodynamic description even beyond the purely hydrodynamic limit, so as to take into account reference scales which may happen to be comparable with the kinetic ones. This is the subject dealt with by the theory of *generalized hydrodynamics* [1–4]. There are several delicate aspects hindering this line of investigation. A first, natural, objection points to the fact that, below a certain length scale, the notion itself of "Local Equilibrium", which is brought about by a sufficiently large number of particle collisions, is questionable. Moreover, from the technical side, one typically deals, in this context, with perturbative methods, such as Hilbert's procedure or the Chapman–Enskog (CE) technique, which, at a certain order of truncation, may give rise to artificial instabilities [5, 6]. In particular, the CE method introduces an expansion of the distribution function in terms of a parameter, the Knudsen number, defined as the ratio of the mean free path to a representative macroscopic length. For small values of the Knudsen number, the CE method recovers the standard Navier-Stokes-Fourier (NSF) equations of hydrodynamics. In more refined approximations, referred to as the Burnett and super-Burnett hydrodynamics, the hydrodynamic modes become polynomials of higher order in the wavevector. In such an extension, the resulting hydrodynamic equations may become unstable and violate the H-Theorem, as first shown by Bobylev [5] for a particular case of Maxwell molecules. This indicates that the CE theory can not be immediately trusted, away from the hydrodynamic limit. Thus, while the mathematical framework concerning the hydrodynamic limit of the Boltzmann equation is well-established [7, 8], there is no consolidated counterpart addressing the short scales domain. Thus, developing a theory of Microfluidics, is a novel challenge for theorists, and has also been fostered by recent technological trends [9, 10], which call for an extension of the hydrodynamic description to the regime of finite Knudsen numbers. In this work we describe the application of the Invariant Manifold theory, which makes it possible to derive the equations of *exact* linear hydrodynamics from the Boltzmann equation. The adjective "exact" refers to the fact that the method allows one to perform an exact summation of all the contributions of the CE expansion. We will show, through the analysis of some solvable model, that the divergences of the hydrodynamic modes can be actually removed by taking into account also the very remote terms of the expansion. This is made possible by solving a closed integral equation, called *invariance equation*, which connects the microscopic evolution of the distribution function with its "projected" (in a sense to be specified below) dynamics, triggered by the set of hydrodynamic fields.

This work is structured as follows. In Sect. 3.2 we will outline some standard model reduction techniques, which allow to derive hydrodynamics from the Boltzmann equation. In Sect. 3.3 we will derive the equations of linear hydrodynamics from certain kinetic models of the Boltzmann equation, thus providing the desired bridge between the kinetic and the hydrodynamic descriptions, valid even at short length scales. Conclusions will be drawn in Sect. 3.4.

3.2 Bridging Time and Length Scales: From Kinetic Theory to Hydrodynamics

In this section we will offer a bird's eye view on some of the analytical methods which yield approximate solutions of the Boltzmann equation. In particular, we will outline the structure of the Hilbert and Chapman–Enskog perturbation techniques and will also comment on the essential features of the Invariant Manifold method [1, 2], which is based on the assumption of time scale separation and applies also beyond the strict hydrodynamic limit.

Before introducing the wealth of different techniques, we shortly review the notion of hydrodynamic limit of the Boltzmann equation, and shed also light on the role of the (often invoked) time scale separation, which is one of the main ingredients underpinning the onset of a collective behavior in a many-particle system.

3.2.1 Hydrodynamic Limit of the Boltzmann Equation

Let $f(\mathbf{r}, \mathbf{v}, t)$ denote the single-particle distribution function, depending on the position $\mathbf{r}$, on the velocity $\mathbf{v}$ and on time t, which describes the statistics of a dilute gas made of N particles of mass m, inside a box Λ_ε with volume V. In absence of external forces, we assume that the distribution f obeys the Boltzmann equation [8]

$$\partial_t f(\mathbf{r}, \mathbf{v}, t) + \mathbf{v} \cdot \frac{\partial f}{\partial \mathbf{r}} f = Q(f, f) \quad , \tag{3.1}$$

where $Q(f, f)$ denotes a nonlinear integral collision operator whose detailed analytical structure is not relevant here. We just need to recall that $Q(f, f)$ vanishes when the distribution function attains the so-called local Maxwellian structure:

$$f^{LM} = n(\mathbf{r}, t) \left(\frac{m}{2\pi k_B T(\mathbf{r}, t)} \right)^{\frac{3}{2}} e^{-\frac{m(\mathbf{v}-\mathbf{u}(\mathbf{r},t))^2}{2k_B T(\mathbf{r},t)}} \quad , \tag{3.2}$$

which is parameterized by the fields n (number density, i.e. number of particles per unit volume), $\mathbf{u}$ (bulk velocity of the fluid), and T (temperature). A point of remarkable interest, in kinetic theory, concerns the study of the scaling properties of the Boltzmann equation (3.1). In particular, one may investigate the structure of the solutions of the Boltzmann equation in the so-called *hydrodynamic limit*, which is obtained by taking the limits $N \to \infty$, $V \to \infty$, with N/V finite. Following [7], we introduce a small parameter ε, and let the side of the box Λ_ε be proportional to ε^{-1}. We assume, then, that the total number of particles contained in the box, obtained

by integrating f over Λ_ε and over the whole velocity space, is proportional to the volume of the box itself:

$$\int_{\Lambda_\varepsilon \times \mathbb{R}^3} f(\mathbf{r}, \mathbf{v}, t) d\mathbf{r} d\mathbf{v} = \varepsilon^{-3} \quad , \tag{3.3}$$

and introduce the following scaling:

$$\hat{\mathbf{r}} = \varepsilon \mathbf{r}, \quad \tau = \varepsilon t \quad , \tag{3.4}$$

with $\hat{\mathbf{r}} \in \Lambda = [0, 1]$, and

$$\hat{f}(\hat{\mathbf{r}}, \mathbf{v}, \tau) = f(\mathbf{r}, \mathbf{v}, t) \quad . \tag{3.5}$$

It is readily seen that the rescaled distribution $\hat{f}(\hat{\mathbf{r}}, \mathbf{v}, \tau)$ describes the statistics of particle system on the scale of the box, and is normalized to unity:

$$\int_{\Lambda \times \mathbb{R}^3} \hat{f}(\hat{\mathbf{r}}, \mathbf{v}) d\hat{\mathbf{r}} d\mathbf{v} = 1 \quad . \tag{3.6}$$

While the description afforded in terms of the distribution f is called *mesoscopic* (or *kinetic*), the description provided by the rescaled distribution $\hat{f}$ can be thought of as a *macroscopic* one, because it describes the particle system in the limit of large length and time scales. Using (3.4) and (3.5), the Boltzmann equation, in the absence of external forces, can be shown to attain the following rescaled structure [8]

$$\partial_\tau \hat{f}(\hat{\mathbf{r}}, \mathbf{v}, \tau) + \mathbf{v} \cdot \nabla_{\hat{\mathbf{r}}} \hat{f} = \frac{1}{\varepsilon} Q(\hat{f}, \hat{f}) \quad , \tag{3.7}$$

which will be the starting point of the methods of reduced description to be described below.

3.2.2 The Bogoliubov Hypothesis and Macroscopic Equations

Let us denote by $\mathbf{M}_f = [M_1, \mathbf{M}_2, M_3]$ the lower-order moments of the distribution function f, defined as:

$$\mathbf{M}_f(\mathbf{r}, t) = \int \boldsymbol{\psi}(\mathbf{v}) f(\mathbf{r}, \mathbf{v}, t) d\mathbf{v} \quad , \tag{3.8}$$

where $\boldsymbol{\psi}(\mathbf{v})$ are known as the *collisional invariants*:

$$\boldsymbol{\psi}(\mathbf{v}) = [\psi_1, \boldsymbol{\psi}_2, \psi_3] \quad , \tag{3.9}$$

with

$$\psi_1 = m, \quad \boldsymbol{\psi}_2 = m\mathbf{v}, \quad \psi_3 = \frac{m}{2}v^2 \quad , \tag{3.10}$$

and $v \equiv |\mathbf{v}|$. Thus, by integrating, one finds:

$$\begin{aligned} M_1 &= \rho(\mathbf{r},t) = \int m f(\mathbf{r},\mathbf{v},t) d\mathbf{v} \quad , \\ \mathbf{M}_2 &= \rho(\mathbf{r},t)\mathbf{u}(\mathbf{r},t) = \int m\mathbf{v} f(\mathbf{r},\mathbf{v},t) d\mathbf{v} \quad , \\ M_3 &= \frac{1}{2}\rho(\mathbf{r},t)u^2 + \rho(\mathbf{r},t)e(\mathbf{r},t) = \int \frac{m}{2}v^2 f(\mathbf{r},\mathbf{v},t) d\mathbf{v} \quad , \end{aligned} \tag{3.11}$$

where $\rho(\mathbf{r},t) = mn(\mathbf{r},t)$ is the mass density, and

$$e(\mathbf{r},t) = \frac{3}{2}\frac{k_B}{m}T(\mathbf{r},t) \quad ,$$

denotes the internal energy per unit mass, which is related, via the equipartition theorem, to the temperature T. The hydrodynamic fields $[\rho, \mathbf{u}, T]$ are thus related to the moments $\mathbf{M}_f$ via:

$$\rho = M_1, \quad \mathbf{u} = M_1^{-1}\mathbf{M}_2, \quad T = \frac{2m}{3k_B M_1}\left(M_3 - \frac{1}{2}M_1^{-1}\mathbf{M}_2 \cdot \mathbf{M}_2\right) \quad . \tag{3.12}$$

We consider, from here onwards, a special class of distribution functions called *normal solutions* of the Boltzmann equation [8]. These are distribution functions whose dependence on the variables $(\mathbf{r}, t)$ is parameterized by a set of fields $\mathbf{x}(\mathbf{r}, t)$, which may correspond to the hydrodynamic fields themselves, but in certain models may also include higher-order moments of the distribution function [11–13]. Thus, we start writing the single-particle distribution function in the form:

$$f(\mathbf{r},\mathbf{v},t) = f(\mathbf{x}(\mathbf{r},t),\mathbf{v}) \quad . \tag{3.13}$$

A physical *rationale* behind Eq. (3.13) can be traced back to the Bogoliubov hypothesis [14–16]. In his seminal work, Bogoliubov introduced three different time scales, labeled τ_{int}, τ_{mf} and τ_{macro}: the time interval τ_{int} is the time during which two molecules are in each other's interaction domain, τ_{mf} denotes the mean time between collisions, and τ_{macro} corresponds to the average time needed for a molecule to traverse the container in which the gas is confined. The Bogoliubov hypothesis thus states that the existence of a vast time scale separation

$$\tau_{int} \ll \tau_{mf} \ll \tau_{macro} \tag{3.14}$$

Table 3.1 Bogoliubov length and time intervals for a gas with mean molecular speed of 300 m/s at standard conditions (container edge length $\lambda_{macro} = 3$ cm), cf. [15]

	λ_{int}	λ_{mf}	λ_{macro}
cm	3×10^{-8}	3×10^{-5}	3
	τ_{int}	τ_{mf}	τ_{macro}
s	10^{-12}	10^{-9}	10^{-4}

Table 3.2 Epochs in the Bogoliubov hypothesis

$t < \tau_{int}$	Initial stage
$\tau_{int} < t < \tau_{mf}$	Kinetic stage
$t \sim \tau_{macro}$	Hydrodynamic stage

When describing the particle system on time intervals $t < \tau_{int}$, the full phase space description is required. If the description is confined between τ_{int} and τ_{mf}, one can employ the framework of kinetic theory and the Boltzmann equation provides an efficient statistical description of the dynamics of a sufficiently dilute particle system. Finally, for $t \simeq \tau_{macro}$, the dynamics of the distribution function is driven by the evolution of the hydrodynamic fields

is a prerequisite underpinning the relaxation of a gas towards equilibrium and the onset of a hydrodynamic behavior. In a similar fashion, it is possible to introduce three corresponding displacements, denoted as $\lambda_{int}, \lambda_{mf}, \lambda_{macro}$. The displacement λ_{int} corresponds the range of particle interaction, λ_{mf} is the mean free path and λ_{macro} denotes a macroscopic reference length, such as the edge length of the confining container. Typical values of these parameters are listed in Table 3.1.

The Bogoliubov hypothesis addresses the structural form of the phase space density $F(\mathbf{z}_1, \ldots, \mathbf{z}_N, t)$ (we used the shorthand notation $\mathbf{z} = (\mathbf{r}, \mathbf{v})$) pertaining to three different stages during the relaxation of the gas to equilibrium, cf. also Table 3.2.

In the initial interval there is no collisional exchange between the particles, and the gas experiences no equilibrating force. Therefore, Bogoliubov conjectured that, in such initial stage, the full N-particle density is required to properly describe the state of the gas. In the kinetic stage, the molecules experience a sequence of collisions, which give rise to the onset of Local Equilibrium in the gas. According to Bogoliubov's hypothesis, during this stage all s-particle marginals may be expressed as functionals of the single-particle density, i.e.

$$F_s = F_s(\mathbf{z}_1, \ldots, \mathbf{z}_s, F(\mathbf{z}_1, t)) \quad , \tag{3.15}$$

where the time dependence of F_s is entirely contained in $F_1(\mathbf{z}_1, t)$. For instance, if the particles are statistically independent from each other, F_s factorizes as follows:

$$F_s = \prod_{i=1}^{s} F_1(\mathbf{z}_i, t) \quad . \tag{3.16}$$

Finally, in the hydrodynamic stage, the relevant time scale is τ_{macro}, which characterizes the time evolution of the macroscopic variables $\mathbf{x}(\mathbf{r}, t)$. It is worth noticing that, in the course of the relaxation, a crucial loss of information occurs [15]: while, in the initial stage, the microscopic state of the particle system is described by the full phase space density, close to equilibrium the statistical description is suitably afforded only in terms of the single-particle distribution function, parameterized by the variables $\mathbf{x}$.

We also remark that the condition $\tau_{int} \ll \tau_{mf}$ is essential in order to write the Boltzmann equation in the form (3.1). The distribution function $f(\mathbf{r}, \mathbf{v}, t)$ must be regarded as an *average* of the single-particle distribution in a time interval dt, with

$$\tau_{int} < dt < \tau_{mf} \quad . \tag{3.17}$$

This condition, in fact, allows one to disregard the variation experienced by the distribution function of the hitting particle, $f(\mathbf{r}, \mathbf{v}_1, t)$, during the time τ_{int} of interaction with the target particle. If the condition (3.17) does not hold, one should use, in Eq. (3.1), the distribution function $f(\mathbf{r}, \mathbf{v}_1, t - \tau_{int})$ evaluated at an earlier time and the rate of change of f at time t would depend not only on the instantaneous value of f, but also on its previous history [17]. This would make the Boltzmann equation a *non-markovian* process. We see, hence, that the separation between τ_{int} and τ_{mf} makes it possible to identify an intermediate scale dt, which guarantees the markovian character of the Boltzmann equation. We can also conceive one further time scale, which we denote by Δt, which corresponds to the characteristic "mesoscopic" time scale characterizing the onset of Local Equilibrium. A macroscopic description of a particle system, based on the hydrodynamic fields $\mathbf{x}(\mathbf{r}, t)$, can be obtained by confining the description to time scales not shorter than Δt, which is typically intermediate between τ_{mf} and τ_{macro}. The role of the time scale Δt can be better evinced by introducing a partition of the volume of the gas into mesoscopic cells of linear size ℓ_{meso}, as portrayed in Fig. 3.1. Local equilibrium is reached, within each cell, after the time interval Δt. Therefore, although the hydrodynamic variables may vary over macroscopic length and time scales, within each cell they obey, after the time interval Δt, the usual relations of equilibrium thermodynamics [18].

The dimensionless parameter ε is the Knudsen number [8, 19] and is defined as the ratio of λ_{mf} to λ_{macro}. The aim of a generalized hydrodynamic theory is, hence, to extend the macroscopic description to finite Knudsen numbers, well beyond the standard hydrodynamic limit (corresponding to $\varepsilon \ll 1$). This, in turn, requires a proper estimate, for the model under consideration, of the magnitude of the length

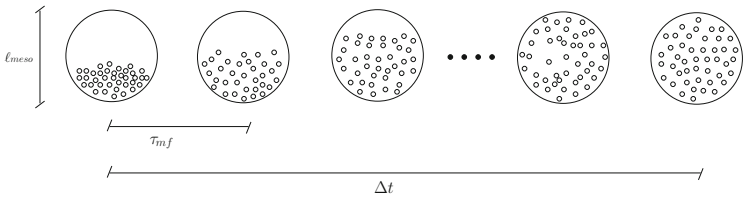

Fig. 3.1 The onset of Local Equilibrium in mesoscopic cells of size ℓ_{meso}, taking place after a time interval Δt. Local Equilibrium results from a large number of collisions, occurring on time scales of the order of τ_{mf}. The hydrodynamic fields attain a local value within each of the cells, and evolve on a time scale τ_{macro} (not shown in the picture) much larger than Δt, according to the time scale separation hypothesis

scale ℓ_{meso}, below which Local Equilibrium no longer holds. Thus, if we consider macroscopic length and time scales compatible, respectively, with ℓ_{meso} and Δt, it makes sense to discuss the derivation of macroscopic equations from the Boltzmann equation and to investigate their properties. To this aim, we integrate Eq. (3.1), multiplied by the collision invariants (3.9), over the velocity space, and obtain:

$$\begin{aligned}
\partial_t \rho &= -\nabla_{\mathbf{r}}(\rho \mathbf{u}) \quad , \\
\partial_t (\rho \mathbf{u}) &= \nabla_{\mathbf{r}} \cdot (\rho \mathbf{u}\mathbf{u} + \mathbf{P}) \quad , \\
\partial_t \left[\rho \left(\frac{1}{2} u^2 + e \right) \right] &= -\nabla_{\mathbf{r}} \cdot \left[\rho \mathbf{u} \left(\frac{1}{2} u^2 + e \right) + \mathbf{P} \cdot \mathbf{u} + \mathbf{q} \right] \quad ,
\end{aligned} \tag{3.18}$$

where the non-hydrodynamic fields $\mathbf{P}$ and $\mathbf{q}$, called pressure tensor and heat flux, are defined as:

$$\mathbf{P} = \int m(\mathbf{v} - \mathbf{u})(\mathbf{v} - \mathbf{u}) f(\mathbf{r}, \mathbf{v}, t) d\mathbf{v} \quad , \tag{3.19}$$

$$\mathbf{q} = \int m(\mathbf{v} - \mathbf{u})(v^2 - 2\mathbf{v} \cdot \mathbf{u} + u^2) f(\mathbf{r}, \mathbf{v}, t) d\mathbf{v} \quad . \tag{3.20}$$

The pressure tensor can be written as $\mathbf{P} = p\mathbf{I} + \boldsymbol{\sigma}$, where $\mathbf{I}$ is the identity matrix, the scalar p, defined as:

$$p = \frac{1}{3} tr\,[\mathbf{P}] = n k_B T = \frac{2}{3} \rho e \quad , \tag{3.21}$$

corresponds to the hydrostatic pressure and $\boldsymbol{\sigma}$ is a symmetric tensor (it is also, typically, a traceless one, depending on the magnitude of the bulk viscosity, defined below). A visible feature of Eq. (3.18) is that the equations are not closed, because of the presence of the non-hydrodynamic fields $\boldsymbol{\sigma}$ and $\mathbf{q}$. As discussed by C. Cercignani in [8], [Eq. (3.18)] "*constitute an empty scheme, since there are* 5 *equation for* 13 *quantities. In order to have useful equations, one must have some expressions for*

$\boldsymbol{\sigma}$ and $\mathbf{q}$ in terms of ρ, $\mathbf{u}$ and e. Otherwise, one has to go back to the Boltzmann equation (3.1) and solve it; and once it has been done, everything is done, and Eq. (3.18) are useless!". This corresponds to the well known problem of seeking a suitable closure to the macroscopic equations. This problem can be tackled either from the kinetic theory standpoint, i.e. by employing some model reduction or coarse-graining techniques [11], or from a purely macroscopic perspective, i.e. by employing macroscopic balance or phenomenological relations which disregard the underlying particle-like picture. In particular, the following set of constitutive equations, written in component notation,

$$\boldsymbol{\sigma}_{i,j} = 0 \quad , \tag{3.22}$$

$$q_i = 0 \quad , \tag{3.23}$$

with $i, j = 1, 2, 3$, yields the so-called Euler equations of inviscid hydrodynamics, which can be also derived from the Boltzmann equation by retaining only the Maxwellian contribution to the distribution function. The Navier-Stokes-Fourier (NSF) equations, instead, are obtained from the following constitutive equations:

$$\boldsymbol{\sigma}_{i,j} = -\eta \left(\frac{\partial u_i}{\partial r_j} + \frac{\partial u_j}{\partial r_i} \right) + \left(\frac{2}{3}\eta - \zeta \right) \frac{\partial u_k}{\partial r_k} \delta_{ij} \quad , \tag{3.24}$$

$$q_i = -\lambda \frac{\partial T}{\partial r_i} \quad , \tag{3.25}$$

where we used the repeated index summation convention and η, ζ, λ correspond to the transport coefficients called, respectively, shear viscosity, bulk viscosity (usually negligible) and thermal conductivity. The NSF equations deserve a special mention in fluid dynamics, because Eqs. (3.24) and (3.25) may be derived not only from the macroscopic principles of conservation of mass, momentum, and energy, but also, rigorously, from kinetic theory [8, 19, 20]. The latter derivation can be performed by using some perturbative schemes, such as those discussed in the next section, which refer to the hydrodynamic limit of the Boltzmann equation.

3.2.3 The Hilbert and the Chapman–Enskog Methods

We provide, here, an overview about the Hilbert and the Chapman–Enskog (CE) methods of solution of the Boltzmann equation in the hydrodynamic limit. The reader is referred to [2, 8] for an exhaustive treatment of the subject. To simplify the notation, we omit, hereafter in this section, the hat over the single-particle distribution referring to a rescaled Boltzmann equation of the form (3.7), introduced in Sect. 3.2.1.

In the Hilbert method, the normal solutions are expanded in powers of the Knudsen number ε, i.e.:

$$f = \sum_{i=0}^{\infty} \epsilon^i f^{(i)} \quad , \tag{3.26}$$

which, substituted in Eq. (3.7), yields a sequence of integral equations

$$Q\left(f^{(0)}, f^{(0)}\right) = 0 \quad , \tag{3.27}$$

$$L\ f^{(1)} = \left(\partial_t + \mathbf{v}\cdot\nabla_{\mathbf{r}}\right) f^{(0)} \quad , \tag{3.28}$$

$$L\ f^{(2)} = \left(\partial_t + \mathbf{v}\cdot\nabla_{\mathbf{r}}\right) f^{(1)} - 2Q\left(f^{(0)}, f^{(1)}\right) \quad , \tag{3.29}$$

to be solved order by order. Here L denotes the linearization of collision integral Q in (3.1). From Eq. (3.27) it follows that $f^{(0)}$ corresponds to the local Maxwellian distribution [19]. The Fredholm alternative, applied to (3.28), results in [2]:

- Solvability condition,

$$\int \left(\partial_t + \mathbf{v}\cdot\nabla_{\mathbf{r}}\right) f^{(0)} \boldsymbol{\psi}(\mathbf{v}) d\,\mathbf{v} = 0 \quad , \tag{3.30}$$

  which corresponds to the Euler equations described by Eqs. (3.22) and (3.23);
- General solution $f^{(1)} = f^{(1),1} + f^{(1),2}$, where $f^{(1),1}$ denotes the special solution to the linear integral equation (3.28) and $f^{(1),2}$ a yet undetermined linear combination of the summational invariants;
- Solvability condition, when applied to Eq. (3.29), yields $f^{(1),2}$ which is obtained from solving the linear hyperbolic differential equations

$$\int \left(\partial_t + \mathbf{v}\cdot\nabla_{\mathbf{r}}\right)\left(f^{(1),1} + f^{(1),2}\right)\boldsymbol{\psi}(\mathbf{v}) d\,\mathbf{v} = 0 \quad . \tag{3.31}$$

Hilbert showed that this procedure can be applied up to an arbitrary order n, so that the function $f^{(n)}$ is determined from the solvability condition applied at the $(n+1)$-th order [2]. Loosely speaking, the description provided by the Hilbert method is essentially in terms of the Euler equations, but it is supplemented by corrections which can by computed by solving linearized equations [8]. It is also worth remarking that the Hilbert method can not provide uniformly valid solutions, as it can be evinced by noticing the singular manner in which the Knudsen number enters the rescaled Boltzmann equation (3.7). Nevertheless, a truncated Hilbert expansion can reproduce, with arbitrary accuracy, the solution of the Boltzmann equation in a properly chosen region of time-space, provided that ε is sufficiently small.

The CE approach, developed by D. Enskog and S. Chapman, is based, instead, on an expansion of the time derivatives of the hydrodynamic variables, rather than seeking the time-space dependence of these functions, as in the Hilbert method. Also the CE method starts with the singularly perturbed Boltzmann equation (3.7), and with the expansion (3.26). Nevertheless, the procedure of evaluation of the functions $f^{(i)}$ is different, and reads as follows:

$$Q\left(f^{(0)}, f^{(0)}\right) = 0, \tag{3.32}$$

$$L\ f^{(1)} = -Q\left(f^{(0)}, f^{(0)}\right) + \left(\partial_t^{(0)} + \mathbf{v}\cdot\nabla_{\mathbf{r}}\right) f^{(0)} \quad . \tag{3.33}$$

Equation (3.32) implies, as in the Hilbert method, that the function $f^{(0)}$ is the local Maxwellian. The operator $\partial_t^{(0)}$ is defined from the expansion of the right hand side of the hydrodynamic equations,

$$\partial_t^{(0)}\mathbf{M}_f = -\int \boldsymbol{\psi}(\mathbf{v})\mathbf{v}\cdot\nabla_{\mathbf{r}} f^{(0)} d\mathbf{v} \quad . \tag{3.34}$$

Equation (3.34) correspond to the inviscid Euler equations, and $\partial_t^{(0)}$ acts on various functions $g(\rho, \rho\mathbf{u}, e)$ according to the chain rule

$$\partial_t^{(0)} g = \frac{\partial g}{\partial \rho}\partial_t^{(0)}\rho + \frac{\partial g}{\partial(\rho\mathbf{u})}\partial_t^{(0)}\rho\mathbf{u} + \frac{\partial g}{\partial e}\partial_t^{(0)} e \quad , \tag{3.35}$$

whereas the time derivatives $\partial_t^{(0)}$ of the hydrodynamic fields are expressed using the right hand side of (3.34). Finally, the method requires that the hydrodynamic variables, obtained by integrating over the velocity space the function $f^{(0)} + \varepsilon f^{(1)}$, coincide with the parameters of the local Maxwellian $f^{(0)}$:

$$\int \boldsymbol{\psi}(\mathbf{v}) f^{(1)} d\mathbf{v} = 0 \quad . \tag{3.36}$$

Thus, one finds that the first correction, $f^{(1)}$, adds the terms

$$\partial_t^{(1)}\mathbf{M}_f = -\int \boldsymbol{\psi}(\mathbf{v})\mathbf{v}\cdot\nabla_{\mathbf{r}} f^{(1)} d\mathbf{v} \tag{3.37}$$

to the time derivatives of the hydrodynamic fields. These novel terms yield the dissipative NSF hydrodynamics. However, higher-order corrections of the CE method, which result in hydrodynamic equations with higher derivatives (the so-called Burnett and super-Burnett hydrodynamics) are affected by severe difficulties, mainly related to the onset of instabilities of the solutions [5, 21, 22].

3.2.4 The Grad's Moment Method

An alternative technique to solve the Boltzmann equation was proposed by H. Grad, and is known as the Grad's moment method [12]. The essence of the method relies on the time scale separation hypothesis, introduced in Sect. 3.2.2:

- During the fast evolution, which occurs on a time scale of the order of the mesoscopic time scale Δt, a set of distinguished moments $\mathbf{x}$, cf. Sect. 3.2.2, does not change significantly in comparison to the rest of higher-order "fast" moments of f, denoted as $\mathbf{y}$.
- Towards the end of the fast evolution, the values of the moments $\mathbf{y}$ become determined by the values of the distinguished moments $\mathbf{x}$.
- During a time interval of the order of τ_{macro}, the dynamics of the distribution function is governed by the dynamics of the distinguished moments, while the rest of moments remain to be determined by the distinguished moments [2].

In the Grad's moment method, the distribution function is expanded as:

$$f(\mathbf{x},\mathbf{v}) = f^{LM}(\rho,\mathbf{u},e,\mathbf{v})\left[1+\sum_{k=1}^{N} a_k(\mathbf{x})H_k(\mathbf{v}-\mathbf{u})\right] \quad , \tag{3.38}$$

where $H_k(\mathbf{v}-\mathbf{u})$ are Hermite tensor polynomials, orthogonal with respect to a weight given by the Maxwellian distribution f^{LM}, whereas the coefficients a_k are known functions of the distinguished moments $\mathbf{x}$. The fast moments $\mathbf{y}$ are assumed to be functions of $\mathbf{x}$, i.e. $\mathbf{y} = \mathbf{y}(\mathbf{x})$. By inserting Eq. (3.38) into the Boltzmann equation (3.1) and by using the orthogonality of the Hermite polynomials with respect to the Maxwellian distribution f^{LM}, one can determine the time evolution of the set of distinguished moments $\mathbf{x}$. According to Grad's argument, this approximation can be refined by extending the set of distinguished moments $\mathbf{x}$, as done, for instance in the Grad's 13 moment approximation [12], which set the stage to the development of the theory of Extended Irreversible Thermodynamics [2, 11, 13].

3.2.5 The Invariant Manifold Theory

The Invariant Manifold method can be considered as a generalization of the theory of normal solutions, which is inherent in the Hilbert and CE expansions [2]. The method is based on a projector operator formalism [23–25], which confines the dynamics onto a manifold of slow motion and disregards the fluctuations of the fast variables. The same approach is also at the basis of Haken's slaving principle and of the procedure of adiabatic elimination of fast variables in stochastic processes [26, 27]. The description of the time evolution of the system resembles the picture given in Sect. 3.2.4: from the initial condition, the system quickly approaches a small neighbourhood of the invariant manifold, and, from then onwards, it proceeds

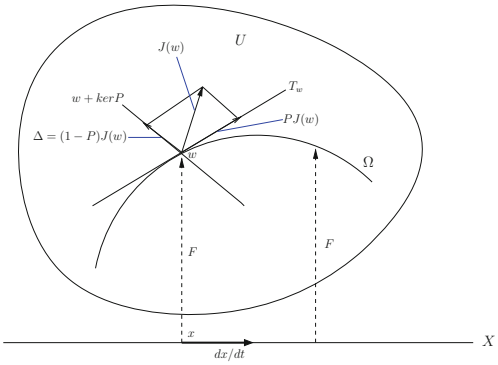

Fig. 3.2 The geometrical structures of the Invariant Manifold method: U is the space of distribution functions, $J(w)$ is the vector field of the system under consideration, Ω is an ansatz manifold, X is the space of macroscopic variables (coordinates on the manifold), the map F maps points $\mathbf{x} \in X$ into the corresponding points $w = F(\mathbf{x})$, T_w is the tangent space to the manifold Ω at the point w, $PJ(w)$ is the projection of the vector $J(w)$ onto tangent space T_w, $d\mathbf{x}/dt$ describes the induced dynamics on X, Δ is the defect of invariance, and the affine subspace $w + ker P$ is the plain of fast motions [2]

slowly along such manifold with a characteristic time scale of the order of τ_{macro}. The main geometrical structures which characterize the Invariant Manifold theory are illustrated in Fig. 3.2.

We summarize, below, the essential mathematical framework of the method. Let U be the phase space, and $\Omega \subset U$ an ansatz manifold, which corresponds to the current approximation to the invariant manifold to be sought. We denote by $J(w)$ the vector field

$$\frac{dw}{dt} = J(w), \quad w \in U, \tag{3.39}$$

which generates the dynamics in U. Let X be the linear space of the macroscopic variables $\mathbf{x}$, which act as coordinates on the manifold Ω, described as the image of the map $F : X \to U$. We remark that the choice of the space X of macroscopic variables is a crucial step of the method: the corrections of the current ansatz manifold correspond to the images of various maps F for a given X. Let us also denote by

$$D_{\mathbf{x}} F = \frac{\partial w}{\partial \mathbf{x}}|_{w=F(\mathbf{x})} \tag{3.40}$$

the derivative of the map F with respect to the set of distinguished variables. We indicate by $\Pi : U \to X$ a regular map which fulfills the condition

$$\Pi \circ F = 1 \quad , \tag{3.41}$$

with 1 the identity operator, and by $D_w\Pi$ the functional derivative of the map $\mathbf{x} = \Pi(w)$ computed at the point w. Thus, the time evolution of the distinguished variables $\mathbf{x}$ reads:

$$\frac{d\mathbf{x}}{dt} = D_w \Pi J(F(\mathbf{x})) \quad , \tag{3.42}$$

where $d\mathbf{x}/dt$ is an element of the tangent space to X. Therefore, joining Eqs. (3.40) and (3.42), one obtains:

$$\frac{dw}{dt}|_{w=F(\mathbf{x})} = D_{\mathbf{x}} F \cdot \frac{d\mathbf{x}}{dt} = [D_{\mathbf{x}} F \circ D_{\mathbf{w}} \Pi]\, J(F(\mathbf{x})) = PJ\,(F(\mathbf{x})) \quad , \tag{3.43}$$

where the operator

$$P = D_{\mathbf{x}} F \circ D_{\mathbf{w}} \Pi$$

projects $J(f)$ onto T_w, which denotes the tangent space to the manifold Ω at the point w. In particular, the projector P determines a decomposition of the motion near Ω: $w + ker[P]$ is the plane of fast motion and T_w the plane of slow motion. We call *slow invariant manifolds* those maps F which fulfill the condition (3.41) and solve the *invariance equation*:

$$\Delta(F) = (1 - P)J(F) = 0 \quad , \tag{3.44}$$

which is a differential equation for the unknown map F. The solutions of Eq. (3.44) are "invariant" in the sense that the vector field $J(F)$ is tangent to the manifold $\Omega = F(X)$ for each point $w \in \Omega$. A crucial aspect of the method concerns the definition of the projector P. Gorban et al. introduced, in [2], the Thermodynamic Projector, which characterizes, in a thermodynamic sense, the plane of fast motion $w + kerP$: the physical entropy grows during the fast motion and the point w is the point of entropy maximum along the plane $w + kerP$.

The geometrical setting described above can be readily adapted to the Boltzmann equation theory. To this aim, one identifies w with the single-particle distribution function f, $\mathbf{x} = \Pi(f)$ denotes a set of distinguished fields which parameterize f and F becomes a "closure", i.e. a distribution function parameterized by the variables $\mathbf{x}$. Moreover, the vector field $J(f)$ attains the form:

$$J(f) = -\mathbf{v} \cdot \nabla_{\mathbf{r}} f + Q(f, f) \quad ,$$

whereas $D_f \Pi$ reads:

$$D_f \Pi[\cdot] = \int \boldsymbol{\psi}(\mathbf{v})[\cdot] d\mathbf{v} \quad ,$$

with $\boldsymbol{\psi}(\mathbf{v})$ defined in (3.10). Therefore, the Thermodynamic Projector P, which depends on f, attains, in this case, the structure:

$$P[\cdot] = \frac{\partial f}{\partial \mathbf{x}} \cdot \int \boldsymbol{\psi}(\mathbf{v})[\cdot] d\mathbf{v} \quad . \tag{3.45}$$

The invariance equation (3.44) constrains the kinetic evolution of the distribution function to coincide with its "macroscopic" evolution, ruled by the projector P (3.45) and driven by the dynamics of the distinguished variables $\mathbf{x}$. It should be noticed that the method does not require the smallness of the parameter ε, hence it is not restricted to the strict hydrodynamic limit. A straightforward application of the formalism described above is obtained by considering an ansatz manifold, Ω_{LM}, given by the locally five-dimensional manifold of local Maxwellians (3.2). We take, hence, the set $\mathbf{M}_f$ of moments (3.11) as the coordinates $\mathbf{x}$ on this manifold. The manifold Ω_{LM} is commonly referred to as the *quasi-equilibrium* manifold for the set of moments $\mathbf{x}$, because f^{LM} corresponds to the unique solution of the variational problem:

$$H(f) \to min \quad ,$$

with $H(f) = \int f \log f d\mathbf{v}$ denoting the celebrated H-function. We thus define the projector $P_{f^{LM}}$ onto the tangent space $T_{f^{LM}}$ as:

$$P_{f^{LM}} J\left(f^{LM}\right) = \frac{\partial f^{LM}}{\partial \mathbf{M}_f} \cdot \int \boldsymbol{\psi}(\mathbf{v}) J(f^{LM}) d\mathbf{v} \quad . \tag{3.46}$$

Returning to the hydrodynamic variables $[\rho, \mathbf{u}, T]$ via the transformations (3.12), one obtains [2]:

$$\begin{aligned} \Delta\left(f^{LM}(\rho, \mathbf{u}, T)\right) = f^{LM}(\rho, \mathbf{u}, T) \Bigg[& \left(\frac{m(\mathbf{v}-\mathbf{u})^2}{2k_B T} - \frac{5}{2} \right) (\mathbf{v}-\mathbf{u}) \nabla_{\mathbf{r}} (\ln T) + \\ & + \frac{m}{k_B T} \left((\mathbf{v}-\mathbf{u})(\mathbf{v}-\mathbf{u}) - \frac{1}{3}(\mathbf{v}-\mathbf{u})^2 \mathbf{I} \right) \nabla_{\mathbf{r}} \mathbf{u} \Bigg] \end{aligned} \tag{3.47}$$

Equation (3.47) reveals that the quasi-equilibrium manifold is not an invariant manifold of the Boltzmann equation, because temperature and bulk velocity It is worth remarking that, strictly speaking, the statistics of the many-particle system is actually not driven towards the local Maxwellian distribution, or, if it accidentally starts in that state, it moves away from it, due to the flow term $\left(\mathbf{v} \cdot \frac{\partial f}{\partial \mathbf{r}} f\right)$ in the Boltzmann equation. The effect of the latter term is, in fact, to smooth out the spatial inhomogeneities [17]. Nevertheless, for small Knudsen numbers, such term acts over time scales much larger than the collisions. Consequently, at all times, the instantaneous single-particle distribution function is very close to the local Maxwellian one, described by Eq. (3.2). The latter may, hence, be regarded

as the standard reference distribution when relying on perturbation theories which are concerned with the hydrodynamic limit of the Boltzmann equation.

3.3 Linear Hydrodynamics from the Boltzmann Equation

Several solution techniques have been introduced in the literature to obtain approximate solutions of the Boltzmann equation. In particular, the CE method extends the hydrodynamics beyond the NSF approximation in such a way that the decay rate of the next order approximations (Burnett and super-Burnett) are polynomials of higher order in k [2, 21, 22]. In such an extension, relaxation rates may become completely unphysical (amplification instead of attenuation), as first shown by Bobylev [5] for a particular case of Maxwell molecules. Therefore, several regularization techniques have been proposed to restore the thermodynamic admissibility of the generalized hydrodynamic equations [28–30]. A promising route, in particular, is based on the notion of Invariant Manifold [2], introduced in Sect. 3.2.5. The method requires a neat separation between hydrodynamic and kinetic (time and length) scales, and postulates the existence of a stable Invariant Manifold in the space of distribution functions, parameterized by the values of the hydrodynamic fields. Following the approach traced in [31], we will employ, here, the Invariant Manifold technique to determine the hydrodynamic modes and the transport coefficients beyond the standard hydrodynamic regime. In particular, we expect to recover the asymptotic form of the dynamic structure factor in the free-particle regime and to shed light on the properties of the hydrodynamic equations in the intermediate regime of finite Knudsen numbers.

This section is structured as follows.

We will review, in Sect. 3.3.1, the eigenvalue problem associated with the linearized Boltzmann equation. In Sect. 3.3.2, we will derive the invariance equation for the Boltzmann equation equipped with an arbitrary linearized collision operator. In Sect. 3.3.3 we will introduce a suitable coordinate system which allows one to highlight the symmetries of the solutions of the invariance equation. In Sect. 3.3.4 we will, then, solve the invariance equation for the linearized BGK model [32]. In Sect. 3.3.5 we will investigate the properties of the solution of the invariance equation for a gas of Maxwell molecules. We will, hence, comment on the structure of the obtained hydrodynamic modes and cast the generalized transport coefficients in the Green-Kubo formalism [33]. We will, finally, determine the spectrum of the density fluctuations and discuss some relevant features of the resulting short wavelength hydrodynamics.

3.3.1 Eigenfrequencies of the Boltzmann Equation

In this section we consider the eigenvalue problem for the linearized Boltzmann equation. Namely, for a inhomogeneous gas, the eigenvalues correspond to k-dependent frequencies (i.e. inverse of characteristic collision rates). The connection

between the fluctuations of the macroscopic variables and the underlying characteristic kinetic rates is a central problem in statistical mechanics [34, 35] which still demands a conclusive understanding. In order to appreciate the problem, we recall that in the NSF approximations, the hydrodynamic modes are quadratic in the wave vector [36] and are unbounded. On the other hand, Boltzmann's collision term features equilibration with finite characteristic rates. Hence, such "finite collision frequency" is at variance with the arbitrary decay rates in the NSF approximation: intuitively, the hydrodynamic modes at large k cannot relax faster than the collision frequencies. In his seminal work [37] on the eigenfrequencies of the Boltzmann equation, Resibois provided an explicit connection between the generalized frequencies of the linearized Boltzmann equation and the decay rate of the hydrodynamic fluctuations. He tackled the problem by solving, perturbatively, the eigenvalue problem associated to the Boltzmann equation and to the NSF equations of hydrodynamics.

Let us rewrite the Boltzmann equation (3.1):

$$\partial_t f = -\mathbf{v} \cdot \nabla f + Q(f, f) \quad . \tag{3.48}$$

We introduce the dimensionless peculiar velocity $\mathbf{c} = (\mathbf{v} - \mathbf{u}_0)/v_T$ and the equilibrium values of hydrodynamic fields: equilibrium particle number n_0, equilibrium mean velocity $\mathbf{u}_0 = \mathbf{0}$, and equilibrium temperature T_0. The global Maxwellian reads: $f^{\mathrm{GM}} = (n_0/v_T^3) f_0(c)$ where $f_0(c) = \pi^{-3/2} e^{-c^2}$ is a Gaussian in the velocity space ($c = |\mathbf{c}|$). We linearize (3.48) by considering only small disturbances from the global equilibrium. Moreover, we write the nonequilibrium distribution function (cf. also Table 3.3) as:

$$f(\mathbf{r}, \mathbf{c}, t) = f^{\mathrm{LM}} + \delta f, \tag{3.49}$$

where f^{LM} denotes the local Maxwellian to be made precise in Sect. 3.3.2, and δf the deviation from local equilibrium. An alternative notation is introduced via $\delta f = f^{\mathrm{GM}} \delta\varphi$. We also consider a reference frame moving with the flow velocity

Table 3.3 Notation used in this manuscript

f	=	f^{LM}			+	δf
	=	f^{GM}	+	$f^{\mathrm{GM}}\varphi_0$	+	$f^{\mathrm{GM}}\delta\varphi$
	=	f^{GM}	+	$f^{\mathrm{GM}}\mathbf{X}^{(0)} \cdot \mathbf{x}$	+	$f^{\mathrm{GM}}\delta\mathbf{X} \cdot \mathbf{x}$
	=	f^{GM}	+	$f^{\mathrm{GM}}\Delta\mathbf{X} \cdot \mathbf{x}$		
	=	f^{GM}	+	Δf		

Terms have been grouped and abbreviated as depicted in this table. f^{GM} and f^{LM} denote global and local Maxwellian, respectively, and Δf and δf their "distance" from f. The third row informs about the closure discussed in this manuscript, while $\mathbf{x}$ is a set of distinguished (lower-order) moments of f

and linearize the collision operator around global equilibrium. When passing over to Fourier space, we seek solutions of the form:

$$f(\mathbf{r},\mathbf{c},t) = e^{\omega t} e^{i\mathbf{k}\cdot\mathbf{r}} f(\mathbf{k},\mathbf{c},\omega) \quad ,$$

where ω is a complex-valued frequency and k is a real-valued wavevector. Thus, the Boltzmann equation (3.48) reduces to:

$$\frac{1}{v_T}\partial_t f(\mathbf{k},\mathbf{c},\omega) = -i\mathbf{k}\cdot\mathbf{c} f + \hat{L}\delta f(\mathbf{k},\mathbf{c},\omega) \; , \qquad \hat{L} = \frac{1}{v_T} L \quad , \tag{3.50}$$

where we made use of the fact that $Lf^{\mathrm{LM}} = 0$. In the sequel of this section, we will investigate the spectrum of the operator $\mathbf{\Lambda} \equiv \hat{L} - i\mathbf{k}\cdot\mathbf{c}$, which determines the time evolution of the single-particle distribution function [38]. This is readily seen by inspection of the inverse Laplace transform:

$$f(\mathbf{k},\mathbf{c},t) = \left[\frac{1}{2\pi i}\oint \frac{e^{zt}}{(z-\mathbf{\Lambda})} dz\right] f(\mathbf{k},\mathbf{c},0) \quad , \tag{3.51}$$

where the closed path encircles the poles of the function inside the integral. According to the Spectral Theorem, these poles correspond to the spectrum of $\mathbf{\Lambda}$. The flow term $-i\mathbf{k}\cdot\mathbf{c} f$ is treated, here, as a small perturbation [17] (this amounts to considering small gradients in the real space). Equation (3.50) can be, hence, written in the form:

$$\Lambda f = \omega f \quad . \tag{3.52}$$

The investigation of the spectrum of the operator Λ, in Eq. (3.52), is a formidable mathematical problem, which can be tackled by considering, first, the hydrodynamic limit $k \to 0$. In this limit, Eq. (3.52) reads:

$$\hat{L}\Psi_i(\mathbf{c}) = \lambda_i \Psi_i(\mathbf{c}) \quad . \tag{3.53}$$

The linear operator $\hat{L}$ can be shown to be self-adjoint with respect to a suitably defined scalar product [1], hence the corresponding eigenfunctions are (or can be made) orthogonal and constitute a complete set. In particular, a subset of them is related to the fivefold degenerate zero eigenvalue. These functions correspond to the collision invariants $f^{\mathrm{GM}}\mathbf{X}^{(0)}$, with $\mathbf{X}^{(0)}$ denoting a set of lower-order Sonine (or associated Laguerre) polynomials:

$$\mathbf{X}^{(0)} = \left[1, 2\mathbf{c}, \left(c^2 - \frac{3}{2}\right)\right] \quad . \tag{3.54}$$

One, also, typically assumes that the eigenvalues of $\hat{L}$ other than 0 have no accumulation point at the origin. This assumption is always implicit in any calculation

of transport coefficients based on kinetic theory. Physically, it corresponds to invoking a separation between the kinetic time scale λ_i^{-1}, and the hydrodynamic time scale $(v_t k)^{-1}$, as discussed in Sect. 3.2.2. For finite values of k, there will be a set of eigenvalues of Λ, denoted by ω_α, with $\alpha = 1, \ldots, 5$, which, in the $k \to 0$ limit, reduce to the aforementioned degenerate zero eigenvalue. Hence, we shortly review, here, the results of a perturbative method, outlined in [37], which allows one to determine the dependence of the set ω_α from k. Denoting by $\Psi_\alpha(k)$ the eigenfunctions corresponding to $\omega_\alpha(k)$, the yet unknown eigenfunctions and eigenvalues can be expanded in powers of the wavevector k:

$$\begin{aligned} \Psi_\alpha &= \Psi_\alpha^{(0)} + k\Psi_\alpha^{(1)} + k^2\Psi_\alpha^{(2)} + \ldots \quad , \\ \omega_\alpha &= \omega_\alpha^{(0)} + k\omega_\alpha^{(1)} + k^2\omega_\alpha^{(2)} + \ldots \quad , \end{aligned} \tag{3.55}$$

where $\Psi_\alpha^{(0)}$ are linear combinations of the collision invariants (3.54), whose detailed expression is not relevant here (cf. [39] for details). The use of a Rayleigh-Schödinger perturbation theory leads to the following polynomial expression for the set $\{\omega_\alpha\}$:

$$\begin{aligned} \omega_1 &= i c_0 k - k^2 \left\langle \Psi_1^{(0)} \middle| \left((c_x - c_0) \frac{1}{\hat{L}} (c_x - c_0) \right) \Psi_1^{(0)} \right\rangle \quad , \\ \omega_2 &= -i c_0 k - k^2 \left\langle \Psi_2^{(0)} \middle| \left((c_x + c_0) \frac{1}{\hat{L}} (c_x + c_0) \right) \Psi_2^{(0)} \right\rangle \quad , \\ \omega_3 &= -k^2 \left\langle \Psi_3^{(0)} \middle| \left(c_x \frac{1}{\hat{L}} c_x \right) \Psi_3^{(0)} \right\rangle \quad , \\ \omega_4 &= -k^2 \left\langle \Psi_4^{(0)} \middle| \left(c_x \frac{1}{\hat{L}} c_x \right) \Psi_4^{(0)} \right\rangle \quad , \\ \omega_5 &= -k^2 \left\langle \Psi_5^{(0)} \middle| \left(c_x \frac{1}{\hat{L}} c_x \right) \Psi_5^{(0)} \right\rangle \quad , \end{aligned} \tag{3.56}$$

where c_0 denotes the speed of sound.

On the other hand, in Fourier space, the linearized NSF equations read:

$$\begin{aligned} \omega n_k &= -i n_0 \, (\mathbf{k} \cdot \mathbf{u}_k) \quad , \\ \omega \mathbf{u}_k &= -\eta k^2 \mathbf{u}_k - \left(\frac{1}{3}\eta + \zeta \right) (\mathbf{k} \cdot \mathbf{u}_k) \, \mathbf{k} - i c_0^2 \gamma^{-1} \rho_0^{-1} \mathbf{k} n_k - i c_0^2 \gamma^{-1} \alpha \mathbf{k} T_k \quad , \\ \omega T_k &= -\frac{\lambda}{\rho_0 c_v} k^2 T_k - i \frac{\gamma - 1}{\alpha} \, (\mathbf{k} \cdot \mathbf{u}_k) \quad , \end{aligned} \tag{3.57}$$

The condition of a non-trivial solvability of the linear system (3.57) with respect to the variables $[n_k(\omega), \mathbf{u}_k(\omega), T_k(\omega)]$, yields the *dispersion relation* $\omega(k)$, i.e. the normal mode frequencies of the system. It can be shown, in particular, that the real

part of these modes is quadratic in the wavevector [2, 37, 39]:

$$Re(\omega) \propto -k^2 \quad ,$$

which can be regarded, in fact, as the hallmark of the NSF approximation. By requiring the equivalence of the hydrodynamic frequencies with the set of kinetic frequencies ω_α, given in Eq. (3.56), leads to approximate expressions for the transport coefficients, which can be shown to be equivalent to the reduced expressions determined by many-body autocorrelation functions [37]. As also pointed out in [17], the results obtained by Resibois, based on the correspondence between hydrodynamic modes and kinetic frequencies, reveals that, in the limit of long wavelengths, the possible modes of motion of the gas correspond to rather ordered motions, such as a sound wave propagation. These modes are referred to, in the literature, as *collective* modes, because they involve the coordinate action of a huge number of particles. The onset of such an ordered motion as a result of the underlying chaoticity of the individual motion of the particles is a striking feature of statistical mechanics. The reason of this can be traced back to the effect of the collisions, which drive very quickly the system towards the local equilibrium state, that is a highly organized one. From then onwards, the flow term produces slow variations in space and time of this basic state, which reduce the local gradients of the hydrodynamic fields. In the sequel of this section, we will employ the Invariant Manifold theory to obtain a generalization of the pioneering approach developed by Resibois.

3.3.2 The Invariant Manifold Technique

Following the notation of Sect. 3.2, we denote by U and $\mathbf{x}(\mathbf{r}, t)$, respectively, the space of single-particle distribution functions and a set of distinguished moments of the latter. We then introduce the *locally finite-dimensional* manifold $\Omega \subset U$ as the set of functions $f(\mathbf{x}(\mathbf{r}, t), \mathbf{c})$ whose dependence on the space-time variables $(\mathbf{r}, t)$ is parameterized through $\mathbf{x}(\mathbf{r}, t)$. In this section, we will identify the distinguished moments $\mathbf{x}(\mathbf{r}, t)$ with the hydrodynamic fields. Moreover, P is the Thermodynamic Projection operator which, as discussed in Sect. 3.2.5, allows to decompose the dynamics into a fast motion on the affine subspace $f + \ker[P]$ and a slow motion, which occurs along the tangent space T_f. The use of the Thermodynamic Projector guarantees the persistence of dissipation: it can be shown [2] that the entropy production rate is unaltered when the dynamic is projected along the manifold of slow motion.

In order to derive exact hydrodynamic equations from the general eigenvalue problem (3.50), we proceed as follows:

1. We determine the invariant manifold, i.e. the distribution function solving the invariance equation

$$(\mathbf{1} - P)\Lambda\Delta f = 0 \quad , \tag{3.58}$$

   where $\triangle f \equiv f - f^{\mathrm{GM}}$ (cf. also Table 3.3).
2. We derive the equations of linear hydrodynamics by integrating the kinetic equation (3.50), with f given by the solution of Eq. (3.58). By construction, the hydrodynamic modes coincide, then, with the set ω_α of eigenfrequencies of the Boltzmann equation, which vanish in the limit $k \to 0$.

We also denote by $\mathbf{x}_k$ the Fourier components of the dimensionless hydrodynamic fluctuations $[\tilde{n}, \tilde{\mathbf{u}}, \tilde{T}]$: $\tilde{n} \equiv (n - n_0)/n_0$ = (particle number perturbation), $\tilde{\mathbf{u}} \equiv \mathbf{u}/v_T$ = (velocity perturbation) and $\tilde{T} \equiv (T - T_0)/T_0$ (temperature perturbation). Further, we split the mean velocity $\tilde{\mathbf{u}}$ uniquely as $\tilde{\mathbf{u}} = u^{\parallel}\mathbf{e}_{\parallel} + u^{\perp}\mathbf{e}_{\perp}$, where the unit vector $\mathbf{e}_{\parallel}$ is parallel to $\mathbf{k}$, and $\mathbf{e}_{\perp}$ orthonormal to $\mathbf{e}_{\parallel}$, i.e., $\mathbf{e}_{\perp}$ lies in the plane perpendicular to $\mathbf{k}$. Due to isotropy, $u^{\perp}$ alone fully represents the twice degenerated (shear) dynamics. By linearizing around the global equilibrium, we write the local Maxwellian contribution to f in (3.49) as $f^{\mathrm{LM}} = f^{\mathrm{GM}}(1 + \varphi_0)$ where φ_0 takes a simple form, $\varphi_0 = \mathbf{X}^{(0)} \cdot \mathbf{x}$ (linear quasi equilibrium manifold), where $\mathbf{X}^{(0)}(\mathbf{c})$ was defined in Eq. (3.54). It is conveniently considered as four-dimensional vector using the four-dimensional version $\mathbf{x}_k = [\tilde{n}_k, u^{\parallel}, \tilde{T}_k, u^{\perp}]$, and is then given by (3.68). It proves convenient to introduce a vector of velocity polynomials, $\boldsymbol{\xi}(\mathbf{c})$, which is similar to $\mathbf{X}^0$ and defined below in Eq. (3.69), such that:

$$\langle \xi_\mu | X_\nu^{(0)} \rangle = \delta_{\mu\nu} \quad .$$

Hence, the fields $\mathbf{x}_k$ are obtained as $\langle \boldsymbol{\xi}(\mathbf{c}) \rangle_{f^{LM}} = \mathbf{x}_k$, where averages are defined, here, as:

$$\langle \boldsymbol{\xi}(\mathbf{c}) \rangle_f = \frac{1}{n_0} \int \boldsymbol{\xi}(\mathbf{c}) f(\mathbf{c}) d\mathbf{v} \quad . \tag{3.59}$$

We introduce yet unknown fields $\delta\mathbf{X}(\mathbf{c}, \mathbf{k})$ which characterize the part δf of the distribution function. As long as deviations from the local Maxwellian are small, we seek a nonequilibrium manifold which is also linear in the hydrodynamic fields $\mathbf{x}$ themselves. Therefore, we set:

$$\delta\varphi = \delta\mathbf{X} \cdot \mathbf{x}_k \quad . \tag{3.60}$$

The "eigen"-closure (3.60), which formally and very generally addresses the fact that we wish to *not* include other than hydrodynamic variables, implies a closure between moments of the distribution function, to be worked out in

detail below. By using the above form (3.60) for $\delta f = f^{\mathrm{GM}}\delta\varphi$, with $\hat{L}\delta f = f^{\mathrm{GM}}L[\delta\mathbf{X}]\cdot\mathbf{x}_k$, and the canonical abbreviations $\triangle\mathbf{X} \equiv \mathbf{X}^0(\mathbf{c}) + \delta\mathbf{X}(\mathbf{c},\mathbf{k})$, Eq. (3.52) reads:

$$\omega f^{\mathrm{GM}}\triangle\mathbf{X}\cdot\mathbf{x}_k = \Lambda\Delta f = -i\mathbf{k}\cdot\mathbf{c}f^{\mathrm{GM}}\triangle\mathbf{X}\cdot\mathbf{x}_k + f^{\mathrm{GM}}\hat{L}\delta\mathbf{X}\cdot\mathbf{x}_k \quad . \tag{3.61}$$

The microscopic projected dynamics is obtained through the projector P, which, when acting upon the vector field $J(f) = \Lambda\Delta f$, gives:

$$P\Lambda\Delta f = D_{\mathbf{x}_k}\Delta f\cdot\int\boldsymbol{\xi}(\mathbf{c})\Lambda\Delta f d\mathbf{v} \quad , \tag{3.62}$$

where $D_{\mathbf{x}_k}\Delta f \equiv \partial\Delta f/\partial\mathbf{x}_k$ and the quantity inside the integral in (3.62) represents the time evolution equations for the moments $\mathbf{x}_k$. These are readily obtained by integration of the weighted (3.52) as

$$\omega\langle\boldsymbol{\xi}(\mathbf{c})\rangle_f = -i\mathbf{k}\cdot\langle\boldsymbol{\xi}(\mathbf{c})\mathbf{c}\rangle_f + \langle\boldsymbol{\xi}(\mathbf{c})\rangle_{\hat{L}\delta f} \quad . \tag{3.63}$$

Due to the eigen-closure (3.60), cf. also Table 3.3, one finds $D_{\mathbf{x}_k}\Delta f = f^{\mathrm{GM}}\triangle\mathbf{X}$, whereas (3.63) is linear in $\mathbf{x}_k$ and can be written as:

$$\omega\mathbf{x}_k = \mathbf{M}\cdot\mathbf{x}_k \quad . \tag{3.64}$$

Equation (3.64) defines the matrix $\mathbf{M}$ of hydrodynamic coefficients, whose explicit structure will be made clear in Eq. (3.74). Using (3.64), Eq. (3.62) can be cast in the form:

$$P\Lambda\Delta f = f^{\mathrm{GM}}\triangle\mathbf{X}\cdot\mathbf{M}\cdot\mathbf{x}_k \quad . \tag{3.65}$$

In the derivation of (3.65), one needs to take into account the constraints $\langle\boldsymbol{\xi}(\mathbf{c})\rangle_{\delta f} = \mathbf{0}$ (because the fields $\mathbf{x}_k$ are defined through the local Maxwellian part of the distribution function only) and $\langle\boldsymbol{\xi}(\mathbf{c})\rangle_{\hat{L}\delta f} = \mathbf{0}$ (conservation laws). The dependence of the matrix elements of $\mathbf{M}$ upon moments of δf is explicitly given in Table 3.4. Combining (3.61) and (3.65), and requiring that the result holds for any $\mathbf{x}_k$ (invariance condition), we obtain a closed, singular integral equation (the invariance equation) for complex-valued $\delta\mathbf{X}$,

$$\Delta\mathbf{X}\cdot\mathbf{M} = -i\mathbf{k}\cdot\mathbf{c}\,\Delta\mathbf{X} + \hat{L}\delta\mathbf{X} \quad . \tag{3.66}$$

Notice that $\delta\mathbf{X} = \Delta\mathbf{X} - \mathbf{X}^{(0)}$ vanishes for $k = 0$, which implies that, in the limit $k \to 0$, the invariant manifold is given by the set of local Maxwellians f^{LM}. The implicit equation (3.66) for $\delta\mathbf{X}$ (or $\Delta\mathbf{X}$, as $\mathbf{X}^{(0)}$ is known) is identical with the eigen-closure (3.60), and is our main and practically useful result.

Table 3.4 Symmetry adapted components of (nonequilibrium) stress tensor $\boldsymbol{\sigma}_k$ and heat flux $\mathbf{q}_k$, introduced in (3.72) and (3.73)

$\sigma_1^{\parallel}$	$\sigma_2^{\parallel}$	$\sigma_3^{\parallel}$	σ_4
$\langle \lambda^{\parallel} \delta X_1 \rangle$	$\langle \lambda^{\parallel} \delta X_2 \rangle$	$\langle \lambda^{\parallel} \delta X_3 \rangle$	$\langle c_{\parallel} c_{\perp} \delta Y_4 \rangle$
$-k^2 B$	ikA	$-k^2 C$	ikD
Real, $\oplus$	Imag., $\oplus$	Real, $\oplus$	Imag., $\ominus$
$q_1^{\parallel}$	$q_2^{\parallel}$	$q_3^{\parallel}$	q_4
$\langle \gamma^{\parallel} \delta X_1 \rangle$	$\langle \gamma^{\parallel} \delta X_2 \rangle$	$\langle \gamma^{\parallel} \delta X_3 \rangle$	$\langle (c^2 - \frac{5}{2}) c_{\perp} \delta Y_4 \rangle$
ikX	$-k^2 Z$	ikY	$-k^2 U$
Imag., $\ominus$	Real, $\ominus$	Imag., $\ominus$	Real, $\oplus$

Row 2: Microscopic expression of these components (averaging with the global Maxwellian). Short-hand notation used: $\lambda^{\parallel} = c_{\parallel}^2 - \frac{c^2}{3}$ and $\gamma^{\parallel} = (c^2 - \frac{5}{2}) c_{\parallel}$. Row 3: Expression of the components in terms of (as we show, real-valued) functions A–Z (see text). Row 4: Parity with respect to z—symmetric ($\oplus$) or antisymmetric ($\ominus$)—of the part of the corresponding δX entering the averaging in row 2, and whether this part is imaginary or real-valued (see Fig. 3.7). Row 3 is an immediate consequence of row 4

3.3.3 Coordinate Representation and Symmetries

In order to calculate the averages occurring in Sect. 3.3.2, we switch to spherical coordinates. For each (at present arbitrary) wave vector $\mathbf{k} = k\mathbf{e}_{\parallel}$, we choose the coordinate system in such a way that its (vertical) z-direction aligns with $\mathbf{e}_{\parallel}$ and that its x–direction aligns with $\mathbf{e}_{\perp}$. The velocity vector we had been decomposed earlier as $\tilde{\mathbf{u}} = u^{\parallel}\mathbf{e}_{\parallel} + u^{\perp}\mathbf{e}_{\perp}$. We can then express $\mathbf{c}$, over which we are going to perform all integrals, in terms of its norm c, a vertical variable z and plane vector $\mathbf{e}_{\phi}$ (azimuthal angle $\mathbf{e}_{\phi} \cdot \mathbf{e}_{\perp} = \cos\phi$; the plane contains $\mathbf{e}_{\perp}$) for the present purpose as:

$$\mathbf{c}/c = \sqrt{1 - z^2}\, \mathbf{e}_{\phi} + z\mathbf{e}_{\parallel} \quad , \tag{3.67}$$

as shown in Fig. 3.3.

The local Maxwellian, linearized around global equilibrium, takes the form: $f^{\mathrm{LM}}/f^{\mathrm{GM}} = 1 + \varphi_0 = 1 + \mathbf{X}^{(0)} \cdot \mathbf{x}_k$, where the four-dimensional $\mathbf{X}^{(0)}$, and the related vector $\boldsymbol{\xi}$, employing four-dimensional $\mathbf{x}_k = [\tilde{n}_k, u^{\parallel}, \tilde{T}_k, u^{\perp}]$, are given by the expressions

$$\mathbf{X}^{(0)}(\mathbf{c}) = \left(1, 2c_{\parallel}, (c^2 - \frac{3}{2}), 2c_{\perp}\right) \quad , \tag{3.68}$$

$$\boldsymbol{\xi}(\mathbf{c}) = \left(1, c_{\parallel}, \frac{2}{3}(c^2 - \frac{3}{2}), c_{\perp}\right) \quad . \tag{3.69}$$

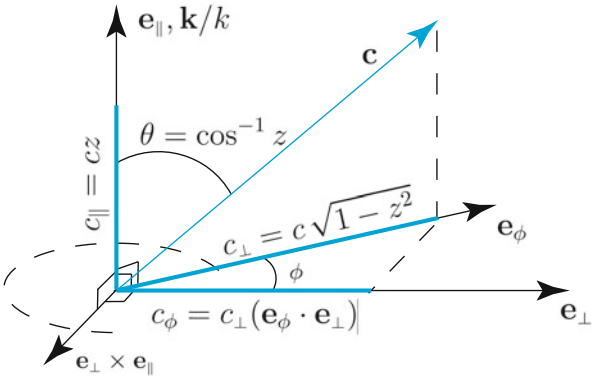

Fig. 3.3 Schematic drawing introducing a orthonormal frame $\mathbf{e}_\parallel, \mathbf{e}_\perp$, and $\mathbf{e}_\perp \times \mathbf{e}_\parallel$ which is defined by the wavevector $\mathbf{k} \parallel \mathbf{e}_\parallel$ and the heat flux $\mathbf{q}$ (not shown), which lies in the $\mathbf{e}_\parallel$–$\mathbf{e}_\perp$–plane. Shown is the velocity vector $\mathbf{c}$ (3.67) relative to this frame (characterized by length c, coordinate z, and angle ϕ) and its various components. The integration over $d\mathbf{c} = c^2 dc dz d\phi$ is done in spherical coordinates with respect to the local orthonormal basis

Here, we introduced, for later use, the abbreviations

$$c_\parallel \equiv \mathbf{c} \cdot \mathbf{e}_\parallel, \qquad c_\perp \equiv \mathbf{c} \cdot \mathbf{e}_\perp, \qquad c_\phi \equiv \mathbf{c} \cdot \mathbf{e}_\phi = \frac{c_\perp}{\mathbf{e}_\perp \cdot \mathbf{e}_\phi}, \tag{3.70}$$

such that $i\mathbf{k} \cdot \mathbf{c} = ikc_\parallel$. We can then rewrite (3.67) as $\mathbf{c} = c_\phi \mathbf{e}_\phi + c_\parallel \mathbf{e}_\parallel$ with $c_\parallel = cz$ and $c_\phi = c\sqrt{1-z^2}$. The latter two components, contrasted by $c_\perp$ (and $\mathbf{e}_\phi$), do not depend on the azimuthal angle. We further introduced yet unknown fields $\delta\mathbf{X}(\mathbf{c}, \mathbf{k})$ which characterize the nonequilibrium part of the distribution function, $\delta\varphi = \delta f / f^{\mathrm{GM}}$.

By analogy with the structure of the local Maxwellian, we postulate that, close to equilibrium, $\delta\varphi$ depends linearly on the hydrodynamic fields $\mathbf{x}_k$ themselves. Equation (3.60) can, hence, be cast in the form:

$$\delta\varphi = \delta\mathbf{X} \cdot \mathbf{x}_k = \delta X_1 \tilde{n}_k + \delta X_2 u^\parallel + \delta X_3 \tilde{T}_k + \delta X_4 u^\perp \quad . \tag{3.71}$$

The functions $\delta X_{1,2,3}$, which are associated to the longitudinal fields, inherit the full rotational symmetry of the corresponding Maxwellian components, i.e. $\delta X_{1,2,3} = \delta X_{1,2,3}(c, z)$, whereas δX_4 factorizes as $\delta X_4(c, z, \phi) = 2\delta Y_4(c, z) \sum_{m=1}^{\infty} y_m \cos m\phi$. In this context it is an important technical aspect of our derivation to work with a suitable orthogonal set of basis functions to represent δf uniquely. The matrix $\mathbf{M}$ in (3.65) contains the non-hydrodynamic fields: the heat flux $\mathbf{q}_k \equiv \langle \mathbf{c}(c^2 - \frac{5}{2}) \rangle_f$ and the stress tensor $\boldsymbol{\sigma}_k \equiv \langle \overline{\mathbf{cc}} \rangle_f$, where $\overline{\mathbf{s}}$ denotes the symmetric traceless part of a tensor $\mathbf{s}$ [40], $\overline{\mathbf{s}} = \frac{1}{2}(\mathbf{s} + \mathbf{s}^T) - \frac{1}{3}\mathrm{tr}(\mathbf{s})\mathbf{I}$, where $\mathbf{I}$ is the identity matrix. Using (3.60) and the above mentioned angular dependence of the $\delta\mathbf{X}$ functions (the only term in δX_4 playing a role in our calculations is the first order term $\cos\phi$, with $y_1 = 1$),

constraints, such as the required decoupling between longitudinal and transversal dynamics of the hydrodynamic fields, are automatically dealt with correctly when performing integrals over ϕ.

More explicitly, the stress tensor and heat flux uniquely decompose as follows:

$$\boldsymbol{\sigma}_k = \sigma^{\parallel} \frac{3}{2} \overline{\mathbf{e}_{\parallel}\mathbf{e}_{\parallel}} + \sigma^{\perp} 2 \overline{\mathbf{e}_{\parallel}\mathbf{e}_{\perp}}, \tag{3.72}$$

$$\mathbf{q}_k = q^{\parallel} \mathbf{e}_{\parallel} + q^{\perp} \mathbf{e}_{\perp}, \tag{3.73}$$

with the moments $\sigma^{\parallel} = (\sigma_1^{\parallel}, \sigma_2^{\parallel}, \sigma_3^{\parallel}) \cdot (\tilde{n}_k, u^{\parallel}, \tilde{T}_k)$ and $\sigma^{\perp} = \sigma_4 u^{\perp}$, and similarly for $\mathbf{q}_k$ (see Row 2 of Table 3.4).

The prefactors arise from the identities $\overline{\mathbf{e}_{\parallel}\mathbf{e}_{\parallel}} : \overline{\mathbf{e}_{\parallel}\mathbf{e}_{\parallel}} = \frac{2}{3}$ and $\overline{\mathbf{e}_{\parallel}\mathbf{e}_{\perp}} : \overline{\mathbf{e}_{\parallel}\mathbf{e}_{\perp}} = \frac{1}{2}$. We note in passing that, while the stress tensor has, in general, three different eigenvalues, in the present symmetry adapted coordinate system it exhibits a vanishing first normal stress difference. Since the integral kernels of all moments in (3.72) do not depend on the azimuthal angle, these are actually two-dimensional integrals over $c \in [0, \infty]$ and $z \in [-1, 1]$, each weighted by a component of $2\pi c^2 f^{\mathrm{GM}} \delta\mathbf{X}$.

Stress tensor and heat flux can yet be written in an alternative form, defined by Row 3 of Table 3.4, in terms of the functions A–Z, which correspond to moments of the nonequilibrium distribution function and are related to the generalized transport coefficients, see [4, 31, 36] and below.

Due to fundamental symmetry considerations, the hereby introduced generalized transport coefficients A–Z are real-valued. To show this, we use the functions A–Z to split $\mathbf{M}$ into parts as $\mathbf{M} = \mathrm{Re}(\mathbf{M}) - i\,\mathrm{Im}(\mathbf{M})$,

$$\mathbf{M} = k^2 \begin{pmatrix} 0 & 0 & 0 & 0 \\ 0 & A & 0 & 0 \\ \frac{2}{3}X & 0 & \frac{2}{3}Y & 0 \\ 0 & 0 & 0 & D \end{pmatrix} - ik \begin{pmatrix} 0 & 1 & 0 & 0 \\ \tilde{B} & 0 & \tilde{C} & 0 \\ 0 & \tilde{Z} & 0 & 0 \\ 0 & 0 & 0 & 0 \end{pmatrix}, \tag{3.74}$$

with abbreviations $\tilde{B} \equiv \frac{1}{2} - k^2 B$, $\tilde{C} \equiv \frac{1}{2} - k^2 C$, and $\tilde{Z} \equiv \frac{2}{3}(1 - k^2 Z)$. The checkerboard structure of the matrix $\mathbf{M}$ (3.74) is particularly useful for studying properties of the hydrodynamic equations (3.65), such as hyperbolicity and stability [21, 22], once the functions A–Z are explicitly evaluated. Moreover, we remind the reader that we use orthogonal basis functions (irreducible moments, cf. Table 3.4) to solve (3.66). In order to show how the above functions enter the definition of the $\mathbf{M}$ matrix, we first notice that its elements are—a priori—complex valued. We wish, then, to make use of the fact that all integrals over z vanish for odd integrands. To this end we introduce abbreviations $\oplus$ ($\ominus$) for a real-valued quantity which is even (odd) with respect to the transformation $z \to -z$. One notices $\mathbf{X}^{(0)} = (\oplus, \ominus, \oplus, \oplus)$, and we recall that A–Z are integrals over either even or odd functions in z, times a component of $\delta\mathbf{X}$ (see Table 3.4). Let us prove the consistency of the specified

symmetry of $\mathbf{M}$ and the invariance condition: start by assuming A–Z to be real-valued functions. Then $M_{\mu\nu} = \oplus$ if $\mu + \nu$ is even, and $M_{\mu\nu} = i\oplus$ otherwise. This implies $\delta X_1 = \oplus + i\ominus$, $\delta X_2 = \ominus + i\oplus$, $\delta X_3 = \oplus + i\ominus$, and $\delta X_4 = \oplus + i\ominus$, i.e., different symmetry properties for real and imaginary parts. With these "symmetry" expressions for $\mathbf{X}^{(0)}$, $\delta\mathbf{X}$, and $\mathbf{M}$ at hand, and by noticing that symmetry properties for $\delta\mathbf{X}$ take over to $\hat{L}(\delta\mathbf{X})$ because the $\psi_{r,l}$ are (i) symmetric (antisymmetric) in z for even (odd) l and (ii) eigenfunctions of $\hat{L}$, we can insert into the right hand side of the equation, $\hat{L}(\delta\mathbf{X}) = (\mathbf{X}^{(0)} + \delta\mathbf{X}) \cdot (\mathbf{M} + i \ominus \mathbf{I})$, which is identical with the invariance equation (3.66). There are only two cases to consider, because $\mathbf{M}$ has a checkerboard structure, i.e., only two types of columns: Columns $\mu = 1$ and $\mu = 3$: $\delta X_\mu = \oplus + i\ominus$ because $M_{1-3,4} = 0$; Columns $\mu \in \{2, 4\}$: $\delta X_\mu = \oplus + i\ominus$ if $M_{\mu,1-3} = 0$ (which is the case for column 4) and $\ominus + i\oplus$ if $M_{\mu,4} = 0$ (which is the case for column 2). These observations complete the proof.

3.3.4 The BGK Kinetic Model

The solution of the invariance equation (3.66) can be obtained in some simple cases amenable to an analytic or numerical treatment. In this section we focus on the linearized version of the BGK kinetic model, which remains popular in applications [8] and is characterized by a single collision frequency. The invariance equation for this model is readily obtained from Eq. (3.66) by using $\hat{L}(\delta\mathbf{X}) = -\delta\mathbf{X}$, which, hence, yields:

$$\delta\mathbf{X} = \mathbf{X}^{(0)} \cdot \left(\mathbf{M} + [ikc_\parallel + 1]\mathbf{I}\right)^{-1} - \mathbf{X}^{(0)}. \tag{3.75}$$

Notice that $\delta\mathbf{X}$ vanishes for $k = 0$, and that (3.75) is supplemented with the basic constraint $\langle \boldsymbol{\xi} \rangle_{\delta f} = 0$, which, however, is automatically dealt with if we only evaluate anisotropic (irreducible) moments with δf, such as those listed in Table 3.4.

The non-perturbative derivation is made possible with an optimal combination of analytical and numerical approaches to solve the invariance equation. The result for the hydrodynamic modes is demonstrated in Fig. 3.4. It is clear from Fig. 3.4 that the relaxation of none of the hydrodynamic modes is faster than $\omega = -1$ which is the collision frequency in the units adopted in this section. Thus, the result for the exact hydrodynamics indeed corresponds to the following intuitive picture: the hydrodynamic modes, at large k, cannot relax faster than the (single) collision frequency itself.

We iteratively calculated (i) $\delta\mathbf{X}$ directly from (3.75) for each k in terms of $\mathbf{M}$, (ii) subsequently calculate moments from $\delta\mathbf{X}$ by either symbolical or numerical integration (both approaches produce same results within machine precision, we found simple numerical integration on a regular 500×100 grid in c, z-space with grid spacing 0.01 on both axes sufficient to reproduce analytical results). Importantly, the

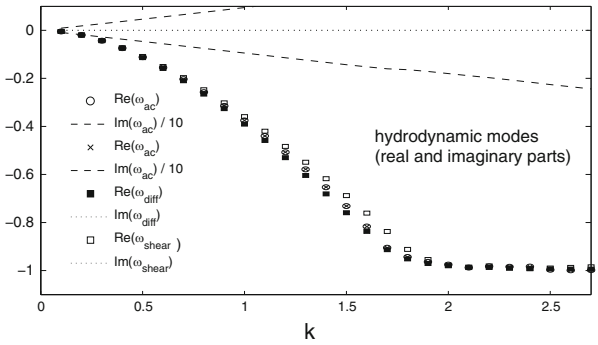

Fig. 3.4 Exact hydrodynamic modes ω of the Boltzmann-BGK kinetic equation as a function of wave number k (two complex-conjugated acoustic modes $\omega_{\rm ac}$, twice degenerated shear mode $\omega_{\rm shear}$ and thermal diffusion mode $\omega_{\rm diff}$). The non-positive decay rates $\mathrm{Re}(\omega)$ attain the limit of collision frequency (-1) in the $k \gg 1$ regime

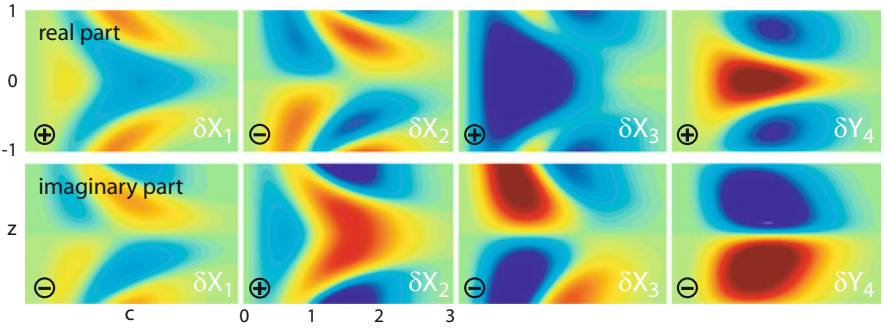

Fig. 3.5 Sample distribution function $f(\mathbf{c}, \mathbf{k})$ at $k = 1$, fully characterized by the four quantities $\delta X_{1,2,3}(c, z)$ and $\delta Y_4(c, z)$. Shown here are both their real (*left*) and imaginary parts (*right column*). In order to improve contrast, we actually plot $\ln|1 + f^{\rm GM}\delta X_\mu|$ multiplied by the sign of δX_μ. Same color code for all plots, ranging from -0.2 (*red*) to $+0.2$ (*blue*)

fix point of the iteration (i)–(ii)–(i)-.. is unique for each k, i.e., does not depend on the initial values for moments A–Z.

In addition, two other computational strategies were implemented: First, we used continuation of functions A–Z from their values at $k = 0$ to solve (3.75) with an incremental increase of k, where the solution at k was used as the initial guess for $k + dk$. Second, we used also a continuation "backwards" in which the solution at some k (obtained by convergent iterations with a random initial condition) was used as the initial guess for a solution at $k - dk$. Both these strategies returned the same values of functions A–Z as computed by iterations from arbitrary initial condition.

The solution $\delta\mathbf{X}$ allows one to calculate the whole distribution function f via (3.60) as illustrated by Fig. 3.5. For the resulting moments A–Z, for a wide

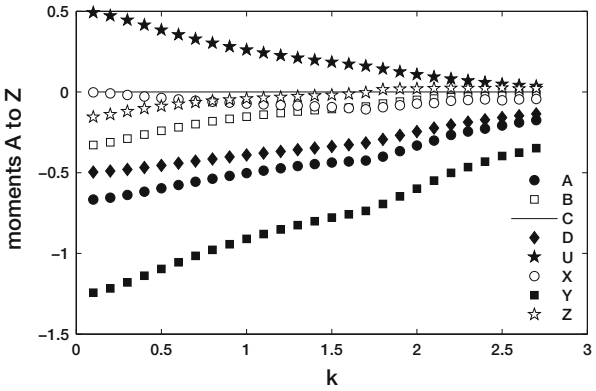

Fig. 3.6 Moments A–Z vs. wave number k obtained with the solution of (3.75)

range of k-values, see Fig. 3.6. With the result for the functions A–Z at hand, the extended hydrodynamic equations are closed.

Let us briefly discuss the pertinent properties of this system. First, the generalized transport coefficients are given by the nontrivial eigenvalues of $-k^{-2}\mathrm{Re}(\mathbf{M})$: $\lambda_2 = -A$ (elongation viscosity), $\lambda_3 = -\frac{2}{3}Y$ (thermal diffusivity), and $\lambda_4 = -D$ (shear viscosity). All these generalized transport coefficients are non-negative (see Fig. 3.6). Second, computing the eigenvalues of matrix $\mathbf{M}$, we obtain the dispersion relation $\omega(k)$ of the corresponding hydrodynamic modes already presented in Fig. 3.4. Third, a suitable transform of the hydrodynamic fields, $\mathbf{z_k} = \mathbf{T} \cdot \mathbf{x_k}$, where $\mathbf{T}$ is a real-valued matrix, can be established such that the transformed hydrodynamic equations read $\partial_t \mathbf{z_k} = \mathbf{M}' \cdot \mathbf{z_k}$, where $\mathbf{M}' = \mathbf{T} \cdot \mathbf{M} \cdot \mathbf{T}^{-1}$ is manifestly hyperbolic and stable; $\mathrm{Im}(\mathbf{M}')$ is symmetric, $\mathrm{Re}(\mathbf{M}')$ is symmetric and non-positive semidefinite. The corresponding transformation matrix $\mathbf{T}$ can be easily read off the results obtained in [21] for Grad's systems since the structure of the matrix $\mathbf{M}$ (3.74) is identical to the one studied in [21, 22]. It can be explicitly verified that matrix $\mathbf{T}$ with the functions A–Z derived herein is real-valued and thus render the transformed hydrodynamic equations manifestly hyperbolic and stable.

We note that this result—hyperbolicity of exact hydrodynamic equations—strongly supports a recent suggestion by Bobylev to consider a hyperbolic regularization of the Burnett approximation [30]. Similarly, using the hyperbolicity, an H-theorem is elementary proven as in [22, 30]. Finally, using the accurate data for functions A–Z, we can write analytic approximations for the corresponding hydrodynamic equations in such a way that hyperbolicity and stability is not destroyed in such an approximation [21].

In conclusion, we derived exact hydrodynamic equations from the linearized Boltzmann-BGK equation [36]. The main novelty is the numerical non-perturbative procedure to solve the invariance equation. In turn, the highly efficient approach is made possible by choosing a convenient coordinate system and establishing symmetries of the invariance equation. The invariant manifold in the space of

distribution functions is thereby completely characterized, that is, not only equations of hydrodynamics are obtained but also the corresponding distribution function is made available.

The predicted smoothness and extendibility of the spectrum to all k is expected to have some implications for micro-resonators where the quality of the resonator becomes better at very high frequency: that is compatible with our prediction. The damping of all the modes saturates while the imaginary part of the acoustic modes frequency grows. The pertinent data can be used, in particular, as a much needed benchmark for computation-oriented kinetic theories such as lattice Boltzmann models, as well as for constructing novel models [41].

It is worth remarking that the above derivation of hydrodynamics is done under the standard assumption of local equilibrium, however the assumption itself is open to further study [42].

3.3.5 The Maxwell Molecules Gas

In this section we investigate another kinetic model for which an exact solution of the invariance equation (3.66) can be obtained: the Maxwell molecules gas, i.e. a gas constituted by particles repelling each other with a force proportional to the inverse fifth power of the distance. Wang Chang and Uhlenbeck [43] provided an analytical solution to the eigenvalue problem for the linearized collision operator L pertaining to this case. For the Maxwell molecules gas, the collision probability per unit time, $g\sigma(g,\theta)$, is independent of the magnitude of the relative velocity g. Since the collision operator is spherically symmetric in the velocity space, the dependence of the eigenfunctions upon the direction of $\mathbf{c}$ is expected to be spherically harmonic. Indeed, the eigenvalue problem admits the following solutions:

$$\begin{aligned} \hat{L}[\psi_{r,l}(c,z)] &= \lambda_{r,l}\psi_{r,l}(c,z) \quad , \\ \psi_{r,l}(c,z) &= \sqrt{\frac{r!(l+\frac{1}{2})\sqrt{\pi}}{(l+r+\frac{1}{2})!}}\, c^l P_l(z) S^{(r)}_{l+\frac{1}{2}}(c^2) \quad , \end{aligned} \tag{3.76}$$

where $S^{(r)}_{l+1/2}(x)$ are Sonine polynomials, and $P_l(z)$ are Legendre polynomials which act on the azimuthal component of the peculiar velocity $\mathbf{c}$. The Legendre and Sonine polynomials are each orthogonal sets, i.e.:

$$\int_{-1}^{1} P_l(z)\,P_n(z)\,dz = \frac{2}{2l+1}\delta_{ln} \quad ,$$

$$2\pi\int_0^\infty c^2 e^{-c^2} c^{2l} S^{(r)}_{l+\frac{1}{2}}(c^2) S^{(p)}_{l+\frac{1}{2}}(c^2)\,dc = \frac{\pi(l+\frac{1}{2}+r)!}{r!}\delta_{rp} \quad .$$

Accordingly, the $\psi_{r,l}$ are normalized to unity with the weight factor $f_0(c)$:

$$\delta_{rr'}\delta_{ll'} = 2\pi^{-1/2}\int_{-1}^{1}\int_{0}^{\infty} c^2 e^{-c^2}\psi_{r,l}(c,z)\psi_{r',l'}(c,z)\,dcdz$$
$$\equiv \pi^{-3/2}\int e^{-c^2}\psi_{r,l}(\mathbf{c})\psi_{r',l'}(\mathbf{c})\,d\mathbf{c} \quad . \tag{3.77}$$

The corresponding eigenvalues for Maxwell molecules are given by:

$$\lambda_{r,l} = 2\pi\int_0^{\pi}\sin(\theta)F(\theta)T_{rl}(\theta)\,d\theta \quad ,$$
$$T_{rl}(\theta) \equiv \cos^{2r+l}\left(\frac{\theta}{2}\right)P_l\left(\cos\frac{\theta}{2}\right) + \sin^{2r+l}\left(\frac{\theta}{2}\right)P_l\left(\sin\frac{\theta}{2}\right) - (1+\delta_{r0}\delta_{l0}) \quad .$$

The collision operator $\hat{L}$ is negative semidefinite, i.e. all eigenvalues are negative except $\lambda_{0,0}$, $\lambda_{0,1}$, and $\lambda_{1,0}$ which are zero and correspond to the elementary collision invariants. As shown by Wang Chang and Uhlenbeck [43], the spectrum of $\hat{L}$ for Maxwell molecules is discrete and, for $r \to \infty$, the eigenvalues $\lambda_{r,l}$ tend to $-\infty$. Chang and Uhlenbeck's investigation on the dispersion of sound in a Maxwell molecules gas was based upon writing the deviation from the global equilibrium as:

$$(\varphi_0 + \delta\varphi) = \sum_{\{r,l\}=0}^{\infty} a^{(r,l)}\psi_{r,l}(\mathbf{c}) \quad , \tag{3.78}$$

so that (3.52) reduces to an algebraic equation for the coefficients $a^{(r,l)}$:

$$\omega a^{(r,l)} = -i\mathbf{k}\cdot\sum_{\{r',l'\}=0}^{\infty}\mathfrak{C}_{r,l,r',l'}a^{(r',l')} + \lambda_{r,l}a^{(r,l)} \quad , \tag{3.79}$$

with:

$$\mathfrak{C}_{r,l,r',l'} = \langle\psi_{r,l}|\mathbf{c}\;\psi_{r',l'}\rangle \quad .$$

The hydrodynamic modes for the Maxwell-molecules gas are determined, as seen in Sect. 3.3.1, from the condition of non-trivial solvability of the linear system (3.79). This approach allows to solve the eigenvalue problem (3.50) for an arbitrary number of modes, which is made possible just by tuning the number of eigenfunctions taken into account in (3.78).

Another approach [31] is based, instead, on the expansion of the functions $[\mathbf{X}^{(0)}, \delta\mathbf{X}]$ in terms of the orthonormal basis $\psi_{r,l} = \psi_{r,l}(c,z)$:

$$X_\mu^{(0)}(c,z) = \sum_{r,l}^{N} a_\mu^{(0)(r,l)} \psi_{r,l}(c,z) \quad , \tag{3.80}$$

$$\delta X_\mu(k,c,z) = \sum_{r,l}^{N} a_\mu^{(r,l)}(k) \psi_{r,l}(c,z) \quad . \tag{3.81}$$

The equilibrium coefficients $a_\mu^{(0)}$ are known, and can be determined, by taking advantage of the orthogonality of the eigenfunctions, as follows:

$$a_\mu^{(0)(r,l)} = \pi^{-\frac{3}{2}} \int e^{-c^2} \psi_{r,l}(c,z) X_\mu^{(0)}(c,z)\, d\mathbf{c} \quad . \tag{3.82}$$

Inserting (3.80) and (3.81) into the invariance equation (3.66), we obtain the following nonlinear set of algebraic equations for the unknown coefficients $a_\mu^{(r,l)}(k)$:

$$b_\mu^{(r,l)} M_{\mu\nu} = -i\mathbf{k} \cdot \sum_{r',l'}^{N} b_\nu^{(r',l')} \mathfrak{C}_{(r,l,r',l')} + \sum_{r',l'}^{N} a_\nu^{(r',l')} \mathfrak{L}_{(r,l,r',l')} \quad , \tag{3.83}$$

with, $\forall_{\mu,r,l}$, $b_\mu^{(r,l)} = \left(a_\mu^{(0)(r,l)} + a_\mu^{(r,l)}\right)$, and

$$\mathfrak{L}_{(r,l,r',l')} = \langle \psi_{r,l} | \hat{L}\ \psi_{r',l'} \rangle \quad .$$

For any order of expansion, the solutions of (3.83) characterize an invariant manifold in the phase space. The matrix elements $\mathfrak{L}_{(r,l,r',l')}$ can be easily evaluated in few kinetic models, such as the linearized BGK model [36] and Maxwell molecules [31]. In particular, the Maxwell molecules case is recovered by setting:

$$\mathfrak{L}_{(r,l,r',l')} = \lambda_{r,l} \delta_{r,r'} \delta_{l,l'} \quad .$$

whereas the linearized BGK model is recovered by setting all nonvanishing eigenvalues equal to $\lambda = -1$. The calculation of the coefficients $\mathbf{a}^{(r,l)}$, via the reformulated invariance equation (3.83), is easily achieved. Through these coefficients, the invariant manifold is fully characterized: the distribution function is determined and the corresponding matrix $\mathbf{M}$ of linear hydrodynamics as well as moments A–Z, are made accessible.

Solving the invariance equation (3.66) and thus obtaining the distribution function via the coefficients $\mathbf{a}^{(r,l)}$, cf. Fig. 3.7, required minor computational effort

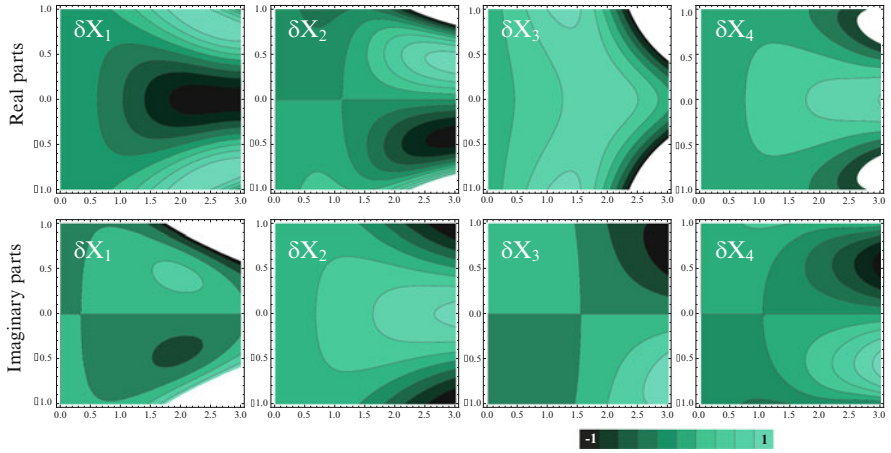

Fig. 3.7 All contributions $\delta X_{1-4}(\mathbf{c},\mathbf{k})$ vs. c (horizontal, $c = |\mathbf{c}|$) and $z \in [-1,1]$ (vertical axis, z is the cosine of the angle between $\mathbf{k}$ and peculiar velocity $\mathbf{c}$) to the nonequilibrium distribution function $\delta f = f^{\mathrm{GM}}\delta\mathbf{X}\cdot\mathbf{x}_k$ (3.60) at $k = 1$, obtained with the fourth order expansion, $N = 4$. Shown here are both their real (*top*) and imaginary parts (*bottom row*)

[31]. The components A–Z of $\mathbf{M}$ are related to the coefficients $\mathbf{a}^{(r,l)}$ by the expressions:

$$
\begin{aligned}
&A = -\frac{i a_2^{(0,2)}}{\sqrt{3}k}\,, \quad B = -\frac{a_1^{(0,2)}}{\sqrt{3}k^2}\,, \quad C = -\frac{a_3^{(0,2)}}{\sqrt{3}k^2}\,, \\
&X = -\frac{i\sqrt{5}a_1^{(1,1)}}{2k}\,, \quad Y = -\frac{i\sqrt{5}a_3^{(1,1)}}{2k}\,, \quad Z = -\frac{\sqrt{5}a_2^{(1,1)}}{2k^2}\,, \\
&D = -\frac{i}{k}\sum_{r,l}^{N} a_4^{(r,l)}\langle c_\parallel c_\phi|\psi_{r,l}\rangle\,, \quad U = -\frac{1}{k^2}\sum_{r,l}^{N} a_4^{(r,l)}\left\langle\left(c^2-\frac{5}{2}\right)c_\perp|\psi_{r,l}\right\rangle\,.
\end{aligned}
\tag{3.84}
$$

In the regime of large Knudsen numbers the coefficients $\mathbf{a}^{(r,l)}$ may be used to, e.g., directly calculate phoretic accelerations onto moving and rotating convex particles [44], while in the opposite limit of small k we recover the classical hydrodynamic equations.

3.3.6 *Hydrodynamic Modes and Transport Coefficients*

With $\mathbf{M}$ at hand, the hydrodynamic modes are obtained from the condition of non-trivial solvability of the linear system (3.64). Figure 3.8 illustrates the damping rates

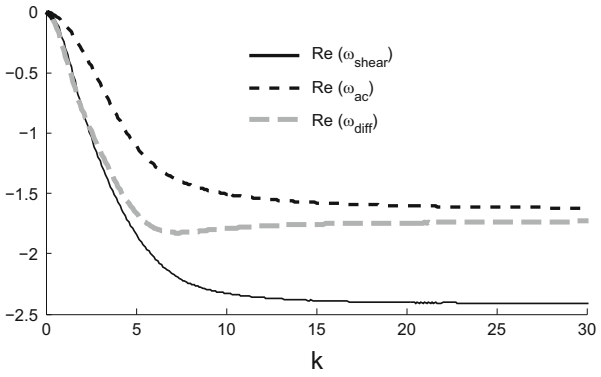

Fig. 3.8 Hydrodynamic modes ω of the Boltzmann kinetic equation with Maxwell molecules collision operator as a function of wave number k. Shown are two complex conjugated acoustic modes $\omega_{\rm ac}$, twice degenerated shear mode $\omega_{\rm sh}$ and a thermal diffusion mode $\omega_{\rm diff}$

of the fluctuations given by the real part of the hydrodynamic modes, obtained by truncating the series (3.80) and (3.81) at the fourth order. The picture does not qualitatively change upon further increase of the order N. For any given order of expansion, the modes extend smoothly over all the wavevector domain and, for large k, they attain an asymptotic value, which is clearly in agreement with the asymptotic behavior of the hydrodynamic modes obtained for the linearized BGK model discussed in Sect. 3.3.4.

The generalized transport coefficients are obtained by the nontrivial eigenvalues of $-k^2\mathrm{Re}(\mathbf{M})$: $\lambda_2 = -A$ (elongation viscosity), $\lambda_3 = -\frac{2}{3}Y$ (thermal diffusivity) and $\lambda_4 = -D$ (shear viscosity). In the limit $k \to 0$, one recovers the hydrodynamic limit. This limit had been worked out in detail in [21, 22]. In that limit, the generalized transport coefficients A–Z become the classical transport coefficients. As can be seen from Fig. 3.9, and by also inspecting the invariance equation (3.66), in the limit of small k, all moments A–Z approach constant values in the limit of small k. These constants are compatible with those obtained in [21, 22] for the case of Navier-Stokes equations and the Burnett correction [45].

The stress tensor and heat flux are given in terms of these moments in Table 3.4. For example, the parallel component of the stress tensor related to density fluctuations, $\sigma_1^{\parallel}$, cf. Eq. (3.72), is given by $-k^2 B$, so that it approaches $-k^2$ for small k, as it results from the Burnett approximation [2].

Moreover, under suitable assumptions, one may also cast the matrix of hydrodynamic coefficients $\mathbf{M}$ in the structure of a Green-Kubo formula [33]. We summarize below the main steps of the proof given in [46], to which we refer the reader for an exhaustive derivation. From Eqs. (3.64) and (3.66), the time evolution of the hydrodynamic fields can be formally written as:

$$\mathbf{x}_k(\tau) = e^{\mathbf{M}\tau}\mathbf{x}_k(0) = \left\langle \boldsymbol{\xi} \middle| e^{\Lambda\tau}\delta\mathbf{X} \right\rangle \mathbf{x}_k(0) \quad , \tag{3.85}$$

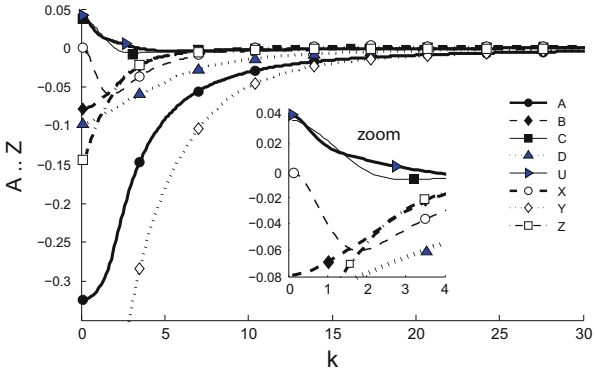

Fig. 3.9 Moments A–Z of the distribution function (see Table 3.4 and Eq. (3.84)) vs. wave number k obtained with the solution of (3.66). *Non-triangles* (*black symbols*): Moments entering only the longitudinal component of hydrodynamic equations. *Triangles* (*blue symbols*): Moments entering the transverse component of hydrodynamic equations

where we skipped, for brevity, the spatial dependence of the fields. In Eq. (3.85) the time τ is of the order of τ_{macro}, which denotes a characteristic time scale related to the evolution of the hydrodynamic fields. As discussed in Sect. 3.2.2, the presence of a definite time scale separation, in a particle system, entails that $\tau_{macro} \gg \tau_{mf}$, where τ_{mf} denotes a kinetic time scale (i.e. the mean time between collisions). Hence, by invoking the Bogoliubov hypothesis of time scale separation, the time τ becomes large with respect to the characteristic time scale of the dynamics of the distribution function (r.h.s. of the second equality in (3.85)). Thus, from Eq. (3.85), we can write the matrix of hydrodynamic coefficients in the form:

$$\mathbf{M} = \lim_{\tau\to\infty} \frac{1}{\tau} \log \left\langle \boldsymbol{\xi} \left| e^{\Lambda\tau} \delta\mathbf{X} \right\rangle \right. \tag{3.86}$$

Next, we use the operator identity:

$$e^{\Lambda\tau} = 1 + \Lambda\tau + \Lambda\tau \left[\frac{1}{\tau} \int_0^\tau (\tau - t) e^{\Lambda t} dt \right] \Lambda \quad , \tag{3.87}$$

and make the following assumptions:

(i) The underlying kinetic evolution is such that the term between square brackets, in Eq. (3.87), can be approximated, for large τ, by $\int_0^\infty e^{\Lambda t} dt$.
(ii) The expansion of the logarithm to first order in τ is a valid approximation *before* the limit $\tau \to \infty$ is taken.

Thus, using the symmetry of the operator Λ, and neglecting, for simplicity, *kinematic contributions* [46] of the form $\langle \boldsymbol{\xi}(0) | \Lambda \delta \boldsymbol{X}(0) \rangle$, Eq. (3.86) can be finally written in the form:

$$\mathbf{M} = \int_0^\infty \left\langle \dot{\boldsymbol{\xi}}(0) \delta\dot{\mathbf{X}}(t) \right\rangle_{fGM} dt \quad . \tag{3.88}$$

Equation (3.88) allows one to extend the Green-Kubo formalism, which relates the response function to a suitable time correlation function, to the short wavelength domain. Moreover, it can be evinced from an inspection of Fig. 3.9 that in the free-particle regime, $k \to \infty$, the transport coefficients vanish and dissipative effects fade off. This observation finds a sound confirmation in [18]: "*Operationally, of course, transport coefficients cannot even be defined for a gas of non-interacting particles. A measurement of the thermal conductivity, for example, is only possible if we can apply, quasi-statically, a temperature gradient and maintain it while we measure the heat current. However, only for a system with a finite mean free path can a temperature gradient be maintained quasi-statically. A free gas would "run away", and the standard measurements of transport coefficients cannot be performed. Still, it may be satisfying for some that, in this case, the Kubo expressions give the most sensible result: zero.*"

3.3.7 Short Wavelengths Hydrodynamics

The existence of collective modes at short wavelengths, in real fluids, is a long-standing issue in fluid dynamics [48, 49]. In their seminal work [50], Ford et al. illustrated, on the basis of a model kinetic equation approximating the linearized Boltzmann equation, that the sound modes extended to length scales comparable with the mean free path in the gas. Similarly, our analysis showed that hydrodynamic modes and the generalized transport coefficients extend smoothly over the whole k domain. Therefore, the Invariant Manifold technique allows to refine the hydrodynamic description beyond the strictly hydrodynamic regime. Our results also strengthen those previously reported in [3, 51, 52] on dense fluids, which revealed that the hydrodynamic laws provide a sensible description of fluids even at length scales comparable with λ_{mf}.

It would be interesting, hence, to investigate the features of the equations of generalized hydrodynamics we obtained in the regime of finite frequencies and wavevectors. In Fig. 3.10a comparison is shown about inverse phase velocity and damping for acoustic waves between our results, former approaches [12, 29] and experimental data performed by Meyer and Sessler [47]. As it is seen, our results are very close to the predictions of the regularized 13 (Reg13) moments method [29] and closer to experimental data than (Reg13) concerning the phase spectrum. Our theory also predicts a phase speed which remains finite also at high frequencies, a property which is not enjoyed by any hydrodynamics derived from the CE expansion [28].

A further clue about the features of our model at finite frequencies and wavevectors can be achieved by investigating the spectrum of density fluctuations, $S_{\tilde{n},\tilde{n}}$ [4] From the knowledge of the functions A–Z, it is possible to compute the coefficients D_T and Γ, related to the damping, respectively, of thermal and pressure fluctuations

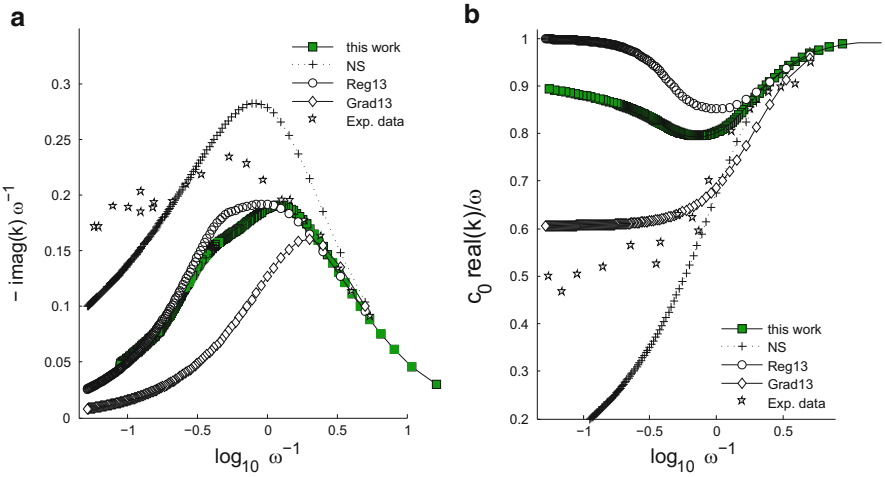

Fig. 3.10 (**a**) Damping spectrum, i.e., the negative imaginary part of k divided by frequency ω vs. the negative logarithm of ω. Results obtained in this work (by solving Eq. (3.66), and subsequently Eq. (3.65) for $w(k)$ with complex-valued k and real-valued ω) are compared with previous approaches including Navier Stokes (NS), regularized 13 moment (Reg13) [29], Grad's 13 moment (Grad13), and experimental data presented in [47]. (**b**) Phase spectrum, i.e, real part of k times velocity of sound c_0 and divided by ω vs. the negative logarithm of ω. Again, we compare with reference results

in fluids. In the limit of small k, and following standard textbooks [39], they read:

$$D_T = \frac{2}{5}(X - Y) \quad ,$$
$$\Gamma = -\left(\frac{1}{2}A + \frac{1}{5}X + \frac{2}{15}Y\right) \quad .$$

It is worth pointing out that, unlike standard treatments of hydrodynamic fluctuations, the generalized transport coefficient X enters the expression of the coefficients D_T and Γ, even though its contribution, as it is evident from Fig. 3.9 is fairly small. The calculation of $S_{\tilde{n},\tilde{n}}$ is a standard textbook exercise [39, 53]. We give, hence, the final result:

$$S_{\tilde{n},\tilde{n}}(k,\omega) = \frac{1}{2\pi} S_{\tilde{n},\tilde{n}}(k) \left[\frac{2}{5}\frac{2D_T k^2}{\omega^2 + (D_T k^2)^2} + \frac{3}{10}\frac{2\Gamma k^2}{(\omega \pm c_0 k)^2 + (\Gamma k^2)^2}\right] \quad . \tag{3.89}$$

Representative plots of $S(k,\omega)$ are shown in Fig. 3.11a, b. For small k (hydrodynamic limit), the obtained spectrum recovers the usual results of neutron (or light) scattering experiments and consists of the three Lorentzian peaks. The one centered

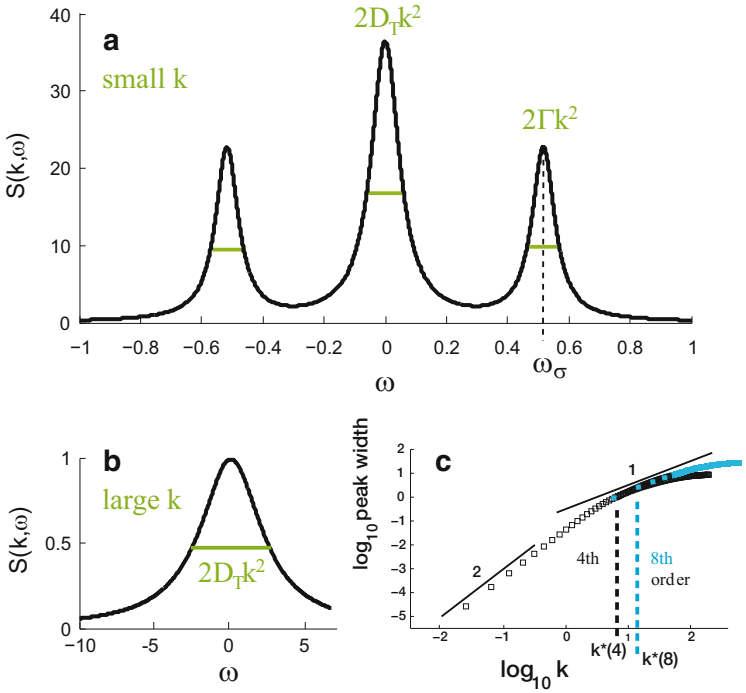

Fig. 3.11 (**a**) Dynamic structure factor $S_{\vec{n},\vec{n}}(k,\omega)$ vs. ω for a small $k = 0.4$ and (**b**) large $k = 100$. $\omega_s = c_0 k$ denotes the hydrodynamic predicted sound mode of the spectrum, and the widths are related to the moments A–Z (see Fig. 3.9). For small k, these are given by $D_T = \frac{2}{5}(X - Y)$ and $\Gamma = -(\frac{1}{2}A + \frac{1}{5}X + \frac{2}{15}Y)$, where A is the generalized longitudinal kinetic viscosity, Y the generalized thermal diffusion coefficient and X is a cross-coupling transport coefficient, relating heat flux to density gradients. (**c**) Width D^2_{Tk} of the Rayleigh peak vs. k (double-logarithmic). At small k, $D^2_{Tk} \propto k^2$ as all moments A–Z, except X, reach a finite value in this limit. The inflection point at $k = k^*(N) \gg 1$ (shown to be increasing with the order of expansion N) denotes the onset of departure from the ideal Maxwellian behavior, where the width of the peak starts to behave sublinearly in k, and is used to quantify the range of validity for results obtained at finite order

in $\omega = 0$ is the Rayleigh peak, which corresponds to the diffusive thermal mode. The two side peaks centered in $\omega \pm c_0 k$ are the Brillouin peaks, and represent the two propagating sound waves.

By increasing the wave-vector, one enters an "intermediate" regime, in which the structure of (3.89) is unchanged, except that the generalized coefficients D_T and Γ must then be replaced by more complicate expressions [31]. The net effect observed is that sound waves get damped and disappear, whereas the central Rayleigh peak decreases and broadens. Density fluctuations are, therefore, driven only by a diffusive thermal mode for large enough k. A deeper look about the behavior of the width at half maximum of the central Rayleigh peak with increasing wavevectors allows us to bridge, hence, the gap between the hydrodynamic and the free-particle regimes. For $k \ll 1$ the width of the central peak increases with the

square wavevector, $\propto k^2$, whereas, in the opposite regime, $k \gg 1$ the width of the central peak is expected to grow up linearly in k.

Our results, see Fig. 3.11, predict a width which is truly quadratic for small enough k, reaches the regime of linear behavior for large k and terminates, for some large k, with a sub-linear dependence on k. The onset of the terminal regime at $k = k^*(N)$ marks the range of validity which can be accessed at a given finite order of expansion N. Increasing N does not alter the overall picture obtained at a moderate order of expansion, and, more generally, results obtained with $N + 1$ will not change those obtained with N below $k^*(N)$, cf. Fig. 3.11c.

By varying the parameter N in the expansions (3.80) and (3.81) one is able to tune the number of nonequilibrium contributions to be included into the distribution function, thus refining the hydrodynamic description to an arbitrary level of accuracy.

The onset of a critical length scale marking the limit of the hydrodynamic description is reminiscent of the discussion made in Sect. 3.2. Namely, we know that hydrodynamics is founded on the notion of Local Equilibrium. Thus, for a given N, one may be tempted to link the length scale at which hydrodynamics breaks down, $[k^*(N)]^{-1}$, with the mesoscopic scale ℓ_{meso}. Further investigation is called for to shed light on this proposal: should such connection be true, this would then endow the generalized hydrodynamic equations obtained via the Invariant Manifold theory with a deeper thermodynamic content.

3.4 Conclusions

In this work, we described the use of the Invariant Manifold technique to derive closed hydrodynamic equations from some kinetic models. The main novelty of our approach stems from the use of a non-perturbative technique, which makes it possible to sum up exactly the classical Chapman–Enskog expansion. The method postulates a separation between slow and fast moments, and allows one to extract the slow invariant manifold in the space of distribution functions.

The obtained equations of exact hydrodynamics, derived by solving the invariance equation, are hyperbolic and admit a H-Theorem. Our solution of the invariance equation was considerably simplified by considering linear deviations from global equilibrium.

The generalized transport coefficients have been numerically determined and settled into expressions which recover the Green-Kubo formulae. Finally, by also comparing with available experimental data and previous approaches, we discussed the range of validity of our approach, which turned out to be amenable of extending the hydrodynamic scenario to length scales comparable with the mean free path. Our approach may help shedding new light on the investigation about the transition between the kinetic, particle-like, description of matter and the macroscopic, "continuum", one.

References

1. Colangeli, M.: From Kinetic Models to Hydrodynamics. Some Novel Results. Springer, New York (2013)
2. Gorban, A.N., Karlin, I.V.: Invariant Manifolds for Physical and Chemical Kinetics. Lecture Notes in Physics, vol. 660. Springer, Berlin (2005)
3. Alder, B.J., Alley, W.E.: Generalized hydrodynamics. Phys. Today **37**, 56 (1984)
4. Boon, J.P., Yip, S.: Molecular Hydrodynamics. Dover, New York (1991)
5. Bobylev, A.V.: Sov. Phys. Dokl. **27**, 29 (1982)
6. Uribe, F.J., Velasco, R.M., Garcìa-Colìn, L.S.: Bobylev's instability. Phys. Rev. E **62**, 5835 (2000)
7. Cercignani, C., Illner, R., Pulvirenti, M.: The Mathematical Theory of Dilute Gases. Springer, Berlin (1994)
8. Cercignani, C.: Theory and Application of the Boltzmann Equation. Scottish Academic Press, Edinburgh (1975)
9. Beskok, A., Karniadakis, G.E.: Microflows: Fundamentals and Simulation. Springer, Berlin (2001)
10. Karabacak, D.M., Yakhot, V., Ekinci, K.L.: High-frequency nanofluidics: an experimental study using nanomechanical resonators. Phys. Rev. Lett. **98**, 254505 (2007)
11. Öttinger, H.C.: Beyond Equilibrium Thermodynamics. Wiley, New York (2005)
12. Grad, H.: On the kinetic theory of rarefied gases. Commun. Pure Appl. Math. **2**, 331 (1949)
13. Jou, D., Casas-Vázquez, J., Lebon, G.: Extended Irreversible Thermodynamics. Springer, Berlin (2010)
14. Bogoliubov, N.N.: In: de Boer, J., Uhlenbeck, G.E. (eds.) Studies in Statistical Mechanics, vol. 1. Wiley, New York (1962)
15. Liboff, R.: Kinetic Theory Classical, Quantum and Relativistic Descriptions. Springer, New York (2003)
16. Liboff, R.: Generalized Bogoliubov hypothesis for dense fluids. Phys. Rev. A **31**, 1883 (1985)
17. Balescu, R.: Equilibrium and Nonequilibrium Statistical Mechanics. Wiley, New York (1975)
18. Forster, D.: Hydrodynamic Fluctuations, Broken Symmetry, and Correlation Functions. W. A. Benjamin, New York (1975)
19. Chapman, S., Cowling, T.G.: The Mathematical Theory of Nonuniform Gases. Cambridge University Press, New York (1970)
20. Lachowicz, M.: From kinetic to Navier-Stokes-type equations. Appl. Math. Lett. **10**, 19 (1997)
21. Colangeli, M., Karlin, I.V., Kröger, M.: From hyperbolic regularization to exact hydrodynamics for linearized Grad's equations. Phys. Rev. E **75**, 051204 (2007)
22. Colangeli, M., Karlin, I.V., Kröger, M.: Hyperbolicity of exact hydrodynamics for three-dimensional linearized Grad's equations. Phys. Rev. E **76**, 022201 (2007)
23. Zwanzig, R.: Memory effects in irreversible thermodynamics. Phys. Rev. **124**, 983 (1961)
24. Zubarev, D.N., Kalashnikov, V.P.: Extremal properties of the nonequilibrium statistical operator. Theor. Math. Phys. **1**, 108 (1969)
25. Grabert, H.: Projection Operator Techniques in Nonequilibrium Statistical Mechanics. Springer, Berlin (1982)
26. Haken, H.: Synergetics: An Introduction: Nonequilibrium Phase Transitions and Self-organization in Physics, Chemistry and Biology. Springer, New York (1978)
27. Gardiner, C.W.: Handbook of Stochastic Methods. Springer, Berlin (2004)
28. Struchtrup, H.: Macroscopic Transport Equations for Rarefied Gas Flows. Approximation Methods in Kinetic Theory. Springer, Berlin/Heidelberg (2005)
29. Struchtrup, H., Torrilhon, M.: H-theorem, regularization, and boundary conditions for linearized 13 moment equations. Phys. Rev. Lett. **99**, 014502 (2007)
30. Bobylev, A.V.: Instabilities in the Chapman-Enskog expansion and hyperbolic Burnett equations. J. Stat. Phys. **124**, 371 (2006)

31. Colangeli, M., Kröger, M., Öttinger, H.C.: Boltzmann equation and hydrodynamic fluctuations. Phys. Rev. E **80**, 051202 (2009)
32. Bhatnagar, P.L., Gross, E.P., Krook, M.: A model for collision processes in gases. I. Small amplitude processes in charged and neutral one-component systems. Phys. Rev. **94**, 511 (1954)
33. Kubo, R.: The fluctuation-dissipation theorem. Rep. Prog. Phys. **29**, 255 (1966)
34. Onsager, L., Machlup, S.: Fluctuations and irreversible processes. Phys. Rev. **91**, 1505 (1953)
35. Lebowitz, J.L., Presutti, E., Spohn, H.: Microscopic models of hydrodynamic behavior. J. Stat. Phys. **51**, 841 (1988)
36. Karlin, I.V., Colangeli, M., Kröger, M.: Exact linear hydrodynamics from the Boltzmann equation. Phys. Rev. Lett. **100**, 214503 (2008)
37. Resibois, P.: On linearized hydrodynamic modes in statistical physics. J. Stat. Phys. **2**, 1 (1970)
38. Blatt, J.M.: Model equations in the kinetic theory of gases. J. Phys. A: Math. Theor. **8**, 980 (1975)
39. Reichl, L.E.: A Modern Course in Statistical Physics. University of Texas Press, Austin (1980)
40. Kröger, M.: Models for Polymeric and Anisotropic Liquids. Springer, Berlin (2005)
41. Chikatamarla, S.S., Ansumali, S., Karlin, I.V.: Entropic lattice Boltzmann models for hydrodynamics in three dimensions. Phys. Rev. Lett. **97**, 010201 (2006)
42. Öttinger, H.C., Struchtrup, H.: The mathematical procedure of coarse graining: from Grad's ten-moment equations to hydrodynamics. Multiscale Model. Simul. **6**, 53 (2007)
43. Wang Chang, C.S., Uhlenbeck, G.E.: The Kinetic Theory of Gases. North-Holland Pub. Co., Amsterdam (1970)
44. Kröger, M., Hütter, M.: Unifying kinetic approach to phoretic forces and torques for moving and rotating convex particles. J. Chem. Phys. **125**, 044105 (2006)
45. Burnett, D.: The distribution of velocities and mean motion in a slight nonuniform gas. Proc. Lond. Math. Soc. **39**, 385 (1935)
46. Gorban, A.N., Karlin, I.V.: Reconstruction lemma and fluctuation-dissipation theorem. Revista Mexicana de Fisica **48**(Suppl. 1), 238 (2002)
47. Meyer, E., Sessler, G.: Schallausbreitung in gasen bei hohen frequenzen and sehr niedrigen drucken. Z. Phys. **149**, 15 (1947)
48. de Schepper, I.M., Cohen, E.G.D.: Very-short-wavelength collective modes in fluids. J. Stat. Phys. **27**, 2 (1982)
49. Gorban, A.N., Karlin, I.V.: Short-wave limit of hydrodynamics: a soluble example. Phys. Rev. Lett. **77**, 282 (1996)
50. Foch, J.D., Ford, G.W. (eds.): Studies in Statistical Mechanics. North-Holland, Amsterdam (1970)
51. Alder, B.J., Alley, W.E.: Generalized transport coefficients for hard spheres. Phys. Rev. A **27**, 3158 (1983)
52. Kirkpatrick, T.R.: Short-wavelength collective modes and generalized hydrodynamic equations for hard-sphere particles. Phys. Rev. A **32**, 3130 (1985)
53. Hansen, J.-P., McDonald, I.R.: Theory of Simple Liquids. Academic, New York (2006)

Part II
Chaos, Synchronization and Complex Networks

Chapter 4
Dynamics of Cluster Synchronisation in Modular Networks: Implications for Structural and Functional Networks

Jake Stroud, Mauricio Barahona, and Tiago Pereira

Abstract Experimental results often do not assess network structure; rather, the network structure is inferred by the dynamics of the nodes. From the dynamics of the nodes one then constructs a network of functional relations, termed the functional network. A fundamental question in the analysis of complex systems concerns the relation between functional and structural networks. Using synchronisation as a paradigm for network functionality, we study the dynamics of cluster formation in functional networks. We show that the functional network can drastically differ from the structural network. We uncover the mechanism driving these bifurcations by obtaining necessary conditions for modular synchronisation.

4.1 Introduction

When using methods from network science to study real-world complex systems, one is faced with the choice of constructing either a structural or functional network that describes the relationship between the interacting components of the system. Sometimes it is more achievable or desirable to measure the dynamics of components and posit that if two components display similar activity, they are in some way dynamically linked. This gives rise to data-driven *functional networks* [4]. Conversely, in other situations, we may have access to *structural networks* representing known physical links between components. The focus of much research in complex network theory is towards gaining a greater understanding of how functional and structural networks relate to each other [12].

J. Stroud
University of Oxford, Oxford, UK
e-mail: jake.stroud@wadh.ox.ac.uk

M. Barahona • T. Pereira (✉)
Department of Mathematics, Imperial College London, London, UK
e-mail: m.barahona@imperial.ac.uk; tiago.pereira@imperial.ac.uk

S. Banerjee, L. Rondoni (eds.), *Applications of Chaos and Nonlinear Dynamics in Science and Engineering - Vol. 4*, Understanding Complex Systems,
DOI 10.1007/978-3-319-17037-4_4

To this end, much analysis has been conducted into network architecture and organisation. Recent results have shown that both functional and structural network representations of real world systems typically display a modular architecture [5, 9, 10, 16, 18, 30, 32]. A network with a modular organization could be described as a network consisting predominantly of highly connected sub-graphs which have comparatively fewer connections to nodes outside the module. We are particularly interested in how functional modules relate to the structural modules of a network.

Synchronisation is a typical paradigm of dynamical network function. Such group collective behaviour appears with ubiquity in nature. Human hearts beat rhythmically because thousands of cells synchronise their activity [27], and the collective behaviour of neurons in the brain has been shown to be linked to Parkinson's disease [28] and epileptic seizures [17]. However, synchronisation does not have to be global, and can occur in particular subgroups or modules.

Over recent decades, synchronisation analysis has benefited from methods in the fields of graph theory and dynamical systems, and theories for global synchronisation have been established in terms of the network structure [1, 3, 11, 13]. Of particular interest is the stability of the synchronised state. If global synchronisation can be maintained, this amounts to a coherent state, while if the synchronised state becomes unstable it can serve to predict a transition in the organisation of the complex system [2, 7, 13, 19, 20, 31].

In this chapter, we will study cluster synchronisation within modular networks of diffusively coupled oscillators. We predict the onset of stable and unstable module synchronisation by obtaining stability conditions within a densely connected module. Our model is based on the following assumptions:

- The network has a modular structure such that nodes in one module have few connections to nodes outside the module.
- Within modules, nodes have a high mean degree and share many common neighbours.

Under these assumptions, we can perform a stability analysis independently for each module, thereby avoiding a spectral decomposition of the network adjacency matrix which poses a significant challenge for large networks. Typically, we would have to analyse as many equations as the number of nodes in a module, but because nodes within modules have a large number of common neighbours, we are able to reduce the analysis to a single equation describing the synchronisation of each module by bounding the dynamics of the external modules. Hence our analysis allows us to tackle the stability of each module independently, yet taking into account their influence on each other.

From our study of the local stability of synchronisation, we establish conditions for the persistence of stability under non-linear and linear perturbations. The stability of module synchronisation is determined as a function of: (1) the module mean degree and matching index (defined in Sect. 4.2.2), and (2) the isolated dynamics and coupling function. This analysis allows us to predict the formation and disintegration of functional modules depending upon the nature of the diffusive coupling between the components of the network. Our results reveal that:

- The mean degree of the module dictates the onset of synchronisation.
- Functional modules may not reflect fully the structural modules of a network.

As a consequence, the functional representation of a network can sometimes drastically differ from the underlying topological structure. Through the use of simulations we validate our analytical results and conclude with a discussion on how the functional network representation of a modular network relates to the underlying topological structure. The remainder of this chapter is organised as follows. Our model assumptions are formalised in Sect. 4.2. Both our analytical and numerical results are presented in Sect. 4.3. The derivation of our analytical results is then presented in Sect. 4.4. Finally we provide a conclusion and discussion in Sect. 4.5.

4.2 The Model

In this section we formalise our model setup. Initially we formalise some basic graph definitions we make use of as well as describing the network class we intend to study. We then present the dynamical model describing the interaction between the components of the network. See Sect. 4.2.1 for remarks regarding notation we adopt throughout the chapter.

4.2.1 Notation

The Jacobian matrix of a function $\boldsymbol{f} : \mathbb{R}^m \to \mathbb{R}^m$ at the point $\boldsymbol{x}$ is denoted by $D\boldsymbol{f}(\boldsymbol{x})$.

When discussing synchronisation in this chapter, we imply a δ-synchronisation; that is, given two trajectories $\boldsymbol{x}(t)$ and $\boldsymbol{y}(t)$ we say that they are δ-synchronised if

the difference in their state vectors are within a neighbourhood of radius $\delta \ll 1$ at all large times t

$$\|\boldsymbol{x}(t) - \boldsymbol{y}(t)\| \leq \delta \quad \forall\, t > T(\delta).$$

The small parameter δ measures the quality of synchronisation, and depends on both the isolated dynamics and coupling function as well as the network structure. This is particularly evident in the numerical simulations. To simplify the notation, we will omit the symbol δ when discussing δ-synchronisation.

We use the small 'o' and big 'O' notation to describe asymptotic behaviour. We write $f(x) = o(x)$ if $f(x)/x$ goes to zero as x tends to infinity, and we write $f(x) = O(x)$ if $|f(x)/x|$ is bounded by a positive constant as x tends to infinity.

4.2.2 Graphs: Basic Definitions

A graph G is a set of N nodes (or vertices) connected by a set of E edges. Here, we will only consider simple, unweighted and undirected graphs; that is, graphs with no loops and where there is no order associated with the two vertices of each edge. We will also use the words 'graph' and 'network' interchangeably although a network commonly denotes a graph structure where some form of dynamics takes place on the nodes.

The adjacency matrix $\boldsymbol{A}$ encodes the topology of the graph, with $A_{ij} = 1$ if i and j are connected and 0 otherwise. Clearly, $\boldsymbol{A} = \boldsymbol{A}^T$ for undirected graphs. The degree of node i is the number of connections it receives, that is

$$k_i = \sum_{j}^{N} A_{ij}.$$

The mean degree for a set of nodes S with cardinality $|S| = n$ is then:

$$\langle k \rangle_S = \frac{1}{n} \sum_{j \in S} k_j.$$

We now define the *matching index* of a graph [32], which will play an important part in our analysis. The neighbourhood of node i is the set of nodes it shares an edge with: $\Gamma(i) = \{j | A_{ij} = 1\}$. Clearly, for simple graphs $|\Gamma(i)| = k_i$. The matching index of nodes i and l is the overlap of their neighbourhoods:

$$I_{il} = |\Gamma(i) \cap \Gamma(l)| = A_{il} + \sum_{n,m=1}^{N} A_{in} A_{ml} = (A + A^2)_{il}.$$

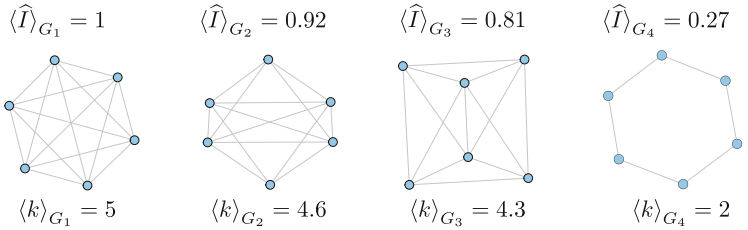

Fig. 4.1 Here we display four graphs, G_1, G_2, G_3 and G_4 with decreasing matching index and mean degree

The normalised matching index is then:

$$\hat{I}_{il} = \frac{|\Gamma(i) \cap \Gamma(l)|}{|\Gamma(i) \cup \Gamma(l)|} = \frac{|\Gamma(i) \cap \Gamma(l)|}{|\Gamma(i)| + |\Gamma(l)| - |\Gamma(i) \cap \Gamma(l)|} = = \frac{(A+A^2)_{il}}{k_i + k_l - (A+A^2)_{il}}. \tag{4.1}$$

It follows that $\hat{I}_{il} = 1$ if and only if i and l are connected to exactly the same nodes, i.e., $\Gamma(i) = \Gamma(l)$; whereas $\hat{I}_{il} = 0$ if nodes i and l have no common neighbours [32]. The mean matching index for a set of nodes S with $|S| = n$ is then:

$$\langle \hat{I} \rangle_S = \frac{1}{n(n-1)} \sum_{\substack{i,j \in S \\ i \neq j}} \hat{I}_{ij}.$$

Figure 4.1 shows graphs with different mean degrees and matching indices.

4.2.3 The Modular Network

A subgraph C of a graph G is a set of nodes and edges of G that connect any two nodes in C. A *structural module* (or cluster) is rather loosely defined as a highly connected sub-graph with comparatively fewer connections to nodes outside the module [10]. Conversely, by taking a dynamical perspective, popularised within the community detection literature, a module (or community) corresponds to a set of nodes and edges were a random walker is likely to become transiently trapped for a longer period of time than that expected at random [8, 9, 26, 33]. A prototypical example of a module would be a complete graph (or clique), where every node is connected to every other node, which is only weakly connected to other nodes. Figure 4.2 provides an example of such a modular network.

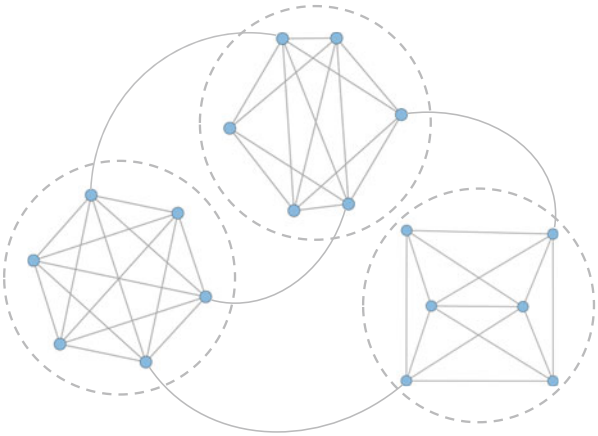

Fig. 4.2 Example of a modular network with modules denoted by *dotted grey lines*

To make this notion more precise, we consider the *mismatch index* between a pair of nodes i and l, which corresponds to the complement of the matching index defined in Eq. (4.1):

$$\mu_{il} = |\Gamma(i) \cup \Gamma(l)| - |\Gamma(i) \cap \Gamma(l)| = |\Gamma(i) \cup \Gamma(l)| - I_{il} \tag{4.2}$$

While the matching index counts all nodes that i and l share, the mismatch index counts all nodes that i and l do not share. Hence the normalised mismatch index is:

$$\hat{\mu}_{il} = \frac{|\Gamma(i) \cup \Gamma(l)| - |\Gamma(i) \cap \Gamma(l)|}{|\Gamma(i) \cup \Gamma(l)|} = 1 - \hat{I}_{il}.$$

Clearly $\hat{\mu}_{il} = 0$ if nodes i and l share exactly the same neighbours (as well as potentially being linked themselves), and $\hat{\mu}_{il} = 1$ if nodes i and l share no common neighbours.

The theory we present in this chapter holds for all modules C of a network G such that

$$\frac{\mu_{il}}{\langle k \rangle_C} = O\left(\frac{1}{\langle k \rangle_C}\right), \quad \forall i, l \in C \tag{4.3}$$

along with the homogeneity condition

$$k_i \approx \langle k \rangle_C, \quad \forall i \in C. \tag{4.4}$$

(continued)

This final relation also implies that

$$\frac{|k_i - k_l|}{\langle k \rangle_C} = O\left(\frac{1}{\langle k \rangle_C}\right), \quad \forall i, l \in C.$$

Therefore from our first relation [Eq. (4.3)], a module will have a high matching index, that is, nodes within a module will have a large number of common neighbours. Our second relation [Eq. (4.4)], allows us to approximate the degree of each node in C by the module mean degree and, certainly for small networks, excludes the possibility of any hubs (highly connected nodes) occurring in a module. As a consequence, module C can be described by the number of nodes it contains q and its mean degree: $C = C(q, \langle k \rangle_C)$.

We note that the matching index does not distinguish between a lack of common neighbours within the module and additional (unshared) links to nodes outside the module. Therefore, a high matching index not only guarantees that nodes within a module share similar neighbours but that they also have a comparatively low number of links to nodes outside the module. In [15], the edges of a graph were decomposed into inter-module and intra-module edges. They showed that this classification of edges distinguishes the formation of functional modules.

4.2.4 *The Dynamical Model: Network of Diffusively-Coupled Bounded Systems*

We now introduce some dynamics on each node of the graph. The dynamics of each node is governed by m-dimensional dynamics:

$$\frac{d\boldsymbol{x}}{dt} = \boldsymbol{f}(\boldsymbol{x}), \tag{4.5}$$

where $\boldsymbol{f} : \mathbb{R}^m \to \mathbb{R}^m$ is a smooth vector field, and we also assume that the solutions of this isolated system are bounded, i.e., for all t there exists a K such that $||\boldsymbol{x}(t)|| < K$. The boundedness of the dynamics of the nodes encompasses a wide variety of stationary and oscillatory (periodic and chaotic) systems [29].

The influence that neighbour j exerts on the dynamics of node i is assumed to depend on the difference of their state vectors: $\boldsymbol{x}_j(t) - \boldsymbol{x}_i(t)$. This type of coupling tries to equalise all states of the nodes and it is in this sense that it is called a *diffusive coupling*. The model accounts for the influence of all neighbours in a network G

with adjacency matrix $\boldsymbol{A}$, which is assumed to be given. The dynamics of node i in a network of N diffusively coupled elements is then given by:

$$\frac{d\boldsymbol{x}_i}{dt} = \boldsymbol{f}(\boldsymbol{x}_i) + \alpha \sum_{j=1}^{N} A_{ij} \left[\boldsymbol{H}(\boldsymbol{x}_j) - \boldsymbol{H}(\boldsymbol{x}_i) \right], \quad i = 1, \ldots, N \tag{4.6}$$

where $\alpha \in \mathbb{R}$ is the overall coupling strength and $\boldsymbol{H} : \mathbb{R}^m \to \mathbb{R}^m$ is the coupling function. Hence the coupling between elements is given in terms of the adjacency matrix and α modulates the influence between connected nodes. Note that we assume identical elements, i.e., in our model, the dynamics $\boldsymbol{f}$ and coupling $\boldsymbol{H}$ are identical for all nodes.

4.3 Results

In this section, we first state briefly our main analytical results, which are derived in detail in Sect. 4.4. We then provide extensive numerical simulations to illustrate our findings.

4.3.1 Summary of Analytical Results

Firstly, we state our assumptions regarding the dynamics of the system.

A1: The coupled node dynamics in Eq. (4.6) are bounded: there is a constant K_x such that

$$\|\boldsymbol{x}_i(t)\| < K_x, \quad \forall i.$$

A2: The variational equation

$$\dot{\boldsymbol{\xi}} = [D\boldsymbol{f}(\boldsymbol{s}(t)) - \sigma D\boldsymbol{H}(\boldsymbol{s}(t))]\,\boldsymbol{\xi}, \tag{4.7}$$

where $\boldsymbol{s}(t)$ is the trajectory of any node, admits a uniformly asymptotic trivial solution for $\sigma \in (\lambda, \Lambda)$, where the both the upper and lower bounds depend on the dynamics and coupling functions: $\lambda = \lambda(\boldsymbol{f}, \boldsymbol{H})$ and $\Lambda = \Lambda(\boldsymbol{f}, \boldsymbol{H})$.[1] That is, the solution of the variational equation is a contraction:

$$\boldsymbol{\xi}(t) = \boldsymbol{T}(t, s)\boldsymbol{\xi}(s) \quad \text{fort} \geq \text{s}$$

[1] We see the equation as a parametric equation in the same spirit as the master stability function approach [3, 21, 24], hence we omit the subindex that explicitly shows the dependence on the node.

with

$$\|\boldsymbol{T}(t,s)\| \leq Ke^{-\eta(t-s)}$$

where $\eta = \eta(\sigma) > 0$ uniformly and $K \in \mathbb{R}$.

Assumption A1 is natural in applications. In particular, if a Lyapunov function exists for the isolated dynamics (4.5) with an absorbing domain, it is possible to show that the network solution satisfies A1 [23]. Assumption A2 is similar to the master stability function approach [21]. The main difference is that in the master stability function, the trajectory $\boldsymbol{s}(t)$ corresponds to the a modified (perturbed) solution of the uncoupled dynamics, whereas here it corresponds to the trajectory of a coupled node. Depending on the structure of the coupling function this difference is immaterial [25]. Our numerical analysis shows that the values of λ and Λ from the master stability function provide a good approximation.

Remark 1 If the coupling function $\boldsymbol{H}$ is a positive definite matrix, then the results of [25] demonstrate that $\lambda = \lambda(\boldsymbol{f}, \boldsymbol{H})$ and $\Lambda \to \infty$. Moreover, the contraction exponent is given by

$$\eta = \beta\sigma - \lambda$$

where β is the smallest eigenvalue of $\boldsymbol{H}$.

Using these two assumptions in combination with the modular structure of the network, we derive, in Sect. 4.4, a stability condition for the synchronisation of modules which does not require a spectral analysis of the network adjacency matrix. This is a consequence of the high matching index within modules. Our results enable the prediction of functional module formation and disintegration depending on the structural properties of the module and the dynamical properties of the nodes.

Our main finding is the following:

Consider the modular network G containing a module $C = C(q, \langle k \rangle_C)$ with $q \gg 1$ nodes and mean degree $\langle k \rangle_C$. Assume that A1 and A2 hold, such that the system in Eq. (4.7) is a contraction for (λ, Λ). If the matching index of the module $\langle \hat{I} \rangle_C$ is high, then the critical coupling strengths α_C^s for synchronisation and α_C^d for desynchronisation are given by

$$\alpha_C^s = \frac{\lambda}{\langle k \rangle_C}(1 + \varepsilon_s) \text{ and } \alpha_C^d = \frac{\Lambda}{\langle k \rangle_C}(1 + \varepsilon_d), \tag{4.8}$$

(continued)

where $\varepsilon_{s,d} = O(1/\langle k \rangle_C)$. *Hence, for* $\alpha \in (\alpha_C^s, \alpha_C^d)$, $\exists T \in \mathbb{R}$ *such that* $\forall t > T$, *the nodes in* C *exhibit stable synchronised dynamics*

$$\|\boldsymbol{x}_i(t) - \boldsymbol{x}_l(t)\| \leq O\left(\frac{1}{\langle k \rangle_C}\right), \forall i, l \in C. \tag{4.9}$$

This result shows that, under these assumptions, the average degree of the module has an effect on the coupling interval that guarantees synchronisation in the module: only if the coupling α is such that $\alpha_C^s < \alpha < \alpha_C^d$ the functional and structural modules coincide. If the coupling strength is too large ($\alpha > \alpha_C^d$) or too small ($\alpha < \alpha_C^s$), the functional module disintegrates and no longer reflects the structural module. We call this change the bifurcation between functional and structural modules. Importantly, the intervals in which synchronisation is stable will be different for different modules, depending on their mean degree.

Remark 2 If the coupling function $\boldsymbol{H}$ is a positive definite matrix, then $\alpha_C^d \to \infty$. Therefore for this class of coupling function and large enough values of the coupling $\alpha > \max\{\alpha_C^s\}$, the functional modules mirror all the structural modules in the network. On the other hand, if $\alpha < \min\{\alpha_C^s\}$ no functional modules will be apparent. In between those two limits, only some of the structural modules will be reflected as functional modules. This is the case of the coupling $H = I$.

Note also that the solutions $\boldsymbol{x}_i$ under cluster synchronisation may not be similar to the solutions of the invariant synchronisation manifold S of the whole network

$$S = \{\boldsymbol{x}_i(t) = \boldsymbol{s}(t) \text{where} \dot{\boldsymbol{s}} = \boldsymbol{f}(\boldsymbol{s}), \forall i = 1, \ldots, N\}.$$

Therefore the dynamics of nodes in different modules can be very different to each other and, in particular, to the global synchronous dynamics of the network. In our analysis, we effectively decompose a modular network into individual modules with low inter-module connectivity and predict the onset of stable synchronisation based upon the mean degree within a module. For the derivation of our analytical results, see Sect. 4.4.

4.3.2 Numerical Simulations

To illustrate our analytical results we consider numerical simulations of the paradigmatic example of a network of diffusively coupled identical Rössler oscillators. The

isolated dynamics of each oscillator i is described by the system of differential equations

$$\dot{\boldsymbol{x}}_i = (\dot{x}_i, \dot{y}_i, \dot{z}_i)^T = \boldsymbol{f}(\boldsymbol{x}_i) = \begin{pmatrix} -(y_i + z_i) \\ x_i + a y_i \\ b + z_i (x_i - c) \end{pmatrix},$$

with the standard parameter values $a = 0.2, b = 0.2$ and $c = 9$. For these values, we know the system exhibits a chaotic attractor and that all trajectories eventually enter a compact set, thereby satisfying our assumptions regarding $\boldsymbol{f}$ from Sect. 4.2.4.

For a network of N diffusively coupled Rössler oscillators, the dynamics of a node i are governed by the diffusive model [Eq. (4.6)], repeated here for clarity

$$\frac{d\boldsymbol{x}_i}{dt} = \boldsymbol{f}(\boldsymbol{x}_i) + \alpha \sum_{j=1}^{N} A_{ij} \left[\boldsymbol{H}(\boldsymbol{x}_j) - \boldsymbol{H}(\boldsymbol{x}_i) \right], \quad i = 1, \ldots, N, \tag{4.10}$$

where $\alpha \in \mathbb{R}$ is the global coupling strength, $\boldsymbol{H} \in \mathbb{R}^{3\times 3}$ is the inner coupling matrix, and $\boldsymbol{A} \in \mathbb{R}^{N\times N}$ encodes the graph topology.

To numerically determine the stability of synchronisation for a system of coupled oscillators, we construct a correlation matrix $\boldsymbol{\rho}(\alpha) \in \mathbb{R}^{N\times N}$ for a particular coupling strength α. This correlation matrix describes the pairwise similarity between the dynamics of all oscillators in the system averaged over some large time T

$$\boldsymbol{\rho}(\alpha) = \boldsymbol{I} - \frac{\boldsymbol{R}(\alpha)}{\hat{R}},$$

where the elements of the matrix $\boldsymbol{R}(\alpha)$ are defined as:

$$R_{ij}(\alpha) = \frac{1}{T} \sum_{t=0}^{T} \|\boldsymbol{x}_i(t) - \boldsymbol{x}_j(t)\|,$$

for nodes i and j and

$$\hat{R} = \max_{i,j,\alpha} R_{ij}(\alpha).$$

Using this notation, we also define the mean correlation between the dynamics of a set S of n nodes

$$\langle \rho \rangle_S = \sum_{\substack{i,j \in S \\ i \neq j}} \frac{\rho_{ij}}{n(n-1)}.$$

We integrated Eq. (4.10) using an Adams-Bashforth multi-step scheme together with an initial fourth order Runge-Kutta algorithm using a step size of 0.001. The initial states of the oscillators were randomised between 0 and 0.05.

We calculated the correlation matrix $\boldsymbol{\rho}$ for a network with a modular structure, varying coupling strengths α and for two coupling schemes: $\boldsymbol{H} = \boldsymbol{I}$ and $\boldsymbol{H} = \boldsymbol{E}$, where

$$\boldsymbol{E} = \begin{pmatrix} 1 & 0 & 0 \\ 0 & 0 & 0 \\ 0 & 0 & 0 \end{pmatrix}.$$

The case $\boldsymbol{H} = \boldsymbol{I}$ corresponds to each variable x, y and z being coupled to the same variable of all its neighbours, while $\boldsymbol{H} = \boldsymbol{E}$ corresponds to only the x variable being coupled to its neighbouring nodes.

4.3.2.1 Dynamics Within a Modular Network

We first present the numerical results of the simulations of the modular network G_1 shown in Fig. 4.3. The network has two modules C_1 and C_2 generated according to an Erdös-Rényi architecture: C_1 contains 60 nodes with $\langle \hat{I} \rangle_{C_1} = 0.95$ and $\langle k \rangle_{C_1} = 58$; C_2 contains 40 nodes with $\langle \hat{I} \rangle_{C_2} = 0.6$ and $\langle k \rangle_{C_2} = 30$. The inter-module connections are low compared with the intra-module links, as implied by the high module matching indices. In these simulations, we use the x-coupling: $\boldsymbol{H} = \boldsymbol{E}$. The results of the functional analysis are presented in Fig. 4.4.

Figure 4.4a–e display heat map representations of the correlation matrix $\boldsymbol{\rho}$ for increasing coupling strengths α. Darker regions correspond to higher correlation between node dynamics. From the analysis of the master stability function of the Rössler system with these parameters and x-coupling, it has been found that the region of stable synchronisation are bounded by $\lambda = 0.186$ and $\Lambda = 4.164$ [13]. We can then use these numbers to approximate the regions of stable synchronisation for modules C_1 and C_2: $\alpha^s_{C_1} \approx 0.186/58 = 3.2 \times 10^{-3}$ and $\alpha^d_{C_1} \approx 4.164/58 =$

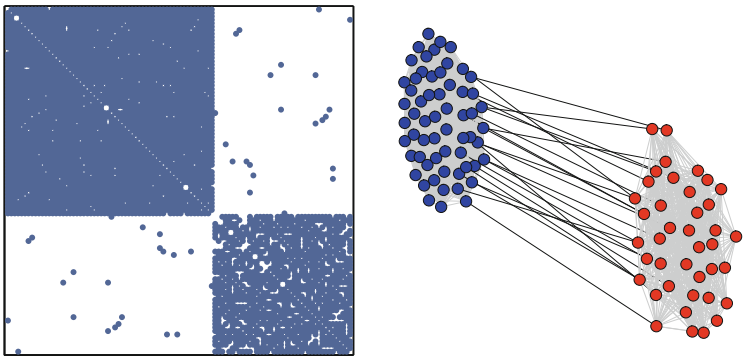

Fig. 4.3 Adjacency matrix (`spy(A)`) and graph visualisation of the network G_1 which contains two weakly connected Erdös-Rényi modules C_1 (*blue*) and C_2 (*red*) with 60 and 40 nodes respectively

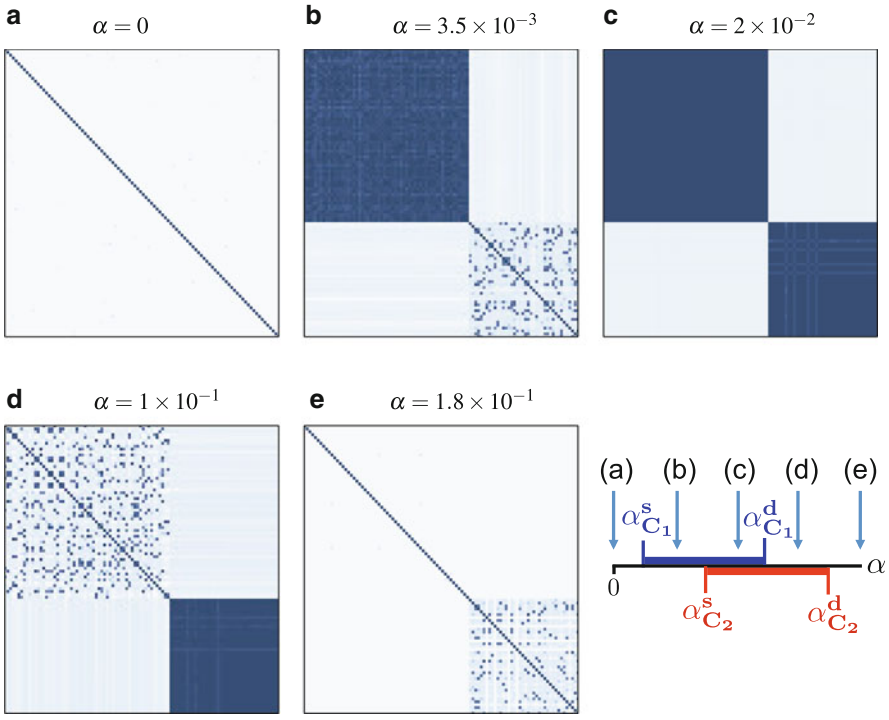

Fig. 4.4 (**a**)–(**e**) display the functional correlation matrix $\boldsymbol{\rho}$ for increasing coupling strengths α of the network G_1 when only the x component of the dynamics is coupled ($\boldsymbol{H} = \boldsymbol{E}$). *Darker coloured areas* correspond to regions of synchronisation. The *inset* illustrates the different synchronisation regions for modules C_1 and C_2 as expected from our analysis. The letter labellings correspond to those in (**a**)–(**e**). Note that $\alpha^{s}_{C_1} \approx 3.2 \times 10^{-3} < \alpha^{s}_{C_2} \approx 6.2 \times 10^{-3} < \alpha^{d}_{C_1} \approx 7.2 \times 10^{-2} < \alpha^{d}_{C_2} \approx 1.39 \times 10^{-1}$, thus giving rise to distinct regions for the functional network

7.2×10^{-2} for C_1; whereas $\alpha^{s}_{C_2} \approx 6.2 \times 10^{-3}$ and $\alpha^{d}_{C_2} \approx 1.39 \times 10^{-1}$ for C_2. These regions are indicated by the illustration inset in Fig. 4.4.

Our numerics show that when $\alpha = 0$ there is no correlation between the dynamics of the nodes. This is expected since there is no interaction between the oscillators. For $\alpha = 3.5 \times 10^{-3}$, C_1 has synchronised and some nodes in C_2 are beginning to show cohesive dynamics. This is expected since the coupling strength has entered the predicted stable synchronisation region for C_1 but not for C_2. For $\alpha = 2{\times}10^{-2}$, both modules have synchronised, but the dynamics of the two modules are *uncorrelated* as indicated by the pale off-diagonal regions. This is a result of the low inter-module connectivity.[2] For $\alpha = 1 \times 10^{-1}$ (Fig. 4.4d), module C_1 has

[2]Under certain conditions, it is possible for two modules to synchronise and this is explored elsewhere such as [14].

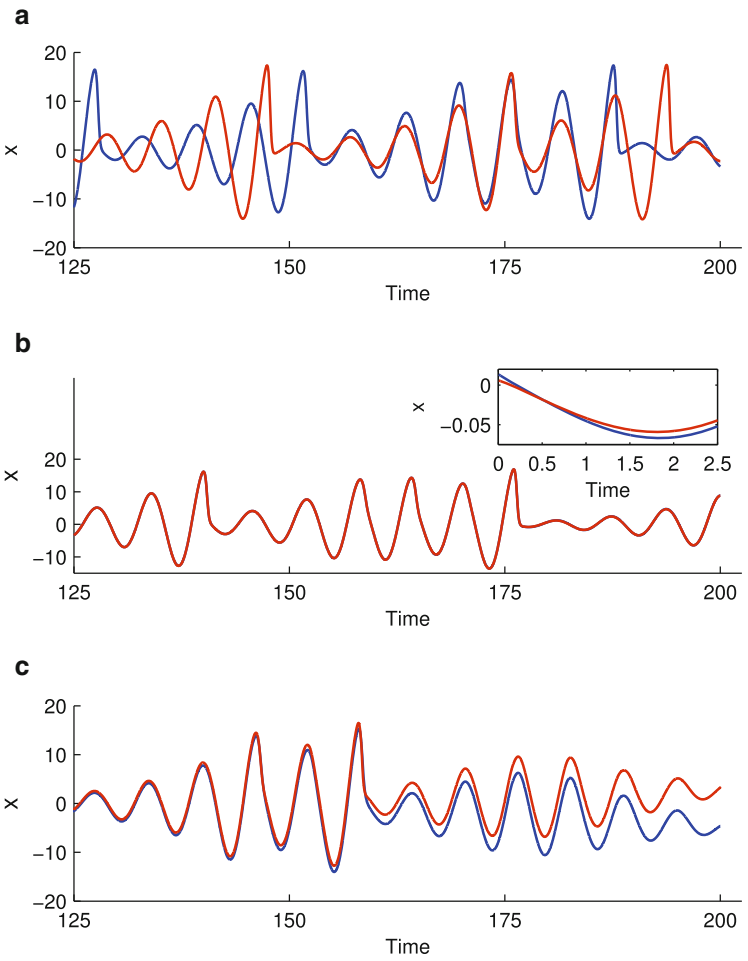

Fig. 4.5 Time evolution of the x component of the dynamics for two oscillators in module C_1 over the time window 125–200. (**a**) For $\alpha = 0$, the dynamics of the two oscillators are uncorrelated. (**b**) When the coupling strength is increased to 3.5×10^{-3}, the two oscillators enter a stable synchronised state. (**c**) As the coupling strength is increased further to 1×10^{-1}, the oscillators initially synchronise for small times before their trajectories diverge and then remain uncorrelated thereafter

already desynchronised, while C_2 remains synchronised. As the coupling strength is increased further, C_2 also desynchronises.

The dynamical behaviour of the clusters is perhaps expressed more clearly when analysing the time evolution of the oscillators. Figure 4.5 displays the evolution of the x variable of two oscillators in module C_1 for increasing coupling strengths. In Fig. 4.5a, where $\alpha = 0$, we observe, as expected, that the dynamics of the two oscillators are uncorrelated. For $\alpha = 3.5 \times 10^{-3}$ in Fig. 4.5b, the two oscillators

synchronise. The inset in this figure demonstrates that the two oscillators have differing but close initial conditions and due to the coupling strength, soon achieve stable synchronisation. Finally, for $\alpha = 1 \times 10^{-1}$ (Fig. 4.5c), the oscillators initially synchronise before diverging after a short time and then remain uncorrelated thereafter.

4.3.2.2 Relation Between the Critical Coupling Strength and the Module Mean Degree

We now examine how the critical coupling strength required for stable synchronisation within a module depends upon its mean degree. To this end we simulated a network G_2 of 100 nodes for varying matching indices between 0.7 and 1 which will act as a paradigmatic example of a module with no inter-module links, thereby removing any external perturbations from other modules. We then determined the coupling strength α such that $\langle \rho \rangle_{G_2} = 0.99$ for both $\boldsymbol{H} = \boldsymbol{I}$ and $\boldsymbol{H} = \boldsymbol{E}$. We repeated simulations five times for varying network adjacency matrices.

Along with the simulations, we indicate the predicted critical coupling strength which depends inversely upon the mean degree of the module as determined by our methodology. We demonstrate this by fitting the simulation results to an expression of the form

$$\alpha_C^s, \alpha_C^d = \frac{a}{\langle k \rangle + b}, \tag{4.11}$$

where a and b are fitting parameters.

Remark 3 The precise bounds for the critical coupling strength depends on the actual node degrees and not only the mean degree (see the derivation of the results in Sect. 4.4 for details). However, since node degrees are close to the mean degree we can approximate $k_i = \langle k \rangle + b$, where b is treated as a free parameter. The parameter b effectively allows for inhomogeneities within the module structure to produce a small perturbation to the critical coupling strength required for stable synchronisation, details on these perturbations can be found in Sect. 4.4.4.

Figure 4.6 displays the results when coupling all components of the dynamics with $\boldsymbol{H} = \boldsymbol{I}$. As expected, all nodes in the module will synchronise given a strong enough coupling strength and the module will remain synchronised as the coupling strength is increased thereafter. The simulations follow an inverse dependence upon the mean degree of the module [Eq. (4.11)], as expected from our results.

Figure 4.7 displays the results when coupling only the x component of the dynamics, corresponding to $\boldsymbol{H} = \boldsymbol{E}$. We see that for a module with a high matching index, all nodes will synchronise above a coupling strength and will then desynchronise as the coupling strength is increased further. Again, from the fitted curves, the critical coupling strengths required for synchronisation and

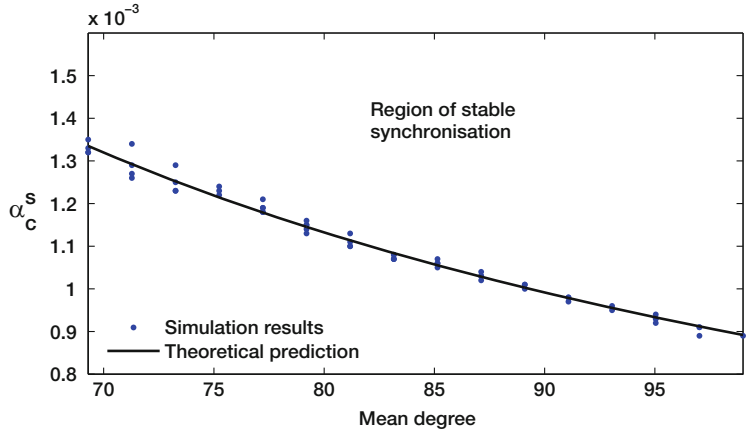

Fig. 4.6 Critical coupling strength required for stable synchronisation for a module of 100 nodes with a varying high matching index plotted against the module mean degree. Simulations were repeated five times with the coupling $\boldsymbol{H} = \boldsymbol{I}$. We also display the fitting curve [Eq. (4.11)], which depends inversely upon the module mean degree

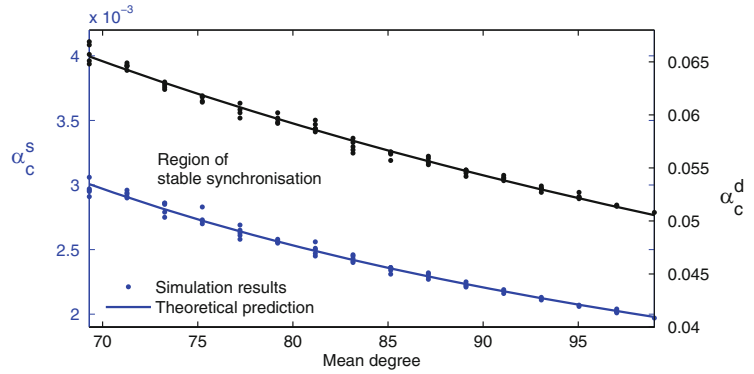

Fig. 4.7 Critical coupling strengths required for stable synchronisation of a module of 100 nodes with varying high matching index plotted against the module mean degree. Simulations were repeated five times with the coupling function $\boldsymbol{H} = \boldsymbol{E}$. We also display the fitting curves, [Eq. (4.11)] which depend inversely upon the module mean degree. Note the different scales on the y-axes, with *blue* corresponding to synchronisation and *black* to desynchronisation

desynchronisation display an inverse dependence upon the module mean degree in line with our results.

Remark 4 When setting $b = 0$ in the curve fitting (corresponding to perfectly homogeneous node degrees), we can directly compare our results with those obtained in the literature from analysing the master stability function, which have shown $\lambda = 0.186$ and $\Lambda = 4.614$ for this system [13]. From our fits, allowing for a stable synchronisation region to be given by $\langle \rho \rangle_{G_2} > 0.99$, we obtain

$\alpha_C^s\langle k\rangle = 0.202$ and $\alpha_C^d\langle k\rangle = 4.750$ in close agreement with the master stability function bounds, as expected from our analytical results.

4.4 Derivation of Our Analytical Results

Before detailing the derivation of our results below, we briefly outline our strategy. Starting from Eq. (4.6), we define

$$z(t) = \boldsymbol{x}_i(t) - \boldsymbol{x}_l(t), \text{foranyi}, \mathrm{l} \in \mathrm{C}, \tag{4.12}$$

where C is a module, and analyse the dynamics of z. To this end, we take the following four steps.

1. First, for z sufficiently small, we obtain the linearised equation for $\boldsymbol{z}(t)$:

$$\frac{d\boldsymbol{z}}{dt} = \boldsymbol{h}(\alpha, t)\boldsymbol{z}(t) + \alpha \boldsymbol{g}(t), \tag{4.13}$$

   where $\boldsymbol{g}$ and $\boldsymbol{h}$ are to be determined and depend on both the node dynamics and network structure. By Taylor's Theorem, the remainder is $O(||\boldsymbol{z}(t)||^2)$ and it can be dealt with in step 2.
2. We then analyse the associated homogeneous equation

$$\frac{d\,\boldsymbol{y}}{dt} = \boldsymbol{h}(\alpha, t)\,\boldsymbol{y},$$

   and, by Eq. (4.7), represent $\boldsymbol{y}(t)$ in terms of its associated evolution operator

$$\boldsymbol{y}(t) = \boldsymbol{T}(t, s)\boldsymbol{y}(s).$$

   Our assumption A2 guarantees that the trivial solution of the above equation is uniformly asymptotically stable, that is, for some $\eta > 0$,

$$\|\boldsymbol{y}(t)\| \leq Ke^{-\eta(t-s)}\|\boldsymbol{y}(s)\|, \text{for} t \geq s.$$

3. We then solve Eq. (4.13) using the method of variation of parameters

$$\boldsymbol{z}(t) = \boldsymbol{T}(t, s)\boldsymbol{z}(s) + \alpha \int_s^t \boldsymbol{T}(t, u)\boldsymbol{g}(u)\,\mathrm{d}u,$$

   and by defining $\|\boldsymbol{g}\| = \sup_u \|\boldsymbol{g}(u)\|$, from the triangle inequality we obtain

$$\|\boldsymbol{z}(t)\| \leq Ke^{-\eta(t-s)}\|\boldsymbol{z}(s)\| + \frac{K\alpha\|\boldsymbol{g}\|}{\eta}.$$

4. Then for large times and using Eq. (4.12), we obtain

$$\|\boldsymbol{x}_i - \boldsymbol{x}_l\| \leq \frac{\tilde{K}\alpha\|\boldsymbol{g}\|}{\eta},$$

where

$$\tilde{K} = K\left(\frac{\eta e^{-\eta(t-s)}||\boldsymbol{z}(s)||}{\alpha||\boldsymbol{g}||} + 1\right).$$

Under our network assumptions, Eqs. (4.3) and (4.4), we can obtain bounds for $\|\boldsymbol{g}\|$ as

$$\frac{\|\boldsymbol{g}\|}{\langle k\rangle_C} = O\left(\frac{1}{\langle k\rangle_C}\right).$$

We now explain these steps in more detail.

4.4.1 Obtaining the Variational Equation

To obtain the first variational equation for $\boldsymbol{z}(t) = \boldsymbol{x}_i(t) - \boldsymbol{x}_l(t)$ we write

$$\begin{aligned}\dot{\boldsymbol{z}} &= \dot{\boldsymbol{x}}_i - \dot{\boldsymbol{x}}_l \\ &= \boldsymbol{f}(\boldsymbol{z} + \boldsymbol{x}_l) - \boldsymbol{f}(\boldsymbol{x}_l) + \alpha\left\{\sum_j (A_{ij} - A_{lj})\boldsymbol{H}(\boldsymbol{x}_j) + \sum_j [A_{lj}\boldsymbol{H}(\boldsymbol{x}_l) - A_{ij}\boldsymbol{H}(\boldsymbol{x}_i)]\right\},\end{aligned}$$

by Eq. (4.6).

For some t such that $\|\boldsymbol{z}(t)\|$ is sufficiently small, we can expand as a Taylor series, and after some manipulations we obtain

$$\dot{\boldsymbol{z}} = D\boldsymbol{f}(\boldsymbol{x}_l)\boldsymbol{z} - \alpha A_{il} D\boldsymbol{H}(\boldsymbol{z}) + \alpha\left\{k_l\boldsymbol{H}(\boldsymbol{x}_l) - k_i\boldsymbol{H}(\boldsymbol{x}_i) + \sum_{j\neq i,l}(A_{ij} - A_{lj})\boldsymbol{H}(\boldsymbol{x}_j)\right\}$$

where k_i is the degree of node i as given in Sect. 4.2.2. Without loss of generality, we assume $k_l \geq k_i$ and set $\bar{k}_i = k_i + A_{il}$ to obtain

$$\dot{\boldsymbol{z}}(t) = \boldsymbol{h}(\alpha, t)\boldsymbol{z} + \alpha\boldsymbol{g}(t), \tag{4.14}$$

where

$$\boldsymbol{h}(\alpha, t) = D\boldsymbol{f}(\boldsymbol{x}_l(t)) - \alpha\bar{k}_i D\boldsymbol{H} \tag{4.15}$$

and

$$\boldsymbol{g}(t) = (k_l - k_i)\boldsymbol{H}(\boldsymbol{x}_l(t)) + \sum_{j \neq i,l} (A_{ij} - A_{lj})\boldsymbol{H}(\boldsymbol{x}_j(t)). \tag{4.16}$$

This is the first variational equation. Note, we truncated our Taylor expansion in z up to first order and by Taylor's Theorem we know the remainder satisfies $\|\boldsymbol{R}(z(t))\| = O(\|z(t)\|^2)$.

4.4.2 The Homogeneous Equation

We now consider the homogeneous part of Eq. (4.14)

$$\dot{\boldsymbol{y}} = \boldsymbol{h}(\alpha, t)\boldsymbol{y}. \tag{4.17}$$

Notice the rescaling $\alpha\bar{k_i} = \sigma$ brings the above equation [Eq. (4.17)] to Eq. (4.7). Therefore, if

$$\lambda < \alpha\bar{k_i} < \Lambda,$$

Eq. (4.17) has an evolution operator satisfying

$$\|T(t,s)\| \leq Ke^{-\eta(t-s)}. \tag{4.18}$$

Now, since modules will have a large number connections and nodes will share many common neighbours, $\bar{k_i}$ will be close to the mean degree $\langle k \rangle_C$ (see our network assumptions Eqs. (4.3) and (4.4)). This means that in leading order in $\langle k \rangle_C$, the stability condition is given by

$$\lambda < \alpha\left(\langle k \rangle_C + \delta\right) < \Lambda,$$

where $|\delta| = o(\langle k \rangle_C)$ takes into account the fluctuation between k_i and the mean degree $\langle k \rangle_C$. After some rearrangements we obtain

$$\frac{\lambda}{\langle k \rangle_C}\left(1 - \frac{\delta}{\langle k \rangle_C}\right) < \alpha < \frac{\Lambda}{\langle k \rangle_C}\left(1 - \frac{\delta}{\langle k \rangle_C}\right). \tag{4.19}$$

Then for $\langle k \rangle_C$ large we see that Eq. (4.19) resembles Eq. (4.8). Furthermore, according to Remark 1, if $\boldsymbol{H}$ is positive definite, we obtain $\Lambda \to \infty$ and

$$\eta = \alpha\beta(\langle k \rangle_C + \delta) - \lambda. \tag{4.20}$$

Then for α satisfying $\eta > 0$ in Eq. (4.20), we obtain a uniform contraction. It remains to show that the perturbations will not destroy the synchronisation property.

4.4.3 The Perturbed Equation

We now turn our attention to the inhomogeneous Eq. (4.14). Using the method of variation of parameters we obtain

$$z(t) = \boldsymbol{T}(t,s)z(s) + \alpha \int_s^t \boldsymbol{T}(t,u)\boldsymbol{g}(u)\,\mathrm{d}u,$$

and by virtue of the triangle inequality we find

$$\|z(t)\| \leq \|\boldsymbol{T}(t,s)\|\,\|z(s)\| + \alpha \int_s^t \|\boldsymbol{T}(t,u)\|\,\|\boldsymbol{g}(u)\|\,\mathrm{d}u.$$

Then, using the bounds for the evolution operator from Eq. (4.18) we obtain

$$\begin{aligned}\|z(t)\| &\leq Ke^{-\eta(t-s)}\|z(s)\| + \alpha \int_s^t Ke^{-\eta(t-u)}\|g\|\,\mathrm{d}u \\ &= Ke^{-\eta(t-s)}\|z(s)\| + \alpha K\|g\|\left[\frac{1-e^{-\eta(t-s)}}{\eta}\right].\end{aligned}$$

For t large we obtain

$$\|z(t)\| \leq \frac{\tilde{K}\alpha\|\boldsymbol{g}\|}{\eta},$$

where

$$\begin{aligned}\tilde{K} &= K\left(\frac{\eta e^{-\eta(t-s)}||z(s)||}{\alpha||\boldsymbol{g}||} + 1\right) \\ &= K + o(1).\end{aligned}$$

Now, under the stability condition Eq. (4.19) for α, we obtain

$$\|z(t)\| \leq \frac{\tilde{K}\Lambda\|\boldsymbol{g}\|}{\langle k\rangle_C \eta}. \tag{4.21}$$

If $\boldsymbol{H}$ is positive definite then from Remark 1

$$\|z(t)\| \leq \frac{\tilde{K}\alpha\|\boldsymbol{g}\|}{\alpha\beta\langle k\rangle_C - \lambda}. \tag{4.22}$$

We must now analyse the bounds for $\boldsymbol{g}$ within a module.

4.4.4 Bounds for the Perturbation

We give the argument for Eq. (4.21). The argument for Eq. (4.22) is similar. We first recall the mismatch index Eq. (4.2):

$$\mu_{il} = \sum_{j=1}^{N} |A_{ij} - A_{lj}| - 2A_{il}.$$

Then since the trajectories are bounded and the coupling function is smooth, we can bound

$$\|\boldsymbol{H}(\boldsymbol{x}_i)\| \leq K_h,$$

for a positive constant K_h, and since

$$\boldsymbol{g}(t) = (k_l - k_i)\boldsymbol{H}(\boldsymbol{x}_l(t)) + \sum_{j \neq i,l} (A_{ij} - A_{lj})\boldsymbol{H}(\boldsymbol{x}_j(t)),$$

from Eq. (4.16), we obtain

$$\frac{\|\boldsymbol{g}(t)\|}{\langle k \rangle_C} \leq \frac{1}{\langle k \rangle_C} K_h(k_l - k_i + \mu_{il}). \tag{4.23}$$

Then, motivated by the matching index notation in Eq. (4.1), we can introduce

$$K_1 = \frac{K_h}{\langle k \rangle_C}(k_i + k_l - (A + A^2)_{il})$$

to obtain

$$\frac{\|\boldsymbol{g}(t)\|}{\langle k \rangle_C} \leq \frac{|k_l - k_i|}{\langle k \rangle_C} K_h + (1 - \hat{I}_{il})K_1. \tag{4.24}$$

Therefore, for the perturbation to be small, we require:

- The difference in node degrees within a module to be low.
- Nodes to share many common neighbours within a module.
- Nodes to have comparatively fewer connections to nodes outside the module.

The final two requirements emerge via the matching index in Eq. (4.24) since $\hat{I}_{il}$ penalises for not only a lack of shared nodes within a module but also for additional (unshared) connections to nodes outside the module. Then, from our network

assumptions (Eqs. (4.3) and (4.4)) along with α satisfying the stability condition Eq. (4.19), by Eqs. (4.21) and (4.23), we obtain

$$\|z(t)\| \leq O\left(\frac{1}{\langle k \rangle_C}\right).$$

Therefore the stability of module synchronisation depends upon the module mean degree and the extent to which synchronisation can be achieved depends upon the matching index within a module. These conditions will clearly vary between modules and our conditions only guarantee individual modules to synchronise independently as opposed to global network synchronisation.

4.5 Conclusion and Discussion

We have shown that the stability of module synchronisation in complex modular networks can be predicted based upon the module mean degree given certain assumptions on the component dynamics and network structure. Our key assumption on the modular structure is that nodes within modules share many common neighbours and inter-module connections are weak in comparison.

Our analysis revealed two basic scenarios for module synchronisation. If the coupling function is linear and positive definite, we showed that the functional modules reflect the structural modules. In this case, as the coupling strength is increased, the module with the largest mean degree synchronizes first, then more and more modules achieve synchronisation. In this case, the dynamics of the network mirror the structural properties of the network.

However, for more general couplings, typically our stability criterion A2 is satisfied, see [13]. In this case, we observe interesting dynamical behaviour as the coupling parameter is increased where, in a first stage, modules of synchronised nodes can form and reflect the structural organization, but for large couplings the synchronisation becomes unstable and functional modules disintegrate. This scenario corresponds to bifurcations between the functional and structural properties.

Our assumptions on the structure of the modules allowed for an analytical treatment of these scenarios and enabled us to determine the critical coupling strengths for synchronisation and desynchronisation. Additionally, we showed that the module matching index dictates the quality of synchronisation. Moreover, our present approach can be used to explain the synchronised dynamics of groups of nodes not necessarily forming modules such as hub synchronization [6, 22], since their matching index may be high and the degrees similar.

These results can be of importance for functional network analysis and enhance our understanding of the relation between the functional and structural network. Indeed, even though a module may possess the structural properties required for synchronisation, the functional modules may not reflect the structural modules of a network.

References

1. Arenas, A., Díaz-Guilera, A., Kurths, J., Moreno, Y., Zhou, C.: Synchronization in complex networks. Phys. Rep. **469**(3), 93 (2008)
2. August, E., Barahona, M.: Obtaining certificates for complete synchronisation of coupled oscillators. Physica D **240**(8), 795 (2011)
3. Barahona, M., Pecora, L.M.: Synchronization in small-world systems. Phys. Rev. Lett. **89**, 054101 (2002)
4. Bassett, D.S., Lynall, M.: Network methods to characterize brain structure and function. In: Cognitive Neurosciences: The Biology of the Mind, 5th edn. In: M. Gazzanigo, R.B. Ivry, G.R. Mangun (eds.) The MIT Press.
5. Bassett, D.S., Wymbs, N.F., Porter, M.A., Mucha, P.J., Carlson, J.M., Grafton, S.T.: Dynamic reconfiguration of human brain networks during learning. Proc. Natl. Acad. Sci. USA **108**, 7641 (2011)
6. Batista, M.S., et al.: Collective almost synchronisation in complex networks. PLoS One **7**(11), e48118 (2012)
7. Belykh, V.N., Belykh, I.V., Hasler, M.: Connection graph stability method for synchronized coupled chaotic systems. Physica D **195**(1), 159 (2004)
8. Delvenne, J.C., Yaliraki, S.N., Barahona, M.: Stability of graph communities across time scales. Proc. Natl. Acad. Sci. USA **107**(29), 12755 (2010)
9. Delvenne, J.-C., Schaub, M.T., Yaliraki, S.N., Barahona, M.: The Stability of a Graph Partition: A Dynamics-Based Framework for Community Detection. Springer, Berlin (2013)
10. Fortunato, S.: Community detection in graphs. Phys. Rep. **486**(3–5), 75 (2010)
11. Heagy, J.F., Pecora, L.M., Carroll, T.L.: Short-wavelength bifurcation and size instabilities in coupled oscillator-systems. Phys. Rev. Lett. **74**(21), 4185 (1995)
12. Honey, C.J., Sporns, O., Cammoun, L., Gigandet, X., Thiran, J.P., Meuli, R., Hagmann, P.: Predicting human resting-state functional connectivity from structural connectivity. Proc. Natl. Acad. Sci. USA **106**, 2035–2040 (2009)
13. Huang, L., Chen, Q., Lai, Y.-C., Pecora, L.: Generic behaviour of master-stability functions in coupled nonlinear dynamical systems. Phys. Rev. E **80**, 036204 (2009)
14. Jian-She, W., Li-Cheng, J., Guan-Rong, C.: Cluster synchronisation in a network of non-identical dynamic systems. Chin. Phys. B **20**, 060503 (2011)
15. Lu, W., Liu, B., Chen, T.: Cluster synchronisation in networks of coupled non-identical dynamical systems. Chaos **20**, 013120 (2010)
16. Meunier, D., Lambiotte, R., Bullmore, E.T.: Modular and hierarchically modular organisation of brain networks. Front. Neurosci. **4**, 200 (2010)
17. Milton, J., Jung, P. (eds.): Epilepsy as a Dynamic Disease. Springer, New York (2010)
18. Mishra, N., Schreiber, R., Stanton, I., Tarjan, R.E.: Clustering social networks. In: Bonato, A., Chung, F.R.K. (eds.) Algorithms and Models for the Web-Graph. Springer, Berlin (2007)
19. O'Clery, N., Yuan, Y., Stan, G.B., Barahona, M.: Observability and coarse-graining of consensus dynamics through the external equitable partition. Phys. Rev. E **88**(4), 042805 (2013)
20. Pecora, L.M., Barahona, M.: Synchronisation of oscillators in complex networks. Chaos Complex. Lett. **1**, 61 (2005)
21. Pecora, L.M., Carrol, T.L.: Master stability functions for synchronized coupled systems. Phys. Rev. Lett. **80**, 2109 (1998)
22. Pereira, T.: Hub synchronization in scale free networks. Phys. Rev. E **82**, 036201 (2010)
23. Pereira, T.: Stability of synchronized motion in complex networks (2012). arXiv:1112.2297
24. Pereira, T., Eroglu, D., Bagci, G., Tirnakli, U., Jensen, H.J.: Connectivity-driven coherence in complex networks. Phys. Rev. Lett. **110**, 234103 (2013)
25. Pereira, T., Eldering, J., Rasmussen, M., Veneziani, A.: Towards a theory for diffusive coupling functions allowing persistent synchronization. Nonlinearity **27**, 501 (2014)

26. Schaub, M.T., Delvenne, J.C., Yaliraki, S.N., Barahona, M.: Markov dynamics as a zooming lens for multiscale community detection: non clique-like communities and the field-of-view limit. PLoS One **7**(2), e32210 (2012)
27. Strogatz, S.: Synch: The Emerging Science of Spontaneous Order. Hyperion, New York (2003)
28. Tass, P., Rosenblum, M.G., Weule, J., Kurths, J., Pikovsky, A., Volkmann, J., Schnitzler, A., Freud, H.J.: Phys. Rev. Lett. **81**, 3291 (1998)
29. Teschl, G.: Ordinary Differential Equations and Dynamical Systems, vol. 140. American Mathematical Society, Providence (2012)
30. Wang, S., Zhou, C.: Hierarchical modular structure enhances the robustness of self-organized criticality in neural networks. New J. Phys. **14**, 023005 (2012)
31. Wu, C.W.: Synchronization in networks of nonlinear dynamical systems coupled via a directed graph. Nonlinearity **18**(3), 1057 (2005)
32. Zamora-Lopez, G., Zhou, C., Kurths, J.: Cortical hubs form a module for multisensory integration on top of the hierarchy of cortical networks. Front. Neuroinform. **4**, 1 (2010)
33. Zhou, H.: Network landscape from a Brownian particle's perspective. Phys. Rev. E **67**, 041908 (2003)

Chapter 5
Synchronous Motions Across the Instrumental Climate Record

Peter Carl

Abstract The Earth's climate system bears a rich variety of feedback mechanisms that may give rise to complex, evolving modal structures under internal and external control. Various types of synchronization may be identified in the system's motion when looking at representative time series of the instrumental period through the glasses of an advanced technique of sparse data approximation, the Matching Pursuit (MP) approach. To disentangle the emerging network of oscillatory modes to the degree that climate dynamics turns out to be separable, a large dictionary of "Gaussian logons," i.e. frequency modulated (FM) Gabor atoms, is applied. Though the extracted modes make up linear decompositions, this flexible analyzing signal matches highly nonlinear waveforms. Univariate analyses over the period 1870–1997 are presented of a set of customary time series in annual resolution, comprising global and regional climate, central European synoptic systems, German precipitation, and runoff of the Elbe river near Dresden. All the evidence from this first-generation MP-FM study, obtained in subsequent multivariate syntheses, points to dynamically excited regimes of an organized yet complex climate system under permanent change—perhaps a (pre)chaotic one at centennial timescales, suggesting a "chaos control" perspective on global climate dynamics and change. Findings and conclusions include, among others, internal structure of reconstructed insolation, the episodic nature of global warming as reflected in multidecadal temperature modes, their swarm of "interdomain" companions across the whole system that unveils an unknown regime character of interannual climate dynamics, and the apparent onset early in the 1990s of the present thermal stagnation.

5.1 Introduction

The Earth's climate is fundamentally shaped by the very fact that phase transitions of water are within reach of normal atmospheric to subsurface conditions. Changes in the water cycle, as a major mediator of the effects of climate and weather on

P. Carl (✉)
ASWEX – Applied Water Research, Climate Dynamics & Signal Analysis Project,
Hausvogteiplatz 5–7, 10117 Berlin, Germany
e-mail: pcarl@wias-berlin.de

S. Banerjee, L. Rondoni (eds.), *Applications of Chaos and Nonlinear Dynamics in Science and Engineering - Vol. 4*, Understanding Complex Systems,
DOI 10.1007/978-3-319-17037-4_5

landscapes, biota and man's society, are often viewed as one-way processes, though (e.g., [51]). Also, a traditional (midlatitude) perspective on climate variability and change is based on the understanding that slow(er) subsystems exert the decisive, solid control. To such a (quasi-equilibrium) view there fits the notion of a hydrologic cycle that merely responds to climate change. It tends to diaphragm out the constitutive impact of atmospheric water on tropic/subtropical climate dynamics and the interactive nature of climatic subsystems across the spatio-temporal scales, including those of astronomical forcing (e.g., [109]).

Latent heat uptake and release in the Tropics and subtropics substantially contribute in driving atmospheric motions. Subtle changes in these motions may result in worldwide hydrologic transformations that feed back on the circulation, and thus on climate and weather; that is, water cycle interactions are integral parts of climate variability and change—and may even take the lead (e.g., [78, 110, 111]). Climatic feedbacks may constitute free oscillations at timescales from intraseasonal to centennial and beyond (e.g., [65, 71, 88]). Such "anomalistic" (not astronomically controlled) oscillatory regimes under active participation of the water cycle are borne in the monsoons (e.g., [62]), the El Niño–Southern Oscillation (ENSO) system (e.g., [47]), and perhaps also in the annular modes of both hemispheres (e.g., [106]). Typically, they show complex, irregular spatiotemporal behaviour and are basically recurrent but difficult to predict. Not only are their quantitative rules of recurrence unknown; qualitative dynamics of the subsystems in the back, and of the whole climate system, are obscure and may well comprise (pre)chaotic regimes at a wide range of scales (e.g., [12, 13, 57, 58, 69, 95, 100, 114]).

Low-dimensional aspects of climate dynamics, as addressed in diverse modelling studies including a "small" yet physically resolved General Circulation Model (GCM) [19], provide reasoning in favour of synchronies in representative data of the real system. Namely, in a high-dimensional dynamic system, low-dimensional behaviour is peremptorily bound to internal dynamic organization as reflected in synchronous, degenerate motions along otherwise largely independent (although not necessarily orthogonal) phase space, resp. signal space, directions. Notably in (pre)chaotic regimes, unstable periodic orbits may become manifest in the data due to episodic or persistent, internal or external synchronization. All this calls for clarification of the role that nonlinear qualitative dynamics may play in the real climate. That the system's dynamical status is largely unknown (as is that of its elaborated GCMs) poses challenges when grasping its past and future evolution.

Time series studies are an established approach toward structural understanding of nonlinear dynamics, not to the least when translating these into geometry [1]. Here the perspective and task have been adopted of unveiling structure in a complex yet organized, dynamically excited system. That is, climate dynamics are empirically addressed which are not primarily "hidden in noise," but are obscured due to their intrinsic complexity. Nonstationary, nonlinear signals are to be coped with to this end—without giving preference by the choice of method to any other notion over the quasi-equilibrium view and its linear implications. Non-probabilistic, dynamic modes are targeted of time series $\chi(t)$ which are viewed as complex yet separable composites, fed by multiple, distributed sources of diverse

signal structure, temporal location, scale etc., i.e. signal space occupation. Accordingly, univariate blind decomposition $\mathcal{T}$ is seeked into a hierarchy of empirical modes $\chi_k(t)$, $\chi(t) \approx \sum_k \chi_k(t) = \sum_k \mathcal{T}\{\mathcal{R}_{k-1}\{\chi\}\}(t)$, where $\mathcal{R}_{k-1}\{\chi\}(t)$ is the time series residue at level $k-1$ ($\mathcal{R}_0\{\chi\}(t) \equiv \chi(t)$). This "greedy" univariate analysis does not necessarily have to bear orthogonality among the extracted modes. Multivariate synthesis to detect mutual dynamic information searches for relations then of the kind $\mathcal{P}_{\gamma_a}\chi_{\mu_i}(t) \sim \mathcal{P}_{\gamma_b}\chi_{\nu_j}(t)$, or

$$\mathcal{P}_{\gamma_a}\mathcal{T}\{\mathcal{R}_{i-1}\{\chi_\mu\}\}(t) \sim \mathcal{P}_{\gamma_b}\mathcal{T}\{\mathcal{R}_{j-1}\{\chi_\nu\}\}(t)\,, \tag{5.1}$$

among modes $\chi_{\mu_i}(t)$, $\chi_{\nu_j}(t), \ldots$ of time series $\chi_\mu(t)$, $\chi_\nu(t), \ldots$ in data set $\mathcal{X}(t) = \{\chi_\kappa(t)\}$. $\mathcal{P}_{\gamma_a}$ and $\mathcal{P}_{\gamma_b}$ represent projections on subspaces γ_a, γ_b of a signal space with index γ; time is left as independent coordinate.

Sparse approximation is achieved this way if superposition of few leading modes $\chi_k(t)$ approximates $\chi(t)$ to "sufficient" accuracy. The system's motion as displayed by these data turns out to be separable then and may be followed (or "shadowed") in a tractable number of signal subspace projections. Low-dimensional behaviour, lately, comes to the fore if Eq. (5.1) holds among the leading modes of the data set. Note that (5.1) does not dictate the specific form of synchrony within the modal structure $\{\{\chi_{\kappa_k}\}\} \equiv \{\mathcal{T}\{\mathcal{R}_{k-1}\{\chi_\kappa\}\}\}$, and that "interdomain" synthesis across different signal space projections ($\gamma_a \neq \gamma_b$) goes beyond multivariate analysis with its methodological stays to the anticipated structure and interaction of data.

The present study comprises global climate time series (insolation, temperatures, precipitation, dynamic indices), central European surface air temperature and synoptic data, aggregate German rainfall, and runoff of the Elbe mainstream, all in annual resolution. Daily discharge data are preprocessed in a blind, inverse operation termed Functional Streamflow Disaggregation (FSD; [21, 22]), aimed at reducing total runoff at catchment outlet to flow components that are conceptualized to reflect different pathways of water until it forms the river. To take into account possible selective climatic impacts on the water body, both total runoff and its components enter the data set of the study. The method of sparse time series approximation of which the bearings are taken, Matching Pursuit (MP) [73], aims to identify then a set of phase space flows, or modes, for each series that enters the study.

Section 5.2 introduces either method and the Gaussian logon used as analyzing waveform which allows for deep frequency modulation (FM) here. Section 5.3 briefly quotes the data sources. Time series analyses of the global climate system are detailed in Sect. 5.4, and their multivariate global-scale ("horizontal") synthesis is completed in Sect. 5.5. Extending beyond the presentation in [18], Sect. 5.6 demonstrates a "vertical" search for synchronies from the global system via central Europe down to the river basin scale of the middle Elbe. A summary is given in Sect. 5.7, and conclusions are drawn in Sect. 5.8. MP-FM details are sketched in the Appendix, where also the performance of the tool is briefly contrasted to a set of other time–frequency (TF) methods and to Singular-System Analysis (SSA) [102].

5.2 Methods

5.2.1 Adaptive Data Modelling

In structural time series analysis one traditionally searches for trends, outliers and harmonic or polynomial components of which significance is tested against a hypothesis about background statistics (e.g., [103]). Though broadband spectra are also typical for chaotic systems, and even a single, localized event generates a white Fourier spectrum, the notion of stationary statistics (Gaussian "white noise") in conjunction with (quasi)equilibrium dynamics bears considerable inertia. A related view appears to be held when searching for covariance in the time domain in testing against the functional shape of time-dependent forcing. A system close to equilibrium or (cyclo)stationarity, maybe traversing such a state during a laminar phase of its forced evolution (e.g., [44]), might obediently follow external forcing—in which case it may be linearized about a reference state. However, as outlined here, such a general dynamical status may be posed into question for the present-day climate, which may bear fluctuations that are structurally borne in a geometrically more complex (yet certainly discernible, e.g., [19]) phase space topology.

Evolving modal structures can be (re)constructed in a variety of ways from time series which fluctuate about a mean. Classical methods (Short-Time Fourier Transform, STFT [3]; Wigner–Ville Distribution, WVD [27]; Maximum Entropy Spectral Analysis, MESA [35]) gave way today to the Wavelet Transform (WT) (e.g., [30]) and the SSA. SSA components are built from eigenvectors and projection coefficients drawn from the data without a functional template or data model. This desirable data-adaptive nature notwithstanding, SSA modal structures are not easily reduced to the sort of tractable parameter sets one needs when tracing, mapping, quantifying and post-processing (synthesizing) the system's trajectories. The WT, on the other hand, yields signal energy distributions in the TF plane which unfortunately obscure details of modal interaction, and a fixed scale–frequency relationship predetermines the TF resolution, irrespective of the demands of the actual time series. Though the analyzing-wavelet approach of the WT would support parameterization of the modal structure, its "tiling" of the TF plane runs counter to this advantage due to high temporal but low frequency resolution in the short-period range, and vice versa for long periods.

More recent data-adaptive methods and tools include the Empirical Mode Decomposition (EMD) [54] and the Matching Pursuit. Both methods overcome the WT shortage of range-dependent TF resolution. EMD exploits the Hilbert transform to construct spectrograms from bandlimited "intrinsic mode functions" (IMFs), which are thought to be analytic signals by construction (AS; cf. Appendix). Its greedy procedure starts with the highest-frequency modes and leaves the slowest one as residue (sparse approximation not being a natural option of EMD). As with the SSA, EMD also misses the means to easily parameterize the modal structures obtained. MP, in contrast, uses an explicit data model, or more than one, and may provide thus concise, tractable "structure books" from the waveform parameters

of each individual mode. The MP selection criterion and ranking are based on the signal energy captured, i.e. how much of the time series (residue) a mode "explains." In the MP version used here throughout, the AS property is technically exploited in addition, but not directly imposed to the waveforms—which even may exhibit deep FM and thus are not necessarily bandlimited.

Projection [55], Basis [24], and Matching Pursuit ideas emerged in the context of sparse data problems, i.e. "almost empty" signal spaces. The sparsity issue and related conceptions are still under discussion (e.g., [32, 97, 98]); for a review cf. [11]. MP seems to have been used only twice as yet in a climatic context. Wang and Wang [108] studied the modal structure of the Southern Oscillation, and the present author addressed the interannual organization of the global climate system [15–17]. This latter work is presented here in more detail than before [18], and is extended "down to the river side," beyond the global climate perspective.

Total streamflow, a temporally convoluted, spatial and functional aggregate, is a key quantity of the terrestrial water balance. Intrinsic data problems notwithstanding, the "integrative capacity" of water mass transduction $\mathcal{A}$ yields an areal measure of part of the hydrologic cycle, in temporal resolution, which cannot be obtained as yet with comparable ease from areal precipitation into basin X_j (coordinates $\mathbf{x}_j$) or from atmospheric water. Transformation of precipitable water w into discharge g at station j (river network coordinates $\mathbf{r}_j$) may be thought to proceed in three major stages:

$$g(\mathbf{r}_j,t) := \mathcal{A}\{f(\mathbf{x}_j,t)\} = \mathcal{GBC}\{w(\acute{\mathbf{x}}_j,t)\}\,. \tag{5.2}$$

Here, rectifier $\mathcal{C}$ imprints synoptic features on (sub)surface hydrology via (effective) rainfall $f(\mathbf{x}_j,t) := \mathcal{C}\{w(\acute{\mathbf{x}}_j,t)\}$, comprising convective, cloud and near-surface processes within the basin's atmospheric reach $\acute{X}_j$ (coordinates $\acute{\mathbf{x}}_j$), and moisture advection across the boundaries. $\mathcal{B}$ represents the impact on flow concentration of geomorphology and anthropogenic impress of the basin, $\mathbf{g}(\mathbf{x}_j,t) = \mathbf{g}(c(\mathbf{x}_j), f(\mathbf{x}_j,t)) := \mathcal{B}\{f(\mathbf{x}_j,t)\}$, where $\mathbf{g}(\mathbf{x}_j,t)$ is the vector of progressively concentrated, parallel surface and subsurface flows (a conceptual entity [112]), and $c(\mathbf{x}_j)$ is the material carrier of infiltration, flow concentration etc. $\mathcal{G}$ stands for final lateral aggregations within range of the river bank ($\mathcal{P}_\perp$) and downstream convolution along the network ($\mathcal{P}_\parallel$) into runoff at catchment outlet, $g(\mathbf{r}_j,t) = \mathcal{G}\{\mathbf{g}(\mathbf{x}_j,t)\} = \mathcal{P}_\parallel\mathcal{P}_\perp\{\mathbf{g}(\mathbf{x}_j,t)\}$ [21].

Classical conceptual discharge components, like base flow $g_b(\mathbf{r}_j,t)$, interflow $g_i(\mathbf{r}_j,t)$, and overland flow $g_r(\mathbf{r}_j,t)$ (e.g., [76]), are thought to represent distinct pathways and response times of surface and subsurface waters. They might thus individually carry the signs of distributed sources and media of flow generation, be it natural or anthropogenic. Consistent inverse (re)construction of such a component structure of historical streamflow should not resort to meteorological data if the results are aimed to unveil the signatures of climate and weather. The FSD strategy performs such an empirical, blind inversion of the (reducible) operator $\mathcal{G}$,

$$\mathcal{T}\{g(\mathbf{r}_j,t)\} \equiv \left[\mathcal{G}^{-1}\{g(\mathbf{r}_j,t)\}\right] =: \mathbf{g}(\mathbf{r}_j,t)\,, \tag{5.3}$$

that infers on a conceptual linear parallel flow aggregation at catchment outlet from the signal structure alone, $g(t) = \sum_k g_k(t) := \sum_k \mathcal{T}_k\{g\}(t)$ ($\mathbf{r}_j$ suppressed heretoforth), has only recourse to elementary constraints, and does neither exploit meteorological information nor require calibration.

5.2.2 *Functional Streamflow Disaggregation (FSD)*

FSD is a hydrologically well-motivated and theoretically founded algorithmic construct based on first principles. The method and tool [21] have been demonstrated first for German and Austrian headwater catchments to reasonably compare with results of distributed hydrologic modelling [22]. More recently, it could be shown that it also provides a natural solution to the intermittency problem; that is, after only a minor technical adaptation, prior (or extra) data treatments are no longer required for ephemeral rivers or time series with data gaps (and/or negatives). In the present application to mainstream data, the version used is that of the original publications.

SSA [102] provides a first guess of slow runoff variations to initialize construction of lower envelopes to the hydrograph via iterative cubic spline interpolation, where the knot selection rules exploit elementary constraints alone (nonnegativity, causality). The utmost envelope separates the fast FSD component, $g_f(t)$, that estimates overland flow $g_r(t)$. The slowest one, attributed in [22] to the classical baseflow $g_b(t)$, is a sort of minimal convolution [74] termed "instantaneous low flow" ($g_\ell(t)$; mode label ilf)—a smoothed running fit from below, using the window and leading eigenvector of the SSA.

A shortcut FSD version leaves the transient component as residue, $g_t(t) = g(t) - g_f(t) - g_\ell(t)$. In a more involved greedy FSD, a hierarchy of lower envelopes is constructed (bounded from below by $g_\ell(t)$) which converges into another slow component, $g_s(t)$, that turned out to differ from $g_\ell(t)$ during periods of enhanced runoff. The shortcut transient component thus splits into two subcomponents, $g_{td}(t) = g(t) - g_f(t) - g_s(t)$ and $g_{tf}(t) = g_s(t) - g_\ell(t)$, coined "driven" and "free" transient, respectively (mode labels dtrans, ftrans; $g_t(t) = g_{td}(t) + g_{tf}(t)$). As a hydrologically active medium [37], the vadose zone may bear structured interflow $g_i(t)$ indeed—to which $g_t(t)$ has been attributed in [22]. As a result of operator iteration, however, the driven-transient subcomponent $g_{td}(t)$ is a (statistically) self-similar construct that might deserve special conceptual attention with a view on the effects of nonlinear dynamics and chaos in hydrologic time series (e.g., [90]). The formulae of the FSD strategy of hydrologic data transformation may be found in [21].

5.2.3 Matching Pursuits with Gaussian logons

MP utilizes projections on elementary functions $\psi(t)$ to pursue the best decomposition of a time series $\chi(t)$ in the sense of filtered signal energy, $\alpha \equiv < \chi, \psi > := \int \chi(t)\bar{\psi}(t)\, dt$, where $\bar{\psi}(t)$ is the complex conjugate of $\psi(t)$. Use is made here of a redundant dictionary of variable waveforms, and the resulting mode-by-mode (greedy) decomposition is "slightly" non-orthogonal in fact, orthogonal methods being less adequate for nonstationary data. To capture complex (quasi)cycles and synchronies that may be drifting and/or appear episodically, high resolution is required in both time and frequency, whatever the location in the TF plane. Besides overcompleteness of the dictionary (which thus extends beyond a basis) and the greedy approach, superresolution near the low-frequency margin of the TF plane and (deep) FM make up essential features of the specific (MP-FM) version used. Here details are given of the analyzing waveform, the Gaussian logon, and its structure book parameters; in the Appendix, the analytic signal is briefly introduced, and both design and performance of the MP-FM tool are outlined.

To assess (quasi)cyclic motions in time series, and their mutual "coalitions" at a variety of scales, the Gabor atom [42]

$$\psi_\gamma(t) := \frac{1}{\sqrt{s}}\, g\left(\frac{t-u}{s}\right) \exp\left(i\left[\omega_c t + \phi\right]\right), \tag{5.4}$$

may be generalized to include harmonic phase (or frequency) modulations, yielding the "Gaussian logon" $\psi_{\tilde{\gamma}}(t) := \psi_\gamma(t) \exp(i\tilde{\varphi}(t))$, or as a real signal:

$$\psi_{r\tilde{\gamma}}(t) := \frac{1}{\sqrt{s}}\, g\left(\frac{t-u}{s}\right) \cos\left(\omega_c(t-u) + \phi' + \tilde{\varphi}(t-u)\right). \tag{5.5}$$

Signal space index $\gamma \equiv (s, u, \omega_c, \phi)$ of the Gabor atom comprises scale s, translation u, angular frequency $\omega_c := 2\pi f_c$ and phase constant ϕ of the carrier mode, and the Gaussian time-window is shaped as $g(\tau) := \sqrt[4]{2}\exp(-\pi\tau^2)$. Harmonic phase modulation $\tilde{\varphi}(\tau) := \beta \sin(\tilde{\omega}\tau + \tilde{\phi}')$ extends this signal space by three dimensions: $\tilde{\gamma} \equiv (s, u, \omega_c, \phi, \beta, \tilde{\omega}, \tilde{\phi})$. Index $\beta := \delta\omega/\tilde{\omega}$ [101] measures the modulation depth ($\delta\omega := 2\pi\delta f$ is peak deviation from carrier frequency ω_c), $\tilde{\phi}$ and $\tilde{\omega} := 2\pi\tilde{f}$ are modulation phase and frequency, respectively.

Phase constants $\phi' := \phi + \omega_c u$ and $\tilde{\phi}' := \tilde{\phi} + \tilde{\omega}u$ refer to the location u of maximum signal energy, not to the time origin; contributions $\omega_c u$ and $\tilde{\omega}u$ are kept explicit to earmark their physical estate. Phase constants also appear in the corresponding complex element $\psi_{\tilde{\gamma}}$, not only for $\psi_{r\tilde{\gamma}} := \Re\{\psi_{\tilde{\gamma}}\} = 0.5\,(\psi_{\tilde{\gamma}} + c.c.)$ to hold—they are maintained as independent parameters in order to untie a signal's phase from its maximum-energy localization.

5.3 Data

The data types, sources, and periods of availability for the present study are summarized in Table 5.1. Global and hemispheric surface air temperatures (SAT) [59] and sea surface temperatures (SST) [80], Central England SAT (CET; [80]), indices of the North Atlantic and Southern Oscillations (NAO [56, 60]; SO [2]), as well as the sea level pressure (SLP) series of their respective centers of action (Iceland, Azores, Tahiti, Darwin), may be found at the website of the Climate Research Unit (CRU) of the University of East Anglia. The Niño3 SST[1] record has been provided by [96], All-India summer monsoon rainfall is tabulated in [94] (AIR-S) for 1844–1992, a second assessment that starts 1871 is given in [81] (AIR-P). Reconstructed solar irradiance (SRAD) [66] has once been found at the website of the Geophysical Data Center (NGDC) of the U.S. National Oceanic and Atmospheric Administration (NOAA). Though this series has been retracted for astronomical reasons [67], the criticism concerns the ranking of its slow secular mode in effect (e.g., [38]), whereas waveforms are of primary interest here. There is due justification to refer to this series, but separate analyses are also given of two related time series: Wolf's sunspot number (SSN) [75] and the cosmogenic Beryllium 10 isotope (Be10) in Greenland ice cores [29]. High-quality Indian summer and winter monsoon (ISM, IWM) onset and retreat dates from peninsular India (MOSK/MONK for ISM onset over South/North Kerala, MRAP for ISM retreat over Andhra Pradesh, NEMO/NEMR for IWM onset/retreat over Tamil Nadu) are published in [4, 5, 82, 83] and [93] for different periods between 1870 and 1990.

Weather regimes (grosswetterlagen, GWLn) over central Europe after Hess & Brezowsky [50] comprise 29 cases [43]. Annual frequencies of occurrence (1881–1997) are used here of four dominating GWLn: High Middle Europe (HM), Ridge Middle Europe (BM), Westerly Cyclonic and Westerly Anticyclonic (WZ, WA). German precipitation and central European SAT are compiled according to Baur [7]. For the Middle Elbe there are daily runoff data of the Dresden gauge available for the whole period, 1870–1997.

5.4 Global Analysis

5.4.1 Structured Insolation

Irradiation at top of the atmosphere carries information from a largely undisturbed, complex dynamic system. Figures 5.1 (left panel) and 5.2 show approximations of the reconstructed insolation [66] and of the Be10 record by their respective

[1] Average over a 5°N/5°S equatorial latitude strip between 150°W and 90°W.

Table 5.1 Data sets, their references and sources (period of interest: 1870–1997)

Parameter	Area/location	Period	Reference	Websource
References to global climate dynamics				
Insolation				
SRAD	Global	1870–1997	[66]	*http://www.ngdc.noaa.gov*
SSN	Global	1870–1997	[75]	*http://www.ngdc.noaa.gov*
Be10	Global	1870–1997	[29]	*http://www.ngdc.noaa.gov*
Global climate				
SAT	Global, NH, SH	1870–1997	[59]	*http://www.cru.uea.ac.uk/cru/data*
SST	Global	1870–1995	[80]	*http://www.cru.uea.ac.uk/cru/data*
	Niño3	1871–1996	[96]	
NAO Index	North Atlantic	1870–1997	[60]	*http://www.cru.uea.ac.uk/cru/data*
Winter NAOI	North Atlantic	1870–1997	[56]	*http://www.cru.uea.ac.uk/cru/data*
SO Index	Tropical Pacific	1870–1997	[2]	*http://www.cru.uea.ac.uk/cru/data*
SLP	Tahiti, Darwin	1870–1997	[2]	*http://www.cru.uea.ac.uk/cru/data*
Indian monsoon				
ISM rainfall	All India	1870–1992	[94]	
		1871–1997	[81]	*http://www.cpc.ncep.noaa.gov/data/india*
ISM onset	South Kerala	1901–1980	[4]	
		1891–1900	[5]	
		1971–1990	[93]	
	North Kerala	1901–1980	[4]	
		1870–1900	[5]	
ISM retreat	Andhra Pradesh	1952–1990	[82]	
IWM onset	Tamil Nadu	1901–1990	[82]	
IWM retreat	Tamil Nadu	1901–1990	[83]	
References to European climate and weather				
SLP	Azores, Iceland	1870–1997	[60]	*http://www.cru.uea.ac.uk/cru/data*
GWL	Central Europe	1881–1997	[43]	
Precipitation	Germany	1881–1997	[7]	
SAT	Central Europe	1881–1997	[7]	
	Central England	1870–1997	[79]	*http://www.cru.uea.ac.uk/cru/data*
Central European streamflow				
Runoff	Dresden, Elbe	1870–1997		Courtesy PIK

leading five MP-FM modes. If the method is suited to uncover organized dynamics in complex data by means of sparse approximation, the solar input should provide a good test case to demonstrate just this. The structure books (Table 5.2) document sparse approximations indeed in terms of captured signal energy: 97.4 % by the modes #1–5 each. Given the great similarity of both time series (save scaling), their modal structures represent alternative, likewise probable pathways in fact of the

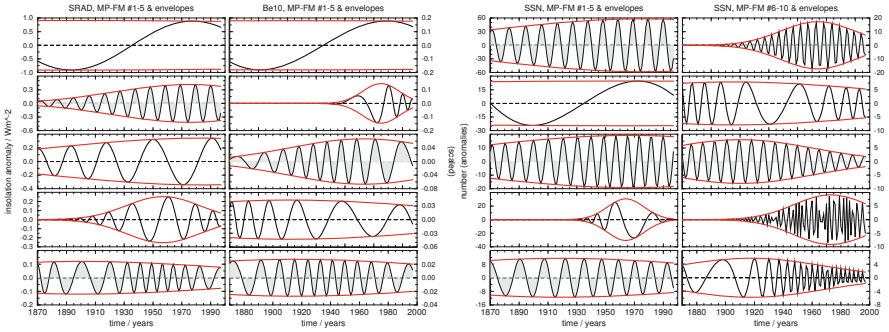

Fig. 5.1 MP-FM analysis, annual SRAD, Be10 and SSN (anomalies), 1870–1997; *left panel*: leading five SRAD and Be10 modes; *right panel*: SSN modes #1–10

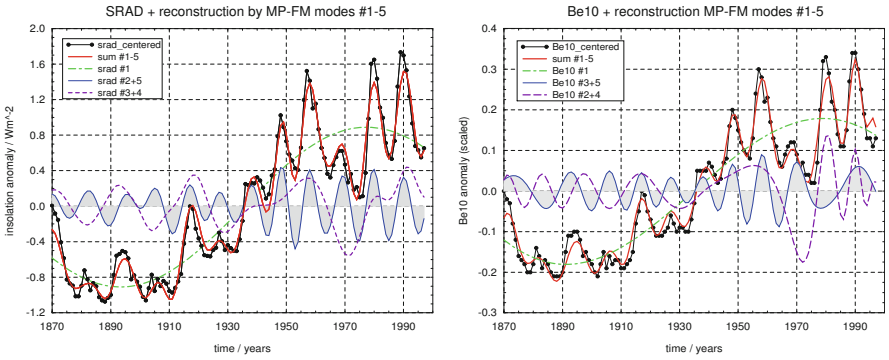

Fig. 5.2 MP-FM analysis 1870–1997, annual SRAD (*left panel*) and Be10 (*right panel*) anomalies: reconstructions by modes #1–5

greedy algorithm. For reasons that will become plausible, the SRAD decomposition is preferred, and that of Be10 is taken to provide supplementary information.

That internal structure in these series has not fully been realized before is small wonder, given this sensitive MP-FM response. Carrier periods $(1/f_c)$ of SRAD #2 and #3 relate to one another like $1:2$—that is, SRAD #3 might bear a "Hale cycle" [52]. Both modes differ in modulation frequency $\tilde{f}$ and index β, however, and traverse different FM phases. In combination with mode #4, some irregular Hale cycle may be inferred indeed (Fig. 5.2, left panel), which appears to perform a period doubling transition (a sort of period doubling is captured by only one mode (#4) in the Be10 decomposition). In relation to the Schwabe cycle, SRAD #2, it runs from a two-cycle pace at lower insolation into a three-cycle one toward the end of the record. This transition is mediated by SRAD #4, which might reflect motion on a "bumpy" torus, some hardly ever studied type of modulational instability (MI; e.g., [113]), or bear the signs of an unstable periodic orbit (UPO; e.g., [91]). SRAD #2 is parameterized as a mode that passes a phase of its multicentennial modulation

Table 5.2 MP-FM structure books of annual insolation [15] and related time series, 1870–1997: anomaly modes #$\langle k \rangle$ and signal energy captured by modes #1–5/#1–10[a]

k	α_k	s_k	u_k	f_k^{b}	ϕ_k	$\tilde{f}_k$	β_k	$\tilde{\phi}_k$
SRAD, in W/m^2 (97.4 %/99.3 % signal energy)								
1	−7.900	1024	23	0.00629	−0.184	0.001065	0.35	2.749
2	2.411	128	105	0.06816	−0.120	0.001715	16.14	0.196
3	2.384	256	115	0.03408	−0.130	0.005769	1.85	−2.553
4	1.200	64	88	0.11463	1.976	0.005290	14.73	−2.945
5	0.868	256	32	0.08839	0.104	0.009291	5.00	3.142
⋯								
7	0.607	1024	14	0.04232	3.070	0.003285	6.77	1.963
13	0.227	32	14	0.01433	0.239	0.000000	0.00	0.000
SSN (91.9 %/97.7 % signal energy)								
1	411.729	256	106	0.05731	−0.931	0.001642	23.71	0.196
2	200.532	1024	99	0.02866	−2.909	0.001213	18.26	−2.945
3	138.301	256	97	0.10977	0.904	0.008158	1.71	−0.196
4	103.574	32	95	0.21953	2.547	0.006570	29.38	2.945
5	85.162	256	51	0.05033	−1.768	0.002762	14.08	−0.982
⋯								
7	57.652	256	37	0.09639	−1.553	0.005290	14.08	2.160
Be10, scaled (97.4 %/99.1 % signal energy)								
1	1.567	1024	43	0.01372	2.588	0.001213	6.76	2.945
2	0.484	32	106	0.20131	1.487	0.006024	29.38	−2.553
3	0.405	128	94	0.06527	3.113	0.006291	6.20	1.178
4	0.319	256	44	0.10066	−2.952	0.002645	29.41	2.356
5	0.204	256	48	0.07117	1.174	0.005524	8.76	−0.785

[a] SRAD #7,13 are referred to in Sect. 5.4.2, Fig. 5.7, SSN #7 in Sect. 5.4.2 (text)
[b] In the structure books heretoforth carrier frequency f_c of component k is written f_k

which beneath the given time window just moves it through the carrier period range of SRAD #5 (11.3 years). It shows the well-known drift toward the shorter-period edge of the $10 \cdots 12$ years Schwabe cycle [40].

Together with marked terrestrial responses to the signal energy of SRAD #4 (envelope synchronization), this Schwabe cycle behaviour lends credence to the SRAD decomposition, the more so since that of Be10 misses the perhaps most striking SRAD feature: interdomain synchrony between modes #1 and #3. FM of the latter leads the time domain evolution of the former by just about one sunspot cycle length ($\sim$11 years) and almost perfectly matches its functional shape ("internal interdomain" [15]; cf. Sect. 5.5, Fig. 5.17). Considering signal energy expenses, the secular change of insolation does certainly drive the frequency drift of SRAD #3—of which also the multidecadal evolution deserves scrutiny. Possible changes notwithstanding for data periods that differ in length and/or are shifted along the time axis ("cross validation" problem), the internal SRAD structure found indicates that the method is capable of unveiling organized dynamics in complex modal

webs—sensitivity of MP-FM response to these data notwithstanding. The SRAD time series itself bears valuable information and should not be shelved.

Structure books (Table 5.2) do not unveil at a glance that SRAD #1 and Be10 #1 are nearly identical in both functional shape and phase, a correspondence that lends further realism to SRAD #1 (yet not necessarily to its leading rank). Be10 #1 and SSN #2 coincide in scale s and modulation frequency $\tilde{f}$. A (bi- to multi-) decadal mode like SRAD #3 or Be10 #4 is missing in SSN, however (Fig. 5.1, right panel): the Schwabe cycle dominates this modal structure, and the slow secular mode (here at rank #2) has a shorter period. Be10 #2 appears to reflect response to, or continuation of, a similarly localized mode in SSN (rank #4). Envelope maxima of both are depart from each other just by one Schwabe cycle length again (parameter u in Table 5.2). Either localized mode contributes in shaping one of the strong solar cycles #19 and #21 with maxima around 1957–1958 and 1979–1980, respectively. SRAD #4 appears to comprise both signals; these in turn may provide hints at different mechanisms behind its growth and decay—and thus perhaps lend weight to UPO interpretation of SRAD #4.

5.4.2 *Thermal Evolution: Into Another Stagnation*

The entire MP-FM structure of customary temperature series of the global climate system bears intriguing features in its leading phase space flows. Modes #1–5 each of global and hemispheric SAT and global SST are presented in Fig. 5.3, and corresponding spectrograms are shown in Fig. 5.4. Secular warming expectedly occupies SAT and SST at rank #1. Their functional shapes are more stretched than those of the slow insolation mode—a fact that offers a certain chance to separate centennial direct solar from thermal effects [15]. Table 5.3 displays the structure books of either global series, Table 5.4 presents those of hemispheric SAT.

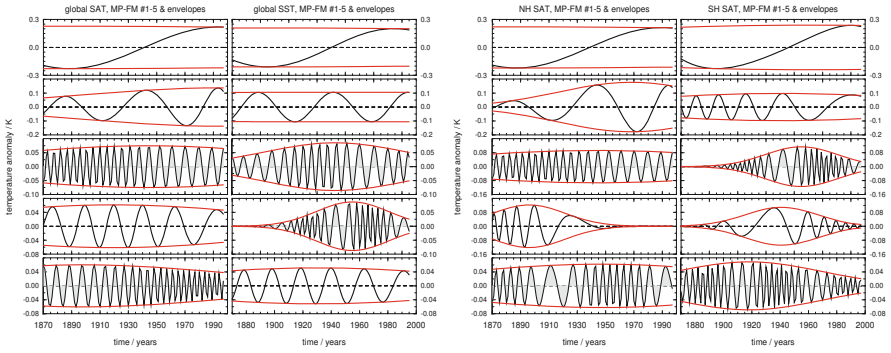

Fig. 5.3 MP-FM analysis (leading five anomaly modes each) of annually aggregated temperatures; *left panel*: global SAT/SST; *right panel*: northern/southern hemispheric SAT

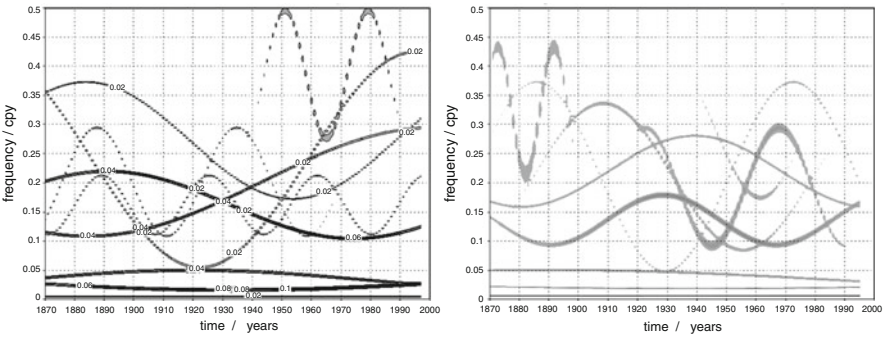

Fig. 5.4 MP-FM spectrograms (leading ten anomaly modes each) of annually aggregated global SAT (*left panel*, 1870–1997 [17]) and global SST (*right panel*, 1870–1995)

Table 5.3 MP-FM structure books of annual mean global SAT and SST (in K); anomaly modes $\#\langle k \rangle$, signal energy captured by modes #1–5/#1–10, and periods of analysis[a]

k	α_k	s_k	u_k	f_k	ϕ_k	$\tilde{f}_k$	β_k	$\tilde{\phi}_k$
Global SAT (86.1 %/93.3 % signal energy), 1870–1997								
1	1.923	1024	18	0.00507	2.983	0.001112	0.30	2.749
2	0.909	256	126	0.03881	1.602	0.002533	9.15	−2.160
3	0.563	256	74	0.16210	2.355	0.006024	9.61	1.963
4	0.462	256	51	0.03408	0.122	0.004448	3.54	0.000
5	0.433	256	30	0.20131	−3.038	0.004260	21.83	−2.749
…								
12	0.221	16	30	0.27263	2.961	0.013139	16.74	2.945
14	0.158	1024	1	0.00000	0.000	0.000000	0.00	0.000
15	0.149	32	80	0.25000	−2.370	0.007481	29.41	2.749
Global SST (87.8 %/95.4 % signal energy), 1870–1995								
1	−1.788	1024	18	0.00577	−0.134	0.001112	0.27	−2.553
2	0.830	1024	70	0.02516	−0.294	0.002426	2.86	3.142
3	0.546	128	74	0.13631	2.639	0.013139	3.26	1.178
4	0.410	64	86	0.19278	0.600	0.022097	4.58	−1.767
5	0.387	256	61	0.02993	−1.408	0.002323	8.76	0.589
…								
11	0.167	128	61	0.04819	−0.677	0.005290	4.79	0.393
12	0.160	128	93	0.00000	0.000	0.000000	0.00	0.000
17	0.096	128	35	0.12500	2.684	0.003741	29.38	2.160

[a] SAT #12,14,15 and SST #11,12,17 are residual slow components (SAT #14 is a highly stretched half-Gaussion that emulates a constant offset, SST #12 is a Gaussian centered 1962)

Modes #3 and #5 of global SAT, both with carriers in the El Niño–Southern Oscillation (ENSO) range of period (∼3–7 years), show secular frequency drifts in nearly perfect (#3, FM inverted) or approximate (#5) interdomain synchrony with rank #1 solar and thermal modes, respectively (cf. also Sect. 5.5, Fig. 5.17, left

Table 5.4 MP-FM structure books of annual mean hemispheric SAT (in K); 1870–1997; anomaly modes #1–5 and signal energy captured by #1–5/#1–10[a]

k	α_k	s_k	u_k	f_k	ϕ_k	$\tilde{f}_k$	β_k	$\tilde{\phi}_k$
NH SAT (82.9 %/92.7 % signal energy)								
1	1.883	1024	11	0.00465	3.002	0.001020	0.24	−0.393
2	1.071	128	99	0.03716	1.216	0.002533	8.77	−2.553
3	0.698	256	74	0.16210	2.308	0.006024	9.61	1.963
4	0.560	64	27	0.14235	−0.820	0.004260	29.38	2.160
5	0.464	256	77	0.13053	2.316	0.011538	6.76	−0.785
...								
8	0.367	64	90	0.25000	−2.079	0.007481	29.41	−2.945
10	0.285	16	12	0.15523	0.627	0.007812	15.36	−2.749
15	0.184	256	84	0.04615	−0.564	0.001381	29.38	2.749
SH SAT (85.1 %/92.8 % signal energy)								
1	1.945	512	91	0.03716	−1.695	0.001112	29.38	−2.945
2	0.746	256	71	0.06250	0.378	0.001870	29.38	2.160
3	0.540	64	86	0.19278	3.108	0.017039	6.76	−1.767
4	0.518	64	72	0.14865	−0.444	0.004448	29.38	−2.749
5	0.437	128	49	0.21022	−0.005	0.019404	4.40	−2.553
...								
6	0.378	512	80	.03263	−2.960	.001791	12.38	−2.160
8	0.301	128	49	.10511	2.026	.003285	24.73	−2.749
12	0.204	64	54	.00265	0.016	.000000	0.00	0.000

[a] NH SAT #8,10,15 and SH SAT #6,8,12 are referred to in Fig. 5.6

panel). Perfect coincidence of NH and global SAT modes #3 (Tables 5.3 and 5.4) hints at the geographic source of this interdomain companion of SRAD #1. This might be taken as endorsing both existence of robust signals here and reliability of the MP-FM method. SST #3 appears to integrate the slower parts of SAT #3 and #5, introducing another modulation period this way—an interpretation that is supported by nearly perfect phase and amplitude coincidence around 1930 of SST #3 with the sum of SAT #3 and #5 [15] (Fig. 5.5, left panel). The two SAT modes just ran into quadrature and were crossing one another at that period (cf. Fig. 5.4, left panel), thus together matching SST #3 there with remarkable precision [15]. The right panel of Fig. 5.5 shows the concurrent evolution of hemispheric SAT #4 modes (cf. also right panel of Fig. 5.3), representing a thermal wave that changes the hemispheres, thereby exhibiting a common "bump" just around 1930 (not rescaled to global in the figure). Notice the remarkable similarity until the 1970s of the sunspot mode SSN #7 (Fig. 5.1, rightmost column) with this combined thermal wave effect. Given distinct growth and decay paths again, the question arises if this might not hint at the terrestrial manifestation of another solar UPO.

The ∼12–15 years in question coincide with the core period of the first global warming shove of the twentieth century (Fig. 5.6) which "kicked" the system from one oscillatory regime into another one at generally higher thermal level. How the

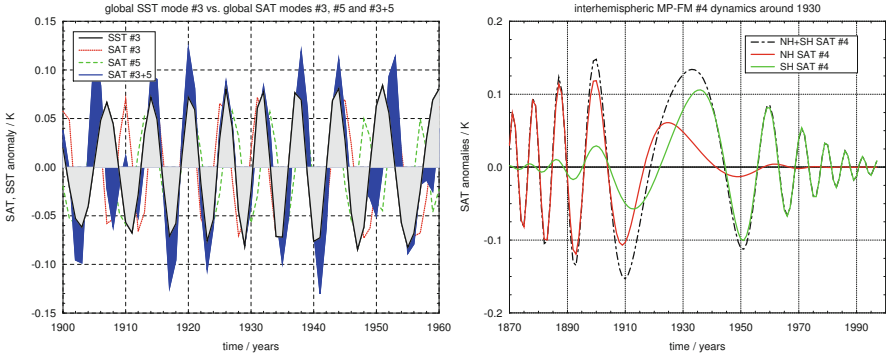

Fig. 5.5 Evolution of MP-FM thermal anomaly modes (in K) around the first twentieth century global warming episode; *left panel*: global SST #3 (*grey shaded*) vs. global SAT #3,5 and their sum, shown for 1900–1960; *right panel*: unstable hemispheric SAT #4 modes (1870–1997) and their common effect (not rescaled to global) during the warming period

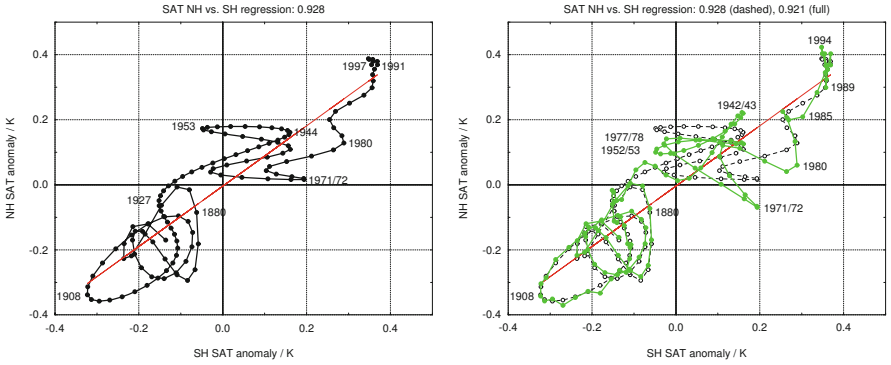

Fig. 5.6 NH vs. SH warming (1870–1997, in K) in terms of the slow MP-FM anomaly modes #1,2,4,10,15 (NH) and #1,2,4,6,8,12 (SH) of hemispheric SAT, and linear regression (*left panel*); inclusion of NH SAT #8 modifies the picture, mainly during the mid-century period of recurrence oscillations (*dashed black line*, *opaque circles* vs. *full green line*, *filled circles*)

climate system is dynamically organized within these regimes is looked at in the sections to follow. Among the thermal features, global multidecadal (SAT & SST #2) and bidecadal modes (SAT #4, SST #5, which bear close resemblance to one another) as well as hemispheric SAT modes #2 (cf. Fig. 5.3) are of special interest.

The stagnation period in all bidecadal-to-centennial temperature modes toward the end of the twentieth century (Figs. 5.3 and 5.6) was unexpected at its discovery around the turn of the century [14, 15]. Coincidentally, the data set does not include the strong El Niño year 1998 with its marked warming pulse (starting with monsoon data of 1870, the 128 year window chosen for technical reasons ends 1997), thus leaving uncertainty about potential boundary effects of the method—the more since "officially" global warming appeared to continue [92]. Only recently, a heated

debate evolved about the "hiatus", the pause in global warming lasting now for 15–20 years, and its absence in GCM based projections [6, 36, 41, 68, 104]. The MP-FM analysis here hints at such a hiatus since the early 1990s, thus supporting the conclusion in [41].

The north-south distribution of slow global warming (Fig. 5.6) shows a dominant NH effect since the beginning of the 1970s. More close inspection (inclusion of NH SAT #8) makes the curve more restless and modifies the shape of oscillations between the mid-1930s and the beginning of the 1980s, thus unveiling a common warming fluctuation of the early 1940s at both hemispheres. The early 1970s, in contrast, have seen a marked "cool NH" excursion, Southern Hemisphere (SH) warming notwithstanding. At the beginning of the 1970s, the NH was as cool as in the late 1920s. The warm NH SAT of the early 1940s, in turn, was reached again not before the mid-1980s, halfway NH warming of this decade. From the early 1930s to the mid-1970s, "global" warming was an SH phenomenon in effect, accompanied by strong fluctuations. Since the 1980s, in contrast, gradual SAT stagnation in the South is accompanied by shorter-scale fluctuations in the North.

Centennial thermal modes #1 most directly fit the idea of "global warming" during the past century, and the multidecadal modes at rank #2 are major carriers of the episodic nature of the process (SH SAT has a weaker multidecadal component at rank #6). A "swarm" of interdomain companions (Sect. 5.5, Fig. 5.17, right panel) bears strong indication of a regime character across the climate system of these dynamics. The oscillatory SAT regime until about 1910 is largely carried by the interplay of bi- and multidecadal modes (Fig. 5.6). The substantial growth of multidecadal signal energy in global SAT, which appears to be borne in the growing NH mode but might have even deeper roots (e.g., the evolving structured solar forcing; Sects. 5.4.1 and 5.5), gradually adopts the lead. It fully dominates since the 1970s until the end of the record, whereby the system is dissolved from the regime of yeasty oscillations around solar cycle #19 (the strongest on record), i.e. from its second oscillatory regime, to run into the present stagnation. Note already here that European SAT does not show any multidecadal mode (Sect. 5.6.1), which hints at a tropic/subtropical origin (cf. also [87]).

That leading slow global SST modes do not exhibit growing signal energy (their Gaussian envelopes show maximum "allowed" spread), might mean the oceans have not "taken over" until the end of the twentieth century to set the global warming rules, including the important multidecadal pace. Centennial modes #1 are least certain under the 1870–1997 time window (showing up only half-periods), but for global SAT and SST #1 identical modulation frequencies $\tilde{f}$ and very similar modulation depths δf have been found, and their carriers f_c are within range of mutual modulation depths.

Figure 5.7 shows slow-mode phase plots of global SAT vs. SST (left panel; data until 1995) and global SAT vs. SRAD (right panel). The left panel also does not hint at a leading role of ocean warming as compared with that of the surface–near atmosphere. The phase plot of modes #1 alone (turquoise) approaches the regression line of balanced SAT/SST evolution and bears almost precise recurrence since the mid-1980s along the warming route, with a state in 1995 very close

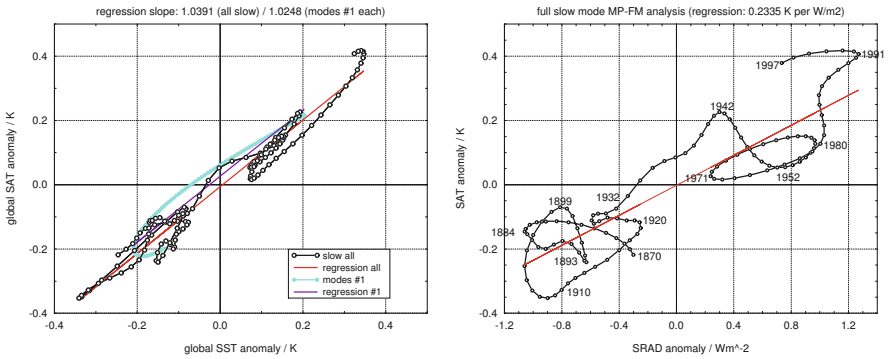

Fig. 5.7 Global warming, slow MP-FM anomalies; *left panel*: global SAT vs. SST modes #1 (*turqouise*) and SAT #1,2,4,12,14,15 vs. SST #1,2,5,11,12,17 (*black* with *opaque circles*), plus respective linear regressions (1870–1995, in K; *right panel*: global SAT (full slow-mode data, cf. *left panel*) vs. SRAD #1,3,4,7,13 (1870–1997, in W/m^2)

to that of 1973. Altogether, this means that multidecadal NH SAT has taken over. Note that stagnation until 1997 in global warming, as represented by SAT, commenced with decreasing slow insolation since 1991 (turning point in the right panel, SAT vs. SRAD). The cyclic mid-century SAT/SRAD excursion calls for further clarification with respect to the potential UPO manifestation in the climate record (forcing/response; recall Sect. 5.4.1). The SAT/SRAD state in 1997 is in line with the discernible trend of the 15 year period 1927–1942. The combined solar–terrestrial system became attracted and temporarily captured then for 40 (or even 55) years by some phase space object (the figure reminds of a homoclinic orbit).

5.4.3 Dynamic Indices

Persistent SLP gradients may drive climatic subsystems and are thus taken as indices to grasp their dynamics in terms of single time series. A customary NAO index is the normalized SLP difference between Azores High (station Ponto Delgada) and Iceland Low (Stykkisholmur). The winter NAO (NAOW; December–March) refers to Lisbon, Portugal, to represent the Azores High [56]. The north–south seesaw of the NAO controls the tracks across central Europe of cyclonic weather systems and is therefore relevant to the hydrology of the region. The east–west seesaw of the SO represents the atmospheric branch of the tropical ENSO system. The SO index (SOI), a normalized SLP difference between Tahiti and Darwin (North Australia), indicates the appearance and strength of El Niño (negative SOI) and La Niña (positive SOI) events which leave their marks in worldwide weather and hydrology (e.g., [84]). Figure 5.8 shows MP-FM spectrograms of either index. The

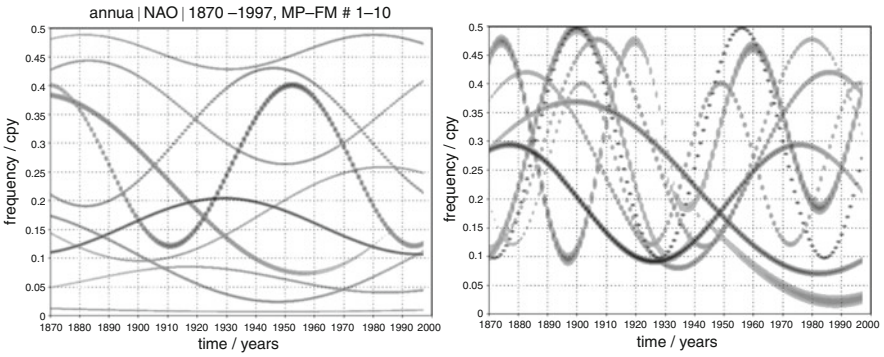

Fig. 5.8 MP-FM spectrograms (leading ten anomaly modes each) of annually aggregated time series of (*left panel*) NAO index [17] and (*right panel*) SO index; 1870–1997 [15]

smoothest one obtained as yet is just that of the NAO—to which slow signatures of other subsystems appear to be imprinted (cf. Fig. 5.10, right panel).

To what extent the NAO is part of a larger system is subject to conceptual debate (e.g., [25, 105, 107]). Accordingly, the pathways remain unclear how the NAO may be affected by other dynamic subsystems (e.g., [70]). Atlantic–Pacific teleconnections are studied for long with a view on NH stormtracks and midlatitude blocking phenomena (e.g., [23, 34]), both in the search for a possible ENSO impact on Europe at interannual to decadal scales (e.g., [39, 45, 46]) and in order to understand the degree and mechanisms of NAO/SO interaction (e.g., [53, 86]). Time domain relationships might episodically exist and be controlled in part by Eastern Pacific equatorial SSTs [53]. A customary measure of the latter is their average over the "Niño-3" area. Table 5.5 presents MP-FM structure books of these three time series.

Systematic FM relationships between NAO #1, SOI #2 and Niño-3 modes #3,4 are shown in Fig. 5.9, as they are found in the TF plane (left panel; cf. also Fig. 5.8) and as normalized departures from their respective carrier modes (right panel). Excepting the initial period, NAO #1 and Niño-3 #3 are interdomain (FM) companions of the slow time domain evolution of NAO #5 (Fig. 5.10, left panel). NAO #1 appertains to a triplet of NAO modes (#1,7,9) with common FM (Table 5.5). Also, FM of NAOW #1 (Table 5.6) approximately fits the multidecadal FM pace of SOI #2 and Niño-3 #4, which are part of the larger set of interdomain companions of the rank #2 thermal modes that have taken over to rule the pace of global warming since the 1970s (cf. Sect. 5.5, Fig. 5.17, right panel). SOI #2 belongs also to a triplet of SOI modes (#2,6,9) with common carrier frequency—throwing another bridge to the monsoon system (Sect. 5.4.4).

Counterintuitive, however, is the fact that a direct rational relationship between the two FMs that make up Fig. 5.9 does not appear to exist; the obvious systematic emerges from a combined $(\tilde{f}, \tilde{\phi})$ effect. A close FM companion to NAO #1, namely NAO #4 (cf. Fig. 5.10, right panel), shows FM relationships to Europe (Iceland SLP

Table 5.5 MP-FM structure books of annual NAO and SO indices and Niño 3 SSTs; anomaly modes $\#\langle k \rangle$, signal energy captured by #1–5/#1–10, and data periods

k	α_k	s_k	u_k	f_k	ϕ_k	$\tilde{f}_k$	β_k	$\widetilde{\phi}_k$
NAOI (61.2 %/85.5 % signal energy), 1870–1997								
1	2.421	256	60	0.15523	0.630	0.007481	6.51	0.000
2	2.326	128	73	0.26107	−0.779	0.012049	11.62	−0.785
3	1.643	128	31	0.22925	−1.447	0.005524	28.20	1.178
4	1.610	256	73	0.31046	1.230	0.007812	15.36	−0.196
5	1.471	512	34	0.02993	0.128	0.001506	15.36	2.749
…								
7	1.272	256	60	0.35355	−2.485	0.007481	12.03	2.160
9	1.130	256	115	0.06250	−1.225	0.007481	2.98	3.142
10	0.988	256	73	0.17678	0.180	0.006024	13.55	−1.571
Niño 3 SST, in K (61.9 %/84.6 % signal energy), 1871–1996								
1	2.945	512	111	0.18460	0.800	0.004079	23.77	−0.196
2	2.419	128	42	0.23940	−0.575	0.013139	9.57	1.178
3	2.160	256	31	0.16210	2.710	0.007481	16.75	−2.553
4	1.894	128	77	0.22925	−1.863	0.017794	8.76	−2.945
5	1.700	128	37	0.32421	2.963	0.008158	13.48	3.142
…								
10	1.120	64	28	0.32421	2.451	0.018581	4.84	2.749
SOI (62.4 %/85.6 % signal energy), 1870–1997								
1	3.863	128	45	0.19278	−2.754	0.010132	9.99	2.356
2	3.068	256	66	0.29730	−1.380	0.017794	11.24	−2.356
3	2.854	128	82	0.21953	−1.267	0.006024	24.76	1.963
4	2.334	64	18	0.28470	−1.743	0.022097	8.60	1.767
5	2.286	64	105	0.32421	−0.880	0.022097	6.34	1.963
6	2.058	64	25	0.29730	1.355	0.015625	12.80	−0.589
…								
9	1.523	128	63	0.29730	−0.095	0.013721	13.12	2.160

& CET #6, Baur's SAT #5, GWL NWZ #4; cf. Tables 5.12, 5.14 and 5.16), but these are links to be expected. It remains thus to decode the time domain behaviour of the leading slow NAO mode #5. In the extreme modulation phase it attains, the mode reaches (below the given time window) an apparent carrier frequency ($f_c - \tilde{f}\beta\ =$) 0.00680, i.e. a ∼147 year period. The secular decline of the NAO during the twentieth century [86] is grasped by this mode as a slow oscillation that evolves into its extreme FM phase with little frequency drift (Table 5.5)—though at the beginning of the record it misfits harmonic FM (Fig. 5.9, right panel). Of the system's slow forcing modes, this matches only the actual apparent carrier period of SSN #2, which in its extreme (slowest) modulation phase here may reach a ∼154 year period. Since about 1900, both modes keep distance to one another in the time domain by about one Schwabe cycle length (Fig. 5.9, right panel; SSN

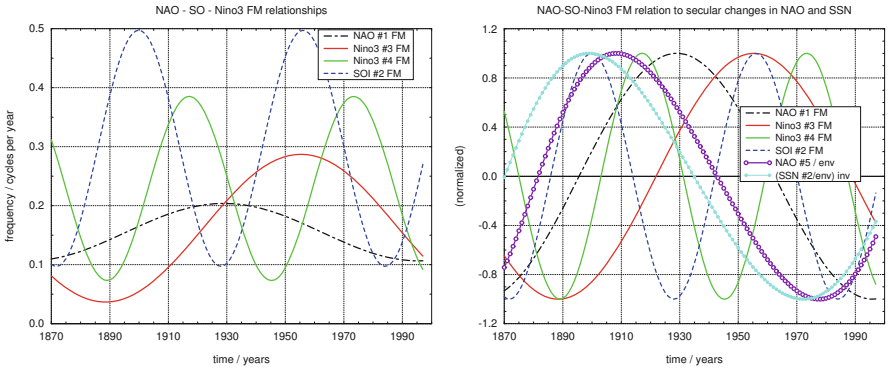

Fig. 5.9 Systematic FM phase relationships between leading anomaly modes of the annual NAO index (#1), Niño 3 modes #3 and #4, and SOI #2; *left panel*: carrier mode position in the TF plane unchanged; *right panel*: normalized fluctuations relative to each carrier mode [17], supplemented by the time evolutions of NAO #5 and inverted SSN #2 (both normalized by their own envelopes; Niño-3 SSTs 1871–1996)

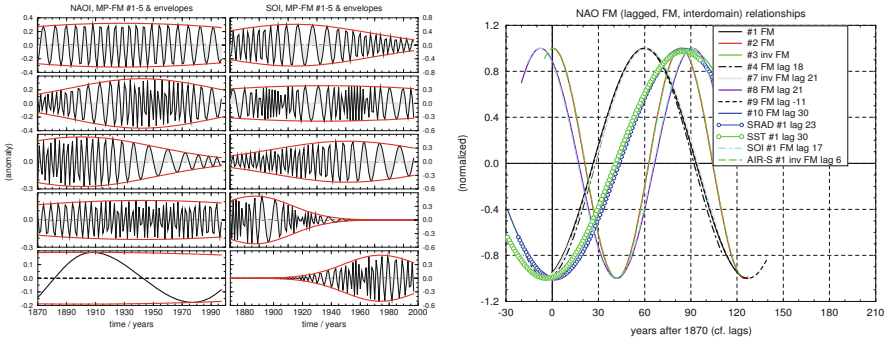

Fig. 5.10 MP-FM analysis of annually aggregated time series; *left panel*: NAO and SO indices (leading five anomaly modes each, 1870–1997); *right panel*: NAO FM relationships to SRAD & SST #1 (time domain) and SOI & AIR-S #1 (frequency domain)

#2 inverted), but toward the end of the record they tend to further synchronize (in counterphase). If NAO #5 is not a robust, genuine European (/North Atlantic) mode, it might thus be increasingly controlled, with growing insolation, by (structured) solar forcing.

Inconclusive observational evidence of NAO–SO relationships notwithstanding, a "small-world" network of modal interactions does exist. "Third-party" mediation as suggested by [53] (cf. also Fig. 5.9), and by [34] in a different context, may be borne in the role that either subsystem plays with respect to the global water cycle. Figure 5.10 (right panel) provides such a hint in showing, among others, lagged FM synchrony between NAO #2 and All-India rainfall (AIR-S) #1 (cf. Sect. 5.4.4). Considering intrinsic uncertainty in period identification of centennial modes beneath a 128-year window, FM of NAO #3 and #10 may also resemble

Table 5.6 MP-FM structure book of the winter NAO (NAOW) index, 1870–1997; anomaly modes #$\langle k \rangle$ and signal energy captured by modes #1–5/#1–10[a]

k	α_k	s_k	u_k	f_k	ϕ_k	$\tilde{f}_k$	β_k	$\tilde{\phi}_k$
NAOW (61.8 %/83.1 % signal energy)								
1	9.321	128	84	0.20131	−2.630	0.017039	4.80	0.589
2	8.507	128	114	0.05488	−2.692	0.003582	10.41	2.945
3	7.977	256	47	0.42045	−0.373	0.002762	21.72	1.767
4	6.767	512	128	0.10977	1.358	0.006291	11.86	3.142
5	5.736	128	42	0.38555	−2.231	0.028656	3.84	0.000
6	5.374	128	80	0.28470	2.593	0.022097	8.60	−1.571
...								
12	3.211	32	83	0.14865	−3.013	0.004448	29.38	2.945

[a] NAOW #12 is referred to in Sect. 5.6.1, Fig. 5.18 (left panel)

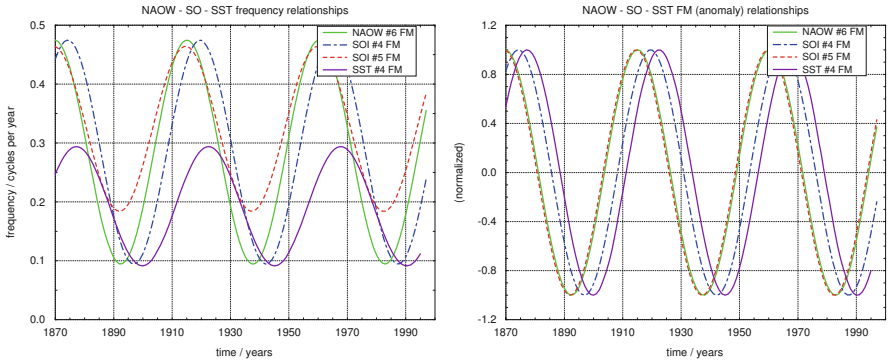

Fig. 5.11 As in Fig. 5.9, but for FM of anomaly modes NAOW #6, SOI #4,5, and global SST #4 (ranges of existence not displayed again; cf. text)

the phase evolutions of SST #1 and SRAD #1, respectively (lagged interdomain synchrony).

Figure 5.10 (left panel) and Table 5.5 show SOI #5 as a continuation of SOI #4, with identical $\tilde{f}$ but changed f_c and δf (cf. also Fig. 5.8). The shift appears around 1930 again. These two SOI modes set the trace to a remarkable weak-coupling link to the NAO in boreal winter (NAOW; cf. Table 5.6), where its strongest signal is found in general. Figure 5.11 shows FM phase relationships between SOI #4,5, NAOW #6, and global SST #4; a clear time domain companion has not been found. NAOW #6 and SOI #4 exactly coincide in all frequency parameters ($\tilde{f}$, δf, f_c) and share their carrier with the leading triplet in ISM onset over South Kerala (MOSK), a key phenomenon and time series of the global water cycle (Sect. 5.4.4, Table 5.7). This extremely improbable coincidence is lost around 1930 with the fading of SOI #4, but the replacement mode SOI #5 fully synchronizes FM phase with NAOW #6 (which overarches SOI #4,5 in their range of existence).

5.4.4 *Atmospheric Water Cycle: Asian Monsoons*

Representing critical transitions in the seasonal march (e.g., [19]), monsoon onsets and retreats bear sensitive indices of the interannual climatic evolution—most directly and simplest by the Julian days of their occurrence. They represent thus a sort of Poincaré maps of global climate dynamics. Remarkably, 1918, the year of the earliest MOSK on record, coincides with startup of the first global warming episode of the twentieth century. Further, the localized MOSK #4 signal and its MONK #3 companion (Fig. 5.12, left panel)—the spot or patch in the spectrograms of Fig. 5.13 which signify an exceptional period of early ISM onset—relate to a phase of reorganized NH circulation [64]. Monsoon anomalies are known to extend to planetary scale (e.g., [110]).

Table 5.7 shows MP-FM structure books of the MOSK, MONK and NEMO series. A prominent feature is the leading MOSK triplet with identical carrier frequency. It also appears as a carrier in other monsoon onset and retreat data (MONK #5, NEMO #6, NEMR #7,10), in All-India rainfall (AIR-S #5), the winter NAO (NAOW #6), the Southern Oscillation (SOI #4; Tahiti SLP #3) and elsewhere. FMs of the leading MOSK pair, though, are solitary among the leading ten modes each across the whole data set analyzed as yet. This is surprising, given the fact that the deep MOSK oscillations (Fig. 5.13, left panel) are most intense during the period of global thermal oscillations (Figs. 5.6 and 5.7) around the height of Schwabe cycle #19. Though signal structures turn out to be more complex there, it is also not unplausible that for technical reasons (limitations to $\tilde{f}/f$ and δf; cf. Appendix) the sparsest approximations have not been reached here.

The localized MOSK/MONK signal of Figs. 5.12 and 5.13 is shown in the left panel of Fig. 5.14 to commence just when the unstable SRAD #4 mode reaches its maximum—at solar cycle #19. It does thus certainly reflect a forcing–response relationship. A related solar connection concerns the leading MOSK pair (right

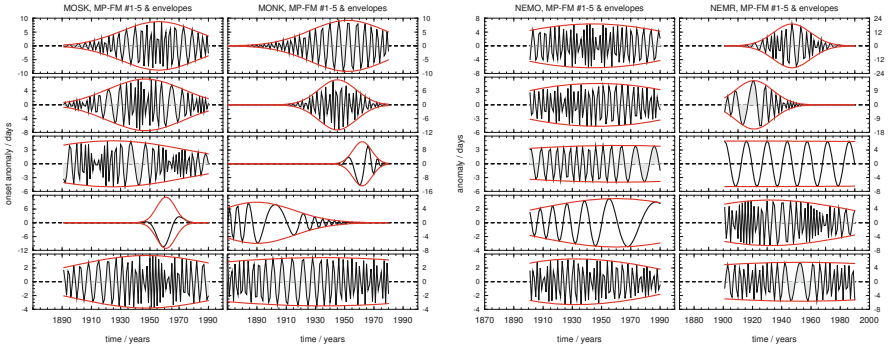

Fig. 5.12 MP-FM analysis (leading five anomaly modes each) of monsoon onset and retreat series over peninsular India [15]; *left panel*: MOSK & MONK; *right panel*: NEMO & NEMR; data periods between 1870 and 1990

Table 5.7 MP-FM structure books of onset dates of the Indian summer and winter monsoons, ISM and IWM (Julian days; leap-years considered); anomaly modes $\#\langle k \rangle$, signal energy captured by #1–5/#1–10, and periods of analysis[a]

k	α_k	s_k	u_k	f_k	ϕ_k	$\tilde{f}_k$	β_k	$\widetilde{\phi}_k$
MOSK (69.5 %/89.9 % signal energy), 1891–1990								
1	41.249	64	66	0.28470	0.352	0.026278	4.95	0.196
2	35.672	64	57	0.28470	−0.902	0.024097	7.47	0.393
3	28.890	128	34	0.28470	−2.701	0.018581	10.76	1.178
4	27.792	16	71	0.02993	−2.571	0.000000	0.00	0.000
5	23.520	128	58	0.31046	2.488	0.012049	14.11	−0.589
...								
7	19.430	64	19	0.15523	−0.465	0.004645	29.38	−2.749
10	12.195	256	83	0.11970	−2.994	0.004645	17.51	−2.749
MONK (67.7 %/90.3 % signal energy), 1870–1980								
1	42.586	64	83	0.27263	1.722	0.010580	11.34	−2.945
2	36.287	32	76	0.36921	0.224	0.065267	1.07	1.963
3	30.928	16	93	0.27263	−2.227	0.013139	16.74	−2.749
4	26.510	64	21	0.23940	−0.820	0.007164	29.38	2.553
5	24.898	256	65	0.28470	2.576	0.008520	17.61	−2.160
...								
9	17.360	512	36	0.04232	−2.940	0.002130	15.36	2.945
NEMO (77.8 %/94.2 % signal energy), 1901–1990								
1	38.259	128	44	0.32421	3.057	0.010580	13.23	0.196
2	27.892	128	47	0.33856	−2.081	0.014328	7.68	1.963
3	25.565	256	61	0.15523	2.455	0.010132	8.05	1.767
4	20.735	128	59	0.09230	0.735	0.003906	18.26	2.356
5	19.550	128	34	0.35355	2.240	0.028656	3.49	−2.160
6	15.801	128	46	0.28470	−2.011	0.011538	18.20	2.356

[a] MOSK #7,10 and MONK #9 are referred to in Sects. 5.4.3, 5.5 and 5.6.1

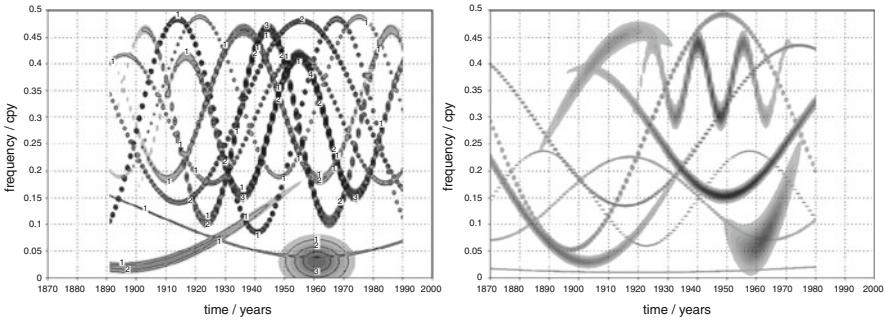

Fig. 5.13 MP-FM spectrograms (leading ten anomaly modes each); *left panel*: MOSK, 1890–1990 [17]; *right panel*: MONK, 1870–1980

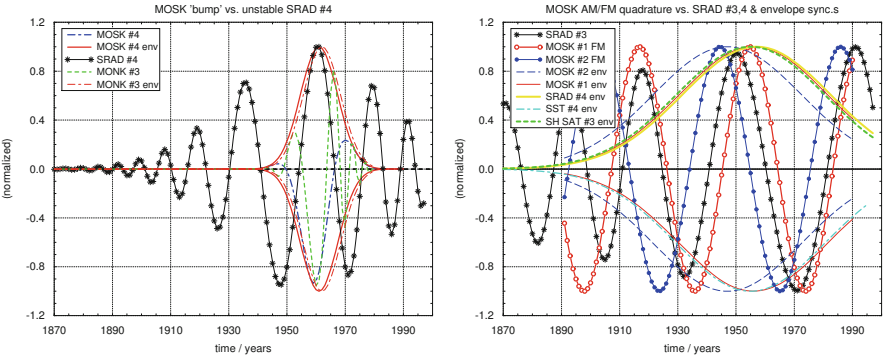

Fig. 5.14 MP-FM based synthesis; *left panel*: annual mean SRAD anomaly mode #4 vs. ISM event around 1960 (MOSK #4 & MONK #3); *right panel*: normalized amplitude and frequency modulations of the leading MOSK pair, in synchrony with SRAD #3 and (envelopes of) SH SAT #3 as well as SRAD & global SST modes #4

panel) which contributes to a signal that comprises interdomain, quadrature, and envelope synchronies at once: Beneath signal envelopes which mirror those of SRAD #4, SST #4 and SH SAT #3, the leading MOSK pair runs into mutual FM quadrature, thereby flanking as interdomain companions the time domain evolution of the (growing, multidecadal) mode SRAD #3. If the MOSK spectrogram (Fig. 5.13, left panel) offers a glance at a real-world UPO manifestation in terms of its signal energy distribution, Fig. 5.14 gives detailed phase information how the solar impact on the terrestrial water cycle might be organized in such a case.

When adopting this suggestive view of marked solar signals in the hydrologic cycle, one may be wondering about one missing signal, the Schwabe cycle mode(s) SRAD #2,5. The issue is difficult to appraise due to technical reasons (cf. Appendix): The solar cycle may have been identified as a combination of two SRAD modes (recall Table 5.2) since MP-FM is not prepared for two simultaneous frequency modulations. That FM is subject here to further technical restrictions, may be relaxed in a second-generation study. A problem that concerns the signal space dimension due to higher-order nonlinearity, however, is more difficult to handle.

All-India rainfall and IWM retreat (AIR-S, NEMR; Table 5.8, Fig. 5.15) also show the signs of higher-order modulations: AIR-S #3,4,6,7,8 form a web of splitting, joining and drifting modes which reflect a complex situation that the present MP-FM does not appear to cope with in sparsest approximation (Fig. 5.15, left panel). The disturbed NEMR spectrogram (right panel) may signify FM drift, i.e. higher order FM as well, carried by modes #2,1,10 (in this sequence; cf. also Fig. 5.12, right panel), of which the latter one mirrors NEMR #1 in FM quadrature, with only slightly differing modulation depths. The accompanying change of carrier frequencies lately falls into the prominent one of the leading MOSK triplet. This

Table 5.8 MP-FM structure books of All-India rainfall (AIR-S; in *mm*), and monsoon retreat dates (MRAP and NEMR); anomaly modes $\#\langle k \rangle$, signal energy as captured by #1–5/#1–10, and periods of analysis[a]

k	α_k	s_k	u_k	f_k	ϕ_k	$\widetilde{f_k}$	β_k	$\widetilde{\phi_k}$
AIR-S (63.0 %/87.0 % signal energy), 1870–1992								
1	374.795	128	86	0.38555	−1.869	0.012049	3.32	2.945
2	336.587	128	65	0.08839	2.738	0.006291	9.55	−1.767
3	296.894	256	18	0.26107	1.434	0.010580	18.90	2.356
4	269.674	64	34	0.26107	−1.444	0.017039	7.63	−0.785
5	268.657	128	46	0.28470	0.762	0.008897	23.60	0.589
6	253.651	64	95	0.31046	0.165	0.027441	5.47	−1.374
7	203.727	32	51	0.21953	−1.698	0.021160	6.20	2.160
8	183.694	64	95	0.36921	−1.921	0.019404	6.18	0.982
...								
11	132.372	128	54	0.01013	−2.311	0.001953	1.11	0.000
MRAP (97.1 %/99.6 % signal energy), 1952–1990								
1	26.346	64	19	0.29730	0.604	0.028656	4.89	2.749
2	23.238	32	13	0.12500	−0.090	0.010580	6.21	2.749
3	17.743	32	25	0.36921	−1.773	0.038808	3.35	−2.356
4	9.012	16	25	0.32421	0.542	0.037163	4.57	1.374
5	6.267	128	15	0.32421	1.759	0.023075	4.77	−2.356
NEMR (69.3 %/92.6 % signal energy), 1901–1990								
1	63.891	32	47	0.29730	−2.383	0.035587	4.22	2.553
2	52.733	32	21	0.27263	−0.927	0.015625	13.44	−2.749
3	43.878	1024	8	0.04819	2.110	0.003285	7.71	−0.785
4	40.245	128	33	0.32421	−1.321	0.020263	8.39	2.356
5	36.508	256	53	0.23940	2.124	0.017039	9.55	−2.945
...								
7	31.540	256	26	0.28470	−0.777	0.010132	19.74	−2.945
10	22.449	64	70	0.28470	1.262	0.035587	3.93	0.196

[a] AIR-S #11 is referred to in Sect. 5.6.1

might indicate completion of a dynamic regime transition, which both for sparse approximation and the present MP-FM version was most challenging.

The terrestrial water cycle, as represented by the monsoon systems here, exhibits most active dynamics across the data set. Its potential (pre)chaotic organization at planetary scale [19] would offer a sea of UPOs on Earth which may be stabilized by even weak external control. “Collision” of solar and terrestrial UPOs might have produced the mid-century recurrence oscillations and their signature notably in the MOSK series.

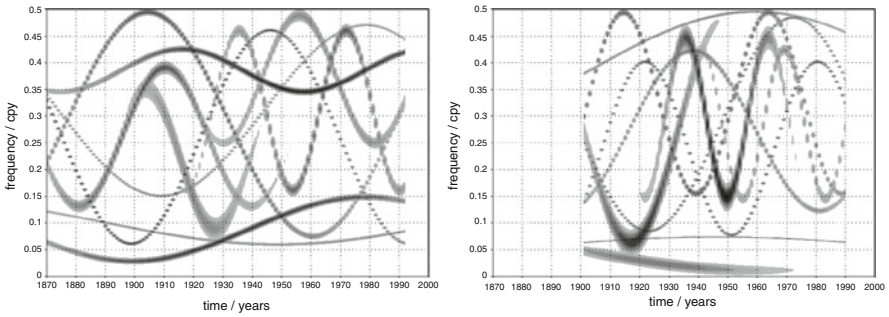

Fig. 5.15 MP-FM spectrograms (leading ten anomaly modes each) of the AIR-S (*left panel*, 1870–1992) and NEMR series (*right panel*, 1901–1990)

5.5 Global Cross-Connections: Dynamic Regimes

Though one might not be inclined to lend too much credit to the short series of ISM retreat over Andhra Pradesh (MRAP) and its decomposition (Fig. 5.16, left panel; Table 5.8), just these data may bear the most direct real-world signature of topology-conditioned interannual climate variability rooted in the atmospheric hydrologic cycle. As found in the GCM study [19], roughly three retreat categories of the boreal summer monsoon may exist, which besides different circulation regimes also bear variable retreat dates ("breathing" seasonal cycle). The MRAP data period centers around the early 1970s, and MRAP #1 shows a deep TF fluctuation shadowed by MRAP #3, with their common turning points just at the height of the "cool NH" excursion (cf. Fig. 5.6). Systematic phase effects in the boreal summer-to-autumn transition (the variable MRAP dates) thus accompanied a marked excursion of the climate system. Note that both MRAP #1 and NEMR #1 fluctuate around a carrier that appears almost as frequently as that of the leading MOSK triplet, notably in the water cycle as well. FM connections to other leading monsoon modes (NEMO and MONK #1, AIR-S #3) also exist for MRAP #2, the low-frequency TF "scar" in Fig. 5.16 (left panel).

Before turning to the right panel of the figure, notice almost perfectly synchronized interdomain motions in Fig. 5.17 of leading insolation (SRAD #1; left panel) and thermal modes of the system (SAT & SST #2; right panel) in the time domain, with leading modes of insolation, temperatures, dynamic indices and the hydrologic cycle in the frequency domain. Whereas the left panel may bear another substantiation of the reality of control by relatively weak irradiance variations of the system's free oscillators, the right panel displays a large "swarm" across the whole climate system of interdomain companions to the important rank #2 multidecadal thermal modes. This may be taken as a clear sign of a regime character of present-day climate dynamics, including modes of the water cycle as integral parts.

SAT and SST #1 do not show likewise broad and perfect global-scale interdomain synchronies, but there is an important exception. MOSK #7 (the "scar" in Fig. 5.13,

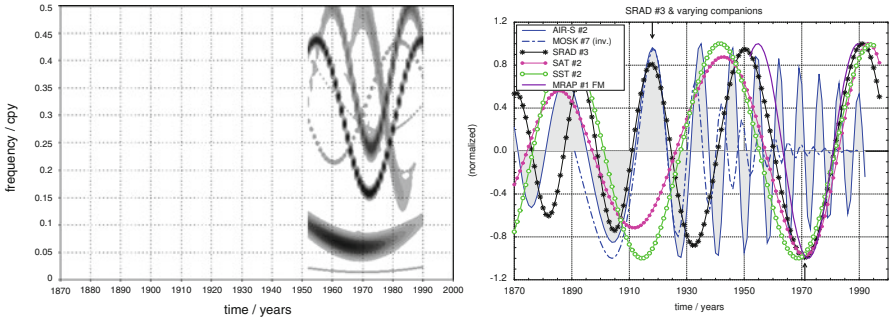

Fig. 5.16 MP-FM spectrogram (leading ten anomaly modes) of the MRAP series (*left panel*, 1952–1990) and episodic time domain synchronies (*right panel*) of SRAD #3, in company with SAT & SST #2 and monsoonal components to shape the exceptional episodes around 1918 and since the 1970s (*arrows* at the upper and lower margins of figure)

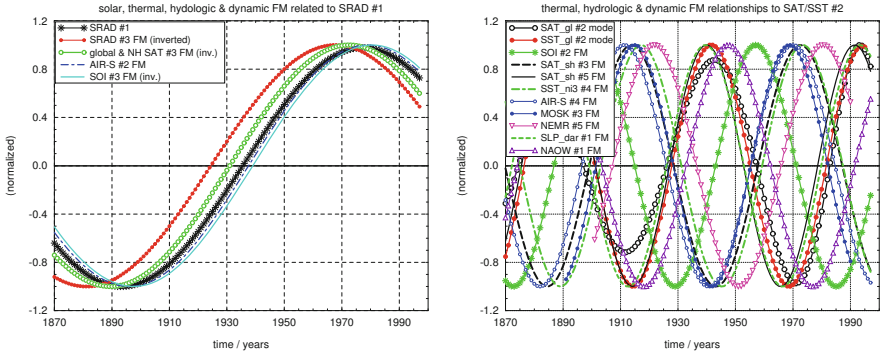

Fig. 5.17 MP-FM based synthesis [15, 17] showing normalized interdomain evolutions; *left panel*: SRAD #1 vs. FM in AIR-S #2 and (inverted) in modes #3 of SRAD itself, global & NH SAT, SOI, as well as in NAOW #4; *right panel*: global SAT & SST #2 vs. FM in the monsoons, ENSO, NAOW and SH SAT

left panel) is a fading decadal mode that evolves in time domain synchrony with AIR-S #2 and SRAD #3 (which are interdomain companions of SRAD #1; Fig. 5.17, left panel) since the turn of the nineteenth century until the mid-1920s [15] (Fig. 5.16, right panel). Decadal MOSK modes #7,10 with identical modulation frequency thereby form the earliest MOSK on record, 1918 (MOSK #10 not shown). SOI #3, and global & NH SAT #3 are interdomain companions of SRAD #1 as well (Fig. 5.17, left panel). FM of MOSK #7, in contrast, fits the time domain evolution of global SAT #1 (Sect. 5.6.1, Fig. 5.23) until it fades away during the 1960s. That is, there was an interdomain link via the water cycle between centennial insolation and thermal modes which has been lost only in the 1960s.

A replacement connection emerges in the 1970s, however, now at multidecadal scale: Time domain synchrony with SRAD #3 and interdomain company by MRAP #1 FM characterize the second warming episode of the study period (Fig. 5.16,

right panel). The solid background regime of this episode displayed in Fig. 5.17 (right panel) includes: NAOW & Darwin SLP #1, SOI #2, MOSK & SH SAT #3, Niño 3 & AIR-S #4, NEMR & SH SAT #5. Whether or not the SRAD #3 synchronization also contributed to growing signal energy in global and NH SAT #2, awaits clarification. Though multidecadal signal energy grows strongest in NH SAT #2, there is no corresponding European SAT signature (Sect. 5.6.1). The centennial-scale multidecadal climate regime hints at a prominent role of the Tropics/subtropics in either warming shove of the twentieth century indeed.

5.6 European "Vertical" Climate Signal Tracing

Tropic/subtropical impacts on European climate and weather might be mediated via teleconnections like the Pacific–North American (PNA) pattern with its eastward extension to the North Atlantic, and a Mediterranean link appears to exist to the South Asian monsoon in boreal summer (e.g., [85]). European floods increased attention to such links (e.g., [26, 77]). Robust connections have been found for paleoclimatic timescales (e.g., [89]), but mechanisms may differ from those of present-day. Recently, quasi-resonant states of circumglobal planetary waves have been detected that may be blamed for extreme hydrologic events in northern midlatitudes [28]. Tropic/subtropical links of these patterns may exist but have apparently not yet been addressed. Here a general low-latitude perspective is adopted with a view on European climate and weather regimes and their hydrologic signatures.

5.6.1 Central European Climate and Weather Regimes

The marked reorganization of NH circulation in concert with the exceptional period of early MOSK around 1960 [64] (Sect. 5.4.4) provides another test for both existence of such a cross-connection in the data and the quality of MP-FM based data modelling. Figure 5.18 (left panel) shows a localized NAOW signal (#12, cf. Table 5.6) which precedes and accompanies the "bump" of MOSK #4. It modifies the growing (bi)decadal NAOW #2 mode, just toward perfect in-phase evolution with MOSK #4 at its foreflank—thereby directly shaping its upcoming multidecadal pace that is about to synchronize with SRAD #3. Combined NAOW #2+12 continues to match the MOSK #4 envelope until the signal terminates. Altogether, this substantiates reality of monsoon/NAO phase interactions and a potential solar influence; recall also the link to sunspot cycle #19 (Sect. 5.4.4, Fig. 5.14).

With positive (negative) NAO index, cyclone tracks are shifted northward (southward), thus reducing (enhancing) precipitation over central and southern Europe [61]. Figure 5.19 (left panel) and Table 5.9 show SLP modal structures at

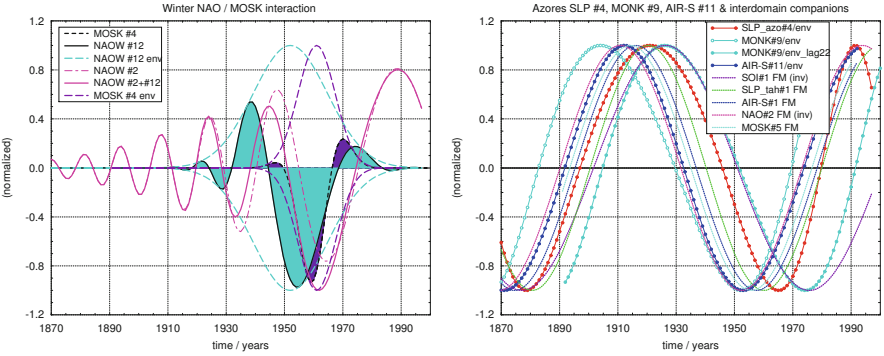

Fig. 5.18 MP-FM based synthesis, *left panel*: NAOW (#2 & #12) coincidence with the MOSK #4 event; *right panel*: slow Azores SLP (#4), MONK (#9), AIR-S (#11) modes and FM companions (Azores SLP, Tahiti SLP, SOI, AIR-S #1, NAO #2, MOSK #5)

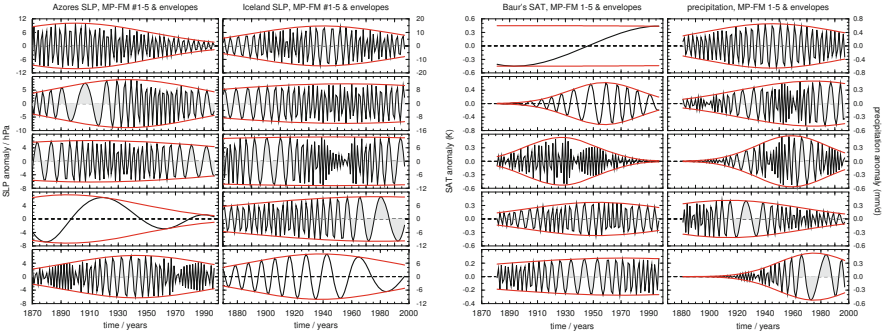

Fig. 5.19 MP-FM analysis (leading five anomaly modes each); *left panel*: annual mean Azores and Iceland SLP (1870–1997, in hPa); *right panel*: Baur's (1881–1997) central European SAT, in K, and German precipitation, in mm/d

the NAO centers of action. Azores SLP #1 and annual NAO #2 are connected with AIR-S #1 via common slow FM. All three are interdomain companions of the slow mode AIR-S #11 (Fig. 5.18, right panel). To further decode functional shapes of the slow modes NAO #5, Azores SLP #4 and MONK #9, note that the latter two show identical bidecadal carrier periods and modulation depths δf, as well as closely neighbouring multicentennial FM. NOA #5, in turn, shares its modulation index β with MONK #9, and both carrier and modulation frequencies of the two relate to one another by a factor of $\sqrt{2}$. Recall also that NAO #5 has NAO #1 and Niño-3 #3 as interdomain companions (Fig. 5.9, right panel).

Slow evolutions in the atmospheric part of the global water cycle thus might exert control over one of the NAO centers of action, the Azores High. Iceland SLP adds a carrier triplet at ranks #1,3,6 which shares the common carrier of retreat modes #1 of ISM (MRAP) and IWM (NEMR), and of the SOI triplet (#2,6,9)—a dominating carrier mode within the global climate system. This network further

Table 5.9 MP-FM structure books of annual mean SLP at NAO centers of action (1870–1997, in hPa); anomaly modes #⟨k⟩ and signal energy captured by modes #1–5/#1–10

k	α_k	s_k	u_k	f_k	ϕ_k	$\tilde{f}_k$	β_k	$\widetilde{\phi}_k$
Azores (59.0 %/82.8 % signal energy)								
1	60.772	128	31	0.33856	0.832	0.012049	4.98	−2.945
2	57.383	128	67	0.19278	−1.284	0.009291	16.04	−1.374
3	45.269	256	43	0.22925	0.607	0.008520	16.08	−0.982
4	43.038	128	26	0.04232	−1.068	0.002224	14.71	2.749
5	40.953	128	74	0.32421	0.527	0.011049	15.39	−2.553
Iceland (58.1 %/84.1 % signal energy)								
1	94.907	128	71	0.29730	2.577	0.016317	7.97	2.749
2	86.862	256	84	0.25000	2.117	0.006860	18.95	0.000
3	81.507	512	75	0.29730	3.095	0.010580	18.90	−0.393
4	69.165	256	110	0.17678	−2.478	0.006291	21.72	2.749
5	64.986	128	69	0.06527	2.039	0.005066	8.76	1.571
6	60.743	128	91	0.29730	2.028	0.007812	24.32	−1.178

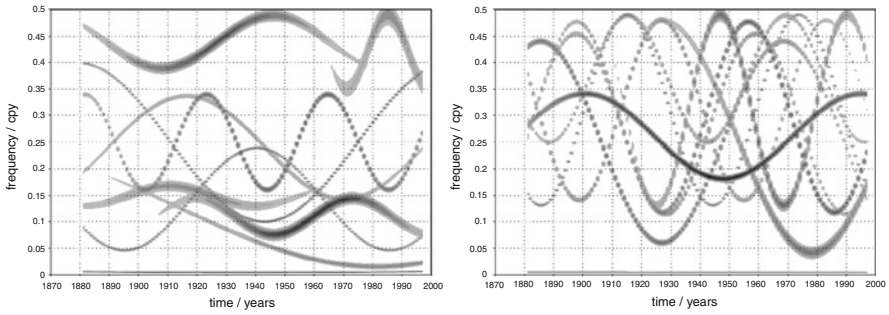

Fig. 5.20 MP-FM spectrograms (leading ten modes each) of annually aggregated Baur's central European SAT (*left panel*) and German precipitation (*right panel*), 1881–1997

extends via common FM of Iceland SLP #3 and leading monsoon modes, which altogether might mark an Arctic Oscillation pathway of monsoon impact on Europe (not shown in detail).

Synoptic systems that accompany circulation types bear typical thermal and precipitation patterns [43]. German precipitation and central European SAT according to Baur [7] (Fig. 5.19, right panel; Table 5.10) thus relate to the temporal succession of weather regimes and its variability and evolution in concert with climate change. There is no central European multidecadal SAT mode, though, that would contribute to global and NH SAT #2 (cf. Sect. 5.5). The same holds for the central England temperature (CET [79]) not discussed here.

Figure 5.20 shows MP-FM spectrograms of Baur's data sets [7]. There are two drifting modulations in the SAT series which the present MP-FM version cannot directly capture, thus selecting two modes each (left panel): Mode #2 has a precursor

Table 5.10 MP-FM structure books of annual mean Baur's central European SAT and German precipitation, 1881–1997; anomaly modes #$\langle k \rangle$ and signal energy captured by modes #1–5/#1–10

k	α_k	s_k	u_k	f_k	ϕ_k	$\tilde{f}_k$	β_k	$\tilde{\phi}_k$
SAT, in K (69.1 %/89.4 % signal energy)								
1	3.546	1024	26	0.02026	0.529	0.001020	15.36	2.945
2	2.932	64	78	0.10977	0.937	0.018581	1.85	−1.767
3	2.469	64	47	0.43906	1.730	0.013139	3.81	−1.571
4	2.306	128	73	0.25000	1.921	0.024097	3.73	−1.767
5	1.919	256	91	0.25000	−0.397	0.007812	19.20	−1.767
...								
8	1.441	64	38	0.14865	0.359	0.017039	1.11	0.785
9	1.437	32	106	0.42045	0.866	0.035587	1.97	0.196
precipitation, in mm/d (68.8 %/89.0 % signal energy)								
1	4.158	128	65	0.26107	−1.925	0.010580	7.56	2.945
2	2.889	128	93	0.29730	0.265	0.017039	10.56	1.767
3	2.669	64	79	0.31046	2.177	0.023075	7.80	1.767
4	2.512	128	34	0.25000	−1.265	0.012049	15.77	2.160
5	2.328	64	95	0.26107	−0.604	0.009702	22.68	2.945
...								
7	−1.797	512	14	0.00552	−0.010	0.001112	0.72	2.356

(#8) with smaller modulation depth and higher carrier frequency, whereas mode #3 is followed by a signal (#9) with substantially shorter FM period. These thermal transitions occur just around 1930 and 1970 again. There is also a bifurcation around 1930 of deeply fluctuating modes in Baur's precipitation (right panel). A variety of further links and modal networks exists, notably of this series. Together with Iceland SLP #3 and GWL WA #2, FM of its leading mode joins a group including leading monsoon onset modes (MONK, NEMO #1) and AIR-S #3. Baur's precipitation #2 joins another prominent group of carriers: the leading monsoon retreat modes (MRAP, NEMR #1) and the SOI triplet (#2,6,9)—plus even a quadruple (#3,4,5,10) of GWL Northwesterly Cyclonic (NWZ; not shown).[2]

Central European weather regimes as represented by four of the leading GWLn here exhibit MP-FM modal structures as shown in Figs. 5.21 and 5.22. The eye-catching behaviour of HM #1 and BM #3 marks a centennial exchange of the dominating patterns (cf. e.g. [43]) of high pressure conditions over the region. The functional shape of (inverted) HM #1 settles between that of global SAT #1 and SST #1; BM #3 is more stretched. The multidecadal mode BM #4 is an interdomain companion of HM #1, and thus an approximate one as well of these two major global warming modes.

[2]To save space, MP-FM structure books are no longer displayed heretoforth; for frequencies f, $\tilde{f}$ consult the summarizing tables in Sect. 5.7. A complete set of structure books of the study may be obtained from the author on request.

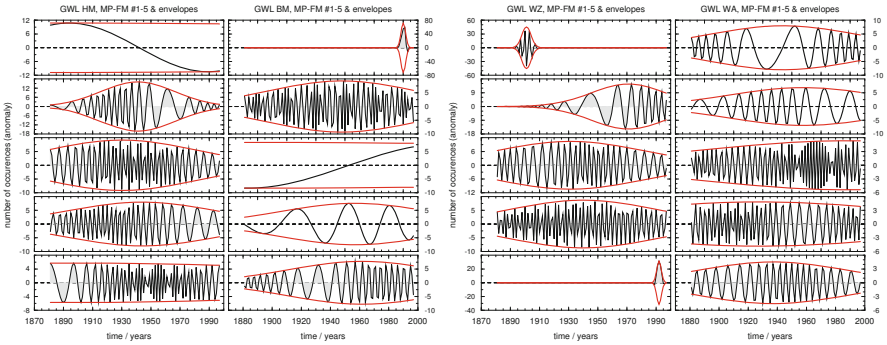

Fig. 5.21 MP-FM analysis (leading five anomaly modes each): annual frequencies of GWL occurrence over central Europe, 1881–1997; *left panel*: High Middle Europe (HM) and Bridge Middle Europe (BM); *right panel*: Westerly Cyclonic (WZ) and Anticyclonic (WA)

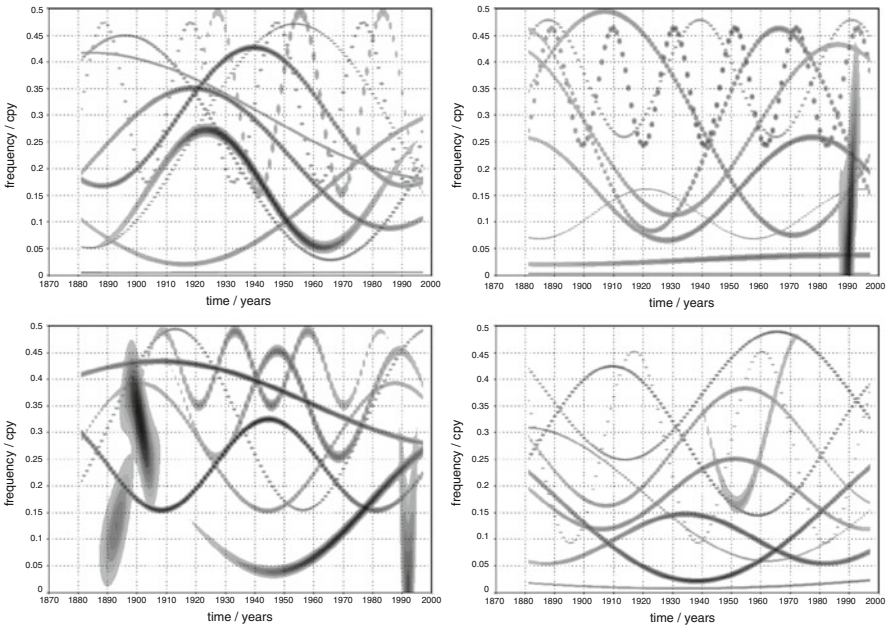

Fig. 5.22 MP-FM spectrograms (leading ten anomaly modes each) of annual GWL occurrences, 1881–1997; *top*: HM (*left*) and BM (*right*); *bottom*: WZ (*left*) and WA (*right*)

At neighbouring carriers, HM #5,6 exhibit identical modulation frequencies and the same modulation depth δf. These modes are arranged in the TF plane so as to support, by their FM phase lags, emergence of HM #2 as a shadowing, apparently resonant enhancement of the signal energy distribution in the TF plane around HM #5,6 until the 1960s (Fig. 5.22, top left panel). HM #6 shares its carrier frequency with the fading mode MONK #4, at even identical modulation frequency and index

β, but different FM phase. During its period of pronounced existence, HM #2 FM fits FM of Azores SLP #1 as well, and thus of AIR-S #1 and NAO #2 in their interdomain relationships with Azores SLP #4, NAO #5, and MONK #9.

For the BM #1 event around 1990 (Fig. 5.22, top right panel) there is no precursor or companion, but an apparent response in WZ #5 (bottom left panel). Given its maximum in 1991, Mt. Pinatubo's eruption in June could have played a role, but recall also the 1991 turning point in the slow motions of global SAT vs. SRAD (Fig. 5.7, right panel). Other exceptional situations in 1991 include Kuwaiti oil well fires and violent East Asian monsoon dynamics [20]. An apparent monsoon response (or common response to solar cycle #19) is also found in a WZ "bump" at rank #14 (not shown) which almost perfectly fits the MOSK #4 signal. The leading WZ patch (#1) follows a common event in WZ #7 and global SAT #12.

In contrast to the patchy WZ modal structure, GWL WA shows a more smooth one. At rank #4 a nearly persistent mode coincides in both carrier and modulation frequencies with NEMR #7, and thus with the leading MOSK carrier triplet (#1–3) at the one hand, and with FM in SOI #1 at the other one. Coincidence with NEMR #7 even extends to scale and translation (lag 2), but not to the phase constant of modulation.

Finally, Fig. 5.23 (left panel) shows clear time domain synchrony over the whole record of the basic modes of global, hemispheric and European centennial warming with the leading slow mode (#7) of Baur's precipitation. Note that this is the only direct signature found as yet of the system's centennial thermal evolutions which serves the traditional view of dynamic correspondence, namely time domain coevolution. Interdomain companions include BM #4, WZ #4—and MOSK #7,10 as noticed in Sect. 5.5.

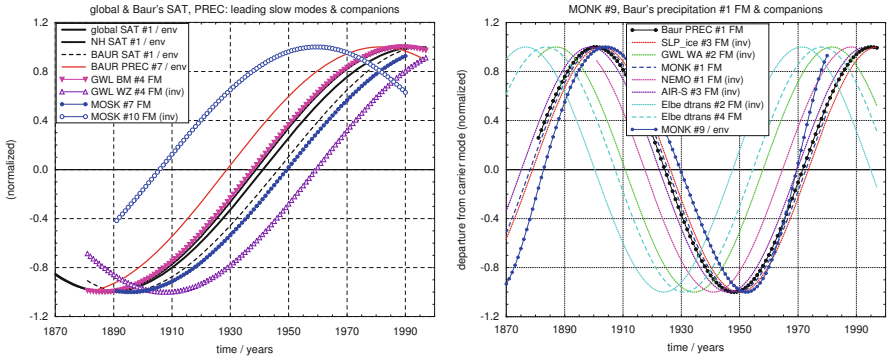

Fig. 5.23 MP-FM synthesis global–regional, *left panel*: normalized global SAT #1 in parallel to hemispheric and central European SAT #1, *Baur*'s German precipitation (#7), plus interdomain companions (GWL BM and WZ #4, MOSK #7,10); *right panel*: normalized MONK #9 and another group of approximate interdomain companions (cf. Fig. 5.18, right panel), including Baur's precipitation #1, GWL WA #2, Iceland SLP #3, MONK and NEMO #1, AIR-S #3, as well as MP-FM modes #2,4 of the driven-transient FSD component of the Elbe river (Dresden gauge; cf. Sect. 5.6.2); centered analyses

Further "vertical" tracing (Sect. 5.6.2) is motivated in the right panel of Fig. 5.23 which shows European and global climate modes as interdomain companions of the slow mode MONK #9 again (cf. also Fig. 5.18, right panel), in concert with modulations found in two MP-FM modes of the driven-transient FSD component of the Elbe mainstream near Dresden. Even SOI #1 FM and its "relatives" (NEMO #3 FM, GWL WA #4 and BM #5, NEMR #7) closely neighbour the modulations shown, and either MP-FM mode of the runoff component bears the rare coincidence in both carrier and modulation frequency with two leading rainfall modes: Baur's German precipitation #1 and AIR-S #3. It makes sense indeed to look further downward.

5.6.2 *Runoff of the Elbe Mainstream Near Dresden*

As with the climate and weather time series, total runoff and its FSD components are treated as complex composites fed by multiple, distributed sources. Figure 5.24 displays the observed daily runoff of the Elbe river near Dresden (left panel). FSD has been applied to overlapping 11-year segments, and the resulting component structures have temporally been aggregated to yield the respective annual time series for the period 1870–1997 (right panel). The combined FSD/MP-FM analysis (Fig. 5.25) of this long daily record has been motivated by a first hint obtained in [22] at possible selective responses in conceptual FSD components to weather and climate variability.

MP-FM modal structures of total runoff $g(t)$ and its fast, driven transient, and slow FSD components ($g_f(t)$, $g_{td}(t)$, $g_s(t)$) as displayed in the figure show close relationships between total and slow runoff in their respective modes #1–4. The highly persistent mode #5 of total flow, in contrast, appears to run into a high-

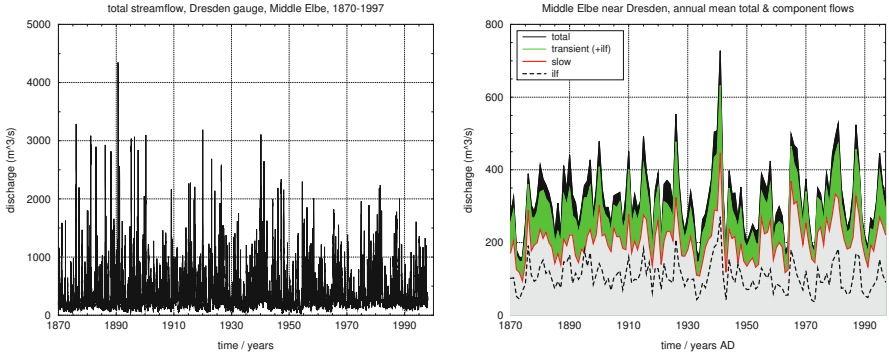

Fig. 5.24 Dresden gauge of the Middle Elbe river mainstream, runoff im m^3/s; daily total flow ($g(t)$, *left panel*) and its annually aggregated FSD component structure (*right panel*): fast (g_f, *black*), driven-transient (g_{td}, *green*), slow (g_s, *red*) and ilf (g_ℓ, *dashed*)

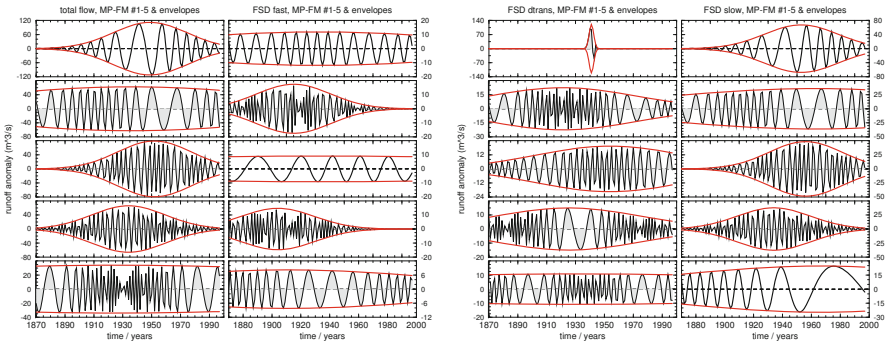

Fig. 5.25 Dresden gauge of the Middle Elbe, MP-FM analysis (leading five anomaly modes each) of annual runoff and its FSD components (1870–1997, in m^3/s); *left panel*: total flow and fast component (g, g_f); *right*: driven transient and slow components (g_{td}, g_s)

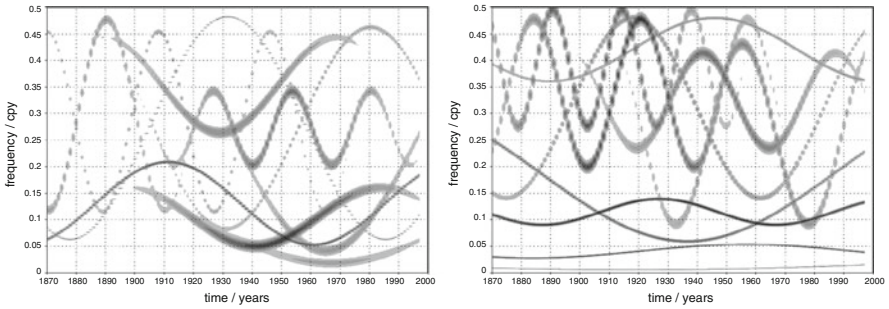

Fig. 5.26 Dresden gauge, MP-FM spectrograms (leading ten anomaly modes each) of annual runoff (1870–1997): total flow (g, *left panel*) and its fast FSD component (g_f, *right panel*)

frequency singularity (modelled as part of a slow, deep harmonic FM) just during the exceptional climate period around 1930. A similar feature in modes #2,4 of the fast component centers around 1918, the year of earliest MOSK on record. MP-FM spectrograms of total runoff and its fast FSD component are given in Fig. 5.26.

During the first half of the record, the fast component, which should comprise any singular contents of total runoff, naturally occupies the high-frequency range of the spectrogram (Fig. 5.26, right panel). Increasing water management since the 1930s at the Czech part of the Elbe mainstream may be blamed for reduced high-frequency activity and should also result in modifications to climatic signatures in the fast and driven-transient components. The solitary rank #1 peak of the latter (the localized scar across the whole frequency range of the spectrogram; Fig. 5.27, left panel) signifies a severe hydrologic event in 1941–1942 (cf. right panel in daily resolution) that coincides with a global climatic anomaly which included a marked El Niño [46], three of the coldest European surface winters of the twentieth century, and midwinter stratospheric warmings in conjunction with an extreme ozone excess anomaly over the continent [10]. Recall also entrance in the early 1940s of the global

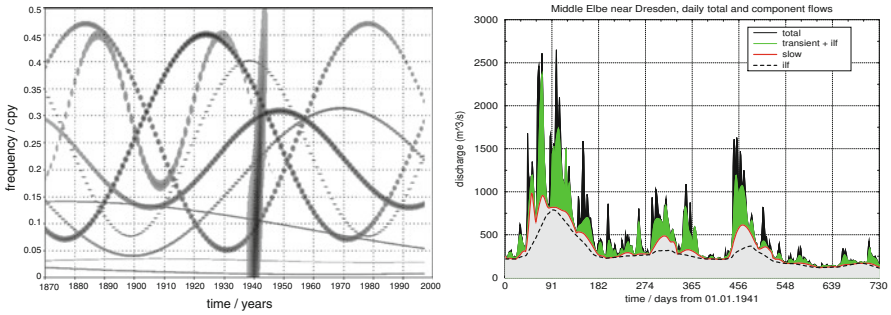

Fig. 5.27 Dresden gauge, MP-FM spectrogram (leading ten anomaly modes) of the annual mean driven-transient FSD component (g_{td}, 1870–1997; *left panel*) and the 1941–42 daily FSD component structure (*right panel*; as in Fig. 5.24, right panel)

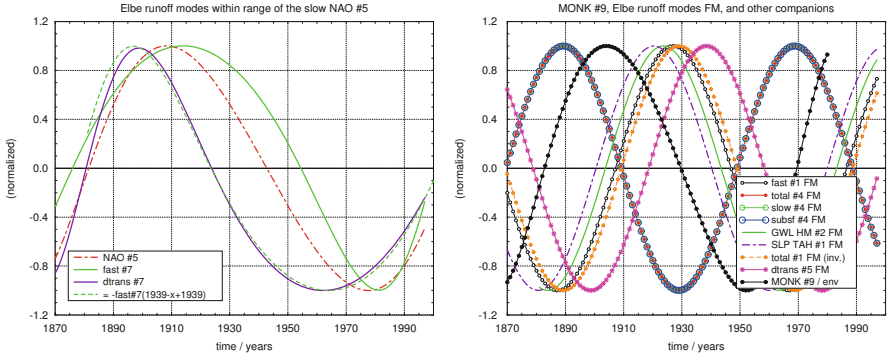

Fig. 5.28 Dresden gauge, 1870–1997; *left panel*: leading slow anomaly MP-FM modes (at rank #7 each) of FSD components fast (g_f) and driven-transient (g_{td}) in mirror antisymmetry around 1939, flanking the slow NAO mode #5; *right panel*: runoff, GWL and SLP interdomain companions of the slow modes MONK #9 (& AIR-S #11); cf. also Fig. 5.23

climate system into its second ("UPO shaped"?) period of thermal oscillations (turning points in Figs. 5.6 and 5.7).

Fast and driven-transient FSD components are complementary in that the former comprises all data contents not grasped by a smooth (lower envelope) approximation, whereas the latter results from an iterate of just this envelope operator. Leading slow MP-FM modes of both, at rank #7 in either case, exhibit mirror (anti-)symmetry across the data period, with its reflection point 1939 close to the 1941–1942 runoff anomaly (Fig. 5.28, left panel). Anti-symmetric synchrony in slow evolutions of these two components, the dominant singular and the regular but (statistically) self-similar one (operator iterate), either might have to do with crossing the basin boundary of the attractor that is going to capture the climate trajectory, may hint at some unknown fundamental interplay at the regular/singular borderline of runoff, may reflect a selective impact of the NAO—or may have

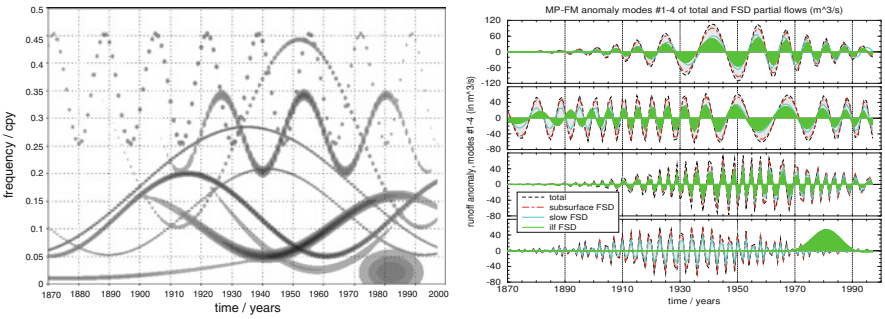

Fig. 5.29 Dresden gauge, 1870–1997; *left panel*: MP-FM spectrogram (leading ten anomaly modes) of the annual ilf component g_ℓ; *right panel*: MP-FM modes #1–4 (*top to bottom*) of total runoff g and its FSD components slow g_s, ilf g_ℓ and subsurface $(g_\ell + g_t)$, respectively

appeared just by chance. The first three cases would deserve scrutiny, though this goes with the risk of falling into speculation. The fact is just noticed here.

Whereas hidden time domain synchronies like this are difficult to carve out, interdomain companions galore are found via structure book screening, notably again with respect to the slow modes MONK #9 and AIR-S #11 (Fig. 5.28, right panel; cf. also Fig. 5.23, right panel). Identical FM of total, slow and subsurface (ilf+transient) MP-FM modes #4 reflects the dominance of slow runoff in the mainstream, as expected. Figure 5.29 (left panel) shows the ilf spectrogram, whereas the right panel displays the leading four MP-FM modes of total, slow, ilf and subsurface runoff. Their only qualitative distinction appears as an isolated "bump" of ilf #4, centered around 1982/1983, the years of an extreme El Niño event. The slow FSD component, in contrast, integrates this hydrologic signature into its deeply modulating mode #5 (Fig. 5.25, rightmost column).

The bidecadal mode #3 of the fast component (Fig. 5.25, second column) is shown in Fig. 5.30 (left panel) to enter for half a century the time domain coalition of global SAT #4 and SST #5 which is accompanied in the frequency domain by GWL BM #2. It leaves this global connection together with the central European interdomain GWL companion in the 1960s—just when the leading slow monsoonal mode MOSK #7 is fading, thus dissolving the global water cycle from its dynamic link to centennial warming (Sect. 5.5).

Finally, another rare coincidence of identical carrier and modulation frequencies as well as modulation indices β (and thus also depths δf in this case) is shown in the time domain evolution in Fig. 5.30 (right panel): Baur's precipitation mode #5, which coincides in these parameters with the largely identical runoff modes subsurface #6 and slow #7, grows up since the 1920s and episodically matches them rather well (perfect matching would require identical phase constants). Localized modes NH SAT #10 and GWL WZ #7 show up further episodic time domain synchrony with these latter two modes at the beginning of the record. There is also a couple of frequency domain companions (not shown) to the precipitation mode,

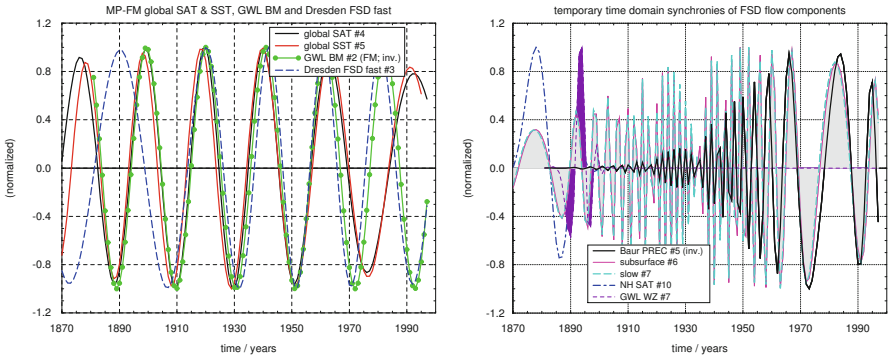

Fig. 5.30 Dresden gauge, normalized time domain evolutions; *left panel*: MP-FM anomaly mode #3 of the fast FSD component, together with global SAT #4 and SST #5, and FM of GWL BM #2; *right panel*: subsurface #6 and slow #7 modes in episodic synchrony with *Baur*'s precipitation mode #5 and localized modes NH SAT #10, GWL WZ #7

including GWL NWZ #1, WA & HM #3, and FSD fast #3 again of which the time domain behaviour has been displayed in the left panel.

Breaking news are not apparent from the present exploratory "vertical" signal tracing down to the river basin scale, but incorporation of this scale into a "small world" network of weakly coupled MP-FM modes has been demonstrated. Borne in prior FSD application, this fact supports the idea of selective hydrologic signatures of regionally external signals. Central Europe is not a core region of the global water cycle, but slow-mode links to Asian summer monsoon dynamics have been identified. Recall that this exploratory study did not focus on extreme events. That the combined FSD/MP-FM procedure is sufficiently robust has been shown in a number of cases. The suspicion has also been substantiated that transient (sub)components may become predicated targets and carriers of selective hydrologic response [22]—a certainly convincing example is the driven-transient runoff response to the leading precipitation mode over Germany (Fig. 5.23, right panel). Lately, it became plausible that FSD is reasonably applied not only to headwater catchments (which use has been made of in its development [21, 22]).

5.7 Summary and Discussion

The present second part of a conceptual modelling and observational data study into the global climate system's "geometry of behaviour" [1] addressed synchronous motions at planetary scale across the instrumental record (1870–1997) and traced their signatures down to the Elbe river basin via the European climatic and synoptic scene. Guided by the GCM study outlined in [19], the search for synchronies (of any kind) aims to uncover hints at potential low-dimensional contributions to climate dynamics. In order to behave low-dimensionally, a high-dimensional

dynamic system like the global climate must undergo substantial synchronizations which to unveil improves the knowledge of its dynamical status and potential evolution.

Data analyses should not prejudice by the choice of method any notion of debate. Accordingly, to provide adequate targets for a broad range of signal types, the dictionary of analyzing signals (Gaussian logons that allow for deep frequency modulation, FM), used here in the sense of best fit, is highly overcomplete, not necessarily orthogonal, and applied in superresolution. It comprises harmonic bases of both Fourier and Wavelet Transforms. Univariate sparse approximations of customary climate time series have been presented first, using a Matching Pursuit approach [73]. Tables 5.11 and 5.12 summarize carrier and modulation frequencies, respectively, of the leading ten MP-FM modes each of the 20 time series analyzed (cf. also Table 5.18).

A multivariate perspective, dismissed in the analysis stage, is provided by subsequent synthesis. "Structure books" of the set of signal parameters provide quantitative support, though visual inspection cannot be dispensed with. A network of leading MP-FM modes has been identified at global scale. Based on this approximation of observed global climate dynamics, European climate and weather data (Tables 5.13 and 5.14) and basin scale hydrology as exemplified by runoff of the Elbe mainstream near Dresden (Tables 5.15 and 5.16) have been investigated for climatic signatures. In contrast to the Indian monsoon region, which has early been perceived as a source, or "nodal," region of global climate dynamics (e.g., [78]), European climate has been viewed here as a non-nodal region, a notion that is largely confirmed by the results.

Six types of synchrony or correspondence may be found in the climate system's motion: (1) phase coherence in the time domain, (2) phase–frequency ("interdomain") synchrony, (3) signal envelope synchrony, (4) quadrature and other phase relationships, (5) rational frequency relationships, and (6) general concurrence in signal parameters (pairs, triplets, quadruples etc. of modes which share certain parameters or their combinations). Phase coherence makes up synchronized motion in the time domain and customary statistical correlation in one. It occurs only temporarily here in most cases, but displays remarkable signals, notably in monsoon–NAO relationships and in changing synchronies to insolation mode SRAD #3. Interdomain synchrony, i.e. frequency drift of one oscillator in parallel to the phase evolution of another one here (maybe lagged), is the dominating type of synchronous motion found—though not normally recognized when applying traditional tools of signal analysis. This sort of synchrony occurs both internally (between different MP-FM modes of one and the same time series, like SRAD #1/#3) and as coevolution between modes of different time series (e.g., SRAD #1 and its centennial companions). Envelope synchrony may uncover kinship between signals that exist in distinct ranges of the TF plane, like those related to the MOSK mode #4. Coincidence in signal parameters scale s and translation u means perfect envelope synchrony, but there are physically justified lags in general.

Though arbitrary phase lags may occur in purely empirical analyses, notably in the frequency domain, quadrature relationships might hint at a specific data type, the

Table 5.11 Distribution of carrier frequency occurrences among the leading ten MP-FM modes each of 20 annual time series (All-India rainfall after [81], AIR-P, not discussed)[a]

#	SRAD		SSN		Be10		glob. SAT		NH SAT		SH SAT		glob. SST		Niño 3		SLP Tah		SLP Dar		#
1	−3	●	−0.5	⊕	−2.5	⋆	−4	⊕	−3.5	△	−0.5	△	−4	⊗	1	⊗	1.5	⋆	2	△	1
2	0.5	⊙	−1.5	⊕	2	●	−1	⋆	−0.5	△	0	⊘	−1	●	2	∘	1.5	⊙	1.5	⊗	2
3	−0.5	⊙	0.5	⋆	−0.5	⊗	1	⊕	1	⊕	2	⊙	1.5	⊙	1	⊕	2.5	●	1	⊗	3
4	0.5	⊕	1.5	⋆	1	●	−0.5	⊙	1.5	●	1.5	△	2	⊙	1.5	⊕	2	⋆	−1	⊗	4
5	0.5	⊘	0	●	0.5	●	2	●	0.5	⊗	2	△	−1	∘	2	⊕	1	⋆	2.5	∘	5
6	1	⊕	2	⊙	1.5	⊙	2.5	⊙	2.5	△	−1.5	⊗	1.5	⋆	1	⊙	2.5	∘	2.5	⊘	6
7	−0.5	∘	1	⊙	1	∘	2	∘	2	⊗	2	△	2	⊕	1.5	∘	1	∘	2	⊘	7
8	1	⊗	1	⊘	1	⋆	1	⊕	2	⊘	1	△	2	△	2.5	∘	3	△	2	∘	8
9	0.5	∘	2	⊗	2	∘	3	⊙	2.5	⊙	2	∘	2	△	1.5	⊙	2	⊙	1	△	9
10	1.5	⊙	1.5	⊘	1.5	△	2	●	1	⋆	2.5	●	2.5	●	2	⊕	−0.5	⋆	1.5	⊗	10
#	SOI		MOSK		MONK		MRAP		NEMO		NEMR		AIR-S		AIR-P		NAO		NAOW		#
1	2	⊙	2.5	●	2.5	⊙	2.5	△	2	⊕	2.5	△	3	⊙	3	⊙	1	⋆	2	●	1
2	2.5	△	2.5	●	2	⊗	1	⊘	2.5	∘	2.5	⊙	0.5	⊘	2	⊘	1.5	⊗	−0.5	⋆	2
3	1.5	⋆	2.5	●	2.5	⊙	2	⊗	1	⋆	0	⊙	1.5	⊗	1.5	⋆	1.5	⊕	3	△	3
4	2.5	●	−1	∘	2	∘	2	⊕	0	⊗	2	⊕	1.5	⊗	1.5	⊙	2	⋆	0.5	⋆	4
5	2	⊕	2	⋆	2.5	●	2	⊕	2.5	⊘	2	∘	2.5	●	3	△	−1	∘	3	⊙	5
6	2.5	△	2	⊕	1.5	△	0.5	⊕	2.5	●	0.5	⊘	2	⋆	−1	⋆	1	△	2.5	●	6
7	1.5	⊘	1	⋆	2.5	⊙	2	⊗	2	∘	2.5	●	1.5	⋆	2	⊗	2.5	⊘	1	⋆	7
8	2	⊘	2.5	△	1.5	⊗	2.5	△	1	⋆	2.5	⊙	2	⊗	1.5	⊗	2.5	⊕	2	⊗	8
9	2.5	△	2.5	∘	−0.5	∘	1.5	⊕	0.5	⊗	3	⊙	1	●	2.5	△	0	⊘	0.5	∘	9
10	1.5	⊗	1	∘	1.5	△	2.5	∘	2.5	△	2.5	●	2	⋆	2.5	●	1.5	⊘	1	∘	10

[a] Symbols mark eight families of carrier modes within the framework of a basically dyadic analysis (cf. Table 5.18); [n ∗] means: [reference frequency of the ∗ family, multiplied by 2^n]. These reference carrier frequencies (f_c; in cycles per year, *cpy*) are as follows: ⊙ ≙ 0.04819, ● ≙ 0.05033, △ ≙ 0.05256, ∘ ≙ 0.05985, ⊘ ≙ 0.06250, ⋆ ≙ 0.07762, ⊕ ≙ 0.08105, ⊗ ≙ 0.09230

Table 5.12 As in Table 5.11, but for modulation frequencies[a]

#	SRAD		SSN		Be10		glob. SAT		NH SAT		SH SAT		glob. SST		Niño 3		SLP Tah		SLP Dar		#
1	−2	⊙	−1.5	△	−2.5	⋆	−2	●	−3	⊗	−2	●	−2	●	−1	⊗	1.5	●	2	△	1
2	−2	⋆	−2.5	⋆	0.5	⊙	−1.5	⊕	−1.5	⊕	−1.5	∘	−1.5	⋆	1.5	△	1.5	⊗	1	⊘	2
3	−0.5	⊗	0	⊗	0.5	●	0.5	⊙	0.5	⊙	2	⊙	1.5	△	0.5	∘	1.5	⊗	2	∘	3
4	0	∘	0.5	△	−1	∘	0	●	0	⊙	0	●	2	⊘	2	●	3	△	0	∘	4
5	1	△	−1	⊘	0	⊘	0	⊙	0.5	⊗	1.5	⋆	−1	△	0	⊗	1	⋆	1	⋆	5
6	1	⊙	1	⊗	2	△	0	⊕	0.5	⊕	−2	⊕	1	⊙	0	∘	1.5	⋆	2	⊗	6
7	−0.5	△	0	∘	−0.5	⊕	0	⋆	−0.5	⋆	0.5	△	3.5	△	−1	⊗	0.5	⋆	1.5	⊙	7
8	0.5	⋆	0.5	⋆	0	⊘	2	⋆	0.5	∘	−0.5	△	1	∘	2	⊕	1	⊘	0.5	△	8
9	0	⊘	3	⊕	−0.5	●	3	●	0	⊗	1	⊘	0.5	⊗	0.5	∘	1.5	△	−0.5	●	9
10	1.5	∘	0	∘	0	●	2	∘	0.5	⊘	0	⊗	2	⊙	2	△	−1.5	⊕	2	△	10
#	SOI		MOSK		MONK		MRAP		NEMO		NEMR		AIR-S		AIR-P		NAO		NAOW		#
1	0.5	⊕	2.5	△	1	∘	2	⊕	1	∘	3	●	1.5	⊙	1.5	●	0.5	∘	2	⊙	1
2	2	●	2.5	⊙	3	⊗	1	∘	1	⊕	1.5	⊘	0.5	●	1	∘	1.5	⊙	−1	⊕	2
3	0.5	⊙	2	△	1.5	△	2.5	⋆	0.5	⊕	−0.5	△	1	∘	0.5	⊕	0	⊘	−1	⊘	3
4	2	⊘	–	—	0	⊕	3	△	−0.5	⊘	1.5	⊕	2	⊙	0.5	⋆	0.5	⊘	0.5	●	4
5	2	⊘	1.5	⊙	1	⊙	1.5	⊗	2	⊕	2	⊙	1	●	0.5	⊗	−1.5	⊙	2	⊕	5
6	1.5	⊘	1.5	⋆	1	⊕	−1	⋆	0.5	⊗	−1	∘	2	⋆	−1	●	0	∘	2	⊘	6
7	0	∘	0	△	0.5	⋆	1.5	●	2	⋆	0.5	⊕	2	∘	0	⊗	0.5	∘	1	⋆	7
8	0.5	⋆	2	⊙	0.5	⊘	1.5	⊕	0	⋆	0.5	⊗	1.5	⋆	2	△	0.5	⊕	−1	⊕	8
9	1	⋆	2	△	−1	⊙	1.5	⊙	1.5	⊘	0	●	0	⊙	0.5	●	0.5	∘	−1.5	⊕	9
10	2	∘	0	△	1	∘	2.5	⊕	0	⋆	3	●	0	⊕	1	⊘	0.5	⊙	0	△	10

[a]Reference modulation frequencies ($\tilde{f}$, in *cpy*) of the individual groups are as follows: ⊙ ≙ 0.004260, ● ≙ 0.004448, △ ≙ 0.004645, ∘ ≙ 0.005290, ⊘ ≙ 0.005524, ⋆ ≙ 0.006860, ⊕ ≙ 0.007164, ⊗ ≙ 0.008158. Carrier frequencies f_c of Table 5.11 designated by the same symbol relate to modulation frequencies $\tilde{f}$ here as $f_c/\tilde{f} = 2^{3.5}$ (an arbitrary choice)

Table 5.13 As in Table 5.11 but for ten annual European time series

#	SLP Azo		SLP Ice		CET		Baur SAT		Baur PRC		GWL.HM		.BM		.NWZ		.WA		.WZ		#
1	2.5	∘	2.5	△	1	∘	−2	⊕	1.5	⊗	−3.5	∘	1.5	△	1	⊗	1.5	⊘	2	⋆	1
2	2	⊙	2	⊘	−3.5	•	0.5	⋆	2.5	△	1	⊕	2.5	⊘	1.5	⊕	1	•	1.5	∘	2
3	1.5	⊕	2.5	△	2.5	⋆	2.5	⋆	2	⋆	2.5	△	−4.5	⊕	2.5	△	2	⊗	2	∘	3
4	−0.5	∘	1.5	⊘	1	∘	2	⊘	2	⊘	1.5	⋆	−1.5	⊕	2.5	△	2.5	•	2.5	⊘	4
5	2	⊕	−0.5	⊗	1	⊗	2	⊘	1.5	⊗	1.5	⊗	1	⊕	2.5	△	1	⊗	1.5	⊘	5
6	1.5	⊗	2.5	△	2.5	⊘	1.5	•	2	⋆	2	∘	2.5	⊙	1	⊕	0	⊘	2.5	⊘	6
7	2	⊕	3	•	1.5	⊕	1	⊘	−3.5	⊘	2	⊕	2.5	•	1	⊗	2.5	⊙	2.5	⊙	7
8	2.5	△	2	⊘	2.5	∘	1.5	△	2	⋆	1.5	∘	2.5	⊙	2	⊗	2.5	⊙	3	△	8
9	2.5	⊙	1	•	0.5	⋆	3	△	2.5	•	2.5	△	2	⊗	2	⋆	1	⊗	2	⊕	9
10	0	⊕	2.5	⊘	2.5	•	2	∘	2	⊗	2	⊕	0.5	⊕	2.5	△	2	⊕	2.5	⊙	10

Table 5.14 As in Table 5.13, but for modulation frequencies

#	SLP Azo		SLP Ice		CET		Baur SAT		Baur PRC		GWL.HM		.BM		.NWZ		.WA		.WZ		#
1	1.5	⊙	1	⊗	1.5	⊙	−3	⊗	1	∘	−2	●	4	⋆	0.5	⋆	0	∘	3.5	∘	1
2	1	△	0	⋆	−2.5	⊘	2	△	2	⊙	1.5	●	3.5	⊙	1.5	△	1	∘	0.5	∘	2
3	1	⊙	1	∘	1.5	△	1.5	△	1.5	⊗	0.5	⋆	–	—	1.5	⊗	0.5	⋆	1	⋆	3
4	−1	●	0.5	●	1	⊙	2.5	⊙	1.5	⊙	0.5	∘	−0.5	⋆	0.5	⊘	0.5	⊕	−0.5	⋆	4
5	1	⊘	−0.5	⊕	2	⊙	0.5	⊘	0.5	⋆	0	⊕	0.5	⊕	1.5	⊗	1	⊘	4	⋆	5
6	1	⊕	0.5	⊘	0.5	⊘	1	⊘	2	⊙	0	⊕	0.5	⊗	−0.5	⊗	−1.5	∘	2.5	⊙	6
7	3	△	−0.5	⋆	1	⊙	−0.5	∘	−2	●	3	⊙	0.5	⊘	0	⊘	1.5	⊗	1.5	⊘	7
8	2	⊕	2.5	⊘	0.5	∘	2	⊙	2	●	−0.5	⊕	1	●	0	⊕	1	∘	2.5	⊕	8
9	3	△	−0.5	⊙	−0.5	△	3	●	1	⊗	−1	⊗	1.5	⋆	0.5	⋆	0.5	⊙	0.5	⊗	9
10	−1	⋆	0	⋆	−0.5	⋆	1	△	2	△	3	●	1	⋆	0	⋆	1.5	⊗	0.5	⊗	10

Table 5.15 As in Table 5.11 but for nine annual time series of the Elbe mainstream near Dresden

#	total (g)		slow (g_s)		dtrans (g_{dt})		fast (g_f)		trans (g_t)		ftrans (g_{ft})		ilf (g_ℓ)		mlow[a]		subsfc		#
1	1	△	1	●	2	⊘	0.5	⊕	2	⊘	1.5	⊘	1	△	0.5	⊘	1	△	1
2	0.5	⊗	0.5	⊗	1.5	⊗	2.5	∘	1.5	●	1	⋆	1	⊘	2	△	0.5	⊗	2
3	2.5	⊙	2.5	⊙	1.5	⋆	−1	⊕	1.5	●	2	⊘	2.5	⊙	1	⊙	2.5	⊙	3
4	2.5	⊘	2.5	⊘	1.5	⊗	3	⊙	2	⋆	1.5	⋆	−1.5	∘	2.5	⊙	2.5	⊘	4
5	2.5	⊙	1	●	2	∘	1	⊗	0	⊗	2.5	⊙	1.5	∘	0.5	⊗	1	●	5
6	1.5	⊗	1.5	⊘	0.5	⊘	2	⊕	2	⊕	2.5	●	2.5	⊘	0	⊘	1.5	⊗	6
7	2.5	△	1.5	⊗	−1	⊗	−1	⊗	−1	∘	2.5	⊙	0.5	⊗	2.5	∘	1.5	⊗	7
8	1.5	△	2	∘	1.5	⊘	1.5	⊗	2.5	△	0.5	∘	2.5	⊙	2	●	2	△	8
9	2.5	●	1.5	⊗	2	⋆	2	⋆	2.5	⊘	2.5	⊙	0.5	∘	2.5	⊘	1.5	△	9
10	2.5	⊙	1.5	⊕	−1	⊘	3	△	2.5	⊘	2	⋆	2	△	−0.5	⊕	0	⊕	10

[a] "mlow" is the traditional monthly low flow not discussed here

Table 5.16 As in Table 5.15, but for modulation frequencies

#	total (g)		slow (g_s)		dtrans (g_{dt})		fast (g_f)		trans (g_t)		ftrans (g_{ft})		ilf (g_ℓ)		mlow		subsfc		#
1	0.5	⊗	1.5	⊙	3.5	⋆	1.5	●	4	●	–	—	0.5	⊗	0.5	⊗	0.5	⊗	1
2	0.5	⊕	0.5	⊕	1	∘	2	⋆	1	⊙	1	⊘	1	⊘	1	△	0.5	⊕	2
3	3	△	3	△	0.5	⊗	0	⋆	0.5	⋆	2	∘	3	△	−1.5	⊗	3	△	3
4	1.5	●	1.5	●	1	∘	3	∘	2	∘	2.5	⊘	–	—	3	△	1.5	●	4
5	1	△	−0.5	⊙	1.5	●	−0.5	⊕	−1.5	∘	0.5	⊕	0	⋆	0.5	⊕	0	⊗	5
6	0.5	⊘	4	⊗	−0.5	⊙	2	⊘	1	⊕	1.5	△	3.5	∘	1.5	⊙	0.5	⋆	6
7	2.5	●	0.5	⋆	−2	⊘	−2	⊘	−1.5	△	0.5	⊘	0.5	⋆	2.5	⋆	0.5	⊙	7
8	0	●	1	⊘	0	⊕	2	⊘	1	∘	−1.5	⊕	1.5	●	0.5	⊗	3	⊗	8
9	2.5	△	1	⊗	2.5	⊙	0.5	⊗	1.5	⊘	0.5	●	−1.5	⊕	2	⊕	2.5	⊙	9
10	0.5	⊕	0.5	⊕	0	⋆	1	●	1	⋆	1.5	⊕	0.5	●	−1.5	⊗	−0.5	⊘	10

analytic signal. Decoding the complex terrestrial signal(s) around Schwabe cycle #19 is a related challenge. Archetypal of internal structure that hints at organized dynamics are low rational frequency relationships as well, and hidden structure may also be found via dyadic exponents that emerge in the definition of the present MP-FM dictionary (cf. Appendix). Generally, given the high signal space resolution used, coincidence in more than one signal parameter between two or more MP-FM modes may rarely occur just by chance and hints thus at potential kinship.

Conceptual background of the "vertical" search for climate signals, via Europe down to the river basin scale, is the notion of a regime character of climate variability and change (e.g., [44]). Of the six types of synchrony or parameter coincidence found to apply at global scale, phase coherence (type 1) bears one of the rare persistent time domain effects throughout the analysis period, the (lagged) parallel evolution of the slow mode #7 of Baur's precipitation for Germany [7] with secular warming as represented by global and European SAT #1. Interdomain (type 2) synchrony is not that dominant over Europe as it is at global scale, but global SAT #1, for example, is accompanied by secular frequency drifts in modes #4 of the central European weather regimes (GWLn) BM and WZ. Such type connection to centennial global warming is largely missing at planetary scale, where multidecadal modes have taken the lead since the 1970s. Signal envelope (type 3) synchrony is regionally encountered in slightly lagged localized signals again. GWL WZ #14, for example, reflects the changing NH circulation around 1959 [64], in company with changes in the boreal summer monsoon and the winter NAO (same scale and time location, but much differing variability).

Among such more general signal parameter coincidences (type 6), perhaps most noticeable with a view on the water cycle are solid links between the Indian monsoon and German precipitation. European climate and weather regimes expectedly show clear signatures of the global climatic evolution. Encouraging with a view on further hydrologic downscaling was the comparably high internal organization and external integration of Baur's precipitation series for Germany, which provides the strongest links to basin-scale hydrology, as demonstrated for the middle Elbe gauging station near Dresden. To identify potential selective response of the water body, a functional streamflow disaggregation technique (FSD [21]) has been applied to generate a set of conceptual flow components which are thought to represent distinct sources and response times of (sub)surface hydrology. Links may be traced down indeed from Indian monsoon rainfall via Baur's precipitation to both driven-transient and slow FSD components of the middle Elbe mainstream. It is certainly remarkable that the most convincing "vertical" connections are found in runoff components that belong to the greedy FSD version, as compared to those of the shortcut one which tended to provide analogues to the classical conceptual components overland flow, interflow, and baseflow [22]. The MP-FM modal structure of FSD components of whatever combination, though, is rather robust. The combination of both methods thus appears to provide an adequate strategy of objective analysis to grasp the signatures of climate variability and change at river basin scale.

The study was exploratory in various aspects:

(i) Existence of sparse approximation of climate dynamics was uncertain, though GCM results indicated substantial low-dimensional shares [19].
(ii) A generic method to obtain the "sparsest" approximation, i.e. to minimize the ℓ^0 norm (number of modes) does not exist as yet (e.g., [11]).
(iii) An established method (and tool) is still missing to efficiently search for diverse types of synchrony in a data base of MP-FM structure books (adding to the fact that structure book screening alone does not suffice).
(iv) Archetypal signs in data structures that point to organized dynamics are low rational frequency relationships at top of the Farey tree of rational numbers [63] (Table 5.17), but the dyadic scheme of the dictionary used (though a reasonable choice) does not directly match Farey's construction rule.
(v) The choice of adequate signal space resolutions, also in scale s and modulation phase constant $\tilde{\phi}$, requires experience.
(vi) Stability of MP-FM modal structures against shifted/varied time windows (cross validation) is an issue that calls for extensive studies.
(vii) There was no prior information about the robustness of the combined FSD/MP-FM approach.
(viii) Though motion across the basin is ruled by the respective attractor, it is not clear how the varying distance of a trajectory from the inertial manifold influences dynamic synchronizations and their visibility.
(ix) Unstable periodic orbits are difficult to identify in time series of natural systems (it is thus of basic interest to learn how their signs may look like).
(x) Allowance for deep FM in the MP dictionary evolved from previous weaker-FM dictionaries which did not show "sparse enough" modal structures.

Major non-technical global scale issues and results of the study include

(a) the fundamental role of FM, even deep FM, for interdomain synchrony;
(b) structured insolation that is basically composed of five MP-FM modes and appears to have been found in "almost sparsest" approximation;
(c) the interplay of centennial, multi- and bidecadal thermal modes to shape the global warming process in an episodic manner, with discernible regimes, marked turning points that signify climatically exceptional situations, and lately unexpected stagnation ("hiatus") near the end of the twentieth century;
(d) systematic FM phase relationships, partly in interdomain synchrony, between NAO and SO, accompanied by SST and monsoonal modes;
(e) complex signals of monsoon response to leading insolation modes, including apparent UPO manifestation which feeds forward to the system's thermal evolution at the height of solar cycles #19 and #21 at least;
(f) centennial scale solar–terrestrial interdomain synchrony between SRAD #1 and top-rank monsoonal, thermal, and (EN)SO modes.

"Vertical" signal tracing via European climate and weather systems down to the Elbe river mainstream near Dresden uncovers inclusion of a network of regional MP-FM modes into globally organized dynamics. Above all,

(g) global centennial warming is found in like manner as leading mode of European SAT, but there is no analogue across Europe of the growing multidecadal modes—which thus appear to be of tropic/subtropical origin.

Remarkably however,

(h) the only persistent time domain companion of centennial warming found as yet is the leading slow mode (#7) of German precipitation as compiled according to Baur [7];

(i) leading slow monsoonal modes also occupy only lower ranks (MONK #9, AIR-S #11) but nevertheless appear to guide a variety of interdomain companions across the climate system, including leading monsoon modes itself (internal interdomain), those of NAO and SO, of European weather regimes, of German precipitation (#1 FM), and of FSD runoff components at the Dresden gauge (total & fast #1, dtrans #2,4,5, among others);

(j) selective global and regional climate and weather signatures in runoff components of the middle Elbe both qualify the river as integral part of the global water cycle and hint at preferred pathways of potential impacts.

5.8 Conclusions

5.8.1 Some Rudimentary Statistics

Though structure book screening is only part of the "track securing" here, this concise quantification of modal structures provided by MP is a unique feature of the method that calls for more extended use. Besides convenient exchange of the results of MP based TF analyses and syntheses in terms of only few numbers (in place of full TF plane distributions), some statistics might be based on these tables. Figure 5.31 shows for both global (left panel) and European data sets (right panel) the distribution of frequencies f_c (top row) and $\tilde{f}$ (bottom row) in the left part each of panel. The right parts display corresponding mappings on the Farey tree of rational numbers (Table 5.17) in terms of (negative, inverse) dyadic exponents $-1/log_2 f_c$ and $-1/log_2 \tilde{f}$ (recall the dyadic scheme used in the MP-FM code, and cf. Table 5.18). Shown are the number of occurrences among the leading 10 MP-FM modes each, the corresponding rank-weighted numbers (weights $(11 - rank)/5.5$), and the total signal energy ratio captured by each frequency, normalized by the average signal energy (90.995 % global/86.740 % Europe) as grasped by the ten leading modes each of all (20/10) time series incorporated. Whereas rank weighting does not much change these distributions, signal energy weighting expectedly accents the leading slow (thermal and insolation) modes.

Weighting aside, the two dominating carrier frequencies at global scale (left panel) are 0.2847 cpy (period ∼3.52 years; MOSK #1–3, Tahiti SLP #3, SOI #4, MONK & AIR-S #5, etc.) and 0.2973 cpy (period ∼3.36 years; MRAP & NEMR #1, SOI #2,6,9, etc.). Variables of the water cycle also contribute in shaping either

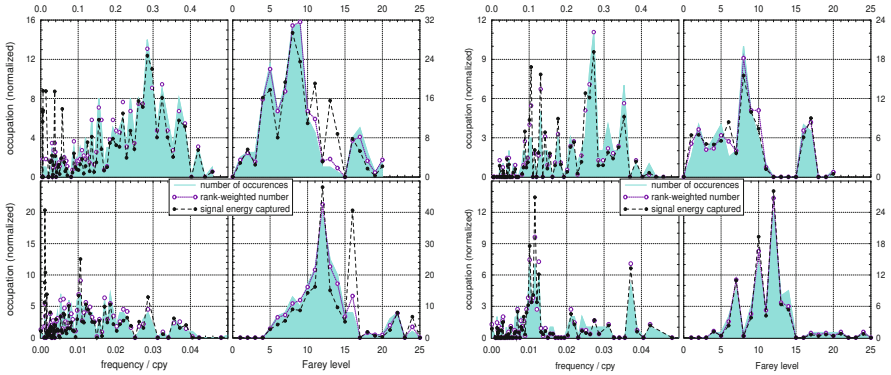

Fig. 5.31 *Left panel*: carrier (*top*) and modulation (*bottom*) frequency distributions (*left*) and their hidden *Farey* tree occupations (*right*) of modes #1–10 each of 20 global climate time series: number of occurrences (*shaded*), rank-weighted number (normalized; *opaque circles* with or without *dotted line*), and signal energy captured (normalized; *dashed line* with *filled circles*); *right panel*: the same for ten European climate and weather time series

first sideband of this central bulk. Excepting solar and thermal slow-mode peaks, the modulation frequency distribution exhibits one dominant centennial peak, made up of leading monsoon modes as well (MONK & NEMO #1, MRAP #2, AIR-S #3). In the Farey tree representation, the central peaks become more slim with signal energy weighting, and sidebands at higher levels (which are exclusively occupied by slow modes) grow up. Farey level 8 dominates among the carrier frequencies, and pronounced sidebands are found at levels 4–5,11,13. Modulation frequencies settle around level 12, with only one substantial (slow mode) sideband at level 16.

For the European time series (right panel), the carrier frequency distribution loses the sidebands of its central peak which itself is located at frequency 0.2973 cpy as well (NWZ quadruple, e.g.). The globally dominating carrier of the MOSK triplet does not play a substantial role regionally, and slow, secular modes do not gain too much relative weight here in terms of captured signal energy. Weighting has practically no effect on the carrier distribution in terms of hidden Farey tree occupations. If compared with the global scene, the regional distribution accents Farey levels 4 and 8, both making up the left (upper) edge of the two broader peaks found for global climate data. Slow-mode (carrier) peak enhancement due to signal energy weighting, as seen at global scale, does not emerge in the European case. As for modulation frequencies, weighting accents the $80 \cdots 100$ years range of FM periods, out of a broader (structured) "bulk" of modulations. In contrast to the global data set, the hidden Farey tree occupation shows a broader peak at levels 12–13, and weighting induces certain growth of a sideband at levels 9–10. Broader (sharper) features of carrier (modulation) frequency distributions in the global data set might reflect the dominance of interdomain effects in its dynamic organization, in contrast to the regional scale.

Table 5.17 Upper 6 levels ($l = 0 \cdots 5$) of the Farey tree of rational numbers [63][a]

l	Rational numbers in terms of *Farey* sums																															
0	$\frac{0}{1}$																															$\frac{1}{1}$
1																	$\frac{1}{2}$															
2									$\frac{1}{3}$																$\frac{2}{3}$							
3					$\frac{1}{4}$								$\frac{2}{5}$							$\frac{3}{5}$								$\frac{3}{4}$				
4			$\frac{1}{5}$				$\frac{2}{7}$				$\frac{3}{8}$				$\frac{3}{7}$				$\frac{4}{7}$			$\frac{5}{8}$				$\frac{5}{7}$			$\frac{4}{5}$		
5		$\frac{1}{6}$		$\frac{2}{9}$		$\frac{3}{11}$		$\frac{3}{10}$		$\frac{4}{11}$		$\frac{5}{13}$		$\frac{5}{12}$		$\frac{4}{9}$		$\frac{5}{9}$		$\frac{7}{12}$		$\frac{8}{13}$		$\frac{7}{11}$		$\frac{7}{10}$		$\frac{8}{11}$		$\frac{7}{9}$		$\frac{5}{6}$	
...	*sequence of rationals [0,1] by projection of levels 0–5 ...*																															
	0	$\frac{1}{6}$	$\frac{1}{5}$	$\frac{2}{9}$	$\frac{1}{4}$	$\frac{3}{11}$	$\frac{2}{7}$	$\frac{3}{10}$	$\frac{1}{3}$	$\frac{4}{11}$	$\frac{3}{8}$	$\frac{5}{13}$	$\frac{2}{5}$	$\frac{5}{12}$	$\frac{3}{7}$	$\frac{4}{9}$	$\frac{1}{2}$	$\frac{5}{9}$	$\frac{4}{7}$	$\frac{7}{12}$	$\frac{3}{5}$	$\frac{8}{13}$	$\frac{5}{8}$	$\frac{7}{11}$	$\frac{2}{3}$	$\frac{7}{10}$	$\frac{5}{7}$	$\frac{8}{11}$	$\frac{3}{4}$	$\frac{7}{9}$	$\frac{4}{5}$	$\frac{5}{6}$	1

[a]Construction via Farey sums of all rational numbers between 0 and 1 follows a continued fraction rule that starts at the seeding level $l = 0$: $\frac{p}{q} = \frac{p_1}{q_1} \oplus \frac{p_2}{q_2} \equiv \frac{p_1+p_2}{q_1+q_2}$, where $\frac{p_1}{q_1}$ and $\frac{p_2}{q_2}$ are nearest neighbour rationals of a projection of all levels above the actual one

Table 5.18 Properties of the MP-FM dictionary in the set of carrier and modulation reference frequencies defined for the present study: 8 families of modes, their mutual relationships in terms of "p/q" rationals and symbols, and corresponding dyadic exponents[a]

f_c,	$-\log_2 f_c$		$\tilde{f}$,	$-\log_2 \tilde{f}$		"p"	"q" family, and field of "p/q" relationships																		
cpy	(dec.)	(rat.)	*cpy*	(dec.)	(rat.)	family	⊙		●		△		○		⊘		⋆		⊕		⊗				
0.04819	4.375	35/8	0.004260	7.875	63/8	⊙	0		4	○	3.5	⊕	4	●	4	⊙	3	⋆	3.5	△	2.5	⊗			
0.05033	4.3125	69/16	0.004448	7.8125	125/16	●			0		4	○	4	△	4	●	3	⊕	3	⋆	3.5	⊙			
0.05256	4.25	17/4	0.004645	7.75	31/4	△					0		3.5	⋆	4	△	3.5	○	3	⊕	3.5	●			
0.05985	4.0625	65/16	0.005290	7.5625	121/16	○							0		4	○	4	⊙	3	⊗	3	⊕			
0.06250	4.0	4/1	0.005524	7.5	15/2	⊘									0		4	●	4	⊙	3.5	○			
0.07762	3.6875	59/16	0.006860	7.1875	115/16	⋆											0		4	○	4	△			
0.08105	3.625	29/8	0.007164	7.125	57/8	⊕													0		3.5	⋆			
0.09230	3.4375	55/16	0.008158	6.9375	111/16	⊗															0				

[a]Families of modes defined by their reference carrier and modulation frequencies ($f_c, \tilde{f}$; left part of the table) are given both in cycles per year (*cpy*) and as negative dyadic exponent ($-\log_2 f_c, -\log_2 \tilde{f}$), where the arbitrary choice $f_c/\tilde{f} = 2^{3.5}$ holds for each family. Note that the definition of symbols here differs from that in [15]. The matrix (right part of the table) presents the quotients of reference frequencies; numerals in front of symbols signify dyadic exponents, i.e. n means a factor of 2^n (for the matrix diagonal, $2^0 = 1$, of course). General relationships, like [$\odot/\oslash = \circ/\star = \oslash/\oplus = \sqrt{2}\bullet/\otimes$], [$\odot/\circ = \bullet/\oslash = \oslash/\star = \sqrt{2}\triangle/\otimes$], or [$\bullet/\circ = \star/\otimes = \triangle/\oslash = \sqrt{2}\odot/\oplus$], directly result from those shown in the table. For carrier frequencies, [$\odot = 2^{2.5}(\otimes)^2 = 2^3(\star)^2$], [$\triangle = 2^3(\oplus)^2$], and [$\oslash = 2^{4.5}(\triangle)^2$] hold in addition, for example; for modulation frequencies analogous relationships exist, with factors of the quadratic terms increased by $2^{3.5}$

Signal distributions of the type presented in Fig. 5.31 have also been constructed for parameters scale s and translation u, and have been followed in their temporal evolution (not shown) in order to find statistics that make appropriate use of structure book collections. Statistically unsettled tendencies have been noticed toward higher frequencies and shorter scales globally, as could be expected for a dynamic system under increasing forcing strength, either internally or externally. Locations u of maximum signal energy over Europe favour the 1940s and 1950s, i.e. the period of dynamic reorganization that followed the first warming episode of the twentieth century.

A set of related standard diagnostics may be developed, not to the least in order to objectively evaluate next-generation analyses. When subspace zooming is applied, Diophantine approximation (rational approximation of irrational numbers) to the system's frequencies, perhaps just using Farey's construction rule [63], might gain even more weight. Rational frequency relationships have only very scarcely been addressed here but may contain additional invaluable information—as might be inferred from Tables 5.11, 5.12, 5.13, 5.14, 5.15, and 5.16. Closer scrutiny is also indicated of phase (or modulation phase) lags; specifically, quadrature relationships may hint at hidden analytic signals.

5.8.2 Final Remarks on Climate Dynamics

An organized global climate system is seen in MP-FM based sparse approximation of its interannual dynamics in terms of representative time series of the instrumental period. Its behaviour hardly indicates that the Earth's climate might obediently follow any forcing scenario: It follows its own dynamic rules governed by a rich variety of internal feedbacks, though in conjunction with the actual degree of forcing. Direct comparison to the GCM study [19], where the focus was on intraseasonal aspects, could not be provided here. A general consequence of low-dimensional behaviour, however, namely a substantial degree of internal synchronization that the (high-dimensional) system necessarily displays, has been uncovered.

A complex, dynamically excited system may act as a sensitive receiver, not to the least in generating a variety of unstable periodic orbits (UPOs) on which it may be temporarily stabilized by external control. It is thus not surprising that relatively weak solar signatures are manifest in the climate record. Paradoxically, if ever higher dynamic excitation parallels increasing anthropogenic forcing, this should increase the system's sensitivity and might thus engrave ever weaker external (e.g., solar) signals into the records—thus perhaps confusing the observer about the very cause of climate change.

Considering projections of the hydrologic cycle, the structured solar input has been found indeed to play an important role. As a straightforward mechanism, uptake of water vapour over large oceanic areas ("solar collector surfaces" in this respect) by the low-level monsoonal circulations, and release of its latent energy in the subsystem's deep convections, may be blamed for these signatures. In addition

to scenarios of anthropogenic impacts, those of insolation might thus be needed as well. Given the "almost sparsest" approximation obtained here for the 128 year insolation series, at enhanced projective power of the method (notably by raising internal restrictions, by subspace zooming, etc.) such solar scenarios might be constructed for the short term, i.e. over a sunspot cycle or two in advance.

That global warming proceeds in an episodic manner bears no surprise if one sheds a glance at the instrumental climate record. What is new and very important, however, is the evolution toward dominance of shorter timescales, notably the apparent takeover by multidecadal modes of the process of global warming. Growing signal energy in corresponding SAT modes appears to be borne in the lower latitudes, under active participation of the tropic/subtropical water cycle. A fundamental question arises about the pathway that climate change has adopted: Is a route to planetary-scale turbulence (rather than obedience to forcing scenarios) imaginable? Whether this would be good or bad news remains an open issue, but couldn't it even undermine a general oceanic takeover (and thus excitation of much longer time scales of climatic change)? Altogether at least, a "chaos control" notion of present-day climate dynamics, variability and change appears to be indicated.

Acknowledgements Thanks are due to Fred Hattermann of the Potsdam Institute for Climate Impact Research (PIK) who provided the Elbe runoff data. Generally, the success of the study hinges on the quality of data, and the author hopes to have expressed his respect to this community in spending substantial effort and using advanced techniques in order to make the best of the data. MP-FM is an own product, but its coding has much profited from the detailed MP description given in [73]. Further sources which helped in own software developments over the years have been acknowledged in [21]. Last but not least, however, graphics solutions as provided by the freely available GrADS [33] and Xvgr packages [99] are explicitly referred to here with due gratitude.

Appendix

Analytic Signal

A deep-rooting question concerns the nature of complex elements like ψ_γ or $\psi_{\tilde{\gamma}}$. The "analytic signal" (AS), a specific complex extension of a real signal (from a sea of possible ones), is defined by a single-sideband (SSB), nonnegative-frequency Fourier spectrum [42]. A sufficient condition for a complex signal $\psi(t)$ to exhibit the SSB property, the quadrature relationship between real and imaginary parts (as is the case with the complex exponential), is guaranteed for Hilbert pairs, $\Im\{\psi(t)\} = \mathcal{H}\{\psi_r(t)\};\ \psi_r(t) = \Re\{\psi(t)\}$, where $\mathcal{H}$ denotes the Hilbert transform (HT)

$$\mathcal{H}\{\psi_r(t)\} := \frac{1}{\pi} \int\!\!\!\!\!\!-_{-\infty}^{\infty} \frac{\psi_r(\xi)}{\xi - t} d\xi \tag{5.6}$$

($\nexists$ is Cauchy's principal value).[3] The linear operator

$$\mathcal{AS}\{\psi_r(t)\} \equiv \psi_{\mathcal{AS}}(t) := \psi_r(t) + i\ \mathcal{H}\{\psi_r(t)\} \tag{5.7}$$

is often (but nevertheless incorrectly) adopted as definition of the AS, though this discards one degree of freedom at least, borne in zero frequency components of the SSB. Whereas extension to harmonic FM does not destroy the AS feature of the complex exponential (the adverse statement in [49] notwithstanding), the Gaussian envelope does so, thus making the Gabor atom only "approximately analytic" [72]. A "true" AS not yet exploited in the present context is the common harmonically amplitude- and frequency-modulated (AM-FM) complex exponential [8].

That the AS of a real signal $\psi_r(t)$ may be obtained without direct computation of the time domain transform $\mathcal{H}\{\psi_r(t)\}$ is technically interesting. The Fourier Transform (FT) $\hat{\psi}_r(\omega) \equiv \mathcal{F}\{\psi_r(t)\}(\omega) := \int_{-\infty}^{\infty} \psi_r(t) e^{-i\omega t} dt$ and its backtransform $\psi_r(t) = \mathcal{F}^{-1}\{\hat{\psi}_r(\omega)\}(t) := \frac{1}{2\pi} \int_{-\infty}^{\infty} \hat{\psi}_r(\omega) e^{i\omega t} d\omega$ offer a convenient way to construct a complex SSB signal: interpreting $\mathcal{H}\{\psi_r(t)\}$ as convolution of $\psi_r(t)$ with the Hilbert kernel $h(t) = 1/\pi t$, i.e. $\mathcal{H}\{\psi_r(t\} = h(t) \star \psi_r(t)$, yields the Fourier domain relations (e.g., [49])

$$\hat{\mathcal{H}}\{\hat{\psi}_r(\omega)\} = \hat{h}(\omega)\ \hat{\psi}_r(\omega) = -i\ \mathrm{sgn}(\omega)\ \hat{\psi}_r(\omega) \tag{5.8}$$

and

$$\widehat{\mathcal{AS}}\{\hat{\psi}_r(\omega)\} = (1 + \mathrm{sgn}(\omega))\ \hat{\psi}_r(\omega)\ . \tag{5.9}$$

AS construction via the Fourier domain thus simply reads

$$\psi_{\mathcal{AS}}(t) = \mathcal{F}^{-1}\widehat{\mathcal{AS}}\mathcal{F}\{\psi_r(t)\}\ . \tag{5.10}$$

From a discussion around Bedrosian's product theorem for the HT [9], there remained a notion of this Fourier domain tour being valid only for narrow-band signals. To the best of the author's knowledge, the narrow-band condition is a sufficient one that can be relaxed.

Design of the MP-FM Tool

The analytic signal regularizes the otherwise ill-posed task of ϕ determination (having dissolved by definition the signal's phase from its energy localization, an implicit regularization has been raised). From $\psi_{\mathcal{AS}}(t)$, phase constant ϕ may

[3] HT definitions in mathematical and signal processing contexts may differ by sign.

be determined, thus reducing the "active" signal space dimensions by one. To relax potential bandwidth restrictions, however, transition to the complex plane is postponed here until the analyzing signal and its translations are projected to the time series (residue). This "convolved inner product" bears a convenient way, again in the Fourier domain, to get the full set of projections in the translation dimension (u) at once with sampling accuracy [96]. It saves explicit exploration of another signal space dimension.

The remaining 5D space has to be traced in high resolution, however, to find the best-matching element $\psi_{r\tilde{\gamma}_k}(t)$. This is done "by brute force" as yet; intelligent searching strategies like subspace zooming, or parallel evaluation of alternative pathways of this greedy algorithm in order to minimize the ℓ^0 norm [11], have not been applied thus far. Dyadic f_c and $\tilde{f}$ spacings with 16 tones per octave result in resolutions of $1/128$ along either frequency axis. A maximum of 26 FM depths δf is traced, the range 2π of modulation phase constants $\tilde{\phi}$ is divided into 32 equidistant angles, and 11 (dyadic) scales are used for the width of the Gaussian window ($s = 2^0 \ldots 2^{10}$). For a time series length of ≤ 128 entries, this signal space resolution bears a web of analyzing wavelets of the order of 10^{10} elements, of which about 10^8 are included in the explicit search. In the frequency plane $(f_c, \tilde{f})$ a dyadic web is spanned, based on 8 families which relate to one another as seen in Table 5.18 (this "coherence" of the dictionary is not exploited in the matching process itself and does not introduce artificial coherence to the data target of the study).

The resulting MP decomposition of a time series, $\chi(t) \approx \sum_k \chi_k(t) = \sum_k \xi_k \psi_{r\tilde{\gamma}_k}(t)$ (where $\xi_k = \alpha_k / \parallel \psi_{r\tilde{\gamma}_k}(t) \parallel$ and $\parallel \cdot \parallel$ is the ℓ^2 norm, i.e. the signal energy), is fixed then in a structure book of eight numbers for each mode k, comprising 7D signal space locations and the projection coefficient α_k. As a rule, ϕ is chosen so as to make α positive, but this is occasionally violated due to a minor software blemish (that affects ϕ but does not bear further consequences). Concise quantification of modal structures is a prominent MP feature, in contrast to other TF methods. Interdomain effects might be studied for any $\widetilde{\gamma_p} \subset \tilde{\gamma}$ on principle, but explicit time dependence is provided in the Gaussian logon only for phase and frequency. Discussion of interdomain synchronies thus focused on time and frequency domains here, where highest resolution applies. In this case, relation (5.1) specifies as $\chi_{\mu_i}(t) \sim \mathcal{P}_{(\tilde{\omega},\tilde{\phi},u)}\{\chi_{\nu_j}\}(t)$.

Overcompleteness of the (homogeneous) dictionary, i.e. its extension beyond a basis, is essential for both sparse approximation and treatment of nonstationary data, but due to a latitude of possible parameterizations synchronies may be obscured then in the structure books. Those redundancies include cases of extreme phase of a slow FM, for example, which beneath the actual time window may pretend different carrier modes. The full tableau of synchronous modal interactions across the data set is thus hardly recognized by structure book screening alone. Visual inspection is also indicated due to technical limitations: At its present state of development, the method is neither well-prepared for two or more simultaneous frequency modulations, nor may it directly cope with a "modulation of modulation." FM itself has been restricted to $\tilde{f} \leq 4\ f_c$, in reminiscence of the radio broadcasting condition $\tilde{f} \ll f_c$ (which allows to clearly grasp the carrier frequency of an FM

signal), and the modulation depth δf is accordingly limited. Finally, by construction of the method (by definition of the analyzing waveform and its signal space), harmonic FM may directly match only those evolutions in the time domain which are largely harmonic; that is, interdomain synchrony between time and frequency domains may best be recognized for MP-FM modes with only small frequency drift beneath the actual time window.

The probability of a specific parameter combination is <0.001 for (s, u) and <0.0001 for $(f_c, \tilde{f})$; envelope synchrony thus may appear by chance with a probability of $<10^{-6}$, frequency domain coincidence with $<10^{-8}$, and for $(f_c, \tilde{f}, \delta f)$ a probability $<10^{-10}$ holds. Searching through the five leading modes each, say, of a set of 20 independent time series, raises all probabilities of coincidence by two orders of magnitude. Since explicit time dependence is provided only for phase and frequency, the system's trajectories may be evaluated for mutual synchronies in three dynamic projections: phase–phase, phase–frequency, and frequency–frequency. For the first case, either phase constant $(\phi, \tilde{\phi})$ is equally important—which makes time domain (phase–phase) synchronies even less probable and more difficult to find empirically. Time delays and otherwise conditioned phase shifts (including shifts in modulation phases), however, do not bear conceptual problems for a purely empirical analysis (and synthesis), like the present one is.

Even if perhaps not the "sparsest" approximations, all MP-FM decompositions here are valid in the sense of proven convergence of the greedy, stepwise extraction of maximum signal energy (e.g., [11, 31, 73, 97]), and de facto exponential convergence of each analysis (e.g., [48]). Given low probability of synchronous motion in the extremely sparse data problem chosen, fake synchronies are highly improbable, and the organized motions found should thus be understood as representing a lower margin of the level of dynamic organization present in the data. Any synchronous motion may add authenticity (and thus should be taken seriously as a potential brick that fits) to an emerging mosaic of low-dimensional climate dynamics.

A technical advantage of using elementary signals like (5.5) rests in the fact that their Wigner–Ville distribution (WVD) [27] is analytically solvable. This may be exploited to build MP-FM spectrograms without masking effects [73]. Due to an "uncertainty principle" (e.g., [72]), though, the temporal extension of a signal relates inversely to the thickness of the WVD trace which represents it: sharp, thin lines mark highly persistent modes, whereas broader "scars" represent signals with shorter timescale. Concerning the graphical resolution, traces in form of sequences of spots should be read as continuous lines.

MP-FM Performance: A Sketch

Structure books of a 128-entries test signal made up of five components, and its MP-FM reconstructions for two types of resolution in δf (fully equidistant, or dyadic over half the frequency axis), are given in Table 5.19. As shown in Fig. 5.32,

Table 5.19 Structure book of the test series and of its (uncentered) MP-FM analyses using either equidistant or (half-) dyadic resolution of modulation depth δf

k	α_k	s_k	u_k	f_k	ϕ'_k	$\tilde{f}_k$	β_k	$\tilde{\phi}'_k$
Test signal components (100 % signal energy)								
(1)	(100)	32	64	0.0000	0.000	0.00000	0.00	0.000
(2)	(100)	128	16	0.2109	0.785	0.00000	0.00	0.000
(3)	(100)	512	32	0.3047	1.571	0.00000	0.00	0.000
(4)	(100)	2048	95	0.2500	0.000	0.03125	2.40	0.000
(5)	(100)	2048	95	0.4375	1.963	0.05469	0.80	0.982
MP-FM equidistant (99.1 % signal energy)								
1	100.00	32	64	0.0000	0.000	0.00000	0.00	0.000
2	58.04	128	28	0.2109	−2.150	0.00000	0.00	0.000
3	41.38	512	5	0.3047	0.139	0.02410	0.41	−1.178
4	21.62	512	85	0.4375	−0.413	0.05488	0.91	−2.356
5	18.26	256	33	0.2500	3.104	0.03125	2.56	0.393
MP-FM (half-)dyadic (99.1 % signal energy)								
1	100.00	32	64	0.0000	0.000	0.00000	0.00	0.000
2	57.78	128	31	0.2102	1.826	0.00000	0.00	0.000
3	41.30	1024	81	0.3242	1.115	0.00098	20.48	3.142
4	21.68	256	36	0.2500	1.393	0.03125	2.24	0.982
5	19.26	256	35	0.4391	0.387	0.05488	0.73	−0.785

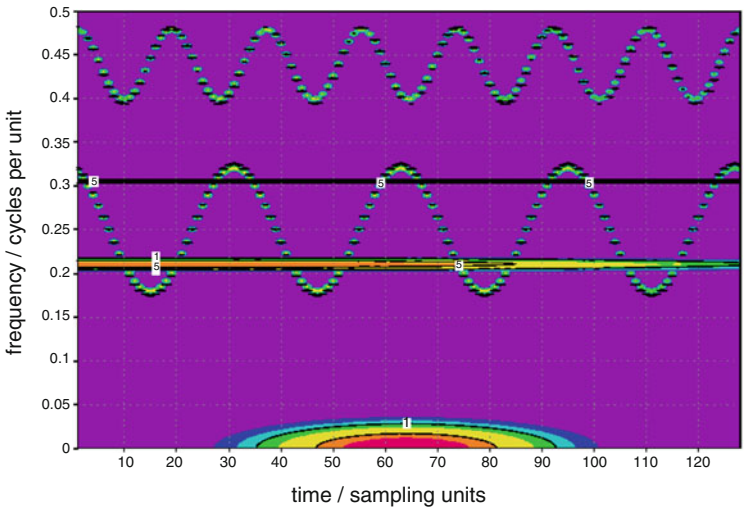

Fig. 5.32 MP-FM reconstruction with half-dyadic resolution of δf spacing: time–frequency view of the test signal (*contour*) and its reconstruction (modes #1–5, *coloured*)

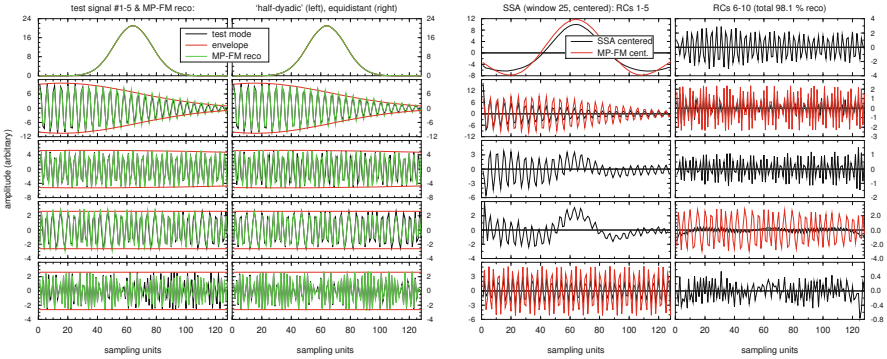

Fig. 5.33 MP-FM vs. SSA test case reconstructions; *left panel*: MP-FM based component reconstructions with half-dyadic (*left*) and equidistant (*right*) δf spacing; *right panel*: SSA reconstruction (window 25, modes #1–10) comprising 98.1 % of signal energy

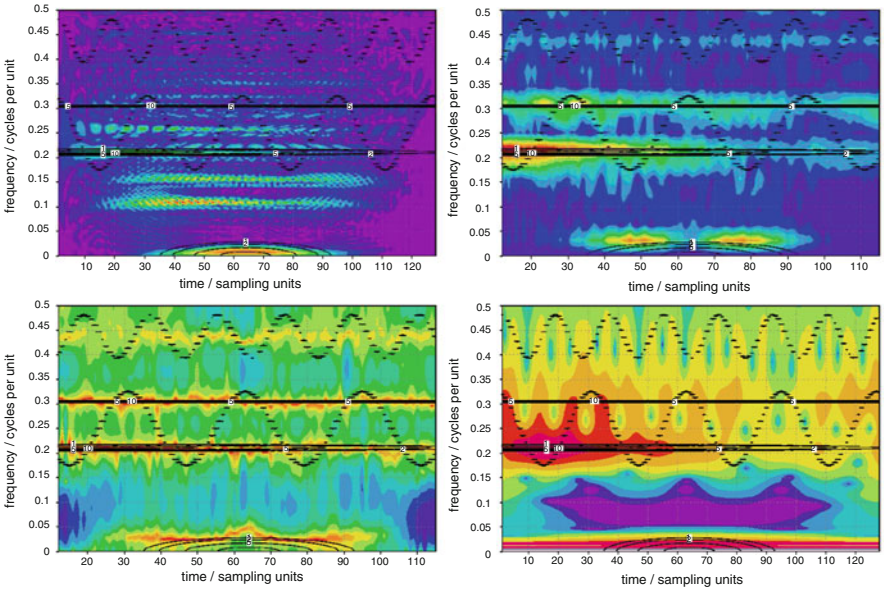

Fig. 5.34 As in Fig. 5.32, but reconstructions via WVD (*top left*), STFT (*top right*; window 25), ST-MESA (*bottom left*; window 25, order 12) and WT (*bottom right*; Morlet)

the linear composition of one Gaussian "bump," two unmodulated components (one decreasing, one nearly persistent), and two persistent FM modes may almost precisely be reconstructed—though in the structure book this is less obvious for the second case than for the first one.

MP-FM reconstruction is contrasted in Fig. 5.33 with results of the SSA, and in Fig. 5.34 with those of customary time–frequency methods, including the WVD, the Short-Time (windowed) FT (STFT; [3]), the evolutionary Maximum Entropy

Spectral Analysis (ST-MESA; [35]), and the Wavelet Transform (WT; [30]) with a "Morlet" as analyzing wavelet. MP-FM clearly outperforms these representations which all do not properly capture FM—though it may be an ubiquitous feature of oscillatory complex systems. The method in its present version (without advanced zooming etc.) may fail if too coarse a resolution has been chosen, or due to other internal restrictions. MP-FM appears to be suited, however, to approach "sparsest" approximations with a further extended signal space (at massively parallel computation).

References

1. Abraham, R.H., Shaw, C.D.: Dynamics. The Geometry of Behavior, 2nd edn. Addison-Wesley, Redwood City (1992)
2. Allan, R.J., Nicholls, N., Jones, P.D., Butterworth, I.J.: A further extension of the Tahiti–Darwin SOI, early SOI results and Darwin pressure. J. Climate **4**(7), 743–749 (1991)
3. Allen, J.B.: Short term spectral analysis, synthesis, and modification by discrete Fourier transform. IEEE Trans. Acoust. Speech Signal Process. **25**(3), 235–238; corrigendum **25**(6), 589 (1977)
4. Ananthakrishnan, R., Soman, M.K.: The onset of the southwest monsoon over Kerala, 1901–1980. J. Climatol. **8**(3), 283–296 (1988)
5. Ananthakrishnan, R., Soman, M.K.: Onset dates of the south–west monsoon over Kerala for the period 1870–1900. Int. J. Climatol. **9**(3), 321–322 (1989)
6. Balmaseda, M.A., Trenberth, K.E., Källèn, E.: Distinctive climate signals in reanalysis of global ocean heat content. Geophys. Res. Lett. **40**, 1754–1759 (2013). doi:10.1002/grl.50382
7. Baur, F., Bartels, J., Bider, M., Sestoft, I.: Langjährige Beobachtungsreihen. In: Baur, F. (ed.) Meteorologisches Taschenbuch, vol. 1, Chap. 11, Tables 2 and 3, pp. 740–748. Geest & Portig, Leipzig (1962)
8. Bedrosian, E.: The analytic signal representation of modulated waveforms. Proc. IRE **50**(10), 2071–2076 (1962)
9. Bedrosian, E.: A product theorem for Hilbert transforms. Proc. IEEE **51**(5), 868–869 (1963)
10. Brönnimann, S., Luterbacher, J., Staehelin, J., Svendby, T.M.: An extreme anomaly in stratospheric ozone over Europe in 1940–1942. Geophys. Res. Lett. **31**(8), L08101 (2004). doi:10.1029/2004GL019611
11. Bruckstein, A.M., Donoho, D.L., Elad, M.: From sparse solutions of systems of equations to sparse modeling of signals and images. SIAM Rev. **51**(1), 34–81 (2009)
12. Cane, M.A., Zebiak, S.E.: A theory for El Niño and the southern oscillation. Science **228**(4703), 1085–1087 (1985)
13. Carl, P.: Monsoon dynamics in a low–dimensional GCM. WCRP-84, WMO/TD-No. 619(II), 773–780. WMO, Geneva (1994)
14. Carl, P.: Growth of thermal signal energy, phase coincidence with insolation—and cooling ahead? Geophys. Res. Abstr. CD-ROM **3**(OA25), 5267 (2001)
15. Carl, P.: Solar vs. thermal signal separation in the global surface air temperature series. In: International Conference on Earth System Modelling, Proceedings on CD-ROM, Hamburg, 15 pp. (2003)
16. Carl, P.: Synchronized motions within the instrumental climate record, 1870–1997. Terra Nostra Schr. Alfred-Wegener-Stiftung **6**, 89–95 (2003)
17. Carl, P.: MP based detection of synchronized motions across the instrumental climate record. In: Proceedings on IEEE Statistical Signal Processing Workshop, pp. 557–560. IEEE, Nice (2011). 978-1-4577-0568-7/11

18. Carl, P.: On the dynamical status of the climate system – II: synchronous motions galore across the records. In: Stavrinides, S.G., Banerjee, S., Caglar, H., Ozer, M. (eds.) Proceedings on Chaos and Complex Systems, pp. 529–539. Springer, Heidelberg (2013). doi:10.1007/978-3-642-33914-1_74
19. Carl, P.: A general circulation model en route to intraseasonal monsoon chaos. In: Banerjee, S., Rondoni, L. (eds.) Applications of Chaos and Nonlinear Dynamics in Science and Engineering. Understanding Complex Systems, vol. 3, Chap. 3, pp. 63–99. Springer, Heidelberg (2013). doi:10.1007/978-3-642-34017-8_3
20. Carl, P.: Atmospheric tracers and the monsoon system: lessons learnt from the 1991 Kuait oil well fires. In: Banerjee, S., Ercetin, S.S. (eds.) Chaos, Complexity and Leadership 2012. Springer Proceedings in Complexity, Chap. 47, pp. 371–410. Springer, Dordrecht (2014). doi:10.1007/978-94-007-7362-2_47
21. Carl, P., Behrendt, H.: Regularity based functional streamflow disaggregation: 1. Comprehensive foundation. Water Resour. Res. **44**(W02420) (2008). doi:10.1029/2004WR003724
22. Carl, P., Gerlinger, K., Hattermann, F.F., Krysanova, V., Schilling, C., Behrendt, H.: Regularity based functional streamflow disaggregation: 2. Extended demonstration. Water Resour. Res. **44**(W03426) (2008). doi:10.1029/2006WR005056; and corrigendum: Water Resour. Res. **44**(W06701) (2008). doi:10.1029/2008WR007105
23. Charney, J.G., DeVore, J.G.: Multiple flow equilibria in the atmosphere and blocking. J. Atmos. Sci. **36**(7), 1205–1216 (1979)
24. Chen, S.S., Donoho, D.L., Saunders, M.A.: Atomic decomposition by Basis Pursuit. SIAM Rev. **43**(1), 129–159 (2001)
25. Christiansen, B.: On the nature of the arctic oscillation. Geophys. Res. Lett. **29**(16), 1805 (2002). doi:10.1029/2001GL014130
26. Christensen, J.H., Christensen, O.B.: Severe summertime flooding in Europe. Nature **421**(6925), 805–806 (2003)
27. Claasen, T.A.C.M., Mecklenbräuker, W.F.G.: The Wigner distribution—a tool for time–frequency analysis. Part 2: discrete–time signals. Philips J. Res. **35**(4/5), 276–300 (1980)
28. Coumou, D., Petoukhov, V., Rahmstorf, S., Petri, S., Schellnhuber, J.: Quasi-resonant circulation regimes and hemispheric synchronization of extreme weather in boreal summer. Proc. Natl. Acad. Sci. **111**(34), 12331–12336 (2014)
29. Crowley, T.J.: Causes of climate change over the past 1000 years. Science **289**(5477), 270–277 (2000)
30. Daubechies, I.: The wavelet transform, time–frequency localization and signal analysis. IEEE Trans. Inf. Theory **36**(5), 961–1005 (1990)
31. Daubechies, I., Grossmann, A., Meyer, Y.: Painless nonorthogonal expansions. J. Math. Phys. **27**(5), 1271–1283 (1986)
32. Donoho, D.L., Elad, M., Temlyakov, V.N.: Stable recovery of sparse overcomplete representations in the presence of noise. IEEE Trans. Inf. Theory **52**(1), 6–18 (2006)
33. Doty, B.E.: Using the Grid Analysis and Display System (GrADS). Manual, Version 1.3.1. University of Maryland, College Park (1992)
34. Duane, G.S., Tribbia, J.J.: Weak Atlantic–Pacific teleconnections as synchronized chaos. J. Atmos. Sci. **61**(17), 2149–2168 (2004)
35. Emresoy, M.K., El-Jaroudi, A.: Evolutionary Burg spectral estimation. IEEE Signal Process. Lett. **4**(6), 173–175 (1997)
36. England, M.H., McGregor, S., Spence, P., Meehl, G.A., Timmermann, A., Cai, W., Gupta, A.S., McPhaden, M.J., Purich, A., Santoso, A: Recent intensification of wind-driven circulation in the Pacific and the ongoing warming hiatus. Nat. Clim. Change **4**, 222–227 (2014). doi:10.1083/NCLIMATE2106
37. Faybishenko, B.: Nonlinear dynamics in flow through unsaturated fractured porous media: status and perspectives. Rev. Geophys. **42**(2), RG2003 (2004)
38. Foukal, P., Fröhlich, C., Spruit, H., Wigley, T.M.L.: Variations in solar luminosity and their effect on the Earth's climate, Nature **443**(7108), 161–166 (2006)
39. Fraedrich, K.: An ENSO impact on Europe? A review. Tellus **46A**(4), 541–552 (1994)

40. Friis-Christensen, E., Lassen, K.: Length of the solar cycle: an indicator of solar activity closely associated with climate. Science **254**(5032), 698–700 (1991)
41. Fyfe, J.C., Gillett, N.P., Zwiers, F.W.: Overestimated global warming over the past 20 years. Nat. Clim. Change **3**, 767–769 (2013)
42. Gabor, D.: Theory of communication. J. Inst Electr. Eng. III **93**, 429–457 (1946)
43. Gerstengarbe, F.-W., Werner, P.C.: Katalog der Großwetterlagen Europas nach Paul Hess und Helmuth Brezowsky, 1881–1998, 5th revised and extended edition. Ber. Dt. Wetterd., 113, Offenbach (1999)
44. Ghil, M., Kimoto, M., Neelin, J.D.: Nonlinear dynamics and predictability in the atmospheric sciences. Rev. Geophys. **29**(Suppl.), 46–55 (1991)
45. Graf, H.-F.: On El Niño/Southern Oscillation and Northern Hemispheric temperature. Gerlands Beitr. Geophys. **95**(1), 63–75 (1986)
46. Graf, H.-F., Zanchettin, D.: Central Pacific El Niño, the "subtropical bridge," and Eurasian climate. J. Geophys. Res. **117**(D01102) (2012). doi:10.1029/2011JD016493
47. Graham, N.E., White, W.B.: The El Niño cycle: a natural oscillator of the Pacific ocean–atmosphere system. Science **240**(4857), 1293–1302 (1988)
48. Gribonval, R., Vandergheynst, P.: On the exponential convergence of Matching Pursuits in quasi-incoherent dictionaries. IEEE Trans. Inf. Theory **52**(1), 255–261 (2006)
49. Hahn, S.L.: Hilbert Transforms in Signal Processing. Artech House, Boston (1996)
50. Hess, P., Brezowsky, H.: Katalog der Großwetterlagen Europas, 1881–1976, 3rd revised and extended edition, Ber. Dt. Wetterd., 15, Offenbach (1977)
51. Houghton, J.T., Ding, Y., Griggs, D.J., Noguer, M., van der Linden, P. J., Dai, X., Maskell, K., Johnson, C.A. (eds.) IPCC: Climate Change 2001: The Scientific Basis. Contribution of Working Group I to the Third Assessment Report of the Intergovernmental Panel of Climate Change. Cambridge University Press, Cambridge (2001)
52. Hoyt, D.V., Schatten, K.H.: The Role of the Sun in Climate Change. Oxford University Press, Oxford (1997)
53. Huang, J., Higuchi, K., Shabbar, A.: The relationship between the North Atlantic oscillation and El Niño–southern oscillation. Geophys. Res. Lett. **25**(14), 2707–2710 (1998)
54. Huang, N.E., Shen, Z., Long, S.R., Wu. M.C., Shi, H.H., Zheng, Q., Yen, N.C., Tung, C.C., Liu, H.H.: The empirical mode decomposition and the Hilbert spectrum for nonlinear and non-stationary time series analysis. Proc. R. Soc. Lond. **454**, 903–995 (1998)
55. Huber, P.J.: Projection Pursuit. Ann. Stat. **13**(2), 435–475; incl. discussion, 475–525 (1985)
56. Hurrel, J.W.: Decadal trends in the North Atlantic Oscillation: regional temperatures and precipitation. Science **269**(5224), 676–679 (1995)
57. Jin, F.-F., Ghil, M.: Intraseasonal oscillations in the extratropics: Hopf bifurcation and topographic instabilities. J. Atmos. Sci. **47**(24), 3007–3022 (1990)
58. Jin, F.-F., Neelin, J.D., Ghil, M.: El Niño on the devil's staircase: annual subharmonic steps to chaos. Science **264**(5155), 70–72 (1994)
59. Jones, P.D.: Hemispheric surface air temperature variations: a reanalysis and an update to 1993. J. Clim. **7**(11), 1794–1802 (1994)
60. Jones, P.D., Jonsson, T., Wheeler, D.: Extension to the North Atlantic Oscillation using early instrumental pressure observations from Gibraltar and South–West Iceland. Int. J. Climatol. **17**(13), 1433–1450 (1997)
61. Kapala, A., Mächel, H., Flohn, H.: Behaviour of the centres of action above the Atlantic since 1881. Part II: Associations with regional climate anomalies. Int. J. Climatol. **18**(1), 23–36 (1998)
62. Krishnamurti, T.N., Bhalme, H.N.: Oscillations of a monsoon system. Part I. Observational aspects. J. Atmos. Sci. **33**(10), 1937–1954 (1976)
63. Lagarias, J.C.: Number theory and dynamical systems. Proc. Symp. Appl. Math. **46**, 35–72 (1992)
64. Lamb, H.H.: Re: the onset of the southwest monsoon over Kerala. Int. J. Climatol. **9**(3), 323 (1989)

65. Lau, K.-M., Peng, L., Sui, C.H., Nakazawa, T.: Dynamics of super cloud clusters, westerly wind bursts, 30–60 day oscillations and ENSO: an unified view. J. Meteorol. Soc. Jpn. **67**(2), 205–219 (1989)
66. Lean, J., Beer, J., Bradley, R.: Reconstruction of solar irradiance since 1610: implications for climate change. Geophys. Res. Lett. **22**(23), 3195–3198 (1995)
67. Lean, J., Wang, Y.-M., Sheeley, N.R., Jr.: The effect of increasing solar activity on the Sun's total and open magnetic flux during multiple cycles: implications for solar forcing of climate. Geophys. Res. Lett. **29**(24), 2224 (2002). doi:10.1029/2002GL015880
68. Lewis, N., Curry., J.A.: The implications for climate sensitivity of AR5 forcing and heat uptake estimates. Clim. Dyn. (2014). doi:10.1007/s00382-014-2342-y
69. Lorenz, E.N.: Can chaos and intransitivity lead to interannual variability? Tellus **42A**(3), 378–389 (1990)
70. Mächel, H., Kapala, A., Flohn, H.: Behaviour of the centres of action above the Atlantic since 1881. Part I: Characteristics of seasonal and interannual variability. Int. J. Climatol. **18**(1), 1–22 (1989)
71. Madden, R.A., Julian, P.R.: Observations of the 40–50-day tropical oscillation—a review. Mon. Weather Rev. **122**(5), 814–837 (1994)
72. Mallat, S.: A Wavelet Tour of Signal Processing, 2nd edn. Academic, San Diego (1999)
73. Mallat, S.G., Zhang, Z.: Matching Pursuits with time–frequency dictionaries. IEEE Trans. Signal Process. **41**(12), 3397–3415 (1993)
74. Maragos, P.: Differential morphology. In: Mitra, S.K., Sicuranza, G.L. (eds.) Nonlinear Image Processing, chap. 10, pp. 289–329. Academic, San Diego (2001)
75. McKinnon, J.: Sunspot numbers: 1610-1985. Report UAG-95, WDC-A for Solar-Terrestrial Physics (1987)
76. Meyboom, P.: Estimating groundwater recharge from stream hydrographs. J. Geophys. Res. **66**(4), 1203–1214 (1961)
77. Mudelsee, M., Börngen, M., Tetzlaff, G., Grünewald, U.: No upward trend in the occurrence of extreme floods in central Europe. Nature **425**(6954), 166–169 (2003)
78. Normand, C.: Monsoon seasonal forecasting. Q. J. R. Meteorol. Soc. **79**(342), 463–473 (1953)
79. Parker, D.E., Legg, M., Folland, C.K.: A new daily central England temperature series, 1772–1991. Int. J. Climatol. **12**(4), 317–342 (1992)
80. Parker, D.E., Jones, P.D., Folland, C.K., Bevan, A.: Interdecadal changes of surface temperature since the late nineteenth century. J. Geophys. Res. **99**(D7), 14373–14399 (1994)
81. Parthasarathy, B., Munot, A.A., Kothawale, D.R.: Monthly and seasonal rainfall series for All-India homogeneous regions and meteorological subdivisions: 1871–1994. RR–065, Indian Institute of Tropical Meteorology, Pune (1995)
82. Raj, Y.E.A.: Objective determination of northeast monsoon onset dates over coastal Tamil Nadu for the period 1901–90. Mausam **43**(3), 273–282 (1992)
83. Raj, Y.E.A.: A statistical technique for determination of withdrawal of northeast monsoon over coastal Tamil Nadu. Mausam **49**(3), 309–320 (1998)
84. Rasmusson, E.M., Wallace, J.M.: Meteorological aspects of the El Niño/Southern Oscillation. Science **222**(4629), 1195–1202 (1983)
85. Rodwell, M.J., Hoskins, B.J.: Monsoons and the dynamics of deserts. Q. J. R. Meteorol. Soc. **122**(534), 1385–1404 (1996)
86. Rogers, J.C.: The association between the North Atlantic Oscillation and the Southern Oscillation in the northern hemisphere. Mon. Weather Rev. **112**(10), 1999–2015 (1984)
87. Selten, F.M., Branstator, G.W., Dijkstra, H.A., Kliphuis, M.: Tropical origins for recent and future Northern Hemisphere climate change. Geophys. Res. Lett. **31**, L21205 (2004). doi:10.1029/2004GL020739
88. Sirocko, F., Sarntheim, M., Erlenkeuser, H., Lange, H., Arnold, M., Duplessy, J.C.: Century-scale events in monsoonal climate over the past 24,000 years. Nature **364**(6435), 322–324 (1993)

89. Sirocko, F., Garbe–Schönberg, D., McIntyre, A., Molfino, B.: Teleconnections between the subtropical monsoons and high-latitude climates during the last deglaciation. Science **272**(5261), 526–529 (1996)
90. Sivakumar, B.: Nonlinear dynamics and chaos in hydrologic systems: latest developments and a look forward. Stoch. Environ. Res. Risk Assess. **23**, 1027–1036 (2009). doi:10.1007/s00477-008-0265-z
91. So, P.: Unstable periodic orbits. Scholarpedia **2**(2), 1353 (2007). doi:10.4249/scholarpedia.1353
92. Solomon, S., Qin, D., Manning, M., Chen, Z., Marquis, M., Averyt, K.B., Tigmor, M., Miller, H.L. (eds.) IPCC: Climate Change 2007: The Physical Science Basis. Contribution of Working Group I to the Fourth Assessment Report of the Intergovernmental Panel of Climate Change. Cambridge University Press, Cambridge (2007)
93. Soman, M.K., Krishna Kumar, K.: Space–time evolution of meteorological features associated with the onset of Indian summer monsoon. Mon. Weather Rev. **121**(4), 1177–1194 (1993)
94. Sontakke, N.A., Pant, G.B., Singh, N.: Construction of All-India summer monsoon rainfall series for the period 1844–1991. J. Clim. **6**(9), 1807–1811 (1993)
95. Suarez, M.J., Schopf, P.S.: A delayed action oscillator for ENSO. J. Atmos. Sci. **45**(21), 3283–3287 (1988)
96. Torrence, C., Compo, G.P.: A practical guide to wavelet analysis. Bull. Am. Meteorol. Soc. **79**(1), 61–78 (1998)
97. Tropp, I.: Greed is good: algorithmic results for sparse approximation. IEEE Trans. Inf. Theory **50**(10), 2231–2241 (2004)
98. Tropp, I.: Just relax: convex programming methods for identifying sparse signals in noise. IEEE Trans. Inf. Theory **52**(3), 1030–1051 (2006)
99. Turner, P.J.: ACE/gr user's manual. Graphics for exploratory data analysis. Software Documentation Series, SDS3, 91-11, Oregon Graduate Institute of Science and Technology (1992)
100. Tziperman, E., Stone, L., Cane, M.A., Jarosh, H.: El Niño chaos: overlapping of resonances between the seasonal cycle and the Pacific ocean–atmosphere oscillator. Science **264**(5155), 72–74 (1994)
101. van der Pol, B.: The fundamentals of frequency modulation. J. Inst. Electr. Eng. III **93**, 153–158 (1946)
102. Vautard, R., Yiou, P., Ghil, M.: Singular-spectrum analysis: a toolkit for short, noisy chaotic signals. Physica D **58**(1–4), 95–126 (1992)
103. Visser, R., Molenaar, J.: Trend estimation analysis in climatological time series: an application of structural time series models and the Kalman filter. J. Clim. **8**(5), 969–979 (1995)
104. von Storch, H., Barkhordarian, A., Hasselmann, K., Zorita, E.: Can climate models explain the recent stagnation in global warming? (2013). http://www.academia.edu/4210419
105. Wallace, J.M.: North Atlantic Oscillation/annular mode: two paradigms – one phenomenon. Q. J. R. Meteorol. Soc. **126**(564), 791–805 (2000)
106. Wallace, J.M., Thompson, D.W.J.: The Pacific center of action of the Northern Hemisphere annular mode: real or artifact? J. Clim. **15**(14), 1987–1991 (2002)
107. Walter, K., Graf, H.-F.: Life cycles of the North Atlantic teleconnections under strong and weak polar vortex conditions. Q. J. R. Meteorol. Soc. **132**(615), 467–483 (2006)
108. Wang, B., Wang, Y.: Temporal structure of the Southern Oscillation as revealed by waveform and wavelet analysis. J. Clim. **9**(7), 1586–1598 (1996)
109. Webster, P.J., Yang, S.: Monsoon and ENSO: selectively interactive systems. Q. J. R. Meteorol. Soc. **118**(507), 877–926 (1992)
110. Webster, P.J., Magaña, V.O., Palmer, T.N., Shukla, J., Tomas, R.A., Yanai, M., Yasunari, T.: Monsoons: processes, predictability, and the prospects for prediction. J. Geophys. Res. **103**(C7), 14451–14510 (1998)
111. Yasunari, T., Seki, Y.: Role of the Asian monsoon on the interannual variability of the global climate system. J. Meteorol. Soc. Jpn. **70**(1B), 177–189 (1992)

112. Young, P.C.: Parallel processes in hydrology and water quality: a unified time series approach. J. Inst. Water Environ. Manag. **6**(5), 598–612 (1992)
113. Zakharov, V.E., Ostrovsky, L.A.: Modulation instability: the beginning. Physica D **238**, 540–548 (2009)
114. Zhao, J.-X., Ghil, M.: Nonlinear symmetric instability and intraseasonal oscillations in the tropical atmosphere. J. Atmos. Sci. **48**(24), 2552–2568 (1991)

Chapter 6
Application of Random Matrix Theory to Complex Networks

Aparna Rai and Sarika Jalan

Abstract The present article provides an overview of recent developments in spectral analysis of complex networks under random matrix theory framework. Adjacency matrix of unweighted networks, reviewed here, differ drastically from a random matrix, as former have only binary entries. Remarkably, short range correlations in corresponding eigenvalues of such matrices exhibit Gaussian orthogonal statistics of RMT and thus bring them into the universality class. Spectral rigidity of spectra provides measure of randomness in underlying networks. We will consider several examples of model networks vastly studied in last two decades. To the end we would provide potential of RMT framework and obtained results to understand and predict behavior of complex systems with underlying network structure.

6.1 Introduction

6.1.1 Complex Networks

Last two decades have been an era of complex systems analyzed in complex network framework. Each complex system can be assumed as a collection of interacting units, and hence can be represented in term of a network where nodes correspond to units of the complex system and links between nodes denoting interactions. This complex networks framework has demonstrated remarkable success in predicting and controlling functional behavior of corresponding complex system [1, 2]. The network concept has been applied to real systems coming from various different fields such as biology (e.g. food-web, nervous system, cellular metabolism,

A. Rai
Complex Systems Lab, Centre for Biosciences and Biomedical Engineering, Indian Institute of Technology Indore, Khandwa Road, Indore 452017, India

S. Jalan (✉)
Complex Systems Lab, Discipline of Physics, School of Basic Sciences, Centre for Biosciences and Biomedical Engineering, Indian Institute of Technology Indore, Khandwa Road, Indore 452017, India
e-mail: sarika@iiti.ac.in

S. Banerjee, L. Rondoni (eds.), *Applications of Chaos and Nonlinear Dynamics in Science and Engineering - Vol. 4*, Understanding Complex Systems,
DOI 10.1007/978-3-319-17037-4_6

protein-protein interaction network, gene regulatory networks), social systems (e.g. scientific collaboration, citation), linguistic networks, and technological systems (e.g. Internet, power-grid) etc. (for reviews, see, e.g., [1]).

The first step towards the success of network framework was the detection of universal features in systems as diverse as human brain and world-wide-web, and its ability to propose simple models capturing these universalities. These network models are based on very simple rules, and contain basic information governing behavior and evolution of corresponding systems.

Traditionally, networks have been studied under graph theory. Random graphs were studied by Erdös and Rényi in a series of papers during late 1950s [3]. According to the random graph model, a complex system can be denoted by nodes N and links, where every pair of nodes are connected with a probability p, and thus creating a graph with approximately pN^2 edges distributed randomly. For about 40 years, the model was a huge success in describing various phenomena. And then came a huge transition, brought by two different groups of A.-L. Barabási and S. Strogatz, which demonstrated that real world systems may not have only random interactions, and indeed they exhibit some universal properties such as scale-free and small-world. Barabási et al. proposed a very simple model based on some physical principles leading to the emergence of scale-free nature of a growing network [4]. According to this model a new node gets attached to a previously existing node based on a preferential attachment. This rule leads to a power law degree distribution, where only few nodes are responsible to carry the whole network and hence are very important. Watts and Strogatz proposed an algorithm to generate popularly known as small-world network [5]. This model captures randomness characterized by small diameter, and regularity characterized by clustering of real-world networks. This model emphasizes on the importance of random connections in networks. Following this came spurt of activities in complex system studies under network framework.

These works have mainly focused on following aspects: (1) direct studies of the real-world networks and measuring their various structural properties such as degree distribution, diameter, clustering coefficient etc., (2) proposing new random graph models motivated by these studies, and (3) computer simulations of the new models and measuring their properties [1, 2].

6.1.2 Structural Properties of Various Model Networks

As discussed above, investigations done by Barabási et al. for various real world systems reveal that they are scale-free, which means that the degree distribution $p(k)$, fraction of nodes that have k number of connections with other nodes, decays as power law, i.e. $p(k) \propto k^{-\gamma}$, where exponent γ depends on the topology of the networks. The scale-free nature of networks suggests that there exist few nodes with very high degree. Some other analysis, by Newman and others, of real-world networks reveal that complex networks have community or module structures [6, 7]. According to these studies, there exists few nodes with very high betweenness,

and are responsible to connect different communities. This direction of looking at the networks focuses on the importance of nodes based on its position in the network. On the other hand, Erdös-Rényi (ER) and Watts-Strogatz (SW) models emphasize on random connections in the networks. In ER model any two nodes are connected with probability p. One of the most interesting characteristics of ER model is a sudden emergence of various global properties; most important one being emergence of giant cluster. For a $p > p_c$, while number of nodes in the graph remain constant, giant cluster emerges through a phase transition. Further, Watts-Strogatz model exhibits the small-world transition with fine tuning of the number of random connections.

6.1.3 Spectral Properties of Model Networks

Apart from the above mentioned investigations which focus on direct measurements of structural properties of networks, there exists a vast literature demonstrating that properties of networks or graphs could be well characterized by the spectrum of associated adjacency and Laplacian matrix [8]. For an unweighted graph, adjacency matrix is defined in following way: $A_{ij} = 1$, if i and j nodes are connected and zero otherwise. For undirected networks, adjacency and Laplacian both are symmetric matrices and consequently have real eigenvalues. Eigenvalues of graph are called graph spectra and they provide information about some basic topological properties of underlying network [8, 9]. Recently, in order to characterize networks, it was proposed to study spectra of eigenvalues of the adjacency matrices as a fingerprint of the networks [10]. The rich information about the topological structure and diffusion processes can be extracted from the spectral analysis of the networks. Studies of spectral properties of the complex networks may also be of a general theoretical interest.

During last 20 years several important applications of the spectral graph theory in physics and chemistry problems have been discovered [8, 9]. For example liquid flowing through a system of communicating pipes are described by a system of linear differential equations. The corresponding matrix appears to be the Laplacian of the underlying graph. Speed of convergence of the liquid flowing process towards an equilibrium state is measured by the second smallest eigenvalue of graph Laplacian [8]. Second smallest eigenvalue of graph Laplacian is called the algebraic connectivity of a graph and is used to understand behavior of dynamical processes on the underlying networks as well [11, 12]. Particularly, Laplacian spectra of networks have been investigated enormously to understand synchronization of coupled dynamics on networks [13, 14]. Extremal eigenvalues of the Laplacian have been shown to exhibit high influence on the synchronizability of a network [15]. Similarly, multiplicity of eigenvalues, particularly at 0 and 1, have direct relations with properties of graphs [16, 17].

6.1.4 Random Matrix Theory

Random matrix theory (RMT) was proposed by Wigner to explain statistical properties of nuclear spectra [18]. Later this theory was successfully applied for studying of spectra of different complex systems including disordered systems, quantum chaotic systems, spectra of large complex atoms etc. [19]. RMT is also shown to be of great interest in understanding the statistical structure of the empirical cross-correlation matrices appearing in the study of multivariate time series. The classical complex systems where RMT has been successfully applied are stock market (cross-correlation matrix is formed by using the time series of price fluctuations of different stock) [20]; brain (matrix is constructed by using EEG data at different locations) [21]; patterns of atmospheric variability (cross-correlations matrix is generated by using temporal variation of various atmospheric parameters) [22], etc.

In the following we describe main RMT tools which have been used to analyze network spectra. Recently there has been considerable amount of work done in the context of random matrix analysis of complex networks. These works have mainly used two most popular tools of RMT, i.e. eigenvalue fluctuations in terms of short range correlations, and spectral rigidity to probe long range correlations in eigenvalues. For completeness we describe these aspects of RMT which have been used to study network spectra. In the random matrix analysis of eigenvalues spectra, one has to consider two kinds of properties: (1) global properties, like spectral density or distribution of eigenvalues $\rho(\lambda)$, and (2) local properties, among which eigenvalue fluctuations around $\rho(\lambda)$ is the most popular one. Spectral density of random matrices, whose elements are Gaussian distributed random numbers, follows Wigner's semicircular law [18].

Nearest Neighbor Spacing distribution: We denote the eigenvalues of networks by $\lambda_i,\ i = 1, \ldots, N$, where N is the size of the network. The eigenvalue fluctuations are generally obtained from the nearest neighbour spacing distribution (NNSD) of the eigenvalues. In order to get universal properties of the fluctuations of the eigenvalues, it is customary in RMT to unfold the eigenvalues by a transformation $\overline{\lambda}_i = \overline{N}(\lambda_i)$, where $\overline{N}$ is the averaged integrated eigenvalue density [18]. Since we do not have any analytical form for $\overline{N}$, we numerically unfold the spectrum by polynomial curve fitting. After the unfolding, the average spacing will be *unity*, which is independent of the system. Using the unfolded spectra, we calculate the spacing as

$$s^{(i)} = \overline{\lambda}_{i+1} - \overline{\lambda}_i \tag{6.1}$$

and due to the above unfolding, the average nearest-neighbor spacing $\langle s \rangle$ becomes *unity* being independent of the system. The NNSD ($P(s)$) is defined as the probability distribution of these s^i's. In case of Poisson statistics, $P(s) = \exp(-s)$,

whereas for GOE, $P(s) = \frac{\pi}{2} s \exp\left(-\frac{\pi s^2}{4}\right)$. For the intermediate cases, the spacing distribution is described by Brody distribution [23];

$$P_\beta(s) = As^\beta \exp\left(-\alpha s^{\beta+1}\right), \tag{6.2}$$

where

$$A = (1+\beta)\alpha \text{ and } \alpha = \left[\Gamma\left(\frac{\beta+2}{\beta+1}\right)\right]^{\beta+1}$$

This is a semiempirical formula characterized by the parameter β. As β goes from 0 to 1, the Brody distribution smoothly changes from Poisson to GOE. We fit the spacing distributions of different networks by the Brody distribution $P_\beta(s)$. This fitting gives an estimation of β, and consequently identifies whether the spacing distribution of a given network is Poisson or GOE or intermediate of these *two*.

The NNSD reflects only local correlations among the eigenvalues. The spectral rigidity, measured by the Δ_3-statistic of RMT, gives information about the long-range correlations among the eigenvalues and is more sensitive test for RMT properties of the matrix under investigation [18, 24]. Following we describe the procedure to calculate this quantity.

Δ_3 statistics: It measures the least-square deviation of the spectral staircase function representing the cumulative density $N(\bar{\lambda})$ from the best straight line fitting for a finite interval L of the spectrum, i.e.,

$$\Delta_3(L;x) = \frac{1}{L} \min_{a,b} \int_x^{x+L} \left[N(\bar{\lambda}) - a\bar{\lambda} - b\right]^2 d\bar{\lambda} \tag{6.3}$$

where a and b are obtained from a least-square fit. Average over several choices of x gives the spectral rigidity $\Delta_3(L)$. The most rigid spectrum is the "picket fence" with all spacings equal (e.g., 1-D harmonic oscillator), therefore maximally correlated with constant $\Delta_3(L)$ $(= 1/12)$. At another extreme, for the uncorrelated eigenvalues, $\Delta_3(L) = L/15$, reflecting strong fluctuations around the spectral density $\rho(\lambda)$. The GOE case is intermediate of these *two* extremes. Here $\Delta_3(L)$ depends *logarithmically* on L, i.e.,

$$\Delta_3(L) \sim \frac{1}{\pi^2} \ln L. \tag{6.4}$$

The article is arranged as follows: after the first introductory section about importance and excitement of network theory, we introduce various RMT tools used to analyze complex networks. The next section provides a short introduction to spectral density of networks. Section 6.3 considers different model networks, viz. random, scale-free, small-world and modular networks one by one, and explain random matrix results for their spectra. Last section lists down major results

of random matrix analysis of networks and discusses future prospective of this framework.

6.2 Spectral Density of Networks

First of all we would review known properties of spectral density of various model networks. The spectral density of the adjacency matrix of ER random graphs, whose elements are randomly 0 or 1, tend to have the asymptotic spectral density with the semicircle shape in accordance with the Wigner theorem which is a classical result of RMT [18]. However, Rodgers and Bray have demonstrated that the density of eigenvalues of a sparse random matrix deviates from the Wigner semicircular distribution and has a tail at large eigenvalues [25, 26]. With the increasing availability of large maps of real-world networks, the analysis of spectral densities of adjacency matrix of real-world networks and model networks having real-world properties have also begun [27–29]. These analyses elucidate that the spectral densities of model networks and real-world networks are not semicircular, instead they have some specific features depending on the minute details of the corresponding models. Spectral density of scale-free model networks exhibits triangular distribution [27, 29] with the tail exhibiting a power law behavior. This power law behavior was analytically confirmed by Dorogovtsev et al. for tree-like scale-free graphs [28, 30]. Explicit solutions reveal that the spectral density of scale-free networks decay as a power law with the decay exponent $\sigma_a = 2\gamma - 1$ [31]. Using replica method Rodgers et al. found a similar power law for Goh, Kahng and Kim's static model in the limit $p \to \infty$ [32]. Spectral density of weighted Laplacian and weighted adjacency matrices for scale-free networks in limit of large mean degree has been derived by Kim and Kahng [33]. Small-world model networks have very complex spectral density with many sharp peaks, while the spectral density of scale-free model networks exhibits triangular distribution [27, 29]. Real world networks exhibit very different spectral density than exhibited by any of the model networks discussed above [34, 35]. In general, they have a very high peak at zero eigenvalue of the adjacency matrix [17, 29, 35].

6.3 Random Matrix Analysis of Network Spectra

One of the most celebrated techniques in RMT is nearest neighbor spacing distribution $\rho(s)$ of eigenvalues. For matrix having Gaussian distributed random numbers, it follows GOE statistics of RMT, as described in Sect. 6.1.4. As seen from the previous section describing spectral density of adjacency matrix of networks, one can notice that network spectra have very different properties than exhibited by those of random matrices. Even spectra of random networks also deviate from Wigner's prediction towards the tail.

Before proceeding further we would like to note few basic differences of adjacency matrix generated for unweighted networks and random matrices. The first most important difference is that the entries in adjacency matrices are 0 and 1. Other differences follow from different types of networks, and networks model based on properties of real world systems. Scale-free networks lead to matrices having very large entries of 1 in few rows and most of the rows having as few as only one non-zero entry. Modular networks have patches of dense 1 entries. Since real world networks are sparse, i.e. they have very less average degree, which leads to most of zeros in corresponding adjacency matrix. Because of all these properties of adjacency matrix of networks, it is but natural to expect that spectral density would differ considerably than that of random matrices, and hardly we get surprised by observing deviation from Wigner's semicircular law and typical structural characteristic being reflected in density distribution.

Upon applying other tools of RMT to network spectra, Jalan and coauthor found that though spectral density deviates from RMT predicted results, eigenvalue fluctuations characterized by nearest neighbor spacing density and spectral rigidity of network spectra do follow GOE statistics of RMT [35]. Furthermore they demonstrated that spectra rigidity test performed by Δ_3 statistics provide a measure for *randomness* in random networks [36]. In the following we review all the results obtained for network spectra under RMT framework.

6.3.1 Random Networks

First we consider an ensemble of random networks generated by using Erdös-Rényi algorithm. Starting with N nodes, random connections between pairs of nodes are made with probability p. The average degree of the graph is $k = 2N_c/N = p(N-1) \sim pN$. There exists a critical probability $p_c(N)$ for which one gets a large connected component. The degree distribution of this random graph is a binomial distribution

$$P(k) = C_k^{N-1} p^k (1-p)^{N-1-k}$$

The corresponding adjacent matrix would have $2pN^2$ entries with 1 and rest $(1-2p)N^2$ entries zero, with summation of row entries depicting binomial distribution as stated in the previous line. For $N = 2{,}000$, value of $p = 0.01$ yields a connected network with average degree $p \times N = 20$. We can see that for such a small value of p, only 1 % entries in the adjacency matrix are nonzero, and rest entries are zero. The motivation behind such a small p values are sparseness observed in real world networks [1].

First, eigenvalue spectrum of the network generated using the above algorithm is calculated. These eigenvalues are unfolded using the technique described in Sect. 6.1.4. This method yields eigenvalues with constant spectral density on the

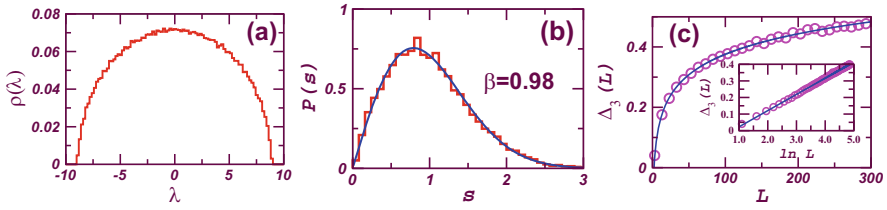

Fig. 6.1 (**a**) Density distribution, (**b**) NNSD and (**c**) Δ_3 statistics for random network with size $N = 2{,}000$ and average degree $\langle k \rangle = 20$. In *middle panel*, the histograms are numerical results and the *solid lines* represent fitted Brody distribution. For *last panel*, the *circles* are numerical results and the *solid curve* is the GOE prediction of RMT. *Inset* plots the $\Delta_3(L)$ in semi-logarithmic scale, in this scale it has the slope 0.0975. All figures are plotted for the average over ten realizations of the networks

average. These unfolded eigenvalues are used to calculate NNSD. The same procedure is repeated for an ensemble of the networks generated for different random realizations. Figure 6.1 plots ensemble average spacing distribution NNSD and Δ_3 statistics [35]. By fitting this ensemble averaged NNSD with the Brody formula given in Eq. (6.2) provides an estimate of the Brody parameter. The estimated value of Brody parameter noted in the figure clearly indicates that NNSD follows GOE prediction of RMT. As explained in the introduction that NNSD only tells about the short range correlations among the eigenvalues. Therefore, to probe for the long range correlations $\Delta_3(L)$ statistic is used. $\Delta_3(L)$ is calculated following Eq. (6.3). Figure 6.1 plots this statistics for the same ensemble as used for the NNSD calculations above [37]. It can be seen that $\Delta_3(L)$ statistic agrees very well with the RMT prediction, given by Eq. (6.4), up to very large value of L, i.e., $L \sim 300$. Inset of this figure exhibits the same in semi-logarithmic scale. Here one can see the expected linear behavior of $\Delta_3(L)$ with slope of 0.0978 which is very close to the RMT predicted value $1/\pi^2 \simeq 0.1013$.

All results discussed here are for ensemble average. Each individual network in the ensemble follows random matrix predictions with very good accuracy, however to make the statistical analysis more credible, one considers results for an ensemble. For smaller network size one needs to take more realization in an ensemble in order to get good accuracy.

6.3.2 *Scale-Free Networks*

Scale-free networks are mostly modeled using algorithm provided by Barabási and Albert [1]. Starting with a small number, m_0 of the nodes, a new node with $m \leq m_0$ connections is added at each time step. This new node connects with an already existing node i with probability $\pi(k_i) \propto k_i$, where k_i is the

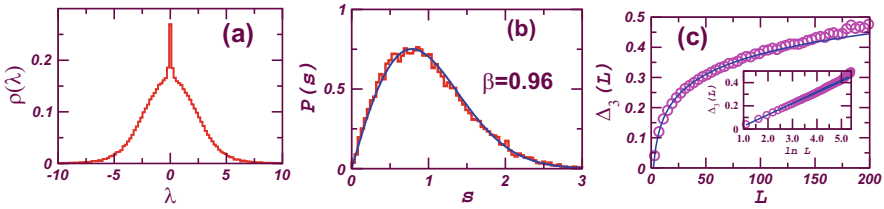

Fig. 6.2 (**a**) Density distribution, (**b**) NNSD and (**c**) Δ_3 statistics for scale-free network with $N = 2{,}000$ and $\langle k \rangle = 20$

degree of the node i. After τ time steps the model leads to a network with $N = \tau + m_0$ nodes and $m\tau$ connections [38]. This model generates a scale-free network, i.e., the probability $P(k)$, that a node has degree k decays as a power law;

$$P(k) \sim k^{-\gamma},$$

where γ is a constant and for the type of probability $\pi(k)$ used here $\gamma = 3$. Other forms for the probability $\pi(k)$ are also possible which give different values of γ. However, nature of spectral density and correlations in eigenvalues are independent of the value of γ. Figure 6.2 presents spectral density, NNSD and Δ_3 statistics plots for network parameters $N = 2{,}000$ and $\langle k \rangle = 20$ [35, 37]. NNSD and Δ_3 statistics are calculated following same procedure as described for random networks. Figure 6.2a demonstrates that spectral density follows typical triangular shape with peak at zero. Figure 6.2b demonstrates that NNSD of scale-free network follows GOE statistics with Brody parameter close to $\beta \sim 1$. Figure 6.2c depicts that Δ_3 statistics for scale-free network agrees very well with the RMT prediction for very large value of L. Inset of this sub-figure depicts the expected linear behavior of $\Delta_3(L)$ in semi-logarithmic scale for this range with slope very close to the RMT predicted value of $1/\pi^2$.

Universality of NNSD for random and scale-free networks seems to give the impression that these networks have same amount of randomness but Δ_3 results tell that the scale-free network is not as much random as the random network. This is obvious from their construction algorithms as well, but Δ_3 statistics captures this property which is a very important result. The finding also suggests that scale-free networks have some specific features that cannot be modeled by RMT. It may be noted that one can generate scale-free networks by using other algorithms as well [39, 40], for these networks also spacing distributions and spectral rigidity results will have qualitatively similar behaviors, except that the range of agreement of L with the random matrix prediction would depend upon the amount of randomness in the networks.

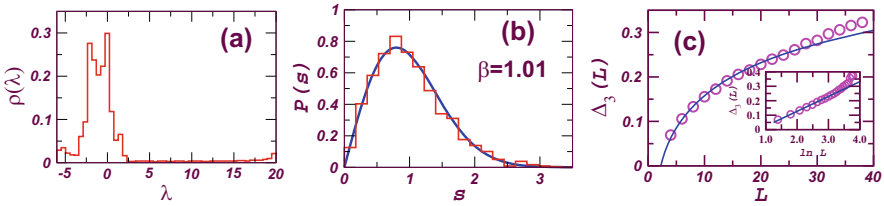

Fig. 6.3 For small-world network with $N = 2{,}000$ and $\langle k \rangle = 20$. (**a**) illustrates the density distribution depicting multi-peak structure. (**b**) depicts that nearest-neighbor spacing distribution (NNSD) $P(s)$ of the adjacency matrices of small-world network follows GOE statistics. The histograms are numerical results and the *solid lines* represent fitted Brody distribution. (**c**) plots $\Delta_3(L)$ statistics for eigenvalues spectra of the random network. The *circles* are numerical results and the *solid curve* is GOE prediction of RMT. *Inset* shows the $\Delta_3(L)$ in semi-logarithmic scale

6.3.3 Small-World Networks

Small-world networks are constructed using the following algorithm of Watts and Strogatz [5]. Starting with an one-dimensional ring lattice of N nodes in which every node is connected to its $k/2$ nearest neighbors, each connection of the lattice is rewired randomly with the probability p such that self-connections and multiple connections are excluded. Thus $p = 0$ gives a regular network and $p = 1$ gives a completely random network. For $N = 2{,}000$ and $\langle k \rangle = 20$, the typical small-world behavior is observed around $p = 0.005$ [36]. Figure 6.3 plots density distribution, NNSD and Δ_3 statistics for ensemble average of networks generated with above parameters. Same procedure as described in Sect. 6.1.4 has been used to calculate NNSD and Δ_3 statistics for the spectra. Figure 6.3a indicate that density distribution is complicated with several peaks. One peak is always at $\lambda = 0$. For different network parameters, the exact positions of other peaks may vary but overall form of spectral density remains similar. Figure 6.3b demonstrates that NNSD of this network follows GOE statistics with β very close to 1. Figure 6.3c plots the $\Delta_3(L)$ statistic for the spectrum of adjacency matrix corresponding to the small-world network with $p = 0.005$. Inset of this figure shows the expected linear behavior of $\Delta_3(L)$ in semi-logarithmic scale for $L \sim 30$ with slope of very close to the RMT predicted value $1/\pi^2$. $\Delta_3(L)$ statistics for the small-world network agrees very well with the RMT prediction for sufficiently large L, (i.e., $L \sim 30$ for these network parameters), but much less than the same for random and scale-free networks, implying that besides randomness, small-world network has specific features also. This again suggests that the behavior of Δ_3 statistics can be used to understand the amount of randomness in the networks. More specifically deviation from the GOE predicted behavior corresponds to the system specific features in the network [36].

All simulations here are quoted for average degree 20. For sparser ($\langle k \rangle < 20$) and denser networks ($\langle k \rangle > 20$ to $\langle k \rangle \sim N$), same universal behavior are found as far as there exists a certain amount of randomness. Problems exist with very sparse

networks, such as degree *two*, and very dense networks such as degree $\sim N$. For sparse networks one gets several degenerate eigenvalues [41]. In those cases, one has to first get rid of the degeneracy to conclude anything under RMT framework. Similarly for dense networks, universal spacing distribution is observed till very large value of average degree. For $\langle k \rangle \sim N$, largest eigenvalue has very high value than the rest of $N - 1$ eigenvalues which are very close to each other, becoming equal in the limiting case of all to all connections $\langle k \rangle = N - 1$. For example, random networks with $p = 0.95$ (which means that the network has 95 % of maximum possible connections), also follow RMT predictions of universal spacing distributions till very large scale. As the number of connections is increased further, one starts getting degenerate eigenvalues and for $p = 0.999$ high degeneracy at various values (such as $\lambda = -1, 0, 1$) are observed keeping it trivially out from the RMT studies.

6.3.4 Modular Networks

In this section we would present results for spectral behavior of networks having community structure under the framework of RMT. The study of community structure helps to elucidate the organization of networks, and eventually could be related to the functionality of groups of nodes [6, 7]. Regardless of the type of real world networks in terms of the degree and other structural properties [1], it is possible to distinguish communities in the whole networks [6]. However, the question of definition of the community is problematic, and usually community is assigned to the nodes which are connected densely among themselves, and are only sparsely connected with other nodes outside the community. This simple approach considers more densely connected nodes as a definition of community, and does not pay attention to the detailed structure of the connections [7].

RMT analysis of network spectra demonstrates that spectra carries signature of community structure. NNSD detects even a small mixing of communities in a network, whereas spectral rigidity test performed by Δ_3 statistics provides signature for larger mixing, which is, in general observed in real world networks.

Let us assume, for simplicity, that communities are modeled by random networks. Random matrices corresponding to unweighted random networks have entries 0 and 1, where number of 1's in a row follows a Gaussian distribution with mean p and variance $p(1 - p)$. This type of matrix is very well studied within the RMT framework [18, 42] and as explained in Sect. 6.3.1. Let us turn our attention to the following structure: (1) Take m random networks with connection probability p; the spectral behavior of the matrix corresponding to each of these sub-networks (blocks) separately follows GOE statistics. The matrix corresponding to the full network would be a m block diagonal matrix. (2) Introduce random connections among these sub-networks with probability q. This configuration leads to m block matrix, with blocks having entries *one* with portability p, and off diagonal blocks

having entries *one* with probability q. The above networks can be casted in the following form [43]:

$$A = A_0 + A_q \tag{6.5}$$

A_0 is a m blocks diagonal random matrix, where each block represents one community, and the off-diagonal block matrix A_q denotes the interactions among the communities. Each block in A_q is a random matrix, which for large N has mean q and deviation $q(1-q)$. The ratio q/p, which can be considered as the relative strength of A_q and A_0, measures the deformation from the block-diagonal form of the matrix, or from the perfect structured network. The value $q/p = 1$, which corresponds to equal strength of inter and intra-community connections, yields complete random network.

Left panel of Fig. 6.4 plots the spectral density for $m = 2$ block matrices having qN^2 non-zero off diagonal entries, corresponding to the two sub-networks connected with probability q. As discussed earlier q varies from $q = 0$, which corresponds to the two completely disconnected sub-networks ($A = A_0$), to $q = p$ leading to a single random network. The cases for $0 < q << p$ correspond to the configurations when the initial community structure is almost preserved. Increase in the value of q leads more entries of *one* in the matrix A_q [Eq. (6.5)]. Finally the $q = p$ case destroys the community structure completely, and the network can be treated as one single random network. Left panel of Fig. 6.4 presents the density distribution of eigenvalues for various values of q. The eigenvalues are scaled with respect to the spectra of the network for $q/p = 1$. With this scaling, the density distributions are not semicircular for values of $q < p$. As the coupling between the two blocks increases ($q > 0$), the density distribution manifest a transition to the semicircular form at $q = p$:

$$\rho(\lambda) = \frac{2}{\pi\lambda_0^2}\sqrt{(\lambda_0^2 - \lambda^2)},$$

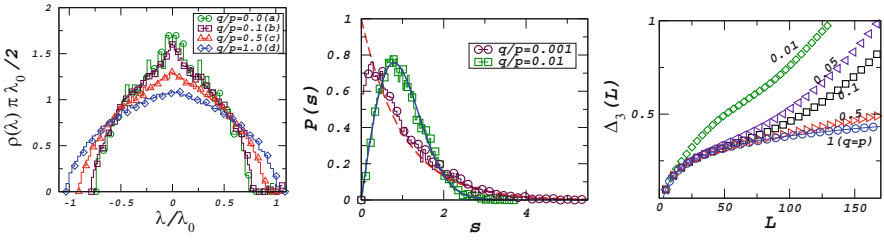

Fig. 6.4 Density distribution (*left panel*), NNSD (*middle panel*), Δ_3 statistics (*right panel*) of the two random sub-networks connecting each other with probability (a) $q = 0$ and $q/p = 0$; (b) $q = 0.001$ and hence $q/p = 0.1$; (c) $q = 0.005$, hence $q/p = 0.5$ and (d) $q/p = 1$ which corresponds to $q = 0.01$. Each block (random network) has size $N = 500$. The axes are scaled in such a way that the semicircle corresponding to $q = p$ has unit radius (see text). All graphs are plotted for 20 realizations of random sets of connections among the two sub-networks

where λ_0 is the radius of the semicircular distribution for $q = p$ calculated from the spectra of network as $\lambda_0 = (\lambda_{max} - \lambda_{min})/2$, λ_{max} and λ_{min} being the highest and the lowest eigenvalue. Now we turn our attention to the statistics of eigenvalue fluctuations.

As can be seen from the middle panel of Fig. 6.4, for $q/p \sim 0.001 (q \sim 10^{-5})$, the value of the Brody parameter $\beta \sim 0.2$, which suggests that distribution is very close to the Poisson $[P(s) = \exp(-s)]$ denoted by the dotted curve in the figure. As the value of q increases, β also increases, and it is of the order of 1 for the value of $q/p \sim 0.01$ (which corresponds to the value of q as less as 10^{-4}), and becomes insensitive for a further increase in q. For larger values of q, we analyze the spectra using the spectral rigidity test of RMT.

As seen from the last panel of Fig. 6.4, the $\Delta_3(L)$ statistics follows RMT predictions of GOE [Eq. (6.4)] up to a certain L. It has a linear behavior in semi-logarithmic scale with the slope of $\sim 1/\pi^2$. The value of L for which it follows GOE statistics depends upon q. For small values of q such as $q/p = 0.01$ and $q/p = 0.05$, Δ_3 follows RMT prediction till very small range of $L \sim 5$ and $L \sim 20$, respectively. As q increases, the value of L for which Δ_3 follows the GOE statistics also increases. For $q/p = 0.1$, it agrees with the RMT predictions of GOE behavior for $L \sim 75$, and after this value, deviation from the RMT prediction is seen. This deviation corresponds to the existence of community structure in the network. As the value of q increases, the communities have more and more random connections between them. For $q = p$ the community structure is destroyed fully, and the network is a complete random network. This fact is reflected in the Δ_3 statistics corresponding to $q/p = 1$. At this value of q, it follows RMT prediction up to a very long-range $L \sim 150$. After this value of L, for the network of size $N \times m = 1{,}000$ we do not have a meaningful calculation of the Δ_3 statistics [24]. For $q = 0.005$ $(q/p = 0.5)$, where the strength of inter-community is as large as $\sim 50\,\%$ of the intra-community connections strength, the Δ_3 statistics correctly reflects the deviation from complete random matrices, suggesting the existence of communities in the network.

6.4 Conclusion and Discussion

In summary, RMT analysis of complex networks demonstrates that these networks follow the universal GOE statistics. These results tell that we can apply random matrix theory, a very well developed branch of Physics, to study and analyze complex networks.

Though the spectral densities of the random, the scale-free and the small-world networks are different, their eigenvalues spacing distributions are same and follow GOE statistics. This universal GOE behavior of NNSD tells that the networks are sufficiently random, or there exists *minimal amount of randomness* in the

network required to introduce the correlations among the neighboring eigenvalues. Δ_3 analysis seems to characterize the level of randomness in the networks based on the range of the correlations among the eigenvalues. Δ_3 analysis of the random network follows RMT prediction for very long range of L, which is not very surprising as random network follows RMT at each level starting from semi-circular density distributions. However interestingly scale-free and small-world networks also follow RMT for sufficiently large value of L. Beyond this value of L, deviation in the spectral rigidity is seen, indicating a possible breakdown of universality. This is quite understandable as small-world network is highly clustered and scale-free network also has specific features like hubs, so it is natural that they are not as random as the random network. Particularly small-world network is generated using Watts and Strogatz algorithm which generates networks with very high clustering coefficient and very less number of random connections. This very small number of random connections makes network *sufficiently* random to introduce the short range correlations among the eigenvalues.

Next, NNSD exhibits transition from Poisson statistics to GOE as network is deformed from perfect community structure to a random one. Poisson to GOE transition is found for many different systems, for example spectra of insulator-metal transition, order-chaos transition etc. [19]. The Δ_3 statistics, which measures long-range correlations among the eigenvalues, detects deformation from a network having two coupled sub-networks, to a single random network. More deformation of the network from community structure, leads to a larger range of L for which Δ_3 follows the GOE statistics. Note that, for the case of sub-networks being completely random, the spacing and the Δ_3 statistics of each of them follows RMT prediction. Therefore, any deviation from GOE statistics is due to the community structure these two sub-networks form when considered as a single network. These indicate that very small random interaction between communities is enough to introduce short-range correlations among them, spreading the randomness in the whole network. Second, further increase in coupling among the sub-networks is reflected by long-range correlations among eigenvalues. For networks having some structure, Δ_3 statistics follows RMT prediction of GOE for very long range of L. Beyond this value of L deviation in the spectral rigidity is seen, indicating a possible breakdown of universality. This means the network under consideration has *sufficient* randomness *which may be due to robustness of the systems* with regularity *which may be to perform some functional task*.

Mixture of random connections and regular structure have been emphasized at various places, for instance information processing in the brain is considered to be random connections among different modular structure [44]. According to the many recent studies, randomness in the connection is one of the most important and desirable ingredients for the proper functionality or the efficient performance of the systems having underlying network structures. Based on above results one can study the role of random connections in behavior and evolution of such systems in a better way under [45]. The RMT approach may be used to detect the connections most responsible to increase the *complexity* of networks. For example effect of oxygen molecule on biochemical networks is recently studied and is shown to increase the

complexity of networks leading to a major transition in the history of life [46]. Furthermore, deviation from the universal RMT predictions can be used to identify system-specific, non-random properties of system under consideration, and it might provide clues about important interactions [45, 47]. Moreover, Δ_3 statistics may be used to address complexity of the systems [48] having network structures under the RMT framework, and thus helping to understand the dynamical behavior [49] and robustness of such systems better.

Results on spectral properties of network with the community structure, on one hand advances the studies of spectral properties of modular networks under the universal RMT framework; on the other hand, variations in the correlations among eigenvalues shed light on the coupling among communities. For the simulations, the community structure in network is modeled by the very simple random or scale-free sub-networks, and the interactions among these sub-networks are considered random, whereas real world networks have richer structure [7]. However, the results achieved so far provide a platform to investigate the community structure of networks using a well developed theory of random matrices; the further investigations in this direction should deal with real world networks with richer and more complicated structure under the deformed random matrix framework [50].

Overall, work reviewed here demonstrates applicability of random matrix theory to complex network spectra, and hence opening a new platform for complex system research. To give an example, we discuss here importance of these RMT results for real world systems, particularly to biological systems. Several studies have revealed that the development of multi-target drugs might give better results than the traditional methods targeting a single protein. Single-target design might not always give satisfactory results, as there might be a backup system, which replaces the function of the inhibited target protein. By using multi-target drugs one can decrease the functionality of entire protein cascades producing more effective results. Multi-target drugs attacking hubs of the protein-protein interaction network, 'hub-links' (links connecting hubs), bridges (inter-modular links having high 'betweenness centrality') or nodes in the overlap of numerous network modules, might give better results [51, 52]. Similarly, targeting genes corresponding to the non-universal part of the spectra may lead to important effect as well.

This review article is restricted only to undirected networks which lead to symmetric matrices. Corresponding spectra has all real eigenvalues. Further new challenges arise when one considers directed networks leading to asymmetric matrices, and hence corresponding spectra may have complex eigenvalues [53]. So far there exist considerably very less understanding of spectral properties of such networks under RMT framework [54–56] though substantial part of real world systems have underlying network structure which are directed. Applicability of RMT framework for undirected networks sets up future directions to analyze directed networks as well under this framework.

Acknowledgements SJ thanks DST and CSIR for financial support, as well acknowledges MPI-PKS for arranging vibrant international conferences ideal for interactions. It is a pleasure to acknowledge discussions on various aspects of random matrix theory with Mahir Hussian, Jayendra N. Bandyopadhyay, M.S. Santhanam and Arul Lakshminarayan. Discussions with T. Kruger on various aspects of graph theory has always been very informative.

References

1. Albert, R., Barabási, A.-L.: Statistical mechanics of complex networks. Rev. Mod. Phys. **74**, 47–97 (2002) and references therein
2. Boccaletti, S., Latora, V., Moreno, Y., Chavez, M., Hwang, D.-U.: Complex networks: structure and dynamics. Phys. Rep. **424**, 175–308 (2006)
3. Erdös, P., Rényi, A.: On the evolution of random graphs. Publ. Math. Inst. Hungar. Acad. Sci. **5**, 17–61 (1960)
4. Barabási, A.-L., Albert, R., Jeong, H., Bianconi, G.: Power-law distribution of the World Wide Web. Science **287**, 2115 (2000)
5. Watts, D.J., Strogatz, S.H.: Collective dynamics of 'small-world' networks. Nature **393**, 440–442 (1998)
6. Girvan, M., Newman, M.E.J.: Community structure in social and biological network. Proc. Natl. Acad. Sci. USA **99**, 7821–7826 (2002); Newman, M.E.J.: A measure of betweenness centrality based on random walks. Soc. Netw. **27**, 39–54 (2005); Newman, M.E.J.: Modularity and community structure in networks. Proc. Natl. Acad. Sci. USA **103**, 8577–8582 (2006)
7. Ravsaz, E., Ravasz, E., Somera, A.L., Mongru, D.A., Oltvai, Z.N., Barabási, A.-L., et al.: Hierarchical organization of modularity in metabolic networks. Science **297**, 1551–1555 (2002) ; Guimerá, R., Amaral, L.A.N.: Functional cartography of complex metabolic networks. Nature **433**, 895–900 (2005)
8. Chung, F.R.K.: Spectral Graph Theory. American Mathematical Society, Providence, RI (1997)
9. Cvetković, D.M., Doob, M., Sachs, H.: Spectra of Graphs: Theory and Applications, 3rd revised edn. Academic, New York (1997)
10. Faloutsos, M., Faloutsos, P., Faloutsos, C.: On power-law relationships of the internet topology. Comput. Commun. Rev. **29**, 251–262 (1999)
11. Pecora, L.M., Carroll, T.L.: Master stability functions for synchronized coupled systems. Phys. Rev. Lett. **80**, 2109–2112 (1998)
12. Zhou, C., Motter, A.E., Kurths, J.: Universality in the synchronization of weighted random networks. Phys. Rev. Lett. **96**, 034101 (2006)
13. Atay, F.M., Biyikoglu, T., Jost, J.: Synchronization of networks with prescribed degree distributions. IEEE Trans. Circuits Syst. I **53**, 92–98 (2006); Network synchronization: spectral versus statistical propertie. Physica D **224**, 35–41 (2006)
14. McGraw, P.N., Menzinger, M.: Analysis of nonlinear synchronization dynamics of oscillator networks by Laplacian spectral methods. Phys. Rev. E **75**, 027104 (2007)
15. Kim, D.-H., Motter, A.D.: Ensemble averageability in network spectra. Phys. Rev. Lett. **98**, 248701 (2007)
16. Grone, R., Merris, R., Sunder, V.S.: The Laplacean spectrum of a graph. SIAM J. Matrix Anal. Appl. **11**, 218–238 (1990)
17. Banerjee, A., Jost, J.: Spectral plots and the representation and interpretation of biological data. Theory Biosci. **126**, 15–21 (2007)
18. Mehta, M.L.: Random Matrices, 3rd edn. Elsevier Academic Press, Amsterdam (2004)
19. Guhr, T., Muller-Groeling, A., Weidenmuller, H.A.: Random matrix theories in quantum physics: common concepts. Phys. Rep. **299**, 190–425 (1998)
20. Pleron, V., Gopikrishnan, P., Rosenow, B., Amaral, L.A.N., Stanley, H.E., et al.: Universal and nonuniversal properties of cross correlations in financial time series. Phys. Rev. Lett. **83**, 1471–1474 (1999)

21. Seba, P.: Random matrix analysis of human EEG data. Phys. Rev. Lett. **91**, 198104 (2003)
22. Santhanam, M.S., Patra, P.K.: Statistics of atmospheric correlations. Phys. Rev. E **64**, 016102 (2001)
23. Brody, T.A.: A statistical measure for the repulsion of energy levels. Lett. Nuovo Cimento **7**, 482 (1973)
24. Bohigas, O., Giannoni, M.-J., Schmidt, C.: In: Casati, G. (ed.) Chaotic Behaviour in Quantum Systems, p. 103. Plenum Press, New York (1985)
25. Rodgers, G.J., Bray, A.J.: Density of states of a sparse random matrix. Phys. Rev. B **37**, 3557–3562 (1998)
26. Semerjian, G., Cugliandolo, L.F.: Sparse random matrices: the eigenvalue spectrum revisited. J. Phys. A **35**, 4837 (2002)
27. Farkas, I.J., Derényi, I., Barabási, A.-L., Vicsek, T., et al.: Spectra of "real-world" graphs: beyond the semicircle law. Phys. Rev. E **64**, 026704 (2001)
28. Dorogovtsev, S.N., Goltsev, A.V., Mendes, J.F.F., Samukhin, A.N.: Spectra of complex networks. Phys. Rev. E **68**, 046109 (2003)
29. de Aguiar, M.A.M., Bar-Yam, Y.: Spectral analysis and the dynamic response of complex networks. Phys. Rev. E **71**, 016106 (2005)
30. Dorogovtsev, S.N., Goltsev, A.V., Mendes, J.F.F., Samukhin, A.N.: Random networks: eigenvalue spectra. Physica A **338**, 76–83 (2004)
31. Chung, F., Lu, L., Vu, V.: Spectra of random graphs with given expected degrees. Proc. Natl. Acad. Sci. USA **100**, 6313–6318 (2003)
32. Rodgers, G.J., Austin, K., Kahng, B., Kim, D.: Eigenvalue spectra of complex networks. J. Phys. A **38**, 9431–9437 (2005)
33. Kim, D., Kahng, B.: Spectral densities of scale-free networks. Chaos **17**(2), 026115 (2007)
34. Palla, G., Vattay, G.: Spectral transitions in networks. New J. Phys. **8**, 307 (2006)
35. Bandyopadhyay, J.N., Jalan, S.: Universality in complex networks: random matrix analysis. Phys. Rev. E **76**, 026109 (2007)
36. Jalan, S., Bandyopadhyay, J.N.: Randomness in random networks. EPL **87**, 48010 (2009)
37. Jalan, S., Bandyopadhyay, J.N.: Random matrix analysis of complex networks. Phys. Rev. E **76**, 046107 (2007)
38. Barabási, A.-L., Albert, R., Jeong, H.: Mean-field theory for scale-free random networks. Physica A **272**, 173–87 (1999)
39. Goh, K.-I., Kahng, B., Kim, D.: Universal behavior of load distribution in scale-free networks. Phys. Rev. Lett. **87**, 278701 (2001)
40. Dorogovtsev, S.N., Mendes, J.F.F.: Evolution of networks. Adv. Phys. **51**, 1079–1187 (2002)
41. Fyodorov, Y.V., Mirlin, A.D.: Universality of level correlation function of sparse random matrices. J. Phys. A **24**, 2273 (1991)
42. Evangelou, S.N.: A numerical study of sparse random matrices. J. Stat. Phys. **69**, 361–383 (1992)
43. Jalan, S.: Spectral analysis of deformed random networks. Phys. Rev. E **80**, 046101 (2009)
44. Cohen, J.D., Tong , F.: Modular vs. distributed representations in the brain. Science **293**, 2405–2407 (2001)
45. Jalan, S., Ung, C.Y., Li, B., et al.: Spectral analysis of Gene co-expression network of Zebrafish. EPL **99**, 48004 (2012)
46. Raymond, J., Segré, D.: Oxygen on biochemical networks and the evolution of complex life. Science **311**, 1764–1767 (2006)
47. Jalan, S., Solymosi, N., Vatty, G., Li, B.: Random matrix analysis of localization properties of gene coexpression network. Phys. Rev. E **81**, 046118 (2010)
48. May, R.M.: Stability and Complexity in Model Ecosystems. Princeton University Press, Princeton (1973)
49. Pikovsky, A., Rosenblum, M., Kurths, J.: Synchronization: A Universal Concept in Nonlinear Dynamics. Cambridge University Press, Cambridge (2001)
50. de Carvalho, J.X., Jalan, S., Hussein, M.S.: Deformed Gaussian-orthogonal-ensemble description of small-world networks. Phys. Rev. E **79**, 056222 (2009)

51. Csemely, P., Ágoston, V., Pongor, S.: The efficiency of multi-target drugs: the network approach might help drug design. Trends Pharmacol. Sci. **26**, 178 (2005); Csemely, P.: Creative elements: network-based predictions of active centres in proteins and cellular and social networks. Trends Biochem. Sci. **33**, 569 (2008)
52. Gyurkó, D., Veres, D.V., Nánási, T., Csermely, P.: Network strategies to understand the aging process and help age-related drug design. Genome Med. **1**, 90 (2009)
53. Girko, V.L.: Circular law. Theory Probab. Appl. **29**, 694–706 (1984)
54. Giraud, O., Georgeot, B., Shepelyansky, D.L.: Delocalization transition for the Google matrix. Phys. Rev. E **80**, 026107 (2009)
55. Georgeot, B., Giraud, O., Shepelyansky, D.L.: Spectral properties of the Google matrix of the World Wide Web and other directed networks. Phys. Rev. E **81**, 056109 (2010)
56. Jalan, S., Zhu, G., Li, B.: Spectral properties of directed random networks with modular structure. Phys. Rev. E **84**, 046107 (2011)

Part III
Attractor Reconstructions and Ecology/Biological Patterns

Chapter 7
Some Time-Delay Finding Measures and Attractor Reconstruction

Sanjay Kumar Palit, Sayan Mukherjee, Santo Banerjee, M.R.K. Ariffin, and D.K. Bhattacharya

Abstract Topologically equivalent attractor reconstruction is one of the major issues in nonlinear analysis. This is because of the fact that the underlying dynamical model of some nonlinear phenomena may not be known and thus it is necessary to retrieve the dynamics from the data it generates. One way to achieve this is the reconstruction of the attractor. The basis of such reconstruction is the famous Taken's embedding theorem, which asserts that an equivalent phase space trajectory,preserving the topological structures of the original phase space trajectory, can be reconstructed by using only one observation of the time series. However, in some cases topologically equivalent attractor reconstructions can also be done by using multiple observations. All these things involve the choice of suitable time-delay(s) and embedding dimension. Various measures are available to find out the suitable time-delay(s). Among them, linear auto-correlation, Average mutual information, higher dimensional mutual information are mostly used measures for the reconstruction of the attractors. Every measures have certain limitations in the sense that they are not always useful in finding suitable time-delay(s). Thus it is necessary to introduce few more nonlinear measures, which may be useful if the

S.K. Palit (✉)
Basic Sciences and Humanities Department, Calcutta Institute of Engineering and Management, Kolkata, India
e-mail: sanjaypalit@yahoo.co.in

S. Mukherjee
Mathematics Department, Sivanath Sastri College, Kolkata, India
e-mail: msayan80@gmail.com

S. Banerjee
Institute for Mathematical Research, University Putra Malaysia, 43400 Serdang, Malaysia
e-mail: santoban@gmail.com

M.R.K. Ariffin
INSPEM and Department of Mathematics, Universiti Putra Malaysia, Selangor, Malaysia
e-mail: rezal@upm.edu.my

D.K. Bhattacharya
Instrumental Music Department, Rabindra Bharati University, Kolkata, India
e-mail: dkb_math@yahoo.com

S. Banerjee, L. Rondoni (eds.), *Applications of Chaos and Nonlinear Dynamics in Science and Engineering - Vol. 4*, Understanding Complex Systems,
DOI 10.1007/978-3-319-17037-4_7

aforesaid measures fail to produce suitable time-delay/time-delays. In this chapter, some comparatively new nonlinear measures namely generalized auto-correlation, Cross auto-correlation and a new type of nonlinear auto-correlation of bivariate data for finding suitable time-delay(s) have been discussed. To establish their usefulness, attractors of some known dynamical systems have been reconstructed from their solution components with suitable time-delay(s) obtained by each of the measures. These attractors are then compared with their corresponding original attractor by a shape distortion parameter *Sd*. This shape distortion parameter actually checks how much distorted the reconstructed attractor is from its corresponding original attractor. The main objective of this chapter is to address the problem of reconstruction of a least distorted topologically equivalent attractor. The reason is that if the reconstructed attractor is least distorted from its original one, the dynamics of the system can be retrieved more accurately from it. This would help in identifying the dynamics of the corresponding system, even when the dynamical model is not known. Out of the three measures discussed in this chapter, the generalized and cross auto-correlation measures produce least distorted topologically equivalent attractor only by consideration of multiple solution components of the dynamical system. On the other hand, by using the measure—new type of nonlinear auto-correlation of bivariate data, one can reconstruct a least distorted topologically attractor from single solution component of the dynamical system. Various numerical results on Lorenz system, Neuro-dynamical system and also on two real life signals are presented to prove the effectiveness of the aforesaid three comparatively new nonlinear time-delay finding measures. Finding of suitable embedding dimension is another important issue for attractor reconstruction. However, this issue has not been highlighted in this chapter because we have restricted this discussion only to three dimensional attractor reconstruction.

7.1 Introduction

Real life phenomena can be broadly classified into two categories—deterministic and stochastic. Deterministic phenomena are generally studied in two ways. The widely used way is to consider a dynamical system as a model of real life phenomena, to develop its qualitative theory to inquire about the behavior of its solutions including its chaotic behavior. The other one is the dual approach, where the nature of the real life phenomenon are explored directly from the output data it generates, by considering its phase space reconstruction [1–16]. Since in most of the cases, the dynamical models fail to reveal the true characteristics of the corresponding phenomena, the dual approach is a better alternative as the phase space that reveals the long term dynamics is reconstructed directly from the data. Phase space is basically a flow or solution space of the underlying dynamical models described by differential equation with initial conditions in continuous case. In this context, a solution with an initial condition of the dynamical model is like a path of a fixed point which is dropped in that flow. This path is called trajectory in

the phase space. Sometimes, it may happen that, whatever the movement of the trajectory, they always [11] converge to a region. The region is called attractor [17]. There are three types of attractor—regular, strange non-chaotic and chaotic [17]. As the dynamical models we have considered in this discussion are all chaotic in nature, we confine our discussion to strange chaotic attractors only. By chaotic attractor [13] we mean, a bounded region with fractal dimension [1], where all the trajectories converge in erratic manner. More precisely, whenever the solution $(y_1(t), y_2(t), y_3(t), \ldots\ldots, y_n(t)) \in \mathbb{R}^n$ of the respective dynamical model with their initial conditions: $(y_1(a_1), y_2(a_2), y_3(a_3), \ldots\ldots, y_n(a_n))$ goes to another position and moves in an eccentric manner with the change of t in the phase space, chaos may occur for the said model. This type of chaos is actually known as deterministic chaos [17]. In this case, trajectories of the system move in a bounded region and form a dense orbit, called chaotic attractor [17]. The existence of chaos can be measured by Largest Lyapunov exponent (LLE) [18]. It plays a very important role in the analysis of a possibly chaotic system, since Lyapunov exponents not only show qualitatively the sensitive dependence on initial conditions but also give a quantitative measure of the average rate of separation or attraction of nearby trajectories on the attractor. Various algorithms are available for calculating Lyapunov exponent details of which are available in [19–29].

The basic problem in formulation of the dynamics from the data is that when analyzing time series, we almost always get only incomplete information. Although more and more multiprobe measurements are being carried out, still the vast majority of time series are single-valued. Even if multiple simultaneous measurements are available, they will not typically cover all the degrees of freedom of the system. However, the missing information can be recovered from time delayed copies of the available data, if certain requirements are fulfilled. The idea of connecting the phase space or state space vector $y(t)$ of dynamical variables of the physical system to the measured time series $x(t)$ was first addressed by Packard et al. [30] in 1980. They proved that reconstruction of a higher dimensional state-space vector was possible by using time delays with the measured scalar time series $x(t)$. Thus, a surrogate vector $z(t) = (x(t), x(t+\tau), x(t+2\tau), \ldots.)$ for $y(t)$could be formed from scalar measurements. These surrogate vectors actually constitute the reconstructed attractor of the said physical system. At this point, the natural query is—Does this reconstructed attractor resemble the original one? The theoretical framework for this approach is set by a number of theorems, all of which specify the precise conditions when an attractor in delay coordinate space is equivalent to the original attractor of a dynamical system in phase space. In fact, it is enough to study the attractor of the phase space instead of studying the entire phase space because most of the important and relevant information of the phase spaces are concentrated on this attractor. Thanks to the celebrated Taken's theorem [11] which ensures such attractor reconstruction from a single time series. It states that "an equivalent phase space trajectory, which preserves the topological structures of the original phase space trajectory, can be reconstructed by using only one observation of the time series respectively". Later on, this study was extended by Sauer et al. [12] in 1991. This reconstruction [1–16] of the dynamics of the system on the

basis of the given data is of paramount importance, as it ensures that under certain generic conditions, such a reconstruction is equivalent to the original attractor. This equivalence ensures that differential information is preserved and it also allows us to consider both qualitative and quantitative analysis. Since its inception Taken' s embedding theorem [11] has been applied in time series analysis of different fields ranging from system characterization and approximation of invariant quantities to noise-filtering and prediction. The embedding theorem asserts that for some systems the true dynamics may not be known, while the equivalent dynamics can be obtained under suitable conditions with the use of time delays of a single time series, treated as a one-dimensional projection of the system trajectory. Thus most of the applications related to embedding theorem are based on uni-variate time series, although measurements of two or more quantities for the same system are often available. One of the first applications of multivariate embedding was in the context of spatially extended systems, where embedding vectors were constructed from data representing the same quantity measured simultaneously at different locations [31–33]. In nonlinear multivariate prediction, the prediction with local models on a space reconstructed from a different time series of the same system was studied in [16, 31]. This study was extended in [34] by having the reconstruction utilizing all the observed time series. Multivariate embedding with the use of independent components analysis was considered in [35] and after that multivariate embedding with varying delay times was studied in [36, 37]. In fact, the time-delay along with the embedding dimension play the vital role in attractor reconstruction, or embedding [12] of a time series. This is because, when time-delay is too short, the attractor will be very narrow or squeezing in nature and when time delay is large, the attractor will be of circular or elliptical nature. Thus for a topologically equivalent attractor reconstruction, it is better to have a moderate time-delay.The state vectors/attractors contain all the information available about the state of the process at a given time and provide the most valuable information in order to forecast the next state of the process. Since the publication of theoretical results about the dimension needed to reconstruct the structure of a series through an embedding in its phase space [11, 12], many methods have been developed for estimating this dimension, such as Correlation dimension [38], False neighbors [36], Box-Counting [12] and minimum dimension [39, 40]. Regarding the time-delay selection [41–47], the common approaches are to use of the auto-correlation (AC) of the series [42, 43], or the Average mutual information (AMI) [44, 45]. The idea of these measures is to select variables as attractor components that are as uncorrelated or independent as possible. However, the AC is a linear measure of dependency. It is only applied in a linear context. The AMI is a non-parametric measure of dependency between variables and is applicable in both linear and nonlinear cases. Though AMI is commonly used for delay selection, it has two major limitations. The first one is that AMI is generally computed between two variables only and hence it can detect only the relations between two attractor values properly, but it cannot provide the information about high-dimensional relationships between all attractor values. The second limitation is that in this process only a unique delay is selected. The attractors are constructed using variables that are equally

distributed in time (as multiples of the chosen delay). This approach artificially limits the attractors in the sense that the delay selection is based on two-dimensional information, while the attractors themselves may be higher dimensional. A more general approach would be to select different delays for the various variables taken into account in the reconstruction of the attractors. The selection of these delays should ideally be performed in a space having dimension equal to that of the attractors. A high-dimensional Mutual information (MI) estimator [46] is one such attempt that addresses this more general problem. In [47], the high-dimensional MI estimator was used for better phase space reconstruction with multiple components of the solution vector of Lorenz [48] and Rössler system [49]. Since Rössler system [49] is a particular case of Lorenz system, so in this case the study was practically concentrated to Lorenz system only. Since MI is not a system dependent nonlinear measure, it cannot vary with different choices of dynamical systems. Hence it may not work for attractor reconstruction of any dynamical systems, in general. As a matter of fact the results, which are found to be true for Lorenz [48] or Rössler dynamical system [49] under the use of high dimensional MI estimator, may not hold good for other systems.

The basic motivation of this chapter is to point out the necessity of modifying the earlier tools for finding time-delay by developing newer and newer sophisticated and finer tools and formulae. This is because it is not possible to reconstruct the topologically equivalent attractor from the data unless we get a proper time-delay. Even when a topologically equivalent attractor is reconstructed, the similarity of this attractor with the original attractor (the attractor that is constructed from the dynamical model which generates the data) needs to be verified. This is done by shape distortion measure introduced in [50]. This similarity checking is important as more similar is the reconstructed attractor with the original attractor, more accurate will be our interpretation of the dynamics from this reconstructed attractor. This would help in better understanding of some real phenomena from its reconstructed attractor without knowing its underlying dynamical model and hence the original attractor. Since the shape of the attractor with its trajectories can be best viewed and can also be geometrically differentiated only up to three dimensional spaces, we restrict the embedding dimension to three in this discussion.

The whole chapter is organized in the following manner. In broader sense, this chapter has two major parts. The first part deals with an improved measure for finding time-delay, which successfully reconstruct the best possible attractor from a single time series. This measure is basically a new type of nonlinear auto-correlation of bivariate data [51] and it produces the best possible reconstructed attractor, which is topologically equivalent to the original attractor. Therefore, when only one measurement of the real data is available, this measure may be used towards getting the reconstructed attractor. In fact, this observation has been confirmed by means of two suitable real life examples. In the next part, topologically equivalent attractors are reconstructed from multiple solution components of the underlying dynamical systems. In this section, the limitations of the mostly used delay finding measures have been highlighted and a comparatively new nonlinear measure namely Generalized Auto Correlation (GAC) with single and different time-delays [52]

have been introduced and validated with suitable examples. The supremacy of this method has also been established by comparing it with the existing delay finding measures. Next, the limitation of GAC with single and multiple delays have also been pointed out with suitable examples and as a remedy to this problem, another much more improved nonlinear measure called Cross Auto Correlation (CAC) [53] has been introduced. The use of multiple solution components for proper attractor reconstruction as mentioned in [47] has also been established in both cases. In fact, the second measure is more useful for finding proper time-delay for attractor reconstruction in almost all cases by including multiple solution components of the original dynamical system. Thus, if multiple measurements of some real data are available, then the aforesaid measures for finding time-delay, more specifically the second measure, stand as most powerful tools. The entire discussion is summarized and concluded in the conclusion section.

7.2 Attractor Reconstruction and Verification of Topological Equivalence

An attractor is a set in which all neighboring trajectories converge. For a scalar time series $\{x_t\}_{t=1}^{N}$, the attractor can be reconstructed by using the method of delays. The basic idea in the method of delays is that the evolution of any single variable of a system is determined by the other variables with which it interacts. Information about the relevant variables is thus implicitly contained in the history of any single variable. On the basis of this an equivalent attractor can be reconstructed by assigning an element of the time series x_t and its successive delays as coordinates of a new vector time series $y_t = \{x_t, x_{t+\tau}, x_{t+2\tau}, \ldots, x_{t+(m-1)\tau}\}$, where τ is referred to as the time-delay. Different measures are available for finding the suitable time-delay for the reconstruction of the attractors of some dynamical systems. However the measures that are more frequently used for this purpose is the linear auto-correlation (AC) and the Average mutual information (AMI)—a general measure.

Once the attractor is reconstructed, the topological equivalence of this attractor with its original one needs to be verified. One way of verification is to make use of the shape distortion parameter *Sd* [50]. *Sd* measures, how much similar is the reconstructed attractor of some dynamical system with its corresponding original attractor. Let us describe the *Sd* measure in brief.

Let A be the original attractor and $\bar{A}$ be the reconstructed attractor. The shape distortion is measured with Mutual False Nearest Neighbors [54–56]. Let y_n be a point on A with y_{n_k} as its nearest neighbor and x_n be the corresponding point on $\bar{A}$ with nearest neighbor x_{n_r}. The shape distortion (*Sd*) [50] is given by

$$Sd = < \frac{||y_n - y_{n_k}||||x_n - x_{n_r}||}{||x_n - x_{n_k}||||y_n - y_{n_r}||} > \tag{7.1}$$

where $< . >$ denotes the average of all points and $||.||$ denotes the Euclidean norm. Larger is the *Sd*, lesser is the distortion on the shape of the dynamics of the attractor. The dynamics may be preserved though the reconstructed attractor is a stretched or squeezed (or both) version of the original attractor. But the preservation of the shape guarantees the preservation of the dynamics, since the shape of the attractor is formed by its dynamics.

7.3 Some Time-Delay Finding Measures for Attractor Reconstruction

One of the most important tasks for the reconstruction of attractors is the choice of suitable time-delay(s). Various time-delay finding measures are available. However, the measures that are most frequently used are linear auto-correlation (AC) [42, 43], Average mutual information (AMI) [44, 45] and higher dimensional mutual information (MI) with same and different time-delays [46, 47]. Some of the measures are useful if the reconstruction is done from either single or multiple time series, while some of them can be used in both cases. In this section, we revisit the aforesaid frequently used measures, discuss their shortfalls and also discuss some comparatively new nonlinear measures for time-delay selection.

We make the entire discussion in two subsections. First one is for the reconstruction of attractor from a single time series and the second one for multiple time-series.

7.3.1 For Single Time Series

7.3.1.1 Auto-Correlation (AC)

Auto-correlation [42, 43] is the correlation of a signal with itself. It refers to the correlation of a time series with its own past and future values. Auto-correlation is sometimes called *lagged correlation* or *serial correlation*, as it refers to the correlation between members of a series of numbers arranged in time. Informally, auto-correlation is the similarity between observations as a function of the time separation between them. It is a mathematical tool for finding repeating patterns. It is often used in signal processing for analyzing functions or series of values, such as time domain signals. In statistics, the auto-correlation of a random process describes the correlation between values of the process at different points in time, as a function of the two times or of the time difference. Let X be some repeatable process, and t be some point in time after the start of that process (t may be an integer for a discrete-time process or a real number for a continuous-time process). Then X_t is

the value (or realization) produced by a given run of the process at time t. Let the process have mean μ_t and variance σ_t^2 for all times t. Then the definition of the auto-correlation between any two time t and t_1 is given by

$$R(t, t_1) = \frac{E[(X_t - \mu_t)(X_{t_1} - \mu_{t_1})]}{\sigma_t \sigma_{t_1}} \tag{7.2}$$

where E is the expected value operator. Note that this expression is not well-defined for all time series or processes, because the variance may be zero (for a constant process) or infinite. If the function R is well-defined, its value must lie in the range $[-1, 1]$, with 1 indicating perfect correlation and -1 indicating perfect anti-correlation. However, if x_t is a second-order stationary process then the mean μ_t and variance σ_t^2 are time-independent, and further the auto-correlation depends only on the difference between t and t_1 . This actually implies that the auto-correlation can be expressed as a function of the time-delay, and this would be an even function of the delay $\tau = t - t_1$. Thus for a stationary process, (7.2) reduces to

$$R(\tau) = \frac{E[(X_t - \mu)(X_{t+\tau} - \mu)]}{\sigma^2} \tag{7.3}$$

So, one can think that auto-correlation for a stationary process is the ratio of auto-covariance and variance.

For the reconstruction of attractors from a single time series $x(t)$, the auto-correlation between $x(t)$ and $x(t + \tau)$ is calculated for different values of τ. These are then plotted against τ to form a correlogram diagram. The suitable value of the time-delay τ is one for which the auto-correlation attains its positive minimum for the first time.

7.3.1.2 Average Mutual Information (AMI)

Though the most known measure of dependence between two random variables is the coefficient of linear correlation, yet its application requires a pure linear relationship, or at least a linear transformed relationship. This is because of the fact that this correlation is nothing but a normalized covariance, which is measured only for linear relationships. However, this statistics may not be helpful in determining serial dependence if there is some kind of non-linearity in the data. In this context, a measure of global dependence is sought, that is, some measure that captures linear and nonlinear dependencies, without requiring the specification of any kind of model of dependence. Mutual Information is one such measure of general dependence of two variables. It is an information theoretic approach, where the famous Shannon's entropy, which provides formalism for quantifying the concepts

of spreading and new information is used. The basic requirement for the use of information theory is that the probabilities of the messages under consideration must exist and are accessible. Strange attractors are ergodic and have well-defined asymptotic probability distributions. Since the information theory is being applied to the strange attractors and the messages under consideration are the values in which the measurements of the strange attractor might take, the probabilities of the messages under consideration must exist and their long time averages converge to the probabilities. The pioneering and most important contributions towards the development and application of mutual information were made by Fraser and Swinney [44].

In this context, Average mutual information (AMI) [44, 45] is a particular type of MI [46] between the signal itself. For a time series $x(t), t = 1, 2, \ldots.., N$, AMI [44, 45] is calculated by

$$AMI(\tau) = \sum_{t=1}^{N-\tau} Prob[x(t), x(t+\tau)] log(\frac{Prob[x(t), x(t+\tau)]}{Prob[x(t)]Prob[x(t+\tau)]}) \tag{7.4}$$

$\tau = 1, 2, 3, \ldots, N-1$, where Prob[.] denotes the probability.

For estimation of τ, two criteria are important. First, τ has to be large enough so that the AMI [44, 45] at time $t+\tau$ is significantly different from the AMI [44, 45] at time t . Then it will be possible to gather enough information about all other system variables that influence the value of x to reconstruct the whole attractor. Second, τ should not be larger than the typical time for which the system loses memory of its initial state. We must be conscious about the second criteria, because chaotic systems are unpredictable or lose memory of its initial state as time goes forward. In [44], it is stated that the optimum time-delay is obtained, where the AMI [44, 45] attains its first minimum value. Since, AMI [44, 45] is a nonlinear version of auto-correlation, so this method is strongly recommended to apply on nonlinear signals for finding suitable time-delay.

7.3.1.3 Nonlinear Auto-Correlation of Bivariate Data

Most of the time series encountered from real life phenomena are nonlinear with different types of non-linearity. The goal is to find a proper time-delay of moderate magnitude for the reconstruction of attractor [1–16] and so there is no loss of generality in considering a small segment (length varies from 150 to 500) of the given time series. This small segment of the time series is then approximated with a nonlinear curve f that gives the best fit. Thus we get two data series, one is the smaller segment of the time series and the other one is what is generated through the nonlinear curve f .

With these two data sets, we now define new type of nonlinear auto-correlation of bivariate data [51] as follows:

Definition 1 Let $X = \{x(t)\}_{t=1}^{N}$ and $Y = \{y(t)\}_{t=1}^{N}$ be two time series and $f(t)$ be the function that approximates $y(t)$ from $x(t), t = 1, 2, 3, \ldots, N$. Let $Y' = \{f(x(t))\}_{t=1}^{N}$. Then the nonlinear correlation between X and Y, denoted by $r_{X,Y}$ is defined as the linear correlation between $Y = \{y(t)\}_{t=1}^{N}$ and $Y' = \{f(x(t))\}_{t=1}^{N}$, which is given by

$$r_{X,Y}(\tau) = \frac{\sum_{t=1}^{N}(y(t) - \overline{y(t)})(f(x(t)) - \overline{f(x(t))})}{\sqrt{\sum_{t=1}^{N}(y(t) - \overline{y(t)})^2}\sqrt{\sum_{t=1}^{N}(f(x(t)) - \overline{f(x(t))})^2}} \tag{7.5}$$

where $\overline{y(t)}$ and $\overline{f(x(t))}$ are the means of the time series $Y = \{y(t)\}_{t=1}^{N}$ and $Y' = \{f(x(t))\}_{t=1}^{N}$ respectively.

Definition 2 Let $X = \{x(t)\}_{t=1}^{N}$ be a time series and $\{f(x(t))\}_{t=1}^{N}$ be its best nonlinear curve fit. Then the nonlinear auto-correlation $r_X(\tau)$ between $X = \{x(t)\}_{t=1}^{N}$ and $Y = \{x(t+\tau)\}_{t=1}^{N}$ is defined as the linear auto-correlation between $Y = \{x(t+\tau)\}_{t=1}^{N}$ and $Y' = \{f(x(t))\}_{t=1}^{N}$, i.e.;

$$r_X(\tau) = \frac{\sum_{t=1}^{N-\tau}(x(t+\tau) - \overline{x(t+\tau)})(f(x(t)) - \overline{f(x(t))})}{\sqrt{\sum_{t=1}^{N-\tau}(x(t+\tau) - \overline{x(t+\tau)})^2}\sqrt{\sum_{t=1}^{N-\tau}(f(x(t)) - \overline{f(x(t))})^2}} \tag{7.6}$$

where $\overline{x(t+\tau)}$ and $\overline{f(x(t))}$ are the means of the time series $Y = \{x(t+\tau)\}_{t=1}^{N-\tau}$ and $Y' = \{f(x(t))\}_{t=1}^{N-\tau}$ respectively and $1 \le \tau \le \frac{N}{2}$, if N is even and $1 \le \tau \le \frac{N-1}{2}$, if N is odd.

If no such best nonlinear fit is available for the smaller segment of the time series, then determination of the suitable moderate time-delay by Eq. (7.6) for attractor reconstruction [1–16] is not possible. This may happen if the time series is highly non-stationary. But this is a very rare case.

Suppose that there exists a nonlinear curve of best fit for the given nonlinear time series. The new nonlinear auto-correlation of bivariate data [51] given by (7.6) is determined between two groups $\{x(t)\}_{t=1}^{l-\tau}$,$\{x(t+\tau)\}_{t=1}^{l-\tau}, 150 \le t \le 500$, by considering a smaller segment $\{x(t)\}_{t=1}^{l}$ of the time series $\{x(t)\}_{t=1}^{N}$. The time-delay τ is determined from the two dimensional correlogram diagram.Thus we get the independent coordinates $(x(t), x(t+\tau), x(t+2\tau)), t = 1, 2, 3, \ldots, N - 2\tau$. The attractor is finally reconstructed with these independent coordinates.

7.3.1.4 Numerical Examples and Discussions

To validate the above new type of nonlinear auto-correlation of bivariate data [51], let us consider the three dimensional Lorenz system [48] described by the following differential equations:

$$\begin{aligned}\frac{dx_1}{dt} &= s(x_2 - x_1),\\ \frac{dx_2}{dt} &= x_1(r - x_3) - x_2,\\ \frac{dx_3}{dt} &= x_1x_2 - bx_3,\end{aligned} \tag{7.7}$$

with the initial condition $x_1(1) = 8, x_2(1) = 9, x_3(1) = 2$ and the parameter values $s = 10, r = 28, b = \frac{8}{3}$.

The above Lorenz system given by (7.7) with the given initial condition gives rise to a chaotic solution, which is shown by the attractor of the system given in Fig. 7.1a.

For the purpose of reconstruction of the above attractor, we have considered 5,000 values of the solution vector $(x_1(t), x_2(t), x_3(t))$ of the aforesaid Lorenz system given by (7.7). Let us first consider the solution component $\{x_2(t)\}_{t=1}^{5000}$ and find a suitable time-delay τ under the new type of nonlinear auto-correlation of bivariate data.

Since the solution component $\{x_2(t)\}_{t=1}^{5000}$ of the aforesaid Lorenz system is nonlinear, this nonlinear measure may be applied. For this purpose, we first take a smaller segment of length 200 and find a best possible nonlinear curve fit f for it.

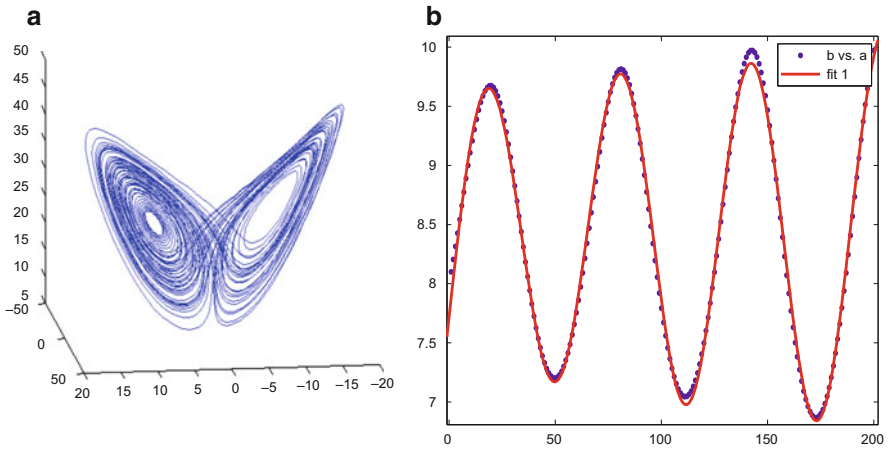

Fig. 7.1 (**a**) Attractor of the Lorenz system given by (7.7), (**b**) best nonlinear curve fit for a smaller segment of the solution component $\{x_2(t)\}_{t=1}^{5000}$ of the Lorenz system

This is given by

$$f(t) = a_0 + a_1\cos(wt) + b_1\sin(wt) + a_2\cos(2wt) + b_2\sin(2wt) + a_3\cos(3wt) + b_3\sin(3wt) + a_4\cos(4wt) + b_4\sin(4wt) + a_5\cos(5wt) + b_5\sin(5wt) \tag{7.8}$$

where $a_0 = 8.44, a_1 = 0.05261, b_1 = -0.04536, a_2 = -0.02356, b_2 = -0.09461, a_3 = -0.1507, b_3 = -0.07338, a_4 = -0.4175, b_4 = 1.353, a_5 = 0.03087, b_5 = -0.04881, w = 0.02525$.

The above best possible curve fit given by Eq. (7.8) is shown by Fig. 7.1b.

Equation (7.5) is then used to determine the nonlinear auto-correlation $r_X(\tau)$ between $X = \{x_2(t)\}_{t=1}^{200}$ and $Y = \{x_2(t+\tau)\}_{t=1}^{200}$. This is actually the linear AC [42, 43] between $Y = \{x_2(t+\tau)\}_{t=1}^{200}$ and $Y' = \{f(x_2(t))\}_{t=1}^{200}$, where f is the best nonlinear fit available for a smaller part of one of the solution components $\{x_2(t)\}_{t=1}^{5000}$ of the aforesaid Lorenz system [48]. Thus $r_X(\tau)$ is obtained for different values of the time-delay τ and the suitable time-delay τ is determined from the two dimensional correlogram diagram [1] given by Fig. 7.2a.

It is evident from Fig. 7.2a that $r_X(\tau)$ comes nearer to zero for the first time, when $\tau = 15$. Thus we get the suitable time-delay and corresponding to this time-delay the attractor of the Lorenz system is reconstructed, which is shown in Fig. 7.2b.

In a similar manner we have also reconstructed the attractor from the other two solution components of the Lorenz system. However, when the *Sd* value is calculated, it is found that the attractor reconstructed from $\{x_2(t)\}_{t=1}^{5000}$ is least distorted from the original attractor. So we have not presented the later attractors.

Next, we try to use the linear AC [42, 43] and AMI [44, 45] to reconstruct the attractor of the Lorenz system. Since AC is a linear measure, but the solution components of the aforesaid Lorenz system are highly nonlinear it is quite impossible

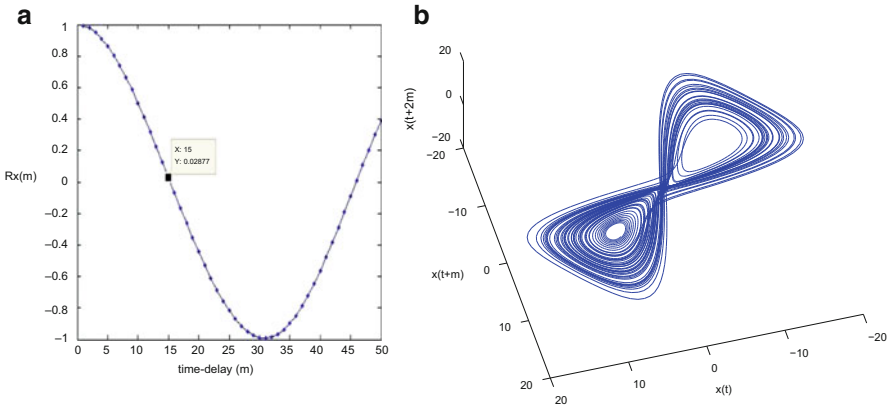

Fig. 7.2 (**a**) Two dimensional correlogram diagram, (**b**) reconstructed attractor of the Lorenz system with time-delay $\tau = 15$ under new type of nonlinear auto-correlation of bivariate data

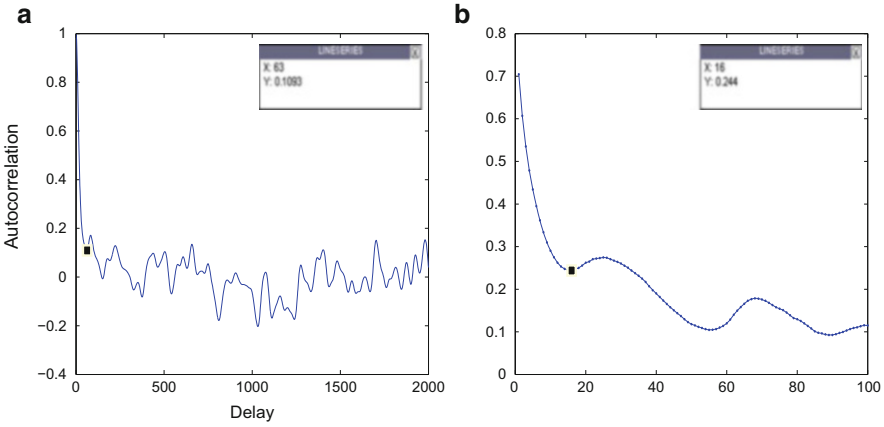

Fig. 7.3 Plot of (**a**) AC versus time-delay, (**b**) AMI versus time-delay for the solution component $\{x_2(t)\}_{t=1}^{5000}$ of Lorenz system given by (7.7). In (**a**), the suitable time-delay is obtained, when AC attains its positive minimum for the first time. In (**b**), the suitable time-delay is obtained, when AMI comes nearer to zero for the first time

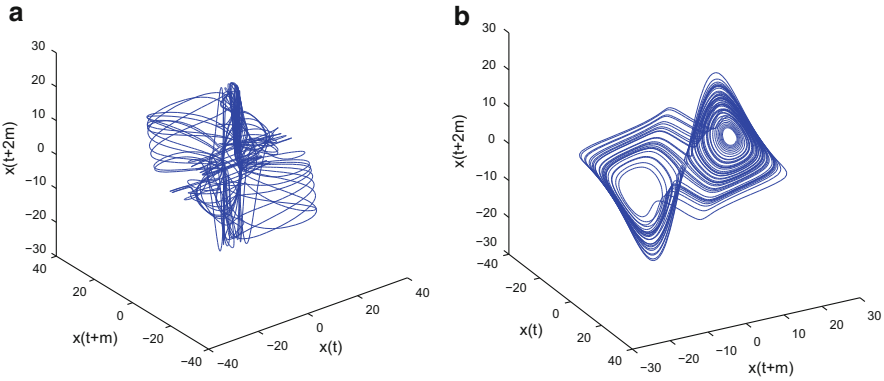

Fig. 7.4 Reconstructed attractor of the Lorenz system (7.7) (**a**) with $\tau = 63$ obtained by AC measure, (**b**) with $\tau = 16$ obtained by AMI measure

to get the proper value of for the reconstruction of the attractor. Figure 7.3a,b show the plot of AC $R_{x_2}(\tau)$ versus time-delay τ and the plot of AMI versus time-delay τ.

It is evident from the above figure that the auto-correlation attains its positive minimum for the first time, when $\tau = 63$ and AMI [44, 45] comes nearer to zero for the first time, when $\tau = 16$. The reconstructed attractor for the above Lorenz system for $\tau = 63$ and $\tau = 16$ are given by Fig. 7.4a, b respectively.

We have also tried to reconstruct the attractor from the other two components of the Lorenz system [48] but both of them were found to be even worsen than the attractors given by Fig. 7.4a, b.

Remarks Obviously, the reconstructed attractor given by Fig. 7.2b looks like the original attractor of the Lorenz system given by Fig. 7.1a. In fact, *Sd* value of this reconstructed attractor is more than that of the same reconstructed under linear AC and AMI. Thus it is established that by using new type of nonlinear auto-correlation of bivariate data, it is possible to reconstruct the attractor of the Lorenz system properly and the attractor is even better and lesser distorted than the same reconstructed under the other measures. Thus this new type of nonlinear auto-correlation of bivariate data can be more effective for attractor reconstruction from a single time series data.

7.3.1.5 Application on Real Data

Since this new nonlinear measure is found to be very effective on Lorenz dynamical system, it is expected to work on real data in getting the least distorted reconstructed attractor out of it. So, we present few applications of this comparatively new measure on some real continuous signals, where the dynamical models behind the generation of the signals are not known. In this context, we have chosen two music signals—both of them are Indian classical Sarod recitals, one is of raga 'Anandi' and the other is of raga 'Bhairavi '. Both of them were played by one of the renowned Sarod player Ustad. Amjad Ali Khan and they were recorded at 16 bits per sample with sample rate 44,100 by using Adobe Audition 1.5 software. None of them were normalized. The reason of choosing music signals is that they are easier to collect by available software, and more importantly the music signals are basically non-stationary and are always found to possess different types of non-linearity. Though these music signals are basically non-stationary as a whole, yet the smaller segments (length varies between 150 and 500) of those signals have some definite form in most of the cases. At this point, one may raise question regarding the loss of generality for choosing such a smaller segment of the music signals. However, when the auto-correlation of a signal is considered, it is basically the correlation between two segments of the signal of finite length differing by one unit only. So, there is no question of making an attempt for a nonlinear fit with the whole signal.

A. Test for Non-stationarity: Q-Q Plot

By non-stationary signal we mean a signal where the pattern of probability distributions of different segments are not equal at all. To test the non-stationarity of the signal, Quantile-Quantile plot (Q-Q plot) [57] is used. Basically it is a graphical technique to determine whether or not two data sets come from populations with a common distribution. More precisely, it is a plot of the quantiles of the first data set against the quantiles of the second data set. If the two sets come from a population with the same distribution, the points must fall approximately along the reference line $y = x$. The greater is the departure from this reference line, the greater is the evidence for the conclusion that the two data sets have come from populations with

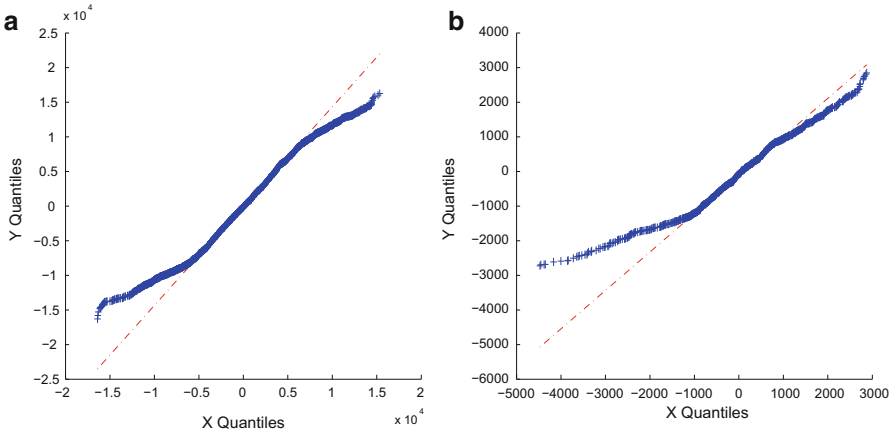

Fig. 7.5 Q-Q plots for the music signal of raga (**a**) 'Anandi' and (**b**) 'Bhairavi'. In both the figures, the points do not fall approximately along the reference line $y = x$ and hence both the signals are non-stationary

different distributions. This proves that the statistical parameters of the segments of equal length are always different. In other words, signal is non-stationary.

Thus for the music signals based on raga 'Anandi' and raga 'Bhairavi', Q-Q plots [57] are drawn (Fig. 7.5a, b) and non-stationarity of both the signals have been established.

B. Test for Non-linearity: Surrogate Data Method

The existence of non-linearity in the underlying experimental data is generally investigated by Surrogate data method, initially introduced by Theiler et al. [58]. In this method, a null hypothesis is formed for a specific process class and the system output is compared with this hypothesis at a level of significance α. In order to do this, $(\frac{2}{\alpha} - 1) - \frac{1}{\alpha}$ surrogates are first generated for a one side (two-side) test. A suitable statistic is then chosen and its value for the original data is compared to the same of the surrogates. If the value of the statistic of the data deviates from that of the surrogates, then the null hypothesis is rejected. In this concern, Schreiber and Schmitz introduced an improved surrogate data method [59] which is used to test non-linearity for all types of stationary and non-stationary signals. In this method, the testing is done with significance level 0.01 in three steps. In the first step 99 surrogate data are generated by Iterative Amplitude Adjusted Truncated Fourier Transform (IAATFT) [59] from the observed data, in the second step the nonlinear version of auto-correlation statistics—Average Mutual Information $(AMI)(\tau = 1)$ is considered as discriminate statistics and finally a null hypothesis is formed against which observations are tested.

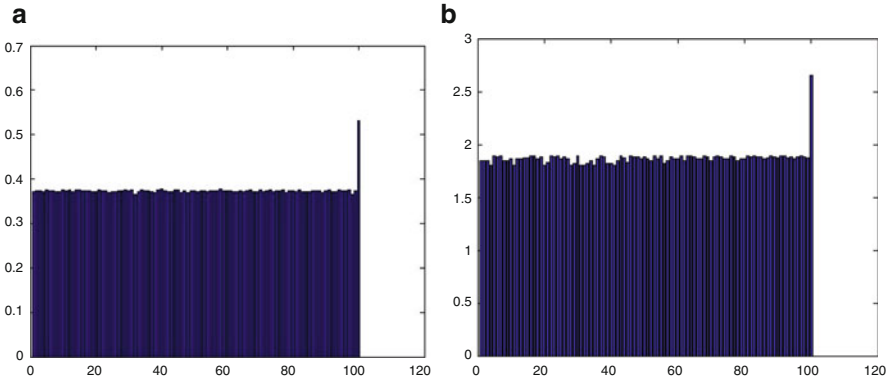

Fig. 7.6 Surrogate data test for the music signal of raga (**a**) 'Anandi' and (**b**) 'Bhairavi' under AMI with $\tau = 1$. The surrogates are represented by the indices 1–99 and the index number 100 represents the original signal measured along X-axis. Y-axis represents the corresponding value of $AMI(\tau = 1)$. In both the figures, the value of $AMI(\tau = 1)$ of the music signal is greater than the same of their respective 99 surrogates and hence both the signals are nonlinear

In this connection, the null hypothesis (H_0) is taken as $H_0 : AMI_{experimentalsignal}(\tau = 1) = AMI_{SUR(experimentalsignal)}(\tau = 1)$. The discriminating statistic AMI [44, 45] is basically a number that quantifies some aspect of the time series. If the value of AMI ($\tau = 1$) for the experimental signal is different from all of its surrogates, then the null hypothesis can be rejected with the given level of significance. If the null hypothesis is rejected, the experimental signal must be nonlinear.

The Surrogate data test [59] with significance level 0.01 and the statistical parameter AMI ($\tau = 1$) of the music signals of raga 'Anandi' and 'Bhairavi' are given in Fig. 7.6a, b.

It is observed from Fig. 7.6a, b that the AMI of surrogate data series is not equal to AMI of the given signals. Hence the null hypotheses $H_0 : AMI_{Anandi}(\tau = 1) = AMI_{SUR(Anandi)}(\tau = 1)$ and $H_0 : AMI_{Bhairabi}(\tau = 1) = AMI_{SUR(Bhairabi)}(\tau = 1)$ are rejected and thus the non-linearity of the music signal of raga 'Anandi' and'Bhairavi' are established by Surrogate data test [59].

C. Test for Chaos: Lyapunov Exponent

Since both the music signal of raga 'Anandi' and raga 'Bhairavi' are nonlinear, the largest Lyapunov exponent (LLE) [18, 21, 29] of these signal is computed to test the existence of deterministic chaos. This largest Lyapunov exponents [18, 21, 29] quantify the exponential divergence of initially close state-space trajectories and estimate the amount of chaos in a system. Several methods of finding this Lyapunov exponent are available but in this case a comparatively new method [18, 21, 29] has been used. The method follows directly from the definition of the LLE and is accurate because it takes advantage of all the available data. The algorithm is fast,

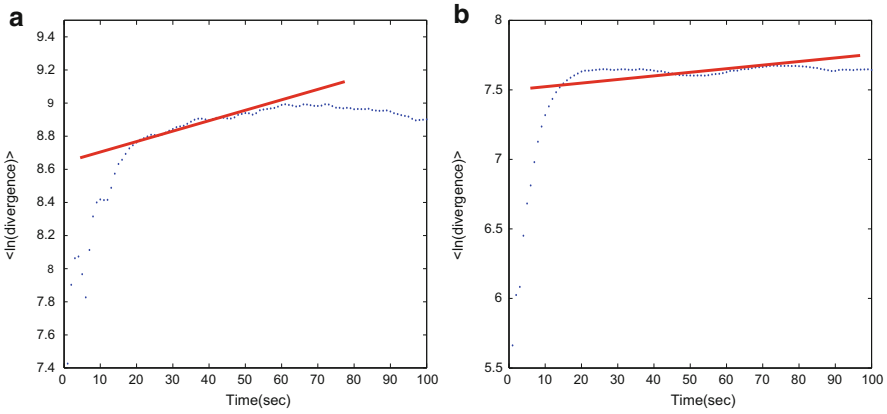

Fig. 7.7 *Straight lines*, fitted on the linear region of < ln(divergence) > for the music signal of raga (**a**) 'Anandi' and (**b**) 'Bhairavi'

easy to implement, and robust to changes in the following quantities: embedding dimension, size of data set, reconstruction delay, and noise level. The LLE is easily and accurately calculated by using a least-squares fit to the 'average' line defined by $y(i) = \frac{1}{\Delta} < ln(d_j(i)) >$, where $< . >$ denotes the average over all values of j and $d_j(i)$ is the distance between the jth pair of nearest neighbors after i discrete-time steps, i.e., $i\Delta t$ seconds.

To find the LLE of both the music signals, straight lines are fitted on the average of log(divergence) of the music signals of raga 'Anandi' and raga 'Bhairavi'. The coefficients a and b of the fitted straight lines $x = at + b$ are given by $a = 0.0044, b = 8.6947$ for the music signal of raga 'Anandi' and $a = 0.00064, b = 7.6042$ for the music signal of raga 'Bhairavi'. These are shown by Fig. 7.7a, b respectively.

The LLE for the music signals of raga 'Anandi' and raga 'Bhairavi' are calculated from the slope of the fitted straight lines in Fig. 7.7a, b. The values are found to be 0.88 and 0.128 respectively (by considering the sampling frequency as 200 Hz). Thus the LLE for both the music signals are found to be positive. This indicates that both the signals possess chaotic attractor.

D. Reconstruction of the Attractors

Let $\{x_A(t)\}_{t=1}^{10000}$ and $\{x_B(t)\}_{t=1}^{10000}$ be 10,000 samples of the recorded north Indian Classical Music (Sarod) based on raga 'Anandi' and 'Bhairavi' respectively. The time series plots of these signals are given by Fig. 7.8a, b respectively.

A best nonlinear curve fit for the smaller segment of length 200 of the music signal based on raga 'Anandi' is then obtained. Similarly another best nonlinear

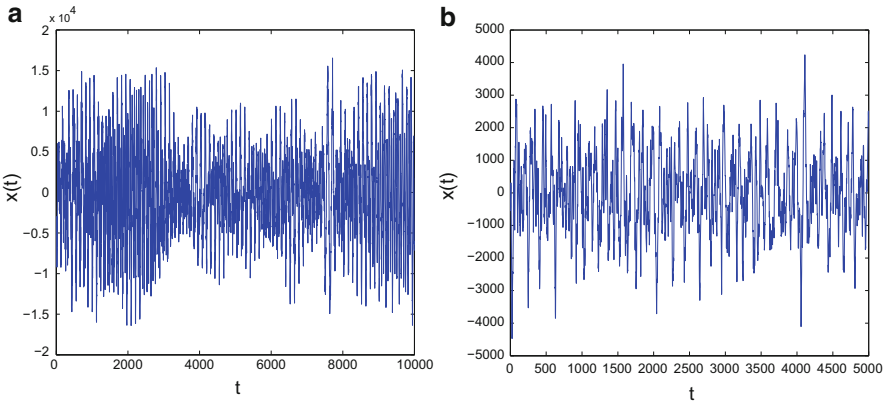

Fig. 7.8 Time series plot of the music signals based on raga (**a**) 'Anandi', (**b**) 'Bhairavi'

curve fit for the smaller segment of length 150 of the music signal based on raga 'Bhairavi' is obtained. These are respectively given by Eqs. (7.9) and (7.10).

$$f(t) = a_1 \exp(-((t-b_1)/c_1)^2) + a_2 \exp(-((t-b_2)/c_2)^2) + a_3 \exp(-((t-b_3)/c_3)^2) + a_4 \exp(-((t-b_4)/c_4)^2) + a_5 \exp(-((t-b_5)/c_5)^2) + a_6 \exp(-((t-b_6)/c_6)^2) + a_7 \exp(-((t-b_7)/c_7)^2) \tag{7.9}$$

where $a_1 = 5,109, b_1 = 172.5, c_1 = 2.314, a_2 = 4,881, b_2 = 182.8, c_2 = 1.539, a_3 = 14,430, b_3 = 72.76, c_3 = 10.7, a_4 = -42,800, b_4 = 226, c_4 = 150.5, a_5 = 44,280, b_5 = 178.9, c_5 = 47.44, a_6 = 20,420, b_6 = 102.3, c_6 = 24.66, a_7 = 15,340, b_7 = 48.09, c_7 = 15.19$.

$$f(t) = a_0 + a_1 \cos(wt) + b_1 \sin(wt) + a_2 \cos(2wt) + b_3 \sin(3wt) + a_4 \cos(4wt) + b_5 \sin(5wt) + a_6 \cos(6wt) + b_6 \sin(6wt) + a_7 \cos(7wt) + b_7 \sin(7wt) + a_8 \cos(8wt) + b_8 \sin(8wt) \tag{7.10}$$

where $a_0 = -5.015 \times 10^{13}, b_1 = -4.742 \times 10^{15}, a_2 = 8,754 \times 10^{13}, b_3 = 4.242 \times 10^{15}, a_4 = -6.004 \times 10^{13}, b_5 = -4.933 \times 10^{15}, a_6 = 4.397 \times 10^{13}, b_6 = 4.319 \times 10^{15}, a_7 = -2.616 \times 10^{13}, b_7 = -1.569 \times 10^{15}, a_8 = 4.83 \times 10^{12}, b_8 = 2.189 \times 10^{14}, w = 0.0816$.

The above curves of best fit for the music signals of raga 'Anandi' (Eq. 7.9) and raga 'Bhairavi' are (Eq. 7.10) are shown by Fig. 7.9a, b respectively.

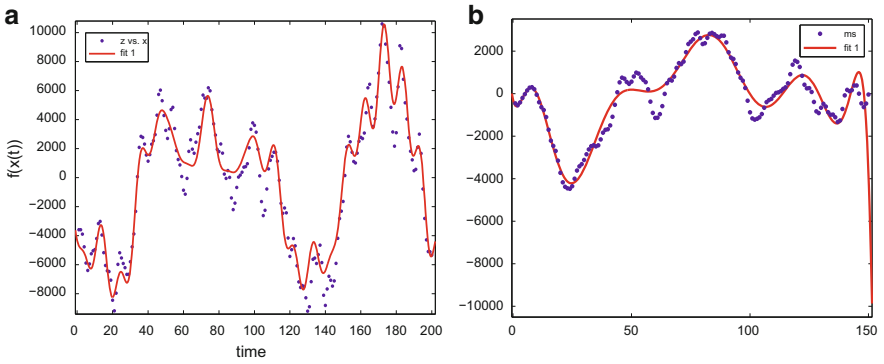

Fig. 7.9 Best nonlinear curve fit for the music signal (**a**) $\{x_A(t)\}_{t=1}^{200}$ of raga 'Anandi', (**b**) $\{x_B(t)\}_{t=1}^{200}$ of raga 'Bhairavi'

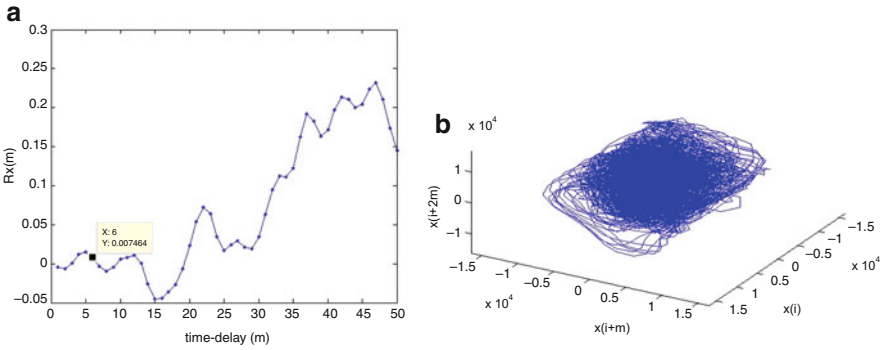

Fig. 7.10 (**a**) Two dimensional correlogram diagram for the music signal based on raga ' Anandi' under new type of nonlinear auto-correlation of bivariate data, (**b**) reconstructed three dimensional attractor of the music signal based on raga 'Anandi' with time-delay $\tau = 6$ obtained from the correlogram diagram

We now reconstruct the underlying dynamics of both the music signals under the notion of new type of auto-correlation of bivariate data [51] one by one. Let us first consider the music signal of raga 'Anandi'.

In this case, the new type of nonlinear auto-correlation $r_X(\tau)$ between $\{x(t+\tau)\}_{t=1}^{200-\tau}$ and $\{f(x(t))\}_{t=1}^{200}$, given by Eq. (7.6) is first computed for different values of τ, where f is the best nonlinear fit of the music signal 'Anandi' given by Eq. (7.9). This $r_X(\tau)$ is then plotted against τ to form the two dimensional correlogram diagram. This is shown by Fig. 7.10a. The suitable value of the time-delay $\tau = 6$ is obtained from this correlogram diagram. The three dimensional attractor is finally reconstructed with the coordinates $(x_A(t), x_A(t+\tau), x_A(t+2\tau)), t = 1, 2, \ldots, (10000 - 2\tau)$. This is given by Fig. 7.10b.

We next reconstruct the attractor of the other music signal based on raga 'Bhairavi'.

To reconstruct the attractor of the aforesaid music signal based on raga 'Bhairavi', Eq. (7.6) is first used to determine the nonlinear auto-correlation [51] $r_X(\tau)$ between $\{x(t+\tau)\}_{t=1}^{150-\tau}$ and $\{f(x(t))\}_{t=1}^{150}$, where f is the best nonlinear fit available for a smaller segment of this music signal, given by Eq. (7.10). The suitable value of τ is obtained from the corresponding two dimensional correlogram diagram as discussed in Sect. 7.3.1.1. In this case, the value of τ is found to be three. Finally, the three dimensional attractor is reconstructed with time-delay $\tau = 3$, which is given by Fig. 7.11.

On the other hand, the linear AC measure is not applicable as both the signals are perfectly nonlinear. However the general measure AMI may be used in these cases. The plot of AMI(τ)against the time-delay τ for the music signals based on raga 'Anandi' and 'Bhairavi' are shown by Fig. 7.12a, b.

It is evident from the above figures that the suitable time-delay for the music signals of raga'Anandi' and 'Bhairavi' are found to be 18. The respective reconstructed attractors are given by Fig. 7.13a, b.

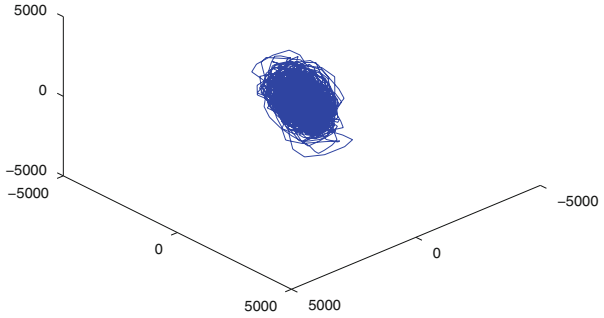

Fig. 7.11 Reconstructed three dimensional attractor of the music signal based on raga 'Bhairavi' with $\tau = 3$ under the new type of nonlinear auto-correlation of bivariate data

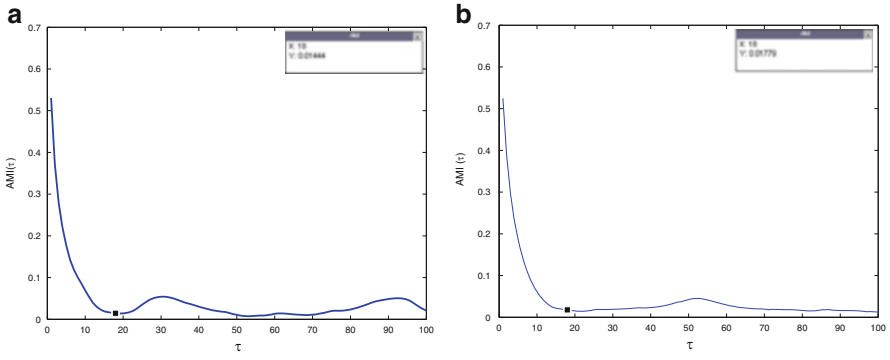

Fig. 7.12 Plot of AMI against time-delay for the music signals of raga (**a**) 'Anandi' and (**b**) 'Bhairavi'

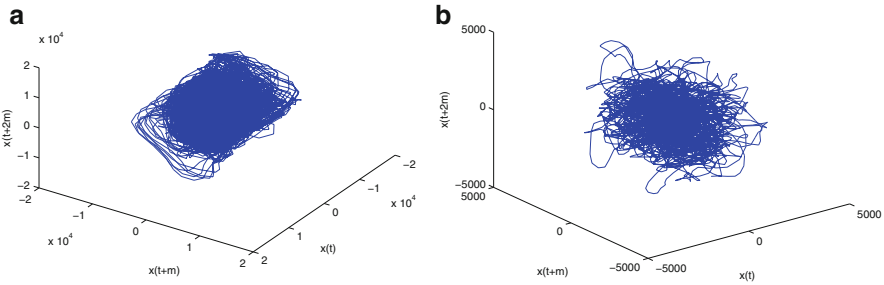

Fig. 7.13 Reconstructed three dimensional attractor of the music signal based on raga (**a**) 'Anandi' and (**b**) 'Bhairavi' with $\tau = 18$ obtained under AMI measure

7.3.1.6 Remarks

Three dimensional reconstructed attractor under AMI measure [44, 45] of the music signals of raga 'Anandi' and 'Bhairavi' given by Fig. 7.13a, b respectively, show lack of density in the orbits and hence they can not be considered as attractors in the proper sense of the term. In fact, the attractor given by Fig. 7.13b possesses many outliers also. However, the three dimensional attractors of both the signals reconstructed under new type of nonlinear auto-correlation of bivariate data, given by Figs. 7.10b and 7.11 show significant improvement over their respective attractors reconstructed under AMI. The three dimensional attractors of Figs. 7.10b and 7.11 reconstructed under this measure exhibit orbits, which are almost dense except for very few outliers. So these attractors are supposed to be the least distorted reconstructed attractor for the music signal of raga 'Anandi' and'Bhairavi' respectively. This not only establishes the applicability of this new type of nonlinear auto-correlation measure, but also it claims the superiority of attractor reconstruction under this new type of nonlinear auto-correlation of bivariate data [51] over those reconstructed under the AMI measure.

7.3.2 For Multiple Time Series

Let us first generalize the procedure for attractor reconstruction from a single component of the solution vector of a system of differential equations such that it is possible to reconstruct the attractor by utilizing multiple components of the solution vector. Since the given Lorenz system [48] consists of three differential equations, the solution vector of the Lorenz system has three components. Let $(x_1(t), x_2(t), x_3(t)$ be the solution vector of the given system. The independent coordinates can be taken as $(u(t), u(t+\tau), u(t+2\tau)), t = 1, 2, 3, \ldots, N - 2\tau$, for the time-delay τ, where u, v, w are chosen from x_1, x_2, x_3. The suitable time-delay

τ is determined from the two dimensional correlogram as described earlier. Finally, the attractors are reconstructed in three dimensions with these points.

In case of different time-delays, the independent coordinates are taken as $(u(t), u(t+\tau_1), u(t+\tau_1+\tau_2)), t = 1, 2, 3, \ldots., N-(\tau_1+\tau_2)$, for the time-delays τ_1, τ_2, where u, v, w are chosen from x_1, x_2, x_3. The suitable time-delays τ_1, τ_2 are determined from three dimensional correlogram diagram. This is basically a three dimensional plot of the time-delays τ_1, τ_2 against the respective correlation measure. The three dimensional attractors are then reconstructed with these independent coordinates.

7.3.2.1 Higher Dimensional MI

One of the major limitation of AMI [44, 45] discussed in Sect. 7.3.1 is that it was computed between two variables $x(t)$ and $x(t-\tau)$ only, where τ is the time-delay. This actually constrains the higher dimensional attractor in the sense that the variables $x(t-2\tau)$,$x(t-3\tau), \ldots..$ etc. are selected automatically, without care of the information content added by these variables to the information already contained in $x(t)$ and $x(t-\tau)$. This problem can be solved in two ways. One way is to evaluate the information contained as a whole by all variables involved in the reconstruction of attractors. The other way is to allow more freedom by removing the constraint that time-delays are multiple one from another. In other words, instead of same time-delay (τ) repeated, different time-delays $\tau_1, \tau_2, \tau_3, \ldots..$ may be used. Thus, a multidimensional criterion needs to be incorporated with the notion of MI. From this view point, the notion of higher dimensional MI [46, 47] was introduced. In this section, we briefly discuss this measure under same time-delay repeated and different time-delays.

A. Same Time-Delay Repeated

Let the attractor to be reconstructed is m dimensional. We define the required m variables as follows: $X_1 = x(t), X_2 = x(t-\tau), X_3 = x(t-2\tau), \ldots., X_m = x(t-(m-1)\tau)$.

Equation (7.4) is then generalized to obtain m-dimensional MI given by Eq. (7.11).

$$MI(X_1, X_2, \ldots., X_m) = \sum_t Prob[X_1, X_2, \ldots., X_m] log\left(\frac{Prob[X_1, X_2, \ldots., X_m]}{Prob[X_1]Prob[X_2]\ldots..Prob[X_m]}\right). \quad (7.11)$$

Thus, MI is a measure of the discrepancy between the probability density of the joint variables and the product of the marginal densities.

The suitable time-delay τ is obtained in exactly the same way as it was obtained for AMI [44, 45].

However, it is very difficult to estimate this higher dimensional MI in practice. This is because, the unknown probability densities cannot be estimated accurately in a high-dimensional space. Thus, it is estimated in an alternative way proposed by Kraskov et al. [46]. This idea is based on a K-NN estimator [46].

B. Different Time-Delays

Higher dimensional MI with different time-delays $\tau_1, \tau_2, \tau_3, \ldots, \tau_{m-1}$is a further generalization of the higher dimensional MI with same time-delay repeated [46]. This measure is determined by similar technique as discussed in the previous section with the exception that the m-variables $X_1, X_2, \ldots, X_m$ are taken as $x(t), x(t - \tau_1), x(t - \tau_2), \ldots, x(t - \tau_{m-1})$ respectively.

7.3.2.2 Generalized Auto-Correlation (GAC)

It has already been highlighted in the introduction section that the best possible approach for understanding real life nonlinear phenomena is to reconstruct the dynamics of the system from the data itself, which involves choice of proper time-delay and proper embedding space. However, most of the real life nonlinear data are non-stationary and thus the linear AC measure and even the AMI measure fail to produce the proper time-delay for phase space reconstruction in such cases. As a remedy to this problem, the earlier strategy was to first make the time series stationary and then to apply the known methods of analysis of stationary time series. But in this process, some important information might be lost. In this section, our purpose is to modify the auto-correlation measure in such a way that it is applicable to any signal (time series), whether stationary or non-stationary. Let $\{x(t)\}_{t=1}^{N}$ be such a non-stationary time series. It is known [42, 43] that the time-delay τ for which $x(t)$ and $x(t + \tau)$ are linearly independent, is the first value of τ corresponding to which the auto-correlation coefficient is positive minimum in the correlogram diagram. Obviously in this case $x(t), x(t + \tau), x(t + 2\tau), \ldots..$ are also linearly independent. At this point, the following limitations may be noted:

1. The very definition of auto-correlation demands that the time series must be stationary, as the means and the variances are taken to be the same in all stages of the signal. Naturally the investigations are not applicable to non-stationary signals;
2. It is not possible to find out the independent coordinates with different delay of the form $(x(t), x(t + \tau_1), x(t + \tau_1 + \tau_2), \ldots\ldots)$, although there is no specific reason in choosing same τ in determining the m linearly independent coordinates $(x(t), x(t + \tau), x(t + 2\tau), \ldots.., x(t + (n - 1)\tau))$.

With a view to overcoming such shortfalls in the earlier discussions, we consider generalizations of auto-correlation functions. Obviously to compare two and three stages of a non-stationary signal, our modified definition of auto-correlation works. Moreover, our generalized definition of auto-correlation [52] works well for any finite dimensional attractor reconstruction [1–16].

A. Different Time-Delays

Let $\{x(t)\}_{t=1}^{N}$ be the given time series. The generalized auto-correlation [52] of the given time series with respect to different time-delays τ_1, τ_2 is defined by

$$R_x(\tau_1,\tau_2) = \frac{\sum_{t=1}^{(N-\tau_1-\tau_2)} \zeta_t \zeta_{t+\tau_1} \zeta_{t+\tau_1+\tau_2}}{\sqrt{\sum_{t=1}^{(N-\tau_1-\tau_2)} \zeta_t^2} \sqrt{\sum_{t=1}^{(N-\tau_1-\tau_2)} \zeta_{t+\tau_1}^2} \sqrt{\sum_{t=1}^{(N-\tau_1-\tau_2)} \zeta_{t+\tau_1+\tau_2}^2}} \tag{7.12}$$

$$\zeta_t = (x(t) - \overline{x(t)}), \zeta_{t+\tau_1} = (x(t+\tau_1) - \overline{x(t+\tau_1)}), \zeta_{t+\tau_1+\tau_2}$$
$$= (x(t+\tau_1+\tau_2) - \overline{x(t+\tau_1+\tau_2)})$$

where $\overline{x(t)}, \overline{x(t+\tau_1)}$ and $\overline{x(t+\tau_1+\tau_2)}$ are the means of the time series $\{x(t)\}_{t=1}^{N-(\tau_1+\tau_2)}$, $\{x(t)\}_{t=1+\tau_1}^{N-\tau_2}$ and $\{x(t)\}_{t=1+\tau_1+\tau_2}^{N}$ respectively and $1 \le \tau_1, \tau_2 \le \frac{N}{2}$, if N is even and $1 \le \tau_1, \tau_2 \le \frac{N-1}{2}$, if N is odd.

The suitable time-delay (τ_1, τ_2) is one, where GAC with different time-delays [52] $R_x(\tau_1, \tau_2)$ given by (7.12) comes nearer to zero for the first time in the three dimensional correlogram diagram.

B. Same Time-Delay Repeated

In particular, when $\tau_1 = \tau_2 = \tau$, Eq. (7.12) reduces to

$$R_x(\tau) = \frac{\sum_{t=1}^{(N-2\tau)} \zeta_t \zeta_{t+\tau} \zeta_{t+2\tau}}{\sqrt{\sum_{t=1}^{(N-2\tau)} \zeta_t^2} \sqrt{\sum_{t=1}^{(N-2\tau)} \zeta_{t+\tau}^2} \sqrt{\sum_{t=1}^{(N-2\tau)} \zeta_{t+2\tau}^2}} \tag{7.13}$$

$$\zeta_t = (x(t) - \overline{x(t)}), \zeta_{t+\tau} = (x(t+\tau) - \overline{x(t+\tau)}), \zeta_{t+2\tau}$$
$$= (x(t+2\tau) - \overline{x(t+2\tau)})$$

where $\overline{x(t)}, \overline{x(t+\tau)}$ and $\overline{x(t+2\tau)}$ are the means of the time series $\{x(t)\}_{t=1}^{N-2\tau}$, $\{x(t)\}_{t=1+\tau}^{N-\tau}$ and $\{x(t)\}_{t=1+2\tau}^{N}$ respectively and $1 \le \tau \le \frac{N}{2}$, if N is even and $1 \le \tau \le \frac{N-1}{2}$, if N is odd.

The suitable time-delay τ is one, where GAC with same time-delay repeated [52] ($R_x(\tau)$) given by (7.13) comes nearer to zero for the first time in the two dimensional correlogram diagram.

7.3.2.3 Cross Auto-Correlation (CAC)

Cross auto-correlation (CAC) [53] is a measure, which basically fits a nonlinear curved surface trend. The problem of attractor reconstruction [1–16] still depends on finding proper time-delay and embedding dimensions [11, 12]. The newly introduced concept of nonlinear method gives better result in determining the suitable time-delay and hence indirectly helping in attractor reconstruction. For geometrical clarity, once again we like to consider the embedding dimension to be three. We first define CAC [53] step by step.

A. Total Correlation

In determining linear regression coefficients, a *line of best fit* is tried for the given two dimensional points by the method of least squares. In case of *two dimensional nonlinear points*, the points do not lie on a line or more precisely they cannot be approximated by a line of best fit. Thus to find the corresponding nonlinear regression coefficients, a *curve of best fit* is tried with the given two dimensional nonlinear points by the method of least squares. Since the points have a nonlinear trend, the method of nonlinear correlation needs to be applied. However, when two sets of data points have nonlinear trend, ultimately by proper substitution, two sets of data points with linear trend are obtained and the same correlation formula for linear trend is used to compute the correlation coefficient even in this case of nonlinear trend.

The difficulty arises when three time series of any suitable size is considered. If the points have a planar trend, then plane of regression may be tried. But this precisely means that variable corresponds to one of the time series must be related with the two other variables correspond to two other time series by a linear function. Thus, a new data set of the approximated time series is obtained. Naturally correlation formula for these two series—one is the given time series and the other one is the approximated time series is calculated, which is defined as the *total correlation* [60] of the given three time series having planar trend.

When n time series are compared simultaneously a *hyper-plane of best fit* of the form $w = a_1u_1 + a_2u_2 + a_3u_3 + \ldots\ldots + a_{n-1}u_{n-1} + a_n$ is tried with the n-dimensional non-planer points $(x_1(t), x_2(t), x_3(t), \ldots.., x_n(t))$ to find total correlation coefficient. By applying the method of least squares and using these given n dimensional points, values of $a_1, a_2, a_3, \ldots\ldots, a_n$ are determined. Thus, a plane of the form $w = f(u_1, u_2, u_3, \ldots.., u_{n-1})$ is obtained, where f is a known linear function of $u_1, u_2, u_3, \ldots.., u_{n-1}$. We call this new data set as $\{w'\}$. The total correlation coefficient [60] is defined as the linear correlation coefficient between

$\{w'\}$ and the set $\{w''\}$, which is given by the nth component of the n-dimensional points $(x_1(t), x_2(t), x_3(t), \ldots.., x_n(t))$.

B. Cross Correlation

Suppose the three time series have a curved surface trend instead of a planar trend. In this case, it is not possible to get two time series with linear trend by proper substitution as done in the two dimensional case. So the correlation of three time series with linear trend is extended to correlation of three time series with nonlinear trend. We call it *cross-correlation* in general and *cross-auto-correlation* in particular. Obviously in this case, the points on the attractor lie on a fractal set consisting of different non-planar, non-smooth points. As a matter of fact, these non-planar points cannot be approximated by plane of best fit. Rather, these points can be better approximated by a smooth hyper-surface, which we call a *hyper-surface of best fit*. Even when more than three time series are compared simultaneously, the same procedure is followed. In this process, the actual non-planar n-dimensional points $(x_1(t), x_2(t), x_3(t), \ldots.., x_n(t))$, where each $x_i(t), i = 1, 2, 3, \ldots\ldots, n$ is a time series, are approximated by fitting a smooth hyper-paraboloid of the form $w = a_1u_1^{n-1} + a_2u_2^{n-1} + a_3u_3^{n-1} + \ldots\ldots + a_{n-1}u_{n-1}^{n-1} + a_n$ and then the method of least square is applied to obtain the *hyper-surface of best fit* given by $w = a_1u_1^{n-1}+a_2u_2^{n-1}+a_3u_3^{n-1}+\ldots\ldots+a_{n-1}u_{n-1}^{n-1}+a_n$, where $a_1, a_2, a_3, \ldots\ldots, a_n$ are determined from the following equations:

$$
\begin{aligned}
\sum w &= a_1 \sum u_1^{n-1} + a_2 \sum u_2^{n-1} + \ldots. + a_{n-1} \sum u_{n-1}^{n-1} + n a_n, \\
\sum u_1^{n-1} w &= a_1 \sum u_1^{2n-2} + a_2 \sum u_1^{n-1} u_2^{n-1} + \ldots. + a_{n-1} \sum u_1^{n-1} u_{n-1}^{n-1} + a_n \sum u_1^{n-1}, \\
\sum u_2^{n-1} w &= a_1 \sum u_1^{n-1} u_1^{n-1} + a_2 \sum u_2^{2n-2} + \ldots. + a_{n-1} \sum u_2^{n-1} u_{n-1}^{n-1} + a_n \sum u_2^{n-1}, \\
&\ldots\ldots\ldots\ldots\ldots\ldots\ldots\ldots \\
&\ldots\ldots\ldots\ldots\ldots\ldots\ldots\ldots \\
\sum u_{n-1}^{n-1} w &= a_1 \sum u_{n-1}^{n-1} u_1^{n-1} + a_2 \sum u_{n-1}^{n-1} u_2^{n-1} + \ldots. + a_{n-1} \sum u_{n-1}^{2n-2} + a_n \sum u_{n-1}^{n-1},
\end{aligned}
\tag{7.14}
$$

Thus a hyper-surface of the form $w = f(u_1, u_2, u_3, \ldots.., u_{n-1})$ is obtained, where f is a nonlinear function of $u_1, u_2, u_3, \ldots.., u_{n-1}$. Let us denote this new data set as $\{w'\}$. The *cross correlation coefficient* is defined as the linear correlation coefficient between $\{w'\}$ and the set $\{w''\}$, which is given by the nth component of the n-dimensional points $(x_1(t), x_2(t), x_3(t), \ldots.., x_n(t))$. Since the equation of the hyper-paraboloid contains one linear term and $n - 1$ nonlinear terms, while the other surfaces like hyper-ellipsoid or hyper-hyperboloid contain n nonlinear terms, the calculation becomes more complex and unmanageable and takes more computational time in the later cases. For this reason, only a hyper-paraboloid

$w = a_1u_1^{n-1} + a_2u_2^{n-1} + a_3u_3^{n-1} + \ldots\ldots + a_{n-1}u_{n-1}^{n-1} + a_n$ is fitted to the given non-planar points, which definitely minimizes the computation time. Moreover, there is no loss of generality in choosing such a simpler form of hyper-surface, because only small segments of the time series have been taken for considering non-linearity of the time series and hence it makes no difference whether we consider a hyper-paraboloid or a hyper-ellipsoid or a hyper-hyperboloid as a hyper-surface of best fit.

C. Cross Auto-Correlation

It is a particular case of cross correlation. Cross-correlation was developed for comparing n time series simultaneously. But when a single time series is considered, cross-correlation becomes cross-auto-correlation (CAC) [53].

Let $x_1(t), x_2(t), x_3(t), \ldots.., x_n(t)$ be the solution component of some n-dimensional dynamical system. To define CAC for a single solution component $\{x(t)\}_{t=1}^{N}$ of the dynamical system with copies under same time-delay repeated and different time-delays, we proceed as follows:

Let us first consider single time series with copies under same time-delay repeated [53].

In this case, we first find the n independent coordinates $(x(t), x(t+\tau), x(t+2\tau), \ldots., x(t+\overline{n-1}\tau))$ with time-delay τ as follows: Firstly, the time series is partitioned into n groups, viz. $\{x(t)\}_{t=1}^{N-(n-1)\tau}, \{x(t)\}_{t=1+\tau}^{N-(n-2)\tau}, \{x(t)\}_{t=1+2\tau}^{N-(n-3)\tau}, \ldots.., \{x(t)\}_{t=1+(n-1)\tau}^{N}$. Thus we have n sets of data in n-dimensional spaces given by $u_{t,1}, u_{t,2}, u_{t,3}, \ldots., u_{t,n}$, where $u_{t,1} = x(t), u_{t,2} = x(t+\tau), u_{t,3} = x(t+2\tau), \ldots\ldots., u_{t,n} = x(t+(n-1)\tau), t = 1, 2, 3, \ldots., N-(n-1)\tau$. $u_{t,1}, u_{t,2}, u_{t,3}, \ldots., u_{t,n-1}$ are then substituted for $u_1, u_2, \ldots, u_{n-1}$ in the equation $w = a_1u_1^{n-1} + a_2u_2^{n-1} + a_3u_3^{n-1} + \ldots\ldots + a_{n-1}u_{n-1}^{n-1} + a_n$ of the best fitted hyper-surface to obtain a new time series $\{w_t\}_{t=1}^{N-(n-1)\tau}$. The cross auto-correlation between these n time series $u_{t,1} = x(t), u_{t,2} = x(t+\tau), u_{t,3} = x(t+2\tau), \ldots\ldots., u_{t,n} = x(t+(n-1)\tau)$ denoted by $r_{n,x}(\tau)$, is defined as the correlation between $\{w_t\}_{t=1}^{N-(n-1)\tau}$ and $\{u_{t,n}\}_{t=1}^{N-(n-1)\tau}$ with respect to the time-delay τ and is given by

$$R_x(\tau) = \frac{\sum_{t=1}^{N-(n-1)\tau}(u_{t,n} - \overline{u_{t,n}})(w_t - \overline{w_t})}{\sqrt{\sum_{t=1}^{N-(n-1)\tau}(u_{t,n} - \overline{u_{t,n}})^2}\sqrt{\sum_{t=1}^{N-(n-1)\tau}(w_t - \overline{w_t})^2}} \tag{7.15}$$

where $\overline{u_{t,n}}$ and $\overline{w_t}$ are the means of the time series $u_{t,n}$ and w_t respectively and $\tau = 1, 2, 3, \ldots., N-1$.

The suitable time-delay τ for the reconstruction of attractor is obtained from the two dimensional correlogram diagram exactly in a similar manner as it was obtained under GAC with same time-delay repeated [52].

We next consider single time series under different time-delays [53].

To find the n independent coordinates $(x(t), x(t+\tau_1), x(t+\tau_1+\tau_2), \ldots\ldots, x(t+\tau_1+\tau_2+\ldots\ldots+\tau_{n-1}))$ for attractor reconstruction with different time-delays $\tau_1, \tau_2, \ldots.., \tau_{n-1}$, the time series is sub-divided into n groups—$\{x(t)\}_{t=1}^{N-(\tau_1+\tau_2+\ldots..+\tau_{n-1})}, \{x(t)\}_{t=1+\tau_1}^{N-(\tau_2+\ldots..+\tau_{n-1})}, \ldots.., \{x(t)\}_{t=\tau_1+\tau_2+\ldots..+\tau_{n-1}}^{N}$.

Proceeding similarly as above, the CAC [53] between the time series $u_{t,1} = x(t), u_{t,2} = x(t+\tau_1), u_{t,3} = x(t+\tau_1+\tau_2), \ldots\ldots, u_{t,n} = x(t+\tau_1+\tau_2+\ldots..+\tau_{n-1}), t = 1, 2, 3, \ldots., N-(\tau_1+\tau_2+\ldots..+\tau_{n-1})$ is defined with respect to the time-delays $\tau_1, \tau_2, \tau_3, \ldots.., \tau_{n-1}$, denoted by $r_{n,x}(\tau_1, \tau_2, \tau_3, \ldots.., \tau_{n-1})$ as the correlation between $\{u_{t,n}\}_{t=1}^{N-(\tau_1+\tau_2+\ldots..+\tau_{n-1})}, \{w_t\}_{t=1}^{N-(\tau_1+\tau_2+\ldots..+\tau_{n-1})}$, given by

$$R_{x,n}(\tau_1, \tau_2, \tau_3, \ldots.., \tau_{n-1}) = \frac{\sum_{t=1}^{\sum_{i=1}^{n-1}\tau_i}(u_{t,n}-\overline{u_{t,n}})(w_t-\overline{w_t})}{\sqrt{\sum_{t=1}^{\sum_{i=1}^{n-1}\tau_i}(u_{t,n}-\overline{u_{t,n}})^2}\sqrt{\sum_{t=1}^{\sum_{i=1}^{n-1}\tau_i}(w_t-\overline{w_t})^2}} \tag{7.16}$$

where $\overline{u_{t,n}}$ and $\overline{w_t}$ are the means of the time series $u_{t,n}$ and $w_t$respectively and $\tau_1, \tau_2, \tau_3, \ldots.., \tau_{n-1} = 1, 2, 3, \ldots., N-1$.

To find the suitable time-delays $\tau_1, \tau_2, \tau_3, \ldots.., \tau_{n-1}$ for the reconstruction of attractor, $R_{x,n}(\tau_1, \tau_2, \tau_3, \ldots.., \tau_{n-1})$ is plotted against $\tau_1, \tau_2, \tau_3, \ldots.., \tau_{n-1}$ to form the n-dimensional correlogram diagram. This is just an extension of the three dimensional correlogram diagram and so the suitable time-delays $\tau_1, \tau_2, \tau_3, \ldots.., \tau_{n-1}$ are obtained similarly as obtained under GAC with different time-delays [52].

For multiple time series with copies under same time-delay repeated, the independent coordinates are taken as $(x(t), x(t+\tau), x(t+2\tau), \ldots\ldots, x(t+\overline{n-1}\tau))$, under single time-delay τ, such that $x(t) = x_{i_1}(t), x(t+\tau) = x_{i_2}(t+\tau), x(t+2\tau) = x_{i_3}(t+2\tau), \ldots\ldots, x(t+\overline{n-1}\tau) = x_{i_n}(t+\overline{n-1}\tau)$ where $i_1, i_2, i_3, \ldots\ldots, i_n \in \{1, 2, 3, \ldots, N\}$. The CAC between these n time series is then obtained by using Eq. (7.15) and suitable time-delay τ is obtained in a similar manner as described earlier for CAC with same time-delay repeated [53].

In case of multiple time series with different time-delays $\tau_1, \tau_2, \tau_3, \ldots.., \tau_{n-1}$, the independent coordinates are taken as $(x(t), x(t+\tau_1), x(t+\tau_1+\tau_2), \ldots\ldots, x(t+\tau_1+\tau_2+\ldots\ldots+\tau_{n-1}))$,$t = 1, 2, 3, \ldots.., N-\sum_{i=1}^{n-1}\tau_i$ such that $(x(t) = x_{i_1}(t), x(t+\tau_1) = x_{i_2}(t+\tau_1), x(t+\tau_1+\tau_2) = x_{i_3}(t+\tau_1+\tau_2), \ldots\ldots, x(t+\sum_{i=1}^{n-1}\tau_i) = x_{i_n}(t+\sum_{i=1}^{n-1}\tau_i)$, where $i_1, i_2, i_3, \ldots\ldots, i_n \in \{1, 2, 3, \ldots, N\}$. The CAC [53] between these n time series is obtained by using Eq. (7.16) and suitable time-delays $\tau_1, \tau_2, \tau_3, \ldots.., \tau_{n-1}$ are obtained in a similar manner from n-dimensional correlogram as described earlier in case of CAC with different time-delays.

It is evident from the above definitions that CAC [53] is a nonlinear measure. Also since $w = a_1u_1^{n-1} + a_2u_2^{n-1} + a_3u_3^{n-1} + \ldots.. + a_{n-1}u_{n-1}^{n-1} + a_n$ represents a family of hyper-paraboloid, so for different sets of values of $a_1, a_2, a_3, \ldots., a_n$ we get different members of the family. Again different sets of values of $a_1, a_2, \ldots., a_n$ are found from the equations given by (7.12) for different set of points $(x_1(t), x_2(t), x_3(t), \ldots.., x_n(t))$, which are points on the

attractor itself. As the dynamical systems vary, their attractors satisfy different $(x_1(t), x_2(t), x_3(t), \ldots.., x_n(t))$ and so the values of $a_1, a_2, a_3, \ldots., a_n$ are also found to be different. Thus this nonlinear measure varies from dynamical system to dynamical system. In other words, CAC [53] is actually system dependent.

7.3.2.4 Experimental Results and Discussion

Let us first consider the Lorenz system given by Eq. (7.7) (Sect. 7.3.1.4).

We have already taken a wrong attempt of reconstructing the attractor of the Lorenz system [48] from each of its solution components separately under the notion of linear AC [42, 43] and AMI [44, 45] (Sect. 7.3.1.4). Therefore, we first try attractor reconstruction of the Lorenz system [48] from a single component of its solution vector under GAC with same time-delay repeated and different time-delays [52].

We apply GAC with same time-delay repeated [52] on the solution component $\{x_2(t)\}_{t=1}^{5000}$ to find a suitable τ for the reconstruction of the attractor for the aforesaid Lorenz system given by (7.7). In this case, the suitable value of τ is obtained from the two dimensional correlogram, where the GAC $R_{x_2}(\tau)$ for different values of τ are calculated by using Eq. (7.13). This is shown in Fig. 7.14a. It is evident from the above figure that the GAC [52] comes nearer to zero for the first time, when $\tau = 32$. The attractor reconstructed with this value of τ is given by Fig. 7.14b.

In a similar manner, we reconstruct the attractor from the other two components $\{x_1(t)\}_{t=1}^{5000}$ and $\{x_3(t)\}_{t=1}^{5000}$ of the solution vector by using GAC measure. The three dimensional attractors thus reconstructed are given by Fig. 7.15a, b respectively.

It is observed that the use of GAC with same time-delay repeated [52] is unable to give the proper value of time-delay towards reconstruction of the best attractor for the Lorenz system [48] by using its single solution component. However, the reconstructed attractors have improved a bit over that reconstructed under the

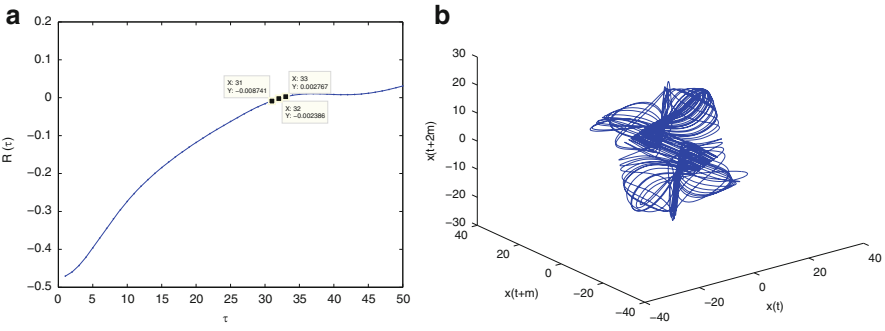

Fig. 7.14 (**a**) Two dimensional correlogram for the solution component $\{x_2(t)\}_{t=1}^{5000}$ of the Lorenz system under the notion GAC with same time-delay repeated, (**b**) three dimensional reconstructed attractor of the Lorenz system with time-delay $\tau = 32$ under the same measure

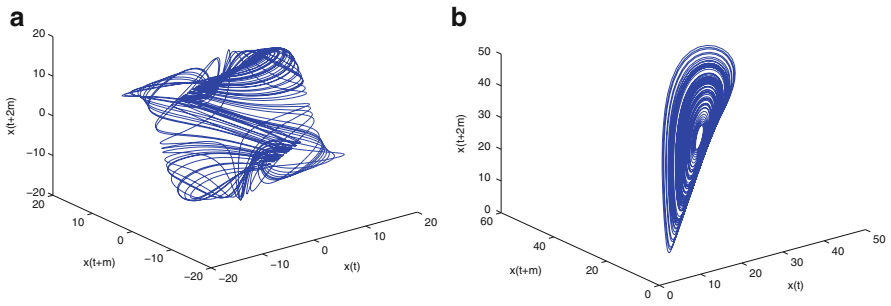

Fig. 7.15 Three dimensional reconstructed attractor of the above Lorenz system from the solution component (**a**) $\{x_1(t)\}_{t=1}^{5000}$ and (**b**) $\{x_3(t)\}_{t=1}^{5000}$ under the notion of GAC with same time-delay repeated

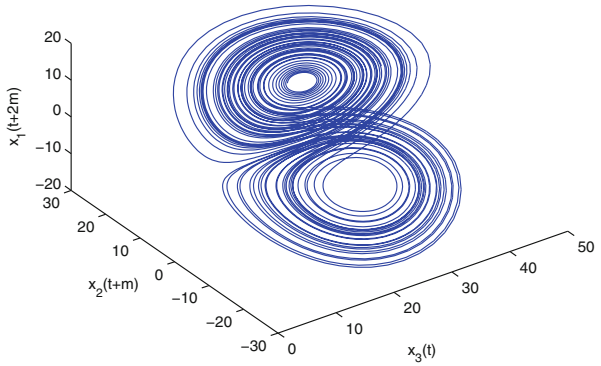

Fig. 7.16 Best form of the reconstructed attractors of the aforesaid Lorenz system with different combinations of the solution components $[(x_3(t), x_2(t+\tau), x_1(t+2\tau))]$ under GAC with same time-delay $\tau = 2$ repeated

standard auto-correlation function, with the use of this newly proposed notion. This motivates us to use this notion with multiple solution components of the Lorenz system.

Thus we next consider multiple solution components to reconstruct the attractor of the Lorenz system. One of the best reconstructed attractors using three components and suitable time-delay is shown in Fig. 7.16.

Actually, most of the reconstructed attractors for the aforesaid Lorenz system [48] show lack of density in the orbits and similarity to the original attractor (Fig. 7.1a). Hence they cannot be considered as attractors in the proper sense of the term. Some of them exhibit orbits, which are almost dense except for some outliers. Hence they may be considered as approximate attractors for the aforesaid Lorenz system. However, the reconstructed attractors given by Fig. 7.16 exhibits complete dense orbits and it may be considered as the least distorted forms of attractors, reconstructed for the Lorenz system. In fact, this attractor reconstructed with the

independent coordinates $(x_3(t), x_2(t+\tau), x_1(t+2\tau))$, $t = 1, 2, 3, \ldots.., N - 2\tau$, with $\tau = 2$ looks almost similar to the original attractor of the Lorenz system given by Fig. 7.1a.

So we finally consider GAC with different time-delays [52] to reconstruct the attractor of the Lorenz system from its multiple solution components. Obviously the reason is to get an attractor, whose distortion from the original attractor is even lesser than that least distorted attractor reconstructed under GAC with same time-delay repeated [52]. In this context, it may be noted that under the notion of GAC with different time-delays [52], it is not possible to obtain proper time-delays for all combinations of the solution components x_1, x_2, x_3. This actually reveals that not all combinations of the solution components are useful for the reconstruction of the attractor of the aforesaid Lorenz system. However, most of the attractors reconstructed under the notion of GAC with different time-delays [52] are almost similar to the actual attractor of the Lorenz system [48]. Among those, the attractors reconstructed with the combinations $(x_1(t), x_3(t+\tau_1), x_3(t+\tau_1+\tau_2))$ and $(x_3(t), x_1(t+\tau_1), x_3(t+\tau_1+\tau_2))$ look exactly same (and obviously topologically equivalent) as the original attractor of the Lorenz system given by Fig. 7.1a. These are shown by Fig. 7.17a, b respectively.

Thus, by the use of GAC with different time-delays [52], it is possible to reconstruct topologically equivalent attractor, which is least distorted from the original attractor of the Lorenz dynamical system [48]. In fact, this new measure can also be used to find proper time-delay for the best possible topologically equivalent attractor reconstruction from multiple time series. This not only establishes the superiority of attractor reconstruction with different time-delays but it also highlights that consideration of a single component of the solution vector of the dynamical system is not always sufficient to reconstruct the best possible attractor for it. However, if the time series data is highly nonlinear, the aforesaid measure may not be workable. One such counter example is a known Neuro-dynamical system [61],

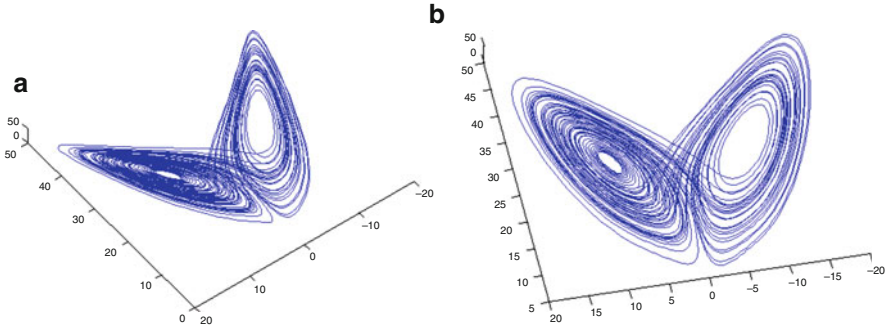

Fig. 7.17 Best forms of the reconstructed attractors of the aforesaid Lorenz system with different combinations of the solution components (**a**) $(x_1(t), x_3(t+\tau_1), x_3(t+\tau_1+\tau_2))$ and (**b**) $(x_3(t), x_1(t+\tau_1), x_3(t+\tau_1+\tau_2))$ under GAC with different time-delays

where this GAC measure with same time-delay repeated or different time-delays [52] do not work properly even by considering multiple solution components. In this connection, we first highlight the inadequacy of the GAC measure [52].

For this purpose, let us consider the Neuro-dynamical system [61] described by the following differential equations:

$$\begin{aligned}
\frac{dx_1}{dt} &= [1 + \exp\{-\beta_1(w_{21}x_2 + w_{31}x_3 - \theta_1)\}]^{-1} - \alpha_1 x_1, \\
\frac{dx_2}{dt} &= [1 + \exp\{-\beta_2(x_1 - \theta_2)\}]^{-1} - \alpha_2 x_2, \\
\frac{dx_3}{dt} &= [1 + \exp\{-\beta_3(x_1 - \theta_3)\}]^{-1} - \alpha_3 x_3,
\end{aligned} \tag{7.17}$$

with the initial condition $x_1(1) = 0.8, x_2(1) = 0.5, x_3(1) = 0.1$ and the parameter values $w_{21} = 1, w_{31} = -6.2, \alpha_1 = 0.62, \alpha_2 = 0.42, \alpha_3 = 0.1, \beta_1 = 7, \beta_2 = 7, \beta_1 = 13, \theta_1 = 0.5, \theta_2 = 0.3, \theta_3 = 0.7$.

Under these values of the parameters, the system gives a chaotic attractor shown by Fig. 7.18.

Solving the above Neuro-dynamical system for x_1, x_2, x_3, we have three time series $\{x_1(t)\}_{t=1}^{10000}$, $\{x_2(t)\}_{t=1}^{10000}$ and $\{x_3(t)\}_{t=1}^{10000}$ as solutions. We try for attractor reconstruction for the aforesaid Neuro-dynamical system [61] by using the notion of GAC under same time-delay repeated and different time delays [52]. For this, we make use of single as well as multiple components of the solution vector of the Neuro-dynamical system [61]. The procedure is discussed in details in Sect. 7.3.2.2. Most of the attractors thus reconstructed under same time-delay repeated and different time-delays are not at all well-formed and they cannot be called attractor

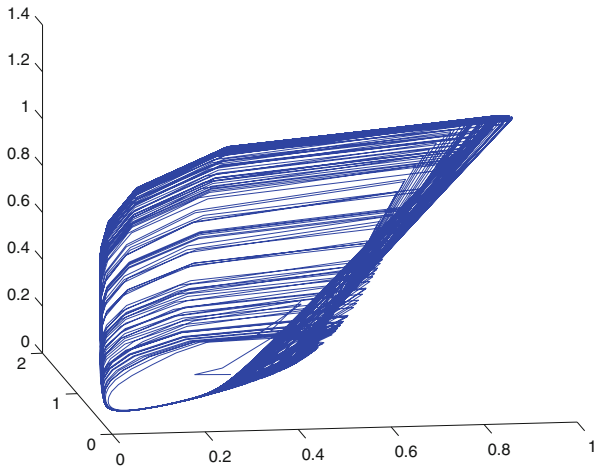

Fig. 7.18 Chaotic Attractor for the aforesaid Neuro-dynamical system given by (7.17)

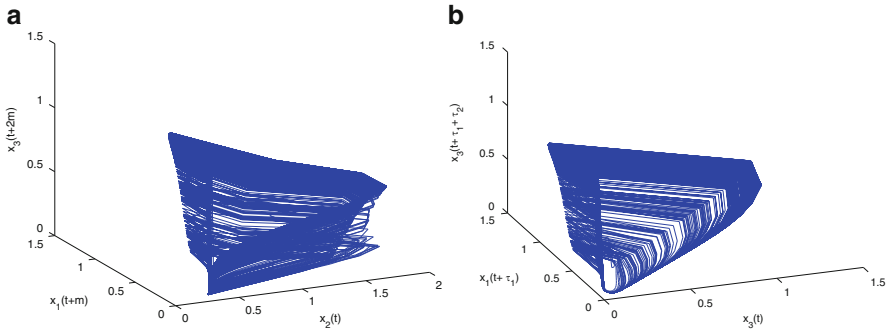

Fig. 7.19 Reconstructed attractors of the Neuro-dynamical system with different combinations of the components of its solution vector under GAC with (**a**) $(x_2(t), x_1(t+\tau), x_3(t+2\tau)$ [under same time-delay repeated], (**b**) $(x_3(t), x_1(t+\tau_1), x_3(t+\tau_1+\tau_2))$ [under different time-delays]

in the proper sense of the term. However, few of them are quite well-formed and among those two best forms of the reconstructed attractors, one under the notion of GAC [52] with same time-delay repeated and the other under different time-delays are given by Fig. 7.19a, b respectively. However, even these best forms of the reconstructed attractors are not at all comparable with the original attractor of the aforesaid Neuro-dynamical system [61]. Thus it is seen that under the notion of GAC [52] it is impossible to find proper time-delay(s) towards better (topologically equivalent) attractor reconstruction for this dynamical system from its single or multiple solution components with same time-delay repeated or different time-delays. Therefore, a new measure is sought in order to resolve this problem.

We next highlight the inadequacy of the other time-delay finding measures viz. AMI [44, 45] and higher dimensional Mutual information (MI) [46, 47] in the reconstruction of the least distorted attractor of the aforesaid Neuro-dynamical system [61].

Note that we have not even considered the linear AC measure [42, 43] as the solution components of the Neuro-dynamical system [61] are non-stationary and highly nonlinear.

Consider the solution component $\{x_3(t)\}_{t=1}^{10000}$ of the above Neuro-dynamical system [61] for the reconstruction of its three dimensional attractor. The plot of AMI [44, 45] against time-delay τ is given by Fig. 7.20a. It is seen from Fig. 7.20a that AMI [44, 45] comes nearer to zero for the first time, when $\tau = 30$. The corresponding three dimensional reconstructed attractor is given by Fig. 7.20b.

It is clear from Fig. 7.20b that it is not at all attractor in the proper sense of the term. The method is then applied for the solution components $\{x_1(t)\}_{t=1}^{10000}$ and $\{x_2(t)\}_{t=1}^{10000}$ of the Neuro-dynamical system [61], but the attractor reconstruction does not improve. In fact, in the later cases the reconstructed attractors [1–16] are even worse than the present one.

We now use higher dimensional MI [46, 47] with same time-delay repeated to find suitable time-delay to reconstruct the attractor of the Neuro-dynamical

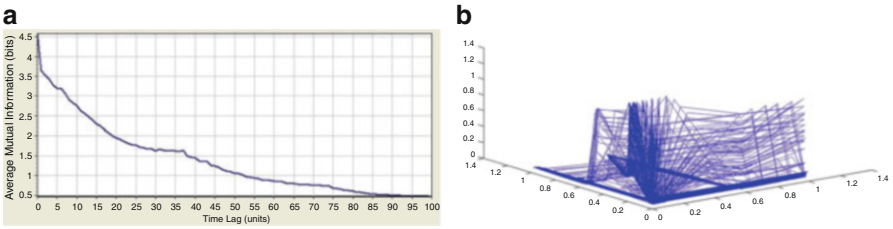

Fig. 7.20 (**a**) Plot of AMI against time-delay for the solution component $\{x_3(t)\}_{t=1}^{10000}$ of the Neuro-dynamical system, (**b**) three dimensional reconstructed attractor of the Neuro-dynamical system with $\tau = 30$ obtained under AMI

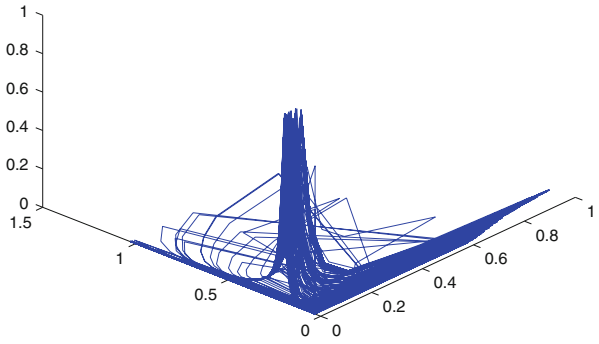

Fig. 7.21 The best form of reconstructed attractor with different combinations of solution components under higher dimensional MI with same time-delay repeated

system [61] from multiple components of its solution vector. The attractors are reconstructed from all possible combinations of the solution component with same time-delay repeated. All the attractors, when judged visually, show that their best form is given as in Fig. 7.21.

Though Fig. 7.21 shows a bit improvement over Fig. 7.20b in the sense that in the present case we get a better dense region with lesser number of outliers but the improvement is not at all remarkable.

We next use higher dimensional Mutual Information with different time-delays [47] to find proper time-delays for reconstruction of the attractor for the Neuro-dynamical system from multiple components of its solution vector. All the attractors reconstructed under higher dimensional MI [47], when judged visually, show that their best form is given as in Fig. 7.22.

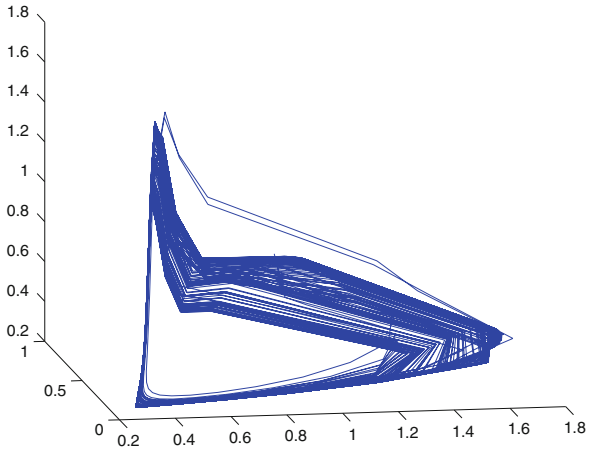

Fig. 7.22 The best form of reconstructed attractors with different combinations of solution components under higher dimensional MI with different time-delays

Figure 7.22 shows a comparatively better dense region with lesser number of outliers as compared to the previous ones. But it still differs much from the original attractor given by Fig. 7.18. As our intention is to reconstruct not only topologically equivalent attractor but also a least distorted attractor, more improvements remain to be achieved. But this cannot be done by existing methods as mentioned above. We now illustrate another nonlinear measure—CAC [53] by means of two examples. One is the aforesaid Neuro-dynamical system [61] for which least distortion attractor cannot be reconstructed by AC [42, 43], AMI [44, 45], higher dimensional MI with same time-delay repeated and different time-delays [46, 47] and even by GAC with same time-delay repeated and different time-delays [52]. The other is the Lorenz system, where our intention is to observe some further improvement in the form of the reconstructed attractor [1–16].

We first reconstruct the attractor of the Neuro-dynamical system [61] under CAC from single component of its solution vector with same time-delay repeated [53]. We consider each of the solution components separately and try to reconstruct the attractors. None of them are found to be satisfactory except one that is reconstructed from the solution component $\{x_2(t)\}_{t=1}^{10000}$. Since the Neuro-dynamical system [61] is three dimensional, CAC [53] $r_{n,x_2}(\tau)$ given by Eq. (7.2) with $n = 3$ is used to find the independent coordinates $(x_2(t), x_2(t+\tau), x_2(t+2\tau))$. The time-delay τ is obtained by plotting $r_{n,x_2}(\tau)$ against τ as given by Fig. 7.23a. The value of τ is found to be 7 and the attractor reconstructed with this τ is shown by Fig. 7.23b.

Obviously, the attractor given by Fig. 7.23b exhibits orbits and it is almost dense and even better than those obtained even under higher dimensional MI with same time-delay repeated and different time-delays [47]. But it does not resemble the original attractor of the Neuro-dynamical system [61].

We next reconstruct the attractors under CAC [53] from single component of the solution vector with different time-delays.

For this purpose, we consider the same solution component $\{x_2(t)\}_{t=1}^{N}$ of the solution vector of the Neuro-dynamical system [61] under different time-delays τ_1

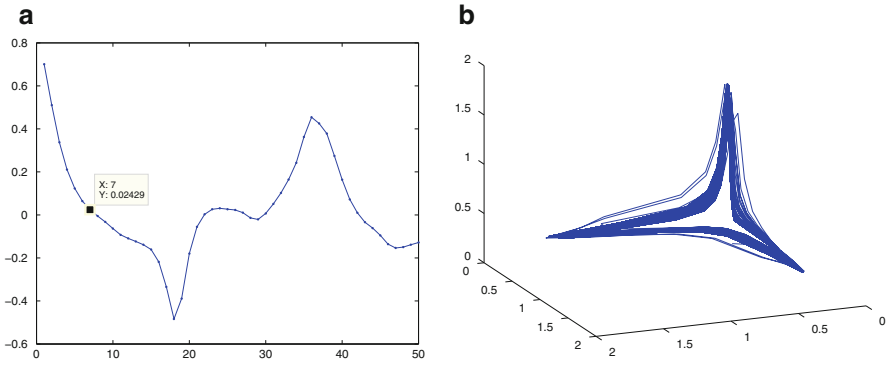

Fig. 7.23 (**a**) Two dimensional correlogram diagram for the solution component $\{x_2(t)\}_{t=1}^{10000}$ of Neuro-dynamical system under CAC with same time-delay repeated, (**b**) three dimensional reconstructed attractor of the Neuro-dynamical system with $\tau = 7$ obtained from the correlogram diagram

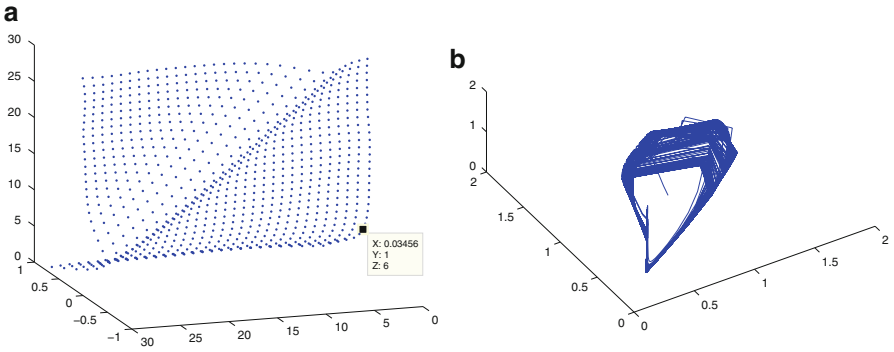

Fig. 7.24 (**a**) Three dimensional Correlogram for the solution component $\{x_2(t)\}_{t=1}^{10000}$ of the Neuro-dynamical system under CAC with different time-delays, (**b**) three dimensional reconstructed attractor of the Neuro-dynamical system with $\tau_1 = 1, \tau_2 = 6$ obtained from the correlogram diagram

and τ_2 and calculate the CAC $r_{n,x_2}(\tau_1, \tau_2)$ given by (7.14) for different values of τ_1 and τ_2. These values of CAC are then plotted against τ_1, τ_2 to form the three dimensional correlogram given by Fig. 7.24a. It is found from Fig. 7.24a that the value of the CAC $r_{n,x_2}(\tau_1, \tau_2)$ comes nearer to zero for the first time when $\tau_1 = 1, \tau_2 = 6$. The reconstructed attractor is shown in Fig. 7.24b.

A further improvement in the quality of the reconstructed attractor is observed in Fig. 7.24b. In fact, the orbits of this attractor reconstructed by CAC [53] measure with different time-delays are much denser even than the previous one reconstructed under same time-delay repeated. Thus so far as reconstruction is concerned from single component, this measure is even better than higher dimensional MI with same time-delay repeated and different time-delays [47]. But still this attractor does not

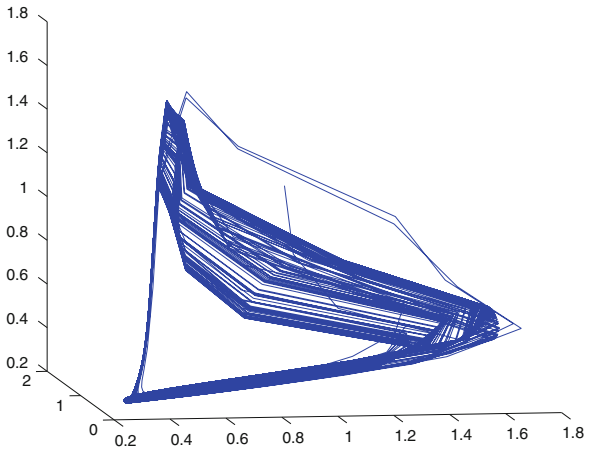

Fig. 7.25 A comparatively less distorted attractor of the Neuro-dynamical system reconstructed from its multiple solution components under CAC with same time-delay $\tau = 2$ repeated

resemble the original attractor given by Fig. 7.18. So we try to improve the quality of this reconstructed attractor by considering multiple solution components of the Neuro-dynamical system [61].

For reconstructing the attractor of the above Neuro-dynamical system [61] from multiple solution components with same time-delay repeated, we first obtain the independent coordinates $(x(t), x(t+\tau), x(t+2\tau))$, where τ is the time-delay and $x(t) = x_{i_1}(t), x(t+\tau) = x_{i_2}(t+\tau), x(t+2\tau) = x_{i_3}(t+2\tau), i_1, i_2, i_3 \in \{1, 2, 3\}$.

However not all of them are attractors in the proper sense of the term. Among all of those attractors, the least distorted form is shown by Fig. 7.25.

Definitely, this attractor reconstructed with the combinations x_2, x_3, x_2 can be considered as a much improved form of the attractor for the Neuro-dynamical system [61], as it exhibits complete dense orbits. Also this reconstructed attractor is less distorted from the original attractor of the Neuro-dynamical system [61] given by Fig. 7.18.

Finally, we reconstruct attractors for the Neuro-dynamical system [61] from its multiple solution components by choosing the independent coordinates $(x(t), x(t+\tau_1), x(t+\tau_1+\tau_2))$, for two different time-delays τ_1, τ_2, where $x(t) = x_{i_1}(t), x(t+\tau_1) = x_{i_2}(t+\tau_1), x(t+\tau_1+\tau_2) = x_{i_3}(t+\tau_1+\tau_2), i_1, i_2, i_3 \in \{1, 2, 3\}$.

The least distorted form among those reconstructed attractors is presented in Fig. 7.26.

Actually, the reconstructed attractor with the combination x_3, x_2, x_1 under different time-delays has remarkably improved compared to that obtained for same time-delay repeated (Fig. 7.25) in the sense that this attractor (Fig. 7.26) contains lesser number of outliers and also a better dense orbit as compared to those obtained under same time-delay repeated (Fig. 7.25). Also it is least distorted to the original attractor of the Neuro-dynamical system given by Fig. 7.18.

In a similar manner, we obtain reconstructed attractors of Lorenz system [48] under CAC [53] measure.

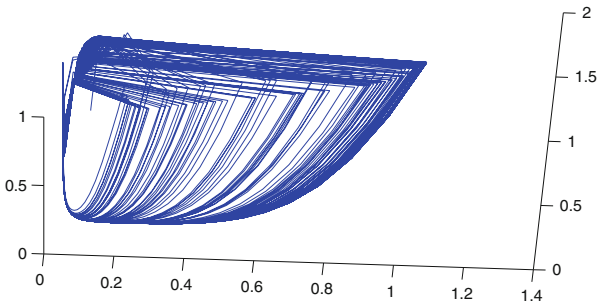

Fig. 7.26 The least distorted reconstructed attractor of the Neuro-dynamical system with different combinations of the components of its solution vector under different time-delays $[(x_3(t), x_2(t + \tau_1), x_1(t + \tau_1 + \tau_2))$ with $\tau_1 = 1, \tau_2 = 3]$ under CAC

We now compute the value of the shape distortion parameter (*Sd*) [50] in each case under all of the time-delay finding measures discussed above for the Neuro-dynamical system [61] and the Lorenz system [48].

The calculation shows that the value of *Sd* [50] is 0.0014 for the attractor reconstructed with $(x_3(t), x_3(t + \tau), x_3(t + 2\tau))$ under AMI [44, 45] measure, 0.0125 for the attractor reconstructed with $(x_1(t), x_3(t + \tau), x_1(t + 2\tau))$ under higher dimensional MI with same time-delay repeated [47], 0.165003 for the same reconstructed with $(x_2(t), x_1(t + \tau_1), x_2(t + \tau_2))$ under higher dimensional MI with different time-delays [47], 0.367 for the attractor reconstructed with $(x_2(t), x_3(t + \tau), x_2(t + 2\tau))$ under CAC with same time-delay repeated [53] and 0.4242 for the same reconstructed with $(x_3(t), x_2(t+\tau_1), x_1(t+\tau_1+\tau_2))$ under CAC with different time-delays [53] for the Neuro-dynamical system [61].

For the Lorenz system [48] the value of *Sd* [50] is 0.5838 for the attractor reconstructed with $(x_1(t), x_1(t + \tau), x_1(t + 2\tau))$ under AMI [44, 45] measure, 0.6298 for the attractor reconstructed with $(x_3(t), x_1(t + \tau), x_2(t + 2\tau))$ under higher dimensional MI with same time-delay repeated [47], 0.8896 for the same reconstructed with $(x_3(t), x_1(t + \tau_1), x_1(t + \tau_2))$ under higher dimensional MI with different time-delays [47], 0.7625 for the attractor reconstructed with $(x_3(t), x_1(t + \tau), x_2(t + 2\tau))$ under CAC with same time-delay repeated [53] and 0.8994 for the same reconstructed with $(x_3(t), x_1(t+\tau_1), x_1(t+\tau_1+\tau_2))$ under CAC with different time-delays [53].

Thus, it is evident from the above results that the largest *Sd* value [50] occurs for CAC measures with different time-delays [53] in both cases. Hence the dynamics is best preserved in these cases. However, in both cases consideration of multiple solution components is mandatory. Thus CAC with different time-delays [53] stands as a best tool for attractor reconstruction, when multiple time-series are considered. Note that we have not calculated the value of *Sd* [50] under GAC [52] measure as for Neuro-dynamical system [61] the attractors reconstructed under this measure are not at all well-formed.

7.4 Conclusions

One of the two important factors in attractor reconstruction [1–16] is the proper selection of the time-delay. The attractor reconstructed from one or multiple ensembles will be topologically equivalent to the original attractor of the corresponding system only when proper time-delay and embedding dimension are chosen. If the time-delay is selected properly, the topological properties are preserved even if the attractor is reconstructed in lesser embedding dimension. Amongst the available time-delay finding measures, the widely accepted and mostly used measures are the AMI [44, 45] and higher dimensional mutual information (MI) [47] for attractor reconstruction from single and multiple observations respectively. The linear AC measure [42, 43] is sometimes found to be handy but as most of the real life phenomena are nonlinear and non-stationary, it is not much useful in most of the cases. In almost all cases the attractors reconstructed under the former two measures are found to be topologically equivalent to its original attractor. However, it is not at all desirable to constrain the study up to this topologically equivalent attractor reconstruction. Rather, it is encouraged to develop newer and newer sophisticated measures for finding proper time-delay(s) in order to get the reconstructed attractor as least distorted from the original one. If this can be done, then more precise information regarding the dynamics behind the generation of the data can be retrieved from its reconstructed attractor. Keeping in view of the above fact, some comparatively newer time-delay finding measures [51–53] have also been presented in this chapter. The basic motivation is not only to reconstruct topologically equivalent attractors [1–16], but also to reconstruct least distorted attractors as much as possible.

Towards this goal, a nonlinear measure—GAC [52] with same time-delay repeated and with different time-delays have been introduced and validated for Lorenz system [48]. It has been observed that it produces a lesser distorted reconstructed attractor of Lorenz system [48] compared to the other time-delay finding measures, especially when multiple solution components of the Lorenz system are considered. However, this measure fails to produce a topologically equivalent attractor of some known three dimensional Neuro-dynamical system [61], even by considering its multiple solution components. As a remedy to this problem, a system dependent nonlinear measure—CAC [53] with same time-delay repeated and different time-delays have also been presented and a remarkable improvement has been achieved. In fact, the attractor reconstructed under this measure especially with different time-delays produces the best possible reconstructed attractor of both Lorenz [48] and Neuro-dynamical system [61], when the multiple solution components of the respective systems are considered. The comparison of all of these reconstructed attractors with their original attractors have been made by a shape distortion measure (*Sd*) [50], which determines, how much distorted are the reconstructed attractors from their original attractors. Because of its dependency on the underlying dynamical systems, the CAC measure [53] especially with different time-delays is expected to work for a least distorted attractor reconstruction in

almost all cases. Thus, the major scope of application of this measure in real world is limited to attractor reconstruction from multiple copies of the real data. Naturally, a similar type of nonlinear measure, which can produce a best possible reconstructed attractor from a single observation of real data is sought for. For this reason, another time-delay finding measure called new type of nonlinear auto-correlation of bivariate data [51] is presented. The beauty of this measure lies in the fact that it takes care off different type of non-linearity present in different data and hence in almost all cases, it produces most suitable time-delay for a best possible attractor reconstruction. This measure is first successfully validated for Lorenz system by the *Sd* measure [50]. Further, some real life applications of this measure have been presented. It has been found that the attractor reconstructed from the music signals of two different ragas—'Anandi' and 'Bhairavi' under this new type of nonlinear auto-correlation is much better than those reconstructed under other measures.

In a nutshell, this chapter highlights the importance of finding suitable time-delay for a more similar attractor reconstruction of the dynamical systems. For this purpose, it presents three comparatively new nonlinear measures and proves that these methods are also useful. One of the measures—CAC [53] produces least distorted topologically equivalent attractors by considering multiple solution components of the respective dynamical system compared to that reconstructed under the mostly used measures in almost all cases. Thus, this measure may be used in attractor reconstruction from multiple copies of real data. Another measure—new type of nonlinear auto-correlation of bivariate data [51] does the same thing from a single solution component of the dynamical systems and so it may be used for attractor reconstruction from a single observation of real data. This type of attempt is extremely necessary as topological equivalence is the minimum criterion for retrieving the dynamics from the reconstructed attractor and so lesser and lesser distorted attractor we can reconstruct, more and more accurately we can retrieve the dynamics responsible behind the generation of the real data. Future scopes of this article includes but not limited to the least distorted attractor reconstruction from multiple ensembles of real data by CAC especially with different time-delays [53].

References

1. Williams, G.P.: Chaos Theory Tamed. Joseph Henry Press, Washington, DC (1997)
2. Kaplan, D.T., Glass, L.: Understanding Nonlinear Dynamics. Springer, New York (1995)
3. Abarbanel, H.D.I.: Analysis of Observed Chaotic Data. Springer, New York (1997)
4. Kaplan, D.T.: Signal Processing. Warwick-exercises.tex, 5–9 (2004)
5. Glass, L., Mackey, M.C.: From Clocks to Chaos: The Rhythms of Life. Princeton University Press, Princeton (1988)
6. Strogatz, S.H.: Non Linear Dynamics and Chaos-with Application to Physics, Biology, Chemistry and Engineering. Advance Book Program (Persueus Books), Cambridge (1994)
7. Banbrook, M., McLaughlin, S.: Is Speech Chaotic? Invariant Geometrical Measures for Speech Data. IEE Colloq. Exploit. Chaos Signal Process. **193**, 1–8 (1994)
8. McLaughlin, S., Banbrook, M., Mann, I.: Speech characterization and synthesis by nonlinear methods. IEEE Trans. Speech Audio Process. **7**, 1–17 (1999)

9. Johnson, T.L., Dooley, K.: Looking for chaos in time series data. In: Sulis, W., Combs, A. (eds.) Nonlinear Dynamics in Human Behavior, pp. 44–76. World Scientific, Singapore (1996)
10. Kugiumtzis, D.: State space reconstruction parameters in the analysis of chaotic time series' the role of the time window length. Physica D **95**, 13 (1996)
11. Takens, F.: Detecting strange attractors in turbulence. In: Rand, D.A., Young, L.S. (eds.) Dynamical Systems and Turbulence. Lecture Notes in Mathematics, vol. 898, pp. 366–381. Springer, Berlin (1981)
12. Sauer, T., Yorke, J., Casdagli, M.: Embedology. J. Stat. Phys. **65**, 579–616 (1991)
13. Gibson, J.F., Farmer, J.D., Casdagli, M., Eubank, S.: An analytic approach to practical state space reconstruction. Physica D **57**, 1–30 (1992)
14. Kantz, H., Olbrich, E.: Scalar observations from a class of high-dimensional chaotic systems: limitations of the time delay embedding. Chaos **7**(3), 423 (1997)
15. Olbrich, E., Kantz, H.: Inferring chaotic dynamics from time-series: on which length scale determinism becomes visible. Phys. Lett. A **232**, 63 (1997)
16. Pecora, L.M., Moniz, L., Nichols, J., et al.: A unified approach to attractor reconstruction. Chaos **17**, 013110 (2007)
17. Ott, E.: Chaos in Dynamical Systems. Cambridge University Press, Cambridge (1993)
18. Rosenstein, M.T., Collins, J.J., De Luca, C.J.: A practical method for calculating largest Lyapunov exponents from small data sets. Physica D **65**, 117–134 (1993)
19. Wolf, A.: Quantity chaos with Lyapunov exponents. In: Holden, A.V. (ed.) Chaos, pp. 273–290. Princeton University Press, New Jersey (1986)
20. Benettin, B., Galgani, L., Giorgilli, A., Strelcyn, J.: Lyapunov characteristic exponents for smooth dynamical systems and for hamiltonian systems: a method for computing all of them Part I, II. Meccanica **15**(1), 9–30 (1980)
21. Wolf, A., Swift, J.B., Swinney, H.L., Vastano, J.A.: Detennining Lyapunov exponents from a time series. Physica D **16**, 285–317 (1985)
22. Eckmann, J.P., Kamphorst, S.O., Ruelle, D., Ciliberto, S.: Lyapunov exponents from time series. Phys. Rev. A **34**, 4971–4979 (1986)
23. Sano, M., Sawada, Y.: Measurement of the Lyapunov spectrum from a chaotictime series. Phys. Rev. Lett. **55**, 1082–1085 (1985)
24. Peitgen, H., Jurgens, H., Saupe, D.: Chaos and Fractals-New Frontiers of Science. Springer, New York (1996)
25. Banbrook, M., Ushaw, G., McLaughlin, S.: How to extract Lyapunov exponents from short and noisy time series. IEEE Trans. Signal Process. **45**, 1378–1382 (1997)
26. Geist, K., Parlitz, U., Lauterbom, W.: Comparison of different methods for computing Lyapunov exponents. Prog. Theor. Phys. **83**, 875 (1990)
27. Kantz, H.: A robust method to estimate the maximal Lyapunov exponent of a time series. Phys. Lett. A **185**, 77–87 (1994)
28. Kennedy, M.P.: Basic concepts of nonlinear dynamics and chaos. In: Toumazou, C. (ed.) Circuits and Systems Tutorials, pp. 289–313. IEEE Press, London (1994)
29. Briggs, K.: An improved method for estimating Liapunov exponents of chaotic time series. Phys. Lett. A **151**, 27–32 (1990)
30. Packard, N.H., Crutchfield, J.P., Farmer, J.D., Shaw, R.S.: Geometry from a time series. Phys. Rev. Lett. **45**, 712–716 (1980)
31. Abarbanel, H.D.I., Carroll, T.A., Pecora, L.M., Sidorowich, J.J., Tsimring, L.S.: Predicting physical variables in time delay embedding. Phys. Rev. E **49**, 1840–1853 (1994)
32. Guckenheimer, J., Buzyna, G.: Dimension measurements for geostrophic turbulence. Phys. Rev. Lett. **51**, 1438–1441 (1983)
33. Palus, M., Dvorák, I., David, I.: Spatio-temporal dynamics of human EEG. Physica A **185**, 433–438 (1992)
34. Cao, L., Mees, A., Judd, K.: Dynamics from multivariate time series. Physica D **121**, 75–88 (1998)
35. Barnard, J.P., Aldrich, C., Gerber, M.: Embedding of multidimensional time-dependent observations. Phys. Rev. E **64**, 046201 (2001)

36. Garcia, S.P., Almeida, J.S.: Multivariate phase space reconstruction by nearest neighbor embedding with different time delays. Phys. Rev. E **72**, 027205 (2005)
37. Hirata, Y., Suzuki, H., Aihara, K.: Reconstructing state spaces from multivariate data using variable time delays. Phys. Rev. E **74**, 026202 (2006)
38. Grassberger, P., Procaccia, I.: Measuring the strangeness of strange attractors. Physica D **9**, 189–208 (1983)
39. Kennel, M.B., Brown, R., Abarbanel, H.D.I.: Determining minimum embedding dimension using a geometrical construction. Phys. Rev. A **45**, 3403–3411 (1992)
40. Cao, L.: Practical method for determining the minimum embedding dimension of a scalar time series. Physica D **110**, 43–50 (1997)
41. Kember, G., Fowler, A.C.: A correlation function for choosing time delays in phase portrait reconstructions. Phys. Lett. A **179**, 72–80 (1993)
42. Theiler, J.: Spurious dimension from correlation algorithms applied to limited time-series data. Phys. Rev. A **34**, 2427–2432 (1986)
43. Kantz, H., Schreiber, T.: Nonlinear Time Series Analysis. Cambridge University Press, Cambridge (1997)
44. Fraser, A.M., Swinney, H.L.: Independent coordinates for strange attractors from mutual information. Phys. Rev. A **33**, 1134–1140 (1986)
45. Liebert, W., Schuster, H.G.: Proper choice of time delay for the analysis of chaotic time series. Phys. Lett. A **142**, 107 (1989)
46. Kraskov, A., Stögbauer, H., Grassberger, P.: Estimating mutual information. Phys. Rev. E **69**(6), 066138 (2004)
47. Simon, G., Verleysen, M.: High-dimensional delay selection for regression models with mutual information and distance-to-diagonal criteria. Neurocomputing **70**, 1265–1275 (2007)
48. Lorentz, E.N.: Deterministic non-periodic flow. J. Atmos. Sci. **20**, 130–141 (1963)
49. Rössler, O.E.: An equation for continuous chaos. Phys. Lett. A **57**(5), 397–398 (1976)
50. Vlachos, I., Kugiumtzis, D.: Non uniform state-space reconstruction and coupling detection. Phys. Rev. E **82**, 016207 (2010)
51. Palit, S.K., Mukherjee, S., Bhattacharya, D.K.: New types of nonlinear auto-correlations of bivariate data and their applications. Appl. Math. Comput. **218**(17), 8951–8967 (2012)
52. Palit, S.K., Mukherjee, S., Bhattacharya, D.K.: Generalized auto-correlation and its application in attractor reconstruction. Bull. Pure Appl. Math. **5**(2), 218–230 (2011)
53. Palit, S.K., Mukherjee, S., Bhattacharya, D.K.: A high dimensional delay selection for the reconstruction of proper phase space with cross auto-correlation. Neurocomputing **113**, 49–57 (2013)
54. Rulkov, N.F., Sushchik, M.M., Tsimring, L.S., Abarbanel, H.D.I.: Generalized synchronization of chaos in directionally coupled chaotic systems. Phys. Rev. E **51**, 980–994 (1995)
55. Marchal, C.: Determinism, random, chaos, freedom. Henri Poincare and the revolution of scientific ideas in the twentieth century. Regul. Chaotic Dyn. **10**, 227–236 (2005)
56. Wichard, J.D., Parltz, U., Lauterborn, W.: Application of nearest neighbor's statistics. In: International Symposium on Nonlinear Theory and Its Applications, Switzerland (1998)
57. Martinez, W.L., Martinez, A.R.: Computational Statistics Handbook with Matlab. Chapman & Hall/CRC, New York (2002)
58. Theiler, J., Eubank, S., Longtin, A., Galdrikian, B., Farmer, J.: Testing for nonlinearity in time series: the method of surrogate data. Physica D **58**, 77–94 (1992)
59. Schreiber, T., Schmitz, A.: Improved Surrogate Data for Nonlinearity Tests. Phys. Rev. Lett. **77**, 635 (1996)
60. Jar, J.H.: Biostatistical Analysis. Pearson International Edition, Harlow (2006)
61. Das, A., Roy, A.B.: Chaos in a three dimensional neural network. Appl. Math. Model. **24**, 511–522 (2000)

Chapter 8
Turing and Non-Turing Patterns in Two-Dimensional Prey-Predator Models

Malay Banerjee

Abstract Spatial patterns are ubiquitous in nature, and study of spatio-temporal pattern formation for prey-predator models are initiated based upon the seminal work of Turing on morphogenesis (Turing, Philos Trans R Soc Lond B 237:37–72, 1952). Interactions between individuals of different species over a wide range of spatial and temporal scales often modify the temporal dynamics as well as stability properties of the population distributed over natural landscape. Segel and Jackson (J Theor Biol 37:545–559, 1972) first used reaction-diffusion systems to explain ecological pattern formation by interacting populations. This idea used afterwards to explain pattern formation in plankton systems, semiarid vegetation patterns, invasion by exotic species and distribution of prey-predator distribution over homogeneous space. After the seminal works by Segel and Jackson (J Theor Biol 37:545–559, 1972) and Levin and Segel (Nature 259:659, 1976), researchers were interested to study the Turing-type pattern formation, but now a days it shifted towards non-Turing patterns and spatio-temporal chaos. Empirical evidence in support of spatio-temporal chaotic patterns in interacting populations remain in vein but the resulting patterns have similarity with the irregular distribution over spatial domain. Further, the formation of spatio-temporal chaotic patterns within Turing-Hopf domain remains a controversial issue, whether it arises near the Turing-Hopf boundary or away from it. This article aims to review the recent development of Turing and non-Turing pattern formations in prey-predator models having prey-dependent and ratio-dependent functional response with special emphasis on spatio-temporal chaos.

8.1 Introduction

The spatio-temporal models of predator-prey interaction are studied to understand the role of random mobility of the species, within their habitat, on the stability and persistence of interacting species. Investigation on spatio-temporal models of

M. Banerjee (✉)
Department of Mathematics and Statistics, I.I.T. Kanpur, Kanpur, India
e-mail: malayb@iitk.ac.in

S. Banerjee, L. Rondoni (eds.), *Applications of Chaos and Nonlinear Dynamics in Science and Engineering - Vol. 4*, Understanding Complex Systems,
DOI 10.1007/978-3-319-17037-4_8

interacting population reveal that the movement of the individuals of one or more species some time act as a stabilizing factor and in some cases they are capable to induce some destabilization. Interestingly, destabilization of homogeneous distribution of population is not a threat towards the survival of population rather it may settle down to inhomogeneous distribution of individuals over their habitats producing localized patches. These localized patches may be time invariant or may not be. Diffusivity of individuals has power to stabilize as well as destabilize the coexistence scenario. As a result, researchers are interested to study various types of stationary and non-stationary spatio-temporal pattern formation by the interacting populations. Mathematical analysis and numerical simulation of spatio-temporal models provide the idea that how individuals of certain species are distributed over two dimensional landscapes or within the aquatic environment. In reality, the distribution of plant and animal populations is not homogeneous rather they are packed in localized patches. These localized patches either remain fixed or change with time [21]. Time invariant patches and the patches moving with time correspond to stationary and non-stationary patterns. Non-stationary patterns may be oscillatory, quasi-periodic or chaotic. Various types of resulting patterns can be classified as spot pattern, labyrinthine pattern, stripe pattern, target pattern, spiral pattern, tip-splitting pattern and interacting spiral pattern [7, 18].

Significance and importance of spatial aspect towards the stabilization and long term existence of certain species was first observed by Gause [24]. His observation was based upon the laboratory experiments to study growth of *paramecium* and *didinum* [9]. Effect of spatial distribution on stability of population and persistence or extinction properties was studied by Luckinbill [39, 40]. A detailed discussion on the role of space and mobility of individuals on the interaction of ecological species are available in the book by Okubo and Levin [48]. All the research works on spatio-temporal pattern formation due to small perturbation to the homogeneous distribution of population are based upon the seminal work of Turing [63]. Turing's idea of pattern formation in reaction-diffusion system was first applied to justify ecological pattern formation by Segel and Jackson [57]. The same idea was carried out to explain to explain patchy distribution in plankton community by Levin and Segel [37] and for semiarid vegetation patterns by Klausmeier [32]. Now a days the literature on pattern formation by interacting populations is very rich as huge number of articles is published in this direction and a wide variety of spatial patterns are reported [2, 8, 9, 11, 12, 15, 16, 21, 23, 30, 32, 41, 44–46, 51–53, 58, 59, 66]. Initially the works in this direction was focused on the Turing patterns only. Recently, attempts are made to study the non-Turing patterns with special emphasis on spatio-temporal chaos. Few recent works demonstrated the mechanism of spatio-temporal chaotic patterns which are biologically realistic to some extent. But empirical evidence and field data supporting spatio-temporal chaos are not abundant. Rather, existence of chaos in ecological system still remains a controversial issue. However, spatio-temporal chaotic patterns are able to explain the irregular distribution of population which is frequently observed in nature.

Majority of literature on spatio-temporal pattern formation in the spatially extended prey-predator models are focused with the models having prey-dependent

functional response and death rate of the predators is directly proportional to their density [23, 41, 51]. These types of models are unable to produce Turing patterns. But the consideration of prey-predator models with nonlinear death rate for predator are capable to exhibit Turing patterns [12, 44, 64]. But Turing and non-Turing pattern formation in case of spatially distributed populations with ratio-dependent functional response are now getting attention from the researchers [2, 6, 8, 9, 68]. As the temporal models of prey-predator interaction with ratio-dependent functional response produce much richer dynamics (see [5, 29, 31, 34, 35, 70] and references cited therein) compared to the models with prey-dependent functional response so it is expected that the spatial extension of ratio-dependent prey-predator model will produce a wide variety of patterns. Initially the ratio-dependent functional response faced strong criticism as it is undefined at the origin [1, 3, 4, 25]. Arditi and Ginzburg [4] argued that the functional response could be a function of the prey-to-predator ratio when interaction is characterized by the heterogeneity of space and time. Further, the dependence of the functional responses upon the densities of prey and predators are now established by the theoretical biologists. The ratio-dependent functional response is more suitable when predators have to search for prey individuals and hence they have to compete among themselves.

Formation of spatio-temporal patterns are obtained by analyzing the partial differential equation models of prey-predator interaction. Most of the models are extension of ordinary differential equation models by incorporating diffusion terms to model the mobility of the individuals of each species. Classical Gause type prey-predator system is governed by the system of coupled ordinary differential equations

$$\begin{aligned} \frac{dN}{dT} &= Q(N,K)N - R(N,P)P, \\ \frac{dP}{dT} &= eR(N,P)P - M(P)P, \end{aligned} \tag{8.1}$$

subjected to non-negative initial conditions [22]. In above formulation, $N \equiv N(T)$ and $P \equiv P(T)$ denote the prey and predator population densities respectively at any instant of time 'T'. $Q(N,K)$ is the density-dependent per capita growth rate of prey in absence of predator and the positive constant K stands for the environmental carrying capacity for the prey. $Q(N,K)$ satisfies some basic properties: $Q(K,K) = 0$, $Q(0,K) > 0$, $\lim_{K\to\infty} Q(0,K) < \infty$, $Q_N(N,K) < 0$, $Q_K(N,K) \geq 0$, $\lim_{K\to\infty} Q_N(N,K) = 0$ and $Q_{NK}(N,K) > 0$. The sole link between the growth of prey and predator populations is the functional response $R(N,P)$, which is a function of both the prey and predator population and stands for the amount of prey biomass consumed by per predator per unit of time. Further, it is assumed for a wide range of prey-predator models that the growth rate of the predators due to prey consumption is simply proportional to the functional response. The proportionality constant is e $(0 < e < 1)$ and is known as the conversion efficiency. Several authors have considered the fact that the consumption of prey biomass by their predators is solely depend upon the abundance of prey biomass only and hence

the functional response is a function of prey population only, $Q(N, P) \equiv Q(N)$. This type of functional response in known as prey-dependent functional response. $Q(N)$ always satisfies two properties, $Q(N) > 0$ for all $N > 0$ and $Q(0) = 0$ and monotonic prey-dependent functional response satisfies additional condition $Q_N(N) > 0$ [19]. There are some non-monotonic functional responses, namely Holling type-IV [33] and Monod-Haldane type functional response [10, 26, 49]. The ratio-dependent functional response can be obtained from the prey dependent functional response, replacing N by N/P. The ratio-dependent functional response, given by $Q(N/P)$, satisfy additional condition $\lim_{(N,P)\to(0,0)} PQ(N/P) = 0$ [34]. There are several evidences like field data, laboratory experiments etc. towards the consideration of functional response as a function of both the prey and the predator population densities. Beddington-DeAngelis functional response [62], ratio-dependent functional response [3, 4] are examples of the functional response involving predator population density also. $M(P)$ is the per capita intrinsic death rate for the predator and mostly it is assumed to be a constant. The Gause type prey-predator model is capable to describe the dynamic behavior of specialist predator's only as the growth rate of predator population is zero in the absence of the prey [13].

Here we first recall the mathematical criteria for the Turing pattern formation for spatio-temporal prey-predator model where individuals are assumed to be distributed over two-dimensional bounded domain. Mathematical model is described in terms of non-homogeneous parabolic partial differential equations subjected to positive initial conditions and no-flux boundary conditions. Then we look at the pattern formation for the models having ratio-dependent functional response terms. The spatial extension of classical Holling-Tanner model is revisited to show the transition in pattern formation and sensitivity of patterns to initial conditions. Most of the results discussed here are already available in literature [8, 9, 65]. Results are recollected here to ensemble the varieties of patterns produced by the interacting prey-predator models whose temporal counterpart exhibit very rich dynamics. The role of temporal instability and spatial instability to induce spatio-temporal chaotic pattern is discussed in the concluding section.

8.2 Basic Spatio-Temporal Model

A general spatio-temporal prey-predator model is governed by the following system of two nonlinear coupled partial differential equations

$$\begin{aligned}\frac{\partial N(T,X,Y)}{\partial T} &= NF(N,P) + D_N\left(\frac{\partial^2 N}{\partial X^2} + \frac{\partial^2 N}{\partial Y^2}\right)\\ \frac{\partial P(T,X,Y)}{\partial T} &= PG(N,P) + D_P\left(\frac{\partial^2 P}{\partial X^2} + \frac{\partial^2 P}{\partial Y^2}\right)\end{aligned} \tag{8.2}$$

subjected to known non-negative initial distribution of populations,

$$N(0, X, Y) = N_0(X, Y) \geq 0,\ P(0, X, Y) = P_0(X, Y),\ (X, Y) \in \Gamma, \quad (8.3)$$

and zero-flux boundary conditions

$$\frac{\partial N}{\partial \nu} = \frac{\partial P}{\partial \nu} = 0,\ (T, X, Y) \in (0, \infty) \times \partial\Gamma. \quad (8.4)$$

$N \equiv N(T, X, Y)$ and $P \equiv P(T, X, Y)$ denote the density of the prey and the predators respectively at any instant of time'T' and at the position (X, Y) within the square bounded domain Γ having boundary $\partial\Gamma$. $F(N, P)$ and $G(N, P)$ are the per capita growth rates of the prey and predator population respectively and D_N, D_P are their rate of diffusions. The governing system (8.2) can be written in terms of dimensionless variables as follows [47]

$$\begin{aligned} \frac{\partial n(t, x, y)}{\partial t} &= nf(n, p) + \left(\frac{\partial^2 n}{\partial x^2} + \frac{\partial^2 n}{\partial y^2}\right) \\ \frac{\partial p(t, x, y)}{\partial t} &= pg(n, p) + d\left(\frac{\partial^2 p}{\partial x^2} + \frac{\partial^2 p}{\partial y^2}\right) \end{aligned} \quad (8.5)$$

subjected to the initial conditions,

$$n(0, x, y) = n_0(x, y) \geq 0,\ p(0, x, y) = p_0(x, y),\ (x, y) \in \Omega, \quad (8.6)$$

and boundary conditions

$$\frac{\partial n}{\partial \nu} = \frac{\partial p}{\partial \nu} = 0,\ (t, x, y) \in (0, \infty) \times \partial\Omega. \quad (8.7)$$

Here n, p are dimensionless population densities, t, x, y are dimensionless independent variables and $d\ (= D_P/D_N)$ is the ratio of diffusivities. Majority of the research works are based upon the dimensionless versions of the nonlinear coupled partial differential equations as they contain less number of parameters. The temporal model corresponding to the spatio-temporal model (8.5) is a system of two nonlinear coupled ordinary differential equations

$$\begin{aligned} \frac{dn(t)}{dt} &= nf(n, p), \\ \frac{dp(t)}{dt} &= pg(n, p), \end{aligned} \quad (8.8)$$

with non-negative initial conditions $n(0),\ p(0) \geq 0$. This type of system admits a trivial equilibrium point $(0, 0)$ (provided $f(.)$ and $g(.)$ are defined at $(0, 0)$), one or two axial equilibrium points and coexisting equilibrium point(s) is(are) solution(s)

of the system of algebraic equations $f(n, p) = 0 = g(n, p)$ [22, 33]. The number of axial and interior equilibrium point solely depends upon the functional forms of $f(n, p)$ and $g(n, p)$. Let $E_*(n_*, p_*)$ denotes interior equilibrium point and for Turing-instability conditions we need the local asymptotic stability condition of E_* only. The Jacobian matrix for the system (8.8) evaluated at E_* is given by

$$J_* \equiv J(n, p)|_{E_*} = \begin{bmatrix} j_{11} & j_{12} \\ j_{21} & j_{22} \end{bmatrix}, \tag{8.9}$$

where

$$j_{11} = n\frac{\partial f}{\partial n}\bigg|_{E_*}, \; j_{12} = n\frac{\partial f}{\partial p}\bigg|_{E_*}, \; j_{21} = p\frac{\partial g}{\partial n}\bigg|_{E_*}, \; j_{22} = p\frac{\partial g}{\partial p}\bigg|_{E_*}.$$

Interior equilibrium point E_* is locally asymptotically stable whenever the following conditions are satisfied,

$$\mathrm{Tr}(J_*) = j_{11} + j_{12} < 0, \tag{8.10}$$

$$\mathrm{Det}(J_*) = j_{11}j_{22} - j_{12}j_{21} > 0. \tag{8.11}$$

According to the Routh–Hurwitz criteria [47], $\mathrm{Tr}(J_*) < 0$ and $\mathrm{Tr}(J_*) > 0$ ensure that the two eigenvalues of J_* are negative or having negative real parts. The interior equilibrium point looses stability through Hopf-bifurcation [28] when $\mathrm{Tr}(J_*) = 0$. Solving the equation $\mathrm{Tr}(J_*) = 0$ in terms any parameter 'α' (say) involved with the system we can find the Hopf-bifurcation threshold (denoted by α_H, for convenience) and instability of interior equilibrium point is ensured when the transversality condition for the Hopf-bifurcation is satisfied. This transversality condition is $\frac{d}{d\alpha}\mathrm{Tr}(J_*)\Big|_{\alpha=\alpha_H} \neq 0$. Small amplitude periodic solution arises through Hopf-bifurcation and interior equilibrium point is surrounded by a limit-cycle. The stability or instability of the limit-cycle is determined through the sign of first Lyapunov number [36, 50].

The components of interior equilibrium point define a homogeneous steady-state for the reaction-diffusion system. $n(t, x, y) = n_*$ and $p(t, x, y) = p_*$ satisfy the system of partial differential equations (8.5) along with the initial and boundary conditions. The condition under which a small heterogeneous perturbation around the homogeneous steady-state develop with the advancement of time is known as the Turing instability condition. The development of small inhomogeneous perturbation leads to spatio-temporal pattern formation.

To obtain the Turing instability condition, the perturbation around the homogeneous steady-state is defined by

$$n(t, x, y) = n_* + u(t, x, y), \; p(t, x, y) = p_* + v(t, x, y), \tag{8.12}$$

where $u = \epsilon_1 e^{\lambda t}\cos(k_x x)\cos(k_y y)$ and $v = \epsilon_2 e^{\lambda t}\cos(k_x x)\cos(k_y y)$. ϵ_1 and ϵ_2 are two small non-zero real numbers and $k = \sqrt{k_x^2 + k_y^2}$ is the wave number. Substituting (8.12) into (8.5) and then linearizing the system about (n_*, p_*) we get the following characteristic equation

$$|J_k - \lambda I_2| = 0, \tag{8.13}$$

where

$$J_k = J_* - k^2 \text{diag}(1, d)\, I_2 = \begin{bmatrix} j_{11} - k^2 & j_{12} \\ j_{21} & j_{22} - dk^2 \end{bmatrix}. \tag{8.14}$$

For Turing instability requires that at least one eigenvalue of the matrix J_k must have positive real root. Violation of at least one of the following two inequalities imply the onset of Turing instability,

$$j_{11} + j_{12} - (1 + d)k^2 < 0, \tag{8.15}$$

$$h(k^2) \equiv d(k^2)^2 - (dj_{11} + j_{22})k^2 + j_{12}j_{21} - j_{12}j_{21} > 0. \tag{8.16}$$

The condition (8.15) is always satisfied when interior equilibrium point of the temporal model is locally asymptotically stable and $d, k^2 > 0$. The only relevant instability condition can be achieved through the violation of the inequality (8.16) for a range of values of k. $h(k^2)$ attains its minimum at $k^2 = k_T^2$, where

$$k_T^2 = \frac{dj_{11} + j_{22}}{2d} > 0. \tag{8.17}$$

As $j_{11} + j_{22} < 0$ and k_T is a real quantity, the feasible existence of k_T demands that j_{11} and j_{22} must be of opposite sign. The models for which $j_{11}j_{22} \geq 0$, one can not find any Turing pattern. As 'd' is a positive parameter, the conditions $j_{11} + j_{22} < 0$ and $\frac{dj_{11}+j_{22}}{2d} > 0$ are satisfied simultaneously whenever j_{11} and j_{22} are of opposite sign, that is, $j_{11}j_{22} < 0$. Substituting $k = k_T$ in the expression of $h(k^2)$, we find a sufficient condition for Turing instability,

$$0 < 2\sqrt{d}\,\sqrt{j_{12}j_{21} - j_{12}j_{21}} < dj_{11} + j_{22}. \tag{8.18}$$

Turing bifurcation curve is given by $h(k_T^2) = 0$ which defines a boundary in the parametric space. Turing instability cannot occur in the case of equal diffusivity (i.e. $d = 1$). For prey-predator models, in general, $j_{22} \leq 0$ and again one can not find the situation of Turing instability whenever $j_{22} = 0$. For $j_{22} < 0$, the occurrence of Turing instability demands the satisfaction of the restriction $d > -\frac{j_{22}}{j_{11}} > 1$.

Now $h(k^2)$ is a continuous function of k^2, which is a parabola, and for Turing instability we need $h(k_T^2) < 0$. In this case we find two values of k^2 (by solving (8.16) for k^2) which are given by

$$k_{1,2}^2 = \frac{dj_{11} + j_{22} \mp \sqrt{(dj_{11} + j_{22})^2 - 4d(j_{11}j_{22} - j_{12}j_{21})}}{2d}, \tag{8.19}$$

such that $h(k^2) < 0$ whenever $k^2 \in (k_1^2, k_2^2)$. This interval gives us range of unstable wave numbers.

8.3 Turing and Non-Turing Patterns

In this section we explore the structure of Turing bifurcation domains and various types of stationary and non-stationary patterns exhibited by two dimensional prey predator models with ratio dependent and prey dependent functional responses. The classical Gauss type prey-predator models with prey dependent function response fail to produce any Turing patterns. Temporal dynamics of those models are governed by the system of nonlinear coupled ordinary differential equations

$$\begin{aligned} \frac{dn}{dt} &= nq(n) - r(n)p, \\ \frac{dp}{dt} &= er(n)p - mp, \end{aligned} \tag{8.20}$$

subjected to positive initial conditions. $q(n)$ is per capita growth rate of prey in the absence of predators, $r(n)$ denotes the rate of grazing by the predators, e ($0 < e < 1$) is the conversion efficiency and 'm' is the intrinsic death rate for predators. Spatio-temporal models with these type of temporal counterpart are unable to produce Turing patterns as $j_{22} = 0$ and hence the condition $j_{11}j_{22} < 0$ can not be satisfied.

In the forthcoming subsections, we are going to discuss three different models for prey-predator interactions which exhibit Turing as well as non-Turing patterns for specific choices of parameter values. Two ratio-dependent prey-predator models and Holling-Tanner model with prey-dependent functional response is considered here as all of them exhibit Turing patterns. To obtain the spatio-temporal patterns, numerical simulations are performed using the Euler scheme for the reaction part and five point explicit finite difference scheme for the diffusion part. All the numerical simulation results presented here are obtained by considering zero-flux boundary conditions and small amplitude random perturbation around homogeneous steady-state (if not specified otherwise) [42]. The choices of the lattice size along with temporal and spatial stepping are mentioned at relevant places. The domain of integration, for all the simulation results presented here, are taken as square domain.

8.3.1 Ratio-Dependent Prey-Predator Model

Dynamical interaction between prey and predator species with ratio-dependent functional response is governed by the following system

$$\begin{aligned}\frac{\partial n(t,x,y)}{\partial t} &= n(1-n) - \frac{\alpha np}{n+p} + \left(\frac{\partial^2 n}{\partial x^2} + \frac{\partial^2 n}{\partial y^2}\right),\\ \frac{\partial p(t,x,y)}{\partial t} &= \frac{\beta np}{n+p} - \gamma p + d\left(\frac{\partial^2 p}{\partial x^2} + \frac{\partial^2 p}{\partial y^2}\right),\end{aligned} \tag{8.21}$$

subjected to the initial and boundary conditions as described in the previous section. The parameters α, β, γ and d are dimensionless positive parameters and detailed description of the model can be found in [9]. In [9], we have obtained spatio-temporal patterns within and outside the Turing domain for specific choices of parameter values.

The temporal dynamics of the system (8.21) is governed by the following system of equations

$$\begin{aligned}\frac{dn(t)}{dt} &= n(1-n) - \frac{\alpha np}{n+p},\\ \frac{dp(t)}{dt} &= \frac{\beta np}{n+p} - \gamma p,\end{aligned} \tag{8.22}$$

with the initial condition $n(0)\, n_0 \geq 0$ and $p(0)\, p_0 \geq 0$. The function $\frac{np}{n+p}$ is not defined at the origin but $\lim\limits_{(n,p)\to(0,0)}\left[n(1-n) - \frac{\alpha np}{n+p}\right] = 0$ and $\lim\limits_{(n,p)\to(0,0)}\left[\frac{\beta np}{n+p} - \gamma p\right] = 0$. To maintain the continuity of the system in $\mathbf{R}^2_{0+} = \{(n,p) \in \mathbf{R}^2 : n, p \geq 0\}$, we can redefine [9] the temporal model as follows

$$\begin{aligned}&\frac{dn(t)}{dt} = n(1-n) - \frac{\alpha np}{n+p}, \quad \frac{dp(t)}{dt} = \frac{\beta np}{n+p} - \gamma p, \ (n,p) \neq (0,0),\\ &\frac{dn(t)}{dt} = \frac{dp(t)}{dt} = 0, \ (n,p) = (0,0).\end{aligned} \tag{8.23}$$

In a similar fashion the spatio-temporal model (8.21) can be redefined easily. The temporal steady-states for the system (8.23) are $(0,0)$ (trivial equilibrium), $(1,0)$ (axial equilibrium) and unique interior equilibrium point $(n_*, p_*) = \left(1 - \frac{\alpha(\beta-\gamma)}{\beta}, \frac{(\beta-\gamma)n_*}{\gamma}\right)$. The feasibility conditions for the existence of

interior equilibrium point are given by $\alpha < \dfrac{\beta}{\beta-\gamma}$ and $\gamma < \beta$. These two conditions are automatically satisfied for $\alpha < 1$.

Nature and stability properties of various equilibrium points are available in [9, 17, 35, 70] and references cited therein. Local asymptotic stability condition of E_* is given by

$$\alpha < \alpha_* \equiv \frac{\beta}{\beta+\gamma}\left(\gamma + \frac{\beta}{\beta-\gamma}\right). \tag{8.24}$$

The stability condition is automatically satisfied for $\alpha \leq 1$ and in fact, E_* is a global attractor. For $\alpha > 1$, interior equilibrium point losses stability when α crosses the threshold magnitude α_* and limit-cycle arises through Hopf-bifurcation. Limit cycle encircling the interior equilibrium point is stable and unique [5].

We now discuss the spatio-temporal pattern formation by the model (8.21). To obtain the Turing patterns, we have to identify the parameter values which satisfy the conditions (8.10), (8.11) and (8.18). $u(t,x,y) = u_*$ and $v(t,x,y) = v_*$ define a homogeneous steady-state for the system (8.21). Diffusive instability never sets in for $\alpha \leq 1$ as $j_{11} = (\alpha-1) - \dfrac{\alpha\delta^2}{\beta^2} \leq 0$ and $j_{22} = -\dfrac{(\beta-\delta)\delta}{\beta} < 0$ ($\beta > \delta$ whenever E_* is feasible). Note that the ratio of diffusivities is always positive and hence the condition (8.17) can not be satisfied for $\alpha \leq 1$. We find Turing patterns for the model (8.21) only for $\alpha > 1$ and suitable choice of the parameter 'd'.

Our next task is to determine the Turing bifurcation domain and obtain Turing and non-Turing patterns for the model (8.21). The parameters β and γ are fixed at the values $\beta = 1$ and $\gamma = 0.6$ (hypothetical parameter set [9]) and consider α and d as bifurcation parameters. For chosen parameter set, the Turing bifurcation curve and Hopf-bifurcation curves are shown in Fig. 8.1. These two bifurcation curves divide the domain into four parts and we obtain stationary as well as non-stationary

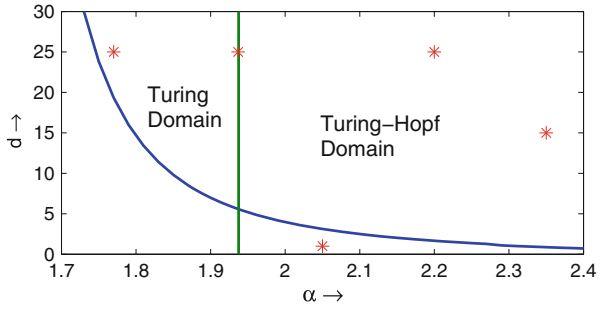

Fig. 8.1 Bifurcation diagram is obtained for $\beta = 1$ and $\gamma = 0.6$, *blue curve* is the Turing-bifurcation curve and the *vertical green line* is Hopf-bifurcation curve. *Red asterisks* represent the points in the $\alpha - d$-parametric space corresponding to which the numerical simulations for the model (8.23) are performed

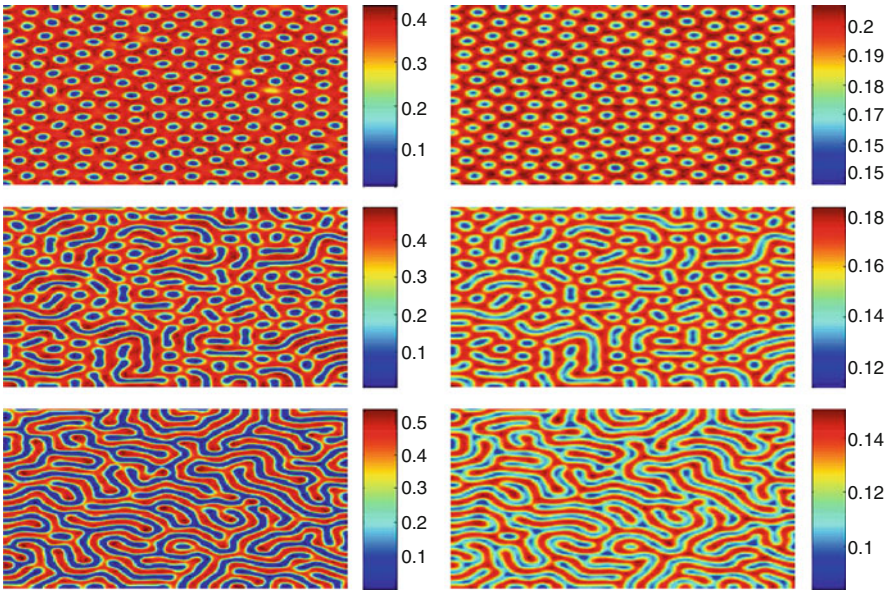

Fig. 8.2 Patterns exhibited by prey (*left column*) and predator (*right column*) for $(\alpha, d) = (1.77, 25)$ (*upper panel*); $(\alpha, d) = (1.9375, 25)$ (*middle panel*); $(\alpha, d) = (2.2, 25)$ (*lower panel*). All the patterns presented here are stationary patterns and obtained at $t = 700$

spatio-temporal patterns for parameter values taken from the Turing domain and Turing Hopf-domain respectively.

We fix the ratio of diffusivity at $d = 15$ and take three different values of α, namely $\alpha = 1.77, 1.9375, 2.2$ and correspondingly the three points lying in the Turing domain, on the Hopf-bifurcation curve and in the Turing-Hopf domain respectively of the parameter space (see Fig. 8.1). For these choices of parameter values, the model (8.21) is simulated over a 400×400 lattices and taking $\Delta t = 0.01$ and $\Delta x = \Delta y = 1$. To ensure that the reported patterns are free from numerical artifacts, the same model is simulated with smaller step sizes and the simulation results remain invariant. Resulting patterns are presented in Fig. 8.2, the reported patterns are observed at $t = 700$. For $(\alpha, d) = (1.77, 25)$ we find cold-spot pattern, these cold spots started coalescing at $(\alpha, d) = (1.9375, 25)$ and ultimately leads to labyrinthine pattern when $(\alpha, d) = (2.2, 25)$. All these patterns are stationary patterns as they remain unaltered with the further increase in time. This stationary property is illustrated in Fig. 8.3, where spatial average of population densities are plotted against time. The labyrinthine pattern sustain for $d = 25$ whenever $\alpha < 2.5$. There is no feasible homogeneous steady-state for $\alpha \geq 2.5$. It is important to note here that the temporal steady-state is unstable and started oscillating for $\alpha > 1.9375$ (the Hopf-bifurcation threshold for $\beta = 1$ and $\delta = 0.6$) but stationary distribution for both the species are obtained here. One natural question arises here, whether we always get stationary patterns for all

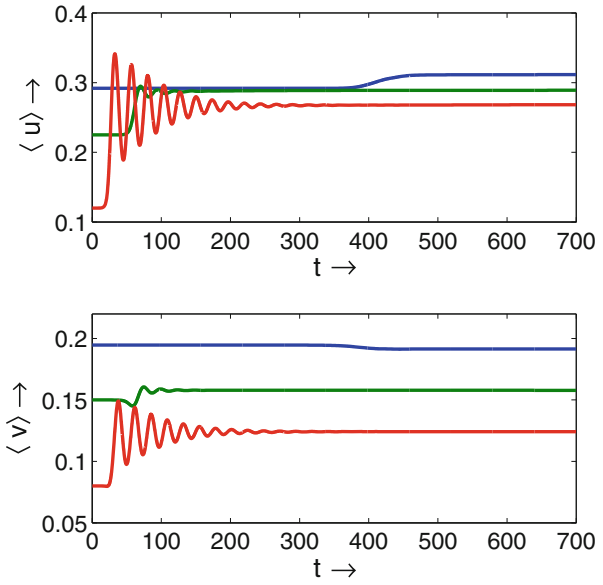

Fig. 8.3 Plot of spatial averages for prey and predator population for $\alpha = 1.77$ (*blue curve*); $\alpha = 1.9375$ (*green curve*); $\alpha = 2.2$ (*red curve*) and $d = 25$

parameter values within the Turing-Hopf domain where the system loses its stability behavior under small amount temporal and spatial perturbation to the homogeneous steady-state. To answer this question we have to examine the patterns for other choices of parameter sets within the Turing-Hopf domain.

There is no mechanism by which one can choose the parameter values within the Turing-Hopf domain for which we find non-stationary patterns. To illustrate such pattern, we choose $\alpha = 2.35$ and $d = 15$. Numerical simulations with this choice of parameter values reveal spatio-temporal chaos and resulting patterns never settle down to any stationary inhomogeneous distribution. Rather they continue to develop irregular patterns which can be classified as spatio-temporal chaotic pattern. In Fig. 8.4 the spatial distribution of prey and predator species is presented at $t = 1{,}500$ along with the spatial average of the two species against time. Phase portrait for the population density of prey verses predator at the location (200, 200) is also plotted in the same figure. The illustrations at the lower panel clearly indicates the chaotic nature of population distributions.

The spatio-temporal patterns we discussed so far for the model (8.21) are obtained for the choice of parameter values inside the Turing domain. Now we can see that the inhomogeneous spatial distribution of prey and predator species can be obtained for the choice of parameter values outside the Turing domain. For this purpose, we choose $\alpha = 2.05$ and $d = 1$. Numerical simulation reveals that the resulting pattern is chaotic. From the sake of brevity the spatio-temporal chaotic nature is not illustrated here. This chaotic nature can be verified in a similar manner as explained in the last paragraph. In Fig. 8.5, the spatial distributions of prey species

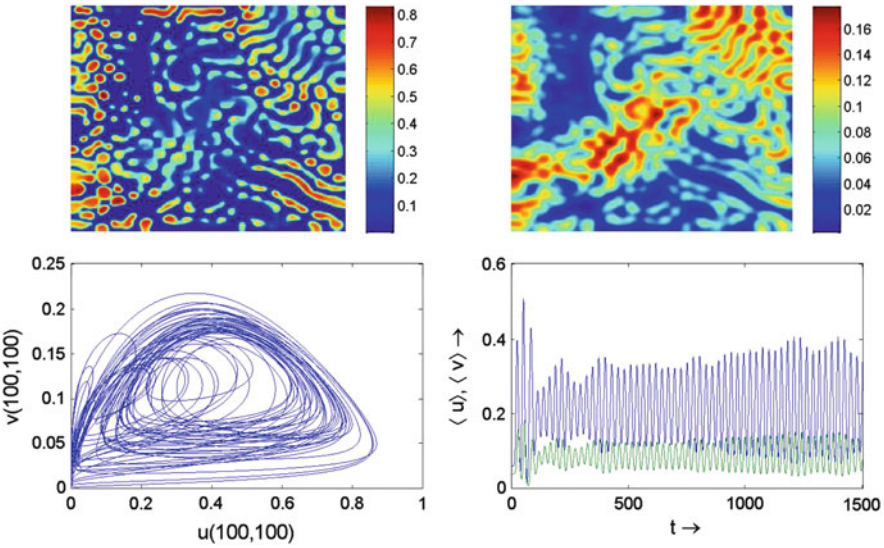

Fig. 8.4 *Upper panel*: Spatial distribution of prey (*left*) and predator (*right*) at $t = 1{,}500$ for $\alpha = 2.35$ and $d = 15$. *Lower panel*: Plot of $u(200, 200)$ against $v(200, 200)$ (*left*) and time evolution of spatial averages of prey and predator density (*right*)

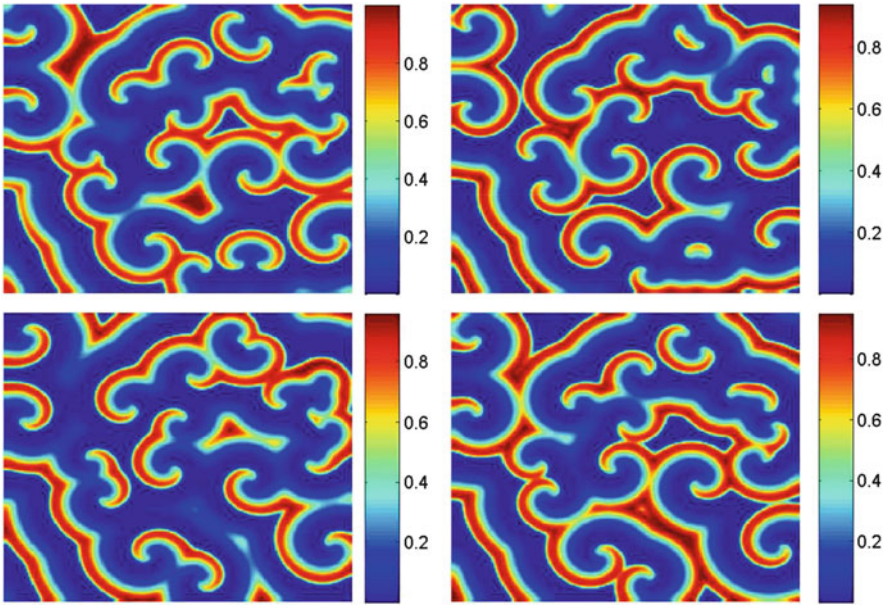

Fig. 8.5 Spatio-temporal chaotic pattern is observed for $\alpha = 2.05$ and $d = 1$. Spatial distribution for prey population at $t = 500$ (*upper-left*); $t = 600$ (*upper-right*); $t = 700$ (*lower-left*) and $t = 800$ (*lower-right*). It is a dynamic pattern

at different time is presented to show the continuous change in the distribution of species. Patterns are presented here for the latest time $t = 800$, but the existence of similar patterns are verified with long time simulations. This type of pattern is classified as interacting spiral pattern and it is a non-Turing pattern.

8.3.2 Ratio-Dependent Holling-Tanner Model

Classical Holling-Tanner type prey-predator was developed to describe the interaction between generalist predator and their most favorable food as prey. Holling-Tanner type prey-predator model with ratio-dependent functional response was proposed and analyzed by Liang and Pan [38]. Recently, we have studied the stationary and non-stationary pattern formation for the spatio-temporal Holling-Tanner model with ratio-dependent functional response [8]. Spatio-temporal dynamics of the Holling-Tanner type prey-predator model with ratio-dependent functional response is governed by the following system of nonlinear coupled parabolic partial differential equations

$$\begin{aligned}\frac{\partial n(t,x,y)}{\partial t} &= n(1-n) - \frac{np}{n+\delta p} + \left(\frac{\partial^2 n}{\partial x^2} + \frac{\partial^2 n}{\partial y^2}\right),\\ \frac{\partial p(t,x,y)}{\partial t} &= \xi\left(\eta - \frac{p}{n}\right)p + d\left(\frac{\partial^2 p}{\partial x^2} + \frac{\partial^2 p}{\partial y^2}\right),\end{aligned} \tag{8.25}$$

subjected to known positive initial conditions $n_0(x, y),\ p_0(x, y) \geq 0, (x, y) \in \Gamma$ and zero-flux boundary conditions $\frac{\partial n}{\partial \nu} = \frac{\partial p}{\partial \nu} = 0$ for $(t, x, y) \in (0, \infty) \times \partial\Gamma$. This model is also undefined at the origin and the reaction kinetics at the origin can be defined in a similar fashion as described in the previous subsection. The non-zero homogeneous steady-state is $(n_*, p_*) = \left(1 - \frac{\eta}{\eta\delta + 1}, \eta n_*\right)$ and the feasibility condition is $\eta < \eta\delta + 1$.

Before going to the pattern formation, here we discuss briefly the local asymptotic stability property of interior equilibrium point $E_*(n_*, p_*)$ for the temporal model corresponding to the spatio-temporal model (8.25). Calculating the quantities $j_{rs}, r, s = 1, 2$ we find,

$$j_{11} = \frac{\eta^2\delta(1-\delta) + 2\eta(1-\delta) - 1}{(\delta\eta + 1)^2},\ j_{12} = -\frac{1}{(\delta\eta + 1)^2},\ j_{21} = \eta^2\xi,\ j_{22} = -\eta\xi.$$

From these expression one can easily verify that the interior equilibrium point E_* is always locally asymptotically stable for $\delta \geq 1$ and we are unable to find any Turing pattern for the associated spatio-temporal model as $j_{11}j_{22} \geq 0$. For $\delta < 1$,

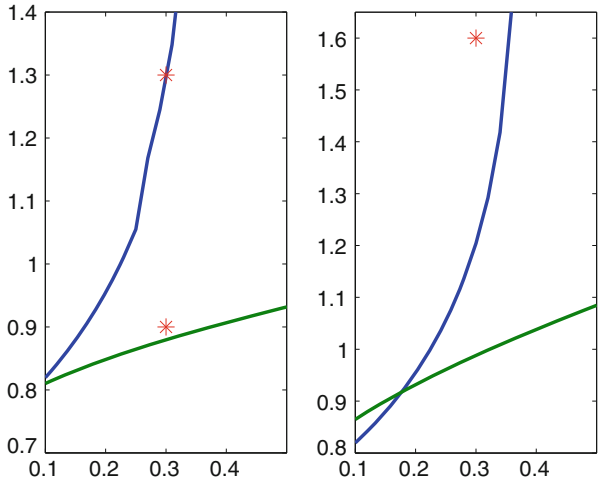

Fig. 8.6 Turing (*blue coloured*) and Hopf-bifurcation (*green coloured*) curves are drawn for $(\alpha, d) = (0.4, 25)$ (*left panel*) and $(\alpha, d) = (0.4, 10)$ (*right panel*) respectively. Hopf-bifurcation curve divides the Turing domain lying above the Turing domain into two regions. Parameter values for which numerical simulations are performed are marked with *red coloured stars*

E_* is locally asymptotically stable if $\xi > \left(\frac{\delta\eta + 2}{(\delta\eta + 1)^2} - \frac{1}{\eta}\right)$ and small amplitude periodic solution bifurcates from the coexisting equilibrium point through Hopf-bifurcation [8, 28]. Clearly, we will look at the Turing patterns for $\delta < 1$.

In the previous subsection, we have considered the ratio of diffusivity as bifurcation parameter and described various types of pattern formation by taking different values for d. Here we consider δ and d at some fixed values and consider η and ξ as bifurcation parameters. In other words, firstly we have to identify Turing and Turing-Hopf domain in the $\eta - \xi$ parameter space and then look at the various stationary and non-stationary patterns for the specific choices of parameter values. In Fig. 8.6 the Turing bifurcation curve and Hopf-bifurcation curve are plotted for $\alpha = 0.4$ and $d = 25$ and $d = 10$ respectively. Numerical simulations are performed for the parameter values within Turing domain and chosen parameter values are marked with red coloured stars in the bifurcation diagram. For the Holling-Tanner model with ratio-dependent functional response we find clod spot pattern and labyrinthine pattern for parameter values taken from Turing domain and Turing-Hopf domain respectively. These two patterns are obtained for $(\xi, \eta) = (0.3, 0.9)$ and $(\xi, \eta) = (0.3, 1.3)$ respectively and both the patterns presented in Fig. 8.7 are stationary patterns. Numerical simulations are performed with $\Delta t = 0.01$, $\Delta x = 1 = \Delta y$ and over 400×400 lattice and using zero flux boundary condition and small random perturbation around homogeneous steady-state as initial conditions.

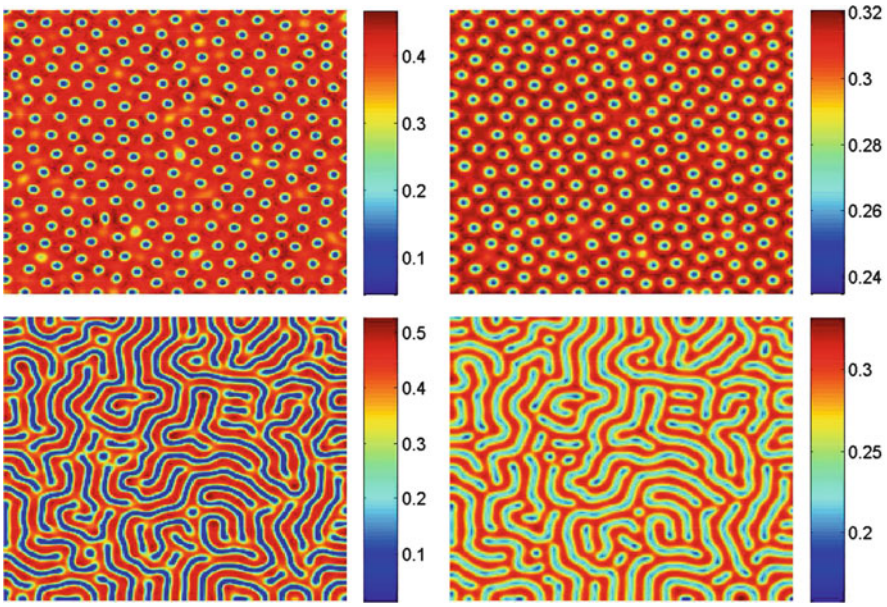

Fig. 8.7 Cold spot (*upper panel*) and labyrinthine pattern (*lower panel*) produced by prey (*left column*) and predator (*right column*) species, involved with the ratio-dependent Holling-Tanner model, at $t = 400$. Both of these patterns are obtained for fixed $\alpha = 0.4$, $\xi = 0.3$, $d = 25$ and $\eta = 0.9$ and $\eta = 1.3$ respectively

In the previous subsection we have considered the ratio of diffusivities as bifurcation parameter and illustrated how spatio-temporal chaos emerges for parameter values within and outside the Turing domain. Here it is important to note that the model under consideration in this subsection is unable to produce chaotic pattern when $d = 25$. Spatio-temporal chaotic pattern is obtained for the model (8.25) when $d \leq 12$, (for $\alpha = 0.4$) and some specific choices of ξ and η in the Turing-Hopf domain. Spatio-temporal chaotic pattern presented in Fig. 8.8 is obtained for $\alpha = 0.4, \xi = 0.3, \eta = 1.6$ and $d = 10$. This spatio-temporal chaos is a dynamic pattern as the distribution of prey and predators over two dimensional space changes continuously with the advancement of time. Patterns are checked for longer times also and it is observed that they never settle down to any stationary level. This model is also capable to produce interacting spiral type spatio-temporal chaotic pattern for $d = 1$ and not presented here to avoid repetitions.

8.3.3 Holling-Tanner Model

In the previous two subsections we have observed spatio-temporal patterns produced by prey-predator models with ratio-dependent functional response. Both the models

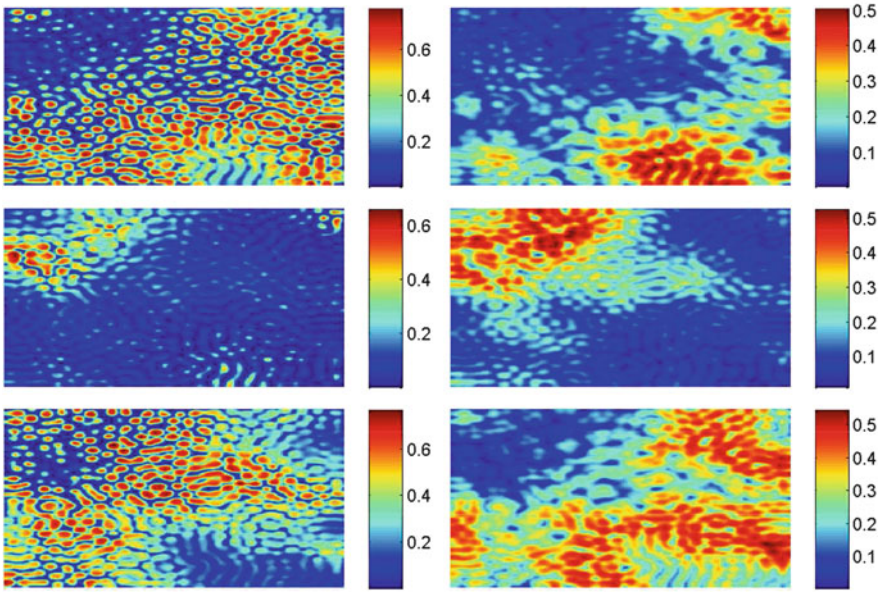

Fig. 8.8 Spatio-temporal chaotic pattern produced by prey (*left column*) and predator (*right column*) for the parameter values $\alpha = 0.4$, $\xi = 0.3$, $\eta = 1.6$ and $d = 10$. Patterns are obtained at $t = 1{,}000$ (*upper panel*); $t = 1{,}250$ (*lower panel*) and $t = 1{,}500$ (*lower panel*) respectively

produce cold spot and labyrinthine patterns as stationary patterns. Here we consider the spatio-temporal version of classical Holling-Tanner type prey-predator model to show the transition of Turing pattern from cold spot to hot spot through labyrinthine pattern and this transition takes place with gradual change in one parameter value. Turing and travelling wave patterns for this Holling-tanner model is recently investigated by Upadhyay et al. [65]. Spatio-temporal model for Holling-Tanner type prey-predator interaction is given by

$$\begin{aligned}\frac{\partial n(t,x,y)}{\partial t} &= n(1-n) - \frac{np}{n+\nu} + \left(\frac{\partial^2 n}{\partial x^2} + \frac{\partial^2 n}{\partial y^2}\right),\\ \frac{\partial p(t,x,y)}{\partial t} &= \theta\left(1 - \frac{\zeta p}{n}\right)p + d\left(\frac{\partial^2 p}{\partial x^2} + \frac{\partial^2 p}{\partial y^2}\right),\end{aligned} \tag{8.26}$$

subjected to the positive initial condition and no-flux boundary condition. Spatio-temporal pattern formation for this model is investigated in details by Upadhyay et al. [65] but the populations are labeled as phytoplankton and zooplankton respectively. The dynamical behavior of the temporal counterpart of the model (8.26) is well-known and available in the literature [43, 47, 62].

To show the transition if spatio-temporal pattern produced by the system (8.26), we consider the fixed parameter set $\nu = 0.1$, $\theta = 0.25$ and consider ζ as free parameter. For the chosen parameter set, we find the co-existing homogeneous steady-state $E_*(n_*, p_*)$ where

$$n_* = \zeta p_*, \quad p_* = \frac{9\zeta - 10 + \sqrt{121\zeta^2 - 180\zeta + 100}}{20\zeta^2}.$$

The condition for local asymptotic stability of co-existing equilibrium point for the associated temporal model can be obtained in terms of ζ. One important observation is that the equilibrium point loses its stability through Hopf-bifurcation at $\zeta_{H1} = 0.3227$ and regains its stability through another Hopf-bifurcation at $\zeta_{H2} = 1.0244$. Hopf-bifurcating limit cycle exist for $\zeta_{H1} \leq \zeta \leq \zeta_{H2}$.

The model (8.26) is simulated numerically keeping fixed the parameters $\nu = 0.1$, $\theta = 0.25$ and $d = 25$. Three different stationary patterns are obtained for $\zeta = 0.28$, $\zeta = 0.7$ and $\zeta = 1.15$. Numerical simulations are performed with the same set up as explained in the previous subsections. Three different Turing patterns are presented in Fig. 8.9.

For the chosen set of parameter values and considering ζ as parameter we find that the interior equilibrium point loses and regains the stability through two consecutive Hopf-bifurcations. The occurrence two successive Hopf-bifurcation

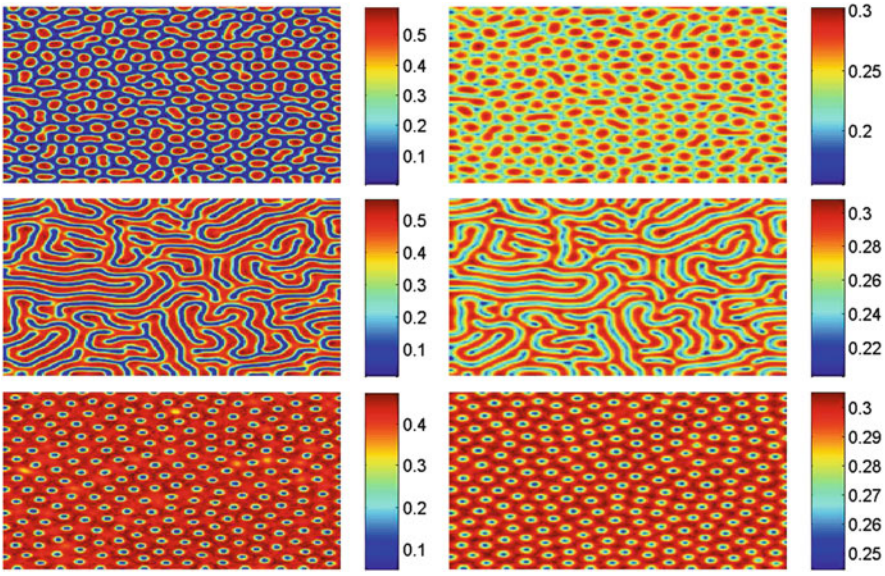

Fig. 8.9 Hot spot (*upper panel*; $\zeta = 0.28$), Labyrinthine (*middle panel*; $\zeta = 0.7$) and cold spot (*lower panel*; $\zeta = 1.15$) patterns are obtained through numerical simulation for varying ζ and keeping other parameters fixed at $\nu = 0.1$, $\theta = 0.25$ and $d = 25$. These stationary patterns are obtained at $t = 600$

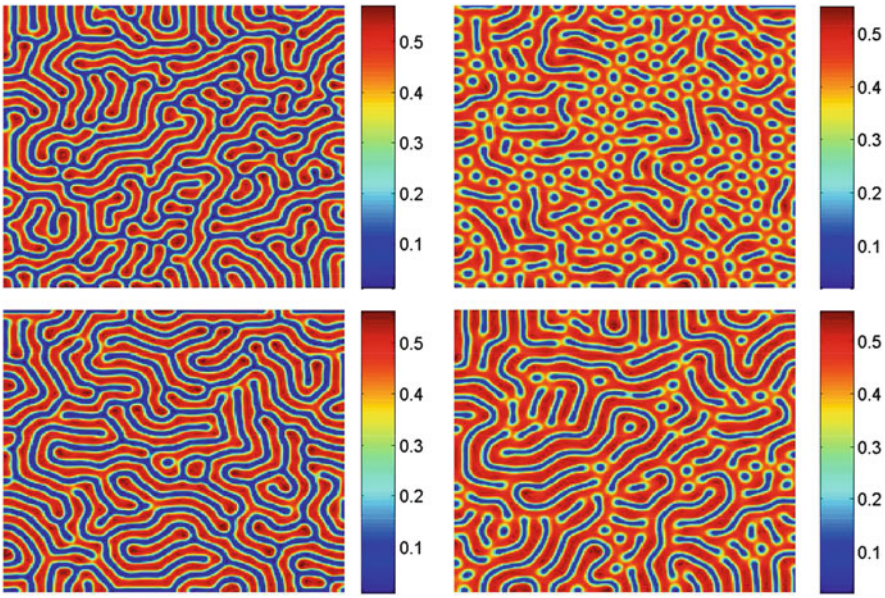

Fig. 8.10 Distribution of prey species over two dimensional landscape for $\zeta = 0.5$ (*left column*) and $\zeta = 0.9$ (*right column*) at $t = 500$, with $\nu = 0.1$, $\theta = 0.25$ and $d = 25$. Patterns presented in the *upper panel* are obtained with small random perturbation around homogeneous steady-state as initial condition and zero flux boundary condition. Patterns presented in the *lower panel* are obtained with the pattern obtained at $\zeta = 0.9$ and $\zeta = 0.5$ as initial conditions

is here responsible to generate hot spot and cold spot type Turing patterns. Labyrinthine pattern is observed for the parameter values lying in the Turing-Hopf domain. There is no spatio-temporal chaotic pattern exhibited by the model (8.26) for chosen set of parameter values.

An interesting phenomena for pattern formation takes place for this Holling-Tanner model when parameter values are inside the Turing-Hopf domain. Patterns produced by the prey and predator population are sensitive to initial conditions. Sensitivity of spatial pattern is presented in Fig 8.10. At the upper panel, patterns are obtained for two different values of the parameter ζ keeping other parameters fixed at the level as described above and with small random perturbation around the homogeneous steady-states as the initial conditions. The patterns are obtained for $\zeta = 0.5$ and $\zeta = 0.9$, they are stationary patterns. In order to check the sensitivity of initial condition, the stationary pattern obtained at $\zeta = 0.9$ is used as the initial condition and the spatio-temporal model is simulated numerically with $\zeta = 0.5$ and the stationary pattern obtained at $t = 500$ is presented at the left of lower panel in Fig. 8.10. Similarly, the pattern obtained for $\zeta = 0.5$ is used as initial condition to obtain the pattern when $\zeta = 0.9$ and we have obtained a different pattern compared to that was obtained with the usual initial condition used here.

8.4 Discussion

Autonomous temporal models of prey-predator interaction always results in either stable stationary coexistence or oscillatory coexistence or extinction of one or both the species. Spatio-temporal models are developed to take care of the mobility of individuals over their habitats. Individuals of various species attempt to find out most favorable habitat as well as patches where availability of their essential foods is abundant. Again carnivorous predators have to chase their prey to get the food and hence they have to run faster from their predators. Similarly, the swimming speed of zooplankton within aquatic environment should be greater than the moving speed of phytoplankton due to water current within the aquatic environment. All these requirements are reflected through the condition $d > 1$, where d is the ratio of diffusivities of the prey and their predators. At the initial stages of the research on pattern formation, it was believed that the inequality in the ratio of diffusivity is essential for spatio-temporal pattern formation. Afterwards, it is revealed that the spatio-temporal patterns can emerge in case of equal diffusivities also [23, 41, 51]. Most important and interesting cases of pattern formation with equal diffusivities are biological invasions and travelling wave-train [42, 45, 46, 58, 59, 61, 66, 67]. Recently, few authors have paid their attention towards the spatio-temporal chaotic pattern formation due to wave of chaos. This scenario arises in most of the cases for $d = 1$, (see [51, 64] and references cited therein).

In this chapter we have discussed pattern formation in prey-predator models within Turing and Turing-Hopf domain with special emphasis on ratio-dependent functional response. Prey-predator models with prey-dependent functional response and intrinsic constant per capita death rate for predators are unable to produce Turing patterns. Three models are considered here, ratio-dependent prey-predator model, Holling-Tanner model with ratio-dependent functional response and classical Holling-Tanner model. The classical Holling-Tanner model is also known as semi-ratio dependent model as the growth equation of the predators contains a term which is proportional to the ratio of predator to prey. For fist two models, we have observed that the stationary Turing patterns are cold spot patterns which indicate the existence of circular patches with lower concentration of prey and predators. In contrary, the stationary Turing patterns observed for the classical Holling-Tanner model are of two types, hot spot pattern and cold spot pattern. Hot spots are generated through the localized circular patches with high concentration of population density. The labyrinthine pattern is observed for some particular choices of parameter values within the Turing-Hopf domain. In the first two models, the stationary cold spot pattern changed to labyrinthine pattern due to coalesce of nearby circular patches with low concentration of population. This transition takes place as parameter moves from Turing domain to Turing-Hopf domain. But the generation of labyrinthine pattern in case of spatio-temporal Holling-Tanner model with Holling type-II functional response can be explained in two ways. If we consider the increase in the magnitude of ζ then labyrinthine pattern is generated by the coalescing of hot spots and the same can be generated due the merging of nearby cold spots due

to decrease in the magnitude of ζ. The three models considered here are capable to generate another kind of stationary patterns which is a mixture of spot and labyrinthine pattern. The stationary patterns obtained for the first two models are independent of initial condition, we have checked this independence numerically but the results are not presented here. The sensitivity of resulting pattern, or in other words the dependence of stationary pattern on the choice of initial condition is illustrated for the spatially extended classical Holling-Tanner model. We have reported here the spatio-temporal chaotic patterns for parameter values within and outside the Turing domain. Obviously the spatio-temporal chaotic patterns are not stationary patterns rather they changes continuously with time and never settle down to any stationary state.

In reality the spot and labyrinthine patterns obtained within Turing domain are not realistic for the distribution of prey and predators distributed over two dimensional landscapes but can be observed for vegetation patterns generated through the interaction between autotroph and their herbivores. Again the patchy patterns resulting from spatio-temporal chaos and labyrinthine type distributions are observed for the vegetation patterns in semiarid regions [8, 14, 45, 69]. Spatio-temporal chaotic patterns are also observed for the distribution of various plankton biomass within aquatic environment. The discrepancy in the observed patterns are either due to the over simplification in the modeling approach or due to the consideration of distribution of individuals over two dimensional domain as a continuum media. The patterns obtained for the models under consideration give us the idea of size and rough shape of stationary patches for the distribution of prey and predator species. Some times they give indication of colony formation by the bacterial species and their predators. Apart from this distribution, the stationarity of patterns provide the information regarding the time invariant distribution of species over their spatial habitat.

Finally, we have addressed the issue of spatio-temporal chaotic patterns produced by prey-predator model with ratio-dependent functional response terms. Spatio-temporal chaotic pattern exists for parameter values within the Turing-Hopf domain as well as outside the Turing domain. Emergence of spatio-temporal chaos for parameter values above and below the Turing bifurcation curve ensures that the interaction between temporal instability and spatial instability is not essential for the onset of spatio-temporal chaos. Again, we have observed the existence of stationary patterns for the parameter values within Turing-Hopf domain, it means the coexistence steady-state of the reaction kinetics is unstable and local kinetics is oscillatory. These observations ensure the fact that the interaction between the temporal and spatial instability are unable to drive the system towards spatial and temporal irregularity under any circumstances. Rather the existence of irregular distribution of population over space and its continuous change with time depend upon the complex interaction is taking place over spatial and temporal scale. There are no unified criteria for the existence of spatio-temporal chaos. Further the mobility of individuals within their habitat has some role towards the patchy distribution of interacting populations. Recent works on continuous spatio-temporal models for interacting populations and vegetation distribution indicate the existence

of spatio-temporal chaos but the conclusive evidence in favor of chaotic patterns in realistic ecosystems are not abundant [20, 27, 46, 52, 54–56, 60]. Effect of cross-diffusion, periodic changes in essential resources, random environmental condition on the pattern formation for interacting population models with rich temporal dynamics needs appropriate attention to understand the complex dynamical behavior associated with the spatio-temporal pattern formation. Derivation of necessary and sufficient analytical conditions for the appearance of spatio-temporal chaotic patterns remain an open as well as challenging problem.

References

1. Akçakaya, H.R.: Population cycles of mammals: evidence for a ratio-dependent predator-prey hypothesis. Ecol. Monogr. **62**, 119–142 (1992)
2. Alonso, D., Bartumeus, F., Catalan, J.: Mutual interference between predators can give rise to turing spatial patterns. Ecology **83**, 28–34 (2002)
3. Arditi, R., Berryman, A.A.: The biological control paradox. Trends Ecol. Evol. **6**, 32–43 (1991)
4. Arditi, R., Ginzburg, L.R.: Coupling in predator-prey dynamics: ratio-dependence. J. Theor. Biol. **139**, 311–326 (1989)
5. Bandyopadhyay, M., Chattopadhyay, J.: Ratio-dependent predator-prey model: effect of environmental fluctuation and stability. Nonlinearity **18**, 913–936 (2005)
6. Banerjee, M.: Self-replication of spatial patterns in a ratio-dependent predator-prey model. Math. Comp. Model. **51**, 44–52 (2010)
7. Banerjee, M.: Spatial pattern formation in ratio-dependent model: higher-order stability analysis. IMA J. Math. Med. Biol. **28**, 111–128 (2011)
8. Banerjee, M., Banerjee, S.: Turing instabilities and spatio-temporal chaos in ratio-dependent Holling-Tanner model. Math. Biosci. **236**, 64–76 (2012)
9. Banerjee, M., Petrovskii, S.: Self-organized spatial patterns and chaos in a ratio-dependent predator-prey system. Theor. Ecol. **4**, 37–53 (2011)
10. Banerjee, M., Venturino, E.: A phytoplankton-toxic phytoplnkton-zooplankton model. Ecol. Complex. **8**, 239–248 (2011)
11. Baurmann, M., Ebenhoh, W., Feudel, U.: Turing instabilities and pattern formation in a Benthic nutrient-microorganism system. Math. Biosci. Eng. **1**, 111–130 (2004)
12. Baurmann, M., Gross, T., Feudel, U.: Instabilities in spatially extended predator-prey systems: spatio-temporal patterns in the neighborhood of Turing-Hopf bifurcations. J. Theor. Biol. **245**, 220–229 (2007)
13. Bazykin, A.D.: Nonlinear Dynamics of Interacting Populations. World Scientific, Singapore (1998)
14. Belsky, A.J.: Population and community processes in a mosaic grassland in the Serengeti, Tanzania. J. Ecol. **74**, 841–856 (1986)
15. Benson, D.L., Maini, P.K., Sherratt, J.: Pattern formation in reaction-diffusion models with spatially inhomogeneous diffusion coefficients. Math. Comp. Model. **17**, 29–34 (1993)
16. Benson, D.L., Sherratt, J., Maini, P.K.: Diffusion driven instability in an inhomogeneous domain. Bull. Math. Biol. **55**, 365–384 (1993)
17. Berezovaskaya, F.S., Karev, G., Arditi, R.: Parametric analysis of ratio-dependent predator-prey model. J. Math. Biol. **43**, 221–246 (2001)
18. Cantrell, R.S., Cosner, C.: Spatial Ecology Via Reaction-Diffusion Equations. Wiley, London (2003)
19. Cheng, K.S., Hsu, S.B., Lin, S.S.: Global stability of a predator-prey system. J. Math. Biol. **12**, 115–126 (1981)

20. Ellner, S., Turchin, P.: Chaos in a noisy world: new methods and evidence from time-series analysis. Am. Nat. **145**, 343–375 (1995)
21. Fasani, S. Rinaldi, S.: Factors promoting or inhibiting turing instability in spatially extended prey-predator systems. Ecol. Model. **222**, 3449–3452 (2011)
22. Freedman, H.I.: Deterministic Mathematical Models in Population Ecology. Marcel & Dekker, New York (1980)
23. Garvie, M.R.: Finite difference schemes for reaction-diffusion equations modeling predator-prey interactions in MATLAB. Bull. Math. Biol. **69**, 931–956 (2007)
24. Gause, G.F.: The Strugle for Existence. Williams and Wilkins, Baltimore (1935)
25. Gutierrez, A.P.: The physiological basis of ratio-dependent predator-prey theory: a metabolic pool model of Nicholson's blowflies as an example. Ecology **73**, 1552–1563 (1992)
26. Haldane, J.B.S.: Enzymes. Longman, London (1930)
27. Hanski, I., Turchin, P., Korplmakl, E., Henttonen, H.: Population oscillations of boreal rodents: regulation by mustelid predators leads to chaos. Nature **364**, 232–235 (1993)
28. Hassard, B.D., Kazarinoff, N.D., Wan, Y.H.: Theory and Application of Hopf-Bifurcation. Cambridge University Press, Cambridge (1981)
29. Hsu, S.B., Hwang, T.W., Kuang, Y.: Global analysis of the Michaelis–Menten type ratio-dependent predator-prey system. J. Math. Biol. **42**, 489–506 (2001)
30. Huisman, J., Weissing, F.J.: Biodiversity of plankton by oscillations and chaos. Nature **402**, 407–410 (1999)
31. Jost, C., Arino, O., Arditi, R.: About deterministic extinction in ratio-dependent predator-prey model. Bull. Math. Biol. **61**, 19–32 (1999)
32. Klausmeier, C.A.: Regular and irregular patterns in semiarid vegetation. Science **284**, 1826–1828 (1999)
33. Kot, M.: Elements of Mathematical Biology. Cambridge University Press, Cambridge (2001)
34. Kuang, Y.: Rich dynamics of Gause-type ratio-dependent predator prey system. Fields Inst. Commun. **21**, 325–337 (1999)
35. Kuang, Y., Beretta, E.: Global qualitative analysis of a ratio-dependent predator-prey system. J. Math. Biol. **36**, 389–406 (1999)
36. Kuznetsov, Y.A.: Elements of Applied Bifurcation Theory. Springer, New York (2004)
37. Levin, S.A., Segel, L.A.: Hypothesis for origin of planktonic patchiness. Nature **259**, 659 (1976)
38. Liang, Z., Pan, H.: Qualitative analysis of a ratio-dependent Holling-Tanner model. J. Math. Anal. Appl. **334**, 954–964 (2007)
39. Luckinbill, L.L.: Coexistence in laboratory populations of *Paramecium aurelia* and its predator *Didinium nasutum*. Ecology **54**, 1320–1327 (1973)
40. Luckinbill, L.L.: The effects of space and enrichment on a predator-prey system. Ecology **55**, 1142–1147 (1974)
41. Malchow, H.: Spatio-temporal pattern formation in nonlinear nonequilibrium plankton dynamics. Proc. R. Soc. Lond. B **251**, 103–109 (1993)
42. Malchow, H., Petrovskii, S.V., Venturino, E.: Spatiotemporal Patterns in Ecology and Epidemiology. Chapman & Hall, London (2008)
43. May, R.M.: Stability and Complexity in Model Ecosystems. Princeton University Press, New Jersey (2001)
44. Medvinsky, A., Petrovskii, S., Tikhonova, I., Malchow, H., Li, B.L.: Spatiotemporal complexity of plankton and fish dynamics. SIAM Rev. **44**, 311–370 (2002)
45. Morozov, A.Y., Petrovskii, S.V.: Excitable population dynamics, biological control failure, and spatiotemporal pattern formation in a model ecosystem. Bull. Math. Biol. **71**, 863–887 (2009)
46. Morozov, A.Y., Petrovskii, S.V., Li, B.L.: Bifurcation, chaos and intermittency in the predator-prey system with the Allee effect. Proc. R. Soc. Lond. B, **271**, 1407–1414 (2004)
47. Murray, J.D.: Mathematical Biology II. Springer, Heidelberg (2002)
48. Okubo, A., Levin, S.: Diffusion and Ecological Problems: Modern Perspectives. Springer, Berlin (2001)

49. Pal, R., Basu, D., Banerjee, M.: Modelling of phytoplankton allelopathy with Monod–Haldane-type functional response—a mathematical study. Biosystems **95**, 243–253 (2009)
50. Perko, L.: Differential Equations and Dynamical Systems. Springer, New York (2001)
51. Petrovskii, S.V., Malchow, H.: A minimal model of pattern formation in a prey-predator system. Math. Comp. Model. **29**, 49–63 (1999)
52. Petrovskii, S.V., Malchow, H.: Wave of chaos: new mechanism of pattern formation in spatio-temporal population dynamics. Theor. Popul. Biol. **59**, 157–174 (2001)
53. Petrovskii, S.V., Li, B.L., Malchow, H.: Quantification of the spatial aspect of chaotic dynamics in biological and chemical systems. Bull. Math. Biol. **65**, 425–446 (2003)
54. Petrovskii, S.V., Li, B.L., Malchow, H.: Transition to spatiotemporal chaos can resolve the paradox of enrichment. Ecol. Complex. **1**, 37–47 (2004)
55. Petrovskii, S., Morozov, A., Malchow, H., Sieber, M.: Noise can prevent onset of chaos in spatio-temporal population dynamics. Eur. Phys. J. B **78**, 253–264 (2010)
56. Scheffer, M.: Should we expect strange attractors behind plankton dynamics—and if so, should we bother? J. Plankt. Res. **13**, 1291–1305 (1991)
57. Segel, L.A., Jackson, J.L.: Dissipative structure: an explanation and an ecological example. J. Theor. Biol. **37**, 545–559 (1972)
58. Sherratt, J.A.: Periodic travelling waves in cyclic predator-prey systems. Ecol. Lett. **4**, 30–37 (2001)
59. Sherratt, J.A., Smith, M.: Periodic travelling waves in cyclic populations: field studies and reaction diffusion models. J. R. Soc. Interface **5**, 483–505 (2008)
60. Sherratt, J.A., Lewis, M.A., Fowler, A.C.: Ecological chaos in the wake of invasion. Proc. Natl. Acad. Sci. USA **92**, 2524–2528 (1995)
61. Shigesada, N., Kawasaki, K.: Biological Invasions: Theory and Practice. Oxford University Press, Oxford (1997)
62. Turchin, P.: Complex Population Dynamics. Princeton University Press, New Jersey (2003)
63. Turing, A.M.: The chemical basis of morphogenesis. Philos. Trans. R. Soc. Lond. B **237**, 37–72 (1952)
64. Upadhyay, R.K., Kumari, N., Rai, V.: Modeling spatiotemporal dynamics of vole populations in Europe and America. Math. Biosci. **223**, 47–57 (2010)
65. Upadhyay, R.K., Volpert, V., Thakur, N.K.: Propagation of Turing pattern in a plankton model. J. Biol. Dyn. **6**, 524–538 (2012)
66. Volpert, V., Petrovskii, S.V.: Reaction-diffusion waves in biology. Phys. Life Rev. **6**, 267–310 (2009)
67. Volpert, A., Volpert, V., Volpert, V.: Traveling Wave Solutions of Parabolic Systems. Translation of Mathematical Monographs, vol. 140. American Mathematical Society, Providence, RI (1994)
68. Wang, W., Liu, Q.X., Jin, Z.: Spatiotemporal complexity of a ratio-dependent predator-prey system. Phys. Rev. E **75**, 051913 (2007)
69. White, L.P.: Brousse tigrée patterns in southern Niger. J. Ecol. **58**, 549–553 (1970)
70. Xiao, D., Ruan, S.: Global dynamics of a ratio-dependent predator-prey system. J. Math. Biol. **43**, 268–290 (2001)

Part IV
Chaos and Field Programmable Gate Array

Chapter 9
Realizing Chaotic Systems on Field Programmable Gate Arrays: An Introduction

Bharathwaj Muthuswamy and Santo Banerjee

Abstract In this chapter, we discuss an overview and give examples of how one could leverage the functionality of twenty-first century Field-Programmable Gate Arrays (FPGAs) for implementing nonlinear dynamical systems that exhibit chaotic behaviour. An FPGA is basically a "blank-slate" of hardware that can be "programmed" to emulate a plethora of digital systems. The purpose of this chapter is to expose this exciting engineering product for investigating scientific phenomenon. As a result, this chapter is a guide line on how to implement chaotic systems on an FPGA (the Altera Cyclone IV on a DE2-115 board).

9.1 Overview

In this chapter, we will explore how we can use Field Programmable Gate Arrays or FPGAs to implement nonlinear ordinary differential equations or ODEs (that exhibit chaotic behaviour). To illustrate the robustness of FPGAs, these differential equations could also include time delay(s). There are a myriad of references on chaos theory. Therefore this chapter will primarily focus on FPGAs, as used to realize nonlinear dynamics.

The FPGA industry originated from the programmable read-only memory and programmable logic devices industry of the 1970s [2]. Xilinx co-founders Ross Freeman and Bernard Vonderschmitt invented the first commercially viable FPGA in 1985—the XC2064 [2].

Over the last three decades, the FPGA industry has evolved rapidly. Hence, in the twenty-first century, FPGA development platforms have a variety of on-board peripherals—from gigabit ethernet to audio codec (coder/decoder). In this chapter

B. Muthuswamy (✉)
Electrical Engineering and Computer Sciences, Milwaukee School of Engineering, S342 Fred Loock Engineering Center, 1025 N. Broadway, Milwaukee, Wisconsin, USA 53202
e-mail: muthuswamy@msoe.edu

S. Banerjee
Institute for Mathematical Research, University Putra Malaysia, 43400 Serdang, Malaysia

S. Banerjee, L. Rondoni (eds.), *Applications of Chaos and Nonlinear Dynamics in Science and Engineering - Vol. 4*, Understanding Complex Systems,
DOI 10.1007/978-3-319-17037-4_9

we will utilize the audio codec's digital-to-analog converter (DAC) to help visualize chaotic trajectories as analog voltage waveforms.

Because FPGA technology evolves rapidly, this chapter can only provide a high level overview, with an example for illustrative purposes. It is up to the interested reader to pursue this exciting topic further!

The chapter is organized as follows: we will first discuss the big picture behind implementing ODEs on FPGAs. Next we will discuss an example of implementing the Ikeda Delay Differential Equation (DDE) on the FPGA, by highlighting the important steps involved in realizing an ODE on an FPGA.

For notation used in this chapter: key ideas and steps will be highlighted in **bold**. The mathematical notation used is standard. For example, t represents time, $x(t)$ (or x) represents the state variable with $\mathbf{x}$ (**boldface**) invariably reserved for vectors. $\dot{x}$ is $\frac{dx}{dt}$. τ would represent time delay.

9.2 Implementing Ordinary Differential Equations on FPGAs: The Big Picture

Consider Eqs. (9.1) through (9.3).

$$\dot{x_1} = f_1(x_1, \ldots, x_n) \tag{9.1}$$

$$\dot{x_2} = f_2(x_2, \ldots, x_n) \tag{9.2}$$

$$\vdots$$

$$\dot{x_n} = f_n(x_1, \ldots, x_n) \tag{9.3}$$

We can use forward-Euler's method[1] [5] and rewrite Eqs. (9.1) through (9.3) as Eqs. (9.4) through (9.6).

$$x_1(t + \delta t) = x_1(t) + f_1(x_1(t), \ldots, x_n(t))\Delta t \tag{9.4}$$

$$x_2(t + \delta t) = x_2(t) + f_2(x_1(t), \ldots, x_n(t))\Delta t \tag{9.5}$$

$$\vdots$$

$$x_n(t + \delta t) = x_n(t) + f_n(x_1(t), \ldots, x_n(t))\Delta t \tag{9.6}$$

But let us generalize Eqs. (9.1) through (9.3) to include time delay. Hence the system of equations that we will discuss in this chapter is given by Eq. (9.7).

$$\dot{\mathbf{x}} = \mathbf{f}(t, \mathbf{x}(\mathbf{t}), \mathbf{x}(t - \tau_i)) \tag{9.7}$$

[1] For a very brief discussion on FPGA numerical methods, refer to Sect. 9.3.

Again utilizing forward-Euler method, we get Eq. (9.8).

$$\mathbf{x}(t + \delta t) = \mathbf{x}(t) + \mathbf{f}(\mathbf{x}(t), \mathbf{x}(t - N_i))\Delta t \tag{9.8}$$

In Eq. (9.8), we have slightly abused our notation and have used continuous time t whereas the equation is actually discrete.

When implementing Eq. (9.8) on an FPGA, we define for the n-th time delay ODE:

$$xNNew \triangleq x_n(t) + f_n(x_1(t), \ldots, x_n(t - N_i))\Delta t \tag{9.9}$$

$$xN \triangleq x_n(t + \delta t) \tag{9.10}$$

In Eqs. (9.9) and (9.10), $xNNew$ and xN are VHDL[2] signals with $N = 1, 2, \cdots, n$. Δt is the step-size in Euler's method. δt is the clock period for the D flip-flop that results in synchronized xN. The delay N_i is related to Δt and τ_i by $\Delta t \triangleq \frac{\tau_i}{N_i - 1}$ (refer to Sect. 9.6).

A block diagram representation of Eqs. (9.9) and (9.10) is shown in Fig. 9.1.

The block diagram in Fig. 9.1 will utilize a combination of Altera's Simulink (MATLAB) library—DSP Builder Advanced Block Set (blocks highlighted in *yellow*) and VHDL. Although the entire design can be implemented within the FPGA software framework provided by the FPGA vendor, utilizing Simulink will illustrate the power of abstraction, that has become so prevalent in twenty-first century FPGA designs.

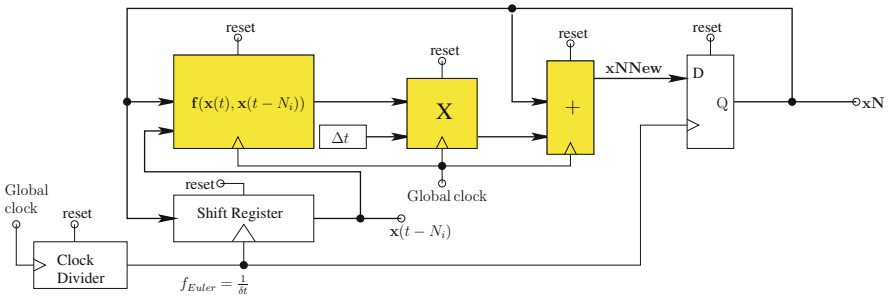

Fig. 9.1 Hardware block diagram for specifying nonlinear ODEs using forward-Euler's method [2]. We have highlighted the vector nature of $xNNew$ and xN from Eqs. (9.9) and (9.10) as **xNNew** and **xN** resp

[2]A detailed description of VHDL (**V**ery high speed integrated circuit **H**ardware **D**escription **L**anguage), FPGA software tools and the underlying FPGA hardware is beyond the scope of this chapter. For details, please refer to our book [2].

In Fig. 9.1 the shift register is unnecessary for non-delay systems. The clock divider block is configured to divide the global clock (usually obtained from the FPGA board clock) so propagation delays associated with the various sub-modules (such as the shift register) can be accommodated. Hence the clock divider output clock (with frequency $f_{Euler} = \frac{1}{\delta t}$) is used as clock input for the shift register and the D flip-flop synchronizer. Since the overall design is synchronous, all sequential logic components have a well-defined reset state. **xN** ($\mathbf{x}(t + \delta t)$) and $\mathbf{x}(t - N_i)$ also serve as inputs to the audio codec DAC.

To complete the implementation of a nonlinear (chaotic) differential equation on an FPGA, the following steps are required:

1. Thoroughly understand the hardware requirements for implementing the nonlinear differential equation.
2. Discretize the system and simulate in Simulink to verify functionality.
3. Specify the necessary subsystems in DSP Builder Advanced Blockset.
4. Complete Euler's method in VHDL.
5. Simulate design in ModelSim to verify VHDL functionality.
6. Fully synthesize the design (along with the necessary external audio codec interface) onto the FPGA.

The next few section(s) will illustrate the steps above, using the Ikeda DDE [2] as an example:

$$\dot{x} = \mu \sin(x(t - \tau)) - \alpha x(t) \tag{9.11}$$

Parameter values are: $\mu = 6, \tau = 1, \alpha = 1$.

9.3 Hardware Requirements for the Ikeda DDE

The hardware platform that we will use in this chapter is a DE2-115 board from Terasic corporation that incorporates a Cyclone IV FPGA from Altera [2]. This platform highlights the hardware requirements for implementing nonlinear ODEs: a modern FPGA that has on-chip peripherals such as Phase-Locked Loops (PLLs), multipliers and RAM blocks. Moreover the associated board has our requisite Wolfson WM8731 audio codec.

Note however that we are implementing a numerical algorithm on a discrete platform (FPGA) for solving a continuous-time differential equations. Hence a sound understanding of the numerical algorithm and the underlying FPGA architecture is a must. In this chapter, we chose to use Euler's method. Although we can implement more complicated numerical methods (such as 4th order Runge-Kutta), these methods will also have issues converging to the correct solution, if a sufficiently large step size is taken [4]. Thus we chose to use Euler's method for simplicity. As a rule of thumb, one should use a sufficiently small step size to ensure that the numerical algorithm converges to the correct solution.

We should also take into consideration the amount of memory required for implementing the ODE. In this chapter, we will utilize only on-chip FPGA memory for design simplicity. The on-chip memory requirements are dominated by the shift register. Therefore when implementing a DDE, we can use the fact: $\Delta t = \frac{\tau}{N-1}$ (for the Ikeda DDE, $\tau_i = \tau, N_i = N$). Suppose we choose $\Delta t = 0.001$. For the Ikeda DDE, we chose parameter $\tau = 1$. Thus $N = 1{,}001$. Hence we need 1001 D flip-flops with a 32-bit datapath. This is not too stringent of a requirement for the Cyclone IV.

A further detailed discussion of FPGA architecture,[3] effects of sampling clock and data path quantization is beyond the scope of this chapter, for details, please refer to [2]. We can however continue to the next step: simulating the discretized Ikeda DDE. A discrete system simulation is a must because we can quickly determine if our step-size is too large or if our on-chip FPGA memory requirements are too small.

9.4 Discrete System Simulation

The general discretized system equations were discussed in Sect. 9.2, an elegant block diagram representation is in Fig. 9.2.

A specific block diagram for the Ikeda DDE is shown in Fig. 9.3. The discrete-time integrator and delay blocks can be found under the Discrete library in Simulink. The Trigonometric function, Gain and Sum blocks can be found under Math Operations. The Constant block can be found in the Sources library.

Simulation results are shown in Fig. 9.4.

The complete reference design (including the Simulink .mdl file for this section and all files for subsequent sections) can be downloaded from http://www.harpgroup.org/muthuswamy/pubs/code/2014/DDEs/DE2ChaoticDDEs.zip.

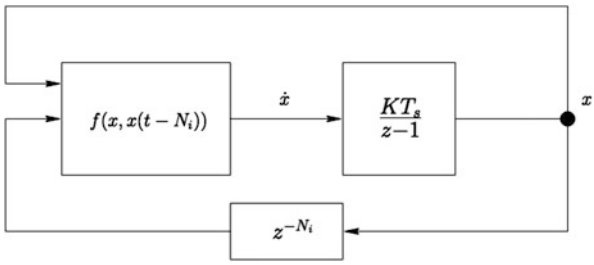

Fig. 9.2 Simulating a DDE in Simulink, block diagram adopted from [2]. We utilize the discrete-time integrator but inherit the sample time from the fixed-point simulation period

[3]The discussion so far should also highlight the advantages of an FPGA as compared to a microcontroller: a dedicated truly-parallel datapath for implementing nonlinear ODEs. The disadvantage of an FPGA is the necessity to visualize the underlying hardware from the specification (VHDL) in FPGA software.

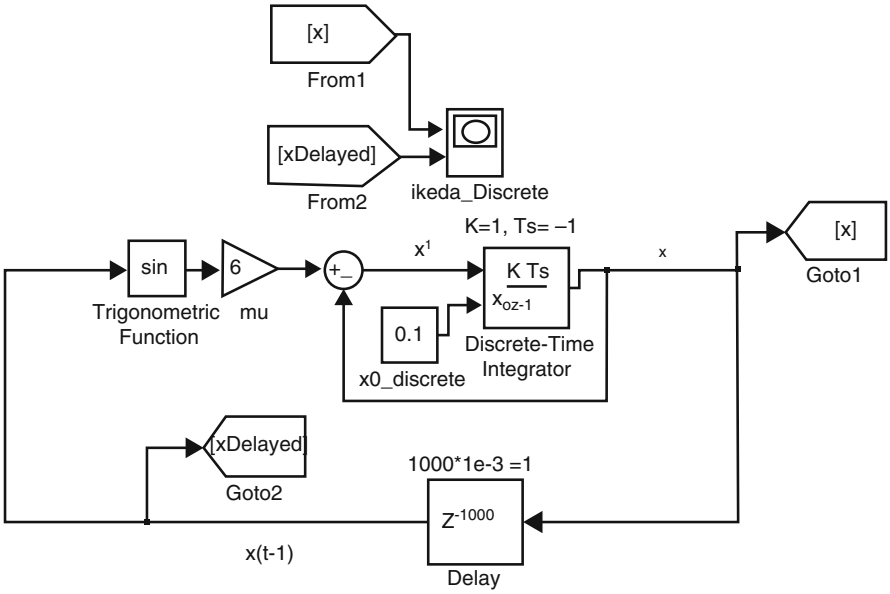

Fig. 9.3 Block diagram from Fig. 9.2, adopted to the Ikeda DDE. We have used Goto and From blocks (Simulink signal routing library) for clarity

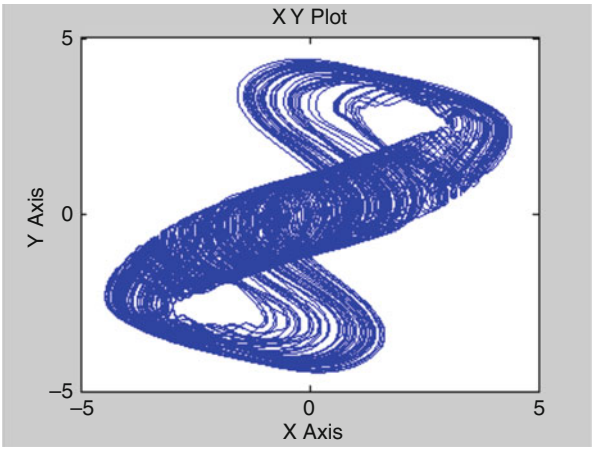

Fig. 9.4 Ikeda DDE phase plot, simulation time is 500 units. x-axis is $x(t)$, y-axis is $x(t-\tau)$

The large file size is because the reference design is fully synthesized for Quartus version 12.0. and the design also implements other DDEs (refer to Sect. 9.9).

Now that we have verified our discretization is functionally correct, the next step would be to implement the appropriate modules using DSP builder, the topic of Sect. 9.5.

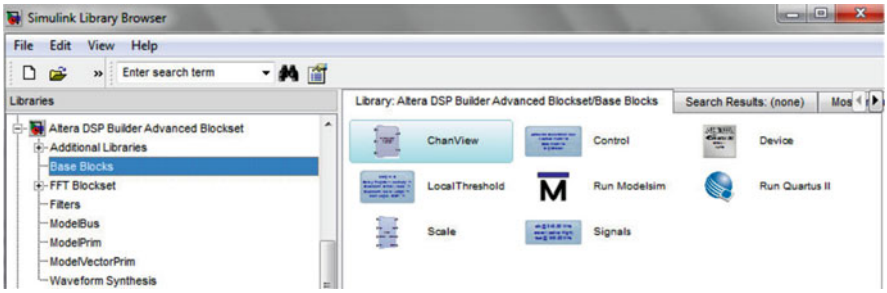

Fig. 9.5 The Base blocks library in the DSP builder advanced blockset

9.5 DSP Builder Advanced Blockset Subsystems

The concept behind DSP builder is to create a synthesizable subsystem that incorporates our mathematical abstraction. The detailed steps are:

1. We first access the **Altera DSP Builder Advanced Blockset**[4] library from Simulink, as shown in Fig. 9.5.
2. We create a new Simulink model and then place the **Control** and **Signals** block from the **Base Blocks** library in Fig. 9.5. Figures 9.6 and 9.7 show the configuration parameters for these blocks. These parameters should be satisfactory for practically all nonlinear ODEs.
3. We next set the solver configurations as shown in Fig. 9.8. The completed top level is shown in Fig. 9.9. We have created a subsystem at the top level. Within this subsystem, we will realize the nonlinear synthesizable subsystem.
4. Within the nonlinear subsystem, we place a **Device** block from the **Base Blocks** library and configure the **Device** block as shown in Fig. 9.10. Figure 9.11 shows the subsystem from the top level that incorporates the **Device** Block.
5. Inside the nonlinear synthesizable subsystem from Fig. 9.11, we specify our design mathematically. In order to do this, we will use blocks from the **ModelPrim** library, shown in Fig. 9.12.
6. There are two main blocks that should be part of any nonlinear synthesizable subsystem: the Convert block shown in Fig. 9.13 and the SynthesisInfo block shown in Fig. 9.14.
7. We finally enable port data types as shown in Fig. 9.15 as a visual debugging tool, in case of errors.

Once we **Run** our top level in Simulink, DSP builder should generate the appropriate hardware in the directory specified via the Control block (Fig. 9.6). Make sure the constant input(s) from the Source library at the top level have single as the output data type. The default is double and will generate 64-bit bus widths.

[4] Altera recommends the use of Advanced Blockset instead of Standard Blockset for newer designs.

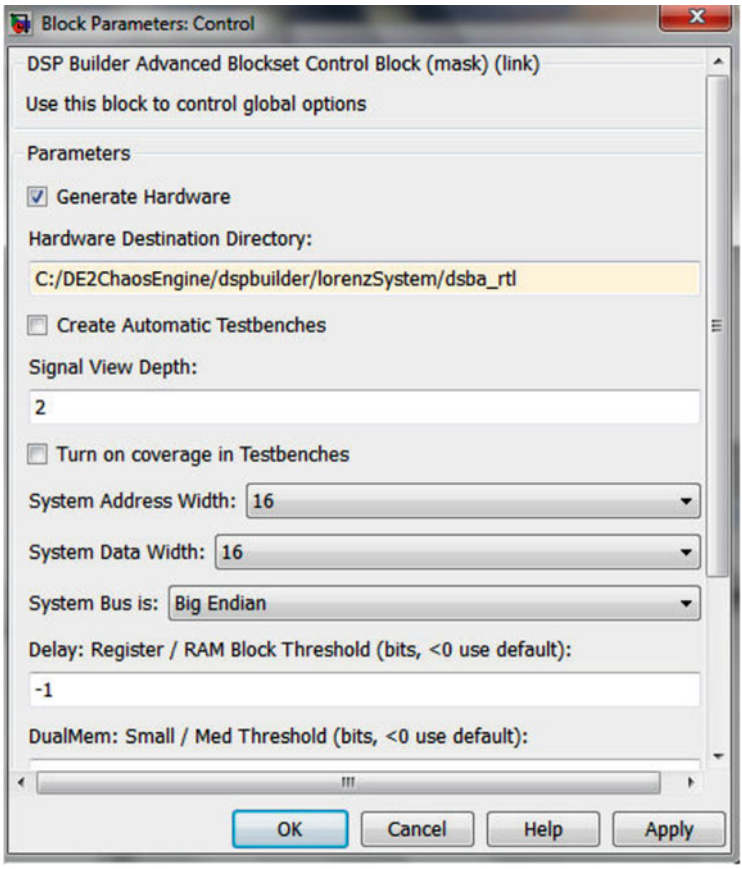

Fig. 9.6 In the control block, make sure generate hardware is checked and use an absolute path for the hardware destination directory. Turn off automatic test benches. Set both address and data width to 16-bits

We will next complete in Sect. 9.6 the shift register and the D flip-flop from Fig. 9.1.

9.6 Completing Euler's Method in VHDL

Listing 9.1 shows one approach to implement the shift register from Fig. 9.1 using parameterization (**generic** keyword in VHDL) and the **for** keyword. Also, Line 22 in Listing 9.1 declares the internal delay lines to be 32 bits wide. However, we need an array of these internal delay lines and hence we have declared it as "memory". Hence Listing 9.1 specifies a tapped delay line in VHDL.

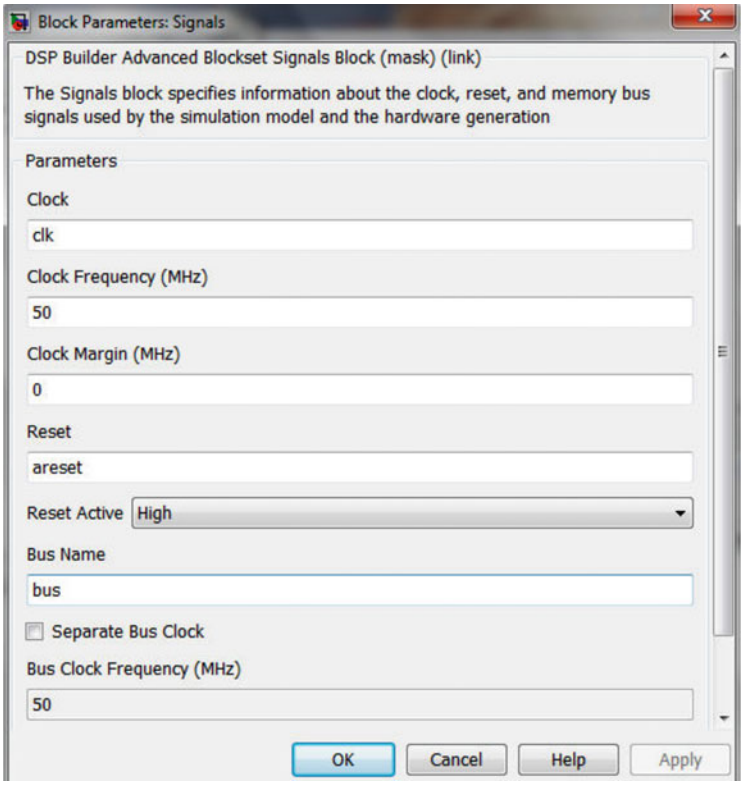

Fig. 9.7 In the signals block configuration, set the clock frequency to 50 MHz (the DE2 board clock). There is no need to use a separate bus clock. Make sure the reset is active high

Listing 9.1 Realization of VHDL delay

```
1  library ieee;
2  use ieee.std_logic_1164.all;
3  use ieee.numeric_std.all;
4
5  entity addressableShiftRegister is
6            generic (numberOfFlipFlops : integer := 0;
7                           delay : integer := 0);
8            port (
9            clk,areset : in std_logic;
10               In_x : in std_logic_vector(31 downto 0);
11           Out_xDelayed : out std_logic_vector(31 downto 0));
12 end addressableShiftRegister;
13
14 architecture behavioral of addressableShiftRegister is
15
16     component dFlipFlopWithAsyncReset is port (
17         clock,reset : in std_logic;
18         d : in std_logic_vector(31 downto 0);
19         q : out std_logic_vector(31 downto 0));
20     end component;
```

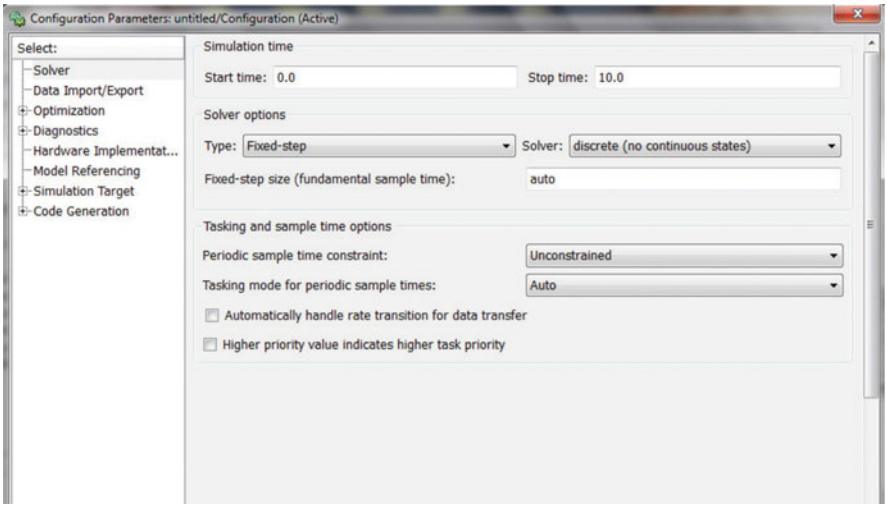

Fig. 9.8 The solver should be configured as fixed-step and with no discrete states

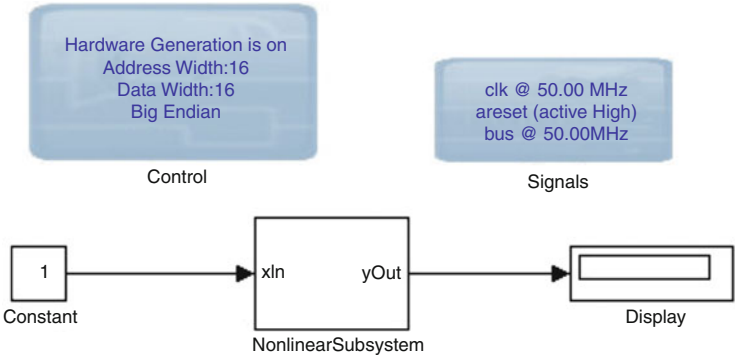

Fig. 9.9 The top level of our design. According to DSP Builder syntax, the synthesizable portion of our design must be specified as a subsystem within the top level

```
21
22      type memory is array(0 to numberOfFlipFlops) of std_logic_vector(31 downto 0);
23      signal internalDataArray : memory;
24
25  begin
26
27      internalDataArray(0) <= In_x;
28      generateFlipFlops:
29          for i IN 0 to numberOfFlipFlops-1 generate
30              nFlipFlops : dFlipFlopWithAsyncReset port map (
31                  clock => clk,
32                  reset => areset,
33                  d => internalDataArray(i),
34                  q => internalDataArray(i+1));
35          end generate;
```

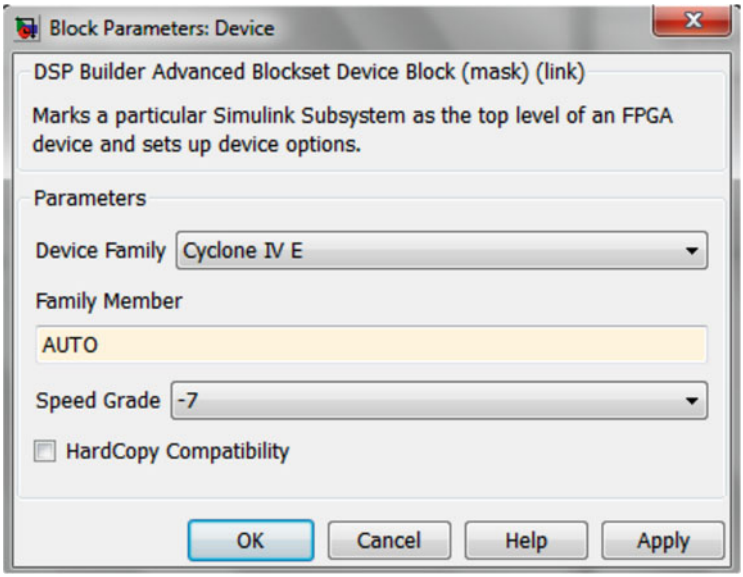

Fig. 9.10 Device block configuration. We don't have to explicitly set the Cyclone IV part number since we are only going to be synthesizing a subsystem, not a stand-alone FPGA project from DSP builder

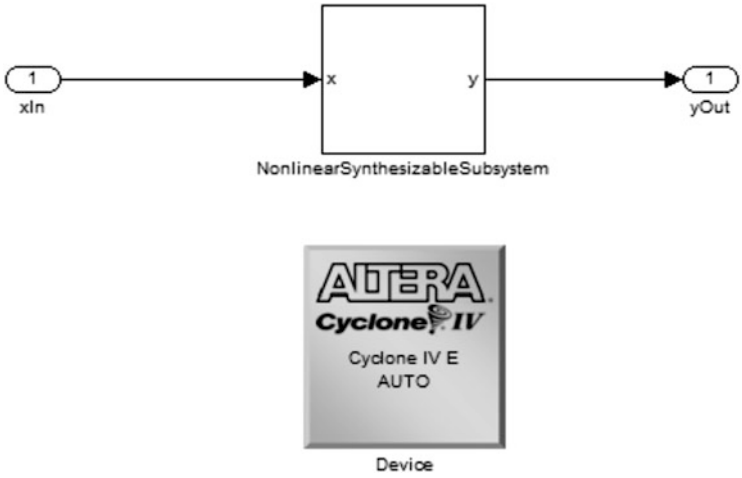

Fig. 9.11 The device block must be placed within a subsystem, not at the top level that has the control and signals blocks

```
36
37      Out_xDelayed <= internalDataArray(delay-1);
38  end behavioral;
```

Listing 9.2 is a simple D flip-flop in VHDL.

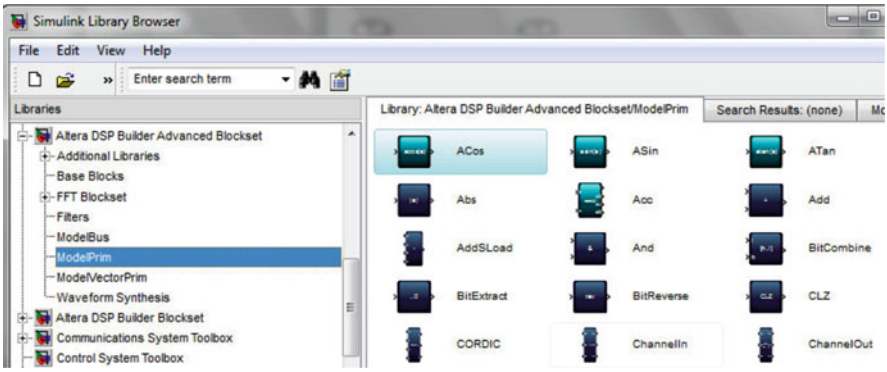

Fig. 9.12 The ModelPrim library from the DSP builder advanced blockset

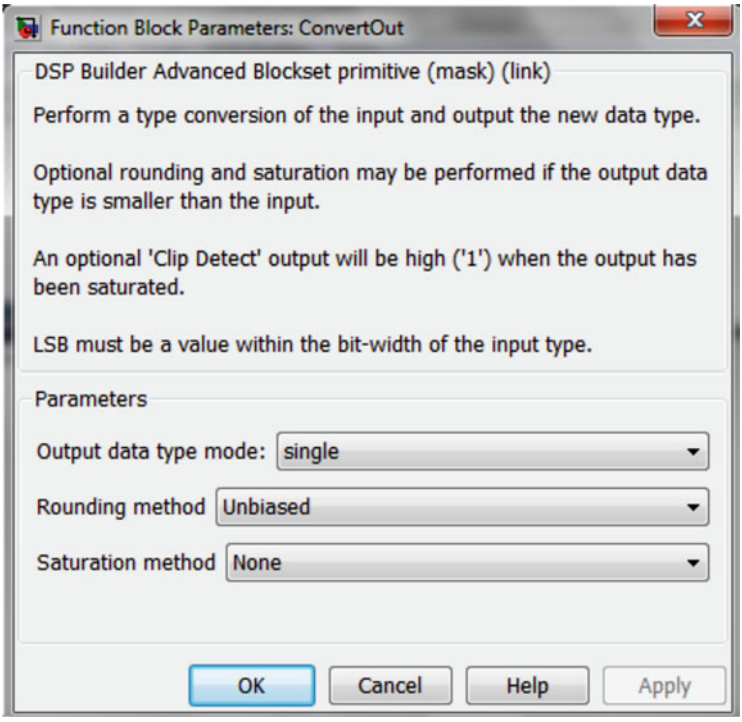

Fig. 9.13 This block is used to convert inputs and outputs to single precision (32-bit) floating point

Fig. 9.14 We need a SynthesisInfo block for controlling synthesis flow. By using the default option of scheduled, we let DSP builder use a pipelining and delay distribution algorithm that create fast hardware implementations from an easily described untimed block diagram

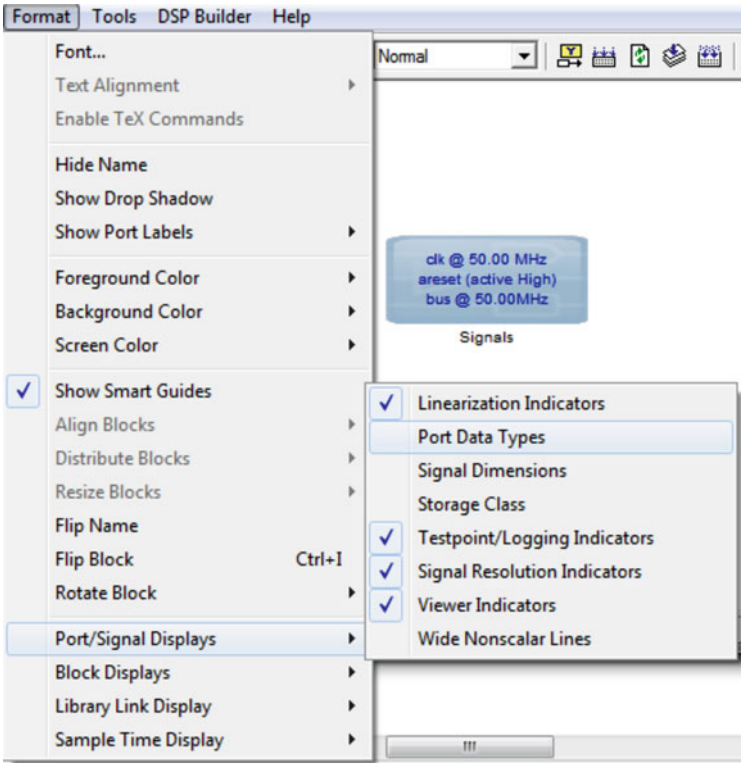

Fig. 9.15 Enable port data types helps us debug the design more easily. In our experience, the most common error is incorrect data types. In the case of incorrect data types, functionally speaking, we have domain and range errors

Listing 9.2 VHDL specification of D flip-flop with asynchronous reset

```
library ieee;
use ieee.std_logic_1164.all;

entity dFlipFlopWithAsyncReset is port (
    clock,reset : in std_logic;
    d : in std_logic_vector(31 downto 0);
    q : out std_logic_vector(31 downto 0));
end dFlipFlopWithAsyncReset;

architecture structuralDFlipFlop of dFlipFlopWithAsyncReset is

begin
    process (clock,reset)
    begin
        if reset = '1' then
            q <= X"00000000";
        else
            if rising_edge(clock) then
                q <= d;
            end if;
        end if;
    end process;

end structuralDFlipFlop;
```

Listing 9.3 shows the Ikeda DDE specification in VHDL that also incorporates the Altera DSP builder advanced block set as a subsystem.

Listing 9.3 VHDL specification of the Ikeda DDE

```
-- This subsystem includes synchronization
-- but we do not use it in this chapter.

library ieee;
use ieee.std_logic_1164.all;
use ieee.std_logic_signed.all;

entity ikedaDDESystem is port (
        resetn, clockIn : in std_logic;
        xFloatOut,xDelayedFloatOut : out std_logic_vector(31 downto 0);
        xOut,xDelayedOut : out std_logic_vector(15 downto 0);
        syncIn : in std_logic_vector(31 downto 0);
        syncClock : out std_logic);
end ikedaDDESystem;

architecture behavioral of ikedaDDESystem is

signal reset : std_logic;
-- constants
signal  dt : std_logic_vector(31 downto 0);
-- state variables
signal x,xDelayed,xNew,xFixed,xDelayedFixed : std_logic_vector(31 downto 0);
-- prescalar
signal count: integer range 0 to 64;
signal addressableShiftRegisterCount  : integer range 0 to 128;
signal addressableShiftRegisterClock : std_logic;
```

```
signal internalSyncClockCount  : integer range 0 to 2048;
signal internalSyncClock : std_logic;

-- DSP builder top level.   Add both the nonlinear subsystem and nonlinear
    -- synthesizable
-- subsystem VHDL files to project.
component ikedaDDE_NonlinearSubsystem is
    port (
        In_dt : in std_logic_vector(31 downto 0);
        In_sync : in std_logic_vector(31 downto 0);
                In_x : in std_logic_vector(31 downto 0);
                In_xDelayed : in std_logic_vector(31 downto 0);
                y : out std_logic_vector(31 downto 0);
                clk : in std_logic;
                areset : in std_logic;
             h_areset : in std_logic);
end component;
-- END DSP builder top level.

component addressableShiftRegister is
          generic (numberOfFlipFlops : integer := 0;
                          delay : integer := 0);
          port (
            clk,areset : in std_logic;
                In_x : in std_logic_vector(31 downto 0);
            Out_xDelayed : out std_logic_vector(31 downto 0));
end component;


-- latency : 6 clock cycles
component floatingPointToFixed IS
    PORT
    (
        aclr        : IN STD_LOGIC ;
        clock       : IN STD_LOGIC ;
        dataa   : IN STD_LOGIC_VECTOR (31 DOWNTO 0);
        result  : OUT STD_LOGIC_VECTOR (31 DOWNTO 0)
    );
END component;

begin
    reset <= not resetn;
    -- Euler's method
    -- We first synchronously update state variables at 781.250 KHz
        -- (64 counts of 50 MHz clock)
    -- Since dt = 1/1024, time scale is actually (781.250e3/1024) = 762 Hz
        -- (approximately)
    -- state memory
    process(clockIn, resetn)
    begin
            -- constants (place outside reset and clock to avoid latches)
              dt <= X"3A800000"; -- 1/1024
            if resetn = '0' then
            -- initial state
               x <=   X"3DCCCCCC";-- 0.1
               count <= 0;
               addressableShiftRegisterCount <= 0;
               addressableShiftRegisterClock <= '0';
            else
        if rising_edge(clockIn) then

            if count = 64 then
                count <= 0;
```

```
90              else
91                  count <= count + 1;
92              end if;
93
94              if count = 63 then
95                  x <= xNew;
96              end if;
97
98              if addressableShiftRegisterCount = 128 then
99                  addressableShiftRegisterCount <= 0;
100             else
101                 addressableShiftRegisterCount <= addressableShiftRegisterCount + 1;
102             end if;
103
104             if addressableShiftRegisterCount >= 63 then
105                 addressableShiftRegisterClock <= '1';
106             else
107                 addressableShiftRegisterClock <= '0';
108             end if;
109
110             -- for synchronizer period
111             if internalSyncClockCount = 2048 then
112                 internalSyncClockCount <= 0;
113             else
114                 internalSyncClockCount <= internalSyncClockCount + 1;
115                 end if;
116
117             if internalSyncClockCount >= 1023 then
118                 internalSyncClock <= '1';
119             else
120                 internalSyncClock <= '0';
121             end if;
122
123         end if;
124     end if;
125     end process;
126
127 -- this design also includes synchronization
128 -- since y(t+dt)=y(t)+(-alpha*y+mu*sin(y(t-tau))+k(t)(x(t)-y(t)))*dt,
129 -- we also send in the sync signal into the DSP builder nonlinear subsystem.
130 staticNonlinearities : ikedaDDE_NonlinearSubsystem port map (
131           In_dt => dt,
132   In_sync => syncIn,
133           In_x  => x,
134           In_xDelayed => xDelayed,
135           y => xNew,
136           clk => clockIn,
137           areset => reset,
138           h_areset => reset);
139
140
141 delay : addressableShiftRegister generic map (numberOfFlipFlops => 2048,delay => 1024)
142     port map (
143               In_x => x,
144               Out_xDelayed => xDelayed,
145               clk => addressableShiftRegisterClock,
146               areset => reset);
147 -- END Euler's method
148
149 --state outputs : convert scaled floating point variables to
150 -- 5.27 fixed point format DAC (no latency)
151 xOutFinal :  floatingPointToFixed port map (
152         aclr => reset,
```

```
153         clock => clockIn,
154         dataa => x,
155         result  => xFixed);
156     xDelayedOutFinal :  floatingPointToFixed port map (
157         aclr => reset,
158         clock => clockIn,
159         dataa => xDelayed,
160         result  => xDelayedFixed);
161
162         xOut <= xFixed(31 downto 16);
163         xDelayedOut <= xDelayedFixed(31 downto 16);
164
165         xFloatOut <= x;
166         xDelayedFloatOut <= xDelayed;
167
168         syncClock <= internalSyncClock;
169 end behavioral;
```

Once we complete the VHDL specification of our nonlinear ODE, we should include the VHDL audio codec interface and perform a functional simulation using an industry standard tool such as ModelSim. This is the topic of Sect. 9.7.

9.7 Functional Simulation

The idea of functional simulation is a natural followup to the Simulink discrete simulation from Sect. 9.4. Functional simulation simply answers the question: does the hardware perform as it is supposed to?

In the case of chaotic systems, a functional simulation will tell us if our design functionally reproduces chaotic behavior. Functional simulation can also tell us how the signals propagate within our hardware system. Hence a functional simulation tests the fundamental correctness of our digital circuit. We will use the industry standard ModelSim simulator for illustrating functional simulation.

First we need to design a VHDL file called as a "test bench" that mimics a physical lab bench. The test bench for the Ikeda DDE is shown in Listing 9.4.

Listing 9.4 VHDL test bench for the Ikeda DDE

```
1  -- testbench for ikeda system
2
3  library ieee;
4  use ieee.std_logic_1164.all;
5  use ieee.numeric_std.all;
6
7  entity ikedaSystemtb is
8  end ikedaSystemtb;
9
10 architecture testbench of ikedaSystemtb is
11     signal clock,reset,resetn,trigger,increment,pulseOut,
           syncClock : std_logic := '0';
```

```
12      signal xFloatOut,xDelayedFloatOut,syncIn : std_logic_vector
            (31 downto 0);
13      signal xOut,xDelayedOut : std_logic_vector(15 downto 0);
14
15      component ikedaDDESystem is port (
16          resetn, clockIn : in std_logic;
17          xFloatOut,xDelayedFloatOut : out std_logic_vector(31
                downto 0);
18          xOut,xDelayedOut : out std_logic_vector(15 downto 0);
19          syncIn : in std_logic_vector(31 downto 0);
20          syncClock : out std_logic);
21      end component;
22
23  begin
24      ikedaDDESystemInstance :  ikedaDDESystem port map (
25          resetn => resetn,
26          clockIn => clock,
27          xFloatOut => xFloatOut,
28          xDelayedFloatOut => xDelayedFloatOut,
29          xOut => xOut,
30          xDelayedOut => xDelayedOut,
31          syncIn => syncIn,
32          syncClock => syncClock);
33
34      clock50MHzProcess : process
35      begin
36          clock <= not clock;
37          wait for 10 ns;
38      end process clock50MHzProcess;
39
40      stimulus : process
41      begin
42          resetn <= '0';
43          syncIn <= X"00000000"; -- no synchronization
44          wait for 55 ns;
45          resetn <= '1';  -- unreset after 55 ns
46          wait; -- prevent process from being executed again
47      end process stimulus;
48  end testbench;
```

The salient features of the test bench are:

1. The entity statement has no input and/or output ports. This makes sense since the test bench is a virtual environment that cannot be synthesized.
2. We have to generate a board (50 MHz) clock. This is done using the process statement shown.
3. We then provide stimulus inputs to our module under test. Notice that since VHDL processes execute concurrently, our stimulus process has a wait as the last statement to prevent repeated process execution.

ModelSim commands can also be scripted and placed in a .do file, shown in Listing 9.5.

Listing 9.5 ModelSim script file for Ikeda DDE

```
# do vlib work only once!
# vlib work

vmap work work

# compile DSP builder advanced blockset source
vcom D:/altera/12.0/quartus/dspba/Libraries/vhdl/fpc/math_package.vhd
vcom D:/altera/12.0/quartus/dspba/Libraries/vhdl/fpc/math_implementation.vhd
vcom D:/altera/12.0/quartus/dspba/Libraries/vhdl/fpc/hcc_package.vhd
vcom D:/altera/12.0/quartus/dspba/Libraries/vhdl/fpc/hcc_implementation.vhd
vcom D:/altera/12.0/quartus/dspba/Libraries/vhdl/fpc/fpc_library_package.vhd
vcom D:/altera/12.0/quartus/dspba/Libraries/vhdl/fpc/fpc_library.vhd

# compile DSP builder advanced blockset nonlinearities
vcom ../../dspBuilder/ikedaDDE/dspba_rtl/ikedaDDE/NonlinearSubsystem/ikedaDDE_NonlinearSubsystem.vhd
vcom ../../dspBuilder/ikedaDDE/dspba_rtl/ikedaDDE/NonlinearSubsystem/NonlinearSynthesizableSubsystem/ikedaDDE_NonlinearSubsystem_NonlinearSynthesizableSubsystem.vhd

# compile source
vcom ../../floatingPointMultiplyDedicated.vhd
vcom ../../floatingPointToFixed.vhd
vcom ../../ikedaDDESystem.vhd
vcom ../../addressableShiftRegister.vhd
vcom ../../dFlipFlopWithAsyncReset.vhd

vcom ikedaSystemtb.vhd

vsim ikedaSystemtb
# configure wave window to have a white background color
configure wave -background white -foreground red -textcolor blue -timecolor blue -vectorcolor red -wavebackground white -cursorcolor black
add wave -divider "Clock and Reset"
add wave clock
add wave -label delayClock sim:/ikedasystemtb/ikedaDDESystemInstance/addressableShiftRegisterClock
add wave resetn


add wave -divider "Outputs from the ikeda DDE model"
# obtained switch information below by using analog (automatic) formatting in ModelSim
add wave -format analog-step -min -1662 -max 2030 -height 74 xOut
```

```
39 add wave -format analog-step -min -1662 -max 2030 -height 74
       xDelayedOut
40
41 #add wave -divider "ikeda DDE System Module Internal Signals"
42 add wave -label dt -hex sim:/ikedaSystemtb/ikedaDDESystemInstance
       /dt
43 add wave -label count -hex sim:/ikedaSystemtb/
       ikedaDDESystemInstance/count
44 add wave -label addressableShiftRegisterCount sim:/ikedasystemtb/
       ikedaDDESystemInstance/addressableShiftRegisterCount
45 add wave -label xPlus_f1 -hex sim:/ikedaSystemtb/
       ikedaDDESystemInstance/xNew
46
47 add wave -label x -hex sim:/ikedaSystemtb/ikedaDDESystemInstance/
       x
48 add wave -label xDelayed -hex sim:/ikedaSystemtb/
       ikedaDDESystemInstance/xDelayed
49
50 add wave -label xFixed -hex sim:/ikedaSystemtb/
       ikedaDDESystemInstance/xFixed
51 add wave -label yFixed -hex sim:/ikedaSystemtb/
       ikedaDDESystemInstance/xDelayedFixed
52
53 # run 10ms
```

Functional simulation results from the script file in Listing 9.5 is shown in Fig. 9.16. Note the waveforms do seem to exhibit chaotic behaviour. We can now move on to implementation results in Sect. 9.8.

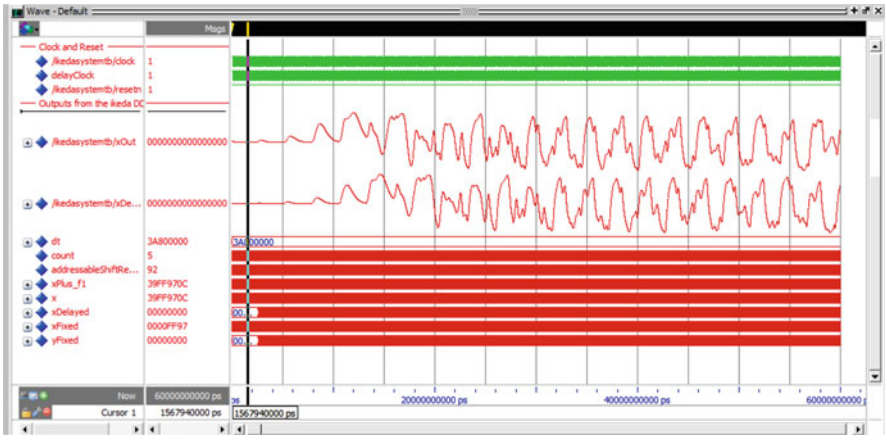

Fig. 9.16 ModelSim wave window results. The simulation has been run for 60 ms and then analog waveforms have been autoscaled after simulation completion

Fig. 9.17 $x(t-\tau)$ vs. $x(t)$ for the Ikeda DDE in Eq. (9.11). Oscilloscope scales are 0.5 V/div for both axis

9.8 Implementation Results

The result of implementing the Ikeda DDE on the DE2-115 and using the audio codec output is shown in Fig. 9.17.

9.9 Conclusion

In this chapter, we showed a glimpse of the robustness of FPGAs in realizing nonlinear (chaotic) differential equations. Understand that utilizing FPGAs for this task involves a lot of engineering—both in hardware and software. However, the results are exceptional. Hence as a concluding note, we show various chaotic ODEs and DDEs in Fig. 9.18 that have been realized on FPGAs [2], to serve as motivation for the reader to pursue this exciting topic further.

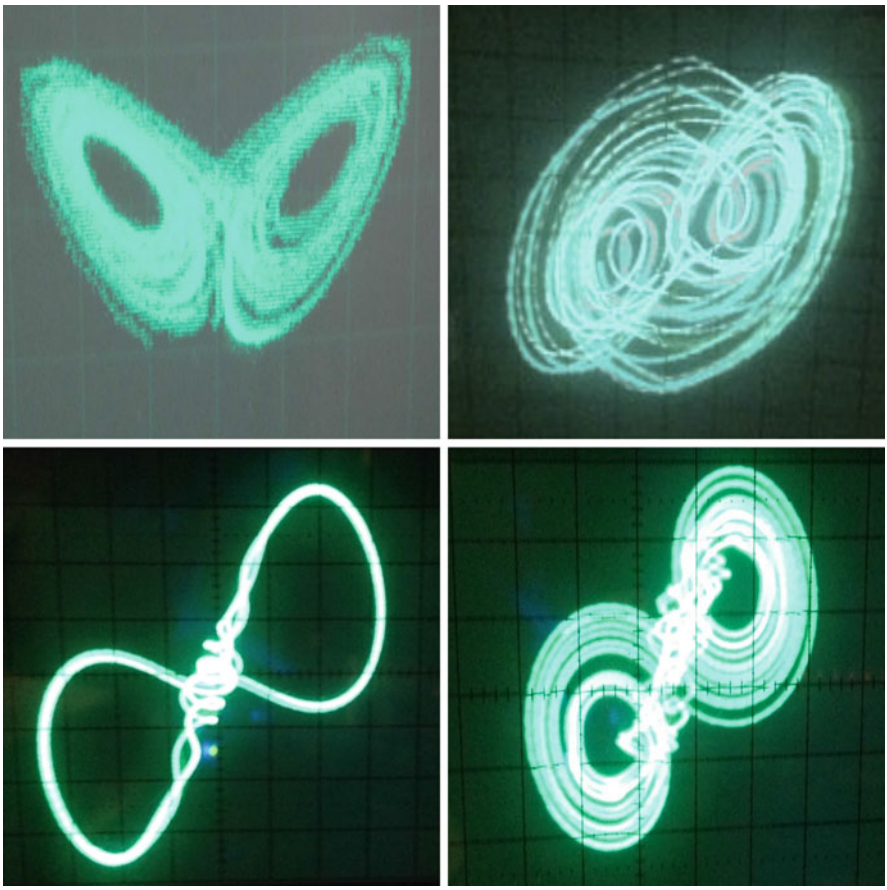

Fig. 9.18 Various chaotic attractors obtained from the DE2-115 board (clockwise from top-left): the classic Lorenz butterfly [1], the highly complex attractor system [3] with a hyperbolic tangent nonlinearity, time-delay system with sigmoid nonlinearity [5] and time-delay system with signum nonlinearity [5]

References

1. Lorenz, E.N.: Deterministic nonperiodic flow. J. Atmos. Sci. **20**, 130–141 (1963)
2. Muthuswamy, B., Banerjee, S.: A Route to Chaos Using FPGAs - Volumes I and II. Springer, Berlin (2015/2016)
3. San-Um, W., Srisuchinwong, B.: Highly complex chaotic system with piecewise linear nonlinearity and compound structures. J. Comput. **7**(4), 1041–1047 (2012)
4. Sprott, J.C.: Chaos and Time Series Analysis. Oxford University Press, Oxford (2003)
5. Sprott, J.C.: Elegant Chaos. World Scientific, Singapore (2010)